PROCEEDINGS

OF THE SECOND

INTERNATIONAL SYMPOSIUM

ON

MAGNETIC BEARINGS

SEIKEN SYMPOSIUM

JULY 12-14, 1990
TOKYO, JAPAN

Edited by Prof. T. Higuchi

Sponsored by Institute of Industrial Science, University of Tokyo

Additional copies of this proceedings are available by
MB Symposium c/o Prof. Higuchi Toshiro
Institute of Industrial Science, University of Tokyo
7-22-1, Roppongi, Minato-ku, Tokyo 106, Japan
Tel.: +81-3-402-6231
Fax.: +81-3-470-9641

Printed in Japan by NISSEI Eblo

PREFACE

This international symposium on magnetic bearings is the second one succeeding to the first one which was organized by professor G. Schweitzer and held at ETH Zurich in 1988. Expecting the rapid progress of magnetic bearing technology and responding to the enthusiasm for continuation, it was decided during the first symposium that the symposium should be held every two years. Following this symposium, the third one will be hosted by the University of Virginia in U.S.A. in 1992. And the fourth is planned to be held in Europe.

The purpose of the symposium is to provide opportunities to exchange new ideas in research and to present the latest experiences in applications about magnetic bearings. Since most of submitted papers are interesting and of great value, we made efforts to list as many papers as possible to the limit of three day sessions. The proceedings contains 53 papers from 12 countries. Topics and interests of these papers extend from theoretical analysis, design, components, vibration control to applications in space, turbo machinery, compressors, vacuum pumps, and machine tools. As to the control of magnetic bearings, digital control is discussed in many papers and applications of recent control theories are reported. Reflecting rapid expansion of areas of application areas, a remarkable number of papers are related to industrial applications in various fields with practical experiences.

I hope that this symposium will serve to broaden and deepen the technical and scientific communications between the participants.

I would like to thank all the people including authors and committee members who have worked to organize, prepare and operate the symposium.
And I would especially wish to thank Nippon Seiko K. K. for offering its convention hall.

This symposium was financially supported by the Foundation for Promotion of Industrial Science. This help is gratefully acknowledged.

Toshiro Higuchi
University of Tokyo

ADVISORY COMMITTEE

P.E. Allaire	University of Virginia, Charlottesville, USA
H. Habermann	Société de Mécanique Magnétique, Vernon, France
T. Higuchi	University of Tokyo, Tokyo, Japan,(chairman)
R. Holmes	University of Southampton, Southampton, UK
F. Matsumura	Kanazawa University, Kanazawa, Japan
G. Schweitzer	ETH Zürich, Zürich, Switzerland

ORGANIZING COMMITTEE

T. Higuchi	University of Tokyo, Tokyo, Japan,(chairman)
K. Ikeda	University of Tokyo, Tokyo, Japan
N. Isogai	Japan Magnetic Bearings Co.,Ltd., Tokyo, Japan
K. Kakuta	Nippon Seiko K.K., Tokyo, Japan
T. Mizuno	Saitama University, Urawa, Japan
K. Oka	University of Tokyo, Tokyo, Japan
M. Ota	Seiko Seiki Co.,Ltd., Narashino, Japan

TABLE OF CONTENTS

2nd International Symposium on Magnetic Beaing
July 12-14, 1990, Tokyo, Japan

A LOW NOISE MAGNETIC BEARING WHEEL FOR SPACE APPLICATION

U. J. BICHLER

Teldix GmbH, Bosch Telecom, Grenzhöfer Weg 36, 6900 Heidelberg, Germany

Abstract

Magnetic bearing momentum wheels can be used as gyroscopic actuators in the attitude control system of spacecraft. If the wheel provides a vernier gimballing capability, three axis attitude control is possible with one wheel only.

A point of increasing interest is the bearing noise which is induced into the spacecrafts environment by the wheel. So called 'micro–gravity' space borne experiments and payloads can only stand very low levels of vibration. The possible noise sources are static and dynamic unbalance movements and the mechanical imperfections of the rotating parts.

One advantage of magnetic bearings is, that it is possible to suppress vibrations in the actively controlled degrees of freedom. Vibration suppression in this context means an isolation of the stator from the rotor in the frequency range of the disturbances rather than the suppression of unbalance movement of the rotor. That means, the rotor can rotate about its axis of inertia, while the sensor surface whirls or wobbles, and the controller will not 'see' this movement and will not make force of it. This has to be done without affecting the bearing stability.

In this paper, different possibilities of active vibration suppression are discussed and compared in simulations. For the best one, practical results are shown as well.

1 Introduction

Almost all spacecraft in orbit are equipped with ball bearing momentum or reaction wheels serving as actuators in the attitude control system. Amongst the various on board system components the wheels have been identified as one of the main sources of vibration noise due to residual unbalances, bearing imperfections, etc. This disadvantage can be avoided by the use of magnetic bearing wheels having all the well known special advantages as higher speed, no contact and lubrication, no stiction etc.. but permitting the acceptance of the increased electronics complexity with the inevitable impacts on mass, volume and reliability [1].

In magnetic bearings – as far as no permanent magnets are involved for direct attraction/repulsion – the bearing forces between the statoric and the rotoric part are fully controllable. They can be designed frequency dependant and with a time varying characteristic for example. Unbalance forces are transmitted to the stator only at an amount proportional to the suspension current. Applying a special control law, the disturbance component in the suspension current can be attenuated while keeping an overall stable levitation of the rotor. This in fact isolates the unbalance forces from the stator and the satellite structure.

A second interesting feature is, that if a vernier gimballing capability is implemented, the use of such a magnetic bearing momentum wheel enables an active satellite nutation damping and a three axis attitude control for small roll and yaw angles with one rotating mass only, that is, a fine pointing system with an accuracy depending only on the performance of the attitude sensors. This may result in overall mass savings and performance enhancements.

Magnetic bearing wheels should be on the first glance ideally suited to exhibit very low noise figures, because they have no mechanical contact between statoric and rotoric parts. But unfortunately there are several possible sources of disturbing forces and torques in magnetic bearing wheels as well. Some of these sources are due to unfavourable design details and should be foreseen and avoided in time. Some others are of principle nature but can be overcome by control means. These sources will be introduced first and then possibilities on how to suppress the disturbances are given.

2. Disturbances in Magnetic Suspension Systems

Unwanted disturbing forces and torques in magnetic bearings can have the following sources:

1. The main source is imbalance, which means that the rotational axis is shifted (resulting in static imbalance) or/and tilted (resulting in dynamic imbalance) against the natural axis of inertia. In a magnetic bearing this rotational axis is the axis of the position sensors measurement surface. Thus if the rotor spins about its natural axis, the measurement surface wobbles. In the subcritical speed range this leads to forces and torques which (try to) keep the rotor rotating about this axis. In the supercritical speed range, the rotor rotates about its natural axis, but the wobbling sensor signal component also causes forces and torques.

2. Mechanical imperfections of the rotating parts as irregularities in a sensor surface, a pole piece or a permanent magnetic field.
3. Poorly damped bearing control loops, for example due to a passive nature, nonlinearities, structural modes or coupling effects between the different loops.
4. Poorly damped gyroscopic oscillations as nutational and precessional motions, which means a whirling motion of the spin axis around the angular momentum vector, in connection with a type of bearing, that transforms motion into force.
5. Sensor types and locations, which do not reject harmonics produced by mechanical imperfections of the rotating measurement surface.

3. Principle of Active Vibration Suppression

In this paper, Active Vibration Suppression (AVS) means to enable the rotor rotating about its natural axis of inertia and to suppress all the resulting noise components from the whirling and wobbling sensor surface without affecting the suspension stability. It does not mean a suppression of the vibrational movement of the rotor surface to achieve a rotation about the geometrical axis [3,5] because then the full imbalance forces and torques would be present at the stator, just like in a ball bearing.

A simple suspension loop model is used to introduce and to discuss qualitatively the different proposed kinds of AVS. It is shown in Fig. 1. It consists of a controller, a power amplifier including the force actuator and the rotor as the plant.

The loop is depicted in a possibly unusual way with the disturbances due to unbalance movement of the measurement surface and other noise as input and the force as output.

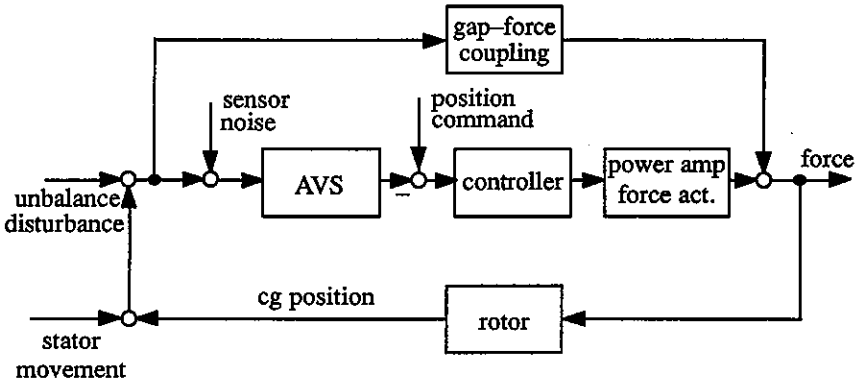

Fig. 1 Simple suspension loop model

AVS means, that the sensor disturbances must be filtered out before reaching the power amplifier and becoming force or torque. Thus a block 'AVS' is introduced in the loop between sensor and controller which must be designed to filter the disturbances out of the measurement signal while keeping the useful information for the suspension loop.

If there is a gap–force coupling in the bearing, the synchronous forces are produced in the bearing before it is possible to filter them out. This is true for all electromagnetic force generation principles, where a change of the gap causes a change of the (bias or permanent) flux and thus of the force. Then these forces must be identified and cancelled by inverse AVS force components. This seems to be more complicated as just to filter, so it is better to have no gap–force coupling. Thus the better choice for a low noise wheel is the electrodynamic principle, where the generated force is independent of the relative position or the relative motion of rotor and stator.

The sensor noise in a magnetic bearing consists of a synchronous component, i.e. of a frequency equal to the rotational speed, and harmonics thereof. Thus an AVS must be either selective and speed adaptive or it must cover the whole frequency range of the disturbances. In the following, several methods of active vibration suppression are discussed, some of them speed tracking, others covering a broad frequency range.

3.1 Tracking Notch Filter (TNF)

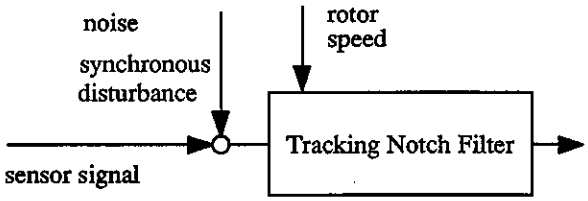

Fig. 3–1 AVS with Tracking Notch Filter

This AVS method [6,4] uses a notch filter, the notch frequency of which is tracking the synchronous speed of the rotor (see Fig. 3–1). Thus, depending on the steepness of the notch, all synchronous noise is removed from the feedback signal more or less.

The disadvantages are that instability occurs in the speed range below the cross–over frequency of the suspension, which must be circumvented by switching the AVS off in the critical speed range. Furthermore, harmonics are not rejected.

3.2 Lead – High order lag (LHL)

The conventional lead lag approach, i.e. a lead in the controller and the parasitic lags in the loop, does not reject sensor noise before becoming bearing force, it even amplifies it, because the highest gain of the loop part between sensor noise input and power amplifier output is at high frequencies, until measurement and parasitic lags are reached.

A possibility to suppress the high frequency noise is to insert a low pass filter between sensor and controller to get a gain decay in the high frequency area of interest (see Fig. 3–2). The higher the order of the filter, the better is the attenuation of the noise.

The advantage of this principle is, that it attenuates all noise beyond the cut off frequency, synchronous noise, harmonics and other. Further it is very simple.

The disadvantage is, that it does not work as long as the speed is below the cut off frequency of the filter.

The impact on the system performance is, that the suspension controller must be adjusted to operate at a very low frequency resulting in a low bandwidth control loop. Thus it will not work in the tilt d.o.f.'s of the wheel, it is applicable only in the translational axes.

With a LHL, the command response becomes very slow and the stiffness very low, but that means no disadvantage in a vibration sensitive environment as long as no external forced displacements exceeding the gap of the bearing are present.

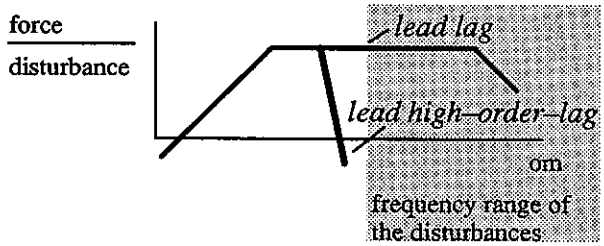

Fig. 3–2 Principal Bode Plot

3.3 Bucket Brigade Device (BBD)

The central component of this approach is a BBD with a positive feedback.

It is fed with the high–pass filtered sensor signal and clocked with a signal taken from the rotor position. The number of clock periods per revolution is equal to the number of states of the BBD.

The idea is depicted in Fig. 3–3. The sensor signal is high-pass filtered and attenuated by a small factor a, say a = 0,1. Then it is fed to the BBD, which is equipped with a feedback with the gain (1 – a) = 0.9. Thus during steady state operation after a few revolutions of the rotor, only the synchronous component and the associated harmonics of the sensor signal are circulating in the BBD loop, because all other frequencies do not match the length of the BBD.

The output is then subtracted from the sensor signal which cancels the unwanted disturbances some revolutions later.

This results in a tracking notch filter for the synchronous disturbance, and, this is the main advantage, for all harmonics. The BBD can be implemented in analogous or digital hardware. From the systems stability point of view, the BBD has the same influence as a simple tracking notch filter, that means it destabilizes the system beyond a certain frequency.

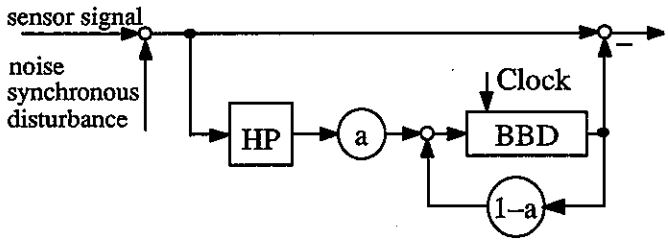

Fig. 3–3 AVS with Bucket Brigade Device

3.4 Synchronous Sampling Control (SSC)

The central idea is that, if the rotor position is sampled only once per revolution, neither synchronous signal components nor their harmonics will be detected. This results in a sampling control system with a speed varying sampling rate.

The implementation of the sampling is very easy, a sample–hold element must be triggered by a mark on the rotor.

The impacts are that the varying sampling rate necessitates adaptive control, and it will not work proper at low speed. Thus the sample–hold element must be switched to permanently transparent below a certain frequency.

If problems arise with unsynchronous frequencies higher then half the sampling rate, they can be overcome by means of a anti–aliasing filter.

The complexity of the whole implementation depends on the application, i.e. whether a wide speed range must be covered necessitating scheduled controller parameter and a tracking anti–aliasing filter or if it is sufficient to have constant parameter set for a certain speed–range.

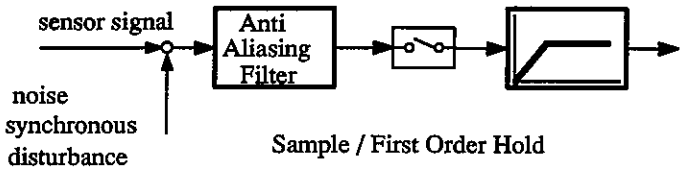

Fig. 3–4 AVS by sampling control

3.5 Model Following Control (MFC)

This is a possibility, which differs from the others because it is not only some kind of filter between the sensor and the controller.

The principle idea of the model following control is to use the output of an observer, simply a double integrator, for the control feedback. The observer output is well suited for low noise purposes, because it does not contain any disturbances. Fig. 3–5 shows the block diagram of the control loop with observer, which is fed with the current command signal. Since there is a linear relationship between current and force in an electrodynamic system, the observers output will be very close to the real position of the rotor.

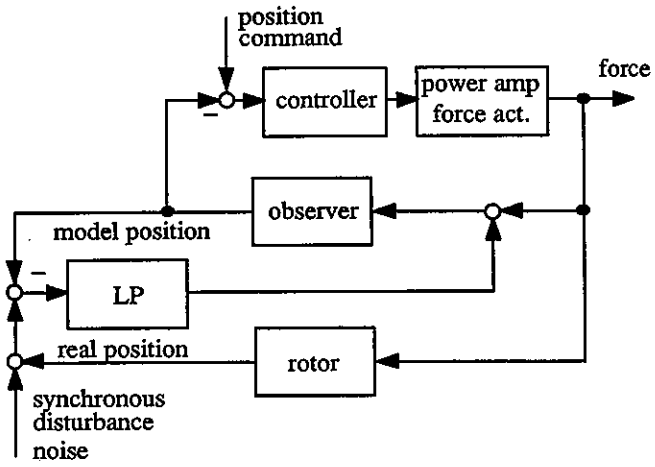

Fig. 3–5 Suspension loop with observer

To prevent the observer from long term drift effects, the low pass filtered difference between the real position signal and the model is used to correct the observers state variables. Thus from the real sensor signal only the lowest (near dc) frequency components are used and the remaining noise in the suspension loop is very small.

4. Comparison of the AVS strategies

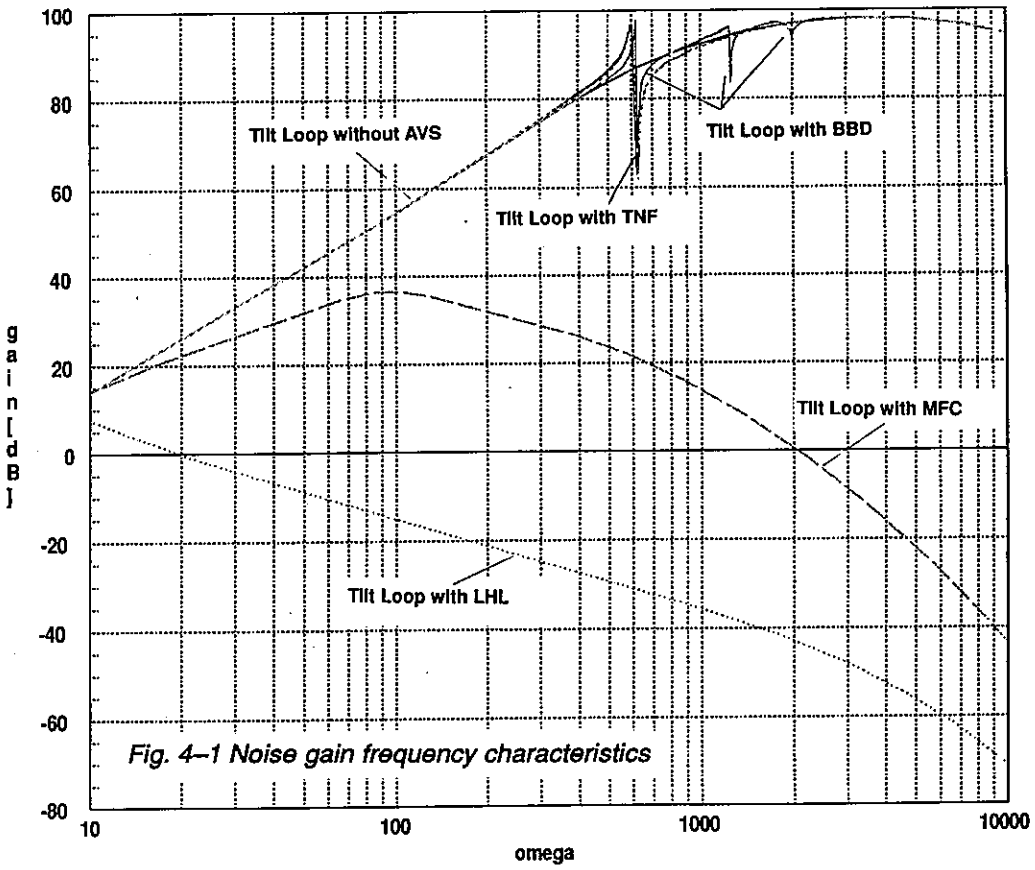

Fig. 4–1 Noise gain frequency characteristics

The different AVS methods have been investigated by linear analysis and time domain simulations of a single suspension loop as representative of the three translational d.o.f.'s and also of the coupled tilt loops.
Fig. 4–1 shows the gain characteristics from the sensor disturbance inputs to the force output. The best results can be achieved with LHL and MFC. TNF and BBD (both calculated for a speed of 6000 rpm) are difficult to distinguish, BBD has just some more notches at the harmonics.
The results in terms of noise suppression figures of the synchronous disturbance and the first harmonic at a speed of 6000 rpm are summarized in the following table together with the most important features, advantages and drawbacks of the different methods.
Some of the investigated methods turned out to be unstable in the coupled tilt loops nearly over the whole speed range, these are LHL and SSC. BBD has been found to be of insufficient performance, because it was not possible to generate all the disturbance cancelling signal components with the correct phase.TNF was discarded because it makes the loops partly unstable and rejects no harmonics.
Finally MFC has been chosen as the superior AVS principle, because it offers very good suppression results and it keeps the active stiffness, i.e. the wheel is usable as tilt actuator in the attitude control loop of spacecraft.
The obtained suppression values are considered as theoretical values, which will presumably not be reached in the real implementation, but can be taken as indicator, that an improvement of about 40 dB at least should be achievable practically.

Noise Suppression in dB compared to the loops withot AVS

AVS Method	Single Loop		Coupled Tilt Loop		Remarks
	Synchronous	1. Harmonic	Synchronous	1. Harmonic	
TNF	25	0	25	0	– single loop unstable from 0 to 4500 rpm – coupled tilt loop unstable from 0 to 2500 rpm – no harmonics rejection! – notch mismatching removes whole suppression effect – poor dynamic behaviour + loop stiffness for external forces not affected + command response not affected
LHL	72	101	unstable in the usable speed range	unstable in the usable speed range	– coupled tilt loops unstable at speeds above 40 rpm! – loop stiffness for external forces extreme low – command response extreme slow + harmonics rejection
BBD	13	8	not further investigated because of insufficient performance	not further investigated because of insufficient performance	– single loop partly unstable – unacceptable performance + harmonics rejection
SSC	? theoretically infinite	? theoretically infinite	unstable in the usable speed range	unstable in the usable speed range	– single loops partly unstable – coupled tilt loops completely unstable + harmonics rejection
MFC	65	108	65	76	– loop stiffness for external forces extreme low (but this can be easily overcome) + command response not affected + harmonics rejection

Fig. 4–2 Summary of the AVS results and characteristics

5. Implementation of the MFC

The MFC is currently being implemented in the Teldix 5 d.o.f. [2], which is short described in the annex.
Two problems remain with this principle. Firstly there is the poor passive stiffness, i.e. the stiffness against externally impressed stator movements. If the satellite fires a thruster for example, the stator moves towards the rotor within fractions of a second and the suspension control cannot react fast enough. This problem can be solved with a second, faster feedback for the observer. This is depicted in Fig. 5–1. The difference of the real position and the observer position is fed through a low pass filter to achieve the long term compensation of drift effects. To control the faster externally impressed stator movements, this difference is additionally fed to a limit switch, which for example detects if the difference exceeds half of the gap. If so, it uses a second, stronger feedback to force the observer position immediately to the real position and, with this, the suspension loop can react and prevent a touch down of the rotor. During the activity of the limit switch, the low noise quality is of course reduced.

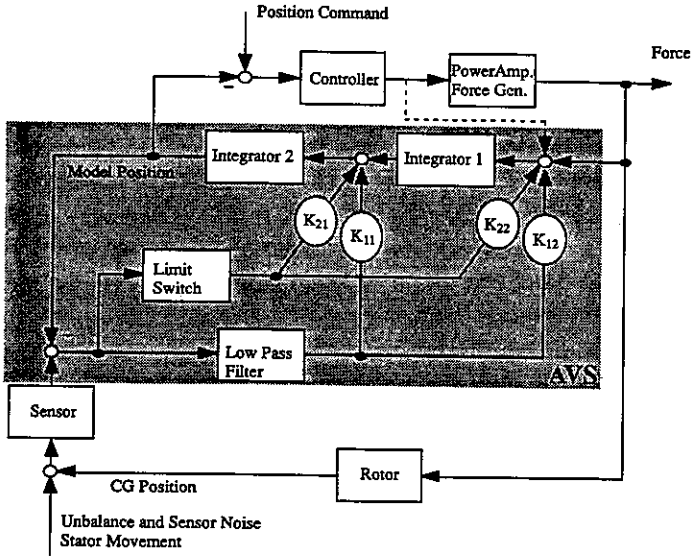

Fig. 5–1 MFC with touch down protection

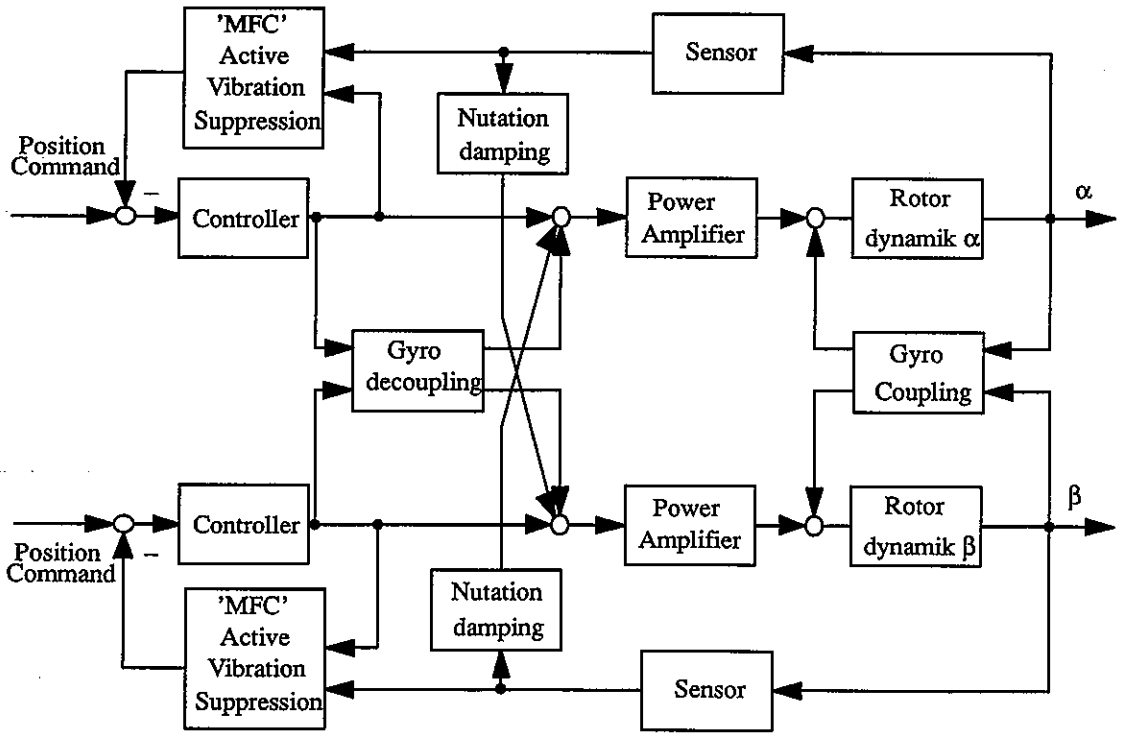

Fig. 5–2 MFC in the tilt loops

The second problem is, that this method is not directly applicable in the gyro–coupled tilt loops, because then the model would not represent the real plant. The gyro–couplings must be either introduced into the observer too, or a decoupling network [2] must be used to distribute the controller outputs over both torque inputs. The second possibility is preferred, because it additionally improves the dynamic behaviour of the tilt loops. Then each controller sees the same plant as if the wheel would stand still and the observer remains the same as before. The overall tilt control system with MFC is shown in the block diagram Fig. 5–2. Additionally a nutational damping cross coupling is foreseen, because the damping of the nutational mode can become poor due to the vibration suppression.

Some results achieved with the MFC in the tilt axes of the real wheel are shown in the next figures. Fig. 5–3 compares the torque that is induced into the wheels mounting base, for example the satellite, at a speed of 2000 rpm. It can be seen, that the suppression works fairly well at this speed already. Considering that the wheel will operate nominally at 6000 rpm and that the unbalance disturbances without AVS would increase quadratic while in the AVS case the disturbance rejection increases with frequency, very good suppression results can be expected at 6000 rpm.

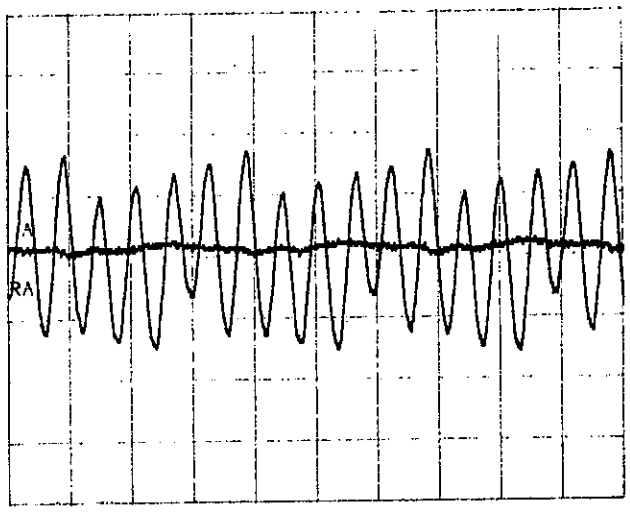

Fig. 5–3 Tilt torque with and without MFC at 2000 rpm

Fig. 5–4 gives some insight in the dynamic behaviour of the system by depicting the responses of the wheel and the observer on a small step applied at the tilt angle reference input. The difference in the superimposed noise is evident and it is obvious that the observer output causes much less disturbance torque in the loop than the real position signal. Furthermore it is demonstrated that the responses are globally of the same time behaviour and thus the vibration suppression does not affect the active stiffness.

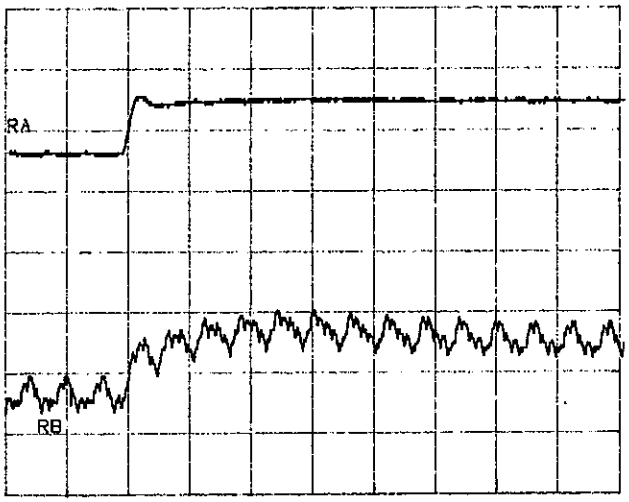

Fig. 5–4 Small signal step response of the tilt loop with MFC at 2000 rpm ; RA: observer , RB: sensor.

6 Summary

The vibration problem in magnetic bearings has been described and the possible sources have been identified. Several strategies of Active Vibration Suppression, different in terms of expenditure and performance, have been discussed.

A comparison between these AVS candidates resulted in the MFC as the superior active vibration suppression system. It provides very good noise suppression results, works in all axes of the magnetic bearing and keeps the active stiffness, which is required if the wheel is used in the attitude control system of a satellite.

First results of the implementation of the MFC in the Teldix electrodynamic bearing wheel have been shown which confirmed qualitatively the theoretical predictions.

A. The Teldix Electrodynamic Bearing Wheel

The Active Vibration Suppression has been developed for the Teldix magnetic bearing wheel [2], which is short described in the following.

It is a 5–d.o.f. electrodynamic bearing wheel, because this type is controllable in all axes which is important for AVS and, furthermore, it has the vernier gimballing capability.

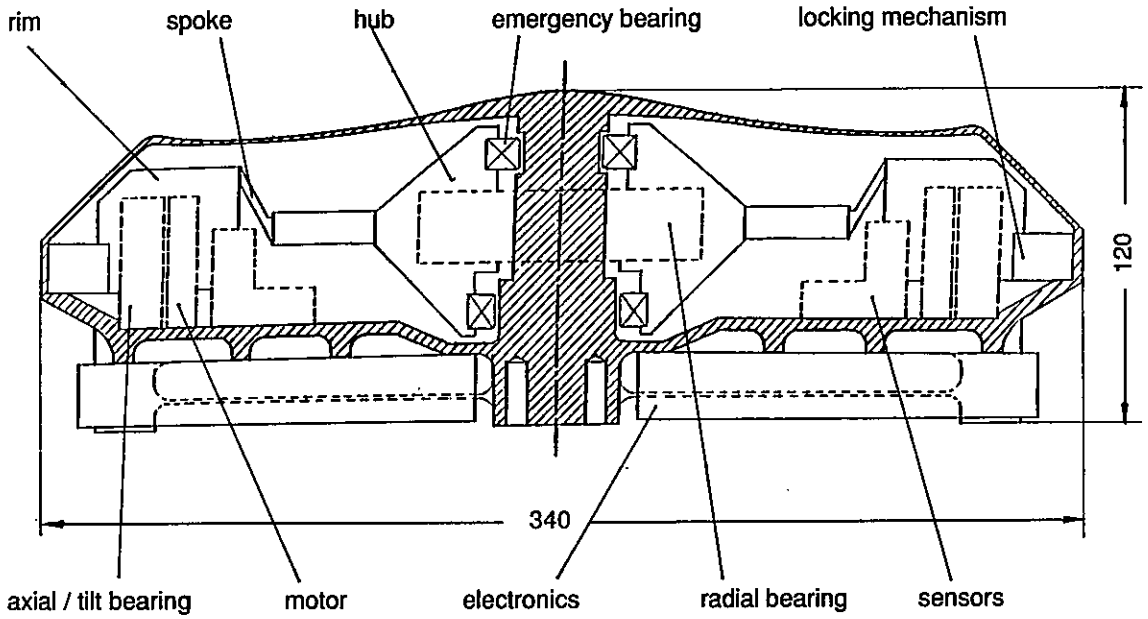

Fig. A–1: Teldix 5–d.o.f. electrodynamic bearing wheel

Fig. A–1 shows a principal sketch of the wheel. The rotor is essentially composed of a rim which is connected to the hub by five titanium springs. Two slots in the rim, which are equipped with Neodymium–Iron magnets, form, together with corresponding epoxi embedded coils on the stator, the axial / tilt actuators and the drive motor. The ironless armature coil consists of four 90° segments. The axial forces are provided by applying a similar current to all coils. The tilting torques about the two perpendicular radial axes are yielded by exciting two opposite coils alternatively.

The hub contains the radial center bearing and carries the emergency bearings.

Any deviation from the nominal rotor position is detected by a set of four axial and two radial position sensors, and – using five control loops – balanced by forces generated in the coils

The drive motor is of the brushless, ironless d.c. type.

The main data are:

Diameter	:	0.34 m
Height	:	0.12 m
Rotormass	:	6.65 kg
Total Mass	:	13 kg
Nom. Speed	:	6000 (10000) rpm
Inertia	:	0.1 kgm2
Momentum	:	60 (100) Nms
Gimballing Angle	:	1.0 °
Slew Rate	:	10 °/s (imax = 3A, 60 Nms)

Angular Momentum
Cross Component: 1 Nms (1°, 60 Nms)

References

[1] Ball Bearing Versus Magnetic Bearing Reaction and Momentum Wheels as Momentum Actuators
W. Auer
AIAA 'Global Technology 2000', Baltimore 1980.

[2] A 5 Degree of Freedom Electrodynamic–Bearing Wheel for 3–Axis Spacecraft Attitude Control Applications
U. Bichler, T.Eckardt
Proceedings of the First International Symposium on Magnetic Bearings, ETH Zurich, June 6–8, 1988.

[3] Magnetic Bearing With Rotating Force Control
H.M.Chen, M.S.Darlow
Transactions of the ASME, VOL. 110, Jan. 1988

[4] Synchronous Response Modelling and Control of an Annular Momentum Control Device
R.Hockney, B.G.Johnson, K.Misovec
NASA Contractor Report 4166

[5] A Design of Robust Servo Controllers for an Unbalance Vibration in Magnetic Bearing Systems
F. Matsumara, M. Fujita, C. Oida
Proceedings of the First International Symposium on Magnetic Bearings, ETH Zurich, June 6–8, 1988.

[6] Vorrichtung zur Kompensation synchroner Störeinflüsse bei einem magnetisch gelagerten Läufer.
H.Habermann, M.Brunet, P.Joly
Patent 2658668

2nd International Symposium on Magnetic Beaing
July 12-14, 1990, Tokyo, Japan

Development of Magnetically-Suspended, Tetrahedron-Shaped Antenna Pointing System

Toshiro HIGUCHI+
Hiroshi TAKAHASHI*, Kenichi TAKAHARA*, Shitta SHINGU*

+ Institute of Industrial Science, University of Tokyo, 7-22-1, Roppongi, Minato-ku, Tokyo, 106, Japan
* Research and Development Center, Toshiba Corporation, 4-1, Ukishima-cho, Kawasaki-ku, Kawasaki, 210, Japan

Abstract

A magnetically-suspended,tetrahedron-shaped antenna pointing system with digital control is proposed for use in a multibeam broadcasting satellite system in the near future. Already, the authors reported a paper emphasizing the advantages of a magnetically-suspended antenna pointing mechanism with the tetrahedral armature using analog controller. According to that paper, it was confirmed to have a 0.002 degree pointing accuracy by tracking tests with a laser beam in the laboratory. However, it remains to be made the most of the features inherent to magnetic suspension, particularly in space, far from human maintenance. Accordingly, we designed the digital controller for magnetic suspension to enhance its function. This paper presents the conception of this system and explains its mechanism, magnetic suspension control system and digital controller with digital signal processor.

1.Introduction

Satellite broadcasting, with aims at regional services such as high definition television, is planned for the future in Japan.[1] An offset Cassegrain antenna constructed with a main reflector, a sub reflector and feed horns will be loaded in the satellite antenna system shown in Fig.1. Since the main reflector is fixed to the satellite body, directly driving its large reflector is almost impossible. Therefore, the small sized sub reflector should be effectively driven by such an antenna pointing mechanism (APM). According to the plan, aperture diameters for the main and sub reflectors are about 3 meters and 0.7 meters. By driving the sub reflector adequately against the satellite perturbation movement, the transmitted and received electric waves should be correctly directed to Japan in conformity. At this time, the allowed pointing error for the antenna system is within 0.01 degree.

In the conventional APMs, the lubricated ball bearings or the flexible pivot is used. On the other hand, the APM using magnetic suspensions has such advantages as simple structure, high pointing accuracy, jitter isolation and mechanism reliability[2,3]. Further, it's possible to change the rotational center by adjusting misalignments between the satellite body and the antenna. Here, the magnetically-suspended, tetrahedron-shaped antenna pointing system (T-MAPS) with digital control is proposed. The important feature of the T-MAPS is to use a tetrahedral armature. The T-MAPS, since it's able to drive the armature contactlessly in 6 degrees of freedom, is clearly superior to other mechanical APMs. Pointing accuracy of the T-MAPS is already confirmed to be 0.002 degree by tracking tests with a laser beam instead of the RF beacon using analog controller[4].

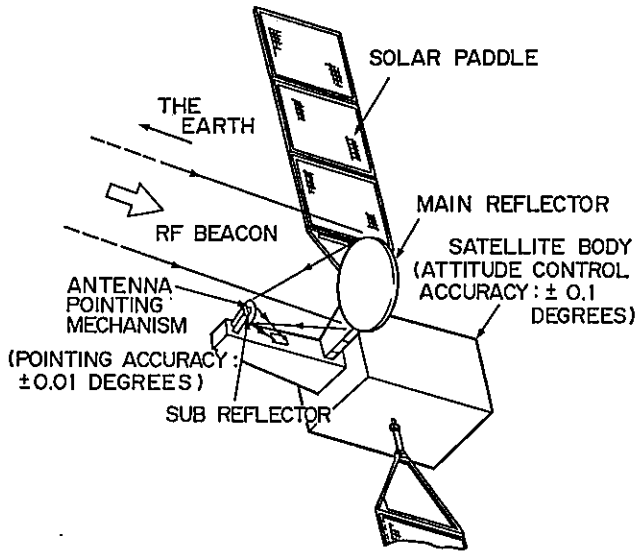

Figure 1 Broadcasting Satellite Antenna System

2.Mechanism Description

Fig.2 shows its photograph, in which the assumptive sub reflector is fixed to the mechanism, and Fig.3 shows its photograph which took out a tetrahedral armature from the mechanism. The T-MAPS consists of a tetrahedral armature made of ferromagnetic material, 9 electromagnets, 9 eddy current type displacement sensors, several support members and a base. The sub reflector is fixed to a support shaft of the armature. 9 electromagnet and displacement sensor units (actuator units) are placed 3 units against bottom face of armature and 6 units against 3 side faces of armature. The clearance gap between individual actuator unit and the armature corresponds to the pointing range for the T-MAPS. The pointing ranges decided on ±1.5 degrees taking account of satellite movements and misalignment between these antennas and the satellite body. The high precision pointing of 6 degrees of freedom of the armature, that is 3 translations and 3 rotations are controlled by the 9 actuator units. The actuator unit is il-

Table 1 DESIGN PARAMETERS

DEGREE OF FREEDOM	6
PAYLOAD MOMENT OF INERTIA	0. 7 kg m²
POINTING RANGE TRANSLATION	± 2 mm
ROTATION	± 1. 5 deg.
NUMBER OF ELECTROMAGNETS	9
NUMBER OF DISP. SENSORS	9
TOTAL WEIGHT	8 kg
<ARMATURE>	
SHAPE	HOLLOW TETRAHEDRON (EDGE LENGTH:180 mm)
MATERIAL	SILICON STEEL
WEIGHT	2. 1 kg
MOMENT OF INERTIA	4×10^{-3} kg m²
<ELECTROMAGNET>	
SHAPE	HORSESHOE SHAPE
YOKE MATERIAL	SILICON STEEL
COIL MATERIAL	COPPER WIRE
WIRE DIAMETER	1. 2 mm
TURNING NUMBER	190 TURNS
MAGNETIC POLE AREA	773 mm²
MAGNETIC CORE AREA	437 mm²
<DISP. SENSOR>	
TYPE	EDDY CURRENT SENSOR
MEASURING RANGE	0 ~ 4 mm
FREQUENCY RESPONSE	0 ~ 20 kHz(-3dB)
RESOLUTION	0. 01 %(FS)
OUTPUT VOLTAGE	0 ~ 5 V

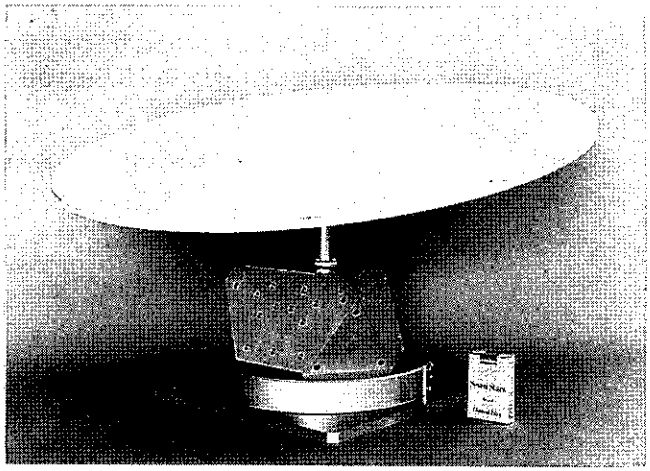

Figure 2 T-MAPS Mechanism with Antenna

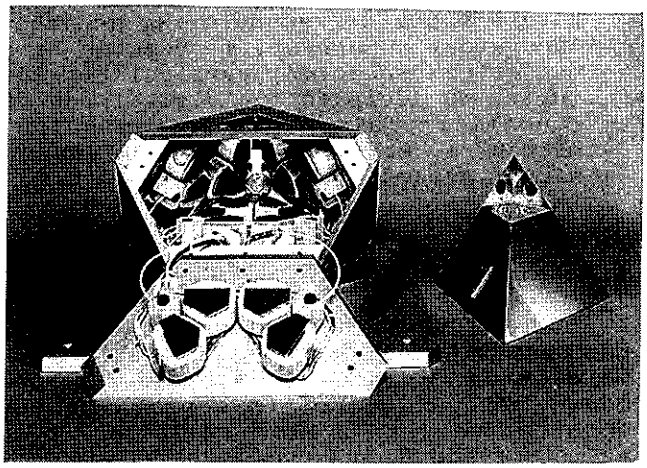

Figure 3 Inside of the Mechanism and Armature.

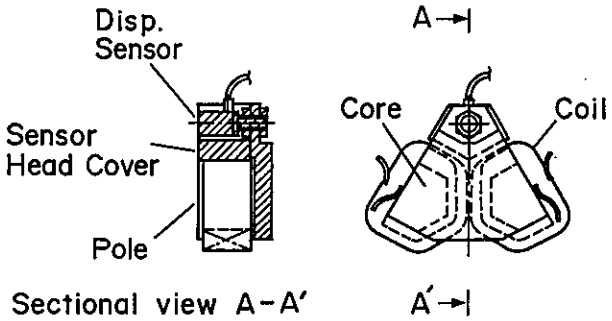

Figure 4 Actuator Unit
(electromagnet/displacement sensor unit)

lustrated in Fig.4. This unit is easy to design and to manufacture for the reason of the same shape and dimension of all units. The design parameters for the T-MAPS are shown in Table 1. These units of this time are designed all the same as the previous[4].

3.Magnetic Suspension Control System

The control closed loop for a magnetically-suspended antenna pointing mechanism consists of the suspension loop and the pointing loop. The former loop stabilizes the armature in the local coordinate system. The latter has a precision pointing capability in a Cartesian coordinate system, and is controlled by the RF beacon (pointing signal) from the earth station. The magnetic suspension control loop is shown in Fig.5. In this servo control system, each actuator unit is independently controlled by an individual compensator in the local coordinate system. The displacement between the armature and the displacement sensor is detected by each displacement sensor. Then these signals are fedback to compensators. In this control block diagram, there are two transformation matrices. One is a command transformation matrix, Max. This matrix transforms commands in a Cartesian coordinates into local ones in the local electromagnet coordinates. The other is a position transformation matrix, Mas. This matrix transforms displacement signals of displacement sensors in the local sensor coordinates into displacement signals in the local electromagnet coordinates. These transformation matrices, are shown below as an example.

$$\mathrm{Max}=\begin{bmatrix} 0.000 & 0.000 & 1.000 & 0.629 & -0.002 & 0.000 \\ 0.000 & 0.000 & 1.000 & -0.311 & 0.541 & 0.000 \\ 0.000 & 0.000 & 1.000 & -0.311 & -0.545 & 0.000 \\ 0.000 & 0.943 & -0.333 & 2.177 & -0.180 & -0.511 \\ 0.000 & 0.943 & -0.333 & 2.177 & 0.182 & 0.513 \\ -0.816 & -0.471 & -0.333 & -0.932 & 1.976 & -0.511 \\ -0.816 & -0.471 & -0.333 & -1.246 & 1.795 & 0.513 \\ 0.816 & -0.471 & -0.333 & -1.246 & -1.795 & -0.511 \\ 0.816 & -0.471 & -0.333 & -0.932 & -1.976 & 0.513 \end{bmatrix}$$

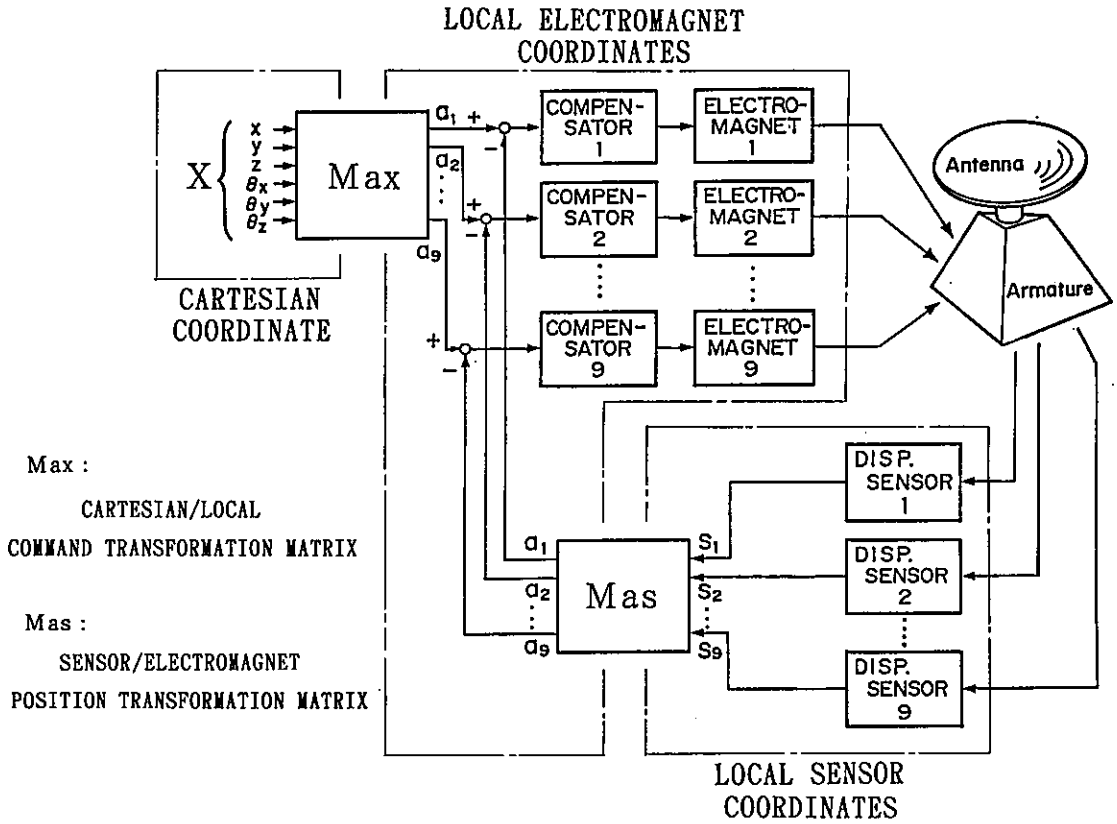

Figure 5 Control Block Diagram for Magnetic Suspension System

$$Mas = \begin{bmatrix} 0.567 & 0.126 & 0.126 & -0.091 & -0.091 & -0.018 & -0.164 & -0.164 & -0.017 \\ 0.126 & 0.566 & 0.126 & -0.164 & -0.018 & -0.091 & -0.091 & -0.018 & -0.164 \\ 0.126 & 0.126 & 0.566 & -0.018 & -0.164 & -0.164 & -0.018 & -0.091 & -0.091 \\ -0.230 & -0.095 & 0.052 & 0.474 & 0.253 & -0.098 & -0.175 & -0.028 & -0.244 \\ -0.230 & 0.052 & -0.095 & 0.254 & 0.474 & -0.245 & -0.028 & -0.175 & -0.098 \\ 0.052 & -0.230 & -0.095 & -0.028 & -0.244 & 0.474 & 0.254 & -0.098 & -0.175 \\ -0.095 & -0.230 & 0.052 & -0.157 & -0.098 & 0.254 & 0.474 & -0.245 & -0.028 \\ -0.095 & 0.052 & -0.230 & -0.098 & -0.175 & -0.028 & -0.245 & 0.474 & 0.254 \\ 0.052 & -0.095 & -0.230 & -0.244 & -0.280 & -0.175 & -0.097 & 0.254 & 0.474 \end{bmatrix}$$

Though an electromagnet generates only a pull force in one direction, a displacement sensor is available in both plus and minus directions. Therefore, essentially only 6 displacement sensors are required. Even in case of damage of any three of the displacement sensors, the T-MAPS maintains normal operation by changing the position transformation matrix, Mas. Similarly, the minimum number of electromagnets, which assures 6 degrees of freedom positioning, is considered to be 7. Therefore, the T-MAPS has redundancy of the electromagnets. It is so effective for the system performance to use the redundant units not only in case of damage but in case of normality. Damage of electromagnet is caused by breakdown of coil due to over current, or wire cut. It is possible to avoid the damage of electromagnet due to over current, by monitoring the current value of the power amplifier. Moreover, displacement sensor damages are caused by wire cut, or by damages of sensor converter due to over heat. When the displacement sensor is broken, sensor output voltage is set -12V or +12V that correspond to the source voltages, or is fixed -2V to +2V that correspond to the normal output voltages. If output voltage is fixed -2V to +2V, it is difficult to find out the broken displacement sensor, even though by monitoring output voltages. Therefore, it's necessary to logically identify the damaged displacement sensors. A method to identify a damaged sensor in a redundant system is reported[5].

4.Digital controller with DSP

4-1.Why digital controller ?

The paper[4] that reported about the T-MAPS laid emphasis to the reliability of the system because of the redundancy. It is true that the function of pointing is maintained even if some of the electromagnets broke down. In other words, the final value of the position for the step input does not depend on the redundant electromagnets. This is the reason why the pointing function is reliable. But, apart from the pointing that is the most essential function in the system, the decoupling function for example that enhance the pointing performance, is lost. On the other hand, on the redundant displacement sensors whose signals are effectively used even in normal condition, depends the pointing accuracy. For that reason, in order to recover the pointing accuracy after the redundant displacement sensor failure, it is necessary to redefine the above mentioned transformation matrix, Mas.

The most important of the features of magnetic suspension, the contactlessness allows to easily remove the injured out of busy area and to start working to the best of its ability. The digital controller is expected to provide the system the adaptability to the time dependent or unexpected change of the system parameters, always realizing nearly the best conditions of pointing as well as dynamic behavior. We developed a digital controller with DSP to improve the function of T-MAPS. The digital controller is considered to be absolutely essential for recovery of system in case of displacement sensor damages.

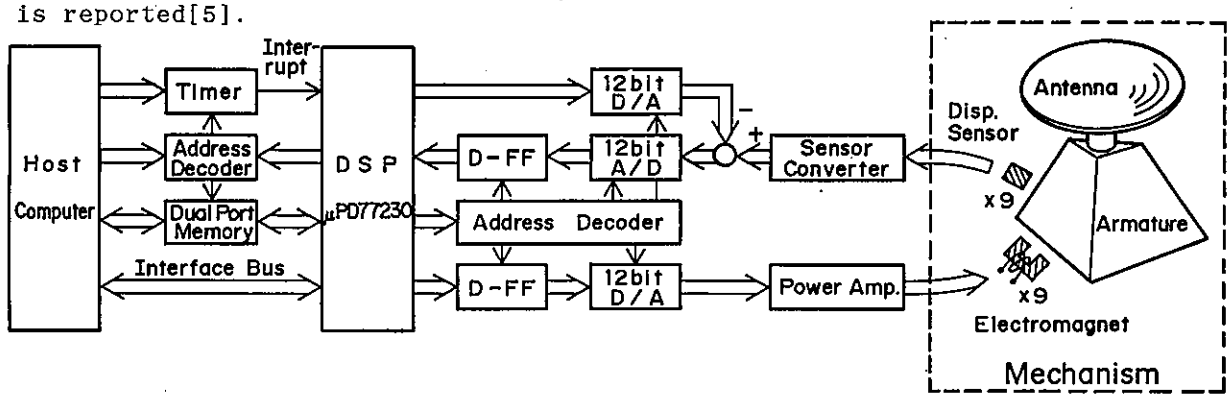

Figure 6 Structure of Digital Controller

4-2.Structure of the digital controller

The structure of the digital controller is shown in Fig.6, and Fig.7 shows its photograph. The structure mainly consists of 12 bit A/D converters, 12 bit D/A converters, sensor converters, DSP and a host computer. The DSP can execute floating point multiplication and adding for a instruction in 150 nsec. The DSP control flowchart is shown in Fig.8. The DSP is driven by the interrupt signal of the external timer. Nine displacement sensor signals which are converted to digital signals by the 12 bit A/D converter are inputted to the DSP, which out of the inputted signals, calculates the control signals to stably suspend the armature. The control signals are converted to the analog signals by the 12 bit D/A converter, which are inputted to the power amplifier and then the control current is supplied to the electromagnets. The displacement sensor signals are adjusted to zero value by means of adding the calculated values to the converted signals. The DSP performs to set the control parameters, such as a sampling period, a stiffness matrix Kc and a damping matrix Pc, and host computer gets the present sensor value from the DSP through the dual port memory. As the dual port memory access from both the DSP and the host computer is impossible at the same time, the data input/output must be performed according to the prescribed hand-shaking rules. The following two flags are provided. One is the host computer access flags. The other is the DSP access flags. These flags are fed through the interface bus in the Fig.6.

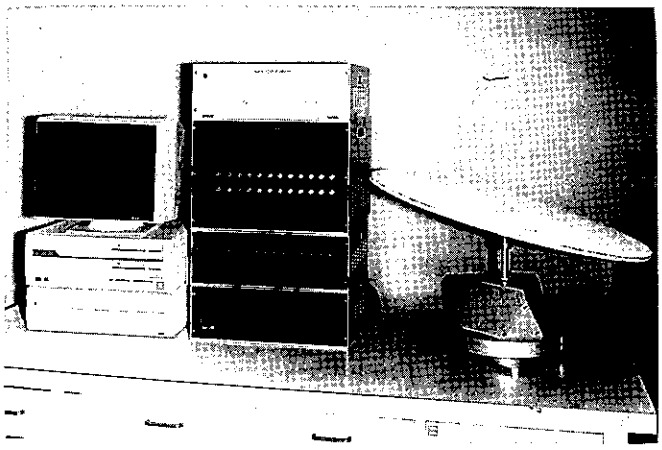

Figure 7 Digital Controller and T-MAPS

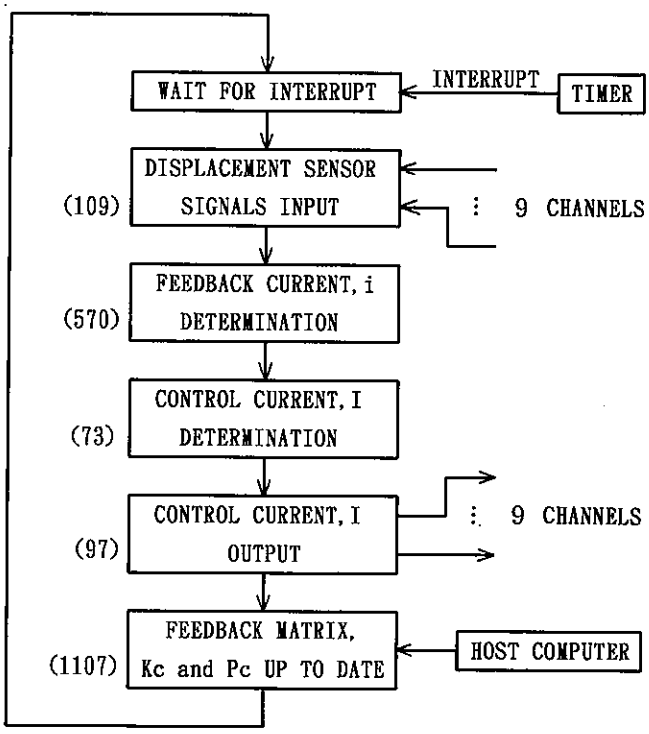

() number of instructions

Figure 8 Flowchart of the DSP Operation

4-3.Suspension control algorithm

The linear equation of motion in a suspension control system is described as follows:

$$m\ddot{x} = F_0 + A_i \cdot i - A_d \cdot d \qquad (1)$$

where m is the armature mass, x is the armature displacement in a Cartesian coordinate, i is feedback current, d is the armature displacement in the local electromagnet coordinates, and the others are as follows:

$$F_0 = Q\,(i_0^{\rho} / d_0^{\sigma}) \qquad (2)$$

$$A_i = \rho Q\,(i_0^{\rho-1} / d_0^{\sigma}) \qquad (3)$$

$$A_d = \sigma Q\,(i_0^{\rho} / d_0^{\sigma+1}) \qquad (4)$$

where Q, ρ and σ are coefficients obtained from the electromagnet characteristics, and the suffix "0" shows the bias value. Applying the linear approximation around the center of the pointing ranges, the eq.(1) becomes :

$$K \cdot M_{ax}^{-1} \cdot d + P \cdot M_{ax}^{-1} \cdot \dot{d} = A_i \cdot i - A_d \cdot d \qquad (5).$$

Furthermore, feedback current i is given as follows:

$$i = K_c \cdot d_s + P_c \cdot \dot{d}_s \quad (6)$$

$$K_c = A_i^{-1} (K \cdot M_{sx}^{-1} + A_d) M_{as} \quad (7)$$

$$P_c = A_i^{-1} \cdot P \cdot M_{sx}^{-1} \cdot M_{as} \quad (8)$$

where ds is displacement sensor signals , Kc and Pc denote the feedback stiffness matrix and the feedback damping matrix, respectively. These feedback matrices,Kc and Pc are determined so as to support the armature stably. The transformation matrix, Msx, transforms displacement signals of displacement sensors in the local sensor coordinates into displacement signals in a Cartesian coordinate. This matrix has only constant elements as follows:.

$$Msx = \begin{bmatrix} 0.000 & 0.000 & 1.000 & 1.223 & -0.002 & 0.000 \\ 0.000 & 0.000 & 1.000 & -0.608 & 1.055 & 0.000 \\ 0.000 & 0.000 & 1.000 & -0.608 & -1.059 & 0.000 \\ 0.000 & 0.943 & -0.333 & 2.474 & -0.352 & -0.996 \\ 0.000 & 0.943 & -0.333 & 2.474 & 0.353 & 0.997 \\ -0.816 & -0.471 & -0.333 & -0.933 & 2.318 & -0.996 \\ -0.816 & -0.471 & -0.333 & -1.542 & 1.967 & 0.997 \\ 0.816 & -0.471 & -0.333 & -1.542 & -1.966 & -0.996 \\ 0.816 & -0.471 & -0.333 & -0.933 & -2.319 & 0.997 \end{bmatrix}$$

The run time of one cycle at this algorithm, becomes 293 micro-sec in 1956 instructions. In the eq.(2) to (4), these coefficients Q, ρ, σ are given by testing the electromagnetic force as follows:

$Q=6.55$
$\rho=2.15$
$\sigma=1.76$

where the calculation units are Newton, millimeter and Ampere.

5.Conclusions

We developed a digital controller with digital signal processor to enhance the function of the T-MAPS. The digital controller is absolutely essential for the recovery of the system in case of displacement sensor damages in a redundant system. And,it is expected that the best dynamic characteristics of the APM is maintained in spite of the damages among redundant elements. The digital signal processor, coupled with the performance of the host computer, provides the feature of the digital controller as follows.

(1) The digital controller has sufficient ability for the magnetic suspension control of 9 axes.

(2) The DSP up date the stiffness matrix Kc and the damping matrix Pc of the control parameters at each sampling period, so it can follow well to the change of the plant parameters.

References

[1] S.Yoshimoto,et al., A Trade-off Study on 22 GHz Band Multibeam Satellite Broadcasting Systems, AIAA 11th Communication Satellite Systems Conference, 1986

[2] W.Anderson and S.Joshi, The Annular Suspension and Pointing(ASP) System for Space Experiments and Predicted Pointing Accuracies, NASA TR R-448, 1975

[3] S.Iwaki and R.Matsuda, Testing Investigation of Magnetically Suspended APM, Proceedings of 15th ISTS, Vol.1, 1986

[4] K.Takahara,et al., Performance Characteristics of a Magnetically Suspended, Tetrahedron-Shaped Antenna Pointing Mechanism, Proceedings of 16th ISTS, Vol.2 1667-1672, 1988

[5] T.Ozawa and S.Shingu, Synthesis of Redundant Control Systems -2nd Rep. Identification of Disordered Sensor-, Proceedings of the 26th SICE Annual Conference, Vol.1 775-776, 1987 (in Japanese)

[6] T.Mizuno and T.Higuchi, Design of the Control System of Totally Active Magnetic Bearings, Proceedings of International Symposium on Design and Synthesis, 534-539, 1984

[7] T.Higuchi,M.Tsuda and S.Fujiwara, Magnetic Supported Intelligent Hand for Automated Precise Assembly, Proceedings of IECON'87:Automated Design and Manufacturing, SPIE Vol. 857 926-933, 1987

2nd International Symposium on Magnetic Beaing
July 12-14, 1990, Tokyo, Japan

A DIGITAL TIME DELAY CONTROLLER FOR ACTIVE MAGNETIC BEARINGS

K. Youcef-Toumi, Associate Professor, S. Reddy, Graduate Student
and T. Vithiananthan, Graduate Student

Department of Mechanical Engineering
Massachusetts Institute of Technology
Cambridge, MA 02139
U.S.A.

Abstract

The successful design of actively controlled magnetic bearings depends greatly on the design of the control system. The function of the controller is to maintain bearing performance in the face of large system dynamic variations and unpredictable disturbances. This paper discusses issues associated with the design and implementation of a digital time delay controller for active magnetic bearings.

The control system evaluation conducted in this research consists of several tests. Various components of the system are identified and their corresponding theoretical models are then validated experimentally. The effectiveness of the digital control algorithm was then validated using several simulations which are based on linear and nonlinear models for the bearing including bending mode effects. Several experiments were conducted for spinning and nonspinning conditions. These include time responses, closed loop frequency responses and disturbance rejection frequency response data. Evaluations were performed at bearing rotational speeds of 10,900 rpm, 20,100 rpm, 30,400 rpm and 34,800 rpm with Time Delay Controller bandwidths of 100, 200 and 400 rad/sec. The digital controller presented shows an extremely high performance for the prototype considered by maintaining almost the same desirable dynamic behavior over the whole range of speeds.

1 Introduction

The use of magnetic bearings to support rotating structures without contact has received considerable attention in the last forty years. There are two main areas of advantages of using magnetic bearings over conventional bearings. The first is due to their contactless nature which eliminates friction which is inherent in conventional bearings. The absence of friction in magnetic bearings not only contribute to efficiency in energy but also to longer life and elimination of mechanical maintenance of the bearing. The contactless nature also eliminates the use of lubrication in the bearing. Lubrication poses problems because its presence precludes operation in many environments. Absence of lubrication in magnetic bearing makes them compatible to environments such as vacuum and other hostile environments. Another advantage is that the magnetic bearings can operate in a wide range of temperature ranging from $-250°C$ to $450°C$ [20].

The other advantages are due to the closed loop control of the bearing such as the elimination of vibrations due to unbalance [20].

The characteristics of active magnetic bearings are inherently nonlinear due to the nonlinearities of electromagnetic fields. The nonlinear nature requires an increase in the modeling complexity, estimation and control of the bearings. Furthermore there exist unpredictable disturbances due to mass unbalances of the rotor, and uncertainty of the model due to changes of the rotor speed. For many applications, the systems are assumed to be linear with no parameter uncertainties. The linear controllers are then designed based on the linearized time invariant model. Additional background and historical review can be found in [16].

The most recent controller design approaches use full-state feedback. Hubbard and McDonald [5] used linear-quadratic design in their pendulous supported flywheel. Stanway and O'Reilly [9] used eigenstructure assignment for the control of suspension systems for rotating machinery. Salm and Schwietzer [7] demonstrated modal control of a flexible rotor. These approaches use linear controllers for linearized models, and therefore ignore all model uncertainties and unexpected disturbances. Additional references are found in [16].

Most of the well-developed control theory, either in the frequency domain or in the time domain, deals with systems whose mathematical representations are completely known. However, in many practical situations, the parameters of the system are either poorly known or operate in environments where unpredictable large parameter variations and unexpected disturbances exist. In such applications, the usual fixed-gain linear controllers will not be adequate to achieve satisfactory performance in the entire range over which the characteristics of the system may vary.

Recently several advanced control techniques have been developed for such systems. One of the primary method is Adaptive Control [1,3,6,10] where the structure of the controller, usually a PD or PID type controller is first selected. The controller gains are then updated so that the plant output closely follows the desired response [2,4]. This method considers slowly varying plant parameters, linear equations and/or bounded uncertainty.

Variable Structure Control (VSC) is another very powerful method to deal with nonlinear systems with uncertain dynamics. VSC was first proposed by Utkin in 1972 [11], and its early application was made by Young in 1978 [18] to robot manipulators. Based on Lyapunov's second method, this control scheme is characterized by a discontinuous function with high frequency chattering, which forces the system to follow the reference signal quickly without the parameter identification process used in adaptive control. This infinite frequency chattering, however, is undesirable in many practical applications such as mechanical systems. Young proposed a linear region to eliminate chattering [19]. In 1983, Slotine and Sastry [8] proposed a modified VSC method to eliminate chattering by introducing a sliding zone. If the uncertainty is large, the sliding zone must be wide enough to cover the uncertainty. In this case the controller tends to be a regular PID controller for the operating range, thus losing the advantages of the VSC approach. That is, SMC is useful only for systems where the plant parameter variations and disturbances are bounded and small.

Learning control is another approach which is based on trial and error. Arimoto and Miyazaki extended it to Multi-Input Multi-Output nonlinear systems. In Learning Control, the generated tracking errors are stored during every iteration. After each iteration, the controller adds a signal, which is proportional to the stored error and/or its derivative, to the previous control input such that the tracking er-

ror will decrease during the next iteration. By repeating this process several times, betterment in performance is obtained. Therefore this approach is restricted to repetitive tasks only.

In 1986, Youcef-Toumi and Ito proposed a novel method, called Time Delay Control (TDC), which is applicable to nonlinear plants with unknown dynamics and unexpected disturbances [12,13,14]. TDC law depends on neither estimation of specific parameters or repetitive actions, nor does it generate a discontinuous signal. Rather, it depends on the direct estimation of the effect of uncertainties. This is accomplished using time delay. The gathered information is used to cancel the unknown dynamics and the unexpected disturbances simultaneously. Then the controller inserts the desired dynamics into the plant. In other words, the TDC uses past observation of the system's response and the control inputs to modify the control actions directly rather than adjusting the controller gains. Thus this algorithm can deal with large unpredictable system parameter variations and disturbances.

In this paper, we first present models of an eight pole attractive magnetic bearing as used in a High Speed turbo molecular pump. The Time Delay Controller for magnetic bearings is briefly presented in Section 3. Section 4 deals with the implementation and evaluation of the Time Delay Controller.

2 System Identification and Model Validation

In this section, the system parameters are identified and the models are experimentally validated. The nonlinear and linearized equations of motion for the bearings are also presented. The theoretical and experimental frequency responses of the system are also presented.

2.1 Plant Dynamics

The dynamic behavior of a rotor under the action of an eight pole attractive magnetic bearing in the radial direction can be modelled by the following equation:

$$m\frac{d^2x}{dt^2} = -f_\ell + f_r + d \tag{1}$$

where m is half of the rotor mass (kg) (since the rotor is controlled by two radial bearings) and the left and right magnet forces (N) are given by

$$f_\ell = \frac{\mu_0 A_g N^2 I_\ell^2}{h_\ell^2} \text{ and } f_r = \frac{\mu_0 A_g N^2 I_r^2}{h_r^2} \tag{2}$$

μ_0 is the permeability of free space and A_g is the air gap area of one pole. N is the number of turns. The left and right bearing clearances h_ℓ and h_r respectively are

$$h_\ell = h_0 + x \text{ and } h_r = h_0 - x \tag{3}$$

h_0 is the nominal bearing radial clearance and x is the deviation of the shaft from the bearing center. d is a disturbance force.

A schematic of the radial bearing is shown in Figure 1. The variable u indicates the control signal. Using Eqn. (2) and Eqn. (3) and introducing a bias current I_0, Eqn. (1) becomes

$$m\frac{d^2x}{dt^2} = -\frac{K(I_0 - 0.5u)^2}{m(h_0 + x)^2} + \frac{K(I_0 + 0.5u)^2}{m(h_0 - x)^2} + \frac{d}{m} \tag{4}$$

At steady state, the current in the left and right electromagnets is I_0, therefore $u = 0$, $x = 0$, and $\dot{x} = 0$. Thus the linearized model becomes:

$$\dot{x}_1 = x_2$$

$$\dot{x}_2 = \frac{4KI_0^2}{mh_0^3}x_1 + \frac{2KI_0}{mh_0^2}u \tag{5}$$

where x_1 and x_2 are the position and velocity. The transfer function of the actuator and plant can be given by the following expression:

$$\frac{X_1(s)}{U(s)} = \left(\frac{\frac{2KI_0}{mh_0^2}}{s^2 - \frac{4KI_0^2}{mh_0^3}}\right) \tag{6}$$

The system parameters are summarized in Table 1.

The bending modes were included in the plant equation to evaluate their effect on the control performance. The first bending mode of the plant can be modelled as a second order single degree of freedom system. Figure 2 shows a single degree of freedom system, where the massless dashpot of damping coefficient D and a spring of stiffness k are mounted between the mass m and the fixed wall. The transfer function between the displacement x and the force F can be written as:

$$\frac{X(s)}{F(s)} = \left(\frac{1}{M}\right)\left(\frac{1}{s^2 + 2\zeta\omega_n s + \omega_n^2}\right)$$

where ω_n^2 is equal to K/M, and ζ is equal to $D/2\sqrt{M/K}$. Since there are more than one bending mode of the rotor, the mass m of the rotor has to be distributed among these modes. Therefore the mass for the first bending mode can be thought of as the effective mass for the first bending mode. The value of stiffness K is very high and the damping D is very low for metals. Therefore the damping ratio ζ of the bending mode is small. The effective mass of the bending mode has to be less than the actual mass of the rotor.

The system was modelled such that the perturbations caused by the input force due to the bending mode was then added to the position of the rigid plant affected by the same force. The block diagram of the modelled system is presented in Figure 3

2.2 System Identification and Model Validation of an Eight Pole Magnetic Bearing

The turbo molecular pump has two radial bearings and a thrust bear-

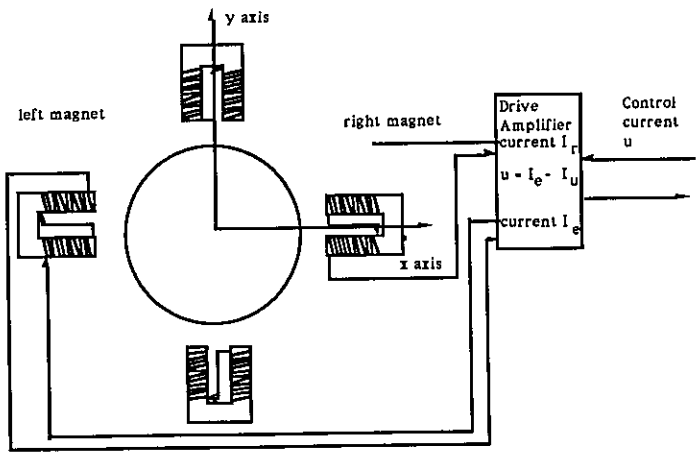

Figure 1: The Control Current Setup for the Bearing in the Radial Direction

K	$= \mu_0 A_g N^2 = 1.23 \times 10^{-6} Nm^2/A^2$
I_0	$= 0.36$ A
m	$= 1.1$ kg
h_0	$= 2.5 \times 10^{-4}$ m
A_g	$= 9.75 \times 10^{-5}$ m^2
N	$= 100$ turns

Table 1: System Parameters

ing. Each radial bearing has two degrees of freedom in the horizontal plane and the thrust bearing has one degree of freedom in the vertical plane. It is assumed that the bearing forces are uncoupled in the five axes (x_1, y_1, x_2, y_2, and z). The controller is similar to a regulator where the system output follows a desired position indicated by the reference input.

Several frequency responses were obtained for comparison with theoretical models. These frequency responses were obtained for both the thrust and the radial bearings. A HP dynamic signal analyzer was used to send a swept sine signal with a frequency range of .1 Hz to 10 kHz. The experimental transfer function is between the output position measured in terms of voltage and the input current measured in terms of voltage. The sensor gain for the radial bearing is 25000 V/m. The analytical transfer function obtained is:

$$\frac{X_1(s)}{U(s)} = \frac{10472}{(s+15700)} \cdot \frac{12.88 \times 25000}{s^2 - 37100} \left(\frac{V}{V}\right) \tag{7}$$

The plant is an unstable plant with two poles at +192.6 rad/sec (30.7 Hz) and -192.6 rad/sec (-30.7 Hz). The experimental plant frequency response is presented in Figure 4. The break frequency of the experimental plant transfer function is 21.8 Hz. The theoretical break frequency is very close to the experimental break frequency. The estimated experimental transfer function is

$$\frac{X_1(s)}{U(s)} = \frac{9 \times 25000}{s^2 - 24670} \cdot \frac{10472}{s + 15700}$$

The experimental frequency response portray the bending mode characteristics of the rotor. The bending mode affects the gain at about 900Hz and at about 2 kHz. The phase response of the plant also shows the effect of the bending mode of the plant.

3 Time Delay Control

This section deals with the Time Delay Controller for magnetic bearings. This controller estimates a feedforward action in order to cancel the unknown dynamics and disturbances present in the system and introduce some desired dynamics. This method is discussed in detail [17].

The nonlinear equations of motion for a given axis of the Active Magnetic Bearing can be written as,

$$\begin{aligned} \frac{dx_1}{dt} &= x_2 \\ \frac{dx_2}{dt} &= g(x_1, u) + d(t) \end{aligned} \tag{8}$$

where $g(x_1, u)$ is a nonlinear function relating $\dot{x}_2$ to x_1, and u; and $d(t)$ is the disturbance force. Time Delay Control law assumes that both the function g and disturbance scheme are unknown. The control as discussed in [17] assumes a reference model which generates the desired trajectory. A second order reference model is chosen as

$$\begin{aligned} \frac{dx_{1m}}{dt} &= x_{2m} \\ \frac{dx_{2m}}{dt} &= -a_{1m}x_{1m} - a_{2m}x_{2m} + b_m r \end{aligned} \tag{9}$$

The values for a_{1m} and a_{2m} are chosen as to satisfy the requirement of the natural frequency, and damping ratio of the second order reference model. The TDC control law derived in the previous section was chosen to satisfy this requirement and therefore given by the equation:

$$\begin{aligned} u(t) = \ & \tfrac{1}{b}[-\ddot{x}_2(t-1) + bu(t-1) - a_{1m}x_1(t) \\ & -a_{2m}(t)x_2(t) + b_m r + k_1 e_1 + k_2 e_2] \end{aligned} \tag{10}$$

where $\ddot{x}_2$ is an estimate of the acceleration of the rotor, x_2 is the velocity of the rotor, and x_1 is the position of the rotor, $e_1 = x_{1m} - x_1$, and $e_2 = x_{2m} - x_2$. The error gains k_1 and k_2 are appropriately chosen. While this control law requires an estimate of the acceleration, a new method has been developed in [17] which does not need such signals.

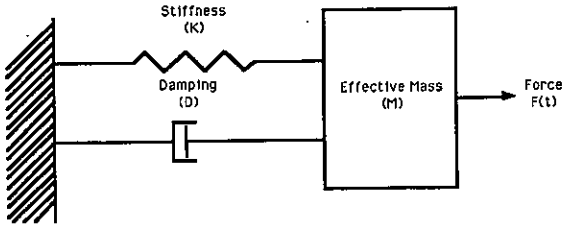

Figure 2: A Single Degree of Freedom System

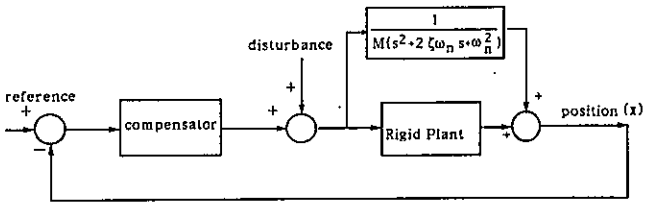

Figure 3: Block Diagram of the Plant including the First Bending Mode

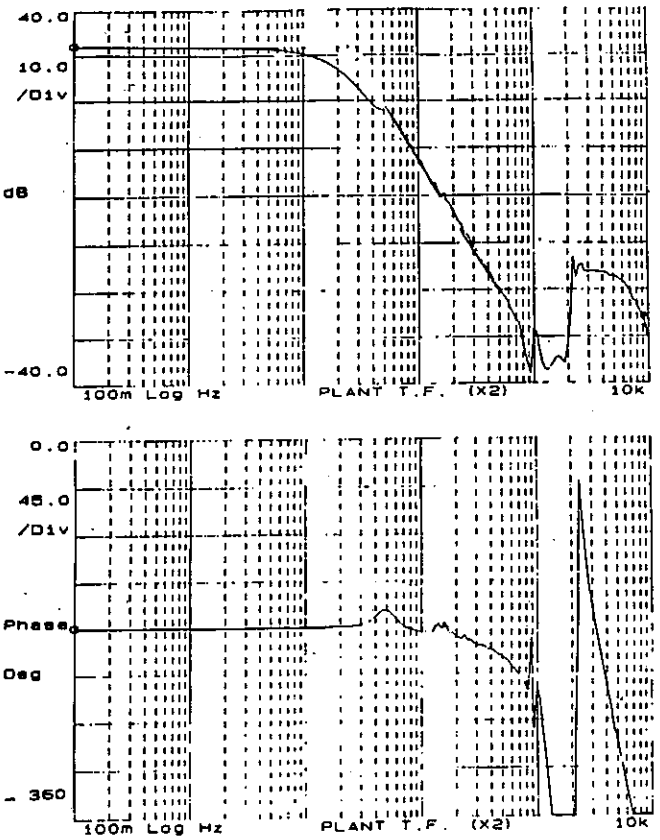

Figure 4: Experimental Frequency Response of the Plant Transfer Function (x_2 axes)

4 Controller Implementation and Evaluation

4.1 Simulation Results

The Time Delay Controller law for the radial bearing was designed under the assumption that the rotor was rigid. The rotor has the first bending mode at frequencies between 800 Hz and 1000 Hz and the second bending mode between 2 kHz and 2.5 kHz. The bending mode natural frequencies were experimentally determined by using an impulse hammer, accelerometer and a signal analyzer. The damping ratio and the effective mass were estimated based on the theory of vibrations discussed in [16]. In the following simulations, $b = 100$, $a_{1m} = 4.0 \times 10^4$, and $a_{2m} = 282.8$ were selected for controlling the thrust bearing (z-axis). $b = 100$, $a_{1m} = 4.0 \times 10^4$ and $a_{2m} = 400$ were used in the case for the radial bearing.

4.1.1 Rigid Model

Simulations were performed for the radial bearing under Time Delay Control with the assumption that the rotor was a rigid body. Figures 5 a, b and c contain the position, the position error, and the control current responses for the radial bearing controller. The specifications for the simulations are as follows: second order reference model with a bandwidth of 200 rad/sec, damping ratio of 1, sampling rate T_s of 4 KHz. The time response of the above mentioned second order reference model should have no overshoot and a settling time of .02 sec. The system time response in Figure 5 behaves as that of a second order system as expected. The settling time of .025 sec obtained from Figure 5 a for the simulation is very close to the expected value of .02 sec. The time response has very negligible or no overshoot as expected. The control current increases in magnitude from 0 A to a maximum value of -0.44 A and then decreases to settle at a steady state value of about -0.01 A.

4.1.2 Flexible Model

The simulations were performed for the case where the closed loop bandwidth of the Time Delay Controller was 200 rad/sec. Figures 6 a, b and c contain the time response, the position error, and the control current of the rotor for the $\mathbf{x_2}$ axis. The specifications for the simulations are as follows: second order reference model with a bandwidth of 200 rad/sec, damping ratio of 1, sampling rate of 4 kHz. The effective mass m_{eff} of the bending mode was .5 kg, the damping ratio was .001, and the natural frequency is 875 Hz. The total rotor mass is 2.2 kg. The time response presented in Figure 6 a looks like the response of a second order system with a settling time of .03 sec and an overshoot of 5%. The time response of the rigid body without the bending mode for the same specifications was similar except that it had a negligible overshoot. The control current of the system does not show any significant change from the rigid body mode. Therefore for the bending mode with the above mentioned specification does not affect the system time response significantly.

4.2 Experimental Implementation and Results

4.2.1 Implementation of the Time Delay Controller

A detailed block diagram of the system is presented in Figure 7. In this experimental setup, we have the option of controlling the system using either a linear analog controller which resides in the compensation block, or a time delay controller implemented digitally in the DSP board.

The position signal for the Time Delay controller is obtained through the test points TP2 and/or TP3 and this signal is then sent into an analog to digital converter (A/D converter) which is linked to the DSP board. The A/D board has an adjustable built in low pass filter where the position signal can be filtered. The control voltage signal is sent out through the D/A converter which has a low pass filter with adjustable cutoff frequency. A switch for implementing the Time Delay Controller was installed in the control board. The system can be switched either to analog or digital from this switch.

4.2.2 Experimental Results

The Time Delay Controller was evaluated for its closed loop responses, disturbance rejection properties, and time responses for both the thrust (z axis) and the radial ($\mathbf{x_2}$ axis) bearing. The closed loop and disturbance rejection properties of the radial bearing were also analyzed while the rotor was spinning at speeds of 10,900 rpm, 20,100 rpm, 30,400 rpm, and 34,800 rpm.

The model reference for the thrust bearing was chosen to have a natural frequency of 200 rad/sec and a damping ratio of .707. The ex-

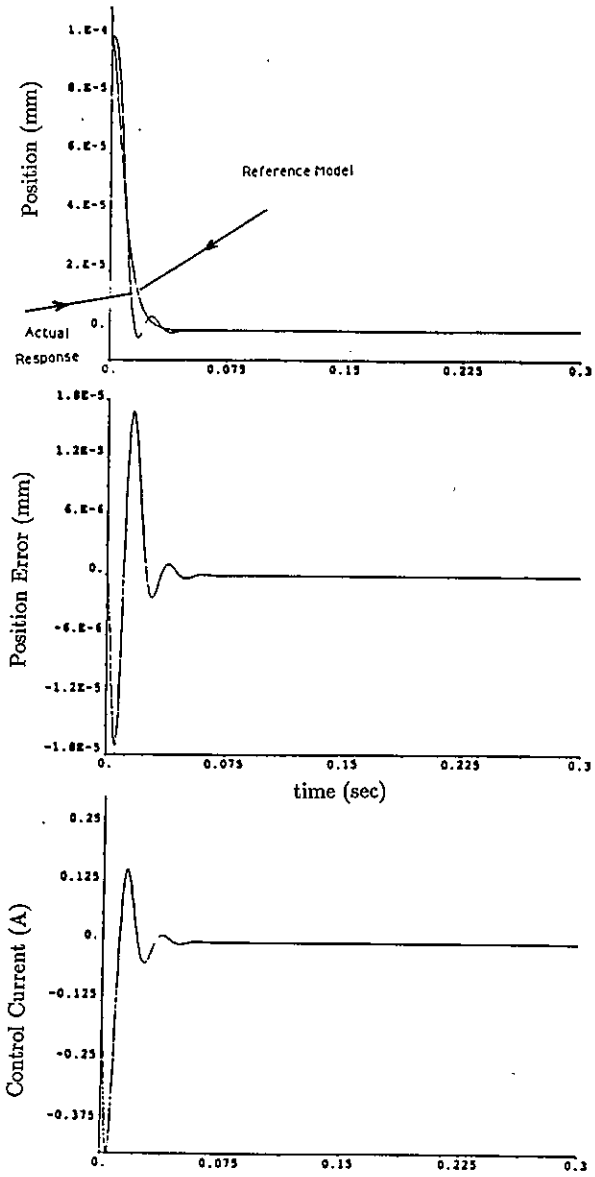

Figure 5: Simulated Rigid Body Model for x_2 Axis. Reference Model: $\omega_n = 200$ rad/sec, $\zeta = 1$, $T_s = 4$ KHz.

perimental data shown in Figure 8 indicate that the actual response tracks the reference model response very closely. In this case, the position moves from 200μm to 0μm which corresponds to the suspended configuration. The error is shown in the same figure and has about less than 10% maximum error. The control current necessary to produce this response is also shown in that same figure with a maximum current of about 1.75 amps. This is an excellent performance considering that the controller has no detailled information about the system. Figure 9 shows the closed-loop frequency response of the thrust bearing. In this case it is clear that the magnitude and phase characteristics are very close to those of the reference model selected. The disturbance rejection properties of the thrust bearing are shown in Figure 10. The controller rejects disturbances up to the bandwidth which is again around 200 rad/sec. The static stiffness is about 100 MN/m and the minimum stiffness is about 300 KN/m at the frequency of 200 rad/sec.

Figure 11 shows the closed loop frequency response for a radial bearing. This is very similar to that of the reference model. Figures 12 shows the disturbance rejection of the radial bearing when the rotor is at rest and while it is spinning at speeds of 10,900 rpm, 20,100 rpm, 30,400 rpm and 34,800 rpm. When the rotor is at rest the stator stiffness is about 200 MN/M and the minimum stiffness is about 500 kN/m at 100 Hz. It is clear that the disturbance rejection properties are almost the same for these different operating conditions. The peaks 800 Hz and 2.2 kHz correspond to the first two bending modes of the rotor. The peaks corresponding to the first bending mode are much more significant when the rotor is spinning at 34,800 rpm. Figure 13 shows the disturbance rejection when the rotor is at rest for reference model bandwidths of 100 and 200 rad/sec. The improvement in disturbance rejection properties with increase in reference model bandwidth is evident in this figure.

5 Conclusions

This paper has presented simple model for active magnetic bearings. The key point of the paper was the implementation of the Time Delay Control to such systems. The effectiveness of the digital control algorithm was first validated using several simulations which are based on linear and nonlinear models for the bearing including bending mode effects. Several experiments were conducted for spinning and nonspinning conditions. These include time responses, closed loop frequency responses and disturbance rejection responses. Evaluations were performed at bearing rotational speeds of 10,900 rpm, 20,100 rpm, 30,400 rpm and 34,800 rpm with Time Delay Controller bandwidths of 100 and 200 rad/sec. The digital controller presented shows an extremely high performance for the prototype considered by maintaining almost the same desirable dynamic behavior over the whole range of speeds.

Acknowledgements

The authors gratefully acknowledge the support of Ebara Research Corporation, Ltd. of Japan. The authors express their special appreciation to Mr. Y. Kanemitsu for his continuous assistance, and to Mr. K. Watanabe for his participation during his visit at M.I.T.

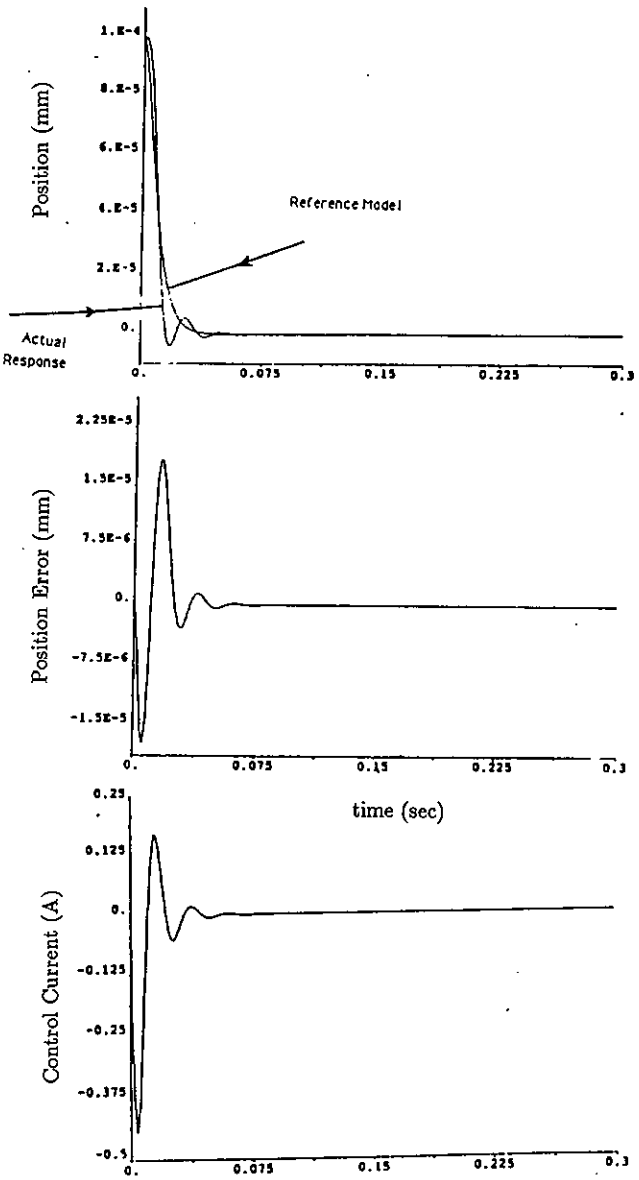

Figure 6: Simulated Flexible Body Model for x_2 Axis. Reference Model: $\omega_n = 200$ rad/sec, $\zeta = 1$, $T_s = 4$ kHz. Flexible Mode: $f_n = 875$ Hz, $\zeta = 0.001$, $m_{eff} = 0.5$ Kg

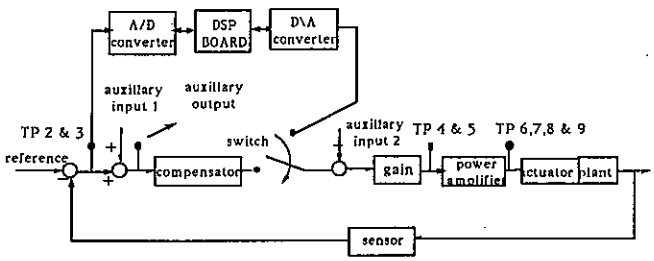

Figure 7: Block Diagram for the Analog and Digital Control

References

[1] Astrom, K. J. and Wittenmark,B. "On Self-Tuning Regulators" Automatica, Vol. 9, 1973, pp. 185-199

[2] Craig, J.J., Hsu, P. and Sastry, S.S. "Adaptive Control of Mechanical Manipulators ." Proceeding of the IEEE International Conference on Robotic and Automation, April 7-10, 1988

[3] Dubowsky, S. and Des Forges, D. T. " The Application of Model Referenced Adaptive Control to Robotic Manipulators." ASME Journal of Dynamic Systems, Measurement and Control, 1979, 101. 193-200

[4] Hsia, T. C. "Adaptive Control of Robot Manipulators. A Review" Proceeding of the IEEE International Conference on Robotics and Automation, April 7-10,1986

[5] Hubbard, M. and McDonald, P. " Feedback Control Systems for Flywheel Radial Instabilities." 1980 Flywheel Technology Symposium Proceedings, Scottsdale, Arizona: October 1980, pp. 209-217.

[6] Kalman, R.E. " Design of Self-optimizing Control" ASME Transaction, Vol. 80, No. 2, 1958, pp. 468-478

[7] Salm, J. and Schweitzer, G. " Modeling and Control of a Flexible Rotor with Magnet Bearings." Proceedings of the Third International Conference on Vibrations in Rotating Machinery, University of York, England, September 11-13, 1984, C277/84

[8] Slotine, J. J. E. and Sastry, S. S. "Tracking Control of Nonlinear Systems Using Sliding Surfaces with Applications to Robot Manipulators " International Journal of Control, 38-2, 1983, pp. 465-492

[9] Stanway, R. and O'Reilly, J. " State Variable Feedback Control of Rotor-Bearing Suspension Systems." Proceedings of the Third International Conference on Vibrations in Rotating Machinery, University of York, U.K., September 11-13, 1984, C274/84

[10] Tomizuka, M. and Horowitz, R " Model Reference Adaptive Control of Mechanical Arm by Trial. " Transaction of Society of Instrument and Control Engineering of Japan, Vol. 14, No.6, December, 1987, pp. 706-712.(Written in Japanese)

[11] Utkin, V. I. "Equations of Sliding Mode in Discontinuous Systems", Automation and Remote Control I (II), 1972

[12] Youcef-Toumi, K. and Ito, O. "Controller Design for Systems with Unknown Dynamics", Proceedings of American Control Conference, Minneapolis, MN, June 1987.

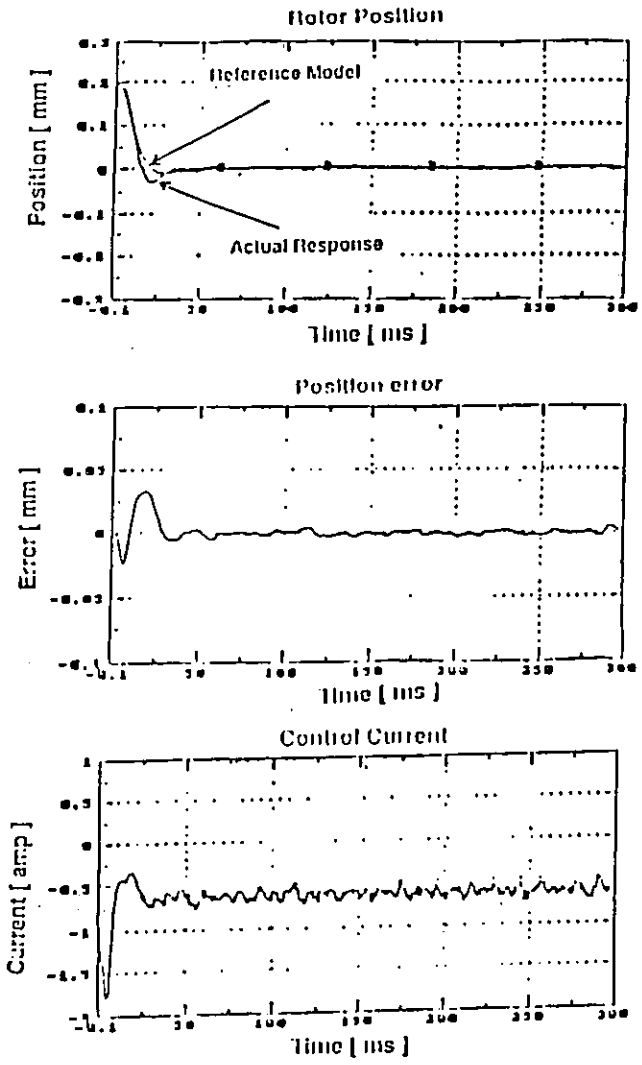

Figure 8: Experimental Time Response Data of the Thrust Bearing

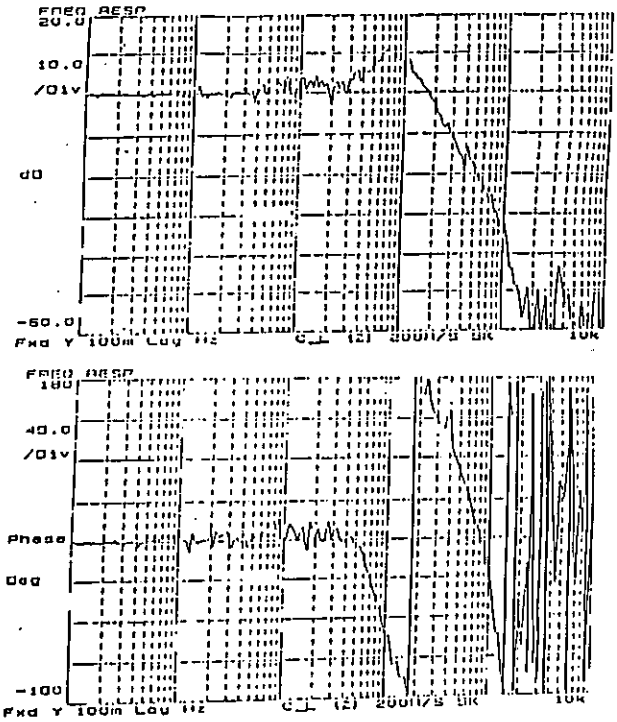

Figure 9: Closed Loop Frequency Response of Thrust Bearing

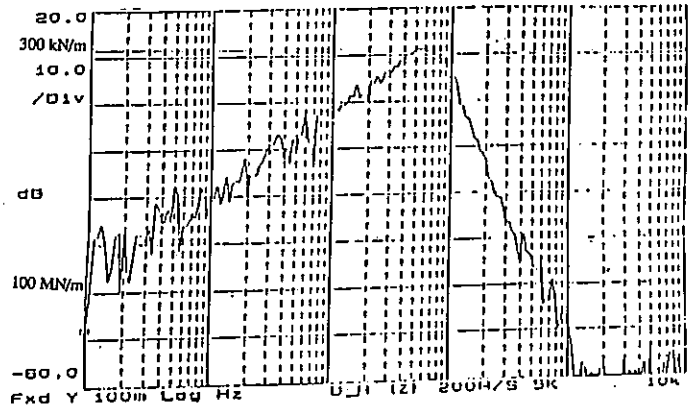

Figure 10: Disturbance Rejection of Thrust Bearing

[13] Youcef-Toumi, K. and Ito, O. "Model Reference Control using Time Delay for Nonlinear Plants with Unknown Dynamics", Proceedings of International Federation of Automatic Control World Congress, Munich, Federal Republic of Germany, July 1987.

[14] Youcef-Toumi, K. and Ito, O. "On Model Reference Control using Time Delay for Nonlinear Plants with Unknown Dynamics", MIT Report, LMP/RBT86-06, June, 1986.

[15] Youcef-Toumi, K. , "The Control of Systems with Unknown Dynamics – Application to Robot Manipulators " M.I.T. Laboratory for Manufacturing and Productivity, Report No LMP-90-003, March 1990.

[16] Youcef-Toumi, K., Reddy, S. and Vithiananthan, I. "Implementation of Time Delay Control to Active Magnetic Bearings", Report, Massachusetts Institute of Technology, 1989.

[17] Youcef-Toumi, K. and Reddy, S. "Stability Analysis of Time Delay Control with Application to High Speed Magnetic Bearings" M.I.T. Laboratory for Manufacturing and Productivity Report No. LMP-90-004, March 1990.

[18] Young, K. D. "Controller Design for a Manipulator Using Theory of Variable Structure Systems", IEEE Transaction, SMC-8-2, pp.101-109, 1978

[19] Young, K.D. and Kwatny, H. G. "Variable Structure Servomechanism Design and Applications to Overspeed Protection Control." , Vol. 18, 1982, pp. 385-400

[20] Zlotykamien, H . "The Active Magnetic Bearing Enables Optimum Control of Machine Vibrations", 4th International Conference Vibrations in Rotating Machinery, Edinburgh, Scotland, Sept. 1988.

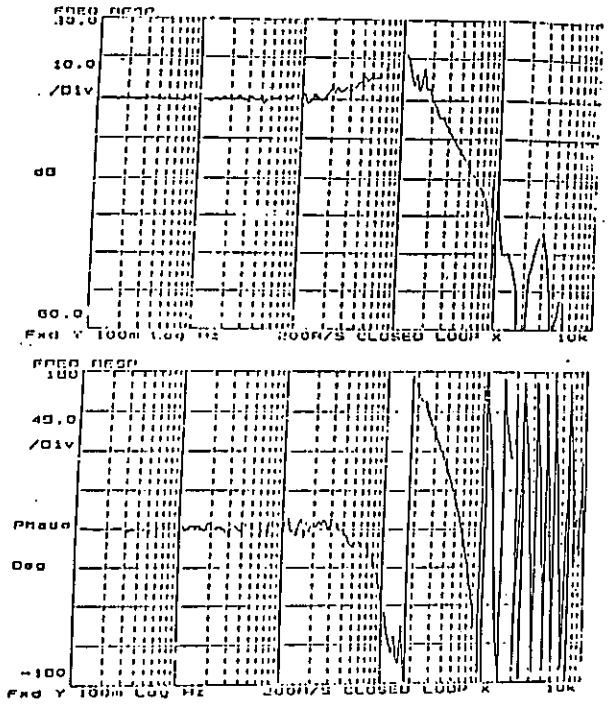

Figure 11: Closed Loop Frequency Response of Radial Bearing

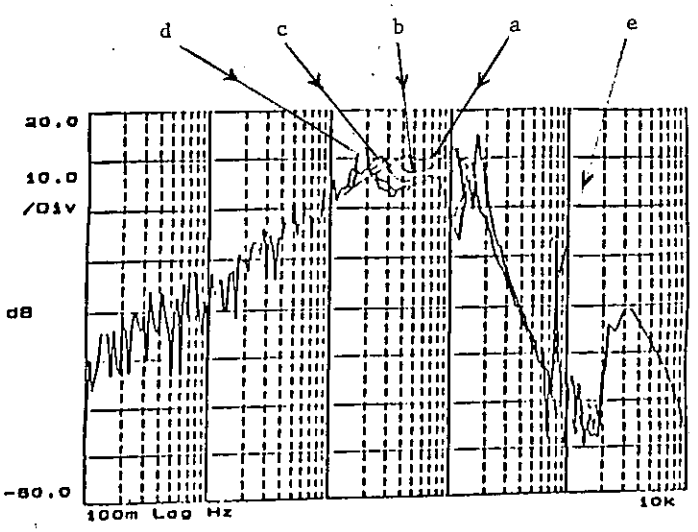

Figure 12: Disturbance Rejection of Radial Bearing: (a) at rest, (b) 10,900 rpm, (c) 20,100 rpm, (d) 30,400 rpm, (e) 34,800 rpm

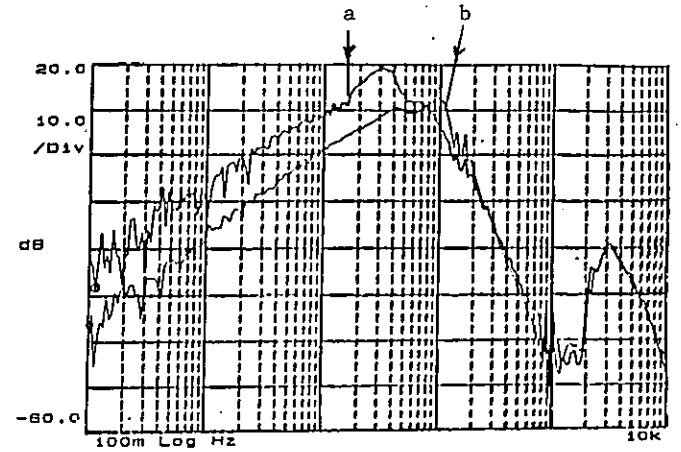

Figure 13: Disturbance Rejection of Radial Bearing with Rotor at Rest (a) bandwidth = 100 rad/sec (b) bandwidth = 200 rad/sec

2nd International Symposium on Magnetic Beaing
July 12-14, 1990, Tokyo, Japan

SELF-TUNING DIGITAL STATE CONTROLLER FOR ACTIVE MAGNETIC BEARINGS

M.BRUNET and J.RIOLAND

S2M, BP 2282, 27950 SAINT-MARCEL (France)

Abstract. State methods are well suited to control Active Magnetic Bearings for supercritical rotors and now digital state controllers implemented on a signal processor system are used by S2M. The mechanical design analysis of the rotor allows a computer-aided design of the optimal observer and controller. The tuning of the observer and controller is automatically done on the actual shaft by the signal processor, thus reducing time and increasing performances, reliability and maintainability of Active Magnetic Bearings.

Keywords. Active magnetic bearings, state variable control, self-optimisation, signalprocessor.

1. INTRODUCTION

The dynamic performances of Active Magnetic Bearings make them well suited to suppress vibrations of flexible shafts allowing them to pass successfully many critical speeds.

The development of digital signal processors gives the opportunity to implement economically complex state variable controls even for very fast rotors (up to 120,000 rpm). The use of state variable controllers in these applications is only possible with a computer-aided commissioning.

Therefore, this paper describes a self-tuning state variable control system for the active magnetic bearings. The necessary state variables are obtained by an observer using only the signals of the position detectors associated with the magnetic bearings. A signal processor system performs the automatic tuning procedure of the controller and observer by means of an identification procedure.

2. COMPUTER AIDED DESIGN OF ROTORS:

2.1. Initial design:

The mechanical design of rotors is always aided by computer using a finite element method. The undamped structure is described by its geometry and the mechanical properties of the materials. The modal method is used for solving the differential system: displacements are then linear combinations of a reduced number of modal deformations associated with the eigen frequencies. The computer gives the critical speeds, the evolution of the natural frequencies and modal damping with the rotation speed, and the associated dynamic deformations.
Using the computed eigenvalues and eigenvectors we can establish a state model (figure 1) of the free-free shaft (without bearings):

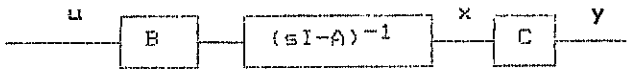

figure 1

$$x' = [A]\,x + [B]\,u$$
$$y = [C]\,x$$

where
x is the state vector (modal coordinates and derivative)
x' is the state vector derivative
y is the observation vector (positions at detectors locations)
u is the control vector (forces applied by the magnetic bearings)
A, B ,C are the state matrix of the system.

This mechanical model is completed by the filtering model (antialiasing filters and feedbacked power amplifiers). The negative stiffness of the electromagnets is corrected by an analog flux feedback in each amplifier in order to avoid non minimum phase system.

This modelisation allows optimisation of actuators and detectors positioning, and if necessary modifications of geometry or materials of the shaft. A first controller can be computed and its performances observed in simulation.

2.2. Modal analysis of the actual shaft:

When it is possible a modal analysis is done on the shaft just after manufacturing and before connecting with the stator. This analysis allows us to verify deviations from the initial design and reveals the influence of damping effects. On turbomachines rotors we can observe hysteretic damping.

This damping, due to the shrinkage of the different parts on the shaft, does not affect the magnitude of the resonances but gives phase rotations between excitation and measurement. The modelisation of this damping can be performed considering complex eigenvectors associated with the eigenvalues.

The transfer function $H_{ij}(w)$ between two nodes i and j at the frequency w is then:

$$H_{ij}(w) = \sum_{r=1}^{n} \Phi_{ri}\ \Phi_{rj} \ / \ (w_r^2 - w^2)$$

where Φ_{ri} and Φ_{rj} are the complex residues associated with the nodes i and j, for the eigen value w_r.

These complex residues cannot be used by the system analysis tools available today and an aproximative model of the phenomena with real parameters had been chosen. These parameters are identified from the measured transfer functions using a least squares method operating with complex values.

Fig 2 shows the geometry of an experimental flexible shaft, fig 3 the modal deformations computed with the finite elements modelisation, fig 4 the transfer function measured on the actual shaft and the response of the model identified with the least squares method.

The initial model can be updated and a better controller can be computed and tested in simulation and programmed in the digital signal processor.

But often the modal analysis is not possible on the free shaft and a self-commissioning procedure must be used on the machine implemented in a process.

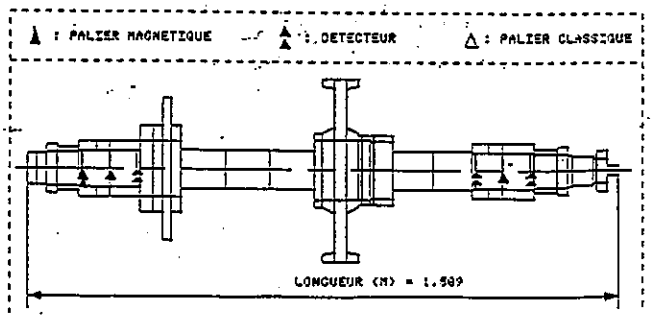

Figure 2

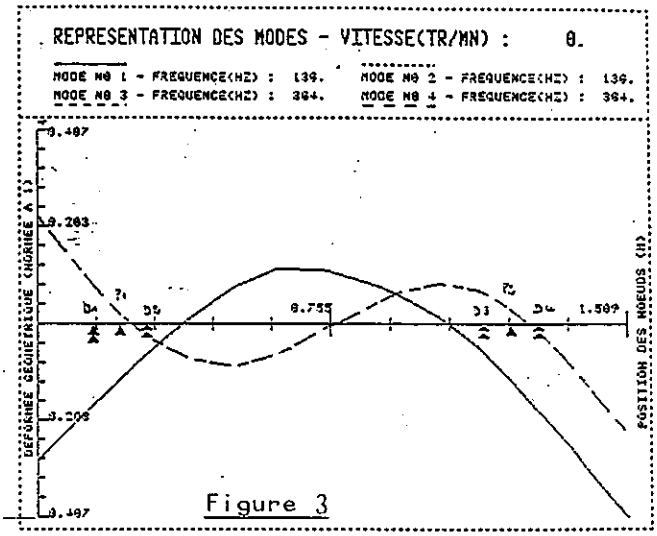

Figure 3

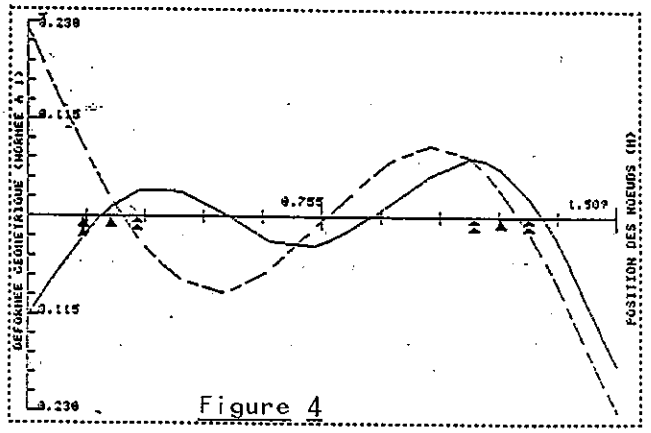

Figure 4

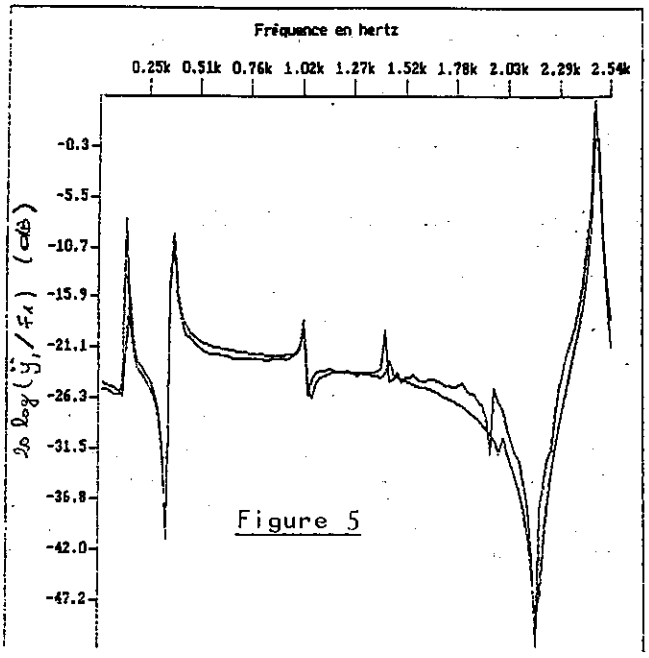

Figure 5

3. COMPUTER AIDED DESIGN OF THE CONTROLLERS:

3.1. Description of the state variable feedback controller:

The state controller consists of the weighted feedback of the modal state variables. The size of the model to use for the controller is determined by the rotation speed of the shaft. Generally, all the modes whose frequencies are under twice the rotation frequency must be damped. In order to have a good phase representation in the interesting bandwidth the complete model can be reduced using a residualisation method . After choosing the sampling frequency we compute the state transition matrix of the system and the state feedback vector F using the linear quadratic method (figure 6).

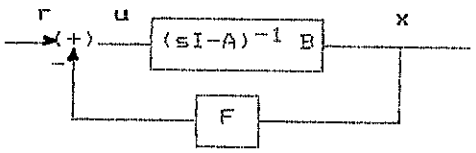

Figure 6

3.2. States observer configuration:

The state variables of the system are not all measurable. Only the position of the shaft is transmitted to the signal processor system. The remaining state variables, as well as the magnetic bearing force, must be computed by the observer. The error signal between the measured and the estimated shaft position $(y_m - y_e)$ is feedbacked by the observer gain vector H.

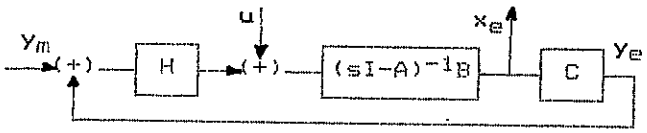

Figure 7

Dependent on the feedback coefficients, the observer error vanishes with an adjustable dynamic performance. The observer gain vector H is computed using Kalman Bucy Filter method.

3.3. Self-tuning control system:

Generally rotors of turbomachines are not available in their final state for modal analysis in laboratory. Then the commissioning of the controller has to be done on a rotor assembled with a complete machine using a self-optimisation procedure. The microcomputer which realizes the state control can compute the auto-commissioning without additional hardware costs.

In order to achieve a secure identification, an off-line procedure is selected. During this step, the shaft is supported by the magnetic bearings with very low stiffness, without damping the natural frequencies. The modal analysis operates automatically using magnetic bearings as actuators and position dectectors as sensors. The frequency response functions are determinated from the impulse response functions by means of a discrete Fourier transformation. Using the identification method described precedently the model parameters are corrected and then the state feedback vector F and the observer gain vector H can be computed and applied to the system. Finally, the integrators associated with each control loop are tuned until the step response of the closed loops matches a desired step response.

3.4. Disturbance observer:

Some machines require an unbalance control system. A digital synchronous observer using moving coordinates axes gives to the regulators information on the unbalance, allowing, for some applications, the rotation of the shaft around its inertial axis or, for other applications, forcing the rotation around the geometrical axis.

4. HARDWARE IMPLEMENTATION:

The system philosophy was conducted with several targets:

-Efficient man/machine interfaces for simple start-up and short repair times in the event of misfunctions,
-Easy adaptation on every rotor,
-Self commissionning of the controller,
-Access to internal system variables and parameters for monitoring and manual tuning,
-Provision for interfaces to serve host computers.

The system was designed using separate subsystem for regulation tasks and for monitoring tasks.

4.1. Regulation system:

The sensors signals are demodulated, filtered and digitized. These 12 bits information are transmitted to a signal processor which realizes state observers, state controllers, and unbalance observer.
The computed control signals are then transmitted, via D/A converters, to power amplifiers.

4.2. Monitoring system:

A microcontroller (for the "small" machines) or a microprocessor (for the other machines) is

interfaced with the digital signal processor system via a dual port RAM. A parallel link allows exchanges with a standard Personal Computer. This computer conducts the self-commissioning procedure from the identification phase to the parameters programming in EEPROM.
When the system is running, the PC allows monitoring of all parameters of the system (currents, deplacements, unbalance, speed of the rotor, temperatures...) and can execute a full diagnosis of the Active Magnetic bearings and its electronic. If necessary, a LCD panel on the electronic cabinet can display information on the machine status or failure diagnosis. Serial links can serve high order control levels.

5. CONCLUSION:

The use of the signal processor system permits the implementation of state variable controllers even for very fast rotors. A good dynamic performance of Active Magnetic Bearings is then achieved. The off-line identification procedure ensures a good model approximation, even if the shaft has a rather complex structure.

REFERENCES

Bühler, H. Réglages échantillonnés Volume 2, Presses polytechniques romandes.

Najim, M. Modélisation et identification en traitement du signal, Masson.

2nd International Symposium on Magnetic Beaing
July 12-14, 1990, Tokyo, Japan

DIGITAL CONTROL SYSTEM FOR MAGNETIC BEARINGS WITH AUTOMATIC BALANCING

T.Higuchi* , T.Mizuno** and M.Tsukamoto***
*Institute of Industrial Science, University of Tokyo,Minato-ku,Tokyo 106,Japan
**Faculty of Engineering, Saitama University,Shimo-Okubo Urawa 338,Japan
***Asahi Chemical Industry Co.,Ltd.,Fuji-shi,Shizuoka 416,Japan

Abstract

The principles and features of a control system for magnetic bearings with an unbalanced rotor are discussed. Unbalance of the rotor causes whirling motion of the rotor and vibratory force acting on bearings. Two special ways to control magnetic bearings with an unbalanced rotor have been presented. One is compensation for unbalance and the other is automatic balancing control. When the spinning axis corresponds with the principal axis of inertia by the automatic balancing control, no reaction force acts on the base of magnetic bearings. In this paper, control system for automatic balancing using observer for totally active magnetic bearing is discussed and implemented by a digital control system. The relationship between the compensation for unbalance and the automatic balancing control is clarified. The effectiveness of the proposed control system is demonstrated by numerical simulation and experiments.

1. Introduction

In a rotating machine unbalance of the rotor causes whirling motion of the rotor and vibratory force transmitting to the base through bearings. These problems can be solved by using a totally active magnetic bearing system, which is able to control its suspension force dynamically. There are two methods to solve the problems caused by unbalance. The first is called compensation for unbalance. With this method, the rotor precisely rotates around the geometrical axis. The other is called an automatic balancing control system in which the spinning axis corresponds with the principal axis of inertia. No reaction force acts on the base of magnetic bearings with this method.

The authors developed a compensator for unbalance using an observer for totally active magnetic bearings[1]. Habermann et al. developed compensation for unbalance and automatic balancing control by utilizing coordinate conversion between fixed coordinate and rotating coordinate and by filtering tuned with the spinning frequency[2][3][4]. Reinig et al. studied compensation for unbalance and automatic balancing control using an observer, but they discussed on only a simplified model of 2 degrees-of-freedom magnetic bearing[5]. In this paper, a compensator for automatic balancing using an observer for totally active magnetic bearing is developed.

The control systems of compensation for unbalance and automatic balancing are implemented by digital controller. The nonlinear characteristics of electromagnet is compensated for linearity. The relationship between compensation for unbalance and automatic balancing control is discussed from the standpoint of the observability. The effectiveness of the proposed control system is demonstrated by numerical simulation and experiments.

2. Modeling

2-1. Structure of magnetic bearings[6]

Fig.1 shows a totally active DC-type magnetic bearing system. It consists of an axial magnetic bearing, two radial magnetic bearings, a motor-stator and a rotor. The axial bearing has a pair of electromagnets and each radial magnetic bearing has two pairs of electromagnets. To describe dynamics of a magnetic bearing system, we define coordinate axes and forces acting on the rotor as shown in Fig.2; in the equilibrium the center of mass of the rotor G is at the coordinate origin O and the axis of the rotor corresponds with z-axis. In this paper, we assume that the rotor is a rigid body and that the rotor spins at a constant angular velocity.

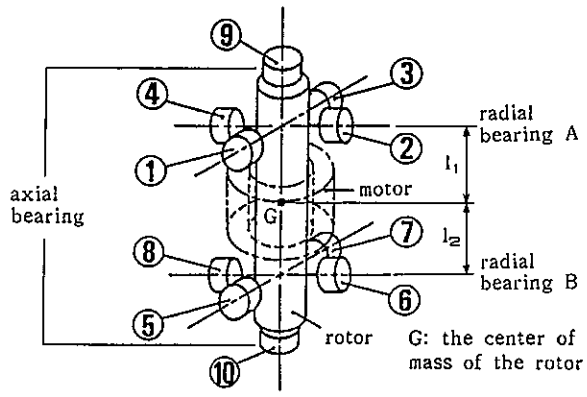

Fig.1 Basic structure of a totally active magnetic bearing system
(①-⑩:electromagnets)

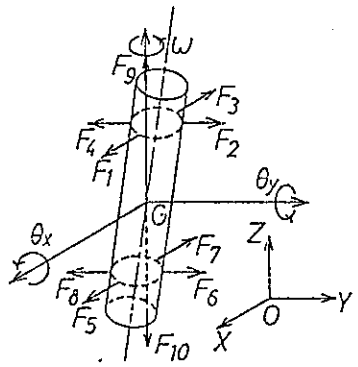

Fig.2 Coordinates and forces acting on the rotor

2-2. Linearization of controlled system

In designing a control system, it is usually assumed that the system to be controlled has linear characteristics. However, electromagnets used for magnetic bearings have nonlinear characteristics as follows:

$$F_n=Q_n\cdot I_n^2/D_n^2, \quad n=1,\ldots,10, \tag{1}$$

F_n: the attractive force of electromagnet n,
Q_n: the coefficient of electromagnet n,
I_n: the coil current,
D_n: the gap between the magnet pole faces and the reaction surface.

In conventional method characteristics of electromagnets are linearized by adding bias current into the coil current. The force of a pair of electromagnets can be given by

$$\begin{aligned}F_p-F_m&=Q_p\cdot I_p^2/D_p^2-Q_m\cdot I_m^2/D_m^2\\&=Q\cdot(I_o+i)^2/(D_o-d)^2-Q\cdot(I_o-i)^2/(D_o+d)^2\\&=4Q\cdot I_o/D_o^2\cdot i+4Q\cdot I_o^2/D_o^3\cdot d\end{aligned} \tag{2}$$

where,
$Q=Q_p=Q_m$, $I_p=I_o+i$, $I_m=I_o-i$, $D_p=D_o-d$, $D_m=D_o+d$,
D_o,d: stationary and incremental component of D_n,
I_o: bias current, i:feedback current,
(p,m)=(1,3),(2,4),(5,7),(6,8),(9,10)
:the numbers of a pair of electromagnets.

To linearize sufficiently, the bias current must be adequately larger than the feedback current. We introduce a direct linearization method[7] which linearize the characteristics of electromagnet by the following nonlinear compensation:

$$F\geqq 0\ ;\ I_p=D_p\sqrt{F/Q}\ ,\ I_m=0 \tag{3a}$$

$$F<0\ ;\ I_p=0\ ,\ I_m=D_m\sqrt{-F/Q} \tag{3b}$$

F: the force acting on the rotor by a pair of electromagnets given by the feedback

This method renders the bias current unnecessary. Therefore, heat generation and consumption of electric power of electromagnet are minimized. The eddy current in the rotor caused by the high speed spinning becomes sufficiently small and so the heat generation of the rotor and rotation loss are also minimized.

2-3. State equations

The state equations of the magnetic bearings with the direct linearization method are developed as the following procedures. The dynamics of the rotor is described as inertial system with the gyroscopic effect. The whole system can be divided to subsystems related to translation and rotation.

The subsystem of translation along x-axis and y-axis is described as

$$\frac{d}{dt}x_t=A_t^c x_t+B_t^c u_t \tag{4}$$

$$x_t=[x_g,v_x,y_g,v_y]^T\ ,\ u_t=[F_x,F_y]^T$$

$$A_t^c=\begin{bmatrix}0&1&0&0\\0&0&0&0\\0&0&0&1\\0&0&0&0\end{bmatrix}\ ,\ B_t^c=\begin{bmatrix}0&0\\b_t&0\\0&0\\0&b_t\end{bmatrix}.$$

The subsystem of rotation around x-axis and y-axis is described as

$$\frac{d}{dt}x_r=A_r^c x_r+B_r^c u_r \tag{5}$$

$$x_r=[\theta_x,\omega_x,\theta_y,\omega_y]^T\ ,\ u_r=[M_x\ ,\ M_y]^T$$

$$A_r^c=\begin{bmatrix}0&1&0&0\\0&0&0&-a_k\\0&0&0&1\\0&a_k&0&0\end{bmatrix}\ ,\ B_r^c=\begin{bmatrix}0&0\\b_r&0\\0&0\\0&b_r\end{bmatrix}.$$

The subsystem of translation along z-axis is described as

$$\frac{d}{dt}x_z=A_z^c x_z+B_z^c u_z \tag{6}$$

$$x_z=[z_g,v_z]^T\ ,\ u_z=F_z$$

$$A_z^c=\begin{bmatrix}0&1\\0&0\end{bmatrix}\ ,\ B_z^c=\begin{bmatrix}0\\b_z\end{bmatrix},$$

where,
x_g,y_g,z_g: displacement of center of mass G,
v_x,v_y,v_z: velocity of center of mass G,
θ_x,θ_y: tilting angle of the rotor axis,
ω_x,ω_y: derivative of θ_x and θ_y,
ω_z: angular velocity of spinning,
F_x,F_y,F_z: force of electromagnet acting on the rotor,
M_x,M_y: moment of electromagnet acting on the rotor,
$a_k=I_a/I_r\cdot\omega_z$,
$b_t=1/m$, $b_r=1/I_r$, $b_z=1/m$,
m: mass of the rotor,
I_a,I_r: polar and transverse mass moments of inertia of the rotor.

The forces F_x,F_y,F_z and the moments M_x,M_y are given by

$$F_x=(F_1-F_3)+(F_5-F_7),M_x=-(F_2-F_4)l_1+(F_6-F_8)l_2, \tag{7a}$$

$$F_y=(F_2-F_4)+(F_6-F_8),M_y=(F_1-F_3)l_1-(F_5-F_7)l_2, \tag{7b}$$

$$F_z=F_9-F_{10}, \tag{7c}$$

where,

l_1, l_2: distance between the center of mass G and the magnets of radial bearing A and B as shown in Fig.1.

3. Control system with automatic balancing

3-1. Model with unbalance

When the rotor is unbalanced, that is, the geometrical axis of the rotor is different from the principal axis of inertia, the rotor spins with whirling motion. Unbalance of the rotor can be divided to static unbalance and dynamic unbalance. The static unbalance affects only the subsystem related to translation along x and y axes. The dynamic unbalance affects only the subsystem related to rotation. If the parameter a_k equals to zero in the subsystem related rotation, it has the same form in the state equations as the subsystem related to translation along x and y axes. There is no influence of unbalance on the subsystem related to translation along z-axis. It is allowed to discuss only the subsystem related to rotation without loosing generality.

To construct a digital control system, we discretize the system (A_r^c, B_r^c) using a zero-order holder and let (A,B) denote the obtained digital system. State variable x_r and input u_r are represented by x and u, respectively, in shortening. The digital system is written as follows:

$$x(k+1)=Ax(k)+Bu(k) . \tag{8}$$

Because of unbalance, disturbance force seems to act on the rotor. It is represented by the following free system:

$$\frac{d}{dt}w_u=A_d^c w_u \ , \ w_u=[M_{dx}, M_{dy}]^T , \tag{9}$$

where,

M_{dx}, M_{dy}: moment caused by unbalance,

$$A_d^c=\begin{bmatrix}0 & -\omega_z \\ \omega_z & 0\end{bmatrix} .$$

To construct a digital control system, we discretize the free system A_d^c using a zero-order holder and let A_d denote the obtained digital free system. Expansion system including disturbance can be written as follows:

$$x_{eu}(k+1)=A_u x_{eu}(k)+B_u u_u(k) , \tag{10a}$$

$$y_u(k)=C_u x_{eu}(k) , \tag{10b}$$

$$x_{eu}(k)=\begin{bmatrix}x_u(k) \\ w_u(k)\end{bmatrix} , \ A_u=\begin{bmatrix}A & B \\ O & A_d\end{bmatrix} ,$$

$$B_u=\begin{bmatrix}B \\ O\end{bmatrix} , \ C_u=[C \ O] , \ C=\begin{bmatrix}1&0&0&0 \\ 0&0&1&0\end{bmatrix} ,$$

where,

x_u: state variable based on the geometrical axis of the rotor,

y_u: output generated from sensor signals.

This augmented system can be represented by another form. Instead of looking upon unbalance as disturbance force, we can think of unbalance as observatory disturbance. That is, the sensors should indicate the tilting angle of the principal axis of inertia. But because of unbalance, sensor outputs include geometrical errors; the difference between the geometrical axis of the rotor and the principal axis of inertia. The geometrical errors can be also represented by the following free system: Note that it is the same form as eq.(9).

$$\frac{d}{dt}w_a=A_d^c w_a \ , \ w_a=[\theta_{dx}, \theta_{dy}]^T , \tag{11a}$$

where,

θ_{dx}, θ_{dy}: difference between the geometrical axis of the rotor and the principal axis of inertia.

An expansion system including geometrical errors can be written as follows:

$$x_{ea}(k+1)=A_a x_{ea}(k)+B_a u_a(k) , \tag{12a}$$

$$y_a(k)=C_a x_{ea}(k) , \tag{12b}$$

$$x_{ea}(k)=\begin{bmatrix}x_a(k) \\ w_a(k)\end{bmatrix} , \ A_a=\begin{bmatrix}A & O \\ O & A_d\end{bmatrix} ,$$

$$B_a=\begin{bmatrix}B \\ O\end{bmatrix} , \ C_a=[C \ I] , \ C=\begin{bmatrix}1&0&0&0 \\ 0&0&1&0\end{bmatrix} ,$$

where,

x_a: state variable based on the principal axis of inertia,

y_a: output generated from sensor signals.

3-2. Structure of controller

The authors developed compensation for unbalance using an observer[1]. In this method, a system to be controlled is represented by eq.(10). The disturbance force is estimated by a minimal order observer and cancelled by bearing force according to the estimation. In this paper we propose an automatic balancing system using an observer for totally active magnetic bearings. In this method, the system to be controlled is represented by eq.(12) and the state variables represent the motion of the principal axis of inertia. By constructing feedback system utilizing these state variables, the rotor spins around the principal axis of inertia. Since the state variables cannot be measured directly, they are estimated by an observer. In this paper, we use a full-order observer. Controllers of compensation for unbalance and automatic balancing are given by follows; ^ shows estimated value.

compensation for unbalance

$$\hat{x}_{eu}(k+1)=(A_u-K_u C_u)\hat{x}_{eu}(k) + B_u u_u(k)+K_u y_u(k) , \tag{13a}$$

$$u_u(k)=F_u \hat{x}_{eu}(k) , \tag{13b}$$

$$\hat{X}_{eu}(k)=\begin{bmatrix}\hat{X}_u(k)\\ \hat{W}_u(k)\end{bmatrix},\quad K_u=\begin{bmatrix}K_{ux}\\ K_{uw}\end{bmatrix},$$

$$F_u=[F\ \ -I],$$

automatic balancing control

$$\hat{X}_{ea}(k+1)=(A_a-K_aC_a)\hat{X}_{ea}(k)+B_au_a(k)+K_ay_a(k), \tag{14a}$$

$$u_a(k)=F_a\hat{X}_{ea}(k), \tag{14b}$$

$$\hat{X}_{ea}(k)=\begin{bmatrix}\hat{X}_a(k)\\ \hat{W}_a(k)\end{bmatrix},\quad K_a=\begin{bmatrix}K_{ax}\\ K_{aw}\end{bmatrix},$$

$$F_a=[F\ \ 0],$$

where,

K_u,K_a: gain matrices of observer

F: feedback matrix of regulator

In these forms, we can hardly understand the structure of the whole system. We rewrite the whole system using estimating errors:

$$\xi_u=\hat{X}_u-X_u,\quad \eta_u=\hat{W}_u-W_u$$
$$\xi_a=\hat{X}_a-X_a,\quad \eta_a=\hat{W}_a-W_a. \tag{15}$$

Then, we get the following equations:

compensation for unbalance

$$\begin{bmatrix}X_u(k+1)\\ \xi_u(k+1)\\ \eta_u(k+1)\\ W_u(k+1)\end{bmatrix}=\begin{bmatrix}A+BF & BF & -B & 0\\ 0 & A-K_{ux}C & B & 0\\ 0 & -K_{uw}C & A_d & 0\\ 0 & 0 & 0 & A_d\end{bmatrix}\begin{bmatrix}X_u(k)\\ \xi_u(k)\\ \eta_u(k)\\ W_u(k)\end{bmatrix}$$

$$y_u(k)=\begin{bmatrix}C & 0 & 0 & 0\end{bmatrix}\begin{bmatrix}X_u(k)\\ \xi_u(k)\\ \eta_u(k)\\ W_u(k)\end{bmatrix}$$

$$u_u(k)=\begin{bmatrix}F & F & -I & -I\end{bmatrix}\begin{bmatrix}X_u(k)\\ \xi_u(k)\\ \eta_u(k)\\ W_u(k)\end{bmatrix} \tag{16}$$

automatic balancing control

$$\begin{bmatrix}X_a(k+1)\\ \xi_a(k+1)\\ \eta_a(k+1)\\ W_a(k+1)\end{bmatrix}=\begin{bmatrix}A+BF & BF & 0 & 0\\ 0 & A-K_{ax}C & -K_{ax} & 0\\ 0 & -K_{aw}C & A_d-K_{aw} & 0\\ 0 & 0 & 0 & A_d\end{bmatrix}\begin{bmatrix}X_a(k)\\ \xi_a(k)\\ \eta_a(k)\\ W_a(k)\end{bmatrix}$$

$$y_a(k)=\begin{bmatrix}C & 0 & 0 & I\end{bmatrix}\begin{bmatrix}X_a(k)\\ \xi_a(k)\\ \eta_a(k)\\ W_a(k)\end{bmatrix}$$

$$u_a(k)=\begin{bmatrix}F & F & 0 & 0\end{bmatrix}\begin{bmatrix}X_a(k)\\ \xi_a(k)\\ \eta_a(k)\\ W_a(k)\end{bmatrix} \tag{17}$$

Let us consider these systems in the standpoint of the observability. Generally, an unobservable system can be written as eq.(18):

$$\begin{bmatrix}X_1(k+1)\\ X_2(k+1)\end{bmatrix}=\begin{bmatrix}A_{11} & 0\\ A_{21} & A_{22}\end{bmatrix}\begin{bmatrix}X_1(k)\\ X_2(k)\end{bmatrix}, \tag{18a}$$

$$y(k)=\begin{bmatrix}C_1 & 0\end{bmatrix}\begin{bmatrix}X_1(k)\\ X_2(k)\end{bmatrix}. \tag{18b}$$

In the case of eq.(18), state variable X_2 cannot be observed from output y and A_{22} is the unobservable subsystem. Comparing eq.(16) and eq.(18), A_d is an unobservable subsystem from output y_u in the system of compensation for unbalance. Therefore, the unbalance gives no influence to output y_u. On the other hand, A_d is an unobservable subsystem from input u_a in the automatic balancing system described by eq.(17). With the automatic balancing control, the state variables are based on the principal axis of inertia and no influence can be transferred to input u_a. Therefore, the rotor rotates around the principal axis of inertia. The compensation for unbalance and the automatic balancing control are opposing each other. The controllers of those methods also have opposing structures; the system of the compensation for unbalance is unobservable from output and the automatic balancing system is unobservable from input.

In these systems the poles of regulator and

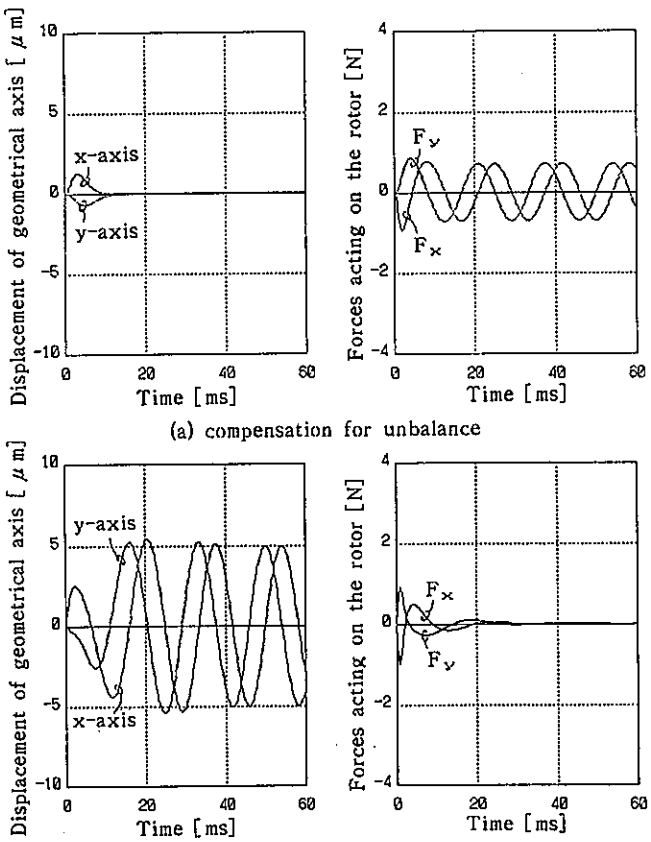

Fig.3 Calculated results

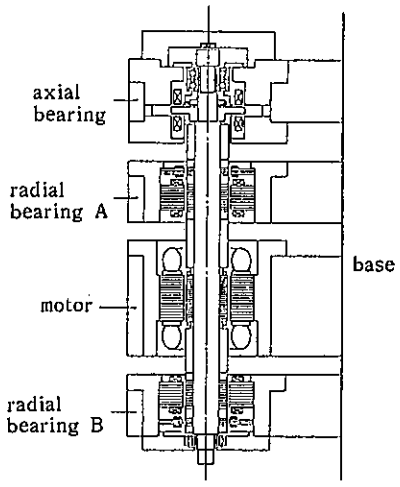

Fig.4 Structure of the experimental setup

Table 1 Parameters of the experimental setup

m	0.998	[kg]
Ir	4.26×10^{-3}	[kg·m^3]
Ia	1.01×10^{-4}	[kg·m^3]
l_1	42	[mm]
l_2	88	[mm]
Q_1~Q_8	2.5	[N·mm^2/A^2]
$D0_1$~$D0_8$	0.3	[mm]

those of observer can be assigned independently. The poles of regulator are assigned by utilizing the linear quadratic optical control theory. The poles of observer are assigned by applying the same theory for its dual system.

4. Simulation and Experiments

The effectiveness of the proposed control system is verified by numerical simulation and experiments. To compare the two control methods, we also examine compensation for unbalance.

Fig.3 shows a calculation result. Displacement of the geometrical axis converges to zero by compensation for unbalance and the forces acting on the rotor converges to zero by automatic balancing control as expected.

Fig.4 shows the section view of the experimental setup. Table 1 explains its parameters. The control system is implemented by digital controller using a digital signal processor[8]. It carries out the above control law and linearization within 0.2 msec.

Fig.5 shows some experimental results. In Fig.5(a) there is a whirling motion in response of a regulator system which is designed as if there were no unbalance. Fig.5(b) shows a result of the compensation for unbalance. The whirling motion are controlled fairly well. In the response of regulator as shown in Fig.5(a), there is an oscil-

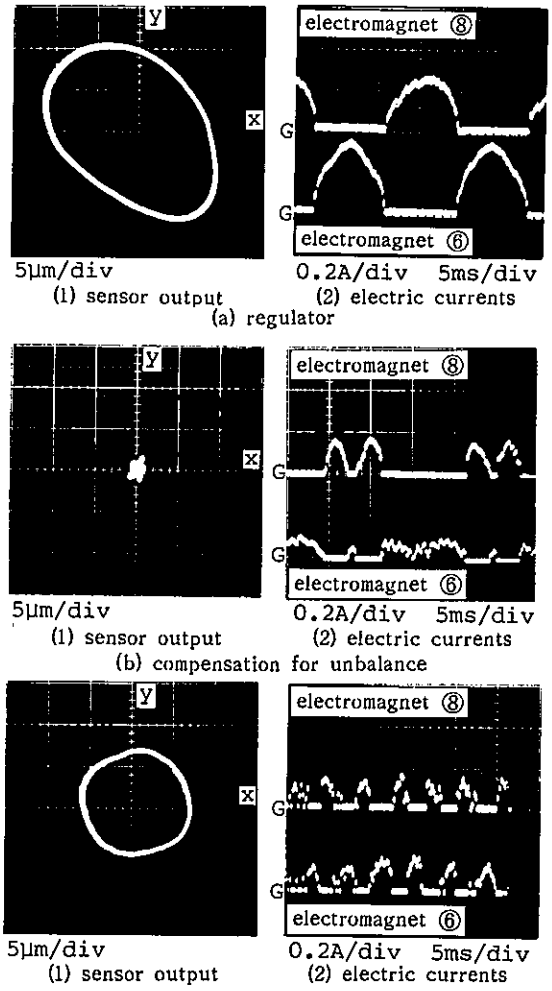

Fig.5 Experimental results

lating magnet-current synchronizing with spinning of the rotor. Fig.5(c) shows a result of automatic balancing. The magnet-current which has the frequency component of the spinning is eliminated in spite of the whirling motion. Therefore, the rotor must be rotated around the principal axis of inertia. Essentially, we have to observe attractive force of magnet. In the case of Fig.5, however, we can substitute magnet-current into attractive force of magnet, because the whirling motion is adequately smaller than the gaps between poles of magnets and the rotor.

5. Conclusion

The control system for automatic balancing using an observer for totally active magnetic bearings was developed.

The relationship between the compensation for

unbalance and the automatic balancing control was discussed from the standpoint of the observability.

The control system for automatic balancing was implemented by a digital controller. The effectiveness of proposed control system was verified by numerical simulation and experiments.

References

[1]Mizuno,T. and Higuchi,T.: Compensation for Unbalance in Magnetic Bearing System(in Japanese). Trans. SICE, Vol.20, pp.1095-1101(1984).

[2]Habermann,H. and Brunet,M.: The Active Magnetic Bearing Enables Optimum Control of Machine Vibrations, ASME International Gas Turbine Conf., 85-GT-221(1985)

[3]Habermann,H. et al.: Device for Damping the Critical Frequencies of a Rotor Suspended by a Radial Electromagnetic Bearing, United States Patent 4,128,795(1978)

[4]Habermann,H. et al.: Device for Compensating Synchronous Disturbances in Magnetic Suspension of a Rotor, United States Patent 4,121,143(1978)

[5]Reinig,K. and Desrochers,A.: Disturbance Accommodating Controllers for Rotating Mechanical Shaft, ASME Journal of Dynamic Systems, Measurement, and Control, 108, March, pp.24-31(1986)

[6]Mizuno,T. and Higuchi,T.: Design of the Control System of Totally Active Magnetic Bearing ---Structures of the Optimal Regulator---, Proc. of 1st Int. Symp. on Design and Synthesis, Tokyo(1984)

[7]Tsuda,M.,Nakamura,Y.,and Higuchi,T.: Design and Control of Magnetic Servo Levitation, Proc. of 20th Int. Conf. on Industrial Robots, pp.693-700(1989)

[8]Tsuda,M.,Nakamura,Y.,and Higuchi,T.: High-Speed Digital Controller for Magnetic Servo Levitation of Robot Mechanism,Proc. of 1st Int. Symp. on Experimental Robotics, pp.229-243(1989)

2nd International Symposium on Magnetic Beaing
July 12-14, 1990, Tokyo, Japan

THE INDUSTRIAL APPLICATIONS OF THE ACTIVE MAGNETIC BEARINGS TECHNOLOGY

Michel DUSSAUX, General Manager
SOCIETE DE MECANIQUE MAGNETIQUE
B.P. 2282 - 2, rue des Champs
27950 SAINT-MARCEL - FRANCE

ABSTRACT

This paper focuses on the main industrial applications of the active magnetic bearings and the status of these applications by the end of 1989.

1. Introduction

Active magnetic bearing (AMB) technology has been developed in S2M since 1969 for numerous different applications. The first commercial product with a rotor suspended on AMB was offered to the market in 1973. Since that date more than 1,000 machines have been equipped with AMB by S2M and its licensees. The bearings diameters manufactured range from 25 mm (1 in) to 1.25 m (50 in).

2. Fields of applications

The AMB applications are usually split in four different domains:
- aerospace applications,
- machine tool applications,
- light industry applications,
- heavy industry applications.

We shall go through the main applications of each domain.

2.1 Aerospace applications

This domain is mostly under development. The only commercial applications in this area today are:
- momentum wheel for satellites,
- turbomolecular vacuum pumps.

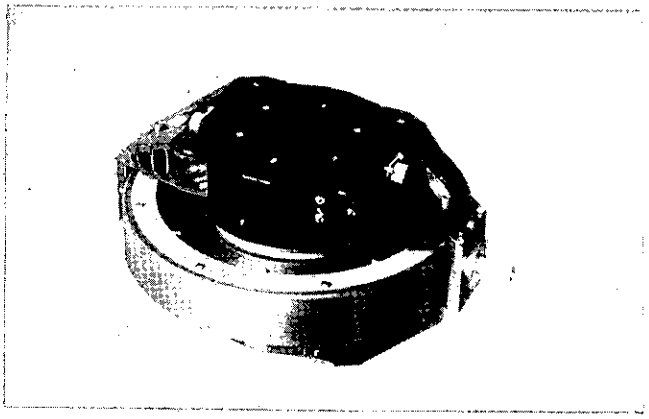

Fig. 1 Momentum wheel for satellite on AMB (Photo S2M)

The main reasons for using active magnetic bearings on momentum wheels for satellites are:
- capability to operate in vacuum,

- no friction and so very limited power consumption,

- unlimited life.

The turbomolecular vacuum pumps such as the one installed on the European space laboratory are very similar to the regular industrial ones we will talk about in paragraph 4.

The major development work going on is related to the application of the AMB technology to:
- rocket engine turbopumps,

- aircraft engines.

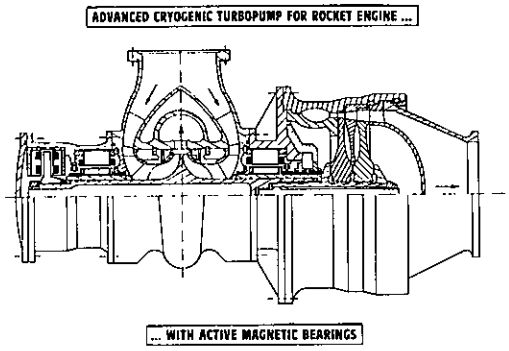

Fig. 2 Cross section of a rocket engine turbopump on AMB (Courtesy of SEP)

The main reasons for applying AMB to rocket engine turbopumps are:

- better capability to withstand high temperature (steam) and low temperature (liquid hydrogen) and temperature gradients,

- higher speed of rotation, so better performances of the machine,

- better control of the rotor dynamics,

- no wear, no lubrication, better reliability.

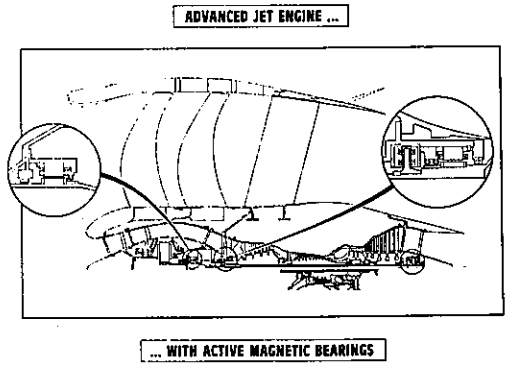

Fig. 3 Cross section of an aircraft engine on AMB (Courtesy of PRATT & WHITNEY)

As far as aircraft engines are concerned, the AMB will allow the concept of the "all electric engine" and mainly for the following reasons:
- higher speed or rotation, so better performance of the engine,
- better control of the rotor dynamics enabling more sophisticated shaft design,
- no wear, no lubrication, better reliability,
- cancellation of all the auxiliaries (pumps, filters, pipings) of the actual lube oil systems.

For both applications there is still a lot of development to perform before commercial products can be offered on the market. This development is engaged, it mostly concerns:
- compatibility of the AMB materials with the environment (eg.: LOX),
- magnetic materials with improved characteristics in order to lower the bearings size and weight,

Demonstration models are being built. The road is opened.

3. Machine tool applications

The AMB applications to the machine tool industry are mostly related to electrospindles.

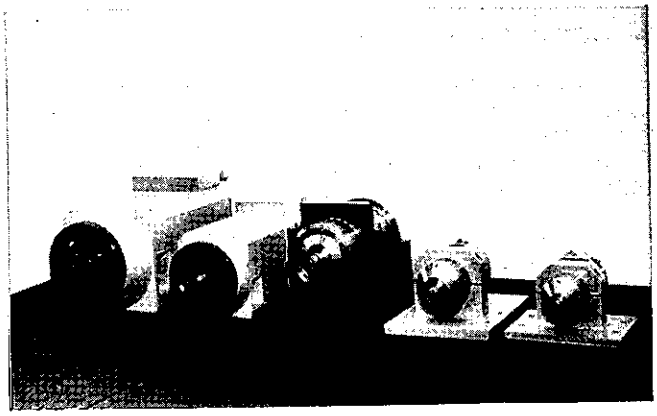

Fig. 4 Electrospindles on AMB (Photo S2M)

These electrospindes ranging from 25 kW - 30,000 rpm to 1 kW - 180,000 rpm, are used in milling and grinding (internal grinding and creep feed grinding).

The main reasons for using AMB on machine tool spindles are:
- high speed, so higher metal removal rate,
- no wear, better reliability,
- no vibrations, better accuracy,
- permanent monitoring of the operating conditions (adaptive control).

These products are now standard products manufactured on an industrial basis.

4. Light industry applications

The light industry is a puzzled family of applications. It includes many different types of machines which common characteristic is to have a light rotor (less than 50 kg) and not to be a machine tool spindle.

Some of the applications are under development such as the X-ray tube applications, others are commercial products but manufactured in limited quantities and on a customized design basis such as the pumps for liquid helium, others are standard products, manufactured on a large scale basis such as the turbomolecular vacuum pumps.

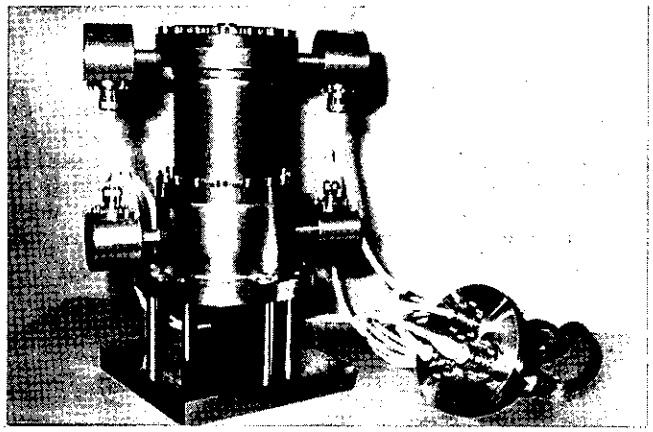

Fig. 6 Pump for liquid helium at 4 K
(Photo S2M)

For liquid helium pumps, it is obvious that the major advantage of the AMB is its capability to operate in a 4 K environment. But there are also many other reasons such as:
- very limited heat input (less than 1 W) in the liquid helium,
- high speed, so better efficiency,
- no thermal barrier, so shorter shaft.

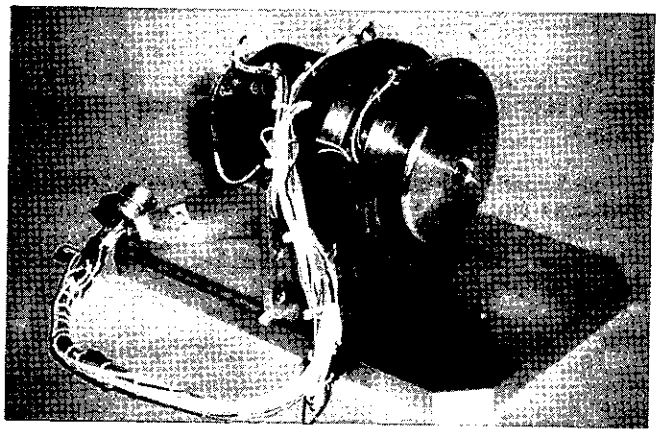

Fig. 5 X-ray tube rotating anode on AMB
(Photo S2M)

The major reasons to use AMB for the supension of the rotating anode of X-ray tubes are:

- higher speed of rotation, so capability to accept higher flux of X-rays enabling better image,

- unlimited life,

- capability to move axially the rotor and to adjust the focusing point of the electron beam on the anode,

- no vibration, no noise.

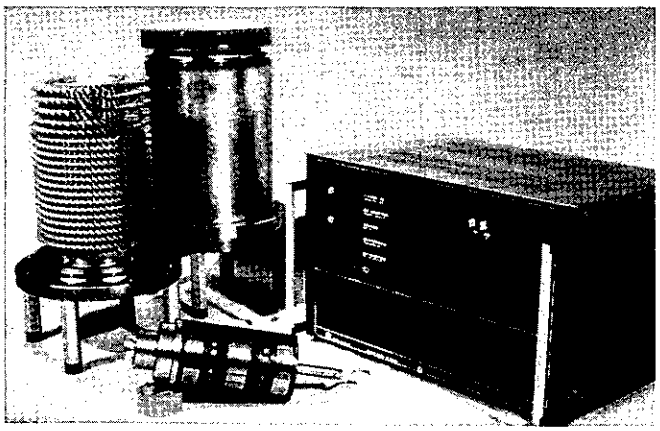

Fig. 7 Turbomolecular vacuum pump on AMB
(Photo S2M)

For turbomolecular vacuum pumps the main reasons for using AMB are:

- no pollution of the vacuum by any lube oil or grease (the auxiliary bearings are dry lubricated),
- high speed and so better level of vacuum,
- no vibrations.

There are many other light industry applications of the AMB such as: neutron chopper, liquid metal centrifuges, medical centrifuges, rotating mirrors, textile electrospindle but today they are either at the development stage or represent a very limited market. But this may change in the future.

5. Heavy industry applications

The heavy industry applications are those related to turbomachines and electrical machines where the rotor mass exceeds 50 kg and for ground (or sea) based applications.

These machines are mostly:

- compressors and drivers,

- turbo expanders,

as shown on the table hereafter.

MACHINE TYPE	QUANTITY	POWER RANGE kW / HP	NOMINAL SPEED RANGE	APPLICATION
TEST COMPRESSORS	7	20 kW to 4,200 kW	10,000 rpm to 16,000 rpm	- TEST STAND
INDUSTRIAL COMPRESSORS	31	3,100 kW to 26,100 kW	3,000 rpm to 15,700 rpm	- PIPELINE - REFINING - CHEMISTRY
HERMETIC MOTOCOMPRESSORS	1	6,000 kW	10,000 rpm	- PIPELINE
MOTORIZED BLOWERS	4	5 kW to 200 kW	3,600 rpm to 12,000 rpm	- TEST STANDS - HOT HELIUM LOOP
GAS TURBINES	1	12,000 kW / 16,300 HP	5,250 rpm	- COMPRESSOR DRIVE
STEAM TURBINES	1	3,000 kW / 4,100 HP	15,000 rpm	- COMPRESSOR DRIVE
TURBOGENERATORS	1	5,000 kW / 6,800 HP	3,000 rpm	- ENERGY RECOVERY (BLAST FURNACE GAS)
TURBO EXPANDERS	31	200 kW to 3,500 kW / 275 HP to 4,700 HP	18,000 rpm to 47,000 rpm	- AIR LIQUEFACTION - DEW POINT

This domain is the largest one for the application of the active magnetic bearings and is also the one which has grown the most drastically over the last three years.
About 10 equipment only were delivered by the end of 1986, more than 60 were delivered by the end of 1989.

The accumulated operating hours on 42 machines by the of 1989 exceeded 200,000 hours.

For all these machines the major reasons for utilizing AMB are:

- completely oil-free machines (elimination of the lube oil system),

- capability to operate at speeds higher than the third critical speed (first shaft bending mode),

- no process gas pollution by lube oil and elimination of fire hazard,
- vibration-free equipment,

- permanent monitoring of the operating conditions (preventive maintenance capability),

- reduced operating cost (lower losses, reduced maintenance),

- better reliability and availability (immediate start up capability).

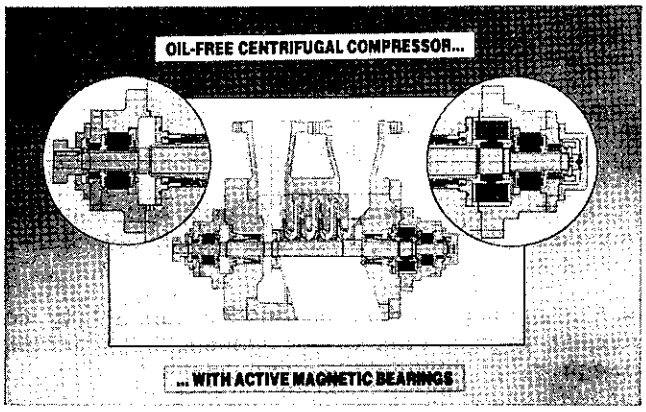

Fig. 8 Typical cross section of a compressor on AMB (Photo S2M)

a) Compressors and drivers:
The major world OEMs have compressors equipped with active magnetic bearings.

The main users are in the field of pipelines, refineries and chemical plants. The application concerns both new machines and retrofit of existing machines.

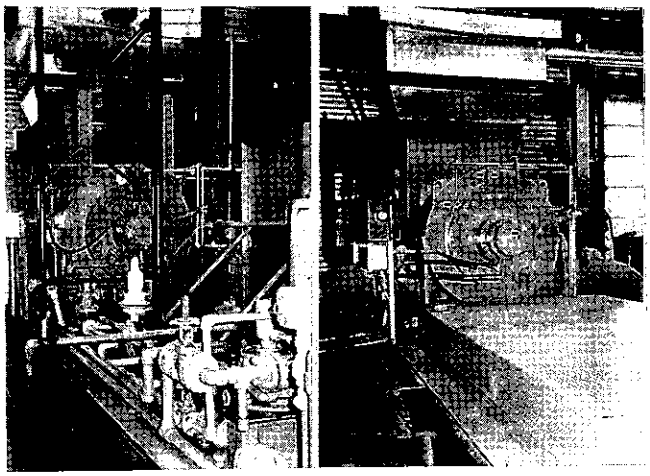

Fig. 9 Pipeline compressor before retrofit (left) and after retrofit (right) with AMB and dry seals (Courtesy of NOVA)

The drivers concerned are steam turbine and power turbines (fed by gas generators).
Development is going on for high speed electrical motors (with low speed electrical motors, a mutliplying gear is necessary and so reintroduces the lube oil).

b) Turbo expanders:

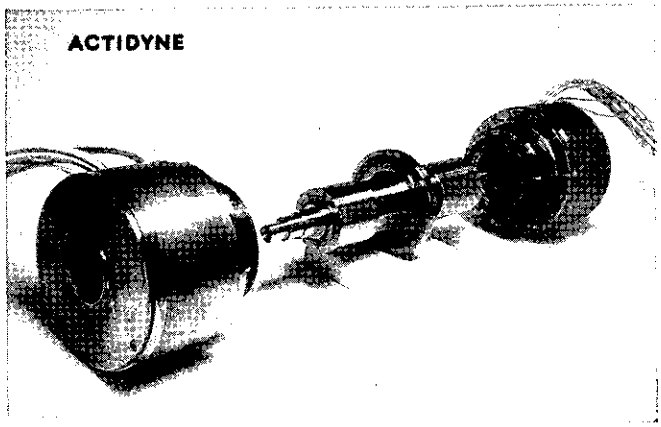

Fig. 10 Magnetic bearings cartridges and shaft of a turbo expander (Photo S2M)

These machines are used in air separation plants and gas fields for dew point control.

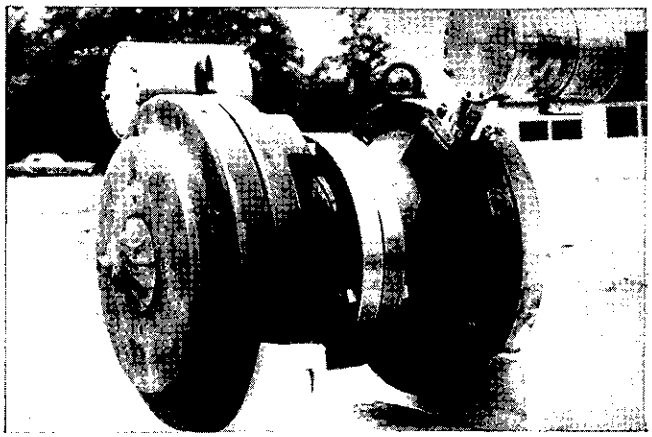

Fig. 11 Turbo expander for air separation plant (Photo S2M)

In addition to the reasons already mentioned one major advantage of the AMB is its capability to withstand a large range of temperature (-150°C on the turbine side, +150°C on the compressor side) and temperature gradients.
Up to now all the turbo expanders equipped with AMB are in operation on shore but the first turbo expanders for offshore will be operating on a North Sea platform by the end of 1990. This shows that this industry has really become very confident in the technology.

c) Other applications:
There are many other applications of the AMB to the heavy industry. The most spectacular one is related to 900 MW and 1,300 MW turbogenerators.

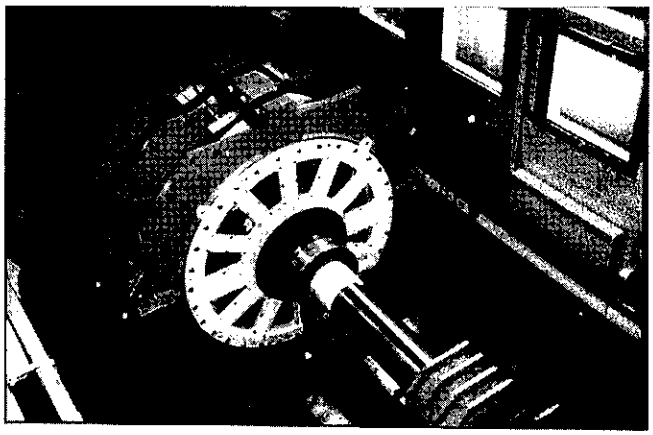

Fig. 12 The largest AMB in the world - diameter at the air gap: 1.25 m (Courtesy of EDF)

These large turbogenerators will be equipped with AMB installed on the couplings between frames and providing a 30 tons rotating force in order to reduce drastically the machine vibrations when crossing critical speed in normal slow down conditions or after a blade loss.

6. Conclusion

The characteristics of the active magnetic bearings are such that this new technology represents a revolution in the suspension of rotating shafts.

The applications already made such as the ones described in this paper, clearly indicate that this technology is no more at the infancy stage.

Of course, development will continue and the AMB technology will incorporate the new materials and components put on the market such as high permeability laminations and microprocessors.

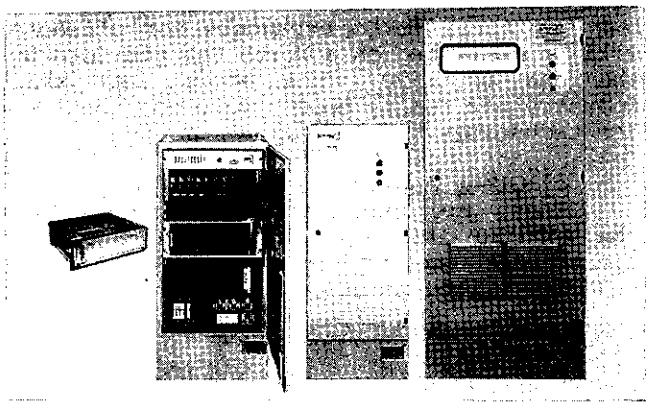

Fig. 13 Electronic controller for AMB with digital monitoring and diagnosis system

But one can say that the AMB technology has reached the level of an industrial technology applicable to industrial machines operating night and day all year long.

REFERENCES

- HABERMANN H., "The Active Magnetic Bearings Enables Optimum Damping of Flexible Rotors", ASME Paper 84-GT-117 presented at Gas Turbine Conference - Amsterdam The Netherlands 1984.

- HABERMANN H. and BRUNET M., "The Active Magnetic Bearing Enables Optimum Control of Machines Vibrations", ASME Paper 85-GT-22, presented at Gas Turbine Conference - Houston, TX, March 18-21, 1985.

- BRUNET, M., 1987, "Applications of the Active Magnetic Bearings to Turbomachinery, paper presented at the 1987 ASME COGEN-TURBO International Symposium on Turbomachinery, Combined-Cycle Technologies and Cogeneration, IGTI vo. 7, p. 191-200.

*
***
*****
****
*****
***
*

2nd International Symposium on Magnetic Beaing
July 12-14, 1990, Tokyo, Japan

Testing of a Magnetic Bearing Equipped Canned Motor Pump for Installation in the Field

Joseph Imlach*, Robert R. Humphris, Barry J. Blair, Paul E. Allaire, and David W. Lewis

*Kingsbury, Inc., Magnetic Bearings Systems Division, Philadelphia, PA, USA
Rotating Machinery and Controls Laboratory, Mechanical and Aerospace Eng. Department, University of Virginia, Charlottesville, VA, USA

Abstract

Magnetic bearings have been installed in an industrial canned motor pump. The rotor of the pump is fully supported by active magnetic bearings. The bearings have been canned in a manner similar to that used to isolate the motor components from the working fluid. Thus, the magnetic fields of the bearings act through a non-magnetic, conducting can.

Several diagnostic procedures using magnetic bearings, reported in an earlier paper by the authors, have been applied to this pump. These diagnostics were performed prior to the start-up of the motor but with the machinery in an assembled configuration. This allowed the pre-determination of optimum control settings prior to delivery. It also provided a baseline indication of the system characteristics for use in future studies and for maintenance purposes.

1. Introduction

1.1 Sealless Pumps. Recently a trend towards the use of sealless pumps has developed in the chemical process pump industry [1]. The driving forces behind this trend are both economic and environmental . The economic benefits associated with the use of sealless pumps are mainly due to the elimination of shaft seals which are the dominant root cause of failure in this pump application. These failures add significantly to the life cycle cost of these pumps. The environmental factors driving the change to sealless pumps include a reduced societal tolerance of chemical emissions of all forms. One source of these emissions is chemical process pumps whose seals leak during normal operations. In the case of a shaft seal failure the leakage becomes much larger. Sealless pumps, when they are made to be reliable, will eliminate these types of leakage.

The present state of the art for sealless pumps, which include both canned motor pumps and magnetic drive pumps, use process fluid lubricated bearings, typically formed from a carbon sleeve. The reliability of these bearing is low, with at least one reported application having an average bearing life span of six months. Thus the maintenance costs associated with these bearings can be high. Additionally, when the bearings fail, the liners are often damaged. This generally results in the loss of the pump as well as potential process fluid leaks. For these reasons a more reliable sealless pump must be developed.

1.2 Magnetic Bearing Application. Magnetic bearings are very well suited to this application. With the magnetic components separated from the working fluid in the same manner as the motor of a canned motor pump, the seal boundary of the pump can be maintained. Because there is no contact between the rotating and stationary components under normal conditions there is no wear and no maintenance associated with the bearings. It is projected that properly designed magnetic bearings may have a life expectancy similar to the 19.7 to 76.3 year average life of electric motors currently operating in this environment [2]. This wide span of life expectancy is due to differences in designs and construction details.

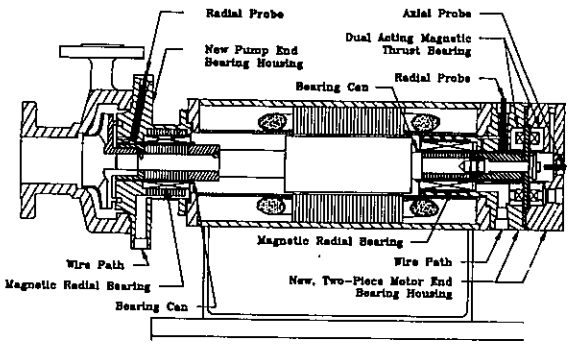

Figure 1 Magnetic Bearing Equipped Pump

1.3 Current Application. Magnetic bearings have been retro-fit into an industrial canned motor pump (figure 1). This pump will be placed in an industrial environment to prove the compatibility of the technology with the application. The installation of the pump in the field represents the conclusion of an ongoing project reported in [4] and [5]. In brief, the project involved two phases: a proof of concept phase in which magnetic bearings were retrofit into an industrial canned motor pump for laboratory use; and a demon-stration phase in which modifications were made to the design to allow a second pump to be configured with magnetic bearings for an industrial application.

The basics of the design procedure used in the development of these bearings is given in [4], while some results from the proof of concept phase were reported in [5]. In the demonstration phase a 7.5 kW (10 hp) pump was selected for the retrofit. The pump specifics are listed in table 1. Figure 1 is a cross sectional drawing of the pump equipped with magnetic bearings. The bearing stators were separated from the working fluid by a .254mm (.010 inch) thick stainless steel can of 316 Stainless Steel (Figure 2).

Motor Rating	7.5 kW	(10 hp)
BEP Flow	1.11×10^{-2} m^3/s	(174 gpm)
Max. Head	5.17×10^{5} Pa	(173 ft)

Table 1 Pump Specifications

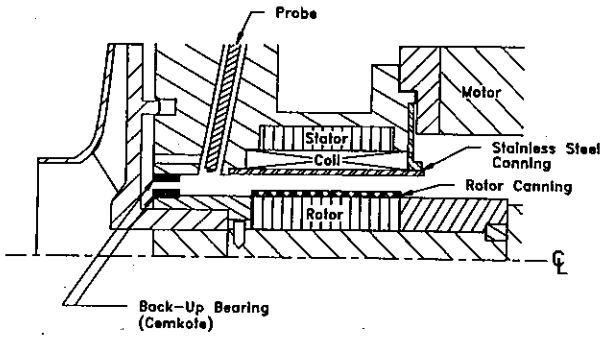

Figure 2 Example of Bearing Canning

The bearings are constructed from .18 mm (.007 inch) thick silicon iron laminations. The bearings were designed to provide the maximum load capacity consistent with the geometric constraints of the retrofit. This general design specification of the load capacity of the bearing resulted from the uncertainty of the end use of the pump. The major load component on the bearings is from the impeller fluid forces which are dependant on the working fluid as well as the hydraulic conditions. Each of these vary with the pump application. For reference, table 2 compares the design loads with the maximum predicted loads, assuming water as a working fluid. It is seen that this design strategy results in a margin of safety regarding bearing load capacity.

Bearing	Design load	Max. Load
PE Radial	1110 N	565 N
ME Radial	445 N	95 N
Thrust	2225 N	555 N

Table 2 Design and Max. Predicted Loads

Prior to the installation of the pump in the field several diagnostic tests were performed on the magnetic bearing equipped pump in order to further demonstrate the capabilities of magnetic bearings reported by Humphris et. al. [3].

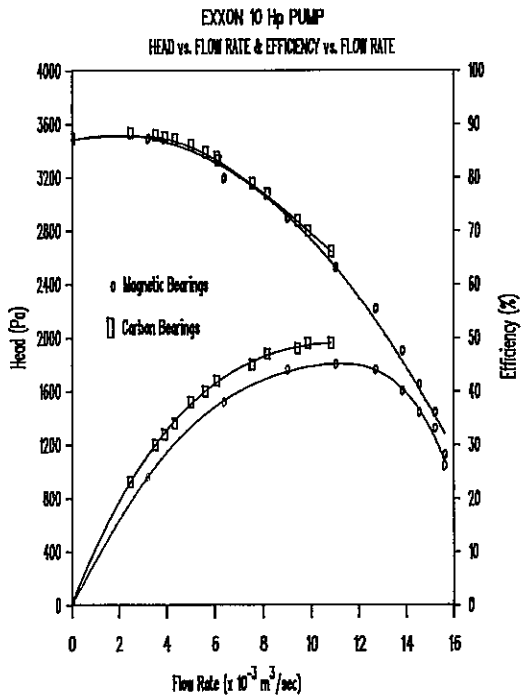

Figure 3 Head and Efficiency Comparison

2. Flow Testing

One of the objectives of this project was to prove that canned magnetic bearings have no adverse effect on pump characteristics. To accomplish this, head and efficiency vs. flow rate data was collected on the "as received" pump. This data was collected again after the magnetic bearings were installed. These sets of data are compared in figure 3. The slight decrease in pump performance in the magnetic bearing equipped pump is attributable to an increase in the by-pass flow recommended by the pump supplier to cool the motor.

3. Diagnostics

In order to investigate the system characteristics prior to operating the machine, the magnetic bearings were used as an investigative tool [3]. This allowed the system to be analyzed and the controller characteristics to be set before the pump was ever run. The diagnostic functions performed in this investigation include: centering the magnetic offset position within the available back-up bearing clearance; measuring the system critical speeds and appropriately adjusting the bearing stiffness, and; measuring the system damping ratio and appropriately adjusting the bearing damping.

3.1 Centering the Bearing There are two possible configurations in which the bearing can be considered centered. The first is when the rotor is centered within the available magnetic clearance. The second, when it is centered within the geometric clearance. Ideally these two will coincide. Practically, however, they will almost always be different by a small amount. Because the magnetic bearing can provide support anywhere within the magnetic clearance it was decided to center the bearing geometrically. To do this for the radial bearings a sinusoidal perturbation signal was injected into the controller of each horizontal axis. Simultaneously, the same signal with a 90 degree phase shift was injected into each vertical axis. This causes the shaft to orbit without rotating about its centerline. The resulting orbits can be observed on the output of the bearing position sensors.

Using this procedure the amplitude of the disturbance can be increased until the backup bearings are contacted by the shaft. The zero position of the shaft can then be adjusted to eliminate the contact. This can be repeated until the bearing is geometrically centered within its available clearance. Figures 4 - 5 show the pump end bearing orbits just prior to contact and with the back-up bearing in full contact. Figures 4 and 5 represent the bearings before and after canning respectively. The gain of the phase shifting portion of the electronics varied slightly from unity resulting in the elliptical shapes of the orbits. Additionally it is noted that the 'before canning' shaft is slightly (approx. .02 mm) more centered than the 'after canning' shaft. This could have been corrected if necessary, but the demonstrated clearances were more than sufficient for the machinery involved.

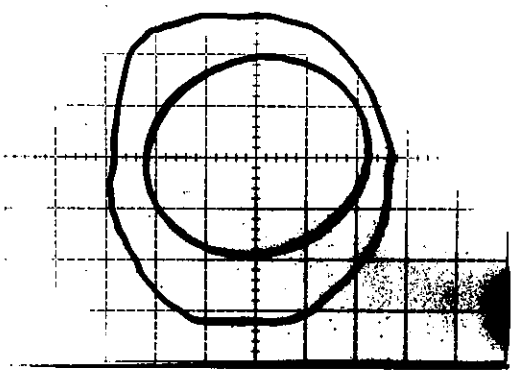

Figure 4 Bearing Orbits Prior to Canning

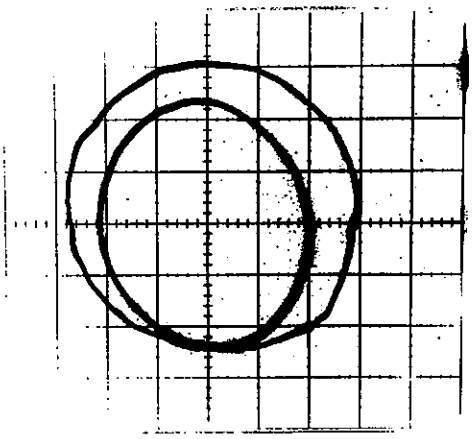

Figure 5 Bearing Orbits after Canning

It is most important to note that the outer orbit, representing full contact with the back-up bearing, is similar in size for the two cases. This shows that the canning of the bearings does not infringe on the back-up bearing clearance at any point. A similar method was used to center the thrust bearing and verify its clearance.

3.2 Measuring System Critical Speeds. The system critical speeds can be investigated in two ways. The first and simplest way is to inject white noise into the perturbation input of the bearing controller and examine the averaged frequency spectrum that results. This is the electrical equivalent of multiple rap tests of the system. The result of this will generally give a broad spectrum peak at each system resonant frequency, whether it is a structural or a rotor critical. No phase information is obtained.

The second method was presented by Humphris et. al. [3] and is based on the orbiting perturbations described in the previous section. To obtain critical speed information, the frequency of the rotating field is varied over the frequency range of interest. The output can be analyzed in the same manner as a machine run up or coast down. This method is preferable to the one described above in that the output is more representative of the actual machinery response and phase information is available.

Figure 6 illustrates some testing results and demonstrates the procedure for selecting an appropriate controller proportional gain (bearing stiffness) for this pump. The first curve represents a stiffness setting of 1.25 on the controller. A comparatively large peak occurs at 43 Hz (2600 rpm) and the phase information verifies that this is the

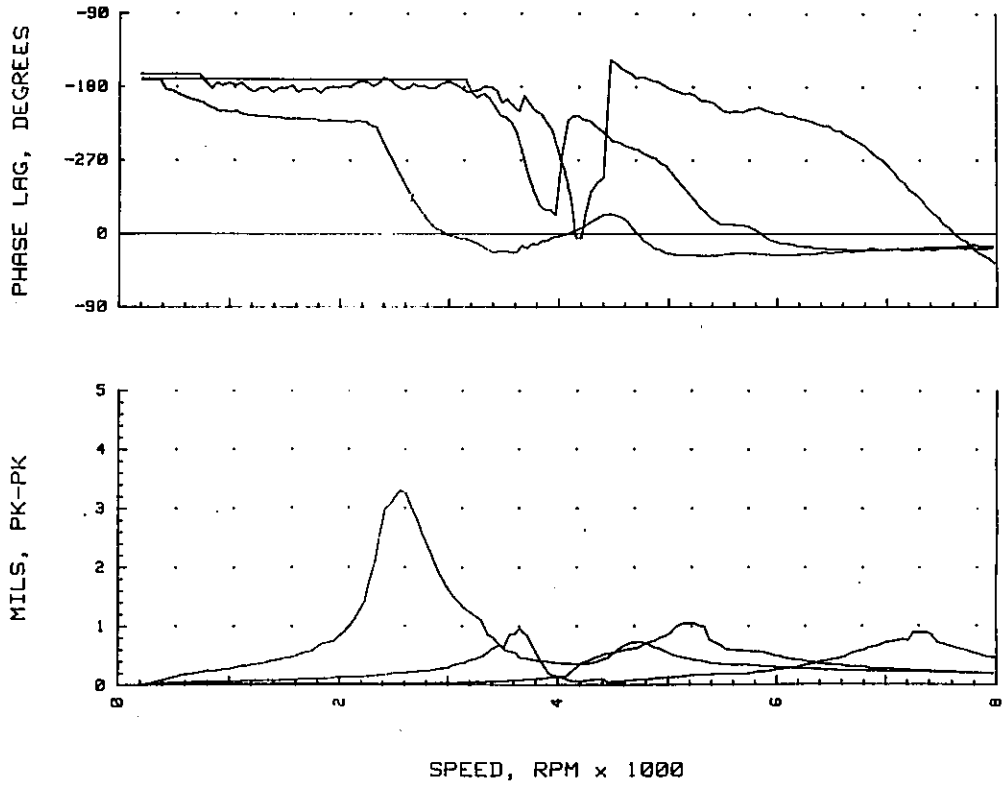

Figure 6 Setting the Bearing Stiffness

first rotor critical. The second curve represents a doubling of the controller gain and a corresponding increase in the first critical to 60 hz (3600 rpm). This is the running speed for this pump, so a further increase in stiffness is desired. The third curve represents another doubling of controller proportional gain. For this case the first critical (from the phase information) is at 67 Hz (4000 rpm) and appears very well damped compared to the previous peaks. This setting is consequently a good candidate for an operating stiffness. This procedure can easily be performed on each axis of support to determine the overall stiffness requirements.

Figures 7 and 8 represent additional examples of this diagnostic method. The figures are representations of identical controller stiffness settings prior to and after canning. The damping differs between the two figures, resulting in the different magnitudes. The curves show the same characteristic shape. The foundation natural frequency (3000 rpm) in the vertical axis is quite evident in both figures. The first rotor critical at approximately 4000 rpm is also apparent in both figures. The curves maintain similar shapes until 5600 rpm when the curves in figure 8 level off and become ragged. This probably indicates a minor contact between the rotor and

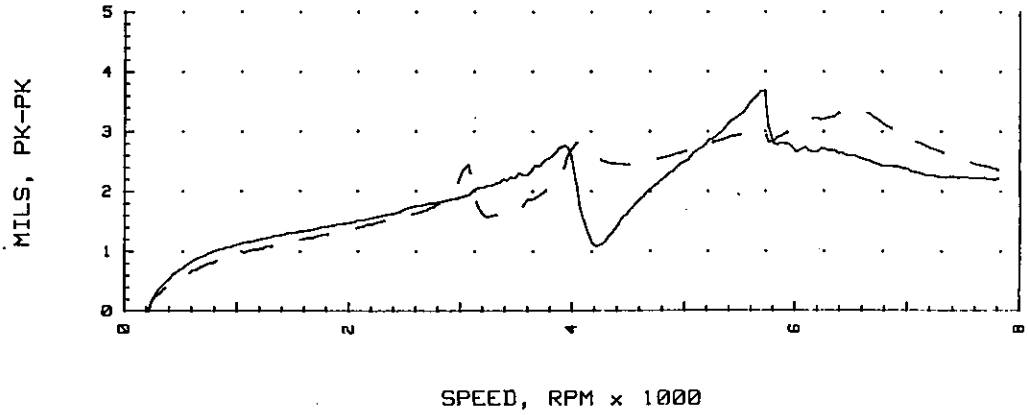

Figure 7 System Criticals for Un-Canned Bearings

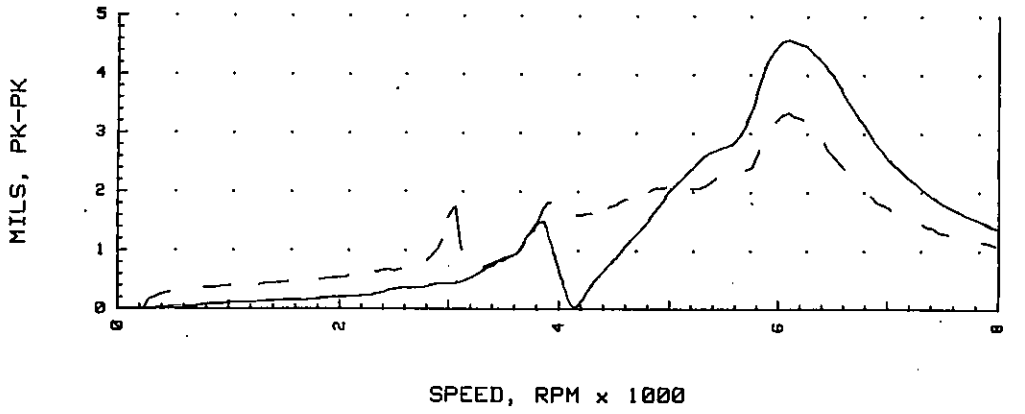

Figure 8 System Criticals for Canned Bearings

stator in the horizontal axis. In general, however, this method is seen to give very repeatable results even though the bearing damping may have changed. Additionally, the comparison between before and after canning shows no significant differences.

3.3 Determining System Damping. The damping of the system can be investigated by inputing a step perturbation and examining the resulting shaft displacement vs time. Damping ratios can be calculated by measuring consecutive peak heights. Usually, however, it is sufficient to adjust the damping such that critical damping is approached. Figures 9 and 10 illustrate this process for the present pump prior to and after canning, respectively. The first plot in each figure corresponds to an initial, poorly damped, setting. The second plot is characteristic of the same system with increased damping. The controller derivative (bearing damping) gains are the same for the two figures. Damping settings similar to the higher ones shown were chosen as the operating points for all of the support axis. When the pump is filled with operating fluid, these derivative settings correspond to over damped system response.

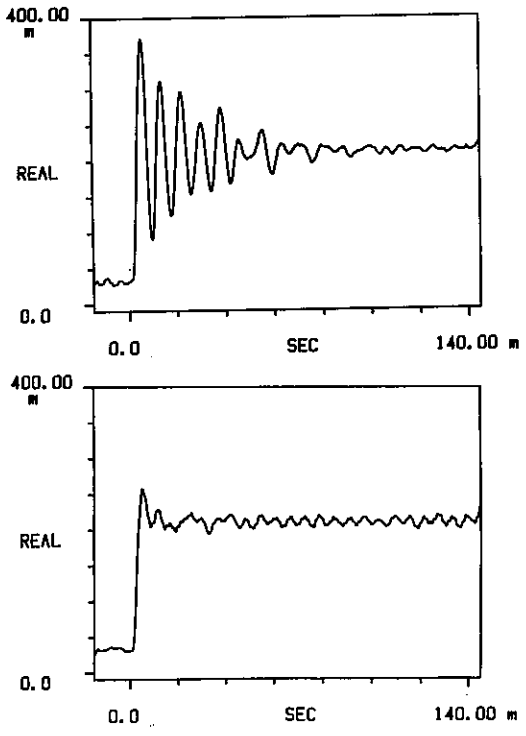

Figure 9 Un-Canned Bearing Damping Characteristics

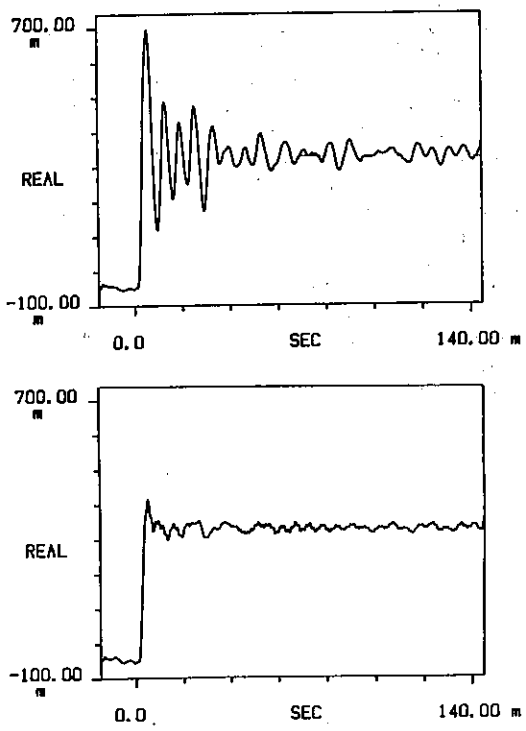

Figure 10 Canned Bearing Damping Characteristics

4. Discussion and Conclusions.

After the above procedures were used to determine the operating point the pump was run. No problems were encountered with the rotordynamic operation of the pump in magnetic bearings. Flow testing was repeated and no significant changes were noted as a result of the magnetic bearing retrofit.

The comparison of physical clearances and bearing damping characteristics before and after canning of the bearings indicate minimal, if any, adverse effects. This was also demonstrated by the pump performance at running speed (60 Hz). The expectation is that canning may effect higher frequency disturbances, but this was not investigated in the current work.

The diagnostic capabilities of the magnetic bearings have been shown to be a valuable tool in setting bearing parameters prior to machine start-up. These same diagnostic methods and capabilities can be used for machine characteristic trending as part of a preventative maintenance program and for diagnostics in the event of machine

problems. Additionally, because these diagnostics can be performed without rotating the shaft, there is less risk of damaging equipment as compared to multiple start-up and run-down tests.

REFERENCES

[1]. Eierman, R.G., "A User's View of Sealless Pumps - Their Economics, Reliability and the Environment," Proceedings of the Seventh International Pump Users Symposium, 5 - 9 March 1990, Houston, Texas, USA.

[2]. Olson, E.A.J. and Grasdal, W.M., "Applications for Magnetic Bearings on Electrical Generating Plant Equipment," Prepared for the Electric Power Research Institute, EPRI RP 2079-21 & 22, December 1988.

[3]. Humphris, R.R., Lewis, D.W., Allaire, P.E., Blair, B.J., and Imlach, J., "System Diagnostics Through Magnetic Bearings - Application to a Canned Motor Pump," Presented at REVOLVE 89, 26-28 September 1989, Calgary, Alberta, Canada.

[4]. Imlach, J., Allaire, P.E., Humphris, R.R., and Barrett, L.E., "Magnetic Bearing Design Optimization," International Conference on Vibrations in Rotating Machinery, Proceedings of the Institution of Mechanical Engineers, 1988, pp 53-60.

[5]. Allaire, P.E., Imlach, J., McDonald, J.P., et. al., "Design Construction and Test of Magnetic Bearings in an Industrial Canned Motor Pump," Proceeding of the Fifth Annual Pump Users Symposium, 24-27 April 1989, Houston, Texas, USA.

2nd International Symposium on Magnetic Beaing
July 12-14, 1990, Tokyo, Japan

Experience with Magnetic Bearings Supporting a Pipeline Compressor

J. SCHMIED

Sulzer Escher Wyss Ltd., CH 8023 Zurich, Switzerland

Abstract

This paper describes theoretical and test results of the vibrational behaviour of a 6MW pipeline compressor supported on magnetic bearings, weighing about 1 ton and running at a maximum speed of 10000rpm. The theoretical model of the rotor bearing sytem, taking into account the bearing transfer function and the non collocation of sensor and actuator describes the behaviour very well in a frequency range up to 300Hz. The vibration level of the machine in operation is far below the limited capacity of magnetic bearings.

1. Introduction

The application of magnetic bearings described in this paper is in a pipeline compressor. A cross section of the machine is shown in fig.1.

The compressor is completely oilfree, assuring that the gas remains clean. This is achieved by the integrated design (the whole rotor is within the housing) and the magnetic bearings. Thanks to the integrated design no sealing against atmospheric pressure is necessary. Normally this is done by oil seals, which are a source of gas contamination. Bearing lubrication has to be avoided, because the bearings are within the housing surrounded by the gas. The compressor is driven by an induction motor of variable speed, which is in the middle of the shaft and which is cooled by the compressed gas.

The rated power of the motor is 6MW. The maximum speed is 10000rpm. The whole rotor weighs 1 ton. According to the S2M reference list of January 90 for heavy turbomachinery applications of magnetic bearings (fig.2) it is presently the heaviest rotor running at a speed of 10000rpm.

In the course of the development of this machine a variety of theoretical

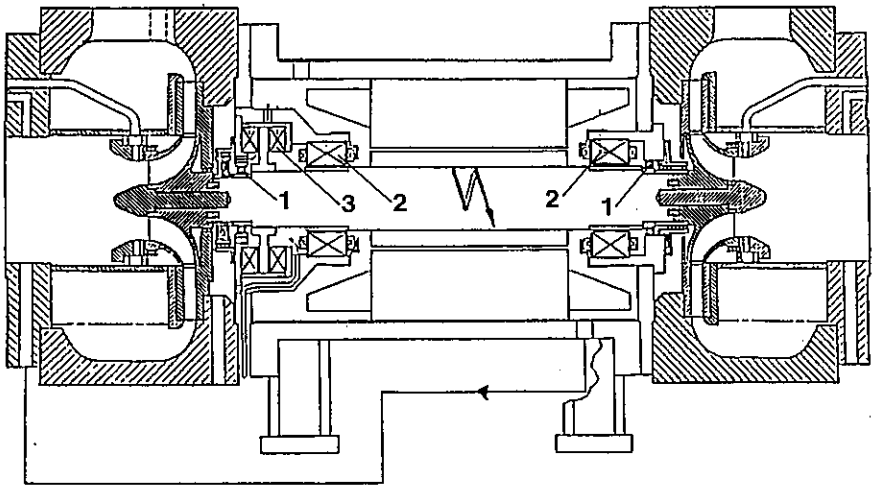

1 auxiliary bearing
2 radial magnetic bearing
3 thrust magnetic bearing

Fig.1
Cross section of the compressor

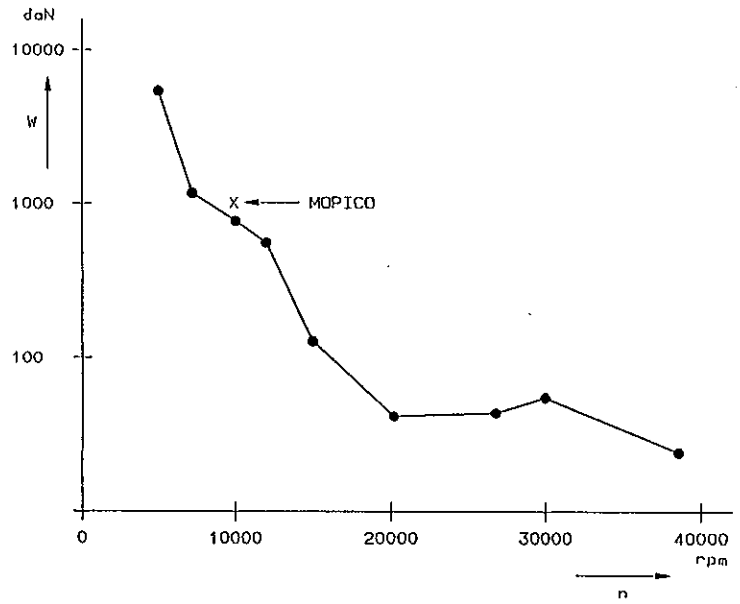

Fig.2
Extreme speeds and weights of large turbomachines supported on magnetic bearings (S2M reference list)

investigations were carried out. The theoretical models of the rotor and the magnetic bearings are described. Theoretical results are reported as well as test results.

2. Modeling the Rotor Bearing System

2.1 The Rotor

Fig.3 shows the finite element model of the rotor. It has 21 elastic shaft elements and three rigid disks. Each node has four coordinates, two for the displacements in direction of the horizontal and vertical axis and two for the rotations around these axis. Hence the model has 88 degrees of freedom. The elements take into account stiffness and all inertia effects (including gyroscopic effects), whereas the disks only have inertia properties.

Table 1 shows the diameter of each element and the additional mass per length modeling the sleeves and laminations shrunk on the rotor. In the region of the motor (element 12 to 15) the given diameter only determines the stiffness, and the added mass per length is the total rotor mass per length.

2.2 The Magnetic Bearing

Fig.4 shows the elements of a magnetic bearing. It consists of a sensor, controller, amplifier and actuator for each direction. The bearing characteristic is basically determined by the controller. Fig.5 shows a block diagram of the analog controller. The filters in the first two blocks condition the measured displacement signal x_m. The phase lead cells produce a damping effect and the integrator prevents a large static deflection. A model of

MB magnetic bearing
AB auxiliary bearing
IP impeller
TB thrust disk

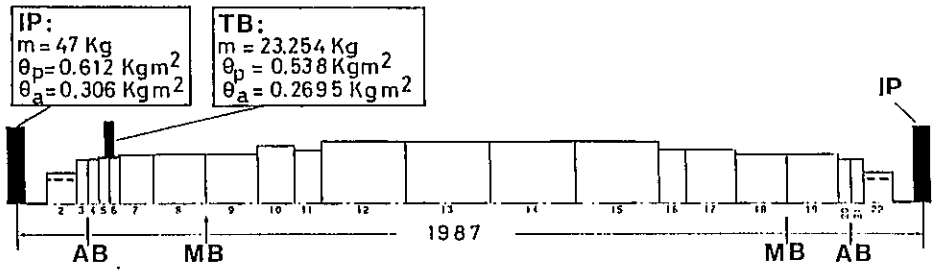

Fig.3
Finite element model of the rotor

Table 1 : Element diameters and added mass per length of the shaft elements

element number	outer diam. [mm]	added mass [kg/m]
2	130.0[1)]	190.0
3/4/20/21	167.6	49.39
5/6	178.0	
7	184.0	73.61
8/9/18/19	186.0	72.20
10	215.0	
11/16	200.0	386.04
12÷15	218.0	735.22[2)]
17	200.0	069.25
22	130.0[1)]	097.46

1) hollow shaft, inner diameter 112.0 mm
2) total mass of the elements 12÷15

the bearing is created by modeling the controller according to fig.5. The sensor, the amplifier and actuator are taken into account by the constant scaling factor SF. In reality the transfer functions of these elements are not a constant. The amplifier plus actuator has a perceptible amplitude and phase loss with

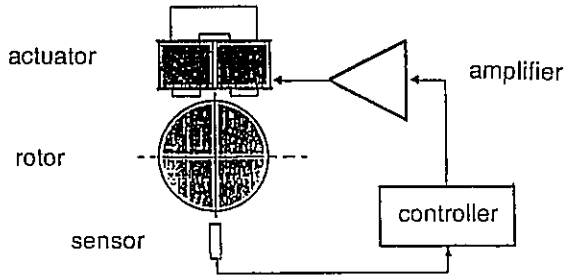

Fig.4 Elements of a magnetic bearing

increasing frequency. At 1000Hz the amplitude and phase lag are about 1% and 30 degree respectively. This effect is neglected as its influence is very small at lower frequencies. Fig.6 shows the open loop transfer function between the bearing force and the measured displacement of the thus modeled bearing.

The bearing only creates damping if the phase angle of the transfer function is between 0 and +90 degrees, which in this case is only for frequencies above 20Hz. This is due to the integral part in the controller. All natural frequencies of the rotor bearing system therefore must be above 20Hz to prevent instability.

The damping and stiffness coefficient of the magnetic bearing can be calculated by

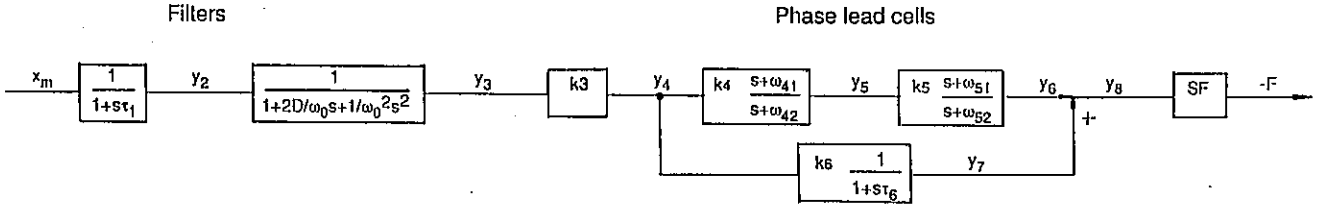

SF = 7 10^7 N/m

τ_1=0.0
ω_0 = 24944 rad/sec
D = 0.32

k_3 = 0.576

k_4 = 4.0
ω_{41} = 222 rad/sec
ω_{42} = 888 rad/sec

k_5 = 4.2
ω_{51} = 1894 rad/sec
ω_{52} = 7955 rad/sec

Integrator

k_6 = 50.0
τ_6 = 1.0 sec

s Laplace Operator

Fig.5 Block diagram of the controller
(with courtesy of Magnetic Bearing Inc.)

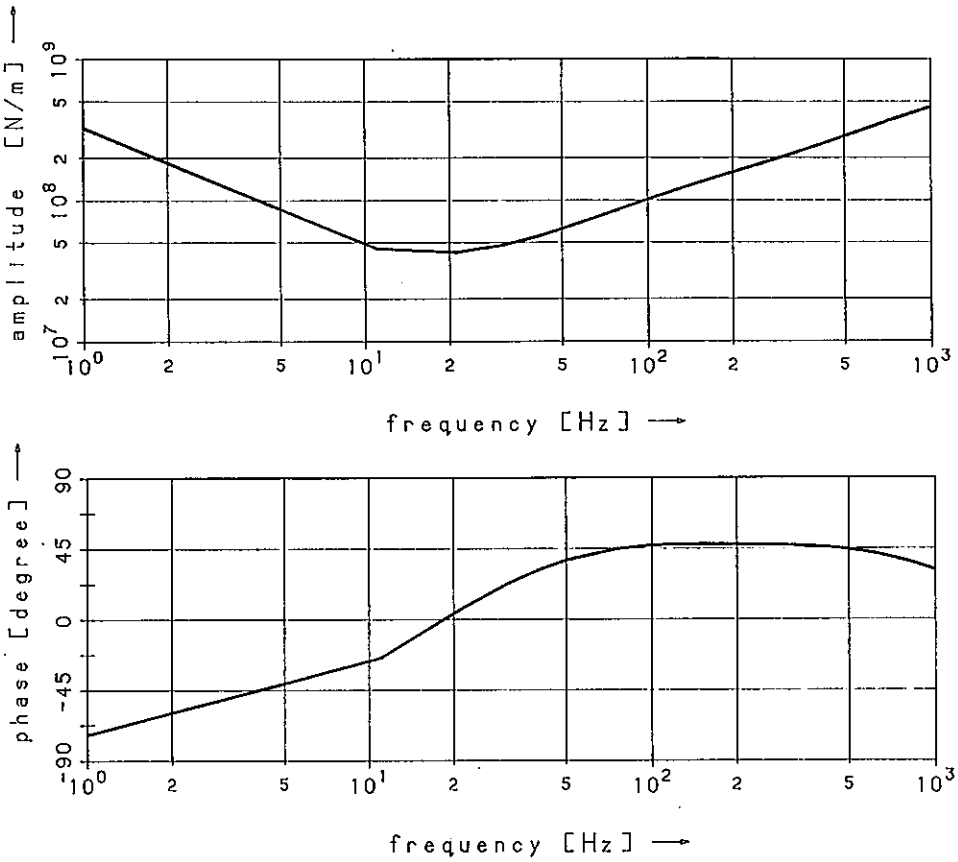

Fig.6
Open loop transfer function of the bearing

taking the real part of the transfer function as the stiffness and the imaginary part divided by the angular frequency as the damping coefficient. Fig.7 shows the thus calculated coefficients as a function of the frequency compared to those of a four tilting pad oil bearing suitable for this rotor. The oil bearing coefficients do not depend on the frequency but on the rotating speed. The shown coefficients are for a speed of 10000rpm. It can be seen that in the frequency range of 30 to 200Hz the magnetic bearing has approximately the same damping coefficient and a stiffness coefficient which is about one third to one sixth.

In the appendix is described how the magnetic bearing is integrated into the finite element model of the rotor. The rotor bearing model thus created also takes into account the slightly different axial position (non collocation) of the sensor and the actuator. The model allows a stability analysis (i.e. to calculate damping factors) of the combined rotor bearing system as well as response calculations to be carried out.

A linear model as described above however is only correct for limited rotor displacements, since the actual bearing force is a nonlinear function of the rotor displacement and velocity /1,2/. The nonlinearities limit the performance of magnetic bearings. Two very important limits are the peak force capacity of the bearing, which is determined by the magnetic saturation and the maximum slew rate, which is limited by the maximum output voltage of the amplifier. Fig.8 shows the maximum amplitude of a harmonic bearing force as a function of the frequency. At lower frequencies the limit is due to the magnetic saturation and at higher frequencies due to the amplifier saturation.

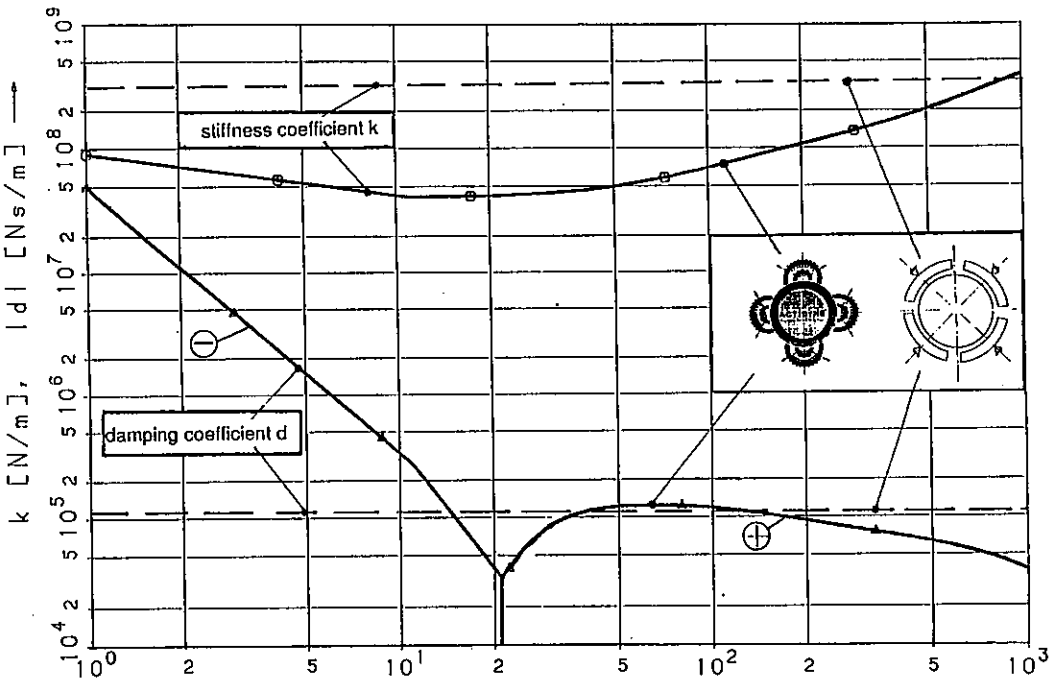

Fig.7 Siffness and damping coefficient of the magnetic bearing and an oil bearing

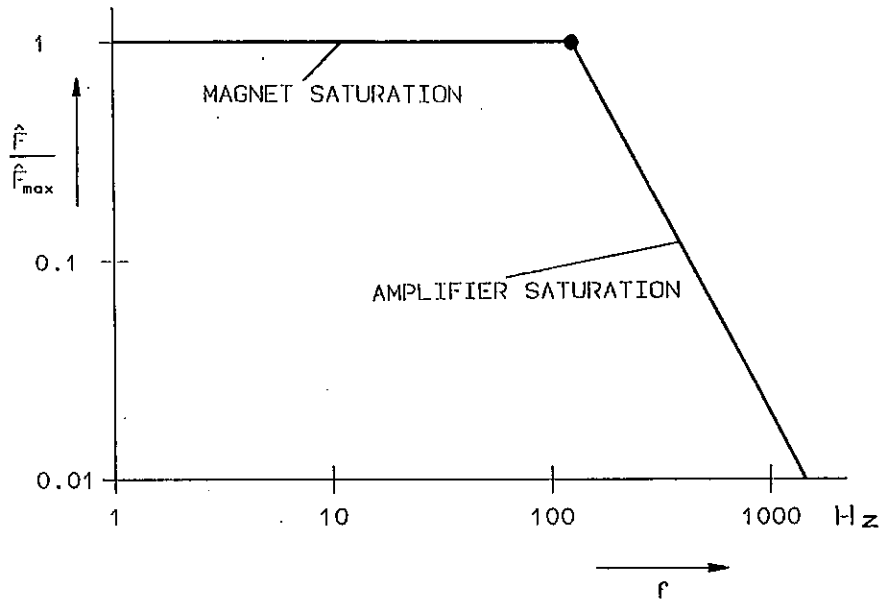

Fig.8
Limits of a harmonic bearing force
F_{max} = 10000N

3. Theoretical and Test Results

All the analyses in this section were carried out by means of the finite element rotor dynamic program MADYN /3/.

Fig. 9 shows calculated damping factors and frequencies of the first three forward whirling modes of the rotor at a speed of 10000rpm. For comparison the diagram also shows results for the rotor supported on the oil bearings with the damping and stiffness coefficients of fig.7 . It can be seen that the first two modes, which are below the maximum operating speed have a lower frequency but a much better damping for a rotor supported on magnetic bearings. This is achieved with a damping coefficient, which is approximately the same as for oil bearings, and a stiffness coefficient, which is much lower.

The theoretical rotor model results as described above are very well confirmed in a frequency range up to 300Hz by comparison of calculated and measured closed loop transfer functions. Fig.10 shows the calculated transfer function for an excitation by means of the magnetic actuators on both sides and a displacement measurement with the bearing sensors. The phase angle of 90 degrees at the frequency 0 is due to the integrator in the controller. The phase angle of -90 degrees at about 45Hz indicates the first mode. A peak in the amplitude is not very clear because of the good damping and the logarithmic scale. A phase shift or peak due to the second mode is not visible, because it is not excited, since the excitation is on both sides. The phase shifts between 130 and 150Hz are due to the changing shape (transition from the first rigid body mode to the first bending mode). The phase angle of -90 degrees and the amplitude peak at about 180Hz indicate the third mode, which is the first bending mode. The frequency is not as high as in fig.9 because the rotating speed here is only 4000rpm instead of 10000rpm in fig.9, hence the gyroscopic effect is less.

The model does not describe the real rotor with a sufficient accuracy at frequencies above 300Hz. Considering the simplifications in the rotor and bearing model (section 2), this is not surprising. The natural frequencies of the fourth and fifth mode (at 380Hz and 640Hz) do still coincide quite well (the maximum deviation is about 5%), but the stability is not predicted well. The fourth and fifth mode in practice became unstable before the controller was properly tuned. The theoretical model did not predict these instabilities. According to the theoretical results the fourth mode has on one side a node between sensor and actuator, hence one

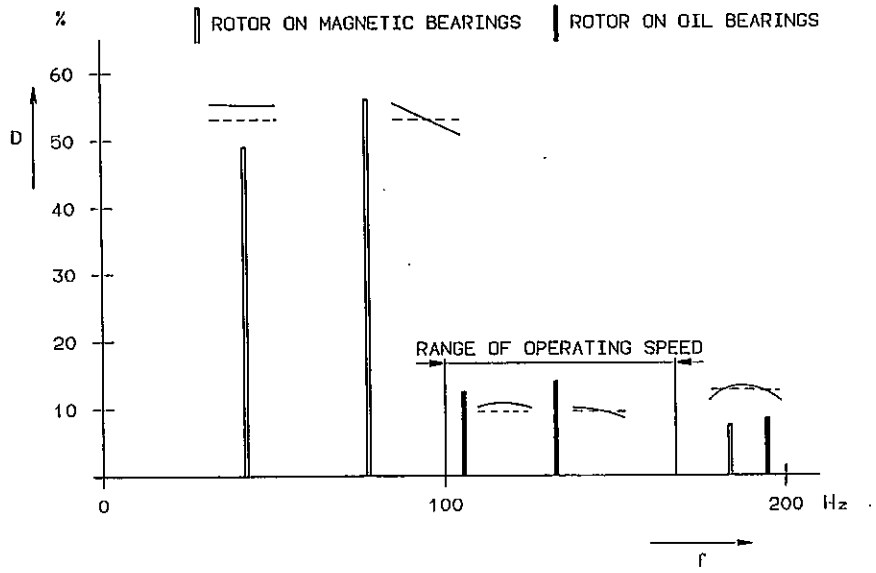

Fig.9
Damping factors and frequencies of the first three forward whirling modes of the rotor in oil and magnetic bearings

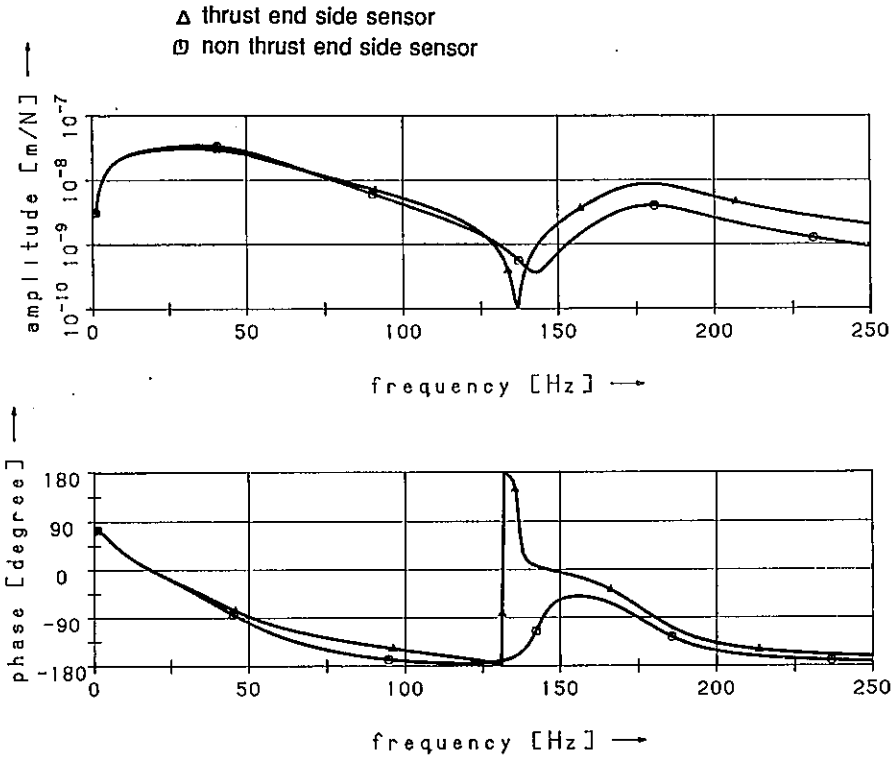

Fig.10
Closed loop transfer function, excitation with the actuators of both bearings, response at the sensors

bearing tends to excite rather than damp the system (also see /4/), but the other bearing still provides enough damping to prevent an instability (the calculated damping factor has the very low value of 0.7%). In practice both mentioned modes had to be stabilized by a notch filter at the natural frequencies of the two modes.

The theoretical model is only unstable at frequencies above 1500Hz due to the non collocation of sensor and actuator and also due to negative phase angles (=negative damping) of the open loop bearing transfer function (not shown in fig.6). At these frequencies however the model is in any case too inaccurate. In practice instabilities at higher frequencies than the fifth mode did not occur. These modes seem to be sufficiently damped by the internal damping to compensate any excitation from the bearing.

Fig.11 shows the measured once per revolution bearing force amplitudes for a run up to 10000rpm with full load in relation to the limits of the bearing mentioned in section 2. It can be seen that at full speed the level is still only 50% of the limit. This is the level for a very fast run up of the cold rotor within 2 minutes, when the rotor is not yet fully thermally balanced. After about 15 minutes, when the rotor is warm, or for a slower run up within 15 minutes, the level is only about half of that shown on fig.11.

Acknowledgements

I want to thank my colleagues from ACEC, the motor manufacturer, and from Magnetic Bearing Inc. for the good cooperation throughout this joint project.

References

/1/ Maslen, E., et al.: Practical Limits to the Performance of Magnetic Bearings: Peak Force, Slew Rate and Displacement Sensitivity. ASME Journal of Tribology, Vol. 111, April 1989.

/2/ Traxler, A.: Eigenschaften und Auslegung von berührungsfreien elektromagnetischen Lagern. Dissertation ETH Zürich 1985.

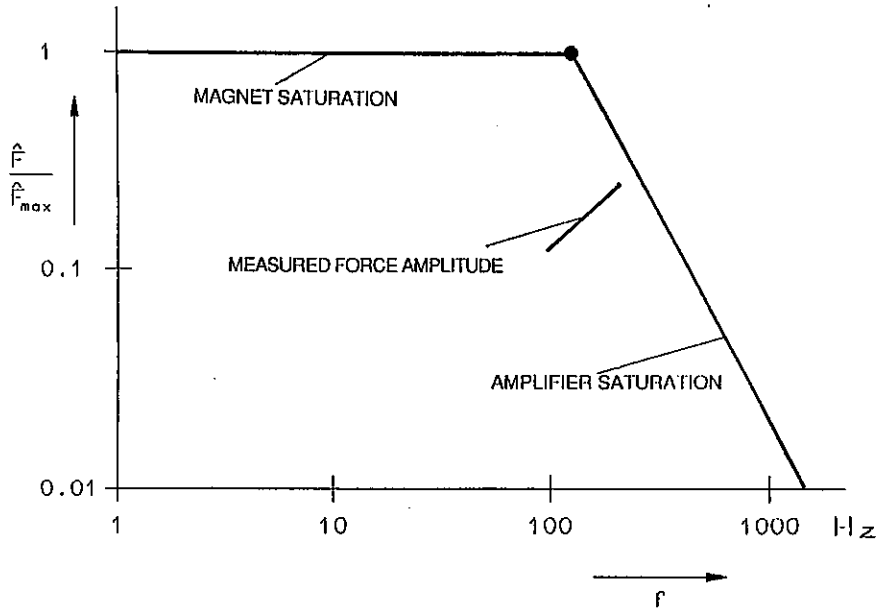

Fig.11
Measured once per revolution force amplitude versus bearing limits

/ 3 / Klement, H.D., Schilling, W.: Schwingungsberechnungen mit dem Programmsystem MADYN. VDI Berichte 786, 1989.

/ 4 / Salm, J., Schweitzer, G.: Modeling and control of a flexible rotor with magnetic bearings. Paper C277/84, Institution of Mechanical Engineers, 1984.

Appendix: Integrating the Magnetic Bearing into the Finite Element Model of the Rotor

For this purpose the finite element rotor model is expanded to include the "controller coordinates" y_2 to y_8 (see fig.5) for each bearing and direction. The coordinate x_m in fig.5 is the translatory coordinate of the finite element model of the rotor at the measuring position in the direction of the sensor. The bearing force F is applied at a node in the middle of the magnetic bearing in the direction of the actuator. The corresponding coordinate is x_F. The direction of the sensor and the actuator coincide, their axial position however does not. The block diagram (fig.5) corresponds to the following equations in the time domain:

$$\tau_1 \dot{y}_2 + y_2 = x_m \qquad \text{(A1)}$$

$$\ddot{y}_3 + 2D\omega_0 \dot{y}_3 + \omega_0^2 y_3 = \omega_0^2 y_2 \qquad \text{(A2)}$$

$$y_4 = k_4 y_3 \qquad \text{(A3)}$$

$$\dot{y}_5 + \omega_{42} y_5 = k_4 (y_4 + \omega_{41} y_4) \qquad \text{(A4)}$$

$$\dot{y}_6 + \omega_{52} y_6 = k_5 (y_5 + \omega_{51} y_5) \qquad \text{(A5)}$$

$$\tau_6 \dot{y}_7 + y_7 = k_6 y_4 \qquad \text{(A6)}$$

$$y_8 = y_6 + y_7 \qquad \text{(A7)}$$

$$-F = SF\, y_8 \qquad \text{(A8)}$$

The coefficients of x_m and the "controller coordinates" y_{2-8}, as well as the coefficients of their first and second derivatives have to be introduced into the appropriate lines and columns of the stiffness, damping and mass matrices of the expanded finite element model, as is shown below. When using the finite element program MADYN /3/ this can be achieved by general matrix addition.

Lines and columns of the expanded mass matrix concerned by the bearing:

	x_m	y_2	y_3	y_4	y_5	y_6	y_7	y_8	x_F
x_m									
y_2									
y_3			1						
y_4									
y_5									
y_6									
y_7									
y_8									
x_F									

Lines and columns of the expanded damping matrix concerned by the bearing:

	x_m	y_2	y_3	y_4	y_5	y_6	y_7	y_8	x_F
x_m									
y_2		τ_1							
y_3			$2D\omega_0$						
y_4									
y_5				$-k_4$	1				
y_6					$-k_5$	1			
y_7							τ_6		
y_8									
x_F									

Lines and columns of the expanded stiffness matrix concerned by the bearing

	x_m	y_2	y_3	y_4	y_5	y_6	y_7	y_8	x_F
x_m									
y_2	-1	1							
y_3		$-\omega_0^2$	ω_0^2						
y_4			$-k_3$	1					
y_5				$-k_4\omega_{41}$	ω_{42}				
y_6					$-k_5\omega_{51}$	ω_{52}			
y_7				$-k_6$			1		
y_8						-1	-1	1	
x_F								SF	

2nd International Symposium on Magnetic Beaing
July 12-14, 1990, Tokyo, Japan

LOADING TEST IN AN AIR TURBINE BORNE BY ACTIVE MAGNETIC BEARINGS

T. INOUE*, M. TAKAGI*, N. TAKAHASHI*, O. MATSUSHITA* and R. KANEKO**
* Mechanical Engineering Research Laboratory , Hitachi Ltd.
** Hitachi Works , Hitachi Ltd.
3-1-1 Saiwai-machi, Hitachi-shi, Ibaraki Pref. 317, JAPAN

Abstract

A conventional air turbine with a load capability of 82 KW is modified with the installation of active magnetic bearings, and loading tests are then performed. The controller unit is constituted by phase compensators and PWM power amplifiers. The phase compensator is principally based upon the conventional PID control law with the addition of several notch filters, which enable the prevention of self-excited oscillations in the bending mode eigen frequencies. During rotational tests, rotor vibration is successfully suppressed to less than 40 μm amplitude. The loading tests are conducted normally without malfunctions in either the analog controller or the digital controller.

1. Introduction

Active magnetic bearings, which have been applied to such compact-size rotary machines as spindles and turbomolecular pumps up until the present time, have recently been applied to such turbomachines as centrifugal compressors. Magnetic bearings are attracting much attention as a mechanical element to be used in place of conventional oil-film bearings for turbomachines, of which maintenance-free operation is very important. Magnetic bearings, having low bearing loss without lubrication, can also contribute towards improvement of fluid performance. Magnetic bearings are now being applied particularly to centrifugal compressors, with subsequent reports written about their operation [1]. It seems, however, that such reports do not have detailed descriptions of what characteristics are realized in the controller, which forms the key to the control of vibrations with electromagnetic bearings. Moreover, while examples of digital control with a model rotor [2] are reported occasionally, it appears that reports concerning turbomachines indicate a controller constructed in an analog circuit with no report yet on test results of turbomachines with digitally controlled electromagnetic bearings.

Therefore, this report presents in detail the vibration characteristics of the shaft system, characteristics of the analog and digital controllers, the open loop transfer function of the entire controlling system, and so forth. These are ascertained in light of tests conducted on a performance test machine formed of an air turbine with electromagnetic bearings. Additionally, a description of the results obtained from the rotational test, the loading test, and the partial loading test.

2. Test rig

2.1 Air turbine with electromagnetic bearings

The schematic construction of the air turbine with electromagnetic bearings subjected to a series of tests is shown in Fig. 1. The turbine rotor is set with a shrink-fit disk in one stage having a diameter of 600 mm. The weight of the rotor is 3.2 kN and the bearing span is 1,060 mm. The turbine rotor is connected by a diaphragm coupling directly with an electric dynamometer rated at the output capacity of 100 kw. However, this rotor is not provided with a damper unit which prevents the occurrence of higher order vibrations. One end of the radial magnetic bearing is set inside the air turbine casing, while the other end is held in the pedestal provided between the turbine casing and the dynamometer. A thrust bearing is also set in this pedestal. Touch bearings are provided in two places on the left side and the right side in order to protect the turbine rotor in the event of trouble occurring in the magnetic bearings.

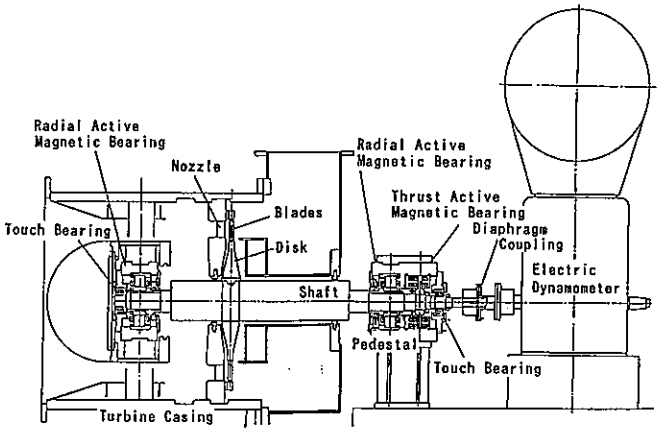

Fig. 1 An air turbine borne by active magnetic bearings

The working air is fed with a blower rated at 600 kw in output. The air flows into the blower from the left and is ejected through the nozzle, turning the turbine blades and being discharged in the upward direction. The turbine has the specified revolutions of 3,600 rpm, with its over-revolution limit set at 4,320 rpm.

The relation between the natural frequency of this rotor system and the spring constant of the magnetic bearings is shown in Fig. 2. The natural frequency which shows a considerable change in relation to the spring constant, occurs in the rigid body mode, in which the rotor oscillates in parallel and in conical modes. On the other hand, the natural frequency in the shaft bending mode shows almost no change, even if the spring constant of the bearings changes. The natural frequency in the shaft bending mode is 210 Hz in the primary value and 440 Hz in the secondary value. Now that the specified revolutions are 3,600 rpm, it is sufficient to pass the two critical speeds of the rigid body, and it is not necessary to pass the critical speed for the primary value in the bending mode.

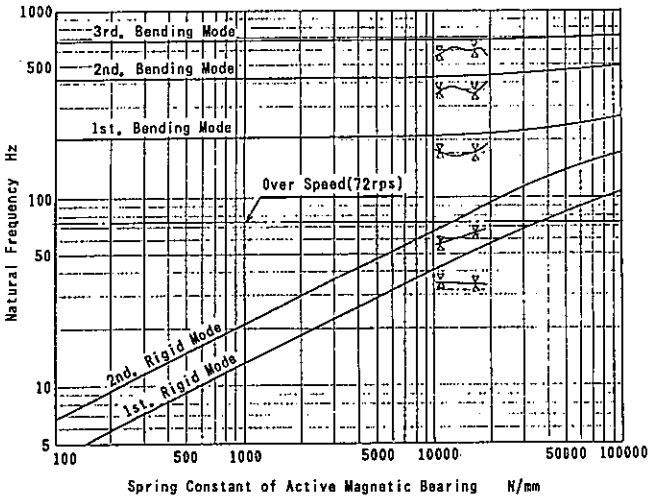

Fig. 2 Natural frequency of the rotor

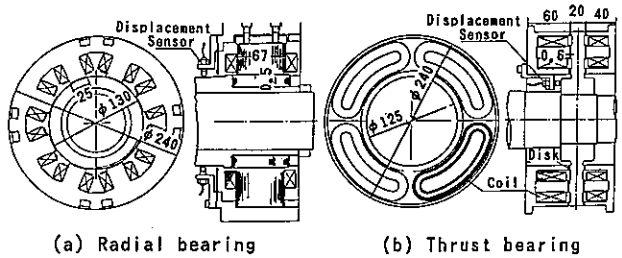

(a) Radial bearing (b) Thrust bearing

Fig. 3 Active magnetic bearing

2.2 Magnetic bearings

2.2.1 Magnetic radial bearings

The magnetic radial bearings are designed with the design radial load set at 2 kN in consideration of the weight of the rotor and the dynamic load, and with the magnetic flux density in the air gap of the magnetic bearings set at 1 T. The construction of the magnetic bearings, as shown in Fig. 3 (a), measures 240 mm in the outer diameter, 130 mm in the inner diameter, 67 mm in the bearing width, and 0.5 mm in the bearing air gap and is formed with a total number of eight magnetic poles. The core is made of a 3% silicon steel sheet with a thickness of 0.5 mm, as laminated in a total of 134 sheets. The magnetic coils are formed of conductive wire with a diameter of 2mm, and with the coil winding in 60 turns. These coils are connected in a series.

2.2.2 Magnetic thrust bearings

The magnetic thrust bearings are designed with the design thrust load set at 10 kN in consideration of the fluid force, and with the magnetic flux density set at 1 T. Their construction, shown in Fig. 3 (b), measures 240 mm in the outer diameter, 125 mm in the inner diameter, 60 mm in bearing length on the loaded side and 40 mm in the bearing length on the opposite side, 0.6 mm in the thrust air gap, and has a total of four magnetic poles. The core is made of low carbon steel. The magnetic coils are made of a conductive wire with a diameter of 1.6 mm wound in a total of 154 turns in the formation of the coil winding. Four such coils are connected in a series.

2.3 Displacement sensor

Eddy current sensors are used as the displacement sensors to detect the position of the rotor shaft core. They are provided opposite each other on the X-axis and the Y-axis. With a form of differential input used for the sensors, temperature drift in the DC output from the displacement amplifier is suppressed, by preventing such external disturbances as changes in temperature. The stability at the point of static equilibrium of the shaft core is thereby secured.

2.4 Controllers

The phase compensation is done by the PID process, performed with the analog controller, which is formed of an operating amplifier, and, with the digital controller composed of TMS 320C25, a DSP made by TI Co. This is shown in Fig. 4. The sampling frequency is 8 kHz. A 12-bit analog-digital converter and a 12-bit digital-analog converter are employed for the input and the

output. Moreover, the PWM system, which attains high efficiency at a low level of heat generation, is used for the power amplifier for feeding an electric current to the magnetic coils. The amplifier has a capacity of 20 kVA for operation at the maximum voltage of 200 V and the maximum current of 20 A per channel.

3. Calculation of stability in control system

Prior to the tests, an analysis of the stability of the rotor and the entire control system was made, with software [3] developed by the present writers and some associates, with a view to simplifying the tuning of the controllers. The block diagram of the control system as a whole, with a notch filter included in the PID, is shown in Fig. 5. The shaft position is detected by the displacement sensor, and the signal generated by the sensor is input into the controllers. The signal is processed for its phase compensation by the proportioning unit, the integrating unit, and the differentiating unit, via the low pass filter at the first stage. Then, the signal is given a further phase compensation by the notch filter with a central frequency almost in agreement with the primary natural frequency and the secondary natural frequency of the shaft. The PWM power amplifier is driven, which feeds an electric current to the magnetic coils, thereby controlling the rotor.

The results obtained from the calculation of the stability of each eigen value in the control system are presented in Fig. 6. The horizontal axis represents the frequency, while the vertical axis indicates the damping ratio. It is observed that the natural frequencies in the primary rigid body mode and the secondary rigid body mode have high damping ratios, so that they offer favorable controllability. The damping factors for the primary and secondary natural frequencies become negative, so that these natural frequencies cause vibrations if the notch filters are not included. On the other hand, it is seen that the damping ratios of these natural frequencies become positive, attaining a state of stabilization, when the notch filters are included. In this figure, the natural frequency with a damping ratio in the proximity of 1 forms the pole for the electrical circuit system.

4. Test results

4.1 Characteristics of control system

4.1.1 PID controller

The transfer functions of the PID controller in the analog control system for radial vibrations are shown in Fig. 7 (a). This Figure

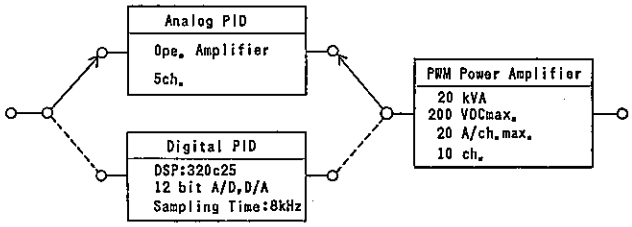

Fig. 4 Controllers

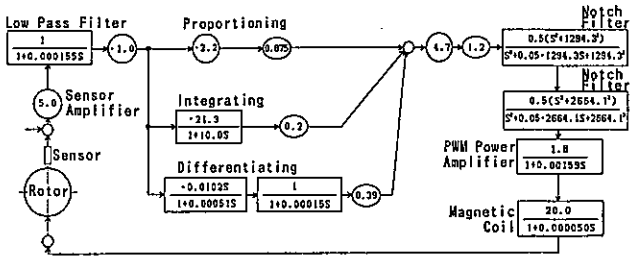

Fig. 5 Block diagram of the entire control system

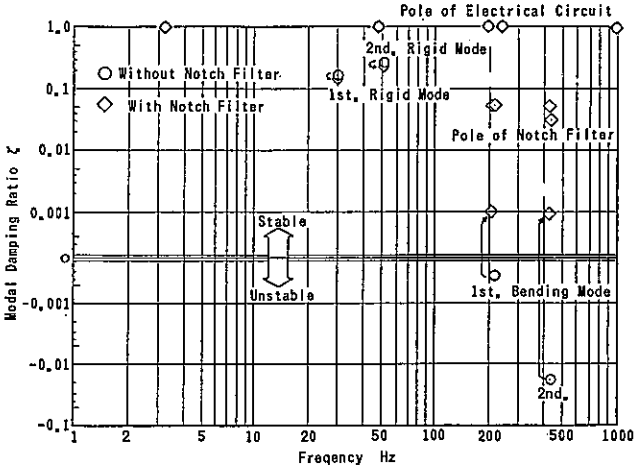

Fig. 6 Results of stability analysis

shows differential characteristics with the gain remaining almost flat up to 20 Hz and incrementing in a monotonous pattern. Moreover, for the purpose of preventing the oscillation of bending modes, notch filters are set up at 200 Hz and 425 Hz in correspondence with the primary and secondary natural frequencies at 210 Hz and 440 Hz in the bending mode. The frequency in the notch filter is set at a level somewhat lower than the natural frequency of the shaft system because the system will not fall into an unstable state even if the natural frequency changes to some extent in the course of its rotation as the frequency has a phase lead in the high frequency region while it has a lag in the phase in the frequency region lower than the notching frequency,

as is clearly observed in the phase characteristics chart. The minor phase delay in the lower frequency region is due to the performance of integrating operations for preventing a steady-state deviation. This presents no problem, since the time constant in the integrating unit is set at a sufficient length.

The transfer functions for the PID controller in the digital control system are shown in Fig. 7 (b). As is evident in comparison with Fig. 7 (a), the digital controller attains approximately the same gain and phase characteristics as those of the analog controller. The notching characteristics of the notching filters in this system are the same as those of the analog controller. It is possible to perceive the accuracy and expediency of the digital controller, which can be constructed through the medium of software. This controller is extremely effective for simplified tuning. Owing to the sampling frequencies set as high as 8 KHz for the analog-digital conversion and digital-analog conversion, the system can amply secure the necessary phase characteristics in the high frequecy region even if it performs arithmetic operations with the PID to the extent just described.

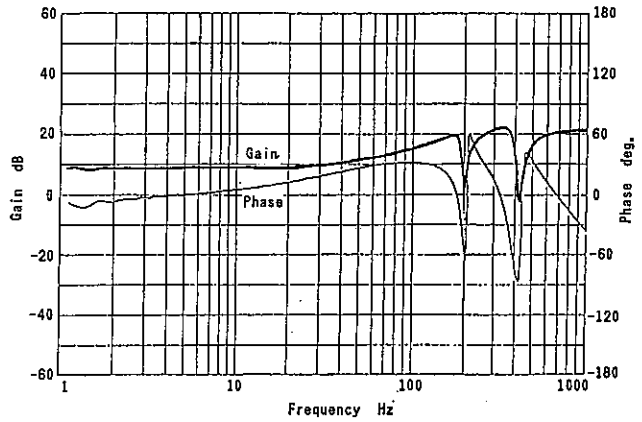

(a) Analog controller

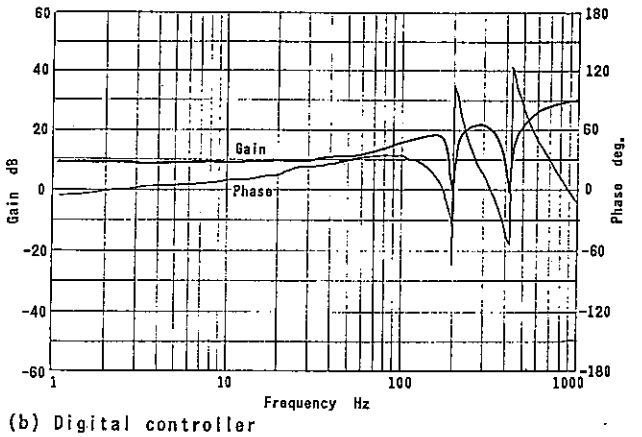

(b) Digital controller

Fig. 7 Transfer function of PID controller

4.1.2 Open loop transfer function

The open loop transfer function of the entire radial control system is presented for the analog control system in Fig. 8 (a) and for the digital control system in Fig. 8 (b). In the analog control system, the gain characteristics show a decline, along with a rise in frequency, and have small peaks at 100 Hz, 210 Hz, and 440 Hz. In this regard, the peak at 100 Hz reflects the natural frequency of the pedestal while the other peaks correspond to the natural frequencies of the bending modes in the shaft system. As the gains at these bending natural frequencies are held down to the order of -15 dB, it is found that the characteristics just described will not cause any vibrations and will have a high degree of latitude to the fluid vibrating force. Also, the phase characteristics feature a lead in phase

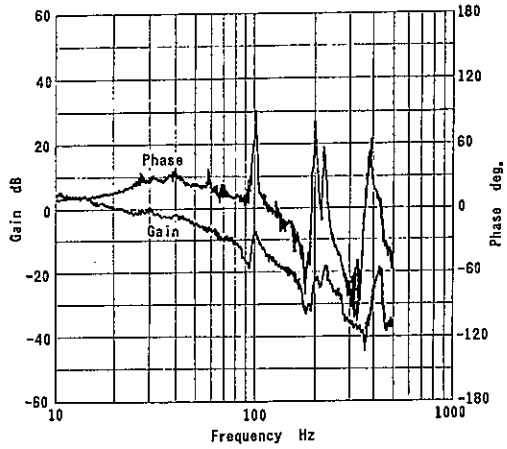

(a) Analog controller

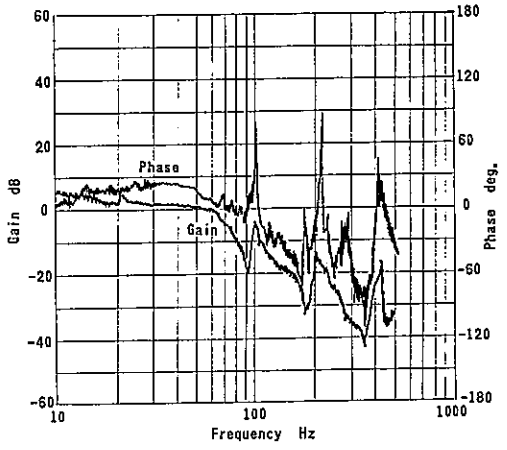

(b) Digital controller

Fig. 8 Open characteristics of the entire control system

up to 130 Hz, and thus it is observed that the characteristics leave an ample margin in reserve for 60 rps, which is the rated speed of this equipment.

The open loop transfer function of the digital control system, as presented in Fig. 8 (b), has small differences either in the gain or the phase characteristics. This control system achieves slightly less phase compensation, with a lead in phase up to 80 Hz, in comparison with the analog control system. In the digital control system, an unavoidable quantizing error takes place when the sensor signals are turned into digital signals by the analog-digital converter. The resulting noises exert vibration in the rigid body mode of the shaft system, thereby causing residual vibrations. Therefore, the gain from the differential operation in this system has been set at a smaller value than in the analog system. However, even at this level of phase compensation, the system has an ample margin of controlling capacity for the rated speed, 60 rps. Hence, there is no problem arising from this.

4.1.3 Free vibration waveforms

Fig. 9 illustrates the free vibration waveforms as measured by an impulse vibrating method applied to the analog control system at a time when the rotor is at a standstill. The radial vibration in the magnetic bearing on the left side is shown in Fig. 9 (a), which radial vibration in the magnetic bearing on the right side is shown in Fig. 9 (b), and the thrust vibration in the axial direction of the rotor is shown in Fig. 9 (c). All these free vibration waveforms are damped after showing approximately four peaks in each, and the damping ratios are at a high level, ranging from 0.3 to 0.5. On the basis of the frequency analysis results, it is found that the natural frequency in the primary rigid body mode is 22 Hz, and in the secondary rigid body mode is about 46 Hz although it is not distinctly discernible, as the peaks are so small in reflection of the high damping ratio. The natural frequency in the axial direction is 20 Hz.

4.2 Rotational test

The shaft vibration responses controlled by the analog system and the digital system, under a no load operation are shown in Fig. 10 (a) and Fig. 10 (b), respectively. On the basis of the vibration responses, it is observed that the critical speed in the primary rigid body mode is at 1,300 rpm (22 Hz). On the other hand, the peak of the critical speed in the secondary rigid body mode, which is not distinctly recognizable, is considered to be in the proximity of 2,800 rpm (46 Hz), as judged in light of the results of the impulse test. The vibration amplitude is approximately 40 μm at most even at the critical speed in the primary rigid body mode, and is 20 μm in the proximity of the rated speed, thus achieving stable vibration characteristics. Yet, the shaft vibration shows a tendency towards its increase at 4,320 rpm (72 Hz), which is an overspeed of 120 %. This is due to an increase occurring in the natural frequency component in the primary bending mode. This increase occurs because a vibrating component three times as large as the rotating frequency N (72 x 3 = 216 Hz), has coincided with the natural frequency of the shaft in the primary bending mode. This tendency is also observed in the form of small peaks in 5N at 2,700 rpm (45 Hz), and in 4N at 3,240 rpm (54 Hz), although these peaks occur at a smaller vibration level.

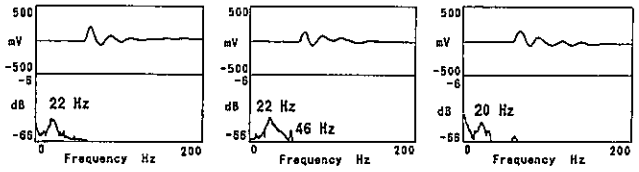

(a) Radial(X_1) (b) Radial(X_2) (c) Axial(Z)

Fig. 9 Free vibration and natural frequency

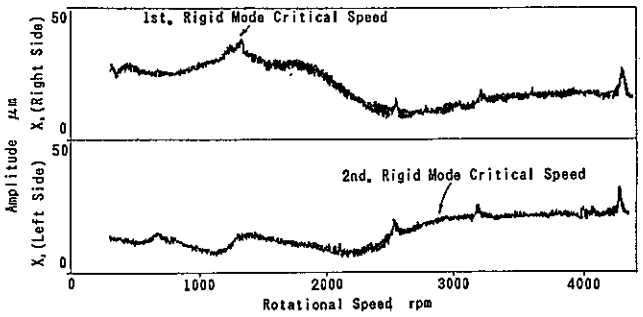

(a) Analog controller

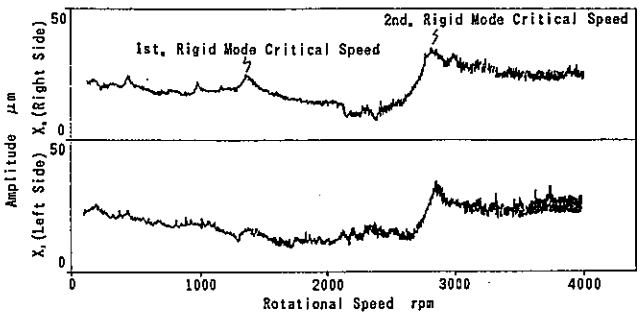

(b) Digital controller

Fig. 10 Rotor vibration response

These states are evident from the spectra of vibrations at the time of rotation, as shown in Fig. 11. The spectrum of vibration at 2,700 rpm shows an example of the coincidence of the vibrating component five times as large as the rotating frequency N with the natural frequency in the primary bending mode. However, the natural frequency components in the primary and secondary bending modes are not observed either at 3,000 rpm or at 3,600 rpm. As it can be estimated from the results described above, it is not sufficient merely to reduce the gain at the higher-order natural frequencies in the shaft bending mode by means of a notch filter. It is in fact important to also maintain a lead in phase in the case of a controller for turbomachines, in which the vibrating force at the degrees of revolution tends to grow larger. For this reason, the frequency in the notch filter is set at a level somewhat lower than the natural frequency of the shaft system. However, the actual tuning job requires much trouble because the natural frequency of the shaft at the time of its revolution deviates from that at the time of its standstill under the influence of the gyro effect. In order to perform the tuning work with high efficiency, taking account of the phase characteristics, it is essential to utilize software for analysis, and the present authors are planning to report on an example [4] of simulations with such software.

The shaft vibration response in Fig. 10 (b) on the unloaded operation of the digital control system shows a somewhat larger amplitude of vibration at the critical speed in the secondary rigid body mode in comparison with that in the analog control system. However, since the amplitude of vibration is on the order of approximately 50 μ m, which marks a fully permissible value, it can be stated that the digital control system has achieved its controlling performance at a level comparable with that of the analog control system. In view of such factors as the simplicity and convenience in tuning and the period necessary for the development work, it can be stated that the digital control is better than the analog control for its use as a controller for magnetic bearings.

4.3 Loading test

Shaft vibration characteristics in which the condition that the loading torque applied to the turbine is increased step by step at 2,000 rpm are shown in Fig. 12. When a load is placed on the turbine, the shaft vibrations in the positions of the two radial bearings show constant values

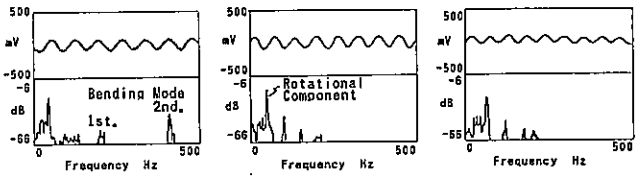

(a) 2700 rpm (b) 3000 rpm (c) 3600 rpm

Fig. 11 Spectra of vibrations at the time rotation

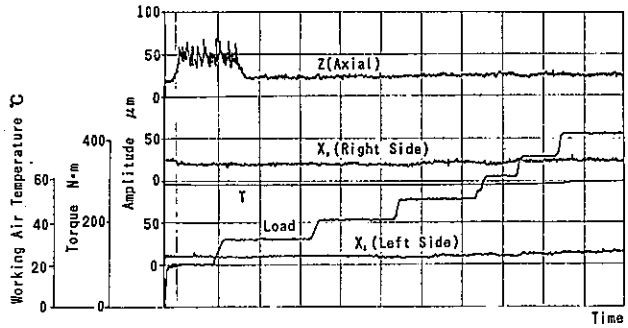

Fig. 12 Vibration characteristics under loading test

regardless of the load. In contrast to this, there appeared a phenomenon marked by a sharp increase of vibrations in the axial direction two times, from 25 μ m to 50 μ m, in terms of the amplitude of vibration under the loading torque of 10 kgf·m. Moreover, as the testing revolutions increased, this phenomenon began to occur on the higher loaded side, but did not occur at 4,000 rpm, where the load became still larger.

Therefore, inquiries were made into the relationship among the load and the current measured by the radial bearings (the radial load), and the thrust bearings (thrust load), at the individual revolutions specified for the test. The results obtained from the study relate to the case of ordinary ejection as shown in Figs. 13 (a) and (b). While the radial bearing current shows a declining tendency in relation to the increase in the output from the turbine, its rate of change is minimal. In contrast to that, the thrust bearing current is placed under the effect of a reverse thrust load in relation to the flow of air when the output from the turbine is low, but is subjected to the effect of a thrust load in the direction of the air flow when the output from the turbine grows larger. That is to say, it is found that the vibration in the axial direction increases sharply with the turbine output at which the thrust load becomes zero by the effect of a reversal in the direction of the thrust load. As no bias current is applied to the magnetic thrust bearings employed for this equipment, the

spring constant of the magnetic thrust bearings will become extremely small under the load condition which reduces the thrust load to zero. Then, the natural frequency in the axial direction decreases, falling into the phase delay zone (differential characteristics) in the lower frequency region for the controller, so that the thrust bearing current becomes unstable.

Therefore, in a turbomachine like this air turbine in which the the thrust load sometimes becomes zero upon the reversal of the direction of the thrust load by the effect of the fluid force, it is necessary to provide an ample flow of bias current, thereby suppressing the fluctuations otherwise likely to occur in the thrust rigidity.

4.4 Partial loading test

The relationship among load applied in the partial loading test, the radial bearing current (radial load), and the thrust bearing current (thrust load) are shown in Figs. 13 (a) and (b). The partial load was simulated by covering one third of the injection nozzle with a shield plate when the rotor was in its counterclockwise rotation, as shown in the figures. In

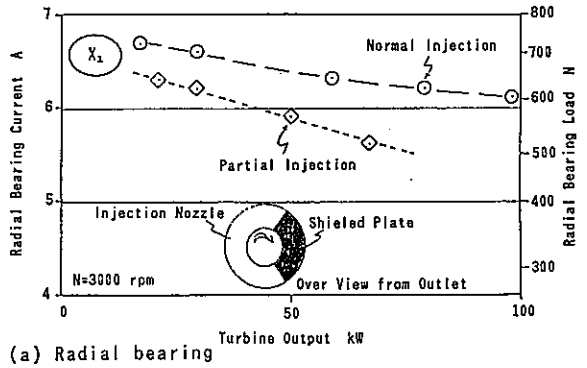

(a) Radial bearing

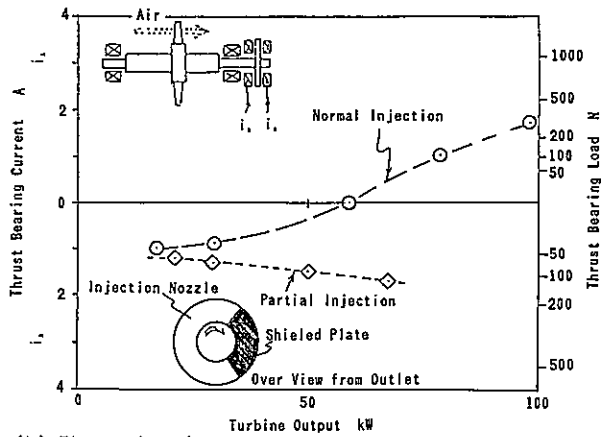

(b) Thrust bearing

Fig. 13 Active magnetic bearing loads

the case of such partial injection, the fluid force tending to push the rotor upward is at work, and the load on the radial bearings decreases as compared with the load at the time of the normal injection. In respect of the increase in the output from the turbine, the same tendency as at the time of the normal injection is observed. Although the thrust load reverses the loading direction in the case of the normal ejection, as mentioned above, the loading direction does not change in the partial injection. As discussed so far, it is considered one of the merits of magnetic bearings with no parallel in the conventional bearings, that it is possible to gain an accurate measure of the fluid force through the measurement of the coil current in the magnetic bearings.

5. Conclusion

With a machine formed by modifying the oil-film bearings into magnetic bearings in a conventional air turbine performance test rig, inquiries were made into the vibration characteristics of the shaft system and the open loop transfer function of the entire control system. A comparison was also made of the control performance of an analog controller and a digital controller of the PID system through rotational and loading tests. The results are as follows:

(1) The test rig provided with magnetic bearings has proved to attain its stable rotating characteristics with low vibration. It has also demonstrated sufficient capability to withstand the fluid force at work at the time of the loading tests up to the overspeed corresponding to 120 % of the rated revolutions of the turbine, either as operated with the analog controller or with the digital controller.

(2) Even with the digital controller by the PID control process, it was possible to attain the same performance in control as with the analog controller.

(3) When any notch filter is used to prevent vibration in the shaft bending mode, it increases the margin of capability of accommodating changes in the natural frequency of the shaft system to set the central frequency for the notch filter at a level somewhat lower than that of the natural frequency at the time of its standstill.

(4) Since the vibration characteristics of magnetic bearings undergo changes when fluid force works on the bearings, it is necessary to perform sufficient simulations in advance with respect to such changes.

References:

[1] KIRK, R. G., HUSTAK, J. F. and SCHOENECK, K. A.: Analysis and Test Results of Two Centrifugal Compressors Using Active Magnetic Bearings. IMechE C278/88, pp. 93-, 1988

[2] BLEULER, H. and SALM, J.: Active Electromagnetic Suspension and Vibration Control of a Signal Processor. IMechE C287/88, pp. 101-, 1988

[3] MATSUSHITA, O.: Stabilization by Cross Stiffness Control of Electromagnetic Damper for Contained Liquid Rotor Unstable Vibration. Intern. Cont. on Vibration in Rotating Machinery, Sep., pp. 13-15, 1988

[4] MATSUSHITA, O., YOSHIDA, T., TAKAGI, T., and TAKAHASHI, N.: Rotor Vibration Simulation with Active Magnetic Bearing Control. 2nd Intern. Sympo., MAGNETIC BEARINGS, July, pp. 12-14, 1990, Tokyo, Japan

2nd International Symposium on Magnetic Beaing
July 12-14, 1990, Tokyo, Japan

MAGNETIC SUSPENSION FOR A TURBOMOLECULAR PUMP

G. GENTA*; L. MAZZOCCHETTI**; E. RAVA**

* Politecnico di Torino, c.so Duca degli Abruzzi 24, 10129 Torino, Italy
** Elettrorava S.p.A., Via Don Sapino 176, 10040 Savonera - Torino, Italy

Abstract

Magnetic bearings allow to solve in a very effective way many of the problems encountered in high vacuum turbomolecular pumps: lubrication under vacuum, hydrocarbon contamination, operating position, vibration and noise.

The development of a magnetically suspended turbomolecular pump based on a "one active axis" configuration is here described. A permanent magnet radial passive bearing and one active axial bearing with its feed-back control loop have been developed and thoroughly tested.

Before building the prototype, a hybrid turbomolecular pump which uses the same radial bearing and one axial ball bearing has been built and tested. As the performance of this machine proved to be very satisfactory, the prototype of the machine with full magnetic suspension is now under construction.

1. Introduction

Rotors operating in high vacuum and at high speed are a very interesting application field for magnetic bearings. The substitution of rolling elements bearings with magnetic suspension systems in turbomolecular pumps, in which both these aspects are present, is very promising.

A turbomolecular pump is a high vacuum device, designed to operate in the range between 1 and 10^{-8} Pa, therefore needing a backing pump, which is normally of the vane type. The rotor is made of a series of bladed discs which look like axial compressor discs but work in a completely different way as they operate in a free molecular flow with the well known principle of molecular pumps [1].

Turbomolecular pumps are powered usually by asyncronous high frequency a.c. motors or d.c. brushless motors located in the vacuum container; types driven by belts through magnetic couplings were also produced.

The spin speed of these machines can range from 10000 up to 90000 rpm depending on the size of the pump, and the bearings must be located within the vacuum container in order to avoid high speed seals on the shaft. It is true that the bearings can be located on the side in which the pressure is higher (output side of the pump) but the pressure is at any rate of about 1 Pa and consequently very low vapour pressure lubricants are needed.

Standard turbomolecular pumps with high speed ball bearings are commercially available since many years, but they cannot completely satisfy the most demanding applications. Although high speed ball bearings can operate under vacuum, there are still some problems to be solved in a completely satisfactory way, mainly due to the presence of lubricants, which can cause vacuum contamination by hydrocarbons, the need for high speed balancing of the rotors and the limited service life.

Residual vibration and noise can also be a problem in some special applications and when the pump is used in a laboratory environment close to people.

All these problems can be avoided with the use of magnetic bearings, which are increasingly used in order to achieve higher speed, cleaner vacuum, lower vibration and noise levels and better reliability.

Hybrid configurations, i.e. configurations employing a combination of magnetic and mechanical bearings, have been used for a few years, but all manufacturers are now involved in the development and sometimes already in the regular production of turbomolecular pumps with total magnetic suspension.

Most of these more advanced solutions are based on five active axes magnetic suspensions which have been developed since some years and run properly, but their cost is still too high and, as a consequence, these pumps have not reached a wide diffusion on the market.

The tendency is now to build turbomolecular pumps with total magnetic suspension reducing to a minimum the number of the actively controlled axes. According to Earnshaw theorem, one of the possible solutions is to have four radial passive axes and only one axial active axis.

This means that permanent magnets or uncontrolled electromagnets are used for the radial bearings, whereas the axial position of the rotor is controlled by an active magnetic bearing.

Another advantage of the total magnetic suspension is that the sensitivity to unbalance is much lower because the rotor tends to rotate around its principal axis of inertia. Therefore the balancing requirements are far less strict than in conventional solutions and in most cases it is not necessary any more to balance the rotor at its operating speed.

The less strict balancing requirements lead to a potential reduction of production costs which can, at least in part, compensate for the higher costs of the suspension system.

Owing to the above mentioned reasons, a new turbomolecular pump with magnetic suspensions is now being developed according to the scheme of fig.1.

The rotor is suspended by means of two passive radial magnetic bearings and one active axial magnetic bearing. This

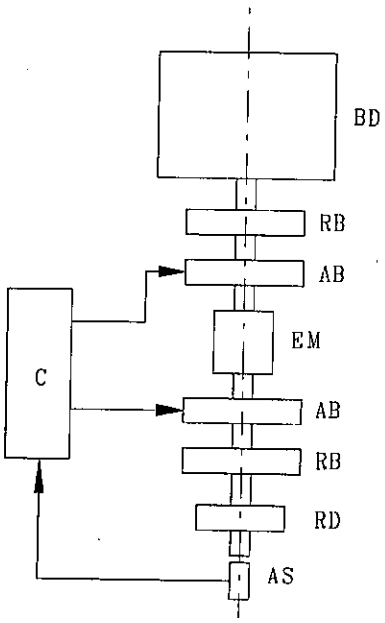

Fig. 1. Scheme of the magnetic suspension system. AB: active axial magnetic bearing; AS: axial position sensor; BD: bladed discs; C: electronic control unit; EM: electric motor; RB: passive radial magnetic bearing; RD: passive radial magnetic damper.

solution is well suitable for a turbomolecular pump, where the radial loads are negligible and the required radial stiffness is within the capabilities of permanent magnets.

Therefore only the axial position has to be controlled actively in order to compensate for the negative stiffness of the passive radial magnetic bearing which are inherently axially unstable. The disadvantage of this configuration is that a passive radial damper is needed in order to be able to accelerate beyond the critical speeds during startup.

A particular type of passive radial magnetic bearing has been developed for this particular application in order to obtain a very simple and low-cost system. In this development stage several bearings of all types shown in fig. 2 have been built and tested. A small turbomolecular pump with hybrid suspension system with one passive radial magnetic bearing of the type considered and one traditional grease lubricated ball bearing has been built and thoroughly tested.

2. Passive radial magnetic bearings

2.1. Bearing type A In order to find the most suitable passive radial magnetic bearing for this application, different types have been examined comparing the following parameters: radial stiffness, axial instability, ease of manufacturing, ease of assembling and cost.

The radial and axial stiffness have been measured experimentally for the four main types shown in fig. 2.

The first type, shown in fig. 2a, is built-up of two concentric sets of annular permanent magnets axially magnetized. The magnets of each set are separated by thin aluminium rings and repel each other axially, forcing the flux lines of each magnet to close on themselves in the radial air gap between the two sets of magnets.

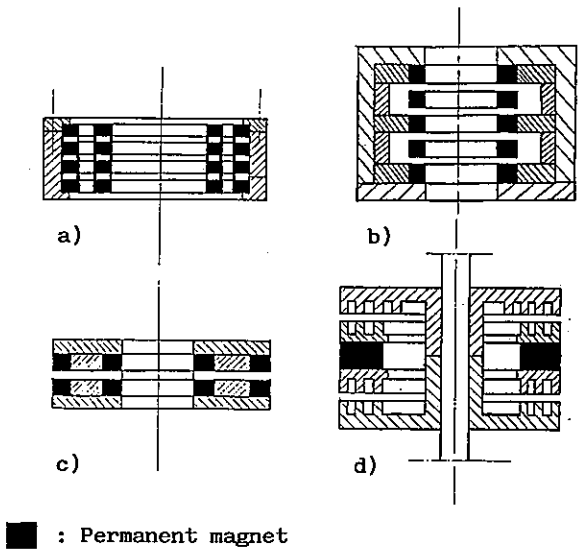

Fig. 2. Configurations of the passive radial magnetic bearing considered for the turbomolecular pump.

The two concentric sets of magnets repel each other radially. The radial stiffness is proportional to the number of magnets that have been employed and of course depends on the material of the magnets. Due to the very high demagnetizing force acting on the magnets, Samarium Cobalt (Sm-Co) or Neodymium Iron Boron (Nd-Fe-B) alloys have to be used for this kind of bearing.

2.2. Bearing type B A number of equal axially magnetized annular magnets attract each other and are alternatively rotating and fixed [2], [3]. At least two magnets are needed, but normally an odd number (5, 7, 9) is used in order to have a vanishingly small axial force when the rotating magnets are axially centred with respect to the fixed ones.

If the rotating magnets are shifted radially, a magnetic radial shear force that tends to restore the central position results. Furthermore, an external iron magnetic path can be built in order to close the flux and maximize the radial stiffness, as shown in fig. 2b.

2.3. Bearing type C Another type of passive radial magnetic bearing is shown in fig. 2c. The fixed and the rotating parts have the same geometry and attract each other. Each part is built up of two concentric axially magnetized annular magnets with an iron disc to close the magnetic flux. The radial stiffness is here again due to radial magnetic shear forces, but the axial force is not zero and increases with decreasing air gap.

2.4. Bearing type D The three types of passive radial magnetic bearings that have been described above have good radial stiffness and have already been employed in turbomolecular pumps for many years, but they have some disadvantages. In

all types there are rotating magnets, which makes the construction more complicated and more costly.

The mechanical strength of Sm-Co and Nd-Fe-B materials used for the magnets is not high enough to withstand the high rotational speeds required in turbomolecular pumps if they are not prestressed by a surrounding aluminium ring. This ring has to be connected to the magnet by adhesive bonding or shrink fitting but in the latter case the thermal cycles could change the magnetic properties of the permanent magnets. Other construction types involving a welded magnet housing are also used.

Furthermore each bearing is built up of many small magnets which are brittle and have to be handled with care, so that the assembly in mass production is critical.

In order to avoid these problems, the passive radial magnetic bearing type D shown in fig. 2d has been developed for the magnetically suspended turbomolecular pump. The main advantage is that there is only one relatively big magnet which is not rotating, and the magnetic flux is guided through the air gap by some small iron annular teeth of suitable shape creating the radial stiffness.

The steel rotor shaft is then used to close the flux. When there are equal air gaps on both sides of the magnet, the axial force acting on the rotor is zero, but this is an unstable equilibrium.

Experimental measurements have been carried out on a passive radial magnetic bearing of the type D with a Sm-Co magnet with outer diameter of 56 mm, inner diameter of 34 mm and axial thickness of 10 mm. The results are shown in fig. 3, where the axial and radial forces are plotted as functions of the axial and radial displacements respectively.

A radial stiffness of about 100 N/mm was found with an air gap of 0.5 mm. The maximum axial force with zero air gap on one side and 1 mm air gap on the other side was 150 N.

3. Hybrid turbomolecular pump

The passive radial magnetic bearing type D has been at first used in a 60 l/s turbomolecular pump running at 72000 rpm. A cross section of the pump is shown in fig. 4.

There is one grease lubricated ball bearing and one passive radial magnetic bearing type D located near the centre of gravity of the rotor. The ball bearing is located at the lower end of the shaft and sustains the axial load. The surface of the iron teeth has to be machined with a spherical shape with the centre in the ball bearing.

The bladed discs are above the passive radial magnetic bearing so that there is no permanent magnet exposed to high vacuum or to other dangerous environmental conditions which can exist inside the vacuum chamber, as high temperatures. The damping of the system is quite low, but the rotor runs properly at 1200 Hz (72000 rpm), which is a much higher frequency than the first critical speed of the system which is at about 46 Hz (2760 rpm).

Quite a large amplitude of the synchronous whirl is obtained when crossing the critical speed and an amplitude limiter consisting of a ring of a special low friction material located around the shaft is used.

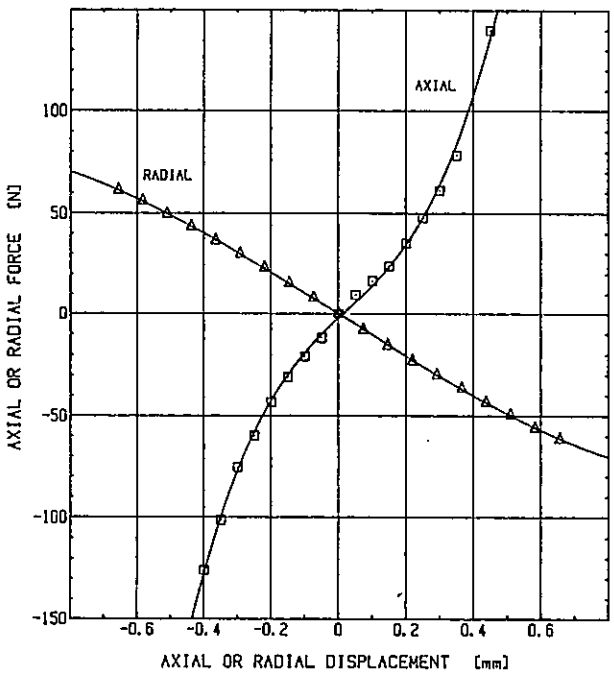

Fig. 3. Experimental characteristics of a passive radial magnetic bearing of type D.

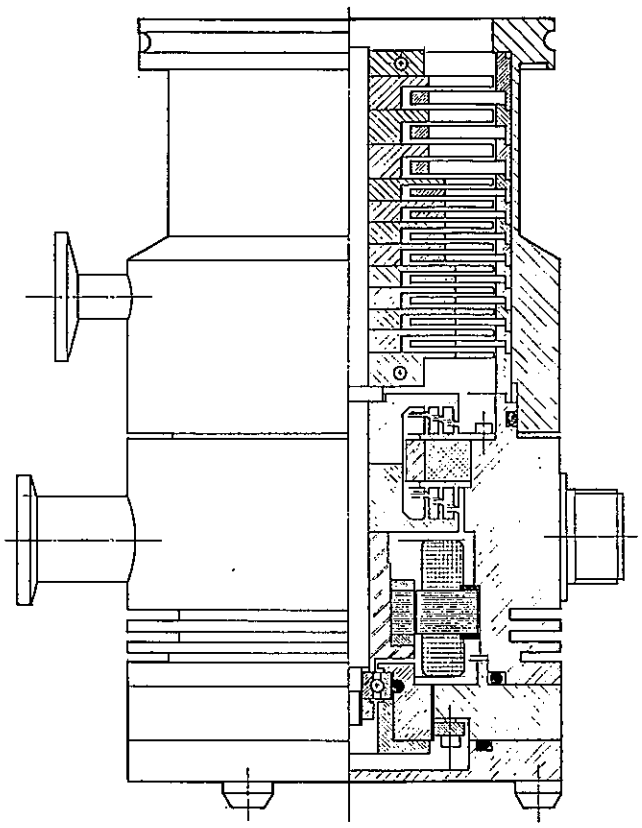

Fig. 4. Cross section of the hybrid turbomolecular pump.

The axial position of the rotor can be adjusted during assembly in order to let the passive radial magnetic bearing work around the zero axial force position. The a.c. squirrel cage motor has a total power consumption of about 30 W under vacuum.

The rotor has been balanced at 1500 RPM on a balancing machine and higher speed balancing was not needed.

The dynamic behaviour of the rotor was investigated using DYNROT finite element code developed at the Mechanics Dept. of Politecnico di Torino [4]. The radial force-displacement characteristic of the magnetic bearing obtained experimentally was linearized about the equilibrium position. A total of 22 nodes and 21 Timoshenko beam elements has been used.

The critical speeds, mode shapes and the Campbell diagram shown in fig. 5 were computed.

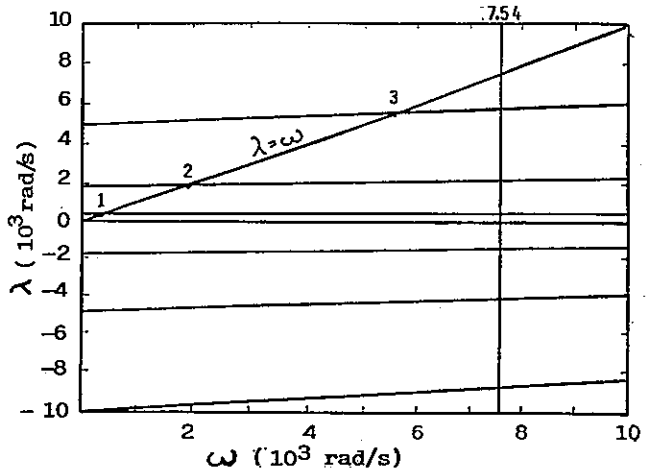

Fig. 5. Campbell diagram of the hybrid turbomolecular pump.

The first critical speed computed by the finite element code is 2730 rpm. Other critical speeds within the working range were obtained, as seen from the Campbell diagram. The analysis of the relevant mode shapes shows however that they are little excited by the static unbalance of the bladed discs and heavily damped by the lower bearing.

The numerical results were later confirmed by vibration measurements on the prototype.

Strong vibrations were detected at a speed of 2760 rpm, with very good accordance with numerical critical speed predictions. As expected, no other critical speed was detected up to operating speed.

The vibration spectrum at 72000 rpm is shown in fig. 6. The four peaks are due to synchronous whirl (1200 Hz), disturbances due to the ball bearing (448 Hz), whirling in the first forward mode (48 Hz) and disturbances coming from the vane backing pump (24 Hz).

The pump was thoroughly tested in operating conditions for some hundred hours with very satisfactory results. In particular the very low energy consumption, about 1/2 of that of conventional solutions and the very low level of vibration without the need of fine balancing were the most interesting features of the machine.

4. Turbomolecular pump with completely magnetic suspension

4.1. General description Owing to the success obtained with the hybrid machine, the design of the pump with a completely magnetic suspension was undertaken.

A cross-section of this machine, a 360 l/s pump running at 48000 rpm, is shown in fig. 7.

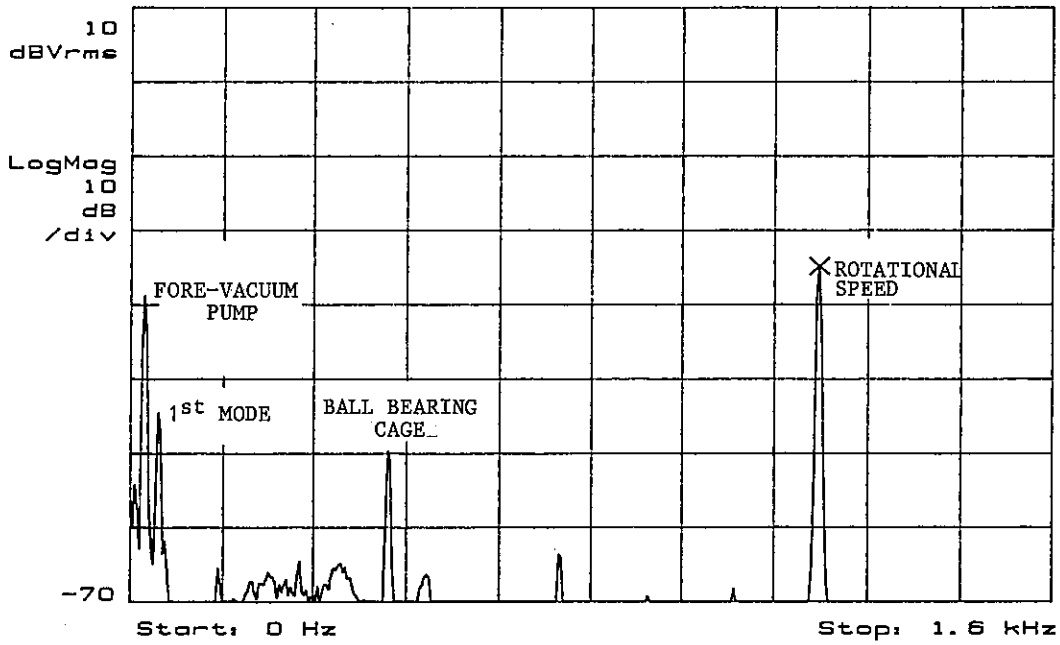

Fig. 6. Vibration spectrum at 72000 rpm.

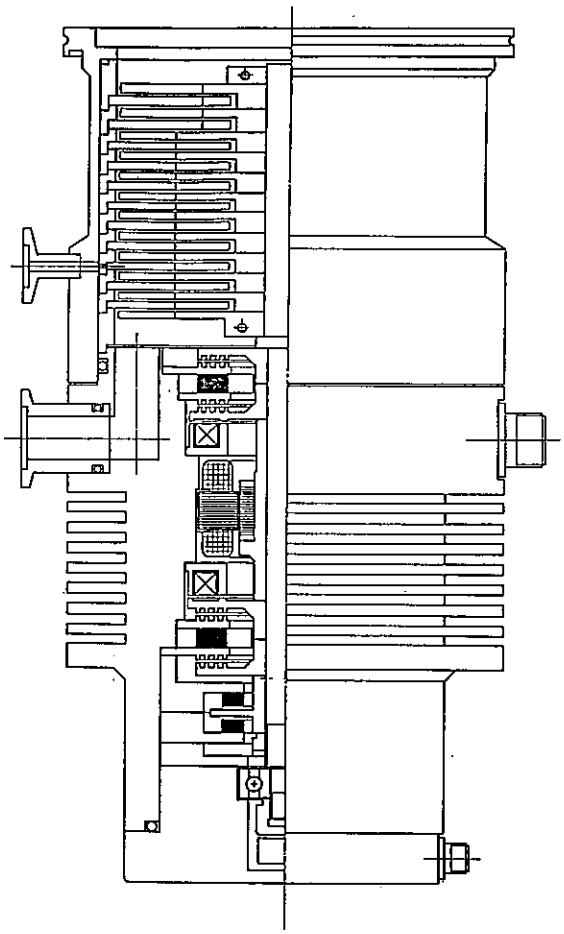

Fig. 7. Cross section of the turbomolecular pump with full magnetic suspension.

Two passive radial magnetic bearings of type D are employed; the upper bearing is located close to the centre of gravity of the rotor. The axial actuator is split into two electromagnets, each one attracting one iron disc of the passive radial magnetic bearing, so that the rotor can be attracted in opposite directions.

The five axes magnetic suspension is completely symmetrical with respect to the a.c. squirrel cage motor. Below the second passive radial magnetic bearing there is an eddy current radial damper [2], [5] consisting of an aluminium disc rotating between two axially magnetized annular Sm-Co permanent magnets. The two magnets attract each other and the flux lines are crossing the conductive disc, whereas an external iron path is closing the flux.

If the disc does not move radially, there is no magnetic flux variation and no current in the disc. But if there is a radial movement of the disc due to whirl motion, eddy currents are induced and the radial motion is damped. At the lower end of the shaft there is a dry-lubricated touch-down ball bearing and the axial inductive sensor to provide the axial position signal to the electronic control system.

It can be seen from the previous description that there is no rotating magnet in the system, which is an advantage from several points of view. Between the magnet of each passive radial magnetic bearing and the rotating shaft there is a ring of a special anti-friction material in order to limit the radial displacement of the rotor if the damper is not sufficient in case of an external shock.

4.2. Active axial bearing The electromagnet used for the axial magnetic bearing is shown in fig. 8a. All relevant data are reported in tab. 1.

If the reluctance of the iron path is neglected the axial force is given by

$$F = \frac{\mu_0 S_g N^2 I^2}{4d^2} \qquad (1)$$

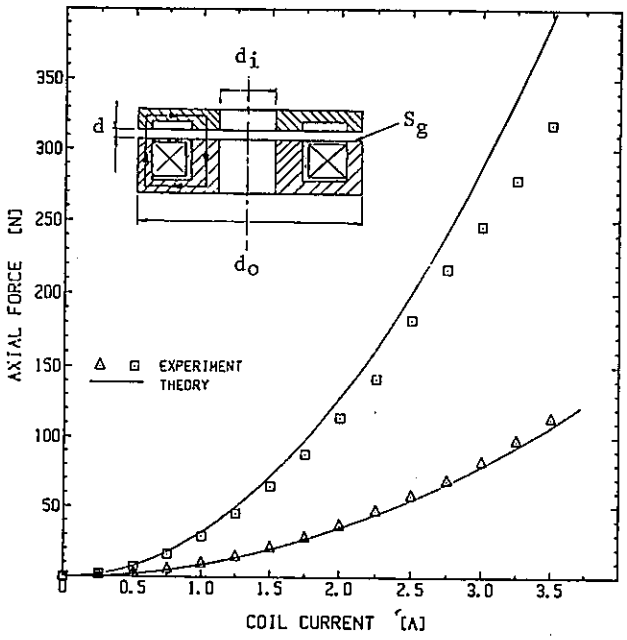

Fig. 8. Axial active magnetic bearing. a) Axial electromagnet. b) Force-current characteristics of the electromagnet.

Outer diameter d_o	80 mm
Inner diameter d_i	20 mm
Air gap surface S_g	1200 mm^2
Number of turns N	160
Wire diameter d_w	1 mm
Nominal air gap d	0.5 mm
Coil resistance R	0.64 Ω
Coil inductance L	35 mH
Nominal load F	410 N
Nominal current density j	4.5 A/mm^2

Tab.1. Data of the axial bearing

It can be seen that the force is proportional to the surface of the air gap, to the square of the current, whereas it decreases with the square of the air gap d.

A plot of the force as a function of the current for the electromagnet of fig. 8a is shown in fig. 8b. The theoretical curve and the experimental points are both plotted and the agreement is quite satisfactory.

The two passive radial magnetic bearing are axially unstable: when the rotor is centred the axial force is zero, but a small deviation from the central position will cause the rotor to move rapidly out of this position. Therefore the axial magnetic bearing must be active and an electronic control unit providing the required stability is needed.

The situation is graphically illustrated in fig. 9, where the force F_{mz} due to the passive radial magnetic bearing acting on the rotor is shown as a function of the axial co-ordinate z of the rotor. As a first approximation in practice it can be assumed that the force F_{mz} increases linearly with z

$$F_{mz} = -K_{mz} z \qquad (K_{mz} < 0) \qquad (2)$$

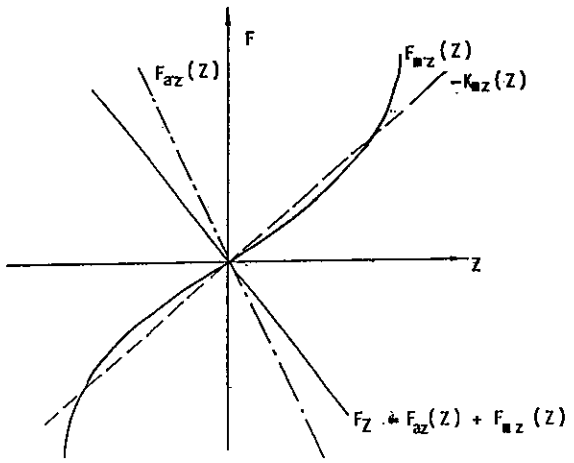

Fig. 9. Force-displacement curves for axial stabilization.

The constant K_{mz} is the negative axial stiffness of the passive radial magnetic bearing. In order to make the system stable, a force

$$F_{az} = -K_{az} \cdot z \qquad (K_{az} > 0) \quad , \qquad (5)$$

generated by the electromagnets driven by the control system that monitors continuously the position of the rotor, must be applied. Constant K_{az} is positive and must overcome the intrinsic axial instability of the passive bearing.

The resulting axial force acting on the rotor is given by

$$F_z = F_{mz} + F_{az} = -K_z \cdot z \quad , \qquad (4)$$

where constant K_z is the overall axial stiffness of the system and has to be positive in order to achieve stability. The condition for stability is then

$$K_z > 0 \quad , \quad \text{i.e. } K_{az} > |K_{mz}| \quad . \qquad (5)$$

As it is shown in fig. 9, the slope of F_{az} has to be greater in absolute value then the slope of F_{mz}. Of course this condition allows to achieve just static stability and other conditions has to be fulfilled by the control system in order to get dynamic stability.

4.3. Control system The block diagram of the control system is shown in fig. 10. The position monitoring is performed by an inductive sensor giving an electric signal which is proportional to the distance between the sensor and the end of the shaft.

The signal is compared with a stable reference signal in order to get a signal proportional to the position z of the rotor. It is then amplified and differentiated to get the information about the axial velocity of the rotor in order to achieve the required damping. The position and velocity signals are then added together to drive the final amplifiers.

The latter are voltage driven current amplifiers that inject the proper current into the coils of the electromagnets. The two electromagnets are working alternatively to attract the rotor towards the central position.

Following a displacement of the rotor in the positive direction z, the current in coil 1 is zero whereas the current in the other coil increases to generate a restoring force attracting the rotor back to its central position.

If otherwise the displacement occurs in the negative direction -z, the current in coil 2 is zero whereas the current in coil 1 increases. Therefore the signal has to be divided in two paths and rectified before driving the final amplifiers. Furthermore another signal must be added to get the stability around the equilibrium point.

The axial force of each electromagnet increases quadratically with the current, and if the current in one coil starts increasing exactly when the current in the other coil approaches zero, the force-displacement curve has a zero derivative in the origin.

This condition is shown in fig. 11, where it can be clearly seen that a negative stiffness is obtained around the origin when the force of the active axial magnetic bearing is added to the axial force of the passive radial magnetic bearing.

This problem can be solved if a current I_o is injected in both coils also when the central position is obtained (z=0), which can be achieved by adding a constant voltage to the signals driving the two power amplifiers, as shown in fig. 10.

4.4. State of development of the project. At present the construction of the prototype has not yet been completed.

Numerical simulations and particularly rotor dynamics computations have been performed using the already mentioned DYNROT code in order to verify the ability of the system to run correctly.

A prototype of the active magnetic axial bearing complete of its control system has been built and thoroughly tested. The conditions for both static and dynamic stability have been achieved.

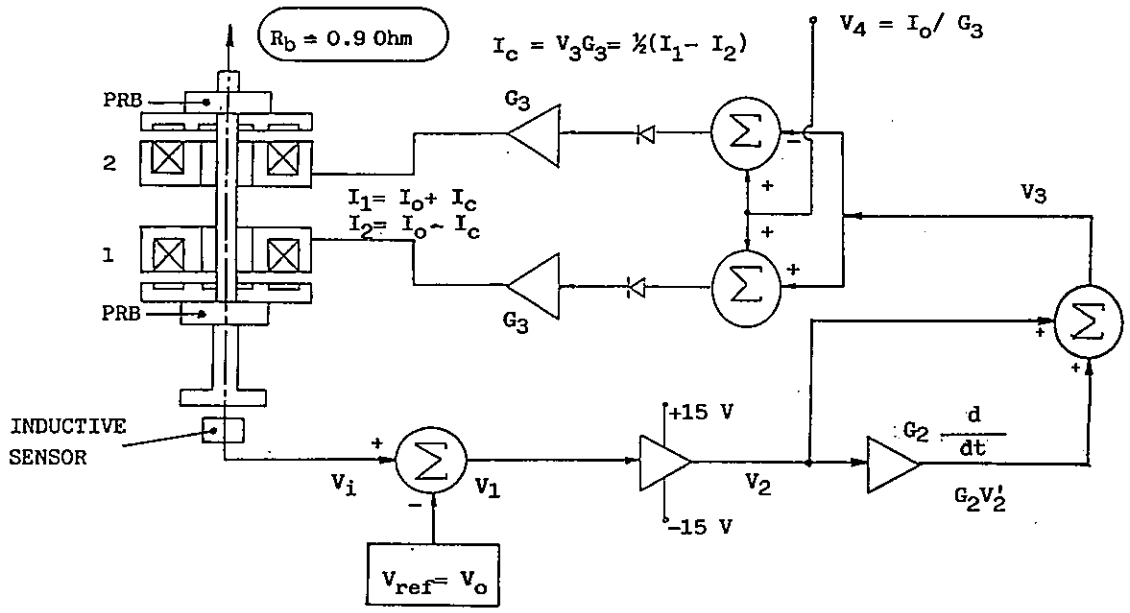

Fig. 10. Block diagram of the control system.

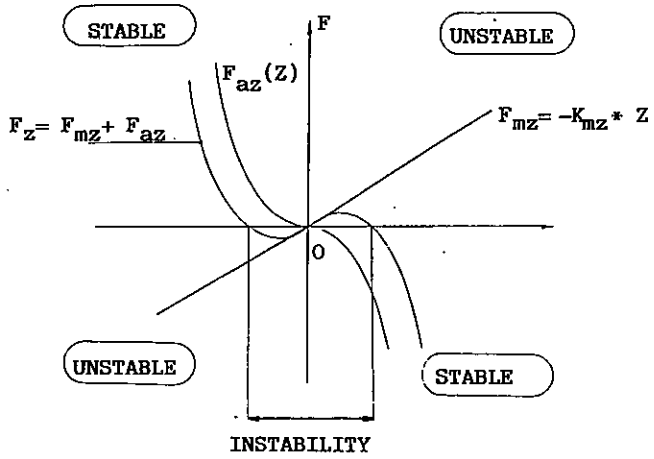

Fig. 11. Instability about the zero-force position.

As all components have been tested separately and some of them have operated in a satisfactory way on the hybrid machine, the turbomolecular pump with full magnetic suspension is expected to fulfil its design goals.

5. Conclusions

The passive radial magnetic bearing of the type shown in fig. 2d seems to be an attractive device for many applications where the manufacturing cost and the ease of assembly are the determining factor in the choice of the magnetic bearing.

Furthermore the absence of rotating magnets makes it very suitable for high rotational speeds. Using this kind of passive radial magnetic bearing a simple total magnetic suspension for turbomolecular pump can be built with only one actively controlled axis.

This leads to a simple control system that has to control only the axial position of the rotor. The main drawback of this type of suspension is the lack of damping of the passive radial magnetic bearing which can create some problems especially during acceleration and deceleration of the rotor. An eddy current damper has been added, but further development can be needed to get better solutions.

In order to verify the suitability of this radial magnetic bearing, a hybrid turbomolecular pump was built and tested.

The hybrid machine fulfilled all design goals, proving to be able to reach the design operating speed and to work satisfactorily for prolonged periods of time.

In particular it showed a very low power consumption and the possibility of operating with very low noise and vibration levels without the need of fine balancing. The use of ball bearings with ceramic rolling elements is now considered in order to improve the performance of hybrid turbomolecular pumps.

The axial active bearing has been tested separately and the final prototype is under construction.

References

[1]. KRUGER, C.H.:"The Axial Flow Compressor in the Free Molecule Range", Ph. D. thesis, M.I.T., 1960.

[2]. FREMEREY, J.K.:"Radial Shear Force Permanent Magnet Bearing System with Zero-Power Axial Control and Passive Radial Damping", First International Symposium on Magnetic Bearings, ETH Zurich, Switzerland, June 6-8, 1988, pp.25-31.

[3]. HACKEMBERG, R. and EBERT W.:"High Precision Particle Beam Chopper", First International Symposium on Magnetic Bearings, ETH Zurich, Switzerland, June 6-8, 1988, pp. 33-40.

[4]. GENTA G.:"A Consistent Matrix Approach for F.E.M. Dynamic Modeling of Rotors", III Conf. on Mech. Des. and Prod., Cairo, Dec. 1985.

[5]. POUBEAU, P.C.:"High Speed Flywheels Operating on "One Active Axis" Magnetic Bearings", 1977 Flywheel Technology Symposium, San Francisco, California, U.S.A., Oct. 1977.

2nd International Symposium on Magnetic Beaing
July 12-14, 1990, Tokyo, Japan

APPLICATION OF MAGNETIC BEARINGS IN A MULTISTAGE BOILER FEED PUMP

Gordon McGinnis and Paul Cooper
Ingersoll-Rand Company (IR)

Gerald Janik
New York State Electric and Gas (NYSEG)

Graham Jones
Gas-Cooled Reactor Associates (GCRA)

Richard Shultz
Magnetic Bearings, Inc. (MBI)

Abstract

Magnetic bearings have been fitted to an eight-stage, 600 hp. boiler feed pump in an effort to bring to the electric utility industry the attendant benefits of longer bearing life, lower maintenance costs and better operability through control of the rotodynamics.

This pump generates 2605 ft of head at 680 gpm and 3560 rpm. It will be subjected to varied and severe operating environment of a power plant, which results in loads that can now be measured at the bearings. The pump will be monitored and evaluated against a similar pump containing conventional bearings for a period of one year in order to establish the feasibility of magnetic bearings for boiler feed pumps.

INTRODUCTION

Magnetic bearing usage in pumps is a natural development when one considers the successes of these bearings in large centrifugal compressors *(1). For pumps of significant power level, the elimination of lubrication systems that would otherwise be needed for conventional bearings and the attendant reduction of maintenance are benefits that should be claimed.

Recently, magnetic bearings were applied to a 20-horsepower, canned-motor, single-stage, centrifugal pump, wherein the conventional bearings were replaced by submerged, canned, magnetic radial and thrust bearings (2).

Application to multistage pumps with orders of magnitude greater power is the next step and is a further test of the feasibility of magnetic bearings, because such pumps often operate with close internal clearances and flexible shafts. Typical of such pumps are those used for boiler feedwater in the electric utility industry. In studies of magnetic bearings for that industry, financial viability was established for applying these bearings in boiler feed pumps (3,4). Increased availability and reduction in operating and maintenance costs were projected, leading to a favorable evaluation (5).

The design of a multistage boiler feed pump is a compromise between allowing sufficient clearance for shaft flexure and thermal distortion and minimizing clearances to increase the efficiency of the impeller ring and the shaft sealing systems. Ideally the bearings would be mounted closer together than is current practice, with a closer tolerance on shaft movement. If submerged magnetic bearings were used, then this could be accomplished by eliminating the outboard (non-drive end) seal and putting the inboard bearing between the first-stage impeller and the inboard seals (6).

Phenomena unique to pumps that could affect magnetic bearing performance are:

(a) The Lomakin Effect. This is the bearing-like stabilizing action that occurs as high-pressure fluid from the discharge of each impeller leaks through the tight annular clearance of the neck ring "seal" back to the impeller suction eye. Shown in Figure 1, this

* Numbers in parenthese denote references listed at the end of the paper.

effect is not always stable - being influenced negatively by swirling of the fluid entering the clearance space. These phenomena can have a confusing influence on otherwise straightforward and understood rotordynamic behavior (7).

(b) Increases in Clearance. Wear of the impeller neck rings or adjacent casing rings leads to loss of stabilization and therefore to adverse changes in rotodynamical behavior.

(c) Loss of Liquid. A further complication would be the loss of any stabilization arising from the Lomakin effect should liquid be momentarily absent from one or more stages of the pump.

(d) Stall Effects. These are the non-uniform flow interruptions or reversals that occur in a pump impeller and diffuser when they operate at reduced flow rates in comparison to that for which they were designed. These effects introduce unsteady, random, radial and axial loads (8).

The mechanical responses to these phenomena become more evident and critical in pumps of high energy level; i.e., those of more concentrated and higher power. For this reason it would be prudent to avoid the extensive and fundamental engineering design effort associated with magnetic bearings for high-power pumps until more is known about their behavior in such pumps in general, their ability to handle these otherwise detrimental situations, and the actual instantaneous loads that might be encountered.

This understanding would appear to be more readily obtainable by first building an intermediate-power pump in the 500 to 1000 hp range with external magnetic bearings running in air and replacing the existing externally mounted conventional bearings.

Since the current in a magnetic bearing is related to the load, readings of current vs. time, speed and pump flow rate should provide the needed insight into the stall effects. Scaling of the loads involved is fairly reliable and should enable one to make a more informed estimate of the loads for a still-higher-power submerged magnetic bearing pump. Also, the ability of the magnetic bearings to cope with the rotordynamic uncertainties mentioned above would be revealed and could be analyzed for the future submerged-bearing application.

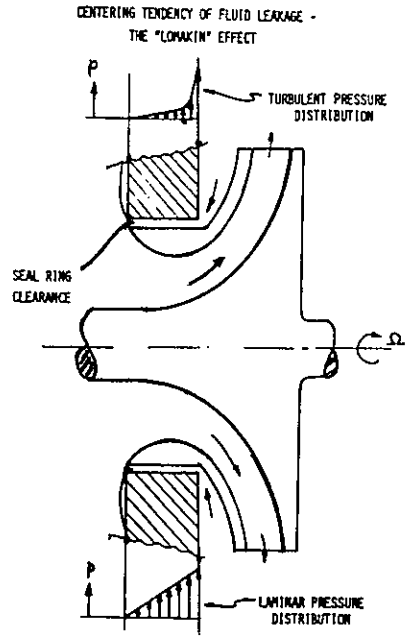

Figure 1. The Lomakin effect.

THE BOILER FEED PUMP APPLICATION

GCRA, part of a team under contract to the Empire State Electric Energy Research Corporation (ESEERCO) initiated a magnetic bearings application study in 1988 (4). The purpose of this study was to identify potential application(s) for magnetic bearing technology in large rotating machinery in a utility application. As a result of this generic study, many potential utility applications/equipment were identified, one of which was boiler feed pumps.

A continuation of this study in 1989 was to identify specific candidate pieces of equipment and a host site to demonstrate this evolving technology in a fossil-fired power plant application.

A boiler feed pump application is felt to be an ideal test/demonstration candidate as it is an energy intensive piece of equipment subject to many operational constraints (upsets). In addition, standard (traditional) boiler feed pump bearings are a big industry problem accounting for more than 11,000 MW-hrs of lost generation (9).

Magnetic bearing technology in a boiler feed pump application offers many potential benefits including improved maintenance techniques, reliability and efficiency. Reduction in failures due to shaft breakage and other mechanical problems caused by vibration, wobbling or thrusting, as well as reduction in forced outages or load loss situations are further benefits.

In mid-1989, New York State Electric & Gas Corporation (NYSEG), an ESEERCO member, became aware of the magnetic bearing technology and its potential application to boiler feed pumps, Since ESEERCO was looking for a host fossil site and NYSEG was planning to replace the boiler feed pumps on Unit No. 3 at its Greenidge Station in the Spring of 1990, NYSEG offered this unit as a host site for this boiler feed pump magnetic bearing test/demonstration.

Greenidge Unit No. 3 is a 58MW (gross) plant with an in-service date of May 1950. This Greenidge Unit No. 3 site was felt to be attractive since the three outmoded existing 50 percent boiler feed pumps were in the process of being replaced, the timing was right for getting a boiler feed pump equipped with a magnetic bearing and the unit is equipped with a spare boiler feed pump. The 700 HP size for this first time electric utility application was ideal. A magnetic bearing installed on a single pump at this location can be tested with a reduced amount of risk to power plant operation since there will also be two 50 percent pumps equipped with conventional bearings and the application will provide a direct comparison of magnetic with conventional bearings.

It was agreed that ESEERCO would fund the fabrication and installation of the magnetic bearing on a single pump and NYSEG would fund the one year test program at its Greenidge Unit No. 3; a two boiler, two feed pump operation.

The one year test program is scheduled to begin in August 1990. Testing will take place over a one year period during normal/usual operation of this base-loaded unit. During the test program, unusual events will be recorded and diagnosed. Upon completion of the test program, performance as well as malfunctions/outages due to pumps equipped with magnetic bearing versus conventional bearing will be determined. From this, it is expected that projections of future pump performance can be made.

PUMP DESIGN

The boiler feed pump is designed to pump 680 gpm (42.9 l/s) of 254 F (123 C) feedwater to a head of 2605 ft. (794 M). Shaft power consumption at this condition is 553 hp (413 kW). a conventional 700 hp (522 kW) induction motor drives the pump at 3560 rpm. The pump is designed as an eight-stage, volute-type, opposed-impeller machine; with four impellers facing the drive end and four facing the non-drive end, as shown in Figure 2.

A high degree of axial thrust balance exists, producing low resultant loads on the axial thrust bearing. Similarly a low resultant radial thrust unbalance results from the use of opposed dual volutes and stage crossovers in the horizontally split pump casing.

Hardened stainless steel rotating and stationary wearing rings have a 0.009 inch (0.23mm) radial clearance. These impeller and casing rings are fitted to each stage of the pump. Ring contact during normal operation is prevented by the self-centering magnetic bearings in the pump so equipped, or by the conventional oil lubricated journal bearings in the other two pumps.

A loss of power to the magnetic bearings when in operation would allow the rotor to drop. To guard against ring contact in this circumstance, three metal filled carbon-graphite auxiliary bushings have been fitted to the magnetic bearing pump as depicted in Figure 2. The two bushings located adjacent to the mechanical seal fitted boxes as well as the center bushings have a radial clearance of 0.005 in. (0.13mm). Metal filled carbon-graphite is successfully used for bearings and bushings in a wide variety of liquid and gaseous applications.

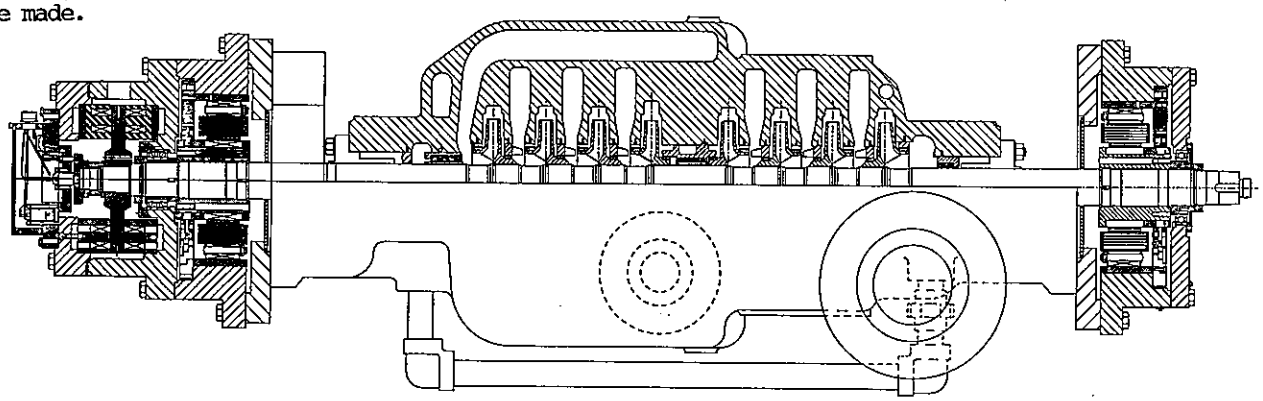

Figure 2. Multistage volute pump fitted with magnetic bearings.

MAGNETIC AND AUXILIARY BEARINGS

The load capacity requirements for each of the magnetic radial bearings are 280 lb. (127 kg) steady-state and an additional 280 lb. (127 kg) for transient conditions. The requirements for the magnetic thrust bearing are 1,000 lb. (454 kg) steady-state and an additional 1,000 lbs. (454 kg) for transient conditions.

In the design of magnetic bearing systems, it is prudent to include load capacity margins to accommodate process induced surge loads and dynamic loads such as abnormal imbalance loads and hydrodynamic loads. Standard magnetic bearing designs were used which provided additional margins over conventional practice. The magnetic radial bearings are designed to provide a maximum steady-state load capacity of 600 lb. (272 kg) and to modulate a force of 400 lb. (181 kg) at a frequency of 60 Hz. The magnetic thrust bearing is designed to provide a maximum steady-state load capacity of 4,000 lb. (1814 kg) and to modulate a force of 1,000 lb. (454 kg.) at a frequency of 60 Hz.

The active magnetic bearing system assemblies are shown on Figures 3 and 4. Each magnetic radial bearing consists of a laminated silicon steel rotor attached to the shaft and a wound stator with a silicon steel lamination stack. The radial bearings have a 6 inch (152.4 mm) diameter bore and a lamination stack length of 2.5 inches (63.5 mm). The magnetic thrust bearing consists of a 11.25-inch (285.8 mm) diameter thrust disk and a laminated wound stator with a 6 inch (152.4 mm) inside diameter and a 11.25-inch (285.8 mm) outside diameter.

All magnet wire insulation and coatings are rated for continuous operation at 200 C. The bearing windings are equipped with RTD's which can be used to monitor operating temperatures.

The electronic control cabinet contains all transformers, control cards, amplifiers, and batteries necessary for the active magnetic bearing system. The cabinet power supply requirement is 208V, 60Hz, 3-phase, 2KVA. The overall cabinet dimensions are 52 inches (1321 mm) high, 21 inches (533 mm) wide, and 20 inches (508 mm) deep and the cabinet is air-cooled. The magnetic radial bearings are powered with eight 120V/15A power amplifiers and the magnetic thrust bearing is powered with two 120V/30A power amplifiers.

The cabinet is equipped with a battery backup power supply. The 208V AC external supply is transformed and rectified to a 93V DC supply. If the 93V DC supply decreases by 15 percent, the external supply is switched out of the circuit and the batteries provide the power for the cabinet. The batteries will power the bearing system for 10 minutes. After 10 minutes the system will maintain operation, but bearing load capacity may be diminished.

The auxiliary bearing at the non-drive end of the machine is a duplexed pair of angular-contact ball bearings. The bearing provides radial and axial load carrying capability if the pump were ever required to coast to a stop upon loss of both primary and backup power to the magnetic bearings. The auxiliary bearing at the drive end of the machine is a Conrad type single radial bearing.

The radial air gap for the magnetic radial bearing is .020 inch (0.51 mm) and the radial air gap for the adjacent auxiliary bearing is .010 inch (0.25 mm). The magnetic axial thrust bearing air gap are 0.028 inch (0.71 mm) and the auxiliary thrust bearing airgaps are 0.014 inch (0.36 mm).

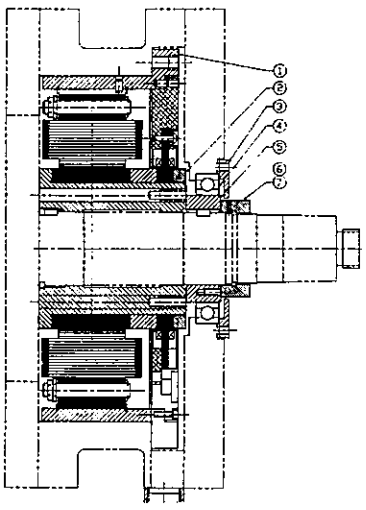

Figure 3. Radial magnetic bearing on drive end of pump.

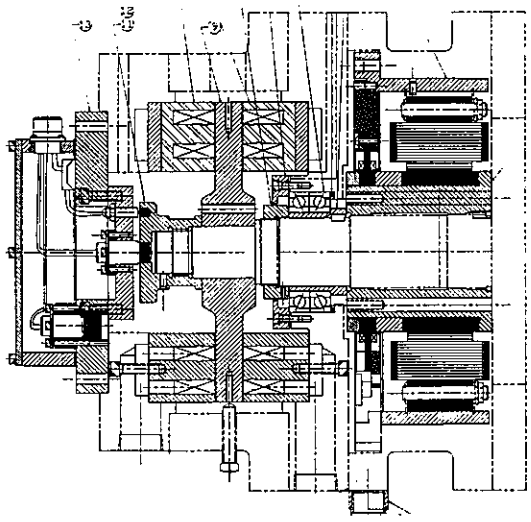

Figure 4. Radial and axial magnetic bearings on non-drive end of pump.

The active magnetic bearing system includes two inductive radial position sensors and one inductive axial position sensor. The radial position sensors are located adjacent to the radial bearing lamination stacks and the axial position sensor is located at the end of the shaft on the non-drive end of the machine. After signal processing, the position sensor signal has a sensitivity of approximately 625 mV per mil. The radial position sensors are designed to reject the third and even number harmonics of any rotor imperfections which would cause position sensor signal noise.

OPERATION

The magnetic bearings, when activated, maintain the rotor position within the clearances mentioned above. Should the power to these bearings be lost - including the reserve power provided by the battery back up system - the shaft will drop. As the pump coasts down, the shaft will then contact the carbon-graphite auxiliary bushings because they have a smaller radial clearance than the rolling element auxiliary bearings.

At first glance it would thus appear that these rolling element auxiliary bearings are not needed. However, if sustained operation on the carbon-graphite bushings should cause them to wear significantly, the rolling-element auxiliary bearings will provide the ultimate protection against magnetic bearing rotor-to-stator contact. Further, the impeller rings will also be protected, because shaft deflection outboard of the carbon-graphite bushings will assure contact with the rolling element auxiliary bearings prior to impeller ring contact with the adjacent casing rings. Protection is assured against sustained loss of magnetic levitation as well as against any upset condition that might occur as a consequence of pump operation in the power plant environment.

SCHEDULE

The magnetic bearing equipped multi-stage boiler feed pump will be assembled and factory tested at IR in June/July 1990. After the radial and axial magnetic bearings and the electronic control cabinet are tuned to the feed pump characteristics by MBI, an operational test will ensue. Using the same 700 hp motor that will drive the pump at Greenidge, the unit will be run at varying flows, and rapidly changing flows, to simulate plant load changes and a load rejection.

Primary power will be shut-off to assure that the back-up battery system functions as intended to maintain the pump rotor levitation. A feed pump trip, following a cessation of all power to the magnetic bearings, will be conducted to demonstrate satisfactory pump coast-down with the pump rotor supported by the auxiliary support system as described above.

Following shipment of the magnetic bearing fitted boiler feed pump, driver and baseplate to Greenidge, the equipment will be installed, and under the direction of IR and MBI any needed additional fine tuning of the electronic/electrical performed.

IR and MBI will train NYSEG operations and maintenance personnel in the performance and care of the magnetic bearing equipped feed pump. At this point the equipment will be released for commercial operation and a one year monitoring program, described in the next section, will commence.

MONITORING

The one-year monitoring program will be undertaken in order to make a reasonably accurate assessment of this overall magnetic bearing demonstration project. The monitoring program will determine,

a) The net benefit to the operating utility relative to conventional bearings - in terms of economics, staffing levels, skill required, and plant availability.
b) Whether operational feed back from this first pump will allow future pumps to be designed that will be more efficient and able to withstand potentially damaging transients,
c) Whether the enhanced diagnostics that include the display or other evidence of shaft loads will increase the operator's ability to protect equipment during transients through a better understanding of these loads and the attendant rotodynamics.

To make the economic assessment, data will be obtained for both the magnetic bearing pump and one of the other conventional-bearing pumps for one year. Demonstration of an expected availability of the bearing system of 40,000 hours will require that data acquisition continue for several more years as well.

Data will be obtained at a greater frequency and in more detail in the first month of operation. This will provide the feedback needed for load analysis and establishment of magnetic bearing design requirements for future higher power pumps. At the power level and configuration of the current machine, there is no reason to expect excessive loads; the low-energy volute-type design with axially opposed stages limiting the radial and axial imbalance. These pumps are thus very suitable for this demonstration as operators will be able to display actual bearing loads under running conditions - thereby allowing the pump designer to determine these loads more precisely for future designs.

Control of pump operation and monitoring will be accomplished by interfacing with the plant computer. This computer has a maximum sampling speed of 1/10 second, which will be adequate except in the first month of operation when the more detailed bearing load data will be obtained on strip charts and viewed on an oscilloscope. Appropriate alarms will be provided from limits on loads, temperature, etc., which can then be acted upon a coordinated manner.

CONCLUSIONS

Boiler feed pumps in an electric utility can benefit from the life and low maintenance advantages of magnetic bearings. Such pumps can provide a comprehensive platform for evaluating the feasibility of magnet bearing technology under a variety of severe operating conditions that can impose strong and random loads on the rotating elements.

By conducting an in-plant demonstration of a 600 hp magnetic-bearing equipped eight stage volute-type boiler feed pump, it is believed possible to more precisely determine the load requirements for such bearings in pumps with an order of magnitude greater power input.

By monitoring the operation of the 600 hp pump, which has the magnetic bearings mounted external to the pump casing and running in air, it should be possible to gain the rotordynamical insights to design improved, higher-power machines with these bearings submerged in fluid within the interior of the casing.

Fabrication of the demonstration pump is underway, with a one-year test, monitoring and benefits evaluation program on two side-by-side new pumps - one with magnetic bearings; the other, with conventional bearings - to begin in the Summer of 1990. If successful, this project could provide an alternate technology to the utility industry resulting in higher availability and more efficient operations.

REFERENCES

1. Hendrickson, T.A.; Leonard, J.S.; and Weise, D.A.: Application of Magnetic Bearing Technology to Vibration Free Rotating Machinery". Naval Engineers Journal, pp.107-111, May 1987.

2. Allaire, P.E.; et al: "Design, Construction and Test of Magnetic Bearings in an Industrial Canned Motor Pump". Proceedings of the 6th International Pump Users Symposium, Texas A&M University, pp 65-73, April 1989.

3. Olson, E.A.J.; et al: "Applications for Magnetic Bearings on Electrical Generating Plant Equipment". Final report on EPRI Research Project 2079-22, prepared for EPRI, ESEERCO, GCRA and Public Service of Colorado by the S.M, Stoller Corp. and Novacorp International Consulting Ltd., EPRI Report RP 2079-21 & -22, December 1988.

4. "Evaluation of Demonstration Options for Magnetic Bearings in Electrical Generating Equipment". Prepared for ESEERCO by GCRA, Report GCRA 89-004, September 1989.

5. Gray, S.; Baxter, B.; and Jones, G.: "Magnetic Bearings can increase availability, reduce O&M costs". Power Engineering, pp 26-29, January 1990.

6. Baxter, B.Z.; Burger, J.M.; and Jones, G.: "Magnetic Bearing Development for the Utility Industry". Proceedings of the American Power Conference, April 1990.

7. Nikolajsen, J.L.; and Gajan, R.J.: "A New Computer Program for Pump Rotordynamic Analysis". Proceedings of the 5th International Pump Users Symposium, Texas A&M University, pp.11-16, May 1988.

8. Cooper, P.; Wotring, T.L.; Makay, E.; and Corsi, L.: "Minimum Continuous Stable Flow in Feed Pumps". Symposium Proceedings: Power Plant Pumps, EPRI CS-5857, pp. 2-97 to 2-132, June 1988.

9. North American Electric Reliability Council: "Generating Availability Data System". Periodic Publication.

ACKNOWLEDGEMENTS

The authors acknowledge the support and sponsorship of ESSERCO for this magnetic bearing program. Acknowledgment is also extended to the managements of NYSEG, IR and MBI for co-sponsoring the program. Special thanks goes to GCRA who has steadfastly promoted the magnetic bearings in power plant equipment.

2nd International Symposium on Magnetic Beaing
July 12-14, 1990, Tokyo, Japan

ACTIVE MAGNETIC BEARING PERFORMANCE STANDARD SPECIFICATION

M. SWANN and W. MICHAUD

M agnetic Bearings, Inc., Groton, Connecticut, 06340, USA

Abstract

Numerous commercial turbomachinery applications utilizing active magnetic bearings are now being undertaken by several manufacturers. A minimum standardization of performance characteristics is proposed in this paper to minimize the difficulty encountered by turbomachinery manufacturers confronted with a new bearing technology. The difficulty of characterizing performance of the complete magnetic bearing system without the rotor is circumvented in this paper by suggestions for specification of bearing static and dynamic load capacity and vibration response of the completed installation.

1. Introduction

Like conventional bearings, active magnetic bearings' characteristics can be sufficiently described to allow assessments of rotor-bearing performance via rotordynamic analysis. Approximate equivalent stiffness and damping coefficients can be developed for magnetic bearings that allow conventional rotordynamic analyses including undamped and damped critical speed analyses and forced response analyses to be conducted. Although this approach allows some insight into rotor-bearing system performance, it partially masks the true nature of magnetic bearings as feedback control systems.

Since the objective of magnetic suspension applications in rotating machinery is to stably locate the rotor during machine operation, a magnetic bearing system is, in essence, a position control system that suffers some complications from rotor rotation. The accuracy of the rotor position control is determined by position sensor measurement accuracy, controller gain, controller bandwidth, and disturbance forces acting on the rotor. However, the fundamental challenge to successful magnetic bearing application is achievement of system stability. Stability of the rotor-bearing system is related to the vibration performance of the machine, an important consideration in specification of any type of bearing system.

Accordingly, it would seem that the most meaningful specification of magnetic bearing system performance would be in classical control parameters related to frequency response, relative stability, and stability robustness to parameter variations. However, this requires complete knowledge of the characteristics of the turbomachinery manufacturer's rotor which comprises the plant of the feedback control system. Furthermore, the controller actuator, the magnetic bearing, is open-loop unstable. The rotor itself may also be open-loop unstable for high-speed operation and this condition generally leads to a minimum and maximum controller bandwidth requirement for achievement of stability over the operating speed range.

The subsequent discussion is directed at an examination of the characteristics of magnetic bearing systems important to overall performance of the rotor-bearing system. This will permit development of performance criteria for inclusion in a standard specification for magnetic bearing application in turbomachinery. Not considered in the following are the physical construction features of the bearing actuators and the controller that will have important effects on system reliability.

2. Discussion

Open-Loop Behavior of Plant

For a general rotor system, a minimum of five axes of motion control are required: four axes of radial motion control, two at each of two radial bearings, and an axial axis of control provided by a thrust bearing. The basic system that is required for active control of one axis of the rotor will consist of at least one state variable sensor, a magnetic control coil, a coil driver, and the electrical network to connect it all together. These elements introduce their own individual characteristics to overall system performance including frequency response limits, eddy current losses, and saturation which must be accounted for in the overall specification of the system. In addition, mechanical resonances of the stator and rotor will interact with the performance of the control system.

Specification of magnetic bearing system performance parameters starts with a discussion of the frequency behavior of the plant of the feedback control system. The components in the upper half of Fig. 1 define the plant in one axis of control as consisting of the suspended rotor, the magnetic negative stiffness, the magnetic bearing, and the power amplifier.

Note that there are two types of disturbances acting on the plant: E_i and E_o. The first, E_i, is the external forces acting on the rotor including rotating unbalance caused by the misalignment of elastic and inertial axes and aerodynamic or hydrodynamic forces. These forces are summed with the magnetic bearing control forces before passing through the rotor to affect the rotor output state variable of position. The second type, E_o, usually ignored in conventional treatments, is the measurement disturbance created by an imperfect state variable measurement. For a position sensor looking at an imperfect shaft surface, the result is a corrupted position measurement that consists of the true center of mass position and components at harmonics of the rotational speed. This corrupted measurement is used as a feedback signal for the magnetic bearing hence producing a disturbance that excites rigid and flexible modes of the rotor system.

The power amplifier and the magnetic bearing have been included in the definition of the plant to emphasize their influence on the control system performance. Mechanical resonances in the rotor are unavoidable and they impose constraints on the frequency dependent characteristics of the power amplifier and the magnetic bearing.

The power amplifiers and magnetic bearing contribute phase lag to the open-loop transfer function for the plant requiring stabilization at high frequencies where structural interaction can occur [1]. Core losses in the magnetic bearing contribute to phase lag by opposing flux changes in the bearing at a frequency below that normally associated with an L-R circuit. Accordingly, the bandwidth of the bearing should be as high as practical as will be shown subsequently. The magnetic bearing is represented in Fig. 1 as a single lag with a break frequency of ω_b and a roll-off thereafter which is first order (slope of -1 or less).

The power amplifier is also represented as a first order lag with a break frequency that should be as high as practical for best performance. Furthermore, the coil driver should have a characteristic which is independent of load inductance and resistance. Unfortunately, this constraint is coupled with power limitations and the complications of design offered by pulse width modulation of the current to the bearing. Preferred designs should operate as a true transconductance amplifier yielding a current output for a voltage input. The amplifier total harmonic distortion at rated output should be as small as possible to avoid nonlinear resonance effects.

Considering a simple rotor system supported by an uncompensated magnetic bearing, the equation of motion for one axis of control is:

$$m\ddot{x} + k^- x = f \qquad (1)$$

where
- m = rotor mass
- k^- = magnetic bearing negative stiffness
- x = rotor displacement
- f = external force

Equation (1) above applies directly to the axial control axis. For a radial control direction, Equation (1) applies if k^- is taken as the effective or combined negative stiffness of all magnetic bearings in the control direction. Equation (1) assumes no cross-coupled motion between axes.

In Laplacian notation, Equation (1) can be expressed as:

$$ms^2 X(s) + k^- X(s) = F(s)$$

$$\frac{X(s)}{F(s)} = \frac{1}{ms^2 + k^-} \qquad (2)$$

where $s = j\omega$ and the capital letters in functions of s denote Laplace transforms. Accordingly, the rotor transfer function, X(s)/F(s), is shown for simplicity in Fig. 1 as $1/ms^2$ with negative feedback of the magnetic bearing uncompensated negative stiffness. Thus, this representation is strictly correct for rigid body motion only but flexible mode effects are added subsequently. The $1/ms^2$ transfer function shows that the rotor acts as a low pass filter rejecting high frequency disturbances.

Flexible mode effects of cross-coupled motion of real rotor systems can be accounted for by incorporating multi degrees of freedom and including gyroscopic and internal damping parameters in the model. Using complex notation to allow a more compact form, the equation of radial motion can be written:

$$[M]\ddot{\{z\}} + [D - j\omega G]\dot{\{z\}} + [K - j\omega D]\{z\} = \{f\} \qquad (3)$$

where
- $[M]$ = rotor mass matrix
- $[D]$ = rotor damping matrix
- $[G]$ = rotor gyroscopic matrix
- $[K]$ = rotor stiffness matrix
- $\{f\}$ = rotor external force vector
- $\{z\}$ = rotor displacement vector $= [.. \; x_i + jy_i \; .. \; \beta_i + j\alpha_i \; ..]^T$
- x_i = translational displacement of the *ith* mass along the x- axis
- β_i = angular displacement of the *ith* mass about the x- axis
- y_i = translational displacement of the *ith* mass along the y- axis

α_i = angular displacement of the *ith* mass about the y- axis
ω = frequency

Following the development of Schweitzer [2], the eigenvalue problem for the above system can be formulated. Solution shows that internal damping can only destabilize if the rotor is spinning. Backward whirls cannot become unstable, but forward whirls can become unstable when the rotor speed exceeds the first flexible mode natural frequency.

The transfer functions for the flexible mode resonances can be expressed as [3]:

$$R(s) = \prod_{i=1}^{n} \left\{ \frac{\left(\frac{s}{\omega_{zi}}\right)^2 + 2\xi\left(\frac{s}{\omega_{zi}}\right) + 1}{\left(\frac{s}{\omega_{pi}}\right)^2 + 2\xi\left(\frac{s}{\omega_{pi}}\right) + 1} \right\} \quad (4)$$

where ω_{zi} is the zero of the *ith* resonance
ω_{pi} is the pole of the *ith* resonance
ξ is the damping ratio including external as well as internal effects

At each resonance there is a gain increase of 40 dB per decade over a frequency range corresponding to the pole-zero separation, and a maximum phase shift of 180° depending on the damping and the pole-zero separation. This damping can easily result in a narrow band gain increase of 40 dB or more.

The complex S plane can be used to describe the relative stability of the open- and closed-loop plant, i.e., before and after compensation. The poles of the rotor transfer function correspond to the eigenvalues of the related characteristic equation for Equation (3); the real part is the damping factor and the imaginary part is the damped natural frequency. Stability requires all poles to be located in the left-half plane (LHP) where the negative real part of the eigenvalue ensures sufficient damping.

The rigid body transfer function of $1/ms^2$ results in two poles at the origin of the complex S plane. These rigid body poles may migrate from the origin due to gyroscopic effects as rotational speed is increased. Generally, the rotor transfer function will also contain a number of complex conjugate poles and zeros as described by Equation (4). These poles and zeros tend to migrate toward the right-half (RHP) of the complex S plane with increasing rotor speed due to the rotor cross-coupled damping effects. Thus, they can easily contribute to rotor instabilities. Fig. 2 shows a representation of the poles and zeros for a typical open-loop rotor system and their direction of travel with increasing speed.

Another important instability in the open-loop plant is that caused by the uncompensated, negative stiffness of the magnetic bearing itself. This aspect of magnetic bearings has been well documented in the literature (e.g., [4]).

The force developed by a magnetic bearing operating on a rotor through an air gap is:

$$F = \frac{\partial F}{\partial I}\partial I + \frac{\partial F}{\partial x}\partial x \quad (5)$$

where x = rotor displacement.
I = bearing current

or expressed as a stiffness,

$$K = K^+ + K^- \quad (6)$$

where the first term is the bearing positive "current" stiffness and the second term is the bearing negative "position" stiffness caused by the increasing attractive force as the gap is reduced. This must be overcome for stable suspension since the homogeneous solution to Equation (1) is in the form of hyperbolic functions indicating that x grows with time. This can be accomplished for a given rotor position in the air gap by ensuring that the first term in Equation (6) is larger, i.e., $K^+ > K^-$.

A Bode plot of the above defined plant for a typical rotor system at zero speed neglecting the bearing negative stiffness is illustrated in Fig. 3. These plots are the steady state magnitude and phase ratios of output position, as produced by an input sinusoidal voltage, versus the frequency of input excitation, ω. It is easy to show that inclusion of the bearing negative stiffness yields undamped poles in the complex S plane. Means of negating this effect will be discussed subsequently.

At low frequencies, the zero speed plant is dominated by the rigid body poles with a second order magnitude roll-off (slope of -2) until the first flexible mode resonance shown arbitrarily at 10^3 rad/sec. The trough of the resonance is caused by the zero of the resonance transfer function and the peak of the resonance is caused by the pole of the resonance transfer function, Equation (4). The pole-zero combination of the flexible mode resonance causes a 180° maximum phase shift. The magnitude slope steepens and the phase falls off from -180° with increasing frequency due to the simple poles of the amplifier and bearing which have been placed arbitrarily in Fig. 3 at 10^4 rad/sec and 10^3 rad/sec, respectively. These characteristics imply that the addition of phase lead is required to stabilize the system. The occurrence of additional flexible mode resonances further complicates the problem of plant stabilization as will be shown subsequently.

The magnitude plot will be somewhat modified with increasing speed if cross-coupled damping or large gyroscopic effects cause migration of the poles and zeros in the complex S plane. Gyroscopic effects may cause the system poles and zeros to move either toward or away from the RHP with increasing speed indicating a destabilizing or stabilizing influence, respectively, according to the values of rotor polar and transverse inertias, rotor flexibility, and geometric parameters. As the rotational speed is increased, cross-coupled

damping may cause some forward whirl poles and zeros of the rotor transfer function to migrate toward the RHP and the rotor can become open-loop unstable when the rotational speed equals a rotor flexible natural frequency. The pole and zero positions in the complex S plane tend to restrict the minimum and maximum gain and bandwidth of a compensating controller as shown by Johnson [5]. Also, the amplifier and bearing bandwidths introduce further gain and bandwidth restrictions to the controller.

In summary, plant variations with speed, open-loop instabilities caused by unfavorable gyroscopic and internal damping effects, component frequency response limitations, and structural interactions combine to make control synthesis of a stabilizing compensator for a typical rotor system a difficult proposition.

Controller Requirements

Since the plant comprises an open-loop system that may have one or more zeros and poles in the RHP, feedback alone is not sufficient for stabilization. Some form of series compensation with lead networks is required for stability. We are interested in stability at nonsynchronous frequencies as well as synchronous frequencies. Furthermore, parameter variations and nonlinear effects within the system components can be expected. Therefore, the controller for a magnetic bearing system has to possess robustness properties that ensure stability under these conditions.

Another requirement of the controller is that the closed-loop system must accommodate disturbances, E_i in Fig. 1, at both synchronous and nonsynchronous frequencies. Nonsynchronous disturbances can come from a variety of sources including coupling misalignment, seal and impeller hydrodynamic effects, rubs, etc. The controller must possess good synchronous response characteristics since the primary exciting mechanism in most turbomachinery applications will be mass unbalance. The synchronous response must be limited by the controller to rotor whirl amplitudes that are less than the magnetic bearing air gap. The corresponding synchronous bearing forces must be consistent with the dynamic load capacity of the magnetic bearings. Accordingly, a relatively flat synchronous response is desirable.

As in other position control systems, optimal control for a magnetic bearing system can generally be achieved with full state feedback, Fig. 4. However, the rotor state variables of velocity and acceleration are not naturally accessible in a magnetic bearing suspension and must be generated with more hardware than a displacement feedback system. The result is additional complexity and cost of the total system. This problem can be circumvented in digital control systems by generating state variables with software.

The negative stiffness of the bearing is a challenging control problem. Here again, state variable feedback and digital technology offers a solution. As shown by Chen [6], a velocity observer implemented into a model based compensator can recover rotor velocity without differentiation of the rotor position signal and ensure system stability despite the magnetic bearing negative stiffness.

Alternatively, flux feedback can minimize the negative stiffness with less control complexity. Since the magnetic force of attraction is given by:

$$F = \frac{B^2 S}{2\mu_o} \qquad (7)$$

where B = magnetic induction
S = bearing projected surface area
μ_o = permeability of free space

it is evident that a linear force vs. rotor displacement is possible if $B \sim \sqrt{x}$. This latter relationship is possible by measuring B. The result is a bearing force characteristic which is independent of the bearing air gap; the unstable effect largely disappears. In fact, reductions in the negative stiffness on the order of five to ten times are achievable.

Some bearing designs utilize linearization of the bearing stiffness by the use of large DC current biases alone to minimize the effect of negative stiffness. This scheme does not eliminate the unstable effect of the negative stiffness and the remaining nonlinearity introduces resonant frequencies into the dynamic system which are subharmonic and ultraharmonic to the main resonance (pole) predicted on the basis of linear theory. These nonlinear resonances can cause further restrictions on stabilizing controllers particularly when the bearing is operating near saturation.

A review of the optimal control technologies seems to indicate that the linear quadratic regulator (LQR) offers everything desirable in a magnetic suspension: good stability, robustness, and flat frequency response properties. Essentially, this design methodology is similar to shaping of the open-loop Bode magnitude plots for performance enhancement. Selection is made of the weighting matrices used to express the relative cost assigned to deviations of the control state from equilibrium and the relative cost assigned to control effort. This technique can be applied to both full state feedback controllers and output controllers using model based compensators. The velocity observer mentioned above is an example of the latter.

The optimal performance of the full state feedback controller using variable gain to account for variation in plant with rotational speed appears ideally suited to magnetic bearing applications. Nevertheless, as shown by Johnson's analysis [5] for his two mass rotor system, output state

feedback using LQR design techniques failed to provide any real advantage over simple lead-lag controllers in terms of nominal stability, synchronous response to measurement error, synchronous response to mass unbalance, stability robustness to speed variation, and stability robustness to variations in structural characteristics of the rotor.

For all the designs studied by Johnson, the open- loop RHP poles and zeros placed minimum and maximum bandwidth restrictions on stabilizing compensators. The above results can be expected to apply as well to general rotor systems with the additional characteristics of variation in pole frequencies with rotation speed and additional bandwidth and gain restrictions caused by higher order structural resonances. Some rotor systems with large disks can also be expected to exhibit unstable gyroscopic modes. Rotors with unsymmetric cross section could be subject to parametric self-excited resonance vibration. However, these are all characteristics that have been successfully addressed in industrial turbomachinery with lead-lag controllers for both direct and cross axis compensation.

Compensation of the typical plant defined in Fig.s 1 and 3 can be readily achieved with a lead-lag controller provided special attention is made to the flexible mode resonances that fall within the bandwidth. To provide stability, the controller gain must be increased to provide a gain crossover in a region where phase is greater than -180°. However, the location of the flexible mode resonances with respect to the low frequency gain crossover dictates the minimum amount of phase necessary for plant stabilization.

This condition can be clearly depicted on a Nichols plot of open-loop magnitude and phase vs. frequency. In this plot, the critical points where instability occurs are the multiple origins of -180° ± n 360° phase and 0 dB magnitude. The gain and phase margins for relative stability are measured, respectively, from the phase crossover at -180° ± n 360° and gain crossover at 0 dB. There may be multiple crossovers at a single critical point due to flexible mode resonances.

Each mode affects the magnitude-phase plot by contributing a counterclockwise loop to the loop transfer function [3], Fig. 4 . A phase stabilized mode is one which for arbitrarily small structural damping ratio is closed-loop stable regardless of how high the loop gain is raised; the mode "loop" never crosses the -180° ± n 360° line, even for zero damping. A gain stabilized mode is one which is closed-loop stable for the actual loop gain and damping ratio, but can become unstable if the gain is raised or the damping ratio is lowered; the mode loop crosses the -180° ± n 360° line if damping ratio is sufficiently small.

The Nichols plot of Fig. 4a was developed for a typical rotor such as shown in Fig. 3 after simple lead-lag compensation. Several flexible modes are depicted. The plot shows the need to stabilize mode 2 by providing additional phase lead to compensate for the amplifier and bearing phase lag thereby avoiding the phase crossover at the mode resonance frequency. The result after higher order lead compensation is shown in Fig. 4b. A phase crossover with reasonable gain margin has been provided between resonances (after mode 2 in Fig. 4b). Higher order modes of large magnitude also have sufficient phase margin (e.g., mode 4 in Fig. 4b).

As discussed above, a simple lead cell is sometimes insufficient to provide acceptable stability margin and higher order lead compensation is necessary. This results in greater loop gain which can destabilize gain stable modes (e.g., mode 3 in Fig. 4b with a lower damping ratio). There is a ready solution to this problem which is used all the time by the authors' company and affiliates: a notch filter to remove the gain at the offending frequency with a minimal increase in the overall gain. Mechanical dampers mounted to the shaft have also been successful in attenuating these resonances at high frequencies thereby stabilizing the offending mode.

The decision to employ an output controller, be it a lead-lag or a model based compensator using a velocity observer, still requires consideration of the feedback measurement system--the position sensor. The sensor must have good sensitivity, temperature stability, high signal to noise and harmonic rejection characteristics, and high linearity with respect to changes in the magnetic bearing air gap. Magnetic bearing systems have been built with capacitive, eddy-current, optical, and inductive devices, but the success of these systems in industrial environments varies in part with the extent to which the above criteria are satisfied.

The inductive sensor with individual coil elements bridged around the rotor for rotor surface harmonic rejection has performed admirably in turbomachinery applications. This sensor intrinsically minimizes the E_o disturbance in Fig. 1 due to an imperfect shaft surface. Output disturbances, due to misalignment of the sensor measurement axis and the bearing axis must be minimized by good machine design practice. This generally requires direct mounting of the sensor to the bearing assembly. Also, where electromagnetic interference is a concern such as in motors and generators, shielding can be implemented to ensure a clean position sensor signal.

Minimum acceptable performance of sensors for both radial and axial position measurement are listed in the summary section which follows. The phase lag characteristics of sensors, particularly inductive types, do not compromise the design of

stabilizing controllers since these are low power devices that can be readily compensated.

Previous considerations of the characteristics of stabilizing controllers assumed colocation of the bearing and sensor. Most practical system will have sensors and bearings separated by an axial dimension along the length of the rotor. Depending on node locations of resonant frequencies relative to the bearing and the sensor, the sensor gain may be affected. Maslen and Bielk [7] show that the effect of sensor noncolocation is generally to reduce the stability of some higher order modes and increase the stability of lower order modes.

Bearing System Load Capacity

The magnetic bearing actuator design must be consistent with frequency and voltage characteristics of the controller in order to develop peak dynamic forces as required over the control bandwidth to maintain contact free suspension. Furthermore, this must be done within current limitations without excessive bearing inductance.

For a four quadrant bearing system, two different operating modes are possible: Class A and Class B. Class A takes advantage of opposing quadrants to react the dynamic load.

As shown by Bornstein [8], neglecting the reluctance of the magnetic core , this configuration can develop a peak dynamic force given by:

$$F = \frac{I_{max} V_{max} S_i N_{pp}}{2 S \varepsilon_0 \omega} \quad (8)$$

where I_{max} = maximum current available from amplifier
V_{max} = maximum voltage available from amplifier
S_i = inductive area of a single magnetic bearing pole
N_{pp} = number of pole pairs in the bearing quadrant
S = projected area of magnetic bearing quadrant
ε_0 = magnetic bearing air gap
ω = frequency of disturbance

and all variables are in consistent MKS units.

Implicit in the development of the above is that the saturation current of the bearing coincides with the amplifier current rating; a usual condition for cost effective designs.

Class B control utilizes current modulation to only one quadrant to react to the dynamically varying load while the opposing quadrant is energized with a small bearing DC current. For horizontal installation, only the upper quadrants modulate the load. The maximum dynamic force developed in a Class B configuration neglecting magnetic core reluctance is [8]:

$$F = \frac{I_{max} V_{max} S_i N_{pp}}{2.83 S \varepsilon_0 \omega} \frac{1}{X_s^{1/2}} \quad (9)$$

where the factor of safety over the static load rating, X_S, has been purposely introduced to illustrate the reduction in dynamic load capacity incurred by overspecification of X_S.

Recommendations for minimum load capacity specifications are contained in the summary.

Overall System Performance Specification Using Vibration Standards

Ideally, performance criteria for a magnetic bearing controller could be specified by the classical control system specifications of gain and phase margin (relative stability), synchronous frequency response, and stability robustness to plant parameter variations. However, as can be concluded from the above discussion, there are a multitude of options for stabilizing controllers and actuator designs for a given rotor system. Identification of suitable criteria is difficult in rotor- bearing systems where rotor open-loop behavior will vary widely across the class of turbomachinery and instability can arise from various sources. This condition makes specification of controller performance requirements difficult.

The problem of practical system performance specifications can be resolved by resorting to the traditional frequency response parameter used for performance evaluation of turbomachinery rotor bearing systems: vibration amplitude. Although vibration standards are often invoked to minimize damaging dynamic loading of conventional bearing systems, satisfaction of appropriate vibration standards for magnetic bearing systems ensures that the previously mentioned attributes of closed-loop stability at synchronous and nonsynchronous frequencies have been met, and that the system is relatively insensitive to disturbances. However, vibration standards do not explicitly indicate relative stability margins and they do not ensure stability robustness. They also unfairly burden the magnetic bearing manufacturer with the task of demonstrating acceptable performance over a rotor system for which he is not completely responsible. Nevertheless, with proper rotor design, manufacture, and balancing, the authors' company has found it possible to meet rigid vibration requirements.

In fact, the proposed vibration standard is the same to which a wide class of turbomachinery are now accepted--the American Petroleum Institute (API) Standards. Fig. 5 shows the various standards for motors (API 541), pumps (API 610), centrifugal compressors (API 617), gas turbines (API 616), and steam turbines (API 611). The herein proposed standard corresponds to API 617 and is cross-hatched in the figure. This standard requires that vibration be limited to $2780/\sqrt{f}$ μm or

50 μm, whichever is less, where f is the frequency in cpm. The authors' company has been able to meet these requirements in all of its installations provided the customer's rotor is multiplane balanced to a minimum of the ISO 1940 standard for the appropriate class of machinery.

3. Summary

The unique performance aspects of magnetic bearing applications to turbomachinery have been reviewed in the context of actively controlled rotors to identify the salient performance requirements that need to be identified by machinery manufacturers in the specification of magnetic bearing systems for their use. While these specifications cannot be totally definitive, they do provide the genesis of a common specification that will help ensure satisfactory performance of the rotor-bearing system.

The results of this review and recommended specification criteria can be summarized as follows:

The bearing system shall permit the driven equipment to run continuously at all speeds within the operating speed range at the maximum unbalance permitted by ISO 1940 for the appropriate class of rotor without exceeding a double amplitude of vibration measured adjacent to the individual bearings of $2780/\sqrt{f}$ μm or 50 μm, whichever is less, and where f is the frequency of vibration in cpm. The controller may use analog or digital technology of any of a variety of algorithms provided it meets the above requirements for vibration and is stable (repeatable) with time. Output or full state feedback using position, velocity, current, flux, or force is permissible provided it meets the above requirements for vibration and is stable with time. Power amplifiers shall be low distortion, linear or switching type with a bandwidth consistent with the above vibration requirements. Bearing bandwidth shall be consistent with the above vibration requirements.

The load capacity of the bearing system shall be a minimum of the total of static plus dynamic loads for the application where static and dynamic loads are as defined below. Static loads consist of weight and steady state aerodynamic, hydrodynamic, or electromagnetic loads of the driven equipment and dynamic loads consist of varying components of the above, plus unbalance loads of the driven equipment. The required dynamic capacity of radial bearings is specified at synchronous frequency and shall be a minimum of 2.5 times the appropriate ISO grade to which the rotor is balanced. The required capacity of axial bearings shall be a minimum of the total of specified static and dynamic loads as indicated above.

The radial position sensors shall feature a linearity and sensitivity that is independent of environmental temperature and that is consistent with stable operation of the magnetic bearing-rotor system. This generally requires linearity for radial sensors to within 2% over the magnetic air gaps and a minimum sensitivity of 10 V over the air gap involved. These requirements may be relaxed for axial sensors. To reduce plant measurement disturbance, the mounting of the radial position sensors shall ensure a concentricity with respect to the radial bearing bore of 50 μm per meter of bearing diameter with a lower limit of 15 μm.

Not previously addressed in this paper, but also important:

All magnetic bearing components shall be compatible with the specified application operating environment of temperature, pressure, humidity, and process fluid. Temperature increase due to joule, hysteresis, eddy current, and windage losses within the magnetic bearing components shall not unduly compromise the performance or the life of the bearing system. Also, operating stress levels due to centrifugal, thermal, electromagnetic, and mechanical loads shall not unduly compromise the performance or the life of the bearing system.

Before design approval, the magnetic bearing manufacturer should be required to conduct and present sufficient analyses to demonstrate that the above requirements are met. However, the equipment manufacturer is ultimately responsible for satisfactory performance of the complete machine with the magnetic bearing system. To this end, the magnetic bearing manufacturer should supply this necessary performance data to enable the equipment manufacturer to make this determination and release the magnetic bearing vendor to proceed with the manufacture and delivery of the complete magnetic bearing system.

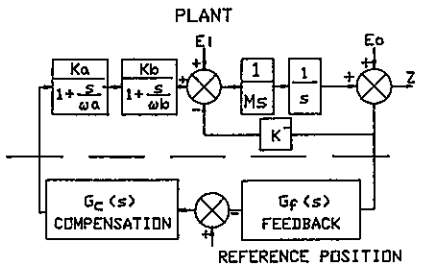

FIGURE 1
MAGNETIC BEARING SYSTEM FOR ONE AXIS CONTROL

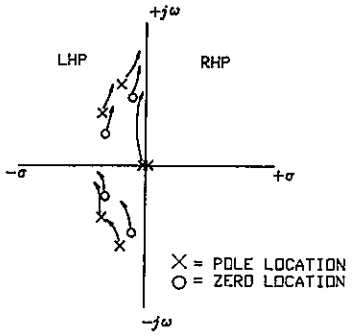

FIGURE 2.
COMPLEX S PLANE. ROOT LOCUS VS. ROTATIONAL SPEED FOR TYPICAL ROTOR SYSTEM-TWO RIGID BODY MODES AND TWO FLEXIBLE MODES (COMPLEX CONJUGATE PAIRS) SHOWN.

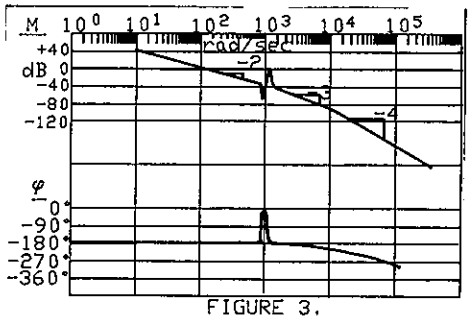

FIGURE 3.
TYPICAL PLANT OPEN LOOP BODE PLOT
ONE FLEXIBLE MODE RESONANCE

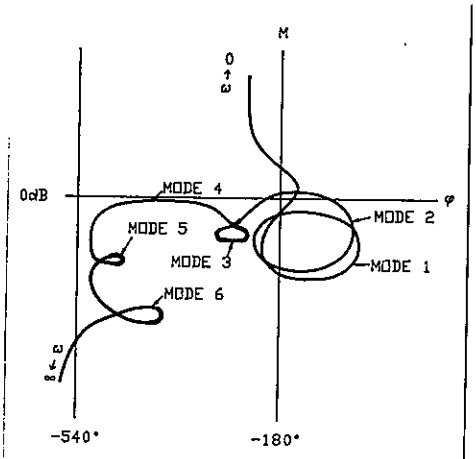

FIGURE 4a
LEAD-LAG COMPENSATED PLANT
BEFORE FLEXIBLE MODE COMPENSATION.

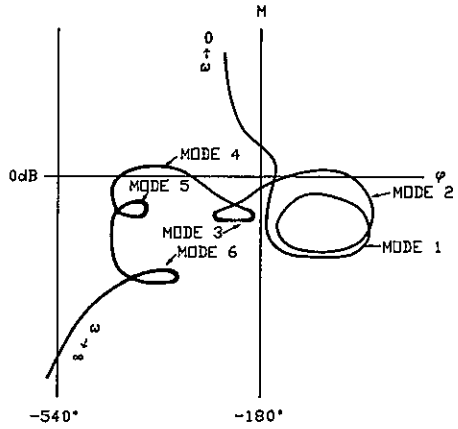

FIGURE 4b
PLANT AFTER FLEXIBLE MODE COMPENSATION.

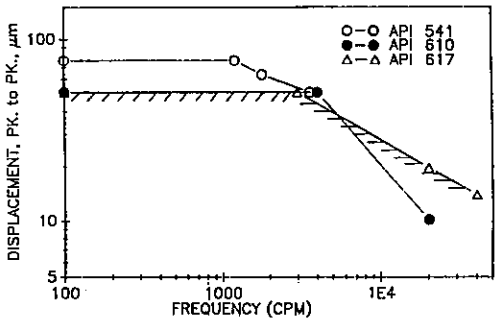

FIGURE 5. PROPOSED VIBRATION STANDARD

[1] Reistad, K., et. al.: Magnetic Suspension for Rotating Equipment, Phase I Project Final Report, National Science Foundation (March 1980).
[2] Schweitzer, G.: Stabilization of Self Excited Rotor Vibrations by an Active Damper, Springer-Verlag, New York (1975).
[3] Yocum, J. F., and Slafer, L. I., Control System Design in the Presence of Severe Structural Dynamics Interactions, Journal of Guidance and Control, Vol. I, No. 2, (March-April. 1978).
[4] Maslen, E. H., et. al.: Practical Limits to the Performance of Magnetic Bearings: Peak Force, Slew Rate, and Displacement Sensitivity.
[5] Johnson, B. G.: Active Control of a Flexible, Two-Mass Rotor: The Use of Complex Notation, Sc. D. Thesis, Massachusetts Institute of Technology (September 1986).
[6] Chen, H. M.: Specification and Performance of Radial Active Bearings with Velocity and Acceleration Observers, Ph.D. Thesis, Rensselaer Polytechnic Institute (1986).
[7] Maslen, E. H., and Bielk, J. R.: Implementing Magnetic Bearings in Discrete Flexible Structure Models (June 8, 1989).
[8] Bornstein, K. R.: Dynamic Capability of Active Electro-Magnetic Bearings, for presentation at the ASME and STLE Joint Conference on Tribology (October 1990).

2nd International Symposium on Magnetic Beaing
July 12-14, 1990, Tokyo, Japan

THE MALVE EXPERIMENTAL CIRCULATOR

THE FIRST LARGE NUCLEAR COMPONENT WITH ACTIVE MAGNETIC BEARINGS

P. BÜHRER, J. ENGEL, D. GLASS
ABB Kraftwerke AG, Mannheim

Abstract
Reliable operation of coolant gas circulators with magnetic bearings is an indispensable prerequisite for the further realisation of the High Temperature Reactor line. Development of the magnetic bearing technology for vertically arranged rotors weighing several tons has therefore been at the center of continuing R&D activities by ABB for a long time. After completion of the design work for a circulator the construction of a full scale prototype has now been started. With a power input of 400 kW, a rotor with magnetic bearings weighing 2 tons, and an overhung impeller of 1.25 m diameter the circulator exhibits features which might be of interest to the conventional compressor business as well. While the construction of the circulator is in progress a test loop will be erected. Tests in air/nitrogen and helium atmospheres are planned. The purpose of the tests is above all to verify the dynamic behaviour of the circulator at different speeds, temperatures, and gas densities. Features of the prototype and of the test loop as well as the milestones of the test program will be described.

1. ESSENTIAL BOUNDARY CONDITIONS FOR THE DESIGN OF THE PROTOTYPE

In high-temperature reactors coolant-gas circulators with magnetic bearings give full freedom of arrangement and orientation without any need to take adverse interactions between the helium gas loops and a lubricant into account, interactions which can only be eliminated by expensive special measures.

On an international scope all modern HTR designs are therefore based on the use of vertically arranged circulators with magnetic bearings. By this means it is still possible to plan cost-effective reactor plants without impairing the availability of safety-related or operational circulator functions. Not only can maintenance needs for potentially contaminated machine elements be eliminated through the use of magnetic bearings, but the enormous fire risks involved in the use of oil as lubricant are also precluded.

The proper functioning of these magnetic bearings verified by a large-scale test is a basic prerequisite for the further advancement of the HTR line, since the benefits of helium circulators fitted with magnetic bearings determine major features of advanced HTR plants.

After the successful completion of the basic experiments with retainer bearings, reported by us during the first symposium in Zurich /1/, ABB was in the late fall of 1989 informed that funds from the Federal German Ministry of Research and Technology will be provided for the construction and testing of a circulator with magnetic bearings in a test loop. This is a R&D project with a term of 5 years involving an expenditure of approx. 16 million Deutschmarks.

The development of the magnetic bearings technology for vertically arranged rotors weighing several tons has for a long time been at the centre of demanding and continuing R&D activities by ABB. At the same time the appearance of an EPRI report /2/, /3/, has made clear that branches of industry which are usually regarded as rather conservative, preferring to wait until new developments have firmly established themselves, are now beginning to become interested in the degree of qualification reached by the magnetic bearings technology. We are therefore rather glad to see that the initiation of our R&D activities in good time has been worth the effort.

The efforts to make use of the benefits involved in magnetic bearings are most obvious in the oil and gas industry /4/. Unfortunately the time when the breakthrough will occur is still uncertain. But there can be no doubt that it will come.

2. DESCRIPTION OF THE DESIGN

With the manufacture of a prototype now started, fully matured design documents will be turned into hardware. They take into account, apart from extensive studies on the dynamic, thermal, and magnetic behavior of circulator components, the results of the nearly completed full scale tests for optimizing the retainer bearings in the retainer bearing test stand fitted with magnetic bearings.

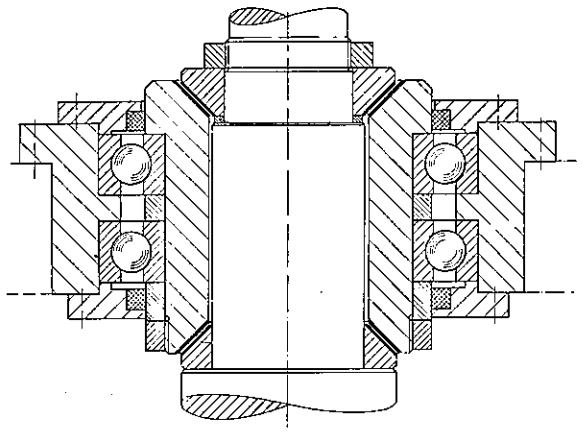

Fig.1 Retainer and centering bearing for vertically arranged rotors

On the basis of the patented design shown in Fig. 1 both grease-free, dry-lubricated retainer bearings and bearings with a grease film are now available. In view of the highly unfavorable friction values in high-purity helium the number of shaft releases (drops) for a set of retainer bearings with grease-film lubrication now exceeds 50 for an unbraked rotor. For dry-lubricated retainer bearings it is higher than 10. The still outstanding optimization of the rolling bearings in the cage region of dry-lubricated retainer bearings is no longer of basic importance since the number of releases achieved under conservative boundary conditions - i.e. unbraked rotor with extended coast-down times - is already adequate for HTR applications.

During the trial operation of the prototype and of the new electronic system for magnetic bearings an increased number of releases is to be expected. For this reason magnetic bearings with grease film lubrication will be used. They will make it possible, taking additional planned and intentional releases into consideration, to complete the extensive test program with a single set of retainer bearings.

The retainer bearing technology itself has been described in detail in a paper presented at the 1st symposium /1/; therefore only the principle shall be explained again by means of Fig.1: In the event of disturbances of the magnetic bearings the rotor will move in axial or radial direction until it comes into contact via friction cones and/or radial friction surfaces with the rolling bearings which areat standstill till then. As a result they will within seconds start to turn at the shaft speed which is to be brought under control. The transfer of power by the impeller wheel to the circulating medium together with an automatically triggered motor cut-out in the case of retainer bearing operation plus simultaneous switchover to electric braking by the motor will result in a short-term and safe coastdown of the rotor in the retainer bearings.

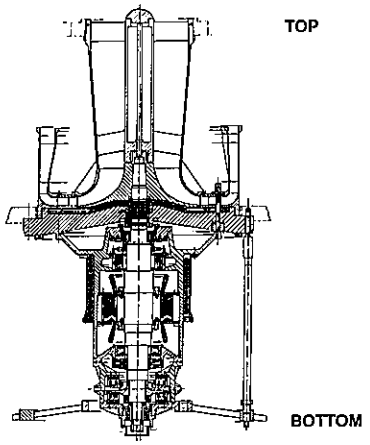

Fig.2 Coolant gas circulator protype MALVE (5300 r.p.m, overhung impeller wheel, 1,25 m diameter, rotorweight 2 t, power input 400 kW)

Fig. 2 is a longitudinal section through the prototype circulator. With a power input of 400 kW, a rotor weight of 2 t held by magnetic bearings, and an overhung impellor wheel of 1.25 m dia., it has features which are of interest to the conventional compressor business as well.

Via the supporting wall the circulator is connected with the test vessel simulating the reactor structure (not shown here). The supporting wall is thermally insulated on its top side, which communicates with the primary loop of the reactor whose temperature is 300 °C, and on the side of the motor it is additionally water-cooled. This arrangement ensures motor compartment temperatures, even if the machine does not turn, that will not jeopardize the electric components.

The shaft penetration is designed as a labyrinth packing and sealing gas can be injected into it. The penetration of any radioactive contaminations from the primary loop into the motor compartment which has a temperature of 80 °C is thereby effectively obstructed. If sealing gas is injected this will, together with the sealing strips of the labyrinth, produce an increased cooling effect at the hot shaft end which is welcome in particular in the event of reactor accidents.

The strength of the supporting wall is designed to withstand the pressure differential which will occur in the event of a depressuri-

zation on the primary gas side or on the motor side as the result of an accident.

In the lower circulator region an additional fixation of the circulator by means of a star-shaped bearing bracket is provided. By this means radial vibrations of the stator are limited. With the assistance of a structure allowing thermal expansion, as it is used in turbine engineering, expansions of the circulator in axial direction are possible.

As for all other ABB circulators designed to date an induction motor is used as drive motor; its electrical insulation is not only radiation-resistant but also takes the much-reduced disruptive strength in helium compared with air into consideration. By means of a static converter the motor speed is infinitely adjustable. During retainer bearing operation resulting from disturbances of the magnetic bearings electric braking, too, is possible by means of a chopper in the static frequency converter.

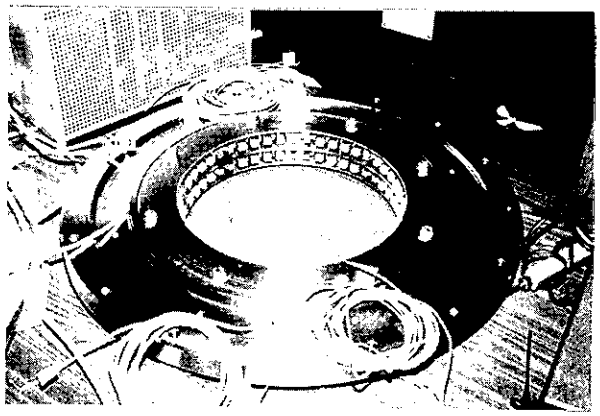

Fig.3 Sensor ring for radial magnetic bearings manufactured by ABB, with redundancy capability for 2-out-of-3 circuits and an additional stand-by sensor.

The magnetic bearings operate with an air gap of approx. 1 mm. Fig. 3 depicts radial magnetic bearing sensors manufactured by ABB during installation. They belong to a partially redundant electronic system for the magnetic bearings and operate in 2-out-of-3 technology.

For the magnetic bearing loads to be expected in nuclear follow-up projects with driving powers in the 5 to 6 MW range the power amplifiers available to date will no longer be sufficient. Under a licensing agreement with the S2M Company ABB has therefore developed a new output stage with a power of 20 to 42 kVA. Fig. 4 is a view of the amplifier which operates during the MALVE application at a maximum of 250 V and 80 A; it shall also be qualified, together with the circulator prototype, during the planned test runs.

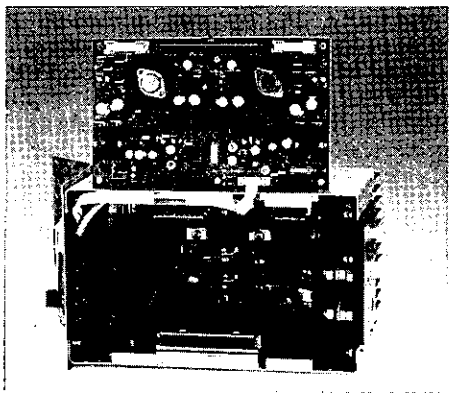

Fig.4 The ABB power amplifier for circulators with magnetic bearings, for power inputs from 5 to 6 MV.

On the basis of extensive calculations with the ABB program system for magnetic stray-field distribution, UNIFELD 4, the design and the materials have been selected such that the magnetic field distribution outside the magnetic bearings is as homogeneous as possible with low values for the magnetic field intensity. This was done because it turned out that even minor field inhomogenities in the hectogauss range, rotating with the rotor or relative to it, can be the cause of undesired, eddy-current-related temperature rises.

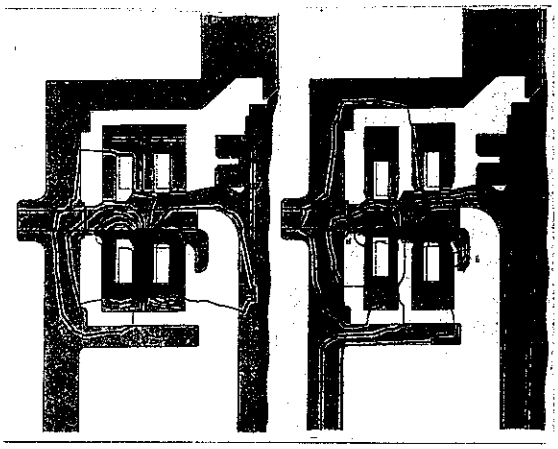

Fig.5 Magnetic stray fields resulting from the structural design of details, illustrated with the example of an axial bearing.

Fig. 5 is a cross section through an axial magnetic bearing with magnetic field pattern for two different bearing designs based on UNIFELD-4 calculations. To understand the magnetic field pattern it is first of all impor-

tant to know that the coils are connected in opposition so that the magnetic induction effect for machine areas further removed from the axial bearing will disappear. In the immediate vicinity it becomes apparent how the compact arrangement of the coil bodies and the elimination of the yoke-leg contraction intended for "flux concentration" will result in a considerable reduction of the stray effect. The rotor shaft region in particular is only slightly affected by it.

Basically the exit of lines of flux outside the pole surfaces always results in a reduction of the bearing capacity, apart from the heat-up due to eddy currents, if the stray fields pass through moving parts. In the present case a bearing capacity improvement from 52.4 kN to 59.1 kN, i.e. of 13%, could be achieved by the design change.

The fact that the circulator comes into contact with the 300 °C of the primary loop causes a not inconsiderable heat input into the motor compartment; this heat plus the dissipation heat from the operation of the magnets in the bearings and of the motor must be removed. A water-filled cooler with helical tubes arranged outside the motor housing is used for this purpose. It serves to cool down the helium circulated in the motor compartment, streaming away from the auxiliary blower integrated in the axial bearing disk. The axial magnetic bearing disk with the integrated ventilator wheel /6/ is shown in Fig. 6 in its interaction with the other elements of the cooling loop.

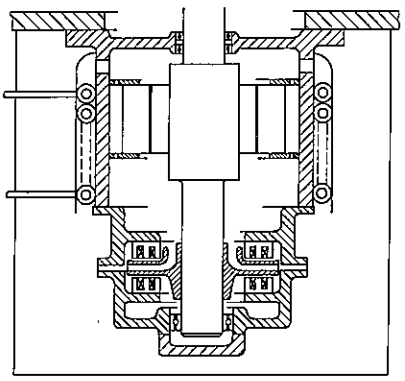

Fig.6 Axial magnetic bearing with integrated impeller for the cooling loop in the motor compartment.

A central shaft boring not shown in Fig. 2 serves to meet the need for reducing the radiation exposure of the assembly personnel of nuclear installations to the minimum. By this means the contaminated impeller wheel of an irradiated circulator may be separated from the shaft, working from the hardly activated rear side of the circulator in the course of maintenance activities which are possible as a matter of principle. Only very low dose rates have then to be taken into account for the handling. To separate the impeller wheel from the shaft by means of the central boring extreme-pressure oil is injected into grooves of the cone interference fit between wheel and circulator.

3. TEST LOOP AND TESTS

While the prototype is being manufactured a test loop is set up. It is conceived such that the circulator prototype in "upright mounting position", i.e. with the impeller wheel on top, can be operated under the effects of pressure and temperature at largely realistic reactor boundary conditions. The gas condition is then set to the temperatures and densities prevailing in the reactor.

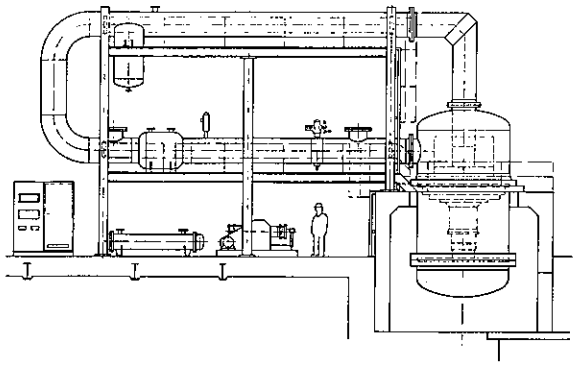

Fig.7 Main componentes of the test loop for testing the coolant gas circulator prototype MALVE.

Fig. 7 gives an impression of the order of magnitude of the project. The circulator is in the pressure vessel visible on the right-hand side. The gas is sucked in from the pipe on top and returned to the loop via the pipe connected to the left-hand side of the vessel. The loop consists basically of heat exchangers for adjusting the gas condition and of a throttling device to achieve different circulator loads for the same gas condition. As part of a "building block philosophy" the expensive large components have been dimensioned such that they may also be used later on for workshop testing of circulators for commercial projects.

Fig. 8 is a schematic diagram showing the interaction of the various gas and cooling loops. At low circulator powers the reactor conditions can be maintained in the thermally

insulated main loop by means of heat tracing.

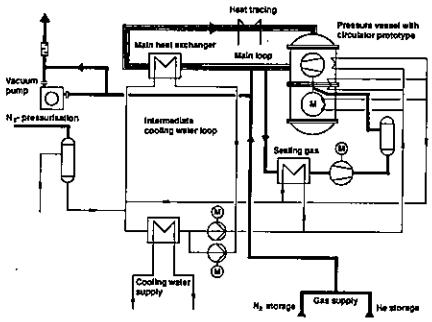

Fig.8 Schematic diagram of the gas and cooling loops in the test stand for the coolant gas circulator prototype MALVE

For large powers the cooler is operated with water from the intermediate cooling loop. The possibility to evacuate the overall loop has been provided for the effective adjustment of the helium purity. The sealing gas supply for the circulator, corresponding to reactor operating conditions, is simulated by means of a separate loop equipped with a cooling device.

The test program envisages tests in air/nitrogen and in helium. The objective of the tests under atmospheric conditions is above all to verify the dynamic behavior of the circulator and the effect of the internal circulator cooling loop at various speeds and gas densities. At first an impeller dummy will be used for the tests; it will later be replaced by the original impeller wheel. During the final tests in helium the circulator will, in particular at full power, be operated with gas densities corresponding to the reactor accident conditions "reactor depressurized", which is important from a safety-engineering point of view.

The instrumentation of the circulator will be much more extensive compared with that for reactor applications later on in order to obtain as much information as possible during the trial phase. The interest here is focussed on material temperatures, vibration and position transducers and on the electric and magnetic parameters which are characteristic for magnetic bearing operation. A suitable concrete foundation for the pressure vessel support structure will ensure that more or less the same highly rigid clamping of the circulator in the reactor structure will exist during the test runs.

The milestones of the planned test program are as follows:

- Testing of all the subassemblies of the coolant gas circulator prototype developed with respect to functionally correct interaction and fulfillment of requirements.

- Evaluation of the running behavior of the circulator and of the rotor dynamics at various speeds, temperatures and gas densities.

- Behavior of the magnetic bearing system during continuous operation and during simulated deviations from normal operating conditions incl. accident boundary conditions to be postulated.

- Investigation of the interaction of the electric subassemblies: static frequency converter, induction motor, and magnetic bearing system.

- Checking the effectiveness of the retainer bearing system; in particular with respect to the repeatability of the release behavior.

- Experimental verification of the temperature drift of circulator subassemblies during simulated, accident-related temperature excursions up to 450 °C in the circulator compartment.

Naturally, ABB attaches to the construction and testing of the coolant gas circulator prototype MALVE the hope that through the use of spin-off effects the magnetic bearings technology of the helium circulator, which is designed for nuclear boundary conditions, will turn out to be applicable to other types of machines as well /7/. The picture of the Magnetic Bearings Test Bay being erected in Mannheim, shown as Fig. 9, makes clear that the activities of ABB in the field of magnetic bearings transcend the scope of normal demonstration projects.

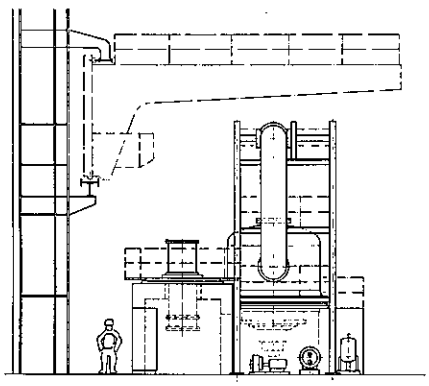

Fig. 9 ABB magnetic bearings test bay

4. TIME SCHEDULE AND FURTHER PROCEDURE

It is planned to continue with the tests in the retainer bearing test stand fitted with magnetic bearings in the 3rd quarter of this year. Besides the remaining optimization activities for the dry-lubrication retainer bearings, component tests in the magnetic bearings area are to be performed.

The commissioning of the test stand with the completed prototype is to start in late 1992; the test program is to be completed by 1994. With the program as presented, sponsored by the Federal German Minister of Research and Technology, ABB wants to safeguard in advance the properties of the HTR reactor line which are to be assessed very favorable in the long term.

Developments in Japan, the USA and the Soviet Union show that despite the decommissioning of the AVR, the TTHTR-300 and the Fort St. Vrain plant, there exists considerable interest in safeguarding the capability to supply operationally reliable, cost-effective and technologically advanced HTR plants.

REFERENCES

/1/ DELL, H., ENGEL, J., FABER, R., GLASS, D.;
Proceedings First Intl. Symposium ETH Zurich,
June 6-8, 1988, Springer-Verlag Berlin Heidelberg 1989;
"Developments and Test on Retainer Bearings for Large Active Magnetic Bearings"

/2/ GRAY, Susan T., Project Manager;
EPRI Final Report RP 2079 -
21 & 22, Dec. 1988;
"Applications for Magnetic Bearings on Electrical Generating Plant Equipment"

/3/ ENGEL, J., GLASS, D.;
VGB Conference 'Kraftwerkskomponenten [Power Plant Components] 1990',
14/15 March 1990, Essen;
"Status of the Magnetic Bearings Technology with Respect to its Potential Use for Power Plant Engineering"

/4/ ACEC SULZER Leaflet 1989,
"MOPICO - Motor Pipeline Compressor for unattended and remotely controlled compressor stations"

/5/ EIERMANN, A., GLASS, D., HERRMANN, R.;
German Patent Application DE 3141841 C2,
published on 28 Sept. 1989; "Centering and retaining device for rotors supported in non-contacting bearings"

/6/ GLASS, D., EIXELSBERGER, W., BÜHRER, P.;
European Patent Application
EP 0 317 946 A2,
published on 31 May, 1989;
"Axial Magnetic Bearing"

/7/ DANGL, G., ENGEL, J., GLASS, D., MAUERSBERGER, T.;
ABB Review 8/9-1989;
"Large 'floating' rotors run, damped and balanced in active magnetic bearings"

2nd International Symposium on Magnetic Beaing
July 12-14, 1990, Tokyo, Japan

APPLICATION AND WORKING CHARACTERISTICS OF HTGR COMPONENTS TEST MACHINES WITH MAGNETIC BEARINGS

H. Shimomura, S. Kawaji, Y. Ohta
Japan Atomic Energy Research Institute
Tokai-mura Ibaraki-ken, 319-11 JAPAN

Abstract

Simulated tests on a helium gas circulator and a reciprocating helium gas compressor with active magnetic bearings had been carried out to improve the High Temperature Gas Cooled Reactor (HTGR) components. A fair prospects has become clarified on application of the active magnetic bearing into the both kinds components. Instability problems in the high speed helium circulators which were experienced in the gas-bearing machines could be easily solved as expected and the friction-less compressor in the cylinder and piston also realized using the magnetic bearing, however, it was found the control stability has difficult problems in the active magnetic bearing system and were not necessarily satisfied the present applications. A lack of technical informations owing to the special situation on the active magnetic bearing makes very difficult analytical considerations on the test results and improvement of those machines.

1. INTRODUCTION

Though the main gas circulator of the High Temperature Gas Cooled Reactor (HTGR) system which uses the helium gas coolant is one of the most important component to keep its safety, the various problems had been encountered in the existent HTGR plants.[1]

Owing to low density of the helium gas, rotating speed of the main gas-circulator for HTGR must be designed more than 10,000rpm or several thousands rpm for one stage or multi-stage compressor respectively. Besides the problem on high speed driving, severe requirements on shaft sealing and lubrication must be satisfied during its long time operation. The shaft sealing mechanism employed mechanical seal and buffered gas seal had been applied in the main gas circulators of existent HTGRs. The submerged electric driven gas circulators had been used with the gas-bearing for the small scale research reactor[2] and are working in the Helium Engineering Demonstration Loop (HENDEL) in Japan Atomic Energy Research Institute(JAERI). They will be also used in the test reactor HTTR[3] just initiated to construct at JAERI.

The former type uses lubricating oil or water as the lubricant or sealing fluid and uses helium for the buffer gas, however, the pressure control of the buffer gas and the lubricant had not worked satisfactorily in the transient condition. This problem caused ingress of the liquid into the coolant gas and had caused fatal defect of the existent HTGR.

In case of the submerged type with gas bearings for the test reactors, weight of the rotor amounts to more than 150 kg including the motor rotor. Thus the dynamic balancing of them become extremely difficult and it tends to cause the half-speed whirling. This phenomenon is feared to grow into the shaft whip condition and to damage the gas bearing mechanism severely.

As the reciprocating compressor for the auxiliary system of HTGR and fuel reprocessing system should be designed to be gas tight and oil free in the cylinder, they could not help using oil free dry-piston or diaphragm type compressors in such applications. The technical problems in those compressors are such those as short life, larger size and radiation exposure resulting from required frequent maintenance.

The experimental works are being carried out on both of the high speed helium circulator and the reciprocating compressor employing the active magnetic bearing. The simulated test apparatus for the practical helium circulators and the small reciprocating compressor were prepared to accomplish these test.

The development test aims to solve problems on the gas bearing circulator and the oil free type reciprocating compressor and to know practical problems on applying the active magnetic bearing on the compressor.

The test results showed that the active magnetic bearing involves favorable characteristics which had never realized by the any conventional bearings, however, it is not always easy to realize the enough stability in the difficult mechanical condition. It was also found that previous analytical considerations on vibrational characteristics are very important for the mechanical components to realize a stable magnetic bearing control system.

2. TESTING APPARATUSES

2.1 SIMULATED GAS CIRCULATOR

Fig. 2.1 shows a sectional view of the simulated gas circulator test apparatus on both of the gas bearing helium circulators in service and predicted one for the test reactor "HTTR". Photo. 2.1 and 2.2 show appearances

of the rotor and the magnetic bearing of the apparatus.

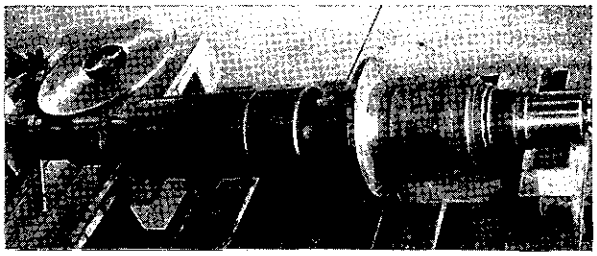

Photo. 2.1 Appearance of Simulated Gas Circulator Rotor

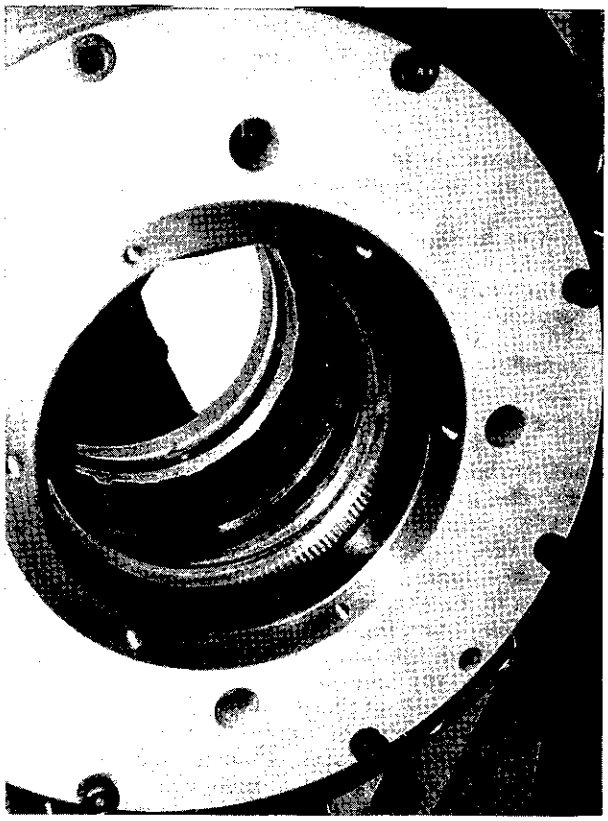

Photo. 2.2 Magnetic Bearing of Simulated Gas Circulator (Lower)

The rotor positions in vertical direction and is driven by the 30kW electric motor in the same manner as the practical circulators.

Main features of the simulated rotor are;

Total rotor length	:	1,227	mm
Max. rotor dia.	:	182	mm
Outer Dia. of	:	169	mm(upper)
journal shaft		109	mm(lower)
Total weight	:	172.9	kg
Moment of inertia	:	0.71	m^2kg(spin)
	:	17.6	m^2kg(transverse)

The practically important two critical speeds among the four first order flexion mode critical speeds ω_1, ω_2, ω_{b1} and ω_{b2} are estimated as 15,540rpm and 13,200rpm for forward ω_1 and backward ω_{b2} respectively.

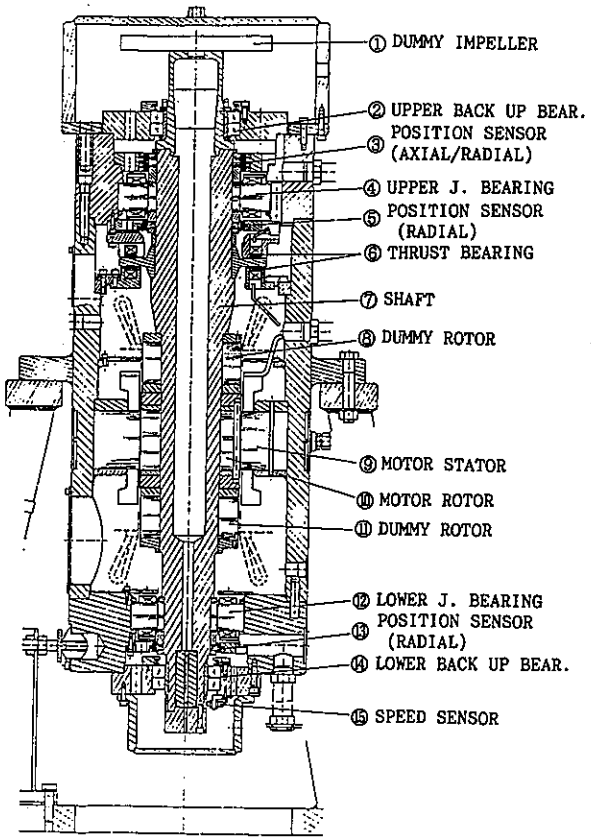

Fig. 2.1 Section of Testing Apparatus for Gas Circulator

The solid disk at upper end of the rotor simulates the impeller and the additional laminations were attached on both side of the motor rotor to simulate the larger power motor in the practical gas circulators which are estimated about 250 to 300kW. The hollow shaft saves total weight of the rotor and contributes to increase the flexion mode frequency of it.

The magnetic bearing positions at both side of the journal shaft and pair of ring shaped axial magnetic bearings are also equipped adjacent to both side of the rotating disk. Both of the journal bearings keep air gaps of 0.5mm and the axial bearing has 0.6mm gap between the rotating disk surfaces. The maximum load capacities of the journal bearings are 3,700N and 2,300N for upper and lower bearings respectively and is 7,650N for the axial bearing.

Auxiliary bearings consisted of conical ball-bearings are attached close to the magnetic journal bearings with 0.175mm radial air gap which is equivalent to 0.25mm for axial

direction.

The magnets in the each bearings are excited with bias current to avoid the zero attractive force during the working condition, because when required attractive force changes across zero, the terminal voltage of the magnet burst out by the induction of the winding and the high voltage impulse might damage the amplifier.

The shaft position sensors are mounted in the levels just below the journal magnetic bearings for radial displacement and axial position is detected by pair of two detectors which positions upper side of the hollow shaft as shown in Fig. 2.1. The additional winding in the magnet detects induced magnetic flux to stabilize the attractive force causing from dependency of the distance between a magnet and the object.

Each control amplifier among five units in the control box feeds the opposite magnets in upper and lower journal bearings of two (X, Y) axes and the axial bearing of one (Z) axis. The auto-balance function is involved in the journal bearing system rejecting the rotating frequency signal component from the shaft vibration signals. This function is a unique technology which could be never realized by conventional bearings owing to the concept of Société de Mécanique Magnétique(S2M). The function makes the rotor rotate around its inertial axis causing zero-stiffness only in the rotating frequency itself. The storage batteries back up power supply system of the control box for five minutes at least.

The displacement signals are available in X, Y and Z axes for the journal bearings and the axial bearing respectively. The dynamic exciting current which is proportional to the force is also measurable for those axes. More than seventy working status signals of the control box are available through the open collector circuits and a part of them are used in this apparatus.

The semi-conductor type frequency converter changes rotor speed from nearly 0 to 12,000rpm changing the frequency from 0 to approximately 220Hz. As the rotor supported by the magnetic bearings keeps rotation without driving power for a long time, it should be rapidly decreased in the emergency condition. Thus the resistors with large heat capacities were equipped in the frequency converter to damp rotating energy of the rotor. Thereby the rotor could be stopped by the regenerative damping in a few seconds from 12,000rpm.

2.2 RECIPROCATING HELIUM COMPRESSOR

Fig. 2.2 shows cross sectional view of upper part of the testing compressor and Photo. 2.3 is an appearance of it. The compressor is being operated practically in the auxiliary circuit of the facility.

Main specifications of this compressor are as follows:

Design gas pressure	:	4.0 Mpa(inlet)
Design gas pressure rise	:	0.5 Mpa
Design gas temperature	:	30 C° (inlet)
Stroke of piston	:	35 mm
Cylinder diameter	:	85 mm
Max. rotating speed	:	1,200rpm
Design shaft power	:	7.5 kW
Weight of piston	:	≃ 1 kg
Design gas temperature	:	30 C° (inlet)
Displacement volume	:	170 lit./stroke
Equivalent mass of reciprocating part (on the level of magnetic bearing)	:	1.82 kg(B.D.C.) 2.04 kg(T.D.C.)

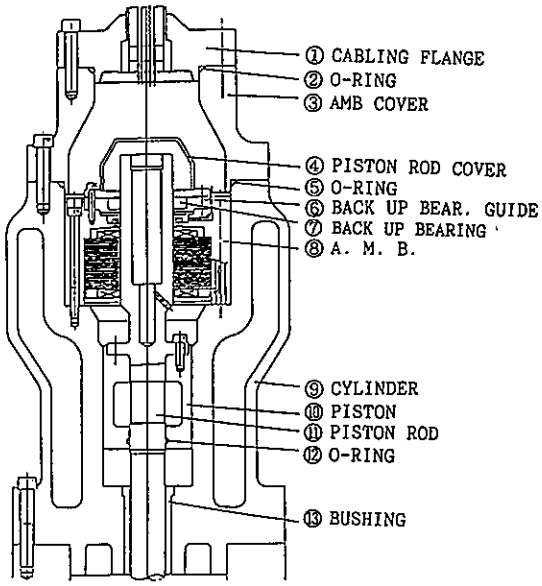

Fig.2.2 Cross Sectional View of Upper Structure of Reciprocating Compressor

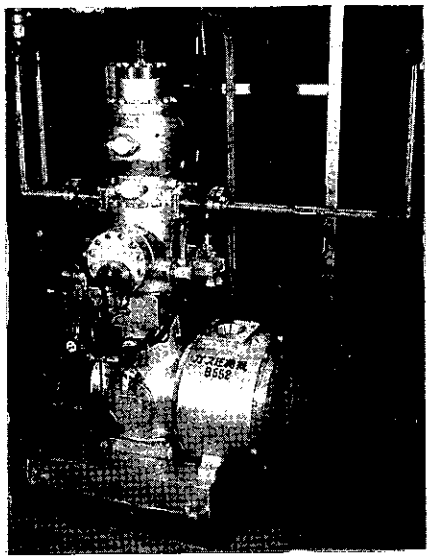

Photo. 2.3 Appearance of Reciprocating Compressor

As shown above, the stroke of piston is designed very short compared to the cylinder diameter thus it makes possible to operate in higher speed.

The magnetic bearing supports the extended piston rod in radial two axes on the top of cylinder. The conventional oil lubricated cross-head supports lower end of the piston rod which fixed with it because the horizontal force component is much larger for the cross head. The oil film in the narrow clearance around the cross-head will contribute to increase the damping factor of the vibrating system. The radial clearance between the extended piston rod and the magnetic bearing is 0.35mm in normal condition. Aluminum alloy was used as a material for main part of the piston to save weight of it. Nominal clearance between labyrinthian piston and cylinder was machined into 150μm, however, this value was found to be reducible into a figure of micro-meter or less as mentioned later.

The magnetic bearing controller involves nominal electric output of 60V, 4A and equips back up batteries of five minutes working time.

An electric motor with 11kW output drives the compressor through a direct coupling and the driving speed is adjustable continuously from 0 to 1,400rpm using a frequency converter.

3. WORKING CHARACTERISTICS

3.1 SIMULATED GAS CIRCULATOR

Vibrational characteristics of the rotor shaft were measured over the whole speed rage using the shaft displacement signals. The vibrational signals were converted into time average amplitude, vibrational traces and frequency spectral maps with the rotating speed.

Fig. 3.1 shows vibrational amplitude with rotating speed of the shaft in upper journal bearing. A thin line in the Figure shows typical amplitude of the practical helium circulator with gas bearings to compare with them for the magnetic bearing. It is very interesting that the shaft amplitude for the magnetic bearing are less in general compared to gas bearing's one and are kept in a constant value in the range over 6,000rpm.

The imbalance of rotor system and stability of the control loop affect amplitude of the shaft of course, however, those values for the test machines with magnetic and gas bearings are roughly the same value 3μm to 5μm and the bending stiffness of the both rotor are almost equally designed. Thus the difference between both types might show that stiffness and damping factor of both bearings are so different. It should be remarked that the auto-balance function reduces the amplitude clearly over 6,000rpm where it works, though the amplitude in the condition must increase because the stiffness become to zero for the rotating frequency component of the vibration force. This provably means that the rotor is very well balanced, however, the control stability of the system made the amplitude relatively large in the condition where the auto-balance was working and the amplitude reduced into the original imbalance when the stiffness become to zero.

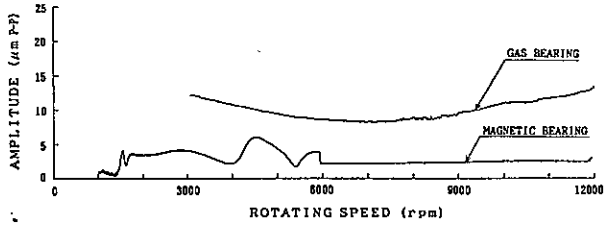

Fig. 3.1 Vibrational Amplitude with Rotating Speed (Upper Journal Bearing)

Fig. 3.2 shows vibrational spectral map measured on upper end of the journal shaft. It will be understood that the amplitude is much lower and no any higher harmonics are found in this figure compared to Fig. 3.3 which shows typical map of the practical helium circulator with gas bearings. It means the stiffness and damping factor is isogonic and the parasitic oscillation is negligible in this test machine.

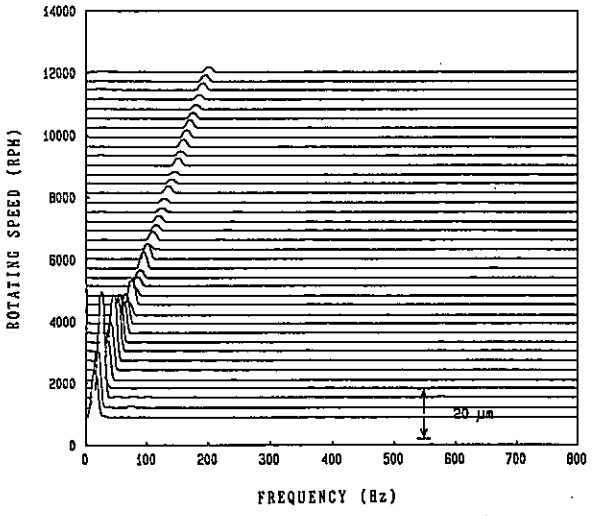

Fig. 3.2 Vibrational Spectral Map of Simulated Gas Circulator on Upper Journal

Fig. 3.4 shows typical trace of the shaft vibration measured on upper journal bearing in radial plane and with time. The almost complete circular trace shows the same characteristics described with Fig. 3.2.

The self-induced weak vibration had been observed at times in higher frequency (KHz) regime. This means stability in the higher frequency regime is insufficient, in other words, the damping factor should be increased more for the control system or steep cut down

of the amplifier gain is necessary without larger phase lag in those frequency regime.

A test on the backup bearing was carried out in the rotating speed of 12,000rpm, however, no any significant problems were happened on it.

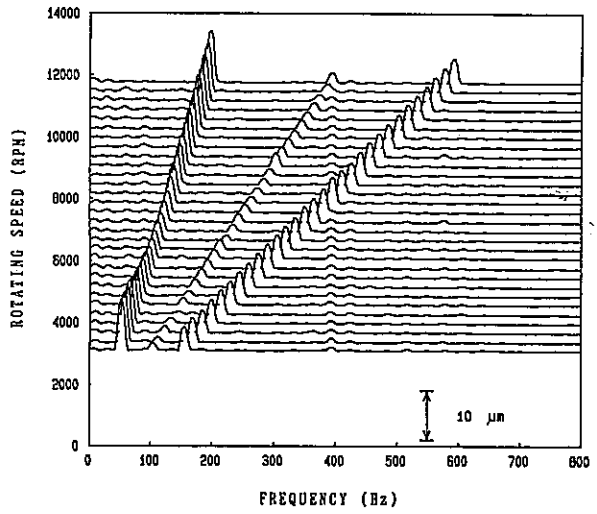

Fig. 3.3 Typical Spectral Map of Practical Helium Circulator with Gas-Bearing

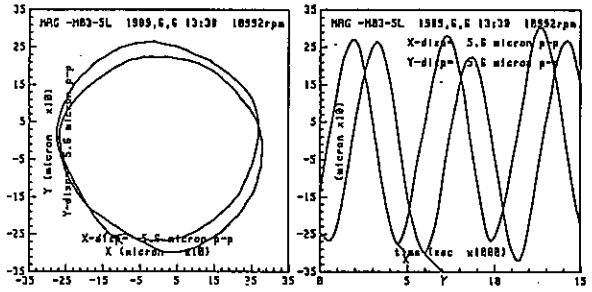

Fig. 3.4 Typical Lissajous' Figure and Time Trace of Upper Journal Vibration

3.2 RECIPROCATING HELIUM COMPRESSOR

The operating tests were accomplished with air and helium as the working gas just after the installation and the compressor have worked more than 4,600 hours on end of April 1990. The volumetric efficiency was more than 60% in rated pressure difference with helium gas and will be improved decreasing the clearance around the piston. The radial vibrational characteristics were measured in two axes using the deflection signals from the magnetic bearing.

The deflection signals were measured as time average amplitude with rotating speed and were transformed into frequency spectra in the same manner as simulated gas circulator. The vibrating trace were also plotted into Lissajous' figure and with time. Figs. 3.5 through 3.7 show typical vibrational data for the operation with helium gas.

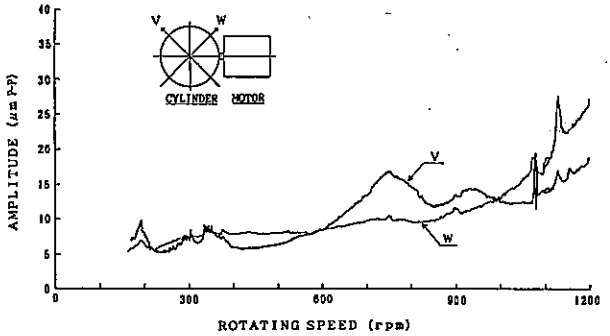

Fig. 3.5 Radial Amplitude of Piston in V and W axes

Among the figures, Fig. 3.5 shows piston amplitude in two axes of magnetic bearing V and W. The amplitude curves for two axes differ each other in general and are steeply increase over 1,100rpm. It will be seen a large peak on 750rpm for V axis, sharp peaks on around 1,100 to 1,150rpm and small peaks on less than 200rpm. The difference with two amplitude curves is thought to be mainly caused from characteristics of the magnetic bearings are not quite equal for two axes. Thus the resonant frequency and the height of peaks are unequal because they depend stiffness and damping factor of the magnetic bearings as understanding from the spectral map shown in Fig. 3.6.

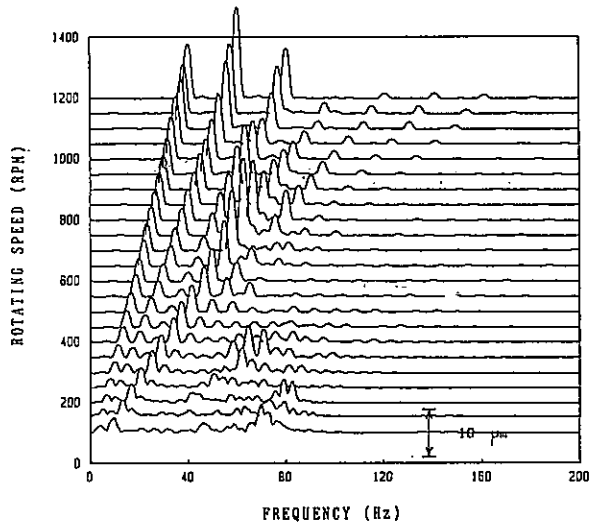

Fig. 3.6 Spectral Map of Radial Vibration of Piston

It should be remarked on Fig. 3.6 that we can find no basic frequency components of vibration but higher harmonics more than second order. These results caused from so called "Peak of Gain" which intensifies gain of the control circuits only for a narrow frequency

band consisted with the rotating speed. Remarkable peaks are also found in Fig. 3.6 on vertical 60Hz line. These are thought to be parasitic vibrations and resonance of forced vibration with resonant frequency decided by stiffness of the magnetic bearing and mass of the object.

The equivalent stiffness is estimated as around 3 x 10^4 kg/m from the resonant frequency and the equivalent mass. The parasitic vibrations and resonant peaks in Figs. 3.5 and 3.6 show insufficient damping of the system. It will be realized by the increased differential gain which is consistent with advancing the phase from lower frequency in the electronic circuits. Instability will be observed from the parasitic vibration in a Lissajous' figure and a time trace for 300rpm shown in Fig. 3.7.

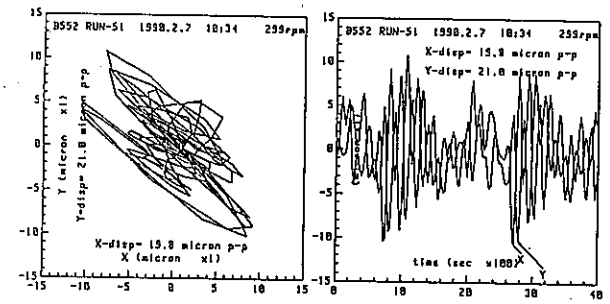

Fig. 3.7 Typical Lissajous' Figure and Time Trace of Radial Piston Vibration

In spite of the insufficient stability, the piston works in very small vibration amplitude and is kept in less than 35μm in peak to peak value. This enables to reduce the clearance around the piston from the present value of 150μm and will cause much improvement on the volumetric efficiency. Farther improvement of the stability is being discussed on dynamic characteristics of the control amplifiers.

4. DISCUSSION ON VIBRATION CHARACTERISTICS

It was found from test results on the two kinds application of the magnetic bearing that the most important technology is to realize a highly stable system. An easy way for this problem will be decreasing total gain of the system, however, it results in low stiffness and low damping factor of the magnetic bearing system which cause relatively low accuracy of control.

The phase lag between the amplifier input and deflection of the object sharply increases at the system resonant frequency in lower damping condition and causes instability of the system. Thus we should realize a large damping factor by the control circuits if the resonant frequencies are relatively low with the operating frequency. The way to solve this problem is not difficult at all in principle, that is advancing phase or enhancing differential gain of the signal for the object deflection in the circuits.

Figs. 3.8a and 3.8b show calculated frequency characteristics on amplitude response and phase respectively for the realistic constants of the compressor.

As shown in Figs. 3.8a and 3.8b, the large damping factor C_1 of the magnetic bearing suppresses the resonant peak and keeps the phase lag less than 90 degree and realizes a stable system. Though the principle way is not difficult to make a stable and accurate system by the circuits, but it is not always easy to realize in the practical circuits.

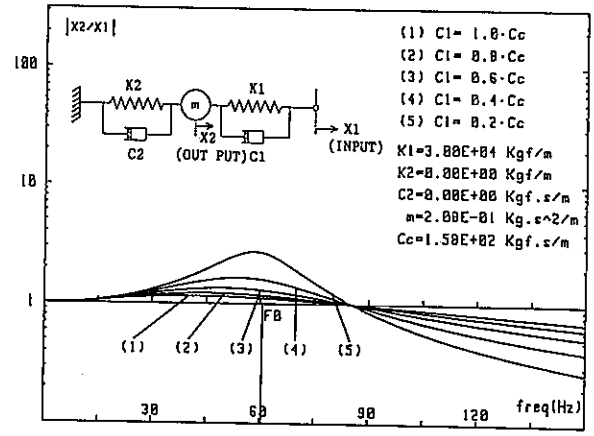

Fig. 3.8a Calculated Amplitude Response of Reciprocating Compressor

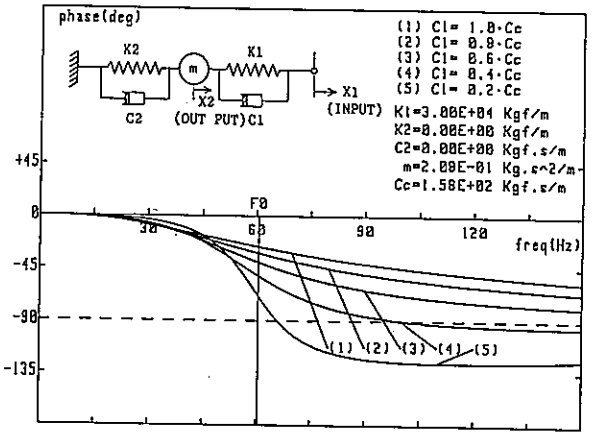

Fig. 3.8b Calculated Phase Lag of Reciprocating Compressor

Understanding the reason why, let us use a logarithmic coordinate system with horizontal frequency axis and vertical gain axis. The proportional gain which means stiffness shows a horizontal line and the differential gain shows a straight line with positive 45° inclination.

Both lines crosses at the cross-over point in the cross-over frequency. As the differential gain line shifts to upper side with the damping factor C_1, the cross-over frequency also shifts to left hand side with it. This means the required gain in higher frequency than cross-over point must be increased proportionally to the damping factor. This is apt to cause a saturation of the output for the limited input signal, furthermore, elevated gain in the higher frequency regime causes over-sensitiveness for noises and makes the electronic amplifier it self unstable.

Thus it is essential to make the imbalance or forced vibration force as small as possible to prevent saturation of the amplifier and to limit the rotational speed to avoid extremely wide frequency range for the circuits. It is so important to improve the electronic amplifier as to endure a wide signal level and as to stabilize the amplifier it self. Intensified gain in the high frequency requires the position signal with very low noises because such amplifier is very sensitive to the noises. From the same reason, electronic devices and signal lines must be carefully selected or designed to reduce the noises.

It is also important to design the mechanical components to be rigid and light weighted so that the resonant frequency could be elevated.

5. CONCLUSION

A fair prospect has become clarified on applications of the active magnetic bearing into the helium circulator and the reciprocating compressor. It was found that the instability problem on the conventional bearing has perfectly solved in the magnetic bearing machines, however, the problems on the control stability had not solved completely even for the magnetic bearing system. From the experiences on experimental studies, we point out the stability consideration is very important when the resonant frequency is relatively low for the operating speed. A lack of technical informations on the control system also makes very difficult analytical considerations on the test results and improvement of those machines owing to the special situation such as patent on the active magnetic bearing.

Nevertheless, the high speed machines and reciprocating compressors were much improved in the vibration amplitude compared to the conventional bearing system. Applying the magnetic bearings, one would have much practical merits on manufacturing, installation, maintenance and operation of the machines such as comparatively easy balancing on the rotor, simple and maintenance free bearing system, very weak vibration to the base, vibration monitoring in service and so on. The maintenance free and wearless machine will greatly contribute to minimize radiation exposure in the nuclear facilities.

The instability due to the insufficient damping factor would be subjected by the high speed digital control system which would be changeable the gain independently from the phase shift in the electronic circuits. Development of the semi-conductor devices with a large power and wide frequency range will be also important to apply the magnetic bearing into high speed and large machines.

It should be emphasized that the magnetic bearing is not only a substitute of the conventional mechanical bearings but is a innovative tool to realize the modern machines which had never produced. The uniqueness on accurate controllabilities of stiffness and damping factor and the special functions such as integral control and auto-balance should be utilized in the advanced mechanical systems.

ACKNOWLEDGEMENTS

The present authors wish to give a cordial thanks to Mr. M. Kato, Mr. S. Watanabe and Mr. K. Sekita who contributed in developing the computer programs and in processing the experimental data with their excellent technical knowledge.

REFERENCES

[1] H. L. Brey, "Fort St. Vrain Circulator Operating Experience", IWGGCR/17, Proc. Specialists' Meeting Gas-Cooled Reactor Coolant Circulator and Blower Tech. in SANDIEGO 30 Nov. - 2 Dec. 1987, pub. by IAEA 1988

[2] C. Mech, "Some Practical Performance Aspects of the Design of Gas Bearing Blowers and Some Performances of Industrial Machines", paper 16, Gas Bearing Symp. Univ. Southampton, April 1967

[3] S. Saito, 1st JAERI Symp. on HTGR Tech., paper 2-11, held in Tokyo JAPAN, March 1990

2nd International Symposium on Magnetic Beaing
July 12-14, 1990, Tokyo, Japan

AN APPLICATION OF MAGNETIC BEARINGS TO TITANIUM POWDER PRODUCTION

T. KIMURA and T. NEGISHI

Mitsubishi Metal Corp. Central Research Institute
1-297 Kitabukuro, Omiya, Saitama 330, Japan

Abstract

Plasma rotary electrode process (PREP) is being used for production of titanium alloy powder. In this technique, titanium billet is rotated and one end of the billet is melted by plasma arc, and droplets are sprayed by centrifugal force and cooled in an inert atmosphere. The rotating mechanism is like a cantilever arm with a heavy weight top and the critical speed is lowered by the weight of the top. Also there are many vibration sources in this system. To avoid this vibrational problem, we adopted the magnetic bearing as the drive mechanism in place of the motor and gear train. The use of the magnetic bearing resulted in an increase of allowable unbalance and a large decrease of the vibration of the machine. These improvements made it possible to produce fine and rapidly solidified particles with a higher productivity.

1. Introduction

Titanium alloys are very attractive as structural materials because of their superior strength to density ratio, fatigue strength and fracture toughness, but they have two problems, i.e., low production yield and high cost. Powder metallurgy route is considered to be very promising to solve these problems and a substantial amount of work has been carried out[1].

Ti alloys are in general hard to work with, but they show enormous elongation up to 1000% and very low flow stress at some strain rate and temperature condition (Superplasticity) [2]. Therefore, National Research Institute for Metals (NRIM) has developed the designing principle and designed new alloy GT-33(Ti-6.5Al-1.4V-1.4Sn-1.0Zr-2.9Mo-2.1Cr-1.7Fe) which has good superplasticity at working temperature and superior mechanical properties at service temperature[3]. We have developed powder production technology to obtain fine particles of this alloys and superplastic forging technology to obtain complex shaped forgings. In this paper, we report the development of powder production technology and application of magnetic bearings in a PREP chamber.

2. Titanium Powder Production Technology

2.1 Outlook

Titanium alloys are chemically active and react with refractory materials, and ordinary powder production technics such as gas atomizing can not be used. Therefore, rotating electrode process (REP) and plasma rotating electrode process (PREP) are developed by Nuclear Metals Inc. and being used for production of titanium alloy powders[4]. In these techniques as shown in Fig.1, titanium billet is rotated and one end of billet is melted by arc or plasma arc, and droplets are sprayed by centrifugal force and cooled in an inert atmosphere. Gas atomizing of titanium alloys using skull melting[5] and centrifugal atomization by rotating disk[6] are attractive alternative technologies to REP. But they are still in development stage.

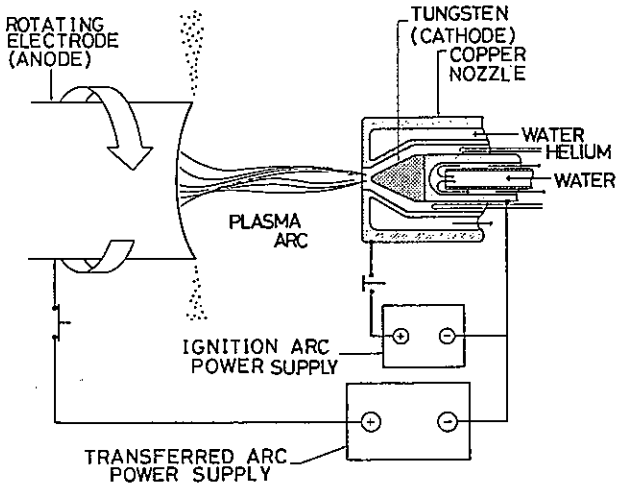

Fig.1 Principle of the transferred arc plasma REP (PREP)[2].

2.2 Particle diameter

In rotating electrode process, molten metal on the top of billet is formed as liquid torus. When the centrifugal force acting on the growing liquid mass overcomes the retaining force of surface tension, liquid protuberances form and drops are ejected from the billet. Considering the balance between these forces, a simple equation is obtained :

$$d=\frac{A}{\omega}\left(\frac{\gamma}{D\rho}\right)^{\frac{1}{2}} \tag{1}$$

d : diameter of particle, μm
ω : angular velocity, rad/s
γ : surface tension of liquid metal, N/m
ρ : density of liquid metal, kg/m^3
D : diameter of billet, m
A : constant

Many authors give the value for constant A and 3.8×10^6 is given for organic liquids[7].

From the regression analysis of many metal atomization experiments, the relation between the mean volume-surface diameter (Sauter diameter) d_{vs} and experimental variables is obtained[8] :

$$d_{vs}=4.63\times10^6\frac{1}{\omega^{0.98}}\frac{1}{D^{0.64}}\left(\frac{\gamma}{\rho}\right)^{0.43}Q^{0.12} \tag{2}$$

Q : melting or flow rate, m^3/s

From these equations, relation between the major parameters are plotted in Fig.2.

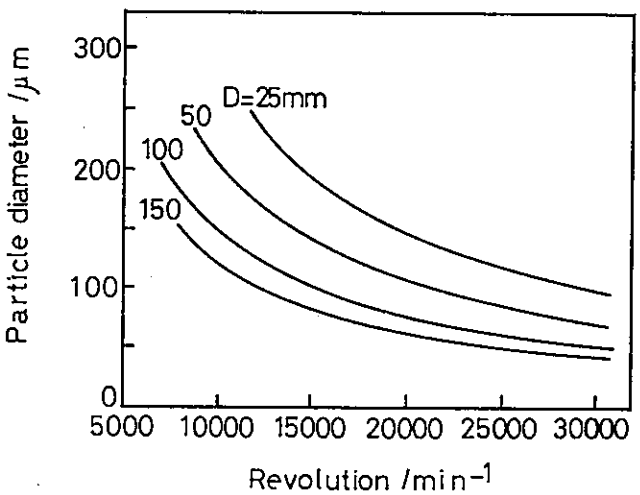

Fig.2 Relation between billet diameter, revolution and particle diameter.

2.3 Cooling rate

A molten droplet is cooled in flight to reflector walls. The mechanisms of heat transfer are radiation and forced convection. The cooling rate of droplets $\dot{T}$(K/s) is given as follows[9] :

$$\dot{T}=\frac{6}{D\rho C_p}\left[h_c\left(T_s-T_g\right)+\sigma\varepsilon\left(T_s^4-T_g^4\right)\right] \tag{3}$$

C_p : specific heat
T_g : temperature of circumferential media
T_s : temperature of droplet
h_c : thermal conductivity
σ : Stephan-Boltzmann constant
ε : emissivity

here h_c is given by

$$h_c=\frac{Nu\cdot\lambda}{d} \tag{4}$$

Nu : Nusselt Number given by

$$Nu=2+0.552Pr^{\frac{1}{3}}Re^{\frac{1}{2}} \tag{5}$$

Pr : Prandtl Number
Re : Reynolds Number

In Eq.3, heat loss by radiation is about several percent of the total heat loss and effect of latent heat is also small.

From the metallurgical point, the relation between cooling (solidification) rate and the secondary dendrite arm spacing (DAS:μm) was studied for Fe, Al, Ni, Cu alloys and formulated as below[10] :

$$\dot{T}=10^5\times\left(DAS\right)^{-3} \tag{6}$$

In Ti alloys, droplet is solidified to the β single phase structure and then decomposes to the $\alpha+\beta$ dual phase structure. The relation between the β grain size $L(\mu m)$ and $\dot{T}$ is given in reference [11] :

$$L=3\times10^6\dot{T}^{-0.9} \tag{7}$$

During the flight, the velocity of droplets is reduced by frictional force and cooling rate is also reduced.

3. Atomizer

3.1 Heat Source and cooling system

Based on the above mentioned formulae, we designed the powder production equipment[12]. The machine was built by ULVAC Corp. Photo.1 shows the appearance of the machine. Photo.2 shows the powder producing condition.

The heat source of this equipment is a plasma torch with a hot hollow cathode discharge[13]. A source gas flows into the heated Ta cathode tube and is excited to plasma, and also thermal electron is ejected out. This system uses the middle position of electron beam and plasma arc, and we named this machine as Plasma Beam Rotary Electrode Process (PBREP).

To obtain rapidly solidified powder, it is necessary to increase circumferential pressure. Therefore, operating pressure is increased gradually and He cooling gas is jet-sprayed perpendicularly into the particle flight path.

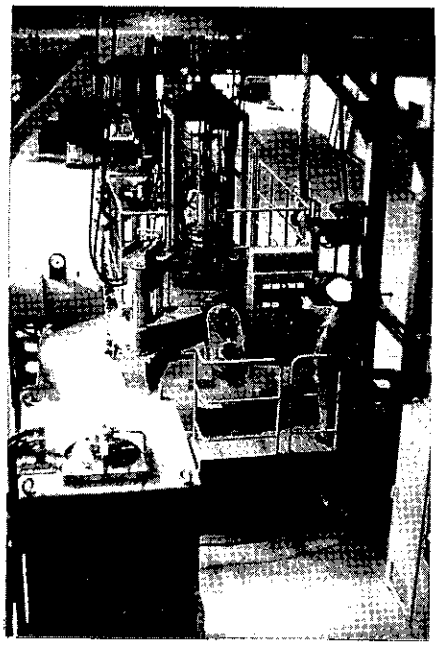

Photo.1 PBREP Machine.

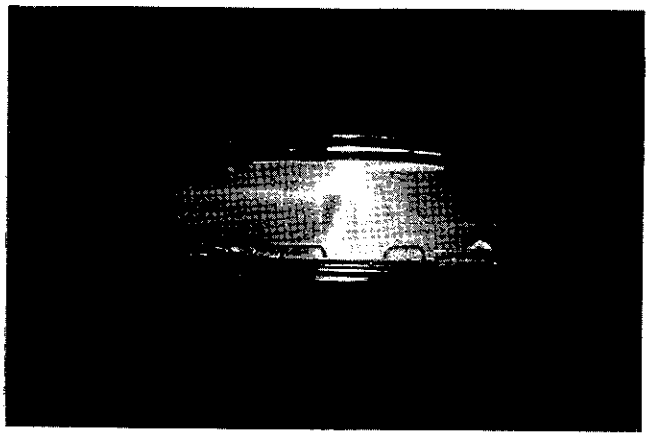

Photo.2 Powder producing condition.

3.2Drive system

To obtain fine and rapidly solidified powder, from Eq.1~7 it is necessary to increase the diameter of billet D and angular velocity ω. These requirements are rather severe for the drive system.

Originally, drive system was made of motor and gear train. Motor and 1st speed increasing gear are in air and transmit to 2nd speed increasing gear in vacuum chamber. As oil with high vapor pressure can not be used in the vacuum, lubrication was not perfect, and high frequency vibration like oil-whip occurred also in gear train.

The output axis fixes the billet. This system is like a cantilever arm with a heavy weight top and the critical speed is lowered by the weight.

When atomizing starts, usually the end of billet is melted nonuniformly and the end portion of the billet heated to just below the melting point deforms by centrifugal force. Consequently the axis starts whirling.

In addition to this, the system is thermally not steady. Heat is conducted from the top end of the billet and is generated in brush assembly by friction, contact resistance and resistivity. As a result, unsymmetrical thermal displacement occurs.

By solving the vibration equation with the boundary conditions of load from the gear and estimated unbalance, maximum operation speed was calculated to be 12,000 RPM.

Then, we redesigned the system to increase the stiffness of axis, and to improve the mounting condition, lubrication, dynamic balance and mechanical tolerances. Further, we avoided the resonance of vibration in each part and installed dynamic damper in the axis. As a result , estimated maximum operation speed is increased to 15,000 RPM. In actual operation, as the atomization proceeds, the vibration amplitude increased and rotation of 4kg billet at 14,000 RPM was the limit.

3.3 Application of magnetic bearing

At that time magnetic bearing was introduced to us by Dr. Harada of NRIM.

The characteristics of magnetic bearing[14] are as follows ;

1. Can be used in vacuum
2. Oil free
3. Increase of natural frequency due to double end free axis
4. Increase of allowable unbalance due to non-contact support
5. Rotation around principal axis of inertia by automatic balancing system

These are very advantageous to the drive system in a vacuum environment.

In this system, motor shaft is levitated by the forces generated by a magnetic field and has 5 degrees of freedom. As shown in Fig.3, the position of the shaft is monitored by sensors, signals are feedbacked and active servo system controls the position.

The stiffness of the bearing is given by

$$K=|F/x|=\left\{\left(k_0-M\omega^2\right)^2+\left(a^+\omega-\frac{b}{\omega}\right)^2\right\}^{\frac{1}{2}} \qquad (8)$$

here

M ; weight of rotor
F ; external force
x ; displacement
k_0 ; spring constant
a^+ ; damping factor
b ; constant for integral term

and its relation to frequency is shown in Fig.4. Static stiffness is given by b/ω and is relatively large value as compared with that of conventional bearings. Damping factor a^+ of the magnetic bearing is also larger and consequently its dynamic stiffness becomes higher.

Furthermore, this control system has automatic balancing system. In this system, signals from the position sensor passes a narrow band tracking filter and signals of the rotating frequency is ignored. Therefore shaft rotates around its principal axes of inertia[15].

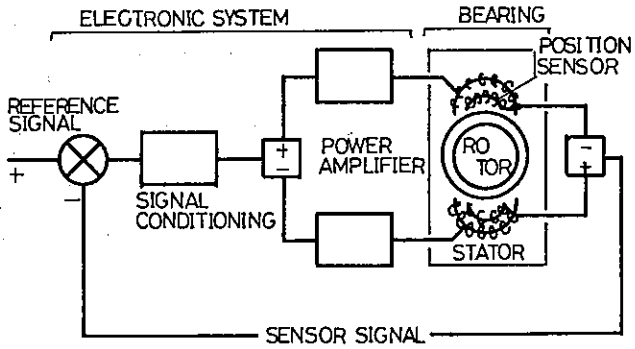

Fig.3 Control loop of magnetic bearings[14].

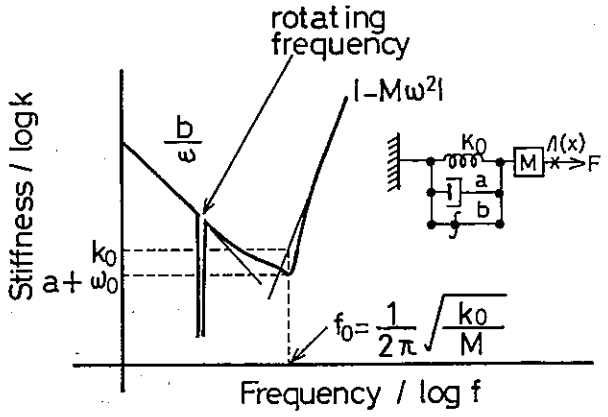

Fig.4 The relation between stiffness and frequency of magnetic bearings[15].

But there was a possibility of mutual electrical interference among electric components in our equipment. The brush assembly was installed just above the end of the motor shaft and transmit DC current up to 2000 A. The brush may cause chattering and arcing. And there existed a magnetic field due to the electric current in the constriction coil of plasma. It was confirmed that there exists no interaction, and we adopted B25/500 magnetic spindle made by S2M as the driving system in place of the motor and the gear train.

Main specification of our magnetic bearings is

Power	15	kw
Maximum rotation speed	24000	RPM
Weight of billet	6	kg
Unbalance	160	gcm max
Maximum load capacity		
upper radial bearing	153	kgf
lower radial bearing	87	kgf
thrust bearing	204	kgf

Fig.5 shows the structure of PBREP after installation of magnetic bearings. By application of magnetic bearings, vibration of the machine decreased drastically as shown in Fig.6. The improvement of overall value of power spectrum reached up to 30dB and there is left only the component of rotating frequency.

In operation, we are now able to produce 5 kg/batch powder at 15000 RPM and it may be possible to increase productivity rate using heavier billets.

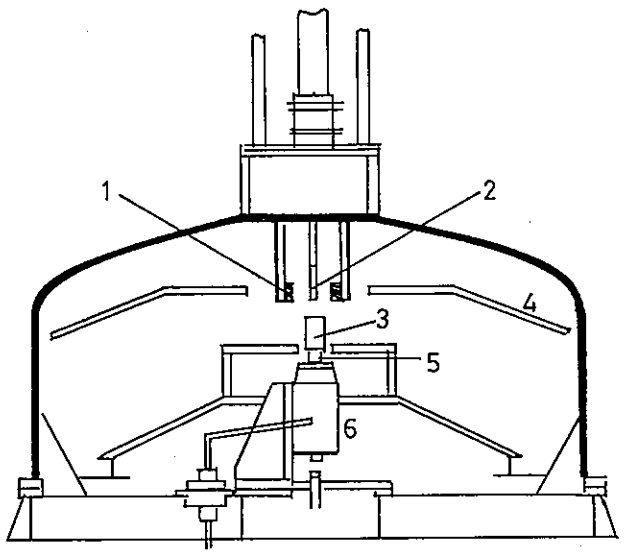

Fig.5 The structure of PBREP after installation of magnetic bearings.
(1) Plasma constriction coil;
(2) plasma torch; (3) billet;
(4) reflector; (5) brush assembly;
(6) magnetic bearings.

As the magnetic bearings give information about the amplitude of vibration and its tendency, the growth rate of unbalance can be calculated. We made several models to explain the phenomena, and now some automatic and manual control are possible. The plasma torch chases the melting billet to keep the distance and is moved to the rim portion of the billet to eliminate the growing unbalance. An example of the change of the vibrational amplitude during atomization is shown in Fig.7. Here, only first portion of atomization procedure is shown. The unbalance is improved gradually by the loss of weight of the billet.

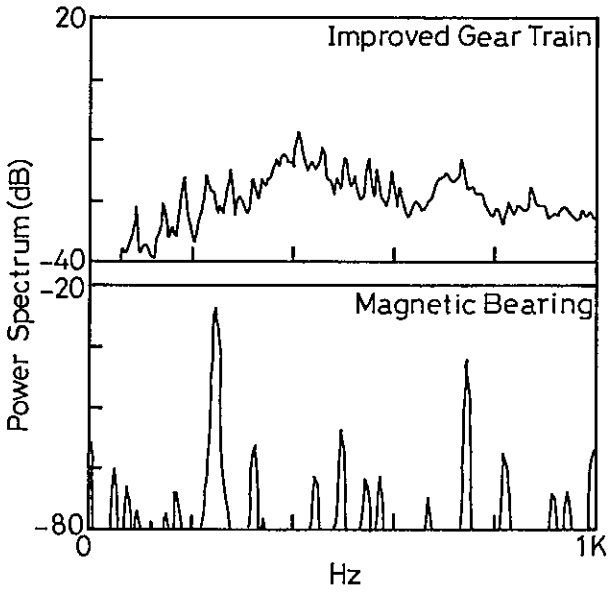

Fig.6 FFT analysis of PBREP (a)before and (b)after the installation of magnetic bearings.

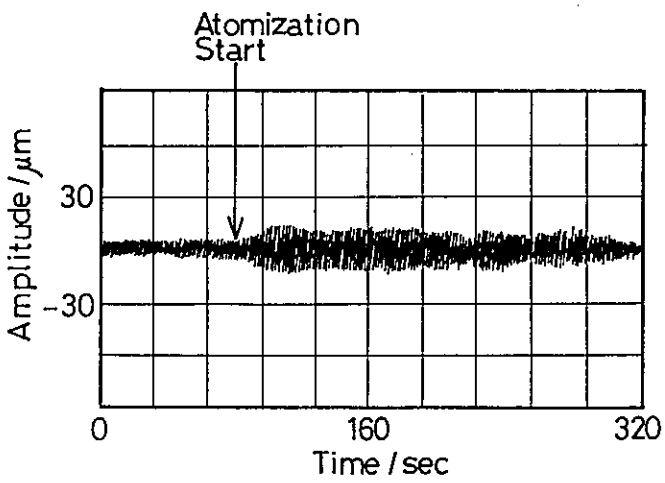

Fig.7 Change of vibration amplitude during the atomization

There are some problems remained in this system. Brush is now used at the speed of twice or more of its permissible speed. From these restriction, up to now we can not rotate the billet at its maximum speed. But improvements are in progress and it will be made possible to rotate the billet with these speeds.

4. Characteristics of Powder

Scanning Electron Microprobe (SEM) image of GT-33 Ti alloy powder produced in our PBREP equipment is shown in Photo.3, which shows that spherical powders were obtained. Powder made by the processes which utilize electron beam as a heat source has the surface α shell, which produced by the evaporation and deposition of alloying element such as Al with high vapor pressure. Such heterogeneity is not observed in our powder as proved by electron probe micro analysis or Auger analysis.

Particle size distribution of Ti-6Al-4V measured by micro track analysis is given in Fig.8. 50% line of vertical axis gives the mean diameter and its relation to rotation speed almost agrees with Eq.1,2 and Fig.2, but as particle diameter becomes finer, mean deviation becomes smaller.

Histogram of GT-33 powder is also given in Fig.9. The change of the drive system to magnetic bearings largely decreased the amount of coarse particles and resulted in a sharp distribution. The mean particle diameter became 86 μm.

Photo.4 shows the SEM image of a cross section of GT-33 powder. The microstructure is uniform in the cross section and is composed of fine cells and dendrites. The relation between the mean cell diameter and the particle size is shown in Fig.10. Each line shows the state of the drive system, and improvement of the cooling system was made together with use of 'improved gear train' and 'magnetic bearing'. It is seen that these improvement refined the substructure.

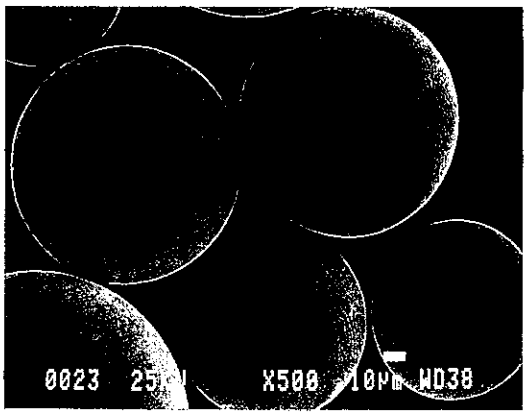

Photo.3 SEM image of GT-33 powder.

Solidification rate is estimated to be increased from $10^{2\sim3}$ at original state to $10^{4\sim5}$ °C/s after the installation of magnetic bearings.

These figures agree also with results obtained from β grain size estimation from microstructural observation of hot isostatic pressed samples and Eq.7.

Improved powder enabled HIP consolidation temperature to decrease about 100 °C. The α grain size after HIP at 750 °C was about 1μm. The flow stress of a HIP'ed preform at 850 °C and strain rate 5×10^{-4} s^{-1} was 1.7 kgf/mm^2, which is one half of that of usual powder.

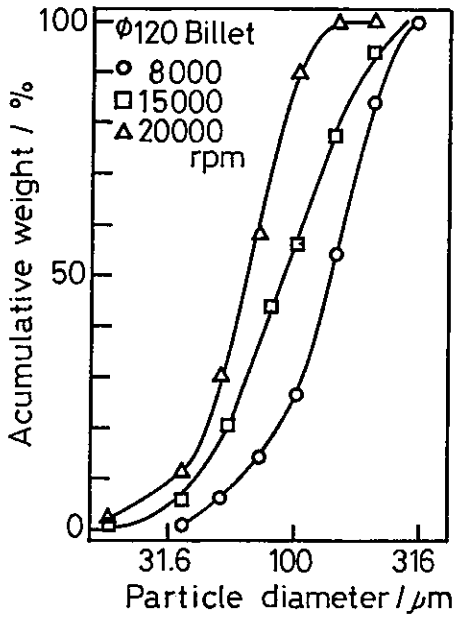

Fig.8 Particle size distribution of Ti-6Al-4V.

These preforms were successfully forged superplastically to a ϕ400mm full scale model disk with blades (blisk) under a very low forging load of 1500 tonf. After double solution heat treatment and aging, this showed ultimate strength 133.0 kgf/mm^2 (strength to density ratio 28.6 km) and elongation 11.3% at 300 °C.

Furthermore, we applied Hydride-DeHydride (HDH) process to control the microstructure of the disk. Hydrogen is a β-phase forming element and it has $10^{1\sim2}$ times larger diffusion coefficient in fine grained body. Using hydrogen as temporary alloying element, partial HDH process enabled to obtain a disk with unique microstructure (dual property disk).

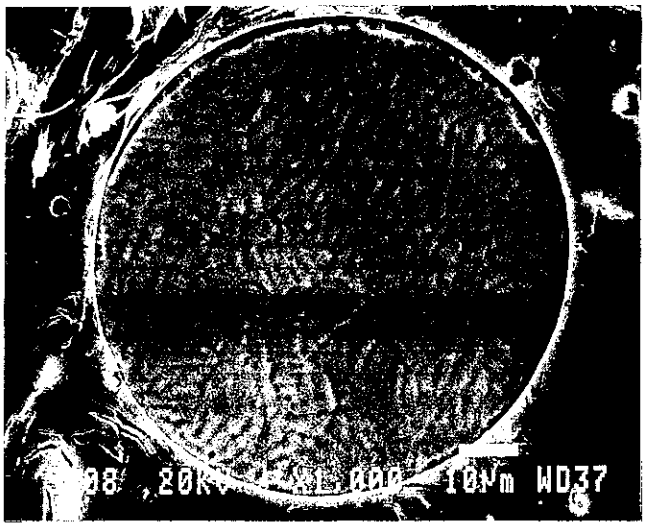

Photo.4 Cross-section of GT-33 powder.

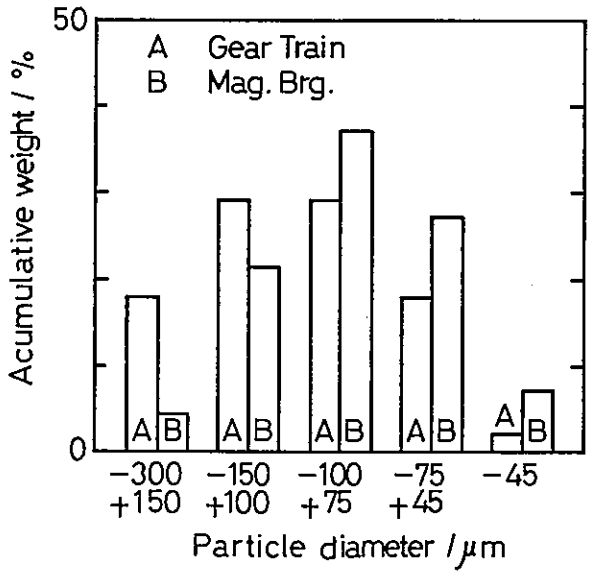

Fig.9 Particle size distributions of GT-33.

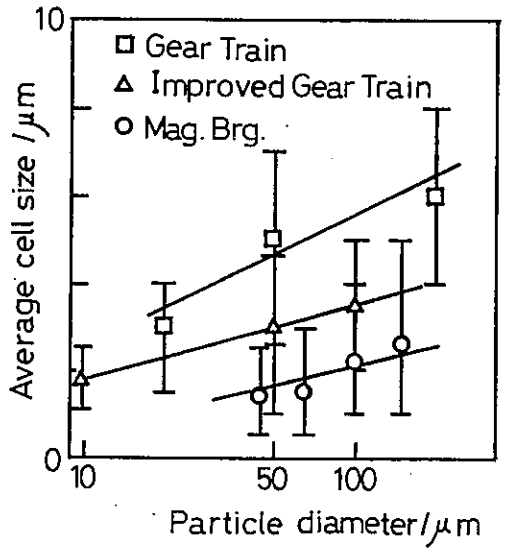

Fig.10 Relation between particle diameter and average cell size.

It consists of two portion ,and the boss part where high strength is necessary has a very fine microstructure and the blade part where creep strength is necessary possesses a coarse microstructure. The creep life of the blade portion is extended to 3 times[16].

Our equipment has not reached its maximum ability yet, but further improvement will make it possible to obtain powders which have finer than 50μm and its solidification rate is more than 10^6 °C/s.

Powder metallurgy (P/M) of Ti alloys is thought to be promising and some case studies of aerospace parts evaluate that the cost of P/M products will be a half of that by ingot metallurgy (I/M) process. But actual applications of P/M are delayed contrary to this prediction. One of the reason of this delay may be high cost of powder because it has not been mass produced. And another reason may be that the mechanical properties of P/M parts are only equal or slightly superior to that of I/M parts and not enough to alter user's mind. The application of magnetic bearings to REP and Rotary Disk process may have possibility to solve these problems by giving higher production rate and finer and more rapidly solidified powder.

5.Conclusions

1. An application of magnetic bearings to PREP decreased drastically the vibration of machine.
2. Weight of the billet and maximum rotation number was increased due to the increase of allowable unbalance.
3. Monitoring of the shaft enabled the control of plasma to eliminate growing unbalance and resulted in stable operation.
4. These improvement enabled us to obtain powders which are finer than 100 μm and more rapidly solidified than 10^5 °C/s.

Acknowledgements

This work was performed under management of Research and Development Institute of Metals and Composites for Future Industries as a part of the R&D project of Basic Technology for Future Industries sponsored by Agency of Industrial Science and Technology, MITI.

Reference

[1] F. H. Froes and J. E. Smugeresly (Eds.) : *Powder Metallurgy of Titanium Alloys*, AIME, 1981.
[2] N. E. Paton and C. H. Hamilton (Eds.) : *Superplastic Forming of Structural Alloys*, AIME, 1982.
[3] H. Onodera, K. Ohno, T. Yamagata and M. Yamazaki : *Proc. 6th Int. Conf. on Titanium*, France, 1988, 1191.
[4] P. R. Roberts and P. Loewenstein : Ref. 1, 21.
[5] J. H. Moll and C. F. Yolton : *Titanium Rapid Solidification Technology*, F. H. Froes and D. Eylon (Eds.), TMS-AIME, 1986, 45.
[6] D. J. Hodkin, P. W. Sutcliffe, P. G. Mardon and L. E. Russell : *Powder Met.*, 16-32(1973), 277.
[7] R. P. Fraser and P. Eisenklam : *Trans.*,Inst. Chem. Eng., London, 34(1956), 294.
[8] B. Champagne and R. Angers : *Int. J. Powder Metall. Powder Technol.*, 16-4(1980), 359.
[9] C. Aerivos : *J. Mat. Sci.*, 11(1976), 1159.
[10] S. J. Savage and F. H. Froes : *J. Metals*, 36-4(1980),20.
[11] F. H. Froes and R. G. Rowe : *Rapidly Solidified Alloys and their Mechanical and Magnetic Properties*, Materials Research Society, 58(1986), 307.
[12] Y. Nishino, T. Kimura, F. Noda and T. Yamauchi : *Progress in Powder Metallurgy*, 41(1986), 509.
[13] S. Kashu, S. Nishino and C. Hayashi : *Trans. Vac. Metall. Conf.*, 1967.
[14] H. Habermann and M. Brunet : 85-GT-221, ASME.
[15] H. Habermann and M. Brunet : 84-GT-117, ASME.
[16] T. Kimura : *Proc. 7th Symposium on Basic Technologies for Future Industries*, 1989, 111 (in Japanese).

MAG-LEV

2nd International Symposium on Magnetic Beaing
July 12-14, 1990, Tokyo, Japan

MAG-LEV SEMICONDUCTOR WAFER TRANSPORTER FOR ULTRA-HIGH-VACUUM ENVIRONMENT

(Application Development of Active Magnetic Bearing)

Masato OTA, Sigenori ANDOH, Hiroyuki INOUE

SEIKO SEIKI Co., Ltd., Narashino, Chiba 275, JAPAN

Abstract

Magnetically levitated linear and tilting movement transfer equipment to operate in an ultra-high-vacuum was developed. This equipment will be used in semiconductor manufacturing equipment for Ultra-Large-Scale Integrated circuit such as dynamic random access memories (DRAMs) with capacities of tens of megabits. Regular electromagnet materials cannot be used in a high vacuum because they emit gases, so we keptthose parts on the outside of a metallic shield wall, with the vacuum inside the wall. It was not easy to develop magnetic bearing control through the conductive wall and across the wide bearing gap. The major problems were vibration of the long and thin transfer rod and axial oscillation of the rod and the floating body.

1. Introduction

It is well known that keeping the environment in a semiconductor manufacturing plant very clean is essential for maintaining high quality and high yield of integrated circuit.

To manufacture even more highly integrated circuits (such as 100 Megabit DRAMs) in the future, it is necessary to process the semiconductor wafers in an ultra-high-vacuum (UHV) to avoid unexpected reaction caused by humidity and impurities of the air.

Wafer transfer equipment, which carries the wafers between UHV process chambers, must not generate particles, release gases, and employ any lubricant.

In these circumstances, rolling or sliding contact bearings cannot be used, we developed a wafer transporter using active magnetic bearings as a contactless motion guide and actuator.

2. Structure of the equipment

Under UHV conditions [$1.33*10^{-6}$Pa ($1.33*10^{-8}$Torr) or lower pressure], ordinary materials for electromagnets such as magnetic steel sheets and enamel-insulated copper wires are cannot be used because they emit gases from their insulating films, contaminating the vacuum. To prevent this contamination we placed ordinary electromagnets outside the vacuum shield and placed the floating body for transportation inside of the shield.

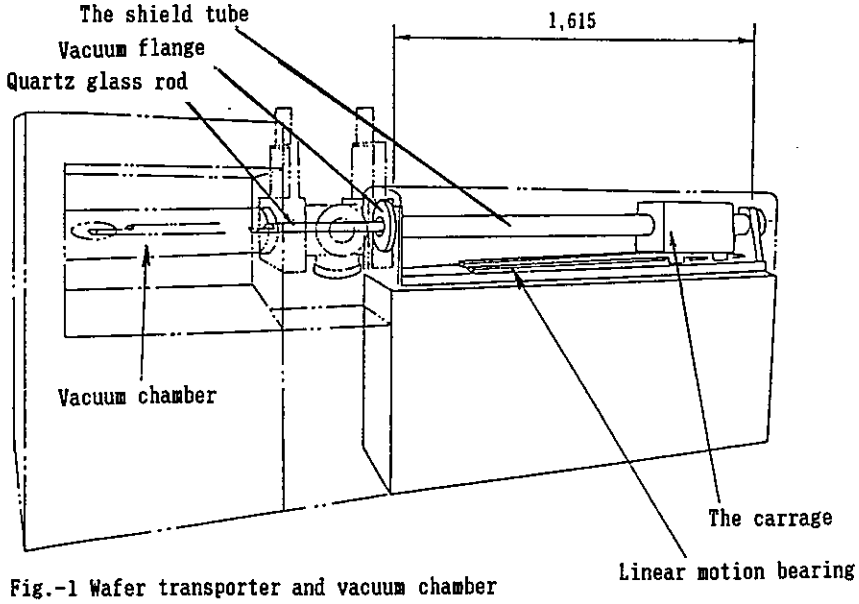

Fig.-1 Wafer transporter and vacuum chamber

Wafer transporter (Figure-1)

From the side wall of the semiconductor UHV chamber, the transfer rod projects into the chamber and moves horizontally. The flat part on one end of the rod scoops the wafer up from the relay point, transfers it to the process (fabricating) spot, unloads it to wait the fabricated wafer.

At the other end of the rod, the transfer rod is connected to the cylindrical floating body. The rod and the floating body are levitated in the middle of a vacuum shield tube which is connected to the vacuum chamber by a vacuum flange. The inside of the shield tube has the same vacuum conditions as the process chamber.

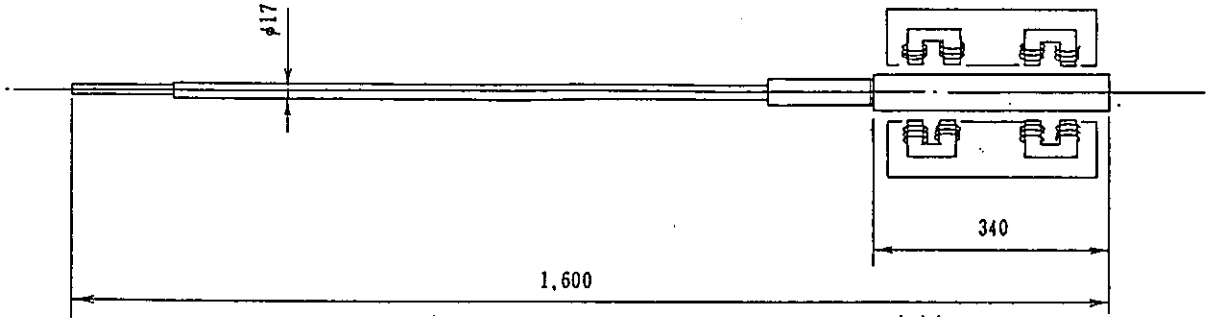

Fig-2 The transfer rod and electromagnets

The transfer rod (Figure-2)

The floating body, is made of magnetic material and is a cylinder about in 50 mm diameter and 340 mm long. The total length of the rod, flat scoop, and floating body is 1.6 meters. The floating body is supported by magnetic attraction through the thin wall of the shield tube.

The radial bearings (Figure-3)

The floating body fits inside the shield tube with a 1 mm gap all around. Four pairs (8 pieces) of electromagnets surround the shield tube, Two groups of two pairs define two points which define the center line of the floating body. The distance between the two groups is decided by the length of the floating body. Also four pairs of inductive position sensors are located on the side of the magnets to detect the radial position of the floating body. Using these sensor signals, four servo control loops keep the floating body and the transfer rod aligned on the center of the shield tube.

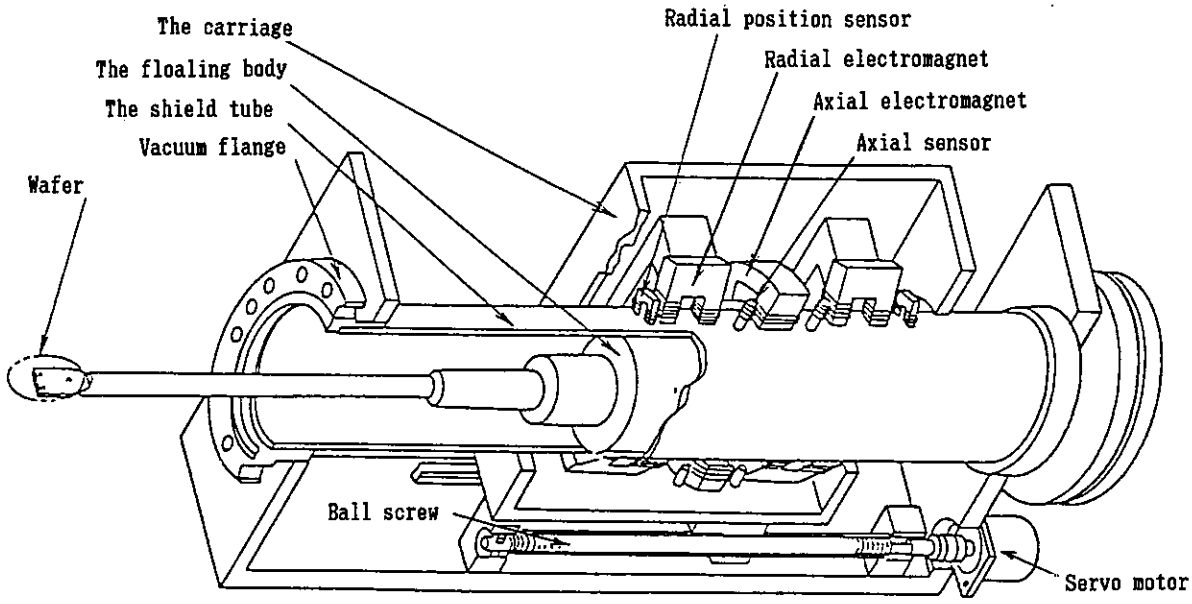

Fig.-3 The carriage and the floating body

Axial motion

The electromagnets and sensors are fixed to the carriage which travels horizontally along the shield tube. Around the floating body's cylindrical surface, 16 lands are formed to match the shape and face the locations of the pole shoes of the 8 electromagnets.

At the time of initial design, we expected that the transfer rod would follow the horizontal travel of the magnets but finally we had to add one control loop to damp axial oscillation at the time of start and stop of traveling.

Restriction of transfer rod rolling

Restoring force to stop the rod rolling is given passively by the radial electromagnets' pole shoes and facing lands on the floating body. When the floating body begins to roll, the electromagnets' pole shoes and the facing lands on the floating body are no longer centered on each other, so the magnetic force brings them back into alignment.

Horizontal motion

The carriage with eight radial electromagnets, their corresponding position sensors, and a set of electromagnets with sensors for damping axial oscillation (explained later), move coaxially with the shield tube. A ball screw and a servo motor drive the carriage guided by linear-motion ball bearings parallel to the shield tube. The levitated floating body and the connected transfer rod are dragged and follow the carriage's movement.

Pick and place motion (Figure-4)

When the floating body is tilted in the vertical plane (pitched), the flat part at the top of the transfer rod scoops up (picks) the wafer from the relay spot or lays down (places) at the process spot.

These movement are given by the input signal for the servo control loops for the radial bearings, and is sequentially changed with the carriage's travel position.

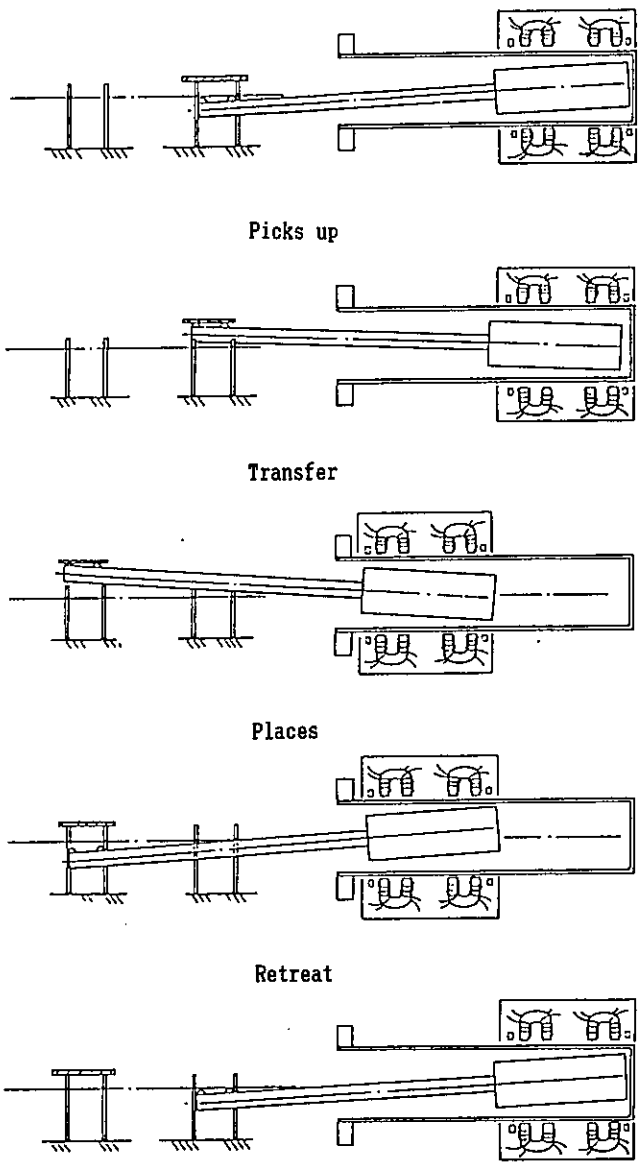

Fig.-4 Pick and Place

3. The subject in design process

Target design specifications and final results are listed in Table-1. The many problems were worked on by trial and error method. The major problem was deciding the bearing gap between the electromagnets and the floating body's lands. The factors for the bearing gap decision are listed below.

* Vertical motion amount (lift) of the flat part at the top of the rod for pick and place.
* Wafer fixture's height diffirence between relay point and process point.
* Geometrical accuracy of the shield tube. (straightness, roundness, taper and wall thickness uniformity)
* Stable control range of the floating body's tilt.
* Maximum payload.

We did not have enough data and experience to design a wide or fluctuating bearing gap, and the bearing was difficult to cotrol through the metal vacuum shield. So we could not optimize the gap, the lift and the size of the electromagnets. The minimum bearing gap was determined by the necessary lift (5 mm) and the estimated geometrical accuracy of the tube.

4 Prototype performance

Unforseen difficulties made it difficult to attain the target specifications. We describe how we overcome those difficulties and where we were obliged to compromise.

Table-1	Design target	Actual results
Transfer travel	1,000/500 mm	Unchanged
Transfer speed	100 mm/s	80 mm/s
Payload /Travel	100 g / 1,000 mm	14 g / 1,000 mm 1,000 g / 500 mm
Lift	5 mm	3.5 mm
Locating accuracy	+/- 0.5mm	+/- 0.1 mm
Vacuum shield (Leak test)	$1 * 10^{-8}$ Torr L/s	$2.7 * 10^{-10}$ Torr L/s

Travel speed

We had hoped to achieve 100 mm/s maximum speed, but had to lower that to 80 mm/s because of axial oscillation of the floating body and the cost of the carriage drive motor servo control system.

We did not adopt any axial control in the initial structure. With this structure, at the carriage's travel end, when the carriage decelerated from its top speed and stopped, the floating body overran and was pulled back by magnetic force. It then started to oscillate at about 2 Hz frequency without amplitude decrement (Figure-5a).

To suppress the oscillation, we put two extra electromagnets and sensors on the carriage and put notches and tapers on the floating body (Figure-6). We also add a control loop for this purpose.

The effect of the additional control is shown in Figure-5b. The oscillation at the carriage stop was damped in 1 second. We were unable to decrease the shock at the carriage travel end because of financial constraints. By using a servo motor with a wider speed range we will be able to increase the maximum transfer speed.

Payload

The main thing limiting the payload was the bending resonance of the transfer rod. When the rod resonates, the wafer falls off the flat part of the rod. Beside thin and long shape, the semiconductor manufacturing process requires that the transfer rod material be quartz glass . That and the rod's long, thin shape meant that it was frequently broken by violent resonance.

There are many resonance frequencies For example with the 1,000 mm distance transfer model, the first-order bending resonance was at 30 Hz and the second-order was at about 100 Hz. To suppress the resonance, we put phase-lead networks in every bearing control loop for the first resonance frequency, notch filters for the second resonance and high-order low-pass filters for the third and higher harmonics.

These countermeasures forced us to compromise and make do with a 14-gram payload instead of the 100 grams we had originally intended.

For bigger payload, we must made the rod stiffer. The model with 500 mm transfer distance reached 1,000 grams payload on a shorter aluminum rod of higher resonant frequencies.

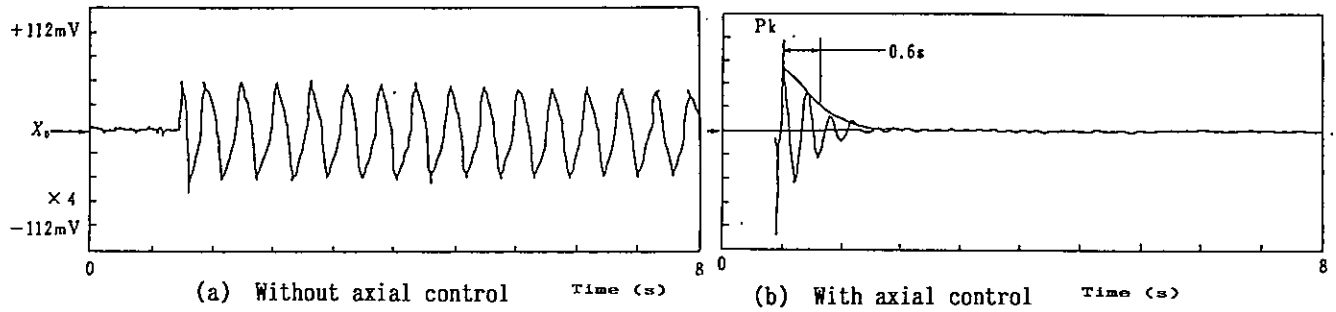

(a) Without axial control (b) With axial control

Fig.-5 Effect of axial damping control

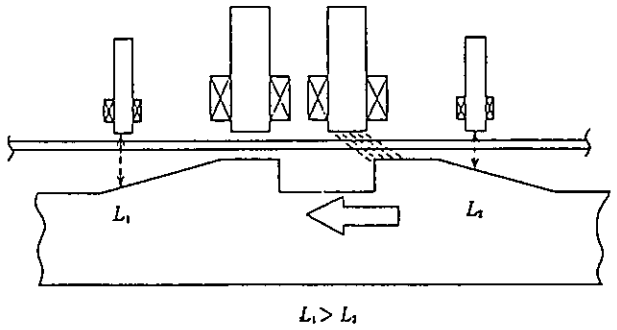

Fig.-6 Components layout for axial damping.

the Electromagnets, Sensors and the Floating body

Lift amount

The wall thickness of the austinite stainless steel of the shield tube was 0.5 mm. The gap between the outside of the tube and the electromagnet was 0.2 mm on average. The gap between the inside of the tube and the lands on the floating body was 1.2 mm on average.

The total gap between the electromagnets' pole shoes and the lands on the floating body was 2.0 mm, including the tube thickness.

The geometrical accuracy of the tube was worse than expected, so we had to increase the bearing gap by 0.2 mm and the lift amount was only 3.5 mm, rather than the 5 mm we had planned.

We note that it is necessary to study the behavior of the inductive position sensor, which senses the magnetic material through the conductive shield.

To avoid lift motion shock, a ramp function for the control signal input was employed, To increase tilt stiffness, the control signal of the front and rear bearing was cross coupled.

Others

Horizontal locating accuracy (repeatability measured in the atmosphere) was better than expected, thanks to the low-friction magnetic bearing and the carriage's high locating accuracy of 0.01 mm.

The vacuum shield test was carried out by helium detecting. The internal surface of the shield tube was polished millor-smooth by an electro-chemical method so that the gases would be released easily from its surface and so that a high grade of vacuum would quickly be reached.

5 Conclusions

We developed and built non-contact, non-lubricated, and dust-free semiconductor wafer transporter, which is levitated and driven by magnetic attraction through the metal vacuum shield.

This transporter can be used in a UHV and will be used in the manufacturing process equipment that will mass-produce 100 Mbit DRAMs in the near future.

* We gathered design data for the stainless steel shielded magnetic bearing including payload limit, gaps, and tilting controllability.
* Without any complicated structure, a wafer could be picked up and placed by tilting the floating body in the gap of the magnetic bearing.
*The suppressing method for axial oscillation of the floating body and the transfer rod was realized by active (controlled) magnetic damping through the metallic shield tube.
* The sensitivity and robustness of the position sensor through the metal vacuum shield must be improved.
* The data and experience gathered during this development are very important for the futures polar coordinate robot, which will work in a UHV.

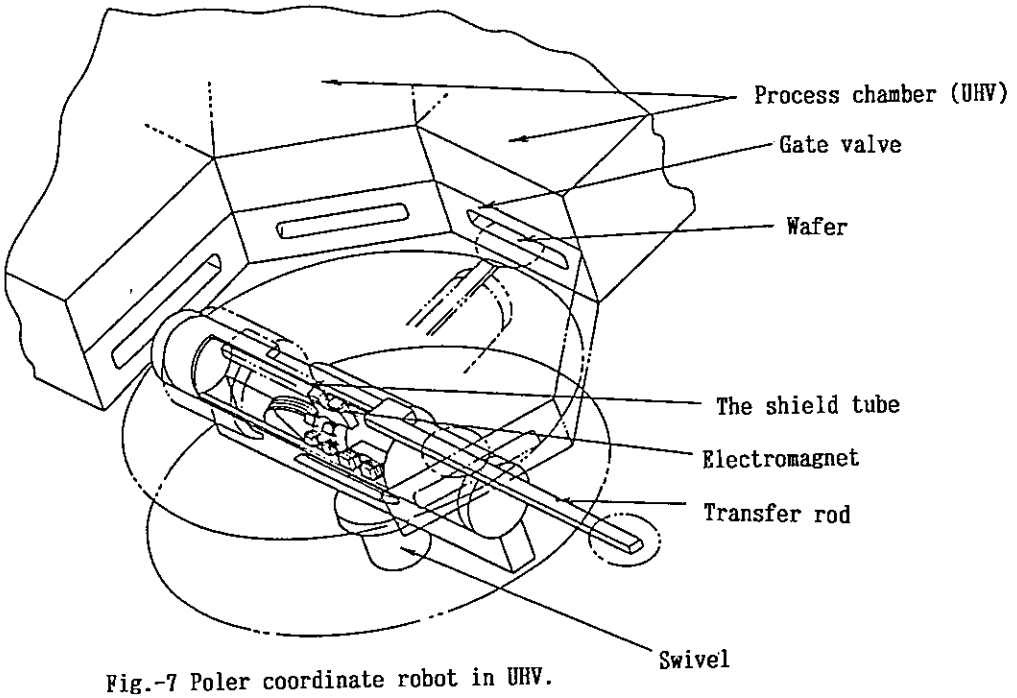

Fig.-7 Poler coordinate robot in UHV.

Acknowledgement

This equipment was developed under the guidance of Professor T. OHMI and Dr. M. MORITA of Tohoku University Electrocommunication Laboratory. The 1,000-mm transfer model was evaluated with an experimental oxidization furness for forming an insulating layer on silicon crystal. This furness, made by SEIKO Instruments, was operated in Tohoku University's famous super-clean room.

2nd International Symposium on Magnetic Beaing
July 12-14, 1990, Tokyo, Japan

DEVELOPMENT OF AN ACTUATOR FOR SUPER CLEAN ROOMS AND ULTRA HIGH VACUA

T.HIGUCHI* A.HORIKOSHI** T.KOMORI**

*Institute of Industrial Science, University of Tokyo, MInato-ku,Tokyo, Japan
**Nippon Seiko K.K., Maebashi-city, Gunma-pre, Japan

Abstract

The Magnetically Suspended stepping motor (MS-type stepping motor) is a new actuator that we are currentry developing. The MS-type motor has the function of both the attractive levitation and the precise positioning of a stepping motor in one construction. By making use of the MS-type stepping motor, a cotactless positioning actuator, which is smaller than one using a simple combination of a conventional magnetic bearing and the conventional positioning motor can be realized. Also, by building in a position sensor (a brushless multipolar resolver), it will be possible to drive the MS-type stepping motor as a servo mortor. That is to say, it will be possible for the contactless actuator to provide velosity control and high speed, precise positioning. Firstly, this paper describes the conception behind the MS-type stepping motor and its structure. Secondly, the structure and performance of the Super Clean Servo Actuator are presented. Further, the development of an actuator for ultra high vacua is explained.

1. Introduction

Since the magnetic bearing does not have any mechanical contact and requires no lubrication, it does not contaminate its environment with dusts or oil vapour. Using this merit of the magnetic bearing, an actuator that is completely free from dusts or oil vapour can be developed. However an actuator which combines a propelling mechanism with a magnetic bearing is apt to be large. Because of the cost of keeping a high degree of cleanliness or vacuity, a super clean environment or an ultra high vacuum environment is very expensive. So actuators that are used in such an environment are required to be as small as possible.

With this in mind, we have developed a new actuator, named the Magnetically Suspended stepping motor(MS-type stepping motor), which has the functions of both a magnetic bearing and a stepping motor. By using the MS-type stepping motor, we can build(or design) not only a more compact actuator for super clean room or ultra high vacuum chamber, but also precise positioning actuator making good use of the functions of a stepping motor.

This paper describes the principle and the structure of MS-type stepping motor and also introduces the structure and the performance of two types of actuators using the developed MS-type stepping motor. One of them is the super clean servo actuator, and the other is the actuator for ultra high vacua with the function of both rotary and thrust positioning in one body.

2. MS-type Stepping Motor Unit

2.1 Structure of MS-type Stepping Motor Unit

Fig.1 (a) shows the structure of the MS-type stepping motor unit. The MS-type stepping motor unit is composed of the motor core and six coils that are wound around the motor core. The motor core is made from laminated silicon steel. Two larger coils(Main coils) are connected in series and produce magnetic flux (Main magnetic flux). Coil A1 and coil A2 are connected in series, but wound in opposite directions so generating opposing magnetmotive forces. The same applies for coils B1 and B2.

The MS-type stepping motor unit has four toothed poles T1,T2,T3,T4. The rack has the same teeth as those of the poles. Let one pitch of the rack be expressed as 2 pi rad., then the phase relationship between the toothed poles may be expressed as;(when the teeth of the toothed pole T1 are in phase with those of the rack) T1 0 rad.; T2 pi rad.; T3 pi/2 rad.; T4 -pi/2 rad..

2.2 Magnetic Suspension Control

Fig.2 shows the equivalent circuit of the MS-type stepping motor unit. 'P1,P2,P3,P4' symbolize the permeance values of the toothed poles T1,T2,T3,T4, and Um symbolizes the magnetomotive force of the Main coils. The Magnetic reluctance and magnetic hysterisis of the motor core were assumed to be negligible. The magnetmotive forces of coils A1,A2,B1,B2 are not indicated in this

figure.

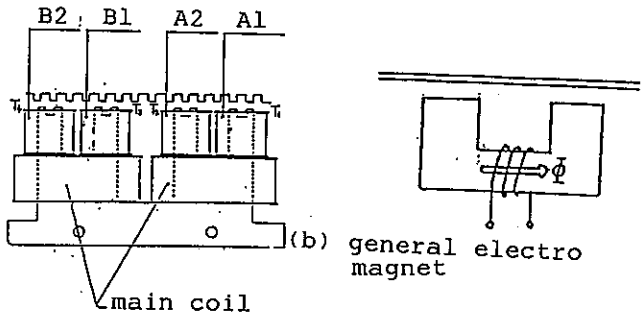

(a) MS-type stepping motor

Fig.1 Structure of the MS-type stepping motor uinit

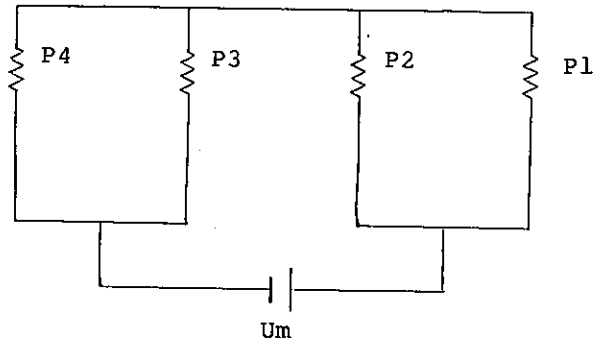

Fig.2 Equivalence circuit of the MS-type stepping motor unit

By using the assumed flux pattern method, permeance P1,P2,P3,P4 of toothed poles T1,T2,T3,T4 are given as functions of tooth width, valley width, gap length, x(the x axis was defined as the direction of propulsion). Due to the toothed pole structure of the motor, permeance P1,P2,P3,P4 fluctuates as the motor moves in the x direction. Fig.3 shows the fluctuation of permeance P1. However, total permeance is more or less constant and insensitive to change of x as shown in Fig.3. This is due to the phase relations of the toothed poles explained in chapter 3.1. The total permeance Pm is calculated using the following equation;

$$Pm = \frac{(P1+P2)*(P3+P4)}{P1+P2+P3+P4}$$

It should be noted that in spite of the toothed pole structure of the motor, the MS-type stepping motor shown in Fig.1.a is equivalent to the general electromagnet shown in Fig.1.b. So a magnetic suspension control circuit, independant of x, may achieve stable suspension.

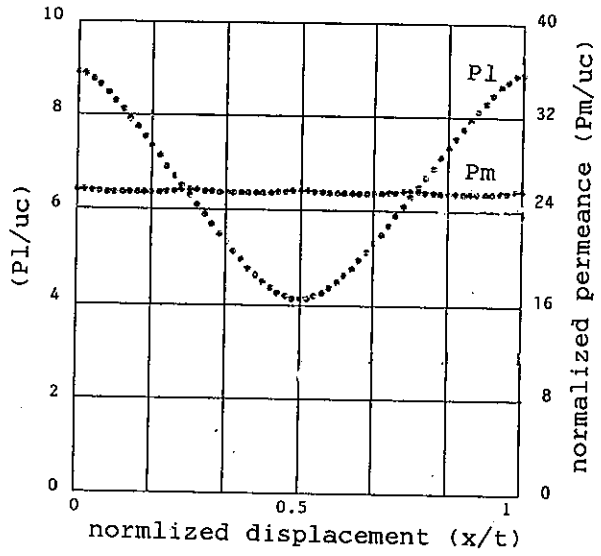

c; thickness of the core
t; pitch of the teeth

Fig.3 Permeance P1 and Pm

2.3 Propulsion Method and Position Control

In the propulsion method of conventional stepping motors the magnetmotive force of coils A1,A2,B1,B2 is changed in a step form as shown in Fig.4. But we made use of another propulsion method, called 'micro step' drive, where the magnetmotive forces of coils A1,A2,B1,B2 take a sinusoidal form. This method was used because acute changes in the step form of Ua and Ub seemed to disturb stable suspension. Moreover, the 'micro step' drive provides smoother motion of the rotor and higher positioning resolution than the conventional method. It has been proved, by simulation and experiment(1),that suspension control and position control scarcely influence each other.

3. Developing Super Clean Servo Actuator

As stated abave,the MS-type stepping motor has the function of positioning without a position detector. However, step out or ripple-full motion due to the resonance that is a characteristic of the stepping motor are apt to occur using open loop control. In the field of micro circuitry production, smooth motion (without speed ripple) is needed in order to provide a uniform chemical reaction on the surface of silicon wafers. Also, an

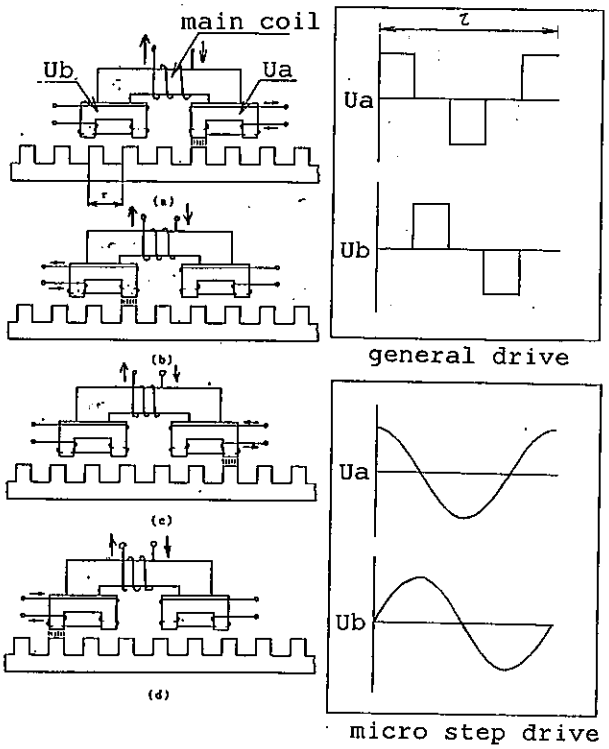

Fig.4 Propulsion method

actuator which has the ability to control speed, torque and position precisely is needed for industrial robots working in the vacuum chambers and the super clean rooms. Therefore, we have developed a servo actuator for super clean rooms by building in a position detector.

In this chapter, the structure and the principle of the built-in position detector are explained, and the developed super clean actuator and its performance are shown.

3.1 Built in Position Detector

The built-in position detector is a sort of brushless multi polar resolver. Fig.5 shows the structure of the built-in position detector. This position detector is part of both the rotor and stator.

The stator has many poles. The coils that are wound around the poles are connected in series. On the pole face and the rotor, the teeth are the same as those of a stepping motor. The gap length between a certain pole of the stator and the magnetically suspended rotor is not always constant. In order to cancel the influence of fluctation of the gap length, the poles are placed point symmetrically. By measuring the current of the coils excited by an A.C. constant voltage power supply, a signal, which is modulated by the variable permeance between the teeth of the rotor and stator can be obtained. Fig.6 (a) shows the carrier signal. Fig.6 (b) shows the modulated signal. Transforming this signal using a resolver to digital converter, we can get a resolution of 1,536,600 pulse per revolution.

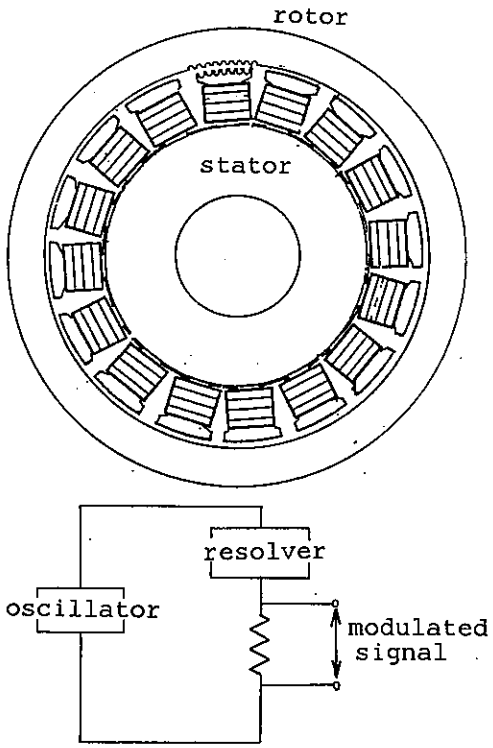

Fig.5 Structure of the built-in position detector(resolver)

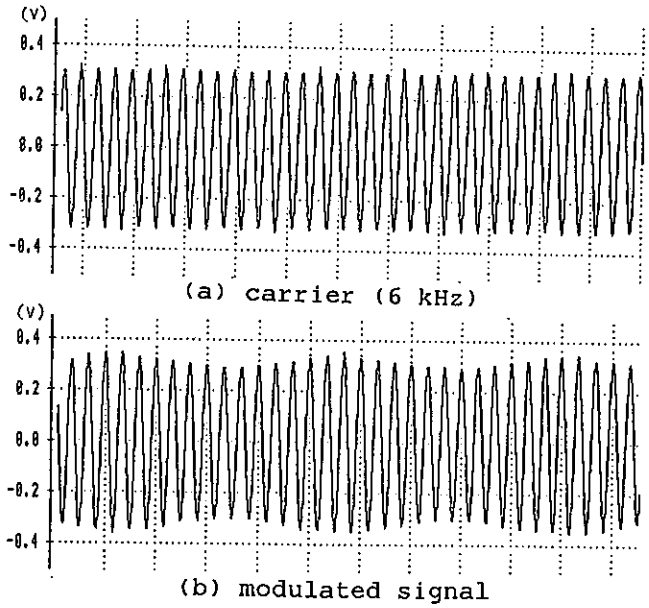

Fig.6 Signal of the resolver

A resolver has the following merits;

(1) A resolver can operate over a very wide temperature range.
(2) Because of its simple structure, a resolver can endure vibration and shocks
(3) Transmission over distance is possible.

3.2 Super Clean Servo Actuator

Phot.1 is the super clean servo actuator. This actuator is an outer rotor type, and it is possible to position the object attached to the rotor directly. Fig.7 shows the section view of the super clean servo actuator. Fig.8 shows MS-type stepping motor unit of this actuator. Four MS-type stepping motor units that are set at regular intervals carry out both the posture control and the position control. Also four electro magnets are set at regular intervals placed face down. They don't have teeth. The gap sensors to detect the motion of the rotor are eddy current-type.

The proportional-differential-feedback control circuit(P.D.control circuit) of Fig.9 is a circuit commonly used for magnetic suspension of conventional magnetic bearings. The magnetic suspension control is done using this P.D. control circuit at each degree of freedom according to the outputs of gap sensors. Four MS-type stepping motor units make up a radial magnetic bearing by their controlled attractive forces. Four electro magnets make up a thrust magnetic bearing.

Fig.10 shows the diagram of the position control circuit. The value of position and velocity of the rotor is given from the resolver to digital-convertor(R.D.C). The position control circuit consists of the position-feed-back-loop and the velocity-feed-back-loop. The integrators are not included in this position control circuit.

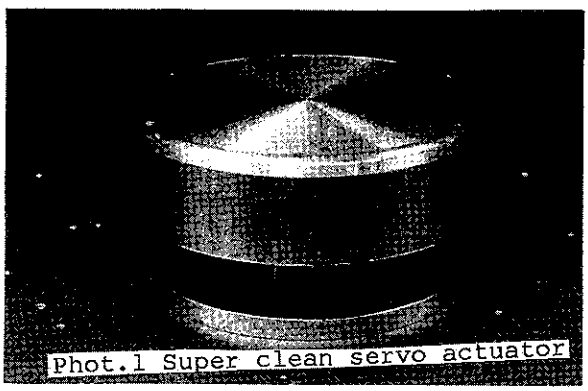

Phot.1 Super clean servo actuator

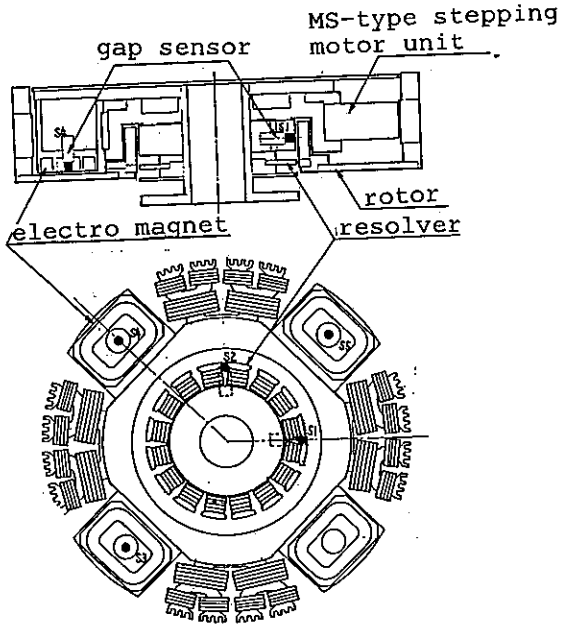

Fig.7 Structure of the super clean servo actuator

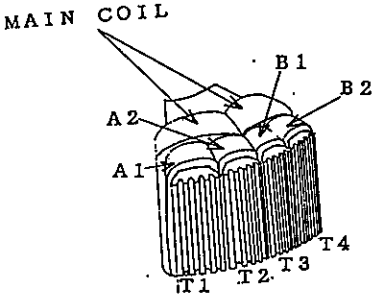

Fig.8 MS-type stepping motor unit of the super clean servo actuator

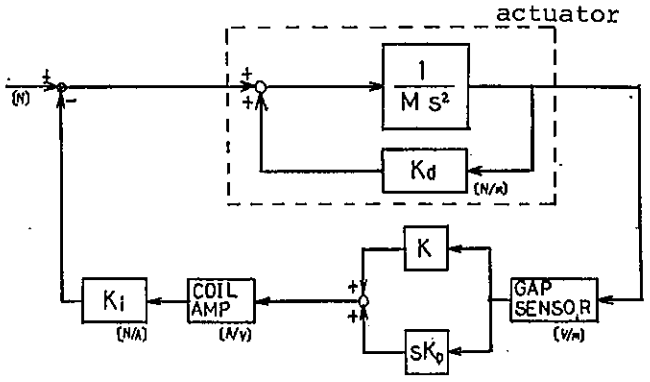

K ; proportional gain
KD; differential gain
Kd, Ki; coefficient of the magnet

Fig.9 Diagram of the P.D. controller

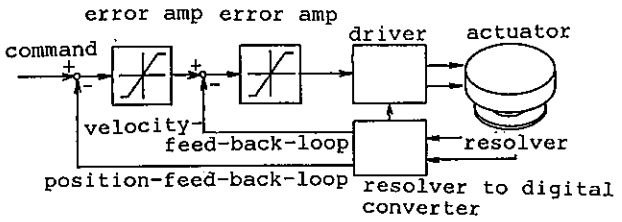

Fig.10 Diagram of the position controller

3.4 Performance of Super Clean Servo Actuator

Fig.11 shows the measured value of the velocity and the position of the rotor during high speed positioning(a rotation of 90 degrees in a counter-clockwise direction and 90 degrees clockwise in one second). The velocity was measured using a tachometer, and the position was measured by detecting the gap between the metal block attached to the rotor and a capacitor-type gap sensor. Fig.12 is the illustration of the actuator and the instruments set for this experiment. In Fig.11, the horizontal axis is time and vertical axis is position and velocity of the rotor. In this experiment, the velocity data which we inputted into the cntrol circuit was 0.52 [r.p.s], and the acceleration data was 2.6 [r.p.s2]. From Fig.11, it can be seen that the rotor followed, precisely, the command which we inputted into the control circuit.

Fig.13 shows the measured rotor position in steps using the minimum step size. (one step is 8.44[arc-sec]). The rotor position is detected by measuring the gap length between the metal block attached to the rotor and the capacitor-type gap sensor. Horizon tal axis is time, vertical axis is the rotated angle

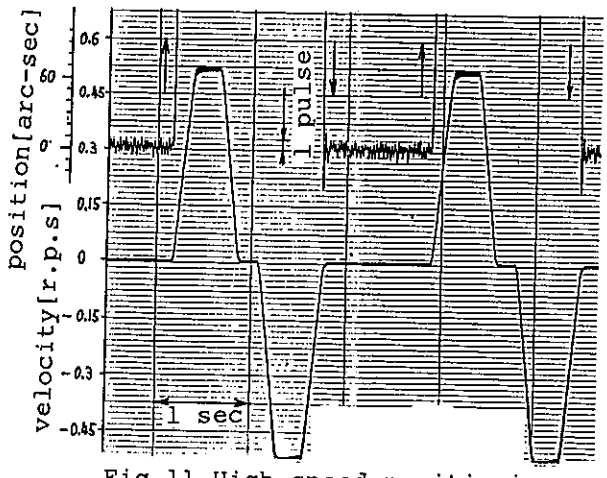

Fig.11 High speed positioning

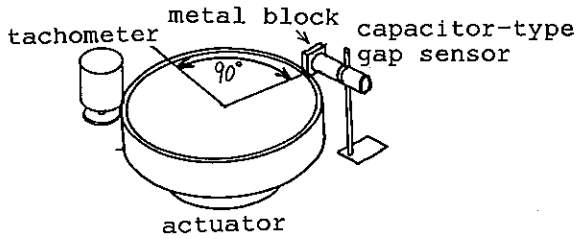

Fig.12 Experiment of high speed positioning

of rotor. However, even though the integrator was not included in the control circuit, the actuator stepped through the same value which was inputted the control circuit. The reason why steady-state error and lost motion are not found in Fig.13 seems to be that mechanical friction doesn't exist between the rotor and the stator.

Fig.14 is the measured velocity ripple of the actuator. This chart is the velocity ripple from the tachometer for the velocity commands 0.4, 0.9, 1.4, 1.9[r.p.s].

Table 1 shows the specification of the super clean servo actuator.

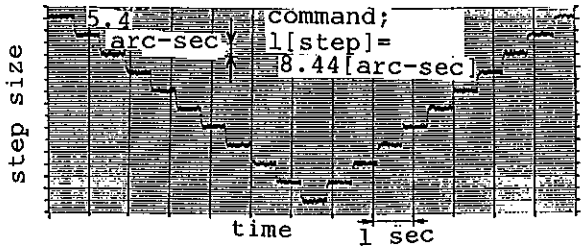

Fig.13 Minimum step size

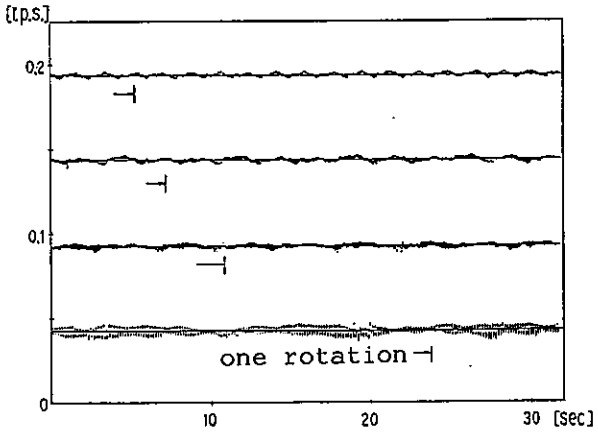

Fig.14 Velocity ripple

Levitation Control	Rotor Mass	8 kg
	Axial Stiffness	4 N/μm
	Gap Fluctuation	10 μm
Position Control	Max. Speed	3 r.p.s
	Max. Torque	1 kgf m
	repeatability	± 1.8 arc-sec

Table 1 Specification of the super clean actuator

4. Development of an Actuator for Ultra High Vacuà

It is possible to build a variety of contactless actuators by interconnecting MS-type motor units.

Because those actuators don't need any lubrication, it seems logical to adapt these actuators for vacuum environments in which it is impossible to use general lubrication. However, these actuators consist of materials which have high exhalation rates of gasses(for example coil wire and resin). So, it is difficult to use these actuators in vacuum chambers. It is nessecary to take measures to cope with this situation. Thus we have decided to seal the stator of the actuator with a sheet of non-magnetic metal. By this countermeasure, materials which exhale a lot of gas are isolated from the vacuum environment.

But there is a problem to solve in this countermeasure too. The problem is that an eddy current-type gap sensor can't detect the position of rotor beyond the sheet metal because of the eddy currents produced in it.Thus we have decided to develop a gap sensor that can detect the position of the rotor beyond the sheet metal.

4.1 Gap Sensor

The gap sensor which have been developed is a sort of inductance-type gap sensor.

An inductance-type gap sensor finds the position of an object by detecting the change of the permeance between the object and the gap sensor. And it is possible to detect the position of the object without using a high frequency carrier as with the eddy current-type. So, an inductance-type gap sensor candetect the position of the rotor beyond the sheet metal by tuning the frequency of carrier so that the influence of eddy currents is small.

Fig.15 shows the basic idea of the gap sensor which has been developed. This gap sensor is composed of a sensor rotor and sensor stator. Fig.15 shows the outer rotor-type. In Fig.15, the shaded area is the rotor. In this figure, there are two rotors, but really, one rotor is linked to another.

The sensor stator consists of a pair of poles which are placed in line with the poles facing outwards. The pole is made from laminated silicon steel and a coil which is wound around the pole core. Two coils(C1,C2) are connected in series, and excited by V*sin wt and -V*sin wt(where w is frequency of the carrier). Then, the amplitude of a central point between C1 and C2 changes according to the position of the sensor rotor. When gap g1 is equal to gap g2, the voltage is zero [v]. Therfore we can detect the position of the sensor rotor by measuring the voltage of the central point between C1 and C2.

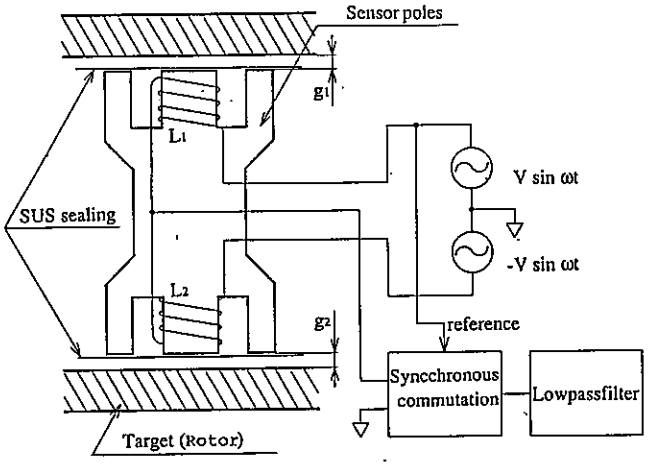

Fig.15 Basic idea of the developed gap sensor

Fig.16 shows the frequency response of developed gap sensor. From fig.16, it can be seen that the gap sensor was able to detect the vibration of 10kHz of rotor beyond the sheet metal, and this gap sensor has enough performance to be used for the magnetic levitation control.

This gap sensor has the following merits

1. It's possible to detect the position of an object beyond the sheet non-magnetic metal.
2. It's hard to be influenced by changes of dimension (caused by fluctuations in temperature), because of the way of detecting the position of an object from the difference between inductance L1 and inductance L2.
3. Because its structure is simple, this gap sensor can endure vibration or shock.

4.This gap sensor can operate over a wide range of temperatures.

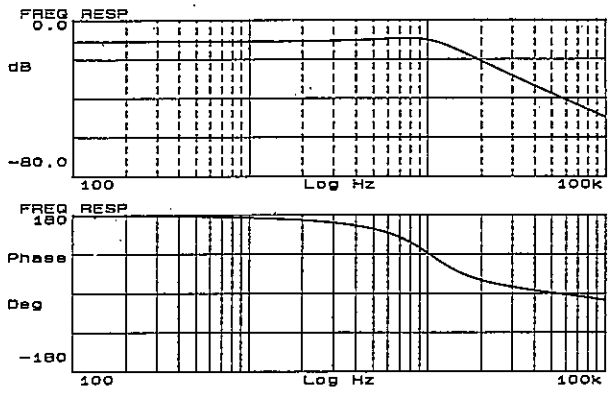

Fig.16 Frequency response of the developed gap sensor

4.2 Actuator for Ultra High Vacua

Phot.2 is the actuator for ultra high vacua which has been developed. The stator is sealed by the sheet stainless steel(which is non-magnetic). The sheet stainless steel is welded to the stator using the electron beam welding. And a metal seal flange which is made of stainless steel is attached to the stator. With this flange, the inside of the vacuum chamber is isolated from the atmosphere. On one side, the rotor is made of magnetic iron and alminium. The magnetic iron is plated with nickel. Therfore, there are not any materials which exhale gas.

This actuator has been built with a view to displacing a silicon wafer in a vacuum environment. For this, we have made this actuator to have the function of two axial positionings. One of them is rotational positioning, and the other is linear positioning.(up & down motion)

Fig.17 shows the section view of this actuator. The use of both a linear unit and a rotary unit enables this actuator to do both the rotational positioning and the linear positioning without mechanical contact at any one point. Fig.18 shows the linear unit and the rotary unit.

Fig.19 shows the structure of the gap sensor. This gap sensor can detect the position of the rotor in two axes at once. Two of these gap sensors are built into this actuator. Therefore, we can detect four degrees of freedum of the rotor.

A radial magnetic bearing is made from the controlled attractive forces of eight linear units. And at once, by the propulsive forces of these eight linear units, the linear positioning is done.

The position control of rotary and linear motion is the micro step driving, explained in chapter 2.3. Table 1 shows the specification of this actuator.

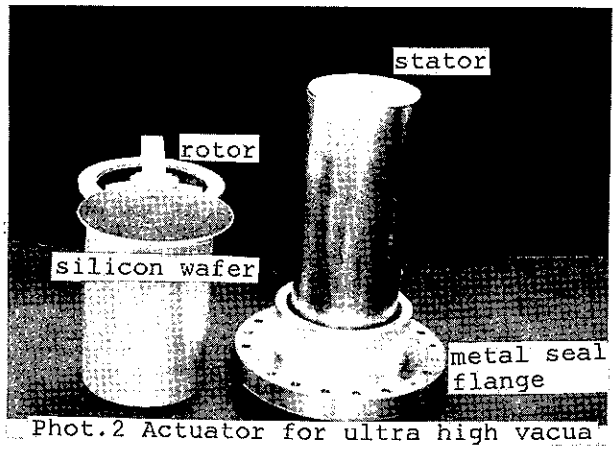

Phot.2 Actuator for ultra high vacua

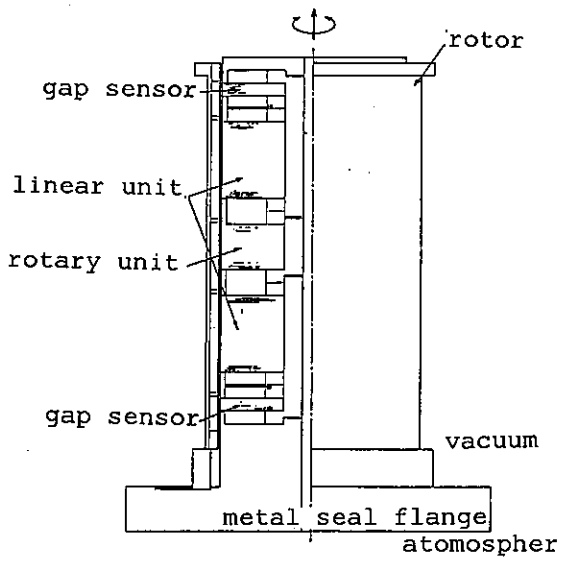

Fig.17 Section view of the actuator for ultra high vacua

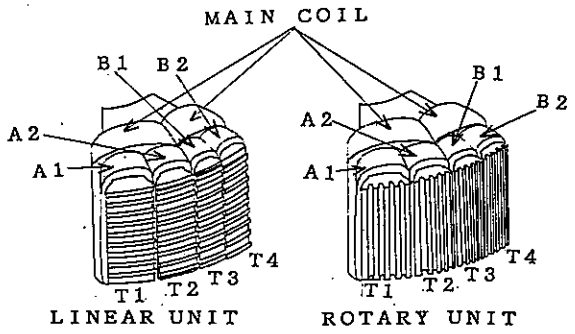

Fig.18 MS-type stepping motor units

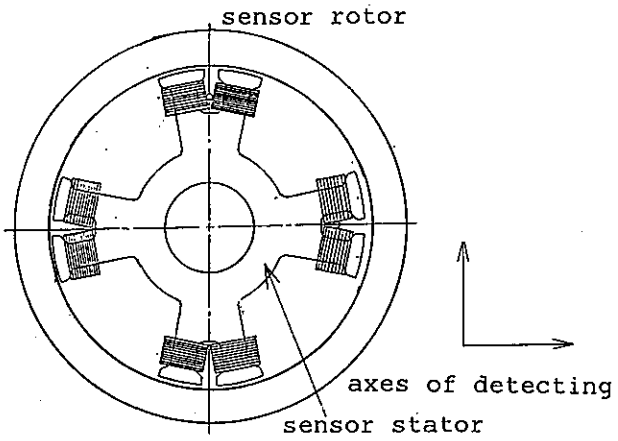

Fig.19 Structure of the gap sensor.

	Up & Down	Revolution
Repeatability	±5μ	±10sec
Max.Propulsive Force	4.5kgf	5kgf·cm
Positioning Resolution	2.9μm/pulse	10.5sec/pulse
Stroke (up & down)	10mm	
Radial Stiffness	2.0N/μm	
Rotor Weight	2.7kg	

Table 2 Specificasion of
Cylindrical Positioning Actuator for Ultra High Vacua

5.Conclusion

By using the MS-type stepping motor which we are currentry developing, we have built the super clean servo actuator and an actuator for ultra high vacua. Also, in order to build the super clean servo actuator, we have developed the position detector which can cancel the influence of fluctuation of the gap length between a rotor and a stator. And, in order to build an actuator for ultra high vacua, we have develpoed the gap sensor which can detect the motion of rotor beyond the sheet metal.

Reference

1. Higuchi, T.; Kawakatu, H.: Super-clean actuator for machines and robots.Proc of IECON'87 (1987) 303-310.

2nd International Symposium on Magnetic Beaing
July 12-14, 1990, Tokyo, Japan

ROBUST MAGNETIC BEARINGS FOR FLYWHEEL ENERGY STORAGE SYSTEMS

R.B. Zmood [(1)(2)], D. Pang [(2)]
D.K. Anand [(2)], J.A. Kirk [(2)]

(1) Department of Communication and Electrical Engineering, Royal Melbourne Institute of Technology, Melbourne, Victoria 3000, AUSTRALIA.

(2) Department of Mechanical Engineering, University of Maryland, College Park, MD 20742, USA.

Abstract

Magnetic bearings are an essential component of flywheel energy storage (FES) systems because of their very low frictional losses, and their extremely long expected operating lifetimes. In this paper recent work on the development of magnetic bearings for a 500 Wh FES system, which is to be used for low earth orbit space applications and is being constructed at the University of Maryland, is described. In this paper two aspects of magnetic bearings are discussed. The first is the design of bearing control systems which prevent large scale self–sustaining non linear oscillations from being established, while the second is the development of an improved inductive displacement transducer which differentiates between rotor growth and rotor displacement.

1. Introduction

The use of magnetic bearings for flywheel suspension in space–borne flywheel energy storage (FES) applications has been studied by Kirk and Studer [1,2] where they have shown that they are essential for such systems to operate efficiently, because of their very low frictional losses, and their extremely long expected lifetimes.

At the University of Maryland design studies of 300 and 500 Wh FES systems for spacecraft applications have shown it is important to maximize the flywheel specific energy density (SED), and a bench mark system design goal of 20 Wh/kg has been set as it exceeds, by an acceptable margin, the 14 Wh/kg of electrochemical systems [3,4,5]. Because of the required SED advanced fibre–composite flywheels are needed, and it has been shown that these need to operate at high rotational speeds, in the range 33 000 to 66 000 rpm, so as to make effective use of these materials. These operating speeds necessitate placing the flywheel in a vacuum to minimize aero–dynamic drag. Since magnetic bearings operate without physical contact and so require no lubricants, and also have no intrinsic speed limitations they appear to be ideally suited for this application. Experience has shown with the electromagnet/permanent–magnet (EM/PM) bearing designs discussed in this paper that the total power losses can be one or even two orders of magnitude smaller than comparable fluid film or rolling element bearings. Also their non–contact operation precludes tribo–physical degradation which limits the life expectancies of the other bearing types mentioned above.

In this paper recent work on the development of magnetic bearings for the 500 Wh FES system, which is to be used for low earth orbit satellite applications is described. Attention will be focussed upon the two aspects of bearing controller design and position transducer configuration, both of which have a significant impact upon the robustness of bearing operation.

2. Flywheel Design

The 500 Wh energy storage system is based upon a "pancake" magnetic bearing stack as shown in Fig. 1. In this arrangement two magnetic bearings are shown with one positioned at the top of the stack and the other at the bottom. Mounted between these two bearings is the motor/generator which is used for converting mechanical into electrical energy and vice versa. It is a three phase brushless D.C. machine having permanent magnets

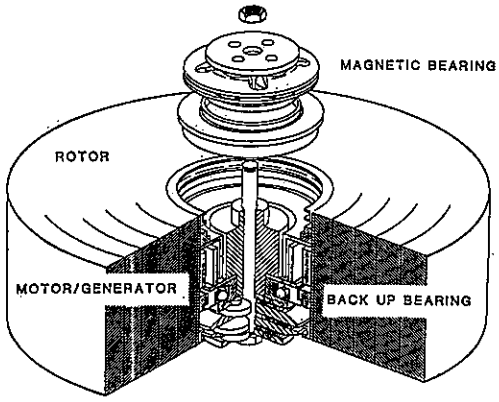

Fig.1. Magetic bearing stack for 500 Wh system.

mounted on the inner surface of the flywheel and a surface mounted winding on the laminated stator core. The design of the motor/generator is discussed in detail by Neimeyer [6] and Neimeyer et.al. [7]. To protect the magnetic bearing actuators and suspension rings as well as the motor/generator when magnetic suspension failure occurs back–up bearings are used. Under normal operating conditions the flywheel is suspended so that there is a uniform clearance of approximately 0.15 mm between the outer ring of the ball bearing and the inner surface of the flywheel. When there is loss of suspension or a large disturbance occurs and the flywheel deflects outside the above range then the flywheel is supported by the ball bearings thus preventing internal damage.

Not shown in the figure, but nevertheless an integral part of the system is the power conditioning electronics for the motor/generator, and the electronic control system for the magnetic bearings. Estimates of the mass of these components has been made and is included when calculating the total system SED.

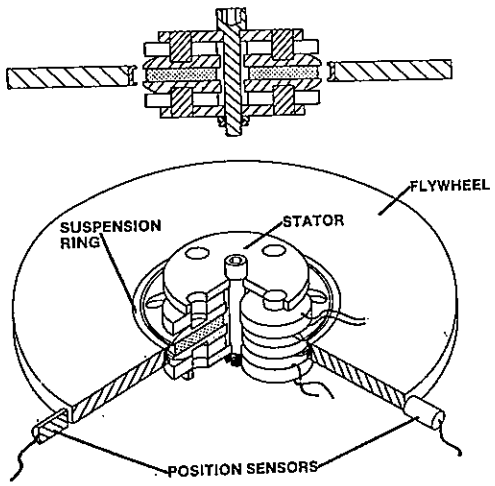

Fig.2. Sectioned view of pancake bearing.

3. Magnetic Bearings

The pancake magnetic bearing used in the 500 Wh energy storage system are EM/PM bearings and a sectioned view of one is shown in Figure 2. In these bearings permanent magnets are used to establish a uniformly distributed bias flux around the airgap between the stator and the suspension ring. In addition electromagnets having controlled currents are used to regulate the magnetic flux in designated quadrants of the pole–faces so as to generate net forces on the flywheel which can be used to control its motion.

These bearings were designed to support a $2g$ axial load without loss of suspension. Based upon experience with earlier designs for the 300 Wh flywheel the static stiffness K_x and current sensitivity K_i for the 500 Wh flywheel bearings were selected to be 981 N/mm (5600 lb/inch) and 249 N/amp (56 lb/amp) respectively. From these values and the estimated flywheel mass the mechanical and electrical design of the actuators was carried out using a suite of computer design programs written at the University of Maryland. In all cases the flux density in the magnetic components was limited to 1.5T.

The design methodology followed involved the iterative computation of the magnetic flux densities in various components for a set of trial physical dimensions. The coil design, which was also performed iteratively, was determined from K_i, and the maximum amplifier output current and voltage. A deficiency of this approach becomes evident when it is realized that the current sensitivity K_i together with the magnetic design determines the required magneto–motive force of the coils. This can be achieved by many combinations of number of coil turns and magnitude of coil current; however it is not clear from static analysis what the optimum choice is for the number of coil turns and the concomitant coil current.

It should be noted though that the coil inductance also increases rapidly with increased number of coil turns, which means that the applied coil voltage must increase significantly if the coil current is to be able to change rapidly under dynamic conditions. Because of uncontrollable oscillation and other difficulties experienced when commissioning the magnetic bearings for the 500 Wh flywheel an investigation of the effects of coil inductance on their operation has been undertaken. The results of this work are discussed below.

The flywheel excursion range was limited to ± 0.15 mm by the touchdown bearings. Theoretical analysis, confirmed by subsequent measurement, showed that the values of K_x and K_i vary as the flywheel traverses from one extreme of the excursion range to the other. It will be seen that these variations in the above parameters as a function of flywheel position can under injudicious circumstances have a profound effect upon the bearing control system robustness.

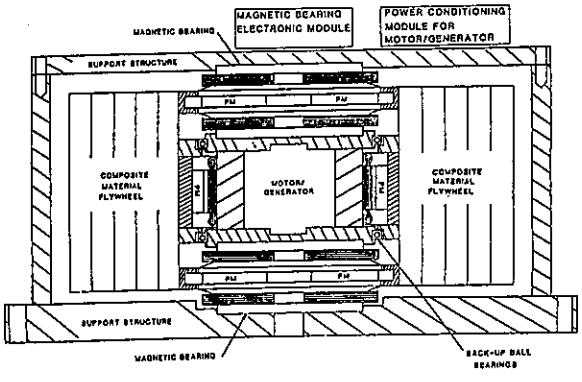

Fig.3. Cross–sectional view of 500 Wh flywheel energy storage system.

4. Robust Magnetic Bearing Control System Design

In the design of the magnetic bearing control systems for the University of Maryland flywheel energy storage system difficulties have arisen from two independant sources. The origin of the first difficulty which appeared quite early in the development phase arose from vibrations of the structure supporting the pancake bearings. Analysis [8] has shown that structural vibrations within the bandwidth of the bearing control systems can seriously affect their operation with the potential risk of instability. These vibrational effects were overcome by progressively improving the mechanical design of the central bearing stack shown in Fig. 1, and by increasing the stiffness of the flywheel support structure, illustrated for the 500 Wh system in Fig. 3. Extensive modal analysis of the final design by Lashley [9] showed that the structural modal frequencies were all well outside the bearing control system bandwidth.

Nevertheless during the commissioning of the bearing control systems for the 500 Wh flywheel great difficulty was experienced in initially suspending the rotor, and any slight disturbance was found to cause the system to break into violent oscillations. In addition, in spite of careful adjustment of the controller time constants and gains it was impossible to make the system self–suspend when the power was first connected. The results of careful investigation has shown that unless the bearing actuator parameters are carefully chosen at the design stage then the control system is likely to break into limit cycle oscillations which cannot be easily controlled by control system parameter adjustment.

The origin of these oscillations has been discussed by Zmood et. al. [10, 11]. They have been found to be due to the combined effect of the power amplifier saturation voltage, the bearing actuator parameter K_x, and the physical constraint of the flywheel displacement. A good understanding of these oscillations can be obtained from studying the operation of the simplified block diagram given in Fig. 4.

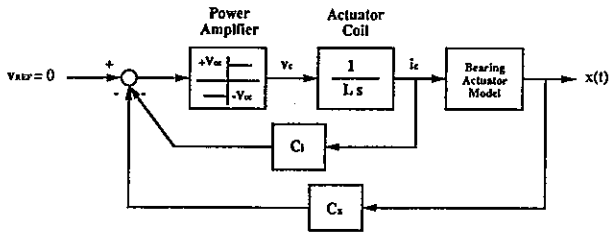

Fig.4. Simplified bearing control system block diagram.

To understand the mechanism of these oscillations imagine for the moment the flywheel mass is zero. In this case the flywheel will move from one physical limit to the other instantaneously, once the threshold current $i_{crit} = \pm K_x x_m / K_i$ is reached. Here K_x and K_i are the magnetic bearing static stiffness and current sensitivity repectively, while x_m is the maximum rotor excursion. Since the coil inductance limits the rate of change of the coil current, the flywheel will oscillate between the physical limits, $\pm x_m$, at a frequency determined by the amplifier supply voltage, the coil inductance, and the current i_{crit}. When the mass is zero the system will oscillate irrespective of the values of the control system parameters C_x and C_i, or the coil inductance L.

In practice, the flywheel mass cannot be neglected. In this case it is shown by Zmood [11] that the control system given in Fig. 4 can be stabilized provided the parameters C_i and C_x are selected correctly. The conditions that need to be satisfied are

$$(1) \qquad \frac{K_x}{K_i} < \frac{C_x}{C_i} < \frac{K_x}{K_i}\left[\frac{1}{2} + \sqrt{\frac{1}{4} + \frac{K_i \alpha'}{K_x x_m}}\right],$$

where the current $\alpha' = V_{cc}/\omega_m' L$, $\omega_m' \approx \sqrt{K_x/M}$, V_{cc} is the amplifier supply voltage, and M is the flywheel mass. Even though the system shown in the above figure is a simplification of the physical bearing control system, the results of experiment and of detailed simulation compare very favourably with the limits given by the above inequalities.

The inequalities given in Eq. (1) are plotted in Fig. 5 using the parameters for the experimentally tested bearing. It will be noted from this figure that the bearing can, in principle, be stabilized by an appropriate choice of the gain parameters C_x and C_i for all coil inductance values. In particular it will be observed that the current gain parameter C_i must be non–zero for stability to be possible. The most important observation to be made from this diagram, however, is that as the coil inductance increases the range of the ratio C_x/C_i for which the system is stable gets narower and narrower. Thus for large values of inductance the values of C_x and C_i need to be selected very carefully.

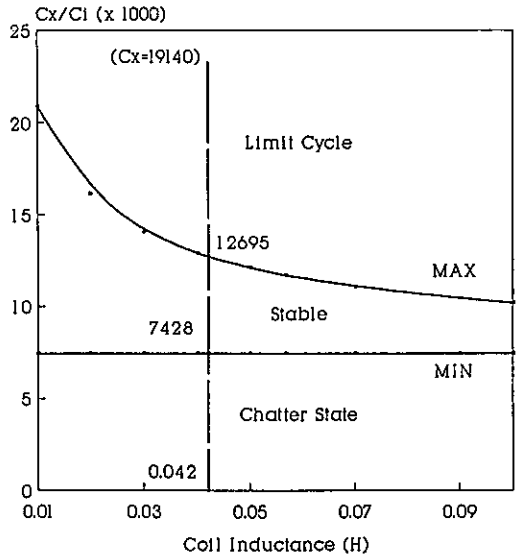

Fig.5. Stability diagram showing variations of C_x/C_i as a function of coil inductance.

Conversely, suppose C_x/C_i is chosen to stabilize the bearing control system for some nominal values of the parameters K_x and K_i. It will be observed from the diagram that if the coil inductance is large then we can only tolerate very small variations of K_x and K_i about their nominal values if stability is to be maintained. Unfortunately, as we have observed above, the uncertainty in the values of these parameters is quite large and varies as a function of the flywheel displacement, so if the coil inductance is too large then it may be impossible to stabilize the rotor. For the bearings tested in the laboratory this was indeed initially the case as self–suspension was impossible, and even when the flywheel rotor was suspended and stabilized by using locking screws it was found that small transient disturbances caused oscillations to develop. When the coil inductance was decreased by a factor of 1:4 by re–winding the coils a marked improvement in bearing robustness was observed, and in particular it was found that it could easily self–suspend when power was applied.

5. Position Transducers and Sensor Positioning

An essential component, of magnetic bearings for use in flywheel energy storage systems, is the non–contacting position transducer which is used to measure the translational displacements of the rotating flywheel relative to the magnetic bearing stators. These transducers convert physical displacements into electrical signals which are fed to the bearing control system. While many techniques are available for non–contact sensing of displacement, to date, no completely satisfactory method has been found which satisfies all requirements. Plant [12,13] has closely examined a number of competing transducers, utilizing inductive, capacitive, and optical techniques. He has also experimentally investigated the performance of a number of commercially available transducers, but has found them all wanting in some respect. It is for this reason that effort has been devoted to developing suitable position transducers for flywheel applications at the University of Maryland, which meet fairly stringent requirements of: reliability, simplicity of concept, robustness, and ease of application.

Of the many techniques considered we have concentrated our attention on those using inductive, capacitive, and optical methods, and in the following we will consider them under the headings:

* Sensitivity
* External disturbing effects
* Packaging

Sensitivity

Both the inner and outer bores of the flywheel grow significantly as it spins from zero to a maximum speed of 66 000 rpm. In the case of the inner bore the radial growth has been estimated to be 0.5055 mm at a speed of 52 000 rpm. On the other hand the rotor translational motion is limited by the touchdown bearings to ±0.15mm about its nominal centre position, which it is observed is significantly less than the radial growth. Consequently any rotor position measuring system which senses the position, of either the flywheel outer rim or its inner bore, must be able to differentiate between displacements due to these two sources.

Currently available commercial transducers, whether of the inductive, capacitive, or optical type, having a single sensor head are incapable of achieving this differentiation, as they sense only at one radial position on, say, the flywheel inner bore. In this case the airgap will be held constant in the region of the sensor and all radial growth will be accommodated by airgap growth in the region diametrically opposite. The nett results of this type of control is that the flywheel geometric axis of symmetry will be displaced away from the bearing stator magnetic centre, so that considerable current will need to be supplied to the control windings to balance the destabilizing forces of the permanent magnets. This situation is highly undesirable as the power consumed by the suspension system will increase considerably.

To overcome this difficulty differential transducers need to be used. In the case of inductive devices this can be achieved by using two inductive elements positioned to sense on diametrically opposite sides of the flywheel inner bore. If these inductors are connected in an electrical bridge circuit the bridge balance will be unaffected by radial growth, and will only sense changes in inductance due to translational motion. A similar situation will occur with differentially connected capacitive and optical sensors. In practice a radial growth to translation rejection ratio of 1:1000 may be achieved with inductive transducers, but the same cannot be said for either capacitive or optical devices. Under worst case conditions for inductive transducers a radial growth of 0.51 mm will only appear as an equivalent 0.00051 mm translational motion, which is less than 0.3 percent of the full scale translational displacement.

Experience has shown that sensitivities in the range 2 to 40 V/mm are achievable with acceptable output signal–to–noise ratios for all of the above transducer types, but the sensitivities are usually limited in applications to the range 2 to 4 V/mm. Commercially available inductive and capacitive transducers appear to operate with carrier frequencies of 1 to 2 MHz, and with low pass output filters having bandwidths of about 10 kHz. The optical transducers which operate on either reflective or interruptive principles are generally of the baseband type and their operating bandwidth is essentially determined by response characteristic of the photo–detector, which can be as high as 100 kHz. Again, in practice this is likely to be limited to approximately 10 kHz to limit the output signal–to–noise ratio.

External Disturbing Effects

Since inductive transducers rely upon magnetic effects they are particularly prone to interference from external magnetic fields generated by the magnetic bearings actuators. Plant [12] has investigated a number of commercially available inductive transducers and has found them to all be sensitive to the presence of external magnetic fields even when sensing displacements relative to aluminium targets. This being in spite of advice to the

contrary from the manufacturers. Subsequent experimental investigation of one commercial transducer has shown the probable cause to be due to the transducer sensor casing. This casing is manufactured from a stainless steel which is mildly, but sufficiently, ferromagnetic so that the transducer calibration is affected by changes in the saturation level of the steel when it is immersed in an external magnetic field. It seems likely that the manufacturer could correct this problem by using a truly non–ferromagnetic material, such a brass. Radio frequency interference can also affect these transducers, but because of the low impedance levels at which they operate this problem can be easily overcome.

Capacitive transducers are totally insensitive to magnetic fields, so they would seem to offer good prospects in this application. However their very high impedance levels, the effect of stray capacitances, and the very small changes in capacitance which needs to be sensed make it quite difficult to achieve satisfactory operation. In addition the high operating impedance levels can lead to serious problems from power frequency and radio frequency interference. Methods of overcoming these problems need to use active guarding and specially shielded cables. Commercial transducers are available but the bulkiness of the sensors together with the high cost has discouraged their use in magnetic bearings.

Two types of optical transducers have been considered. In the reflective type the target must have constant reflectivity, and be preferably a plane surface held at a constant angle to the transmit/send head. For the flywheel the reflective surface is obviously curved and it is extremely difficult to retain constant reflectivity around either its inner or outer perimeter. Experience has shown this method to be highly unreliable in this application. The interruptive optical transducer has been shown to work extremely well with good linearity and sensitivity using commercial light emitting diodes and phototransistors. However strong doubts exist about the stability of the photo transistor sensitivity which is known to drift with time for many devices.

Packaging

Both capacitive and inductive transducers require a metallic target, and if they are to sense displacement on the flywheel outer rim then it must have a metallic surface attached by some means. The limited strength of metals combined with the very high surface speed of the flywheel makes this a difficult task. Interruptive optical transducers on the other hand can operate on the flywheel outer rim because they do not require a metallic target.

While the difficulty of attaching a metal surface to the outer rim may possibly be overcome, mounting the position transducers so as to sense displacement on the outer rim of the flywheel is not recommended for other reasons. Firstly, there are problems in maintaining concentricity between the flywheel outer rim and its inner bore, both during manufacture and especially when it is running at high speed. The latter situation arises due to the effects of large rotor growth with increase in rotor speed, and the inhomogeneity of the composite structure causing an eccentricity to develop between the flywheel outer rim and the inner bore which changes as a function of speed. Secondly the transducer sensors need to be rigidly and accurately fixed to the flywheel outer support structure which in turn must be accurately positioned with respect to the bearing stator; a complicated manufacturing problem. Thus for both manufacturing and operational reasons it is sensible to mount the position sensors internally so as to measure the displacement of the flywheel inner bore relative to the magnetic bearing stators.

Apart from the desirability of mounting the transducer sensors internally it is desirable that they sense along the plane of symmetry of the pancake magnetic bearing actuators, and yet at the same time they must not interfere with the assembly of the flywheel during construction. Neither the inductive nor capacitive types of position sensors need interfere with the flywheel assembly, but the interruptive optical type will, by the nature of its construction and operation, do so. The best mounting position for the inductive and capacitive sensors would be between the two pole faces of each actuator, Fig. 6(a), so that they sense the distance to the suspension rings. However because of restricted space and the presence of strong magnetic fields it is not practical to mount them in this location. Alternative locations which overcome the collocation problem will be discussed below.

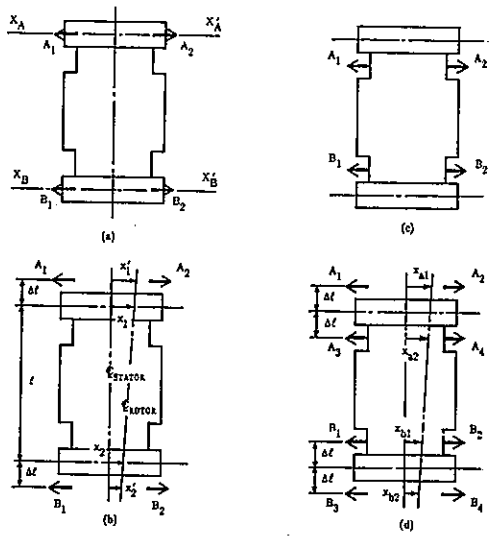

Fig.6. Alternative positions for displacement sensors. Sensor positions indicated by arrowed blocks.

Sensor Positions

The remainder of this discussion will centre on the application of inductive sensors and how they may be used in electrical bridge networks to solve the collocation problem by ensuring the effective displacement sensing planes are along the bearing actuator planes of symmetry, and also to cancel the effects of rotor growth.

Four possible arrangements for the inductive sense coils of the transducers are shown in Fig. 6. The most

ideal arrangement is shown in Fig. 6(a) where the coils are mounted between the pole faces, as this enables direct displacement measurement in the bearing planes $X_A X'_A$ and $X_B X'_B$. For practical reasons this arrangement is difficult to implement and so will not be considered further.

The remaining possible arrangements can measure the displacments in the bearing planes of symmetry provided it is assumed that the bearing actuators and the motor/generator are rigid bodies. For example, let us consider the alternatives shown in Figs. 6(b) and (c) where the inductive sense coils are shown by the arrowed bars in each case. From simple geometry the displacements x_1 and x_2 can be calculated from measurements x_1' and x_2' and for the case shown in Fig. 6(b) are given by

$$x_1 = x_1' \left[\frac{\ell + \Delta\ell}{\ell + 2\Delta\ell}\right] + x_2' \left[\frac{\Delta\ell}{\ell + 2\Delta\ell}\right], \tag{2}$$

and

$$x_2 = x_1' \left[\frac{\Delta\ell}{\ell + \Delta\ell}\right] + x_2' \left[\frac{\ell + \Delta\ell}{\ell + 2\Delta\ell}\right]. \tag{3}$$

When the sensors are inboard of the bearings the errors in the computation of x_1 and x_2 due to uncertainties in $\Delta\ell$ will be larger than for the corresponding outboard case. However as long as $\Delta\ell/\ell$ is small the error in either case can be neglected and the computed values of x_1 and x_2 can be used in place of their exact values in the respective bearing controllers.

If the motor cannot be considered to be rigid then the arrangement shown in Fig. 6(d) needs to be used. Here the sense coils A_1, A_2, coils A_3, A_4, coils B_1, B_2 and coils B_3, B_4 are separately connected in series. Since these coils are symmetrically displaced about the bearing planes of symmetry the transducer outputs will be x_1 and x_2, where

$$x_1 = \frac{x_{a_1} + x_{a_2}}{2}, \tag{4}$$

and

$$x_2 = \frac{x_{b_1} + x_{b_2}}{2}. \tag{5}$$

The Inductive Sensor

In Fig. 7 is shown a simplified schematic of the experimental inductive bridge transducer, which can be used in any of the mechanical arrangements shown in Fig. 6. The sensor inductors are connected in a Maxwell impedance bridge whose ouput is fed to a synchronous demodulator. The output of the demodulator passes through a low pass filter which filters the residual high frequency modulation products as well as any extraneous noise induced into the circuitry. The filter output is an analog signal whose magnitude is proportional to the displacment x. To ensure good balance of the bridge circuit special care needs to be taken to retain symmetry in all parts of the circuit; especially in the wiring of the inductors.

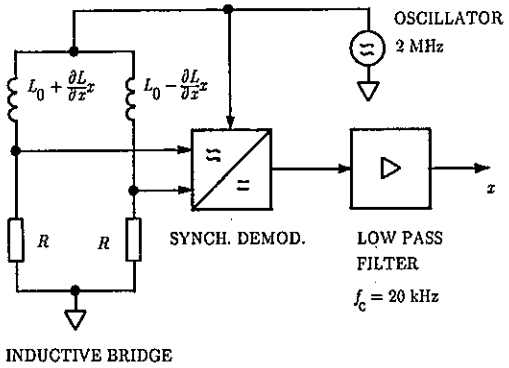

Fig.7. Simplified schematic of inductive bridge transducers.

Heeding the observations made above about the use of stainless steel in the bodies of commercial inductive transducers, care was taken to only use non–ferrous materials, such as aluminium, in the construction of the experimental sensors. Aluminium was also used for the transducer target. Experiments showed that using this construction made the transducers insensitive to changes in external magnetic fields.

6. Concluding Remarks

Two aspects of magnetic bearings for flywheel energy systems which contribute to their robust operation have been considered.

Firstly it has been shown that bearing control systems experience limit cycle oscillations if the actuator coil inductances are too large. The analysis above shows that for the control system to be stable the control gain ratio C_x/C_i must lie within upper and lower bounds which are determined from the characteristics of the bearing actuator. These bounds are particularly sensitive to actuator coil inductance. These considerations profoundly influence the design methodology of the actuators. In the new approach the coil ampere–turns for the actuator are determined as before from static force considerations. Now however the coil inductance is determined from Eq. (1) so as to ensure adequate control system robustness, and from this the number of turns for the control winding can be calculated. From the above information the peak actuator drive current is calculated and the sizing of the control winding amplifiers determined. This approach should be contrasted with the one previously followed, where the winding specifications and the amplifier sizes were largely determined from static considerations. Using the above approach we have found that bearings operates quite robustly, can withstand large transient disturbances, and are easily able to self–suspend.

Secondly it has been shown that the use of differential position transducers enables the rotor displacement to be differentiated from rotor radial growth. As a consequence the bearing control system operation will

be markedly less sensitive to disturbances due to rotor growth than when single–sensor displacement transducers are used. Although inductive transducers can be sensitive to external magnetic field, in most other regards they are much less sensitive to extraneous effects than capacitive and optical transducers. Experience has shown that if care is taken to avoid using ferro–magnetic materials (including stainless steel) in their construction then magnetic effects can be minimized. These types of transducers are currently being included in the design of the 500 Wh flywheel energy storage system.

References

1. Kirk, J.A., "Flywheel Energy Storage – Part I, Basic Concepts", Int. J. Mech. Sci., Vol. 19 (1977), pp. 223–231.

2. Kirk, J.A., and Studer, P.A., "Flywheel Energy Storage – Part II Magnetically Suspended Super–Flywheel", Int. J. Mech. Sci., Vol. 19 (1977), pp. 233–245.

3. Anand, D.K., Kirk, J.A., Frommer, D.A., "Design Considerations for a Magnetically Suspended Flywheel Systems", Proc. 20th Intersoc. Energy Conv. Engrg. Conf., Miami Beach, Florida, Aug. 18–23, 1985, pp. 2.449–2.453.

4. Anand, D.K., Kirk, J.A., Zmood, R.B., et.al., "System Considerations for a Magnetically Suspended Flywheel", Proc. 21st Intersoc. Energy Conv. Engrg. Conf., San Diego, Calif., Aug 25–29, 1986, pp. 1829–1833.

5. Kirk, J.A., Anand, D.K., "Satellite Power Using a Magnetically Suspended Flywheel Stack", J. Power Sources, Vol. 22 (1988), pp. 301–311.

6. Neimeyer, W.L., Design of a High Efficiency Motor for Flywheel Energy Storage, M.S. Thesis, University of Maryland, College Park, Maryland, 1988.

7. Neimeyer, W.L., Zmood, R.B., et.al., "A High Efficiency Motor/Generator for a Magnetically Suspended Flywheel Energy Storage System", Proc. 24th Intersoc. Energy Conv. Engrg. Conf., Washington, D.C., Aug. 6–11, 1989.

8. Zmood, R.B., et. al., "The Effect of Structural Vibrations on Magnetic Bearing Operation", Proc. 24th Intersoc. Energy Conv. Engrg. Conf., Washington, D.C., Aug. 6–11, 1989.

9. Lashley, C.M., et.al., "Dynamic Considerations for a Magnetically Suspended Flywheel", Proc. 24th Intersoc. Energy Conv. Engrg. Conf., Washington, D.C., Aug. 6–11, 1989.

10. Zmood, R.B., et.al., "The Behaviour of Magnetic Bearings Subjected to Large Disturbances". Submitted for publication.

11. Zmood, R.B., et.al., "Non Linear Relaxation Oscillations in Magnetic Bearings". Under preparation.

12. Plant, D.P., "Prototype of a Flywheel Energy Storage System", M.S. Thesis, University of Maryland, College Park, Maryland, 1988.

13. Plant, D.P., Kirk, J.A. and Anand, D.K., "Prototype of a Magnetically Suspended Flywheel Energy Storage System", Proc. 24th Intersoc. Energy Conversion Engrg. Conf., Washington, D.C., August 6–11, 1989.

2nd International Symposium on Magnetic Beaing
July 12-14, 1990, Tokyo, Japan

Design and Testing of a Flexible Rotor-Magnetic Bearing System

M.HISATANI*, S.INAMI*, T.OHTSUKA*, and M.FUJITA*

*Tamano Laboratory, Mitsui Engineering and Shipbuilding,
3-16-1, Tamahara, Tamano, 706 JAPAN

Abstract

A mechanical model analysis of a flexible rotor is combined with an electrical characteristic modelling of control components of a magnetic bearing system. Eigenvalues and system stability are examined for several control strategies. "Quasi-Colocation Pseudo-Inverse" and "Selective Eigenvalue Move" techniques are presented as practical and effective control design methods. Testing result of the flexible rotor in the form of a transfer function is compared with the calculated value, and the effectiveness of these techniques has been ascertained.

1. Introduction

At the design of a control system of active magnetic bearing supporting a rotating body, degrees of freedom of motion around the center of gravity should only be considered when the object rotor can be treated as a rigid body. The design is rather easy if there are no problems of big unbalance excitation or gyroscopic effect.

On the other hand, if the suspended rotor is flexible and the design speed exceeds the eigen-frequencies of bending modes, the rotor should be treated as a multi-mass body connected by flexible shafts with finite spring constants. The design problem becomes complicated as the number of degrees of freedom increases largely. In addition to such a mechanical modelling for modal analysis or eigenvalue analysis, frequency characteristic of the electrical system of the control circuit should also be taken into account as an element which greatly affects the overall eigenvalues.

The control of flexible rotors has been investigated by many researchers [1-5]. If such techniques as optimal regulator or pole assignment using state feedback can be used, system eigenvalues are arbitrarily designated, bringing as desirable system characteristic as possible. Practically, however, the number of sensors to detect the motion of the rotor is limited, so only a part of the whole states are observed, inhibiting state feed-back. As for the constitution of observer to estimate unknown states, it is very difficult to realize in the actual control circuits as its dimension becomes intolerably large. Therefore, it is necessary to approach the preferable characteristic using output feed-back maintaining stable eigenvalues. Many research works have been performed along this approach. As concrete design methods are proposed Quasi-Modal Control [1] and Pseudo-Inverse [2].

In this paper the total control system is expressed for a practical flexible rotor combining mechanical modelling of lumped mass and beam chain system with electrical modelling considering frequency characteristics. Control system design by output feedback is investigated for several methods, and "Quasi-Colocation Pseudo-Inverse" is presented as an original design method. Also presented is "Selective Eigenvalue Move" method which modifies the fine arrangement of system eigenvalues. Finally the effectiveness of these methods are verified experimentally.

2. Mechanical System Modelling

The rotor is modelled as composed of a few disks with masses and moments of inertia and of connecting shafts without mass. Fig.1 shows k-th shaft section with a variation of section profile bound by two disks of k-th and (k+1)-th. Let shearing force at shaft end be F, bending moment M, inclination θ, and deflection x, then

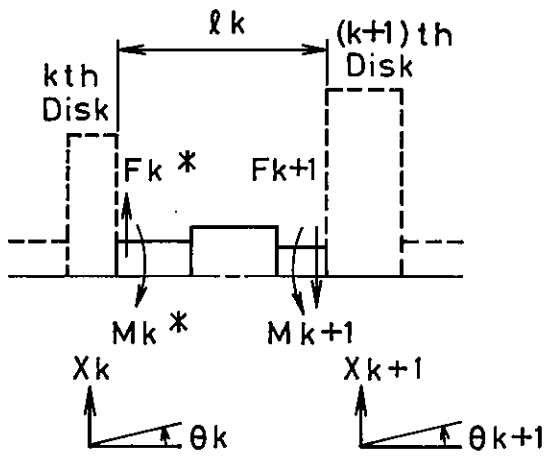

Figure 1 Shaft model

$$\begin{Bmatrix} F_{k+1} \\ M_{k+1} \\ \theta_{k+1} \\ x_{k+1} \end{Bmatrix} = \begin{bmatrix} 1 & 0 & 0 & 0 \\ l_k & 1 & 0 & 0 \\ a_k & b_k & 1 & 0 \\ c_k & d_k & l_k & 1 \end{bmatrix} \begin{Bmatrix} F_k^* \\ M_k^* \\ \theta_k \\ x_k \end{Bmatrix} \quad (1)$$

$$a_k = (l_k^2/2E_kI_k)_a$$
$$b_k = (l_k / E_kI_k)_b$$
$$c_k = (l_k^3/6E_kI_k)_c$$
$$d_k = (l_k^2/2E_kI_k)_d$$

where l_k indicates axial length, E_k modulus of elasticity, and I_k moment of inertia of section. The expression of coefficients $a_k \sim d_k$ with parentheses () indicates that the variation of shaft diameter is considered (see Appendix A), in order to reduce the number of overall degrees of freedom.

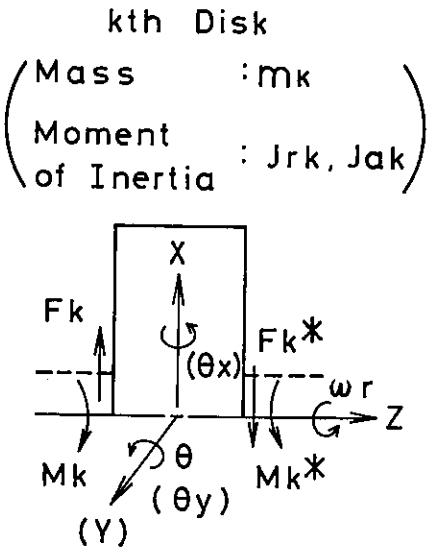

Figure 2 Disk model

From the relation of (1), F and M can be expressed by θ and x as follows;

$$\begin{Bmatrix} F_k^* \\ F_{k+1} \\ M_k^* \\ M_{k+1} \end{Bmatrix} = 1/\Delta_k \begin{bmatrix} b_kl_k-d_k & d_k & b_k & -b_k \\ b_kl_k-d_k & d_k & b_k & -b_k \\ c_k-l_ka_k & -c_k & -a_k & a_k \\ \begin{pmatrix} c_k-l_ka_k \\ +l_k^2b_k \\ -l_kd_k \end{pmatrix} & \begin{pmatrix} l_kd_k \\ -c_k \end{pmatrix} & \begin{pmatrix} l_kb_k \\ -a_k \end{pmatrix} & \begin{pmatrix} a_k \\ -l_kb_k \end{pmatrix} \end{bmatrix} \begin{Bmatrix} \theta_k \\ \theta_{k+1} \\ x_k \\ x_{k+1} \end{Bmatrix} \quad (2)$$

$$\Delta_k = a_kd_k - c_kb_k$$

Referring to Fig.2, the equation of motion of k-th disk without internal damping of the rotor is ;

$$m_k \ddot{x}_k = F_k - F_k^* + u_k \quad (3)$$
$$J_{rk}\ddot{\theta}_k = M_k^* - M_k \quad (4)$$

where u_k is the bearing reaction force, and J_{rk} is around the radius direction.

Relation (2) is substituted into (3) and (4), with a resulting expression ;

$$\begin{Bmatrix} m_k \ddot{x}_k \\ J_{rk}\ddot{\theta}_k \end{Bmatrix} + \{K_{ij}\} \begin{Bmatrix} x_{k-1} \\ \theta_{k-1} \\ x_k \\ \theta_k \\ x_{k+1} \\ \theta_{k+1} \end{Bmatrix} = \begin{Bmatrix} u_k \\ 0 \end{Bmatrix} (i=1,2)\ (j=1,6) \quad (5)$$

where

$$K_{k11} = -b_{k-1}/\Delta_{k-1}$$
$$K_{k12} = (-l_{k-1}b_{k-1}+d_{k-1})/\Delta_{k-1}$$
$$K_{k13} = b_{k-1}/\Delta_{k-1}+b_k/\Delta_k$$
$$K_{k14} = -d_{k-1}/\Delta_{k-1}+(l_kb_k-d_k)/\Delta_k$$
$$K_{k15} = -b_k/\Delta_k$$
$$K_{k16} = d_k/\Delta_k$$
$$K_{k21} = (l_{k-1}b_{k-1}-a_{k-1})/\Delta_{k-1}$$
$$K_{k22} = \{l_{k-1}(b_{k-1}l_{k-1}-d_{k-1}-a_{k-1})+c_{k-1}\}/\Delta_{k-1}$$
$$K_{k23} = (-l_{k-1}b_{k-1}+a_{k-1})/\Delta_{k-1}+a_k/\Delta_k$$
$$K_{k24} = (l_{k-1}d_{k-1}-c_{k-1})/\Delta_{k-1}-(c_k-a_kl_k)/\Delta_k$$
$$K_{k25} = -a_k/\Delta_k$$
$$K_{k26} = c_k/\Delta_k$$

Applying k = 1 $\sim$ n+1 for the rotor partitioned by n, the equation of motion for the whole system becomes as follow;

$$\underline{M}\,\ddot{\underline{x}} + \underline{K}\,\underline{x} = \underline{L}\,\underline{u} \quad (6)$$

$\underline{x} = (x_1, \theta_1, x_2, \theta_2, \cdots, x_{n+1}, \theta_{n+1})^T$
$\underline{u} = (u_1, u_2, \cdots)^T$
$\underline{M} = \mathrm{diag}\{m_1, J_{r1}, m_2, J_{r2}, \cdots, m_{n+1}, J_{r(n+1)}\}$
$\underline{K}$: Band matrix composed of K_{kij} (k=1,n+1)
$\underline{L}$: Matrix indicating bearing locations

Underlined letters indicate vectors or matrices, and diag{} means a diagonal matrix.

The natural boundary condition is applied at both ends of the rotor ;

$$F_1 = M_1 = F_{n+1}^* = M_{n+1}^* = 0$$

3. Undamped Mode Analysis

Let $\underline{u}=\underline{0}$ in (6), and eigenvalues of free-free-mode without damping and bearing spring forces are obtained. Substitution of $\underline{x}=\underline{x}_0\exp(j\omega t)$ into (6) yields the form of normal eigenvalue problem ;

$$\underline{A}\,\underline{x} = 1/\omega^2\,\underline{x} \quad ; \quad \underline{A} = \underline{K}^{-1}\,\underline{M} \qquad (7)$$

Calculated eigenvalues and eigenmodes are used in the formation of control laws stated later.

4. General Damped Modal Analysis with Electrical Modelling and Gyroscopic Effect

A spring term and a damping term are the basic contents of the control input. However, as each element of the control system, sensor, compensation circuit, power amplifier, and control coil, has usually specific frequency characteristic, the complete PD (spring and damping) control is not realized. Therefore, an electrical modelling or a consideration of frequency characteristic is necessary. Also, gyroscopic effect should be taken into account for high speed rotors.

All these effects are included in the following formation.

Transfer function of control input against measured output ;

$$L(u/x)=(k_p+k_d s)\Sigma(a_i s^i)/\Sigma(b_i s^i) \qquad (8)$$

where $L(\ )$ represents Laplace operation, k_p and k_d are gains of P and D control respectively, and a_i and b_i are coefficients of frequency characteristic, which is usually of a low pass filter (LPF) with gain decrease and phase lag at high frequency range.

In the case of 2nd order LPF with cutoff frequency f_c and Q value, equation (8) becomes ;

$$L(u/x)=(k_p+k_d s)/(1+b_1 s+b_2 s^2) \qquad (8')$$

$$b_1=1/Q/(2\pi f_c)\ ,\ b_2=1/(2\pi f_c)^2$$

Equation of motion with gyroscopic effect ;

$$m_k\ddot{x}_k = F_{kx}-F_{kx}^{\cdot}+u_{kx} \qquad (9)$$
$$J_{rk}\ddot{\theta}_{yk}-J_{ak}\omega_r\dot{\theta}_{xk} = M_{ky}^{\cdot}-M_{ky} \qquad (10)$$
$$m_k\ddot{y}_k = F_{ky}-F_{ky}^{\cdot}+u_{ky} \qquad (11)$$
$$J_{rk}\ddot{\theta}_{xk}+J_{ak}\omega_r\dot{\theta}_{yk} = M_{kx}^{\cdot}-M_{kx} \qquad (12)$$

where ω_r is the angular rotational speed of the rotor, J_{ak} is the moment of inertia around the rotating axis and $J_{ak}\omega_r\dot{\theta}_k$ represents cross-coupling gyroscopic terms. θ_k in equation (4) is replaced by θ_{yk} in (10). (Refer Fig.2)

Define extended state vector ;

$$\underline{x}_e=(\underline{x}^T,\dot{\underline{x}}^T,\underline{u}_x{}^T,\dot{\underline{u}}_x{}^T,\underline{y}^T,\dot{\underline{y}}^T,\underline{u}_y{}^T,\dot{\underline{u}}_y{}^T)^T \qquad (13)$$

$$\underline{x}=(x_1,\theta_{y1},x_2,\theta_{y2},\cdots,x_{n+1},\theta_{y,n+1})^T$$
$$\underline{y}=(y_1,\theta_{x1},y_2,\theta_{x2},\cdots,y_{n+1},\theta_{x,n+1})^T$$
$$\underline{u}_x=(u_{x1},u_{x2},\cdots\cdots)^T$$
$$\underline{u}_y=(u_{y1},u_{y2},\cdots\cdots)^T$$

Extended equations of motion (9)-(12) are summarized as follows considering (8') and combining with an identity $\underline{M}\,\dot{\underline{x}}-\underline{M}\,\dot{\underline{x}}=\underline{0}$;

$$\underline{D}\,\dot{\underline{x}}_e + \underline{E}\,\underline{x}_e = \underline{0} \qquad (14)$$

where

$$\underline{D} = \left[\begin{array}{ccc|c} \underline{0} & \underline{M} & \underline{0} & \\ \underline{M} & \underline{0} & \underline{0} & \\ \underline{0} & \{b_1\} & \{b_2\} & \underline{0} \\ \underline{0} & \underline{I} & \underline{0} & \\ \hline & \underline{0} & & \begin{array}{ccc} \underline{0} & \underline{M} & \underline{0} \\ \underline{M} & \underline{0} & \underline{0} \\ \underline{0} & \{b_1\} & \{b_2\} \\ \underline{0} & \underline{I} & \underline{0} \end{array} \end{array}\right]$$

$$\underline{E} = \left[\begin{array}{cccc|cccc} \underline{K}_x & \underline{0} & -\underline{L} & \underline{0} & \underline{0} & -\underline{G}_{yro} & & \\ \underline{0} & -\underline{M} & \underline{0} & \underline{0} & & & & \\ -\underline{G}_{px} & -\underline{G}_{dx} & \underline{I} & \underline{0} & & \underline{0} & & \\ \underline{0} & \underline{0} & \underline{0} & -\underline{I} & & & & \\ \hline \underline{0} & +\underline{G}_{yro} & & & \underline{K}_y & \underline{0} & -\underline{L} & \underline{0} \\ & & & & \underline{0} & -\underline{M} & \underline{0} & \underline{0} \\ & \underline{0} & & & -\underline{G}_{py} & -\underline{G}_{dy} & \underline{I} & \underline{0} \\ & & & & \underline{0} & \underline{0} & \underline{0} & -\underline{I} \end{array}\right]$$

$$G_{yro}=\omega_r\cdot\mathrm{diag}\{0,J_{a1},0,J_{a2},\cdots,0,J_{a,n+1}\}$$

where $\underline{G}_p$ and $\underline{G}_d$ represents proportional and differential feed-back matrices containing k_p and k_d respectively and $\{b_i\}$ means $\mathrm{diag}\{b_i\}$ or diagonal matrix representing filter characteristic of the control system. $\underline{I}$ is the unit matrix.

For this extended system, eigenvalue analysis can be performed similarly to equation (7) ;

$$\dot{\underline{x}}_e = \underline{A}_e\,\underline{x}_e \quad ; \quad \underline{A}_e = -\underline{D}^{-1}\underline{E} \qquad (15)$$

As an eigenvalue analysis technique, QR method using Hessenberg matrix [6] has been employed here.

5. Experimental Apparatus

In order to investigate several control laws as practical design methods for the actual machines, an experimental apparatus was constructed as shown in Fig.3. A disk of weight 1.2Kg is mounted on the shaft of 410mm long and weight 2.2Kg with bearing diameter 40mm. The rotor is divided into 9 disks which have each mass and moment of inertia, with a resulting degree of freedom 36.

A small spring constant of 980 N/m was given to two bearings at ② and ⑦ , and the undamped mode was analyzed with a condition nearly equal to free-free mode, the result of which is shown in Fig.4. 1st(1B) and 2nd(2B) eigenvalues of bending mode lie at 333 Hz and 633 Hz respectively, so this is a flexible rotor which passes critical speeds of bending modes before reaching the design rotational speed (50,000 rpm, 833 Hz). This result is also plotted on the imaginary axis of Fig.5. Between the two main bearings are mounted drive motor ④ and auxiliary bearing ⑤ . The rotor displacements are measured at three points ③ ⑥ and ⑧ .

6. Control laws

Rigid Mode Control

The rotor displacement at the center of gravity is estimated by polynomial curve fit using displacement sensor signals. For three sensors parabola approximation is performed. Neglecting bending modes of the rotor and assuming rigid body, PD control gains are obtained to give appropriate spring and damping to translational and rotational motion of the center of gravity.

With this control law damped eigenvalues are analyzed considering the rotor flexibility, and the result is plotted on Fig.5 with the symbol X. The 2nd bending mode of 627 Hz is unstable.

Pseudo-Inverse (PI)[2]

Let $\underline{T}$ be the modal matrix obtained by the undamped analysis, then using ;

$$\underline{x} = \underline{T}\,\underline{a} \quad \text{or} \quad \underline{a} = \underline{T}^{-1}\,\underline{x} \qquad (16)$$

the equation of motion (6) is transformed into the following equation concerning the modal coordinate $\underline{a}$.

$$\underline{T}\,\underline{M}\,\underline{T}^{T}\,\ddot{\underline{a}} + \underline{T}^{T}\,\underline{K}\,\underline{T}\,\underline{a} = \underline{T}^{T}\,\underline{L}\,\underline{U} \qquad (17)$$

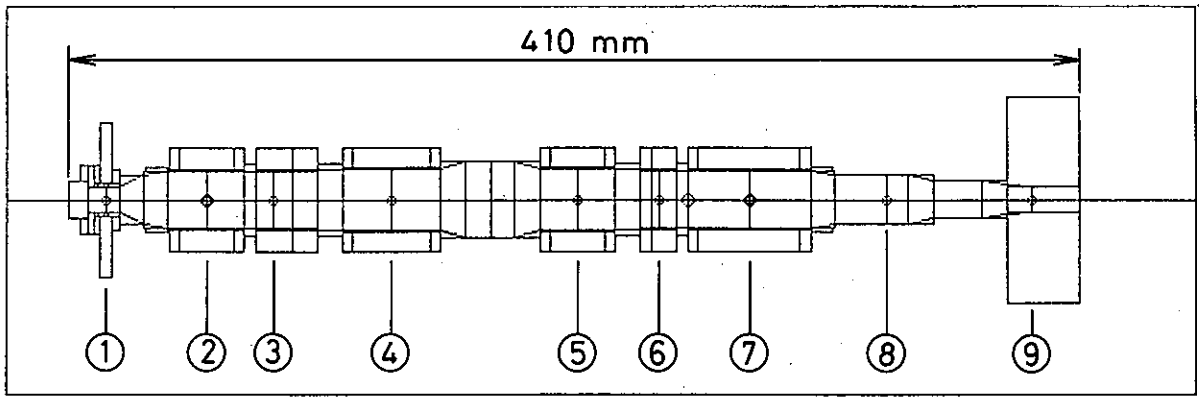

Figure 3 Rotor profile

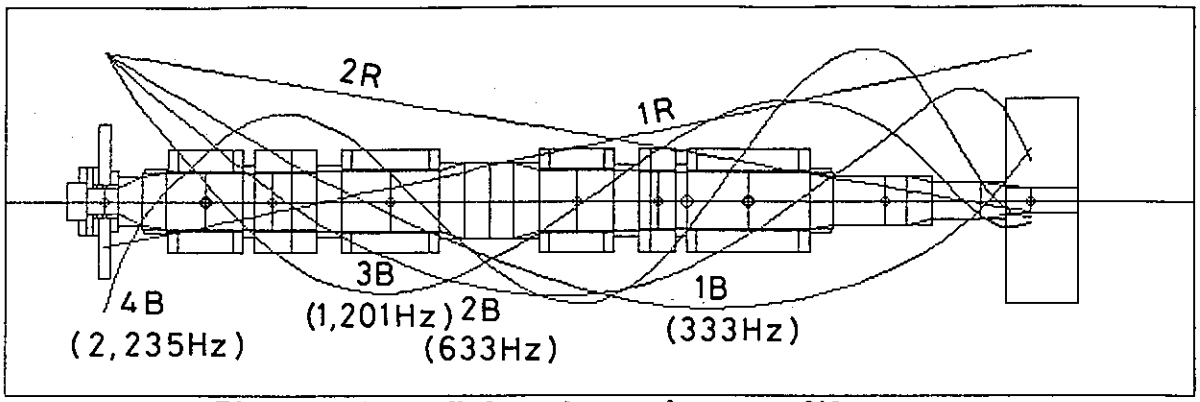

Figure 4 Undamped mode profile

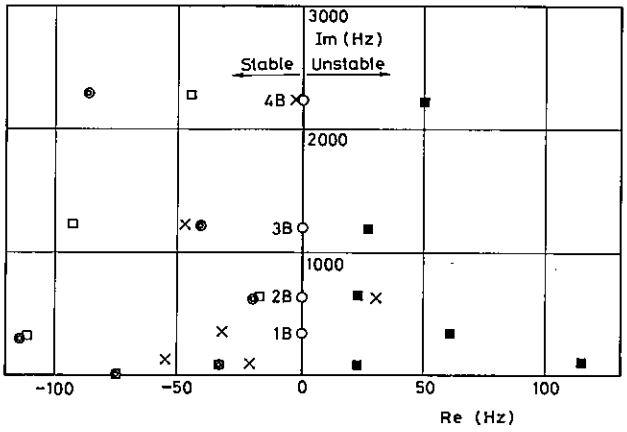

o : Undamped,free-free mode
x : Rigid mode
■ : Pseudo-Inverse,non-colocation
□ : Pseudo-Inverse,with colocation
◎ : Quasi-Colocation Pseudo-Inverse

Figure 5 Eigenvalues by various control laws

where

$$\underline{T}\,\underline{M}\,\underline{T}^{T} = \underline{I}$$
$$\underline{T}^{T}\,\underline{K}\,\underline{T} = \mathrm{diag}\{\omega_1^2, \omega_2^2, \cdots, \omega_n^2\}$$

Therefore, if the following control is realized ;

$$\underline{T}^{T}\,\underline{L}\,\underline{u} = \underline{F}\,\dot{\underline{a}} \;;\; \underline{F}=\mathrm{diag}\{-2\zeta_i\omega_i\} \qquad (18)$$

then this is the ideal modal control which enables arbitrary selections of damping ratio ζ_i for the i-th mode with eigenfrequency ω_i. However, this is actually not realizable.

Let measured output of state $\underline{x}$ be $\underline{S}\,\underline{x}$ and the gain matrix of output velocity feed-back be $\underline{G}$, then

$$\underline{u} = \underline{G}\,\underline{S}\,\dot{\underline{x}} = \underline{G}\,\underline{S}\,\underline{T}\,\dot{\underline{a}} \qquad (19)$$

Combining (18) with (19) ;

$$\underline{T}^{T}\,\underline{L}\,\underline{G}\,\underline{S}\,\underline{T} = \underline{F} \qquad (20)$$

is the ideal relation of $\underline{G}$ and $\underline{F}$. However, (20) cannot be solved for $\underline{G}$, because $\underline{L}$ and $\underline{S}$ are not generally regular and square matrices.

Therefore, using Moore-Penrose's pseudo-inverse (indicated by #, see Appendix B) of $\underline{T}^{T}\,\underline{L}$ and $\underline{S}\,\underline{T}$;

$$\underline{G}_{PI} = (\underline{T}^{T}\,\underline{L})^{\#}\,\underline{F}\,(\underline{S}\,\underline{T})^{\#} \qquad (21)$$

gives an approximated solution.

Eigenvalues calculated by PI method are plotted on Fig.5 with symbols ■. All the eigenvalues plotted are unstable. This is due to "non-colocation" condition that the locations of sensors and bearings differ each other. The importance of colocation condition is emphasized in [2].

Now suppose the case where colocation condition holds. Two sensors are located at points ② and ⑦ which correspond to those of two bearings. In this case the calculated eigenvalues are all stable with sufficient margins as seen from the plots of □ in Fig.5.

Thus PI method is very effective with the condition of colocation, while it is even worse in case of non-colocation, which is often the actual case.

Quasi-Colocation Pseudo-Inverse (QCPI)

In order to modify PI method for non-colocation case, displacement and velocity at the bearing location are estimated by polynomial curve fit using sensor signals as well as the case of rigid mode control. Then PI method is applied for the estimated states at the bearings.

Let measured states be $\underline{x}_m$, estimated states $\underline{x}_b$, and estimating matrix $\underline{E}_s$, then ;

$$\underline{x}_b = \underline{E}_s\,\underline{x}_m = \underline{E}_s\,\underline{S}\,\underline{x} \qquad (22)$$
$$\underline{u} = \underline{G}\,\dot{\underline{x}}_b = \underline{G}\,\underline{E}_s\,\underline{S}\,\dot{\underline{x}} \qquad (23)$$

$\underline{E}_s$ contains curve fitting informations which only depend on locations of each sensor and bearing. The feed-back matrix $\underline{G}$ is calculated as ;

$$\underline{G}_{QCPI} = (\underline{T}^{T}\,\underline{L})^{\#}\,\underline{F}\,(\underline{E}_s\,\underline{S}\,\underline{T})^{\#} \qquad (24)$$

Calculated eigenvalues are shown on Fig.5 with symbols ◎. Eigenvalues of two rigid modes (1R,2R) and 1st(1B) and 2nd(2B) bending modes almost coincide with those of PI method with colocation condition. 3rd and 4th bending modes differ from colocation PI metod but still in the stable region. This means that modal shapes of the rotor of lower modes can sufficiently be approximated by a simple curve, in this case - parabola. The more increaes the number of sensors used, the higher mode shapes are well approximated and corresponding eigenvalues become stabler.

Selective Eigenvalue Move Method

QCPI method stated above has enabled basically stable arrangement of system eigenvalues. For the sake of safe passing of critical speeds or to cope with the change of eigenvalues due to

gyroscopic effect at high rotational speed, it sometimes becomes necessary to move a specific eigenvalue towards stabler region. For this purpose, the following method is presented here.

The characteristic equation of a system of order n is ;

$$s^n+a_{n-1}s^{n-1}+\cdots+a_1s+a_0=0 \qquad (25)$$

Consider following eigenvalue to move ;

$$s_k = s_{kr} \pm j\, s_{ki} \qquad (26)$$

Equation (25) can also be expressed as ;

$$(s^{n-2}+b_{n-3}s^{n-3}+\cdots+b_1s+b_0) *(s^2-2s_{kr}s+s_{kr}^2+s_{ki}^2)=0 \qquad (27)$$

a_i b_i and s_k are supposed to be all known. In order that s_k may change as;

$$s_k = (s_{kr}+\Delta s_{kr}) \pm j\,(s_{ki}+\Delta s_{ki}) \qquad (28)$$

equation(25) changes correspondingly

$$s^n+(a_{n-1}+\Delta a_{n-1})s^{n-1}+\cdots +(a_1+\Delta a_1)s+a_0+\Delta a_0=0 \qquad (29)$$

Also equation (27) changes into ;

$$(s^{n-2}+b_{n-3}s^{n-3}+\cdots+b_1s+b_0)*\{s^2-2(s_{kr} +\Delta s_{kr})s+(s_{kr}+\Delta s_{kr})^2+(s_{ki}+\Delta s_{ki})^2\}=0 \qquad (30)$$

Therefore the increments of coefficients of the characteristic equation are ;

$$\Delta a_m=-2\Delta s_{kr}b_{m-1}+\Delta|s_k|^2b_m \quad (m=0,n-1) \qquad (31)$$
$$\Delta|s_k|^2=(s_{kr}+\Delta s_{kr})^2+(s_{ki}+\Delta s_{ki})^2-s_{kr}^2-s_{ki}^2$$
$$b_{-1}\equiv 0,\ b_{n-2}\equiv 1,\ b_{n-1}\equiv 0$$

Now feed-back gain $\underline{G}$ has to be considered to give Δa_m for specified Δs_{kr} and Δs_{ki}. The characteristic equation (25) is obtained from the system matrix $\underline{A}_e$ (15) as $\det|s\underline{I}-\underline{A}_e|=\underline{0}$. The effect of the change of elements in $\underline{G}$ included in $\underline{A}$ on eigenvalues or coefficients of (25) can be calculated actually conducting eigenvalue analysis. The element g_{ij} of $\underline{G}$ means the feed-back gain for i-th bearing from j-th sensor. Adding 1 to g_{ij}, coefficient increments $\underline{\Delta a}_{m,ij}$ (m=0, n-1) are obtained, and with these as column components a matrix $\underline{Z}_i$ is formed ;

$$\underline{Z}_i\ \underline{\Delta g}_i = \underline{\Delta a} \qquad (32)$$

$$\underline{Z}_i=\{\underline{\Delta a}_{m,i1},\underline{\Delta a}_{m,i2},\cdots,\underline{\Delta a}_{m,ins}\}$$
$$\underline{\Delta a}_{m,ij}=\{\Delta a_{n-1,ij},\Delta a_{n-2,ij},\cdots,\Delta a_{0,ij}\}^T$$
$$\underline{\Delta g}_i=\{\Delta g_{i1},\Delta g_{i2},\cdots,\Delta g_{ins}\}^T$$
$$\underline{\Delta a}=\{\Delta a_{n-1},\Delta a_{n-2},\cdots,\Delta a_0\}^T$$

$\underline{\Delta g}_i$ is the increment of the feed-back gain g_{ij} and should be determined by (32). ns represents the number of sensors and is usually much less than the order of the system n. Therefore (32) cannot be solved strictly for $\underline{\Delta g}_i$. Thus the least square method is applied (see Appendix C). This is basically the same as using pseudo-inverse for column-regular matrix $\underline{Z}_i$. However, when the order of the system is large, each element of $\underline{\Delta a}$ differs by many figures, and the straight forward solution will result in a big error. Therefore each row of (32) is weighted inversely by binomial coefficients.

In the system basically stabilized by QCPI metod, the 2nd bending mode(2B) of 619 Hz has rather poor stability with damping ratio of 0.031. In order to stabilize this mode more, eigenvalue increment Δs_{2B} is specified and the resultant eigenvalues movement is plotted in Fig.6. For this actuator the auxiliary bearing ⑤ was used. It is ideal to move eigenvalue 2B only, but the actual approximation method allows small changes of other eigenvalues. 2B is certainly stabilized as larger values of negative Δs_{2B} are specified, while the second rigid mode (2R) is gradually deteriorated, also 1B turns towards unstable region from halfway. The point where the damping ratio of each eigenvalue approaches would be optimum.

The method stated above deals only one actuator(bearing). To deal plural actuators at the same time will make the equation corresponding to (32) non-

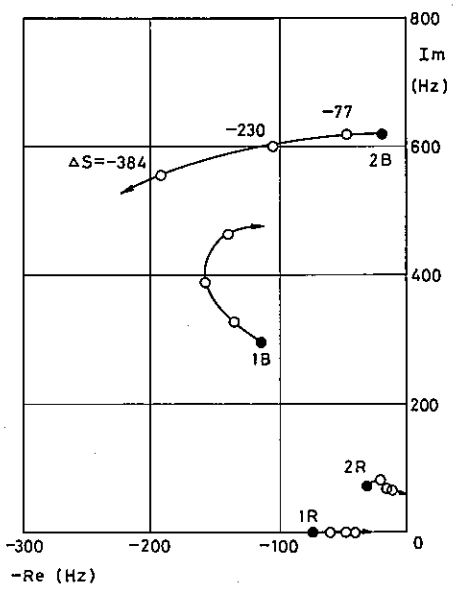

Figure 6 Selective Eigenvalue Move

linear and require iteration. It would be better to deal actuators one by one, watching the location of each eigenvalue and finally obtain the optimum feed-back gain.

7. Experimental Result

In order to test the actual system, a test signal is added to a point in the control system, and the response is measured at another point. The selection of these points is arbitrary, and the measuring point can even be the point located just before or after addition. Here the summing point is selected as input to the power amplifier of the horizontal (in y-direction) bearing ② , and the measuring point is the horizontal sensor ③ . This can simulate the rotor displacement response to a disturbance force, which is expressed as $\underline{f}$ in the equation of motion (14) modified as ;

$$\underline{D}\,\dot{\underline{x}}_e + \underline{E}\,\underline{x}_e = \underline{f} \qquad (33)$$

The response transfer function is ;

$$L(\underline{x}_e/\underline{f}) = (s\underline{I} - \underline{A}_e)^{-1}\underline{D}^{-1} \qquad (34)$$

The response of sensor ③ to the disturbance at bearing ② corresponds to one element of (34), which can be calculated numerically.

Fig.7 shows measured and calculated results in Bode diagram. The rotor is not rotating, so gyroscopic effect is not included. The calculated value of the broken line is of QCPI metod.

The peaks of 1.25 KHz and 2.25 KHz are due to rather small value of damping ratios of 3rd and 4th bending mode. These modes are actually self-oscillated due to more complicated frequncy characteristic than that of (8') and nonlinearity of the control components.

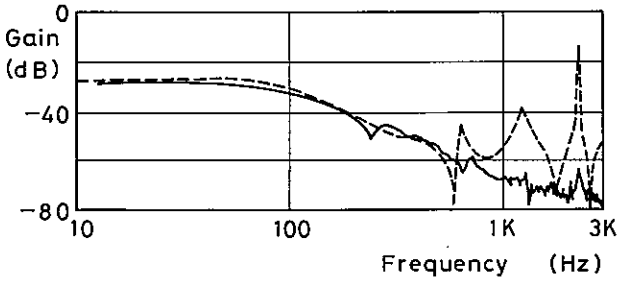

—— : Measured --- : Calculated

Figure 7 Frequency response

These oscillations were suppressed by using Notch filters, and the measured value of the real line in Fig.7 indicates the actual system response finally stabilized. In the lower frequency range, the measured characteristic is well simulated by the calculation indicating the effectiveness of the presented design method.

In the ralization of QCPI method, estimated displacement signals at the bearing are formed and input to the compensation circuit. It is an effective design rule to modify the compensation circuit watching the real system characteristic by the estimated signals[7].

8. Conclusion

(1)QCPI(Quasi-Colocation Pseudo-Inverse) method is effective for the basic design of flexible rotors.
(2)Selective Eigenvalue Move method works well for the fine modification of eigenvalues.
(3)The effectiveness of these techniques were proved experimentally.
(4)Finer modelling of the frequency characteristic of control components is necessary for the precise estimation at high frequency range.

References

[1]Nonami,K.,and Fleming D.P.:"QUASI-MODAL VIBRATION CONTROL BY MEANS OF ACTIVE CONTROL BEARINGS",Proc.Int. Conf. Rotordynamics, 1986,Tokyo
[2]Salm,J.R. "ACTIVE ELECTROMAGNETIC SUSPENSION OF AN ELASTIC ROTOR:MODELLING,CONTROL AND EXPERIMENTAL RESULTS" ASME DESIGN TECHNOLOGY CONFERENCES September,1987
[3]Chen,H.M., "Magnetic Bearings and Flexible Rotor Dynamics" STLE PREPRINT No.88-AM-2D-1
[4]Bradfield,C.D.,et.al. "A PROGRAMMABLE ELECTROMAGNETIC BEARING FOR VIBRATION CONTROL OF A FLEXIBLE SHAFT" ASME Vibration Conf. '89
[5]Burrows,C.R.,and Sahinkaya.M.N. "Control strategy for use with magnetic bearings" I.Mech.E. Int.Conf. on Vibrations in Rotating Machinery, September,1988
[6]Wilkinson,J.H., "The Algebraic Eigenvalue Problem" Oxford Science Publications
[7]Hisatani,M.,"Identification and Optimization of Active Magnetic Bearing Systems Using Measured Nyquist Diagrams" Proc.1st Int.Symp. Magnetic Bearings, June 1988

Appendix A Transfer Matrix of a shaft with variation of section

When there is no variation of section or no change in shaft diameter in Fig.2,

$$\begin{Bmatrix} F_{k+1} \\ M_{k+1} \\ \theta_{k+1} \\ x_{k+1} \end{Bmatrix} = \begin{bmatrix} 1 & 0 & 0 & 0 \\ l_k & 1 & 0 & 0 \\ l_k^2/2E_kI_k & l_k / E_kI_k & 1 & 0 \\ l_k^3/6E_kI_k & l_k^2/2E_kI_k & l_k & 1 \end{bmatrix} \begin{Bmatrix} F_k \\ M_k \\ \theta_k \\ x_k \end{Bmatrix}$$

This relation is expressed as

$$\underline{z}_{k+1} = \underline{T}_k \underline{z}_k$$

$\underline{T}_k$ is the transfer matrix of a shaft section with constant diameter. Now considering the variation of diameter, $\underline{T}_k$ is divided into several parts each representing a shaft section with constant diameter ;

$$\underline{T}_k = \underline{T}_{k,m} \underline{T}_{k,m-1} \cdots \underline{T}_{k,1}$$

Then this represents the transfer matrix of the whole shaft section with diameter variations which is used in equation (1).

Appendix B Moore-Penrose's Pseudo-Inverse [2]

For a column-regular matrix $\underline{B}$;

$$\underline{B}^{\#} = (\underline{B}^T\underline{B})^{-1} \underline{B}^T$$

For a row-regular matrix $\underline{C}$;

$$\underline{C}^{\#} = \underline{C}^T (\underline{C}\underline{C}^T)^{-1}$$

Appendix C Approximation by least square method

Consider the following simultaneous linear equations with the number of equations n larger than the number of unknowns n' ;

$$\sum_{j=1}^{n'} \alpha_{ij} x_j = b_i \qquad (i = 1,n)$$

Define the estimating function as ;

$$f = \sum_{k=1}^{n} \{(\sum_{j=1}^{n'} \alpha_{kj} x_j - b_k)/{}_nC_k\}^2$$

where ${}_nC_k$ is the binomial coefficient and ${}_nC_k = n!/(n-k)!k!$.
Then by partial differentiation ;

$$\partial f/\partial x_j = \sum_{k=1}^{n} 2\alpha_{kj} (\sum_{m=1}^{n'} \alpha_{km} x_m - b_k)/{}_nC_k = 0 \qquad (j = 1,n')$$

Therefore the following equations concerning x_j are obtained ;

$$\{\sum_{k=1}^{n} \alpha_{ki}\alpha_{kj}/{}_nC_k\}\{x_j\} = \{\sum_{k=1}^{n} \alpha_{ki} b_k/{}_nC_k\} \qquad (i,j = 1,n')$$

2nd International Symposium on Magnetic Beaing
July 12-14, 1990, Tokyo, Japan

Rotor Vibration Simulation Method for Active Magnetic Bearing Control

Osami MATSUSHITA, Mechanical Engineering Research Laboratory, Hitachi,
502, Kandatsu-machi, Tsuchiura-shi, Ibaraki-ken
Toyomi YOSHIDA, Mechanical Engineering Research Laboratory, Hitachi, Ltd.
Naohiko TAKAHASHI, Mechanical Engineering Research Laboratory, Hitachi, Ltd.

ABSTRACT Since active magnetic bearings have been employed in turbo-machinery, a corresponding simulation technique combined with rotor dynamics and controller network is required for design, runing operations, and so on. This paper presents the simulation method and its applications to stability estimation, unbalance responses and frequency response of a servo control system.

The rotor system is reduced to a small model by a quasi-modal modeling we developed. The control network is expressed by the usual state equations. Both the model and the equations are then combined for the simulation analysis. In addition to the usual control law, e. g., PID, the observer based state feedback and so on, the developed program is capable to cover the tracking filter with rotational speed and cross talk between x and y channel control, which are related to empirical knowhow of the rotor vibration cntrol.

Some examples of the numerical simulation are presented for demonstrating practical applications of the developed program.

1. INTRODUCTION

Rotordynamics related to ball and oil-film bearings have been the major subject in the study and development of rotor vibration analysis programs. Since present industrial rotating machines such as turbine compressors use passive bearings, such programs can cover almost all types of rotating machines.

Recently, however, electromagnetic bearings, i.e., active bearings, are increasingly used in various types of rotating machines. Currently available commercial control-type rotating machines incorporating electromagnetic bearings are mostly small-scale machines such as turbo molecular pumps and X-ray tubes. However, the application range is increasing to large-scale rotating machines as well.

Electromagnetic bearings are thus becoming more important in the field of rotating machines in general. As a result software to assists in the design and development of rotating machines controlled by electromagnetic bearings is being currently developed.

In the case of an electromagnetic bearing, the output current is determined by an electronic circuit on the basis of input of displacement signals detected and then runs through a coil and induces on electromagnetic force because of vibration restraint. All bearing reaction forces are determined by the electronic circuit according to control rules. Accordingly, the control system of the rotor must be analyzed from the viewpoint of both the conventional rotor dynamics and the control theory.

Rotor vibration is modeled by the quasi-modal method[1], while the electronic circuit is expressed by an set of state equations. The problem is how to combine these two formulations. Rotor vibration is described as a lateral vibration consisting of forward and backward rotor motions. In accordance with this, the electronic circuit is represented as a transfer function, where backward transfer function G $(-j\omega)$ is used in addition to the ordinary forward transfer function G $(j\omega)$.

This study summarizes a method to combine the rotor and electronic circuit by introducing the concept of forward and backward vibration. Some examples are shown to demonstrate the suitability of the developed method for stability analysis, unbalance response analysis, and frequency response analysis.

MOMENCLATURES

M : mass matrix
Cg : gyroscopic effect matrix
K : $= \begin{pmatrix} K_{11} & K_{12} \\ K_{21} & K_{22} \end{pmatrix}$ rotor stiffness matrix ($K_{21}{}^t = K_{12}$).
F : $[F_1, F_2]$: force
U_f, U_b : Unbalance vector
Z : complex displacement vector
$\equiv$: equal by definition
$\overline{\bigstar}$: conjugate of $\bigstar$
Q : bearing reaction force
z_1 : displacement vector of inner coordinates
z_2 : displacement vector of boundary coordinates
ω : natural frequency of rotor inner system mode
ϕ, ϕ_f, ϕ_b : undamped critical speed mode of inner system
δ : deflection mode when boundary coordinates are forcedly displaced
ξ : deflection mode when the boundary is forcedly displaced at unit speed
Ω : rotational speed
$k_2{}^*$: equivalent spring constant at forced displacement of bearing
$C_{g2}{}^*$: equivalent gyroscopic action at forced speed of bearing
S, S_1 : quasi-modal coordinates
G(s), H(s) : transfer functions
i = imaginary unit $= \sqrt{-1}$
B^*_{11} : modal mass corresponding to bending mode
B^*_{12} : modal mass correnponding to relation between bending mode and bearing forced displacement and/or velocity

B^*_{22} : modal mass corresponding to bearing forced displacement

2. SYSTEM STRUCTURE OF A CONTROLLED TYPE ROTOR

2.1 Equation of Motion for Rotor System

Since the displacements x and y in directions X and Y of the rotor vibration are represented, the combination of both rotor vibrations is represented by a complex displacement $Z = x + iy$[2]. Further, displacement of the boundary (the bearing) is denoted by Z_2, and that of the other inner system of the rotor by Z_1. Hereafter, the inner system is represented by suffix 1, and the boundary by suffix 2. Then, the equation of motion is obtained as follows:

$$\begin{pmatrix} M_1 & \\ & M_2 \end{pmatrix}\begin{pmatrix} \ddot{Z}_1 \\ \ddot{Z}_2 \end{pmatrix}+\begin{pmatrix} i\Omega C_{g1} & \\ & i\Omega C_{g2} \end{pmatrix}\begin{pmatrix} \dot{Z}_1 \\ \dot{Z}_2 \end{pmatrix}+\begin{pmatrix} K_{11} & K_{12} \\ K_{21} & K_{22} \end{pmatrix}\begin{pmatrix} Z_1 \\ Z_2 \end{pmatrix}=\begin{pmatrix} F_1 \\ F_2 \end{pmatrix}-\begin{pmatrix} O \\ Q \end{pmatrix}-\begin{pmatrix} O \\ G \end{pmatrix} \quad (1)$$

where F_1, F_2; force

$Q = Q(Z, \dot{Z}, \overline{Z}, \overline{\dot{Z}})$; reaction force of oil-film lubricated bearing

$G = G(j\omega) = G(Z, \dot{Z})$; reaction force of electromagnetic bearing

If the right side of Eq.(1) is represented by force F_A and written a simple form using complex displacement Z, we obtain:

$$M\ddot{Z} + i\Omega C_g \dot{Z} + K Z = F_A \quad (2)$$

From Eq.(2), a state equation is as follows:

$$\begin{pmatrix} M & \\ & K \end{pmatrix}\begin{pmatrix} \ddot{Z} \\ \dot{Z} \end{pmatrix}+\begin{pmatrix} -i\Omega C_g - K & \\ K & O \end{pmatrix}\begin{pmatrix} \dot{Z} \\ Z \end{pmatrix}=\begin{pmatrix} F_A \\ O \end{pmatrix} \quad (3)$$

The following transformation is defined for the quasi-modal transformation shown in Fig.1:

$$\begin{pmatrix} \dot{Z}_1 \\ \dot{Z}_2 \\ Z_1 \\ Z_2 \end{pmatrix}=\begin{pmatrix} i\omega\phi & \delta & O \\ O & \mathbf{1} & O \\ \phi & \xi & \delta \\ O & O & \mathbf{1} \end{pmatrix}\begin{pmatrix} S_1 \\ \dot{Z}_2 \\ Z_2 \end{pmatrix} \equiv [\Phi]\begin{pmatrix} S_1 \\ \dot{Z}_2 \\ Z_2 \end{pmatrix} \quad (4)$$

where $\mathbf{1} = [1, 1, \cdots 1]^t$.

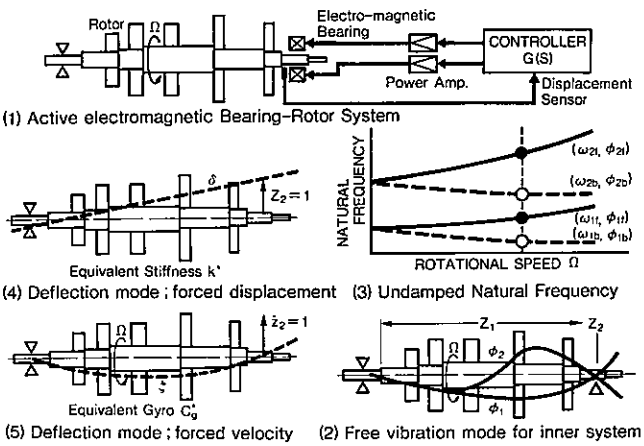

Fig.1 Mode Shapes for Quasi-modal Transformation

Substitute Eq.(4) in Eq.(3) and perform a conjugate transpose of $[\Phi]$ to obtain the following equation:

$$\begin{pmatrix} B_{11}^* & B_{12}^* & 0 \\ B_{12}^{*t} & B_{22}^* & 0 \\ 0 & 0 & k_2^* \end{pmatrix}\begin{pmatrix} \dot{S}_1 \\ \ddot{Z}_2 \\ \dot{Z}_2 \end{pmatrix}=\begin{pmatrix} i\omega B_{11}^* & 0 & 0 \\ 0 & -i\Omega C_{g2}^* & -k_2^* \\ 0 & k_2^* & 0 \end{pmatrix}\begin{pmatrix} S_1 \\ \dot{Z}_2 \\ Z_2 \end{pmatrix} + \begin{pmatrix} -i\omega\phi^t F_1 \\ \delta^t F_1 + F_2 - Q - G \\ 0 \end{pmatrix} \quad (5)$$

where

$B_{11}^* = \omega^2 \phi^t M_1 \phi + \phi^t K_{11} \phi$

$B_{12}^* = -i[\omega \phi^t M_1 \delta + \Omega \phi^t C_{g1} \delta]$

$B_{22}^* = \delta^t M_1 \delta + M_2 - \Omega^2 \xi_g^t C_{g1} \delta$

$k_2^* = k_{21}\delta + k_{22}$

= equivalent spring constant where inner system is viewed from the boundary

$C_{g2}^* = k_{21}\xi_g + C_{g2}$

= equivalent damping factor where inner system is viewed from the boundary

Eq.(5) is the formulation for the portion which corresponds to the rotor system of a controlled type rotating machine. It represents the reduction by a quasi-modal transformation by the use of the eigenmode (marks ○ and ●) of the inner system at a certain rotational speed, as shown in Fig.1(3).

2.2 Dynamic Characteristics of Oil-Film Lubricated Bearings

In the case of a passive oil-film lubricated bearing, the bearing reaction forces Q_x and Q_y in directions X and Y, respectively, are represented by spring constants k_{ij} (i, j = x, y) and damping factors c_{ij} (i, j = x, y), and are defined as 8 parameters of oil-film as follows:

$$\begin{aligned} Q_x &= k_{xx}x + k_{xy}y + c_{xx}\dot{x} + c_{xy}\dot{y} \\ Q_y &= k_{yx}x + k_{yy}y + c_{yx}\dot{x} + c_{yy}\dot{y} \end{aligned} \quad (6)$$

It is generally known that the presence of cross stiffness such as k_{xy} and k_{yx} can cause unstable rotor vibrations.

2.3 Dynamic Characteristics of Electromagnetic Bearings

In the case of an active electromagnetic bearing. These dynamic factors are determined by the adjustment of the controller Generally, isotropic dynamic characteristics of bearings are obtainable by adjustment:

$$k_d = k_{xx} = k_{yy},\ c_d = c_{xx} = c_{yy}$$

$$k_c = k_{xy} = -k_{yx},\ c_c = c_{xy} = -c_{yx}$$

Reaction forces are then given by the following equations:

$$\begin{aligned} Q_x &= k_d x + k_c y + c_d \dot{x} + c_c \dot{y} \\ Q_y &= k_d y - k_c x + c_d \dot{y} - c_c \dot{x} \\ \text{i. e. } Q &= Q_x + iQ_y \\ &= k_d z - ik_c z + c_d \dot{z} - ic_c \dot{z} \end{aligned} \quad (7)$$

Parameter k is an important factor in terms of stability. It indicates a cross talk between channels X and Y of the control circuit.

Generally, a controller accepts displacements x and y as input as shown in Fig.2, and consists of directly coupled transfer function Gd(s) and of cross-coupled transfer function Gc(s). As a result, forces Q_x and Q_y in directions X and Y, respectively, are output via the actuator. Physically, this type of a system is a 2-input, 2-output type system. In the simulation, this form is transformed into 1-input,1-output type as shown below, by using a complex number.

$$Q = (G_d - iG_c)Z \tag{8}$$

Therefore, the problem is reduced to analysis of a control circuit system with one input ($Z = x + iy$) and one output ($Q = O_x + iQ_x$), with a complex transfer function $G(s) = Gd(d) - iG_c(s)$.

A control circuit can also be shown as follows using a state equation and an output equation:

$$B\dot{V} = AV + RinZ$$
$$Q = RoutV + DZ \tag{9}$$

B, A : factor matrix
Rin : vector proportional to input
Rout : vector proportional to output
D : stiffness

where V is the voltage expressed in the complex form, $V = V_x + iV_y$, and V_x and V_y are voltages of the control circuit in directions X and Y, respectively.

3. STABILITY ANALYSIS

For the rotor system, the mode shown in Fig.1 is used to formulate a reduction system using the quasi-modal method. The control circuit is shown by a state equation. Stability analysis is actually performed by introducing a differential equation combining above two and by conducting a complex eigenvalue analysis for the equation.

The equation for a global system consisting of a quasi-modal reduced rotor system and control system be expressed as a matrix shown in Fig.3. From the upper left to the lower right corner of the matrix, the terms along the diagonal are vibration of the inner system of the rotor, vibration of electromagnetic bearing, and voltage of the control circuit.

The inner system starts to vibrate due to the presence of B_{21}. Through the vibration of the bearing, RIN is the bearing vibration, which is an input to the control circuit,while ROUT indicates the effects of reaction forces of the electromagnetic bearing, which the output of the control circuit.

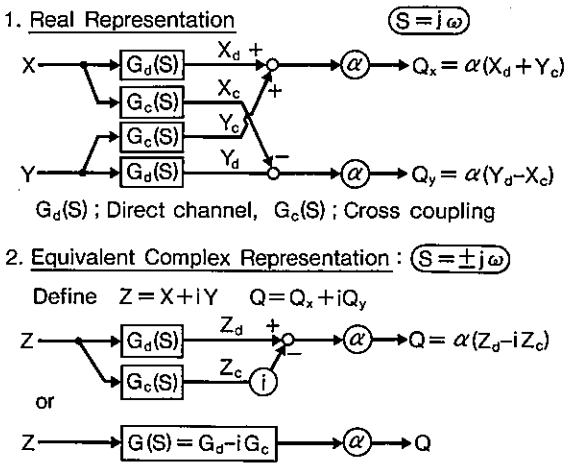

Fig.2 Network with X&Y Cross Coupling

4. UNBALANCE RESPONSE ANALYSIS[3]

Unbalance response of rotors which are supported by oil-film lubricated bearings has been studied for many years. In this Section, contains discussion of the problem of definition of definition of the bearing characteristics when an oil-film lubricated bearing is replaced by an electromagnetic bearing.

4.1 Oil-Film Lubricated Bearing

Generally, the equation of motion for a rotor supported by oil-film lubricated bearings is given as follows:

$$M\ddot{Z} + i\Omega C_g\dot{Z} + KZ + Q = F = U\Omega^2 e^{i\Omega t} \tag{10}$$

Assume the vibration response and the bearing reaction force are given as follows :

$$Z = Z_f e^{i\Omega t} + \overline{Z}_b e^{-i\Omega t} \tag{11}$$
$$Q = Q_f e^{i\Omega t} + \overline{Q}_b e^{-i\Omega t} \tag{12}$$

Then, forward and backward vibration equations are obtained as follows:

$$\begin{aligned} [-\Omega^2(M+C_g)+K]\,Z_f + Q_f &= \Omega^2 U \\ Q_b + [-\Omega^2(M-C_g)+K]\,Z_b &= 0 \end{aligned} \tag{13}$$

If the following 8 parameters are used:

$$k_{xx}\ k_{xy}\ k_{yx}\ k_{yy}\ c_{xx}\ c_{xy}\ c_{yx}\ c_{yy}$$

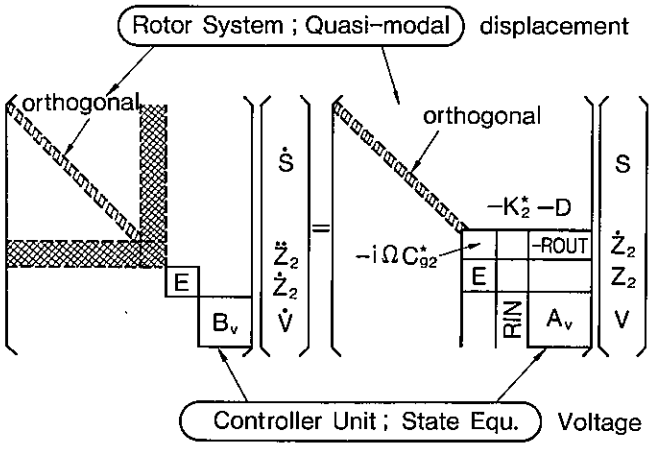

Fig.3 Global State Equation Combining Quasi-modal reduced Rotor with Controller

the characteristics of an oil-film lubricated bearing using complex forms are as follows:

$$K_f=\frac{K_{XX}+K_{YY}}{2}+i\frac{K_{YX}-K_{XY}}{2},\quad K_b=\frac{K_{XX}-K_{YY}}{2}+i\frac{K_{XY}+K_{YX}}{2}$$

$$C_f=\frac{C_{XX}+C_{YY}}{2}+i\frac{C_{YX}-C_{XY}}{2},\quad C_b=\frac{C_{XX}-C_{YY}}{2}+i\frac{C_{XY}+C_{YX}}{2}.$$

Then, the bearing reaction force Q can be expressed as follows:

$$Q\equiv K_f Z+K_b\bar{Z}+C_f\dot{Z}+C_b\dot{\bar{Z}} \tag{14}$$

From Eq.(11), this relation becomes:

$$\begin{aligned}Q_f&=(K_f+i\Omega C_f)Z_f+(K_b+i\Omega C_b)Z_b\\ Q_b&=(\bar{K}_f+i\Omega\bar{C}_f)Z_b+(\bar{K}_b+i\Omega\bar{C}_b)Z_f\end{aligned} \tag{15}$$

Finally, the following forward and backward vibration equations are obtained:

$$\begin{aligned}&\left[(M+C_g)-\frac{K}{\Omega^2}-\frac{K_f+i\Omega C_f}{\Omega^2}\right]Z_f-\frac{K_b+i\Omega C_b}{\Omega^2}Z_b=-U\\ &-\frac{K_b+i\Omega C_b}{\Omega^2}Z_f+\left[(M-C_g)-\frac{K}{\Omega^2}-\frac{K_f+i\Omega C_f}{\Omega^2}\right]Z_b=0\end{aligned} \tag{16}$$

If the vibration force is proportional to the rotational speed the following equation results:

$$F=U_f e^{i\Omega t}+\bar{U}_b e^{-i\Omega t} \tag{17}$$

This equation can be solved in a similar manner.

The rotor portion of Equ.(16) is analyzed using a structure shown in Fig.5, where the quasi-model transformation has been performed using orthogonality of the critical mode of the inner system shown in Fig.4.

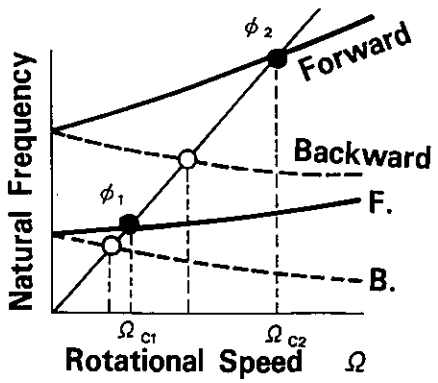

Fig.4 Undamped Critical Speed (Inner System Only)

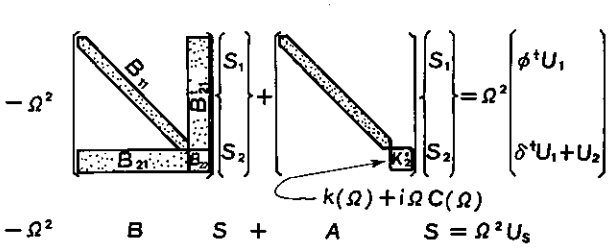

Fig.5 Unbalance Response after Quasi-Modal Transformation

4.2 Electromagnetic Bearing

Transfer function of the electronic circuit of a controller for electromagnetic bearing is represented by G(s). Displacement z is the input, and bearing reaction force Q is the output. This relationship can be shown in the following block diagram:

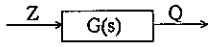

If input Z and output Q are as shown by Eq.(11) and (12), respectively, the following equations are obtained when G(s) is a linear system:

$$\begin{aligned}Q_f&=G(i\Omega)Z_f\\ Q_b&=\overline{G(-i\Omega)}Z_b\end{aligned} \tag{18}$$

By substituting the above in Eq.(13), the dynamic characteristics of electromagnetic bearings can be shown as follows:

$$\begin{aligned}K_f+i\Omega C_f&=G(i\Omega),\quad K_b+i\Omega C_b=0\\ \bar{K}_f+i\Omega\bar{C}_f&=\overline{G(-i\Omega)},\quad \bar{K}_b+i\Omega C_b=0\end{aligned} \tag{19}$$

Eq.(16), which is applicable to oil-film lubricated bearings, is then rewriten to suit the case of the electromagnetic bearing using the above equation, and we obtain:

$$\begin{aligned}&\left[(M+C_g)-\frac{K}{\Omega^2}-\frac{G(i\Omega)}{\Omega^2}\right]Z_f=-u\\ &\left[(M-C_g)-\frac{K}{\Omega^2}-\frac{\overline{G(-i\Omega)}}{\Omega^2}\right]Z_b=0\end{aligned} \tag{20}$$

In this way, an unbalance response analysis can be performed using the quasi-modal modal, Fig.5.

5. FREQUENCY RESPONSE ANALYSIS

Frequency response assumes inputting the electrical input En (n for nodal point) as a force. The matrix of a global system consisting of a rotor and a control circuit system is shown in Fig.6. The upper half of the figure corresponds to the equation for the rotor system, and the lower half to the state equation for the control circuit system. fn is a force working on the state equation, and includes En in its internal

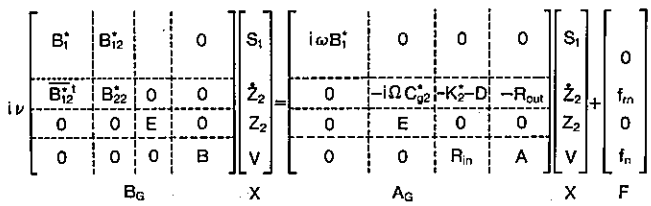

where,

$B_1^*=\omega^2\phi^t M_1\phi+\phi^t K_{11}\phi$ = diagonal matrix

$B_{12}^*=-i\{\omega\phi^t M_1\delta+\Omega\phi^t C_{g1}\delta\}$

$B_{22}^*=\delta^t M_1\delta+M_2-\Omega^2\xi_g^t C_{g1}\delta$

$K_2^*=k_{21}\delta+k_{22}$

$C_{g2}^*=k_{21}\xi_g+C_{g2}$

$\xi=i\Omega\xi_g$

Fig.6 Matrix Structure for Global System (Frequency Response Analysis)

portion.

The force, which is obtained from the output equation of the control circuit system, works as a reaction force to suppress the bearing vibration. For this reason, the portion corresponding to the bearing vibration has a minus sign as shown in Fig.6, before it is stored.

6. EXAMPLES OF NUMERICAL CALCULATION

6.1 Basic Characteristics of Analysis Model

The vertical rotor, shown in Fig.7, was used as the analysis model. A high frequency motor (No. 20) was located between the upper and lower electromagnetic bearings (No. 13 and 28). Thrust bearings were used for the rotor shaft.

To identify the basic characteristics of this rotor, the upper and lower electromagnetic bearings are replaced by spring constants, which are then used as parameters for indicating change in the natural frequency. The results are shown in Fig.8. The horizontal axis shows bearing stiffness,and the vertical axis shows frequencies. The frequencies shown are, from bottom up, 1st and 2nd rigid modes and 1st, 2nd, and 3rd bending modes. The shape of each mode is shown in the lower right corner of the figure.

Since the rated speed of this particular rotor is 300rps, the modes up to the 1st bending mode are covered in the control range, as seen in Fig.8. It is now necessary to adjust so that the 2nd bending mode and higher nodes will not vibrate.

The block diagram of a control circuit is shown in Fig.9. The basic structure comprises a PID circuit with proportional, integral and differential elements. In addition to the PID circuit, a notch filter and a low pass filter with cross stiffness are provided to stabilize the high and low frequency modes, respectively. Further, a tracking filter with cross stiffness is used to prevent resonance.

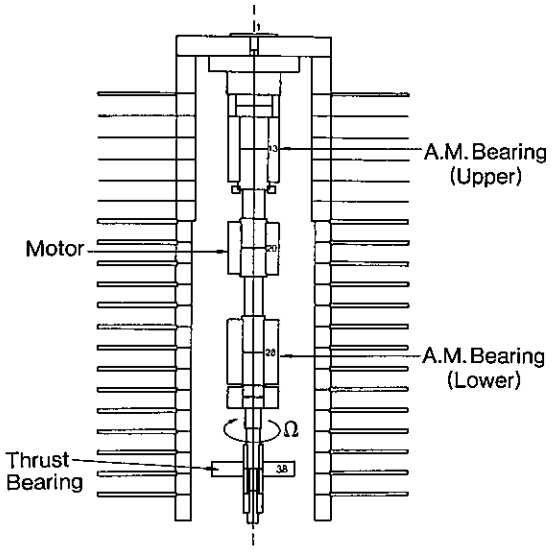

Fig.7 Calculation model

Simulations to rotate the rotor sutably up to the rated speed by using the added portions are performed. The results are discussed below.

6.2 Stabilization of High Frequency Mode

First, stabilization of high frequency mode is described referring to Fig.10. The Bode diagram of transfer characteristics of the PID circuit proper is shown in the upper part of Fig.10. The horizontal axis is for frequencies and the vertical axis for gain and phase. Regarding the phase, the hatched area indicates the phase-advance area, or generally stable area.

If the rotor is rotated using this PID circuit, higher modes (2nd and 3rd bending modes) enter the phase-delay area when the rotor reaches a certain rotational speed resulting in unstable operation. A notch filter was incorporated and the phase-advance area was enlarged in order to stabilize these modes. Cases 1 through 4 in Fig.10 indicate this process, and simply show the phase-advance and phase delay areas.

In case 1, the poles of the notch filter were set at 350Hz ($\zeta = 0.1$)

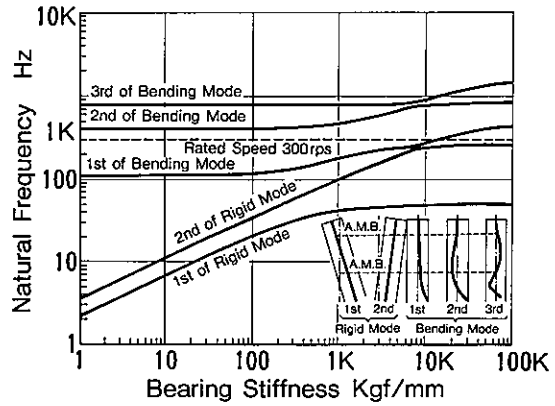

Fig.8 Relationship of natural frequency versus bearing stiffness

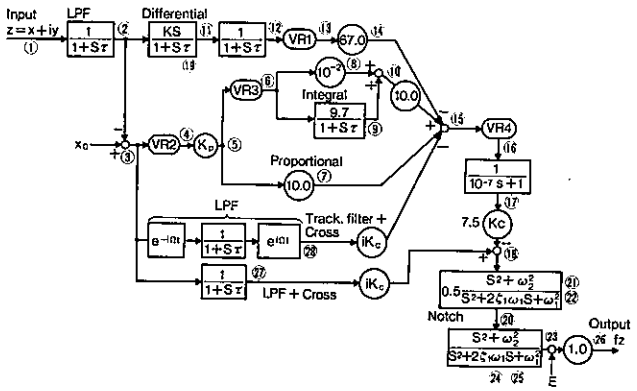

Fig.9 Network of controller (PID + Notch filter, LPF + Cross, Track. filter + Cross)

and 680Hz (ζ = 0.1). The phase-advance area was not large enough, and the modes of -346Hz and 954Hz were unstable. In cases 2 and 3 unstable modes were also observed. The range where all eigenvalues up to the rated speed would move was checked, and the frequency and damping ratio of the notch filter were adjusted so that the filter would cover all of these eigenvalues. As a result, the high frequency mode was stabilized as shown in case 4. Transfer characteristics of the control circuit proper in this instance are summarized in the Bode diagram shown in the bottom part of Fig.10.

6.3 Stabilization of Low Frequency Mode

Fig.11 shows the results of stability analysis made with the use of the PID circuit equiped with a notch filter and adjusted as discussed in Section 6.2. Rotational speed is shown in relation to the horizontal axis. The figure on the left side indicates the change in the each eigenvalue, while the figure on the right side shows the change in the damping ratio. The solid lines are for forward and the dashed lines for the backward mode. The first backward mode is unstable for rotational speed over 200 rps, as shown in the figure. To stabilized the mode, a low pass filter with cross stiffness was added to the control circuit. As a result of parameter adjustment, the first backward mode was improved as indicated by the dashed line pointed by the arrow, and the mode was now stable throughout the range of the rated speed.

6.4 Resonance Prevention

An example of unbalance response calculation is shown in Fig.12.

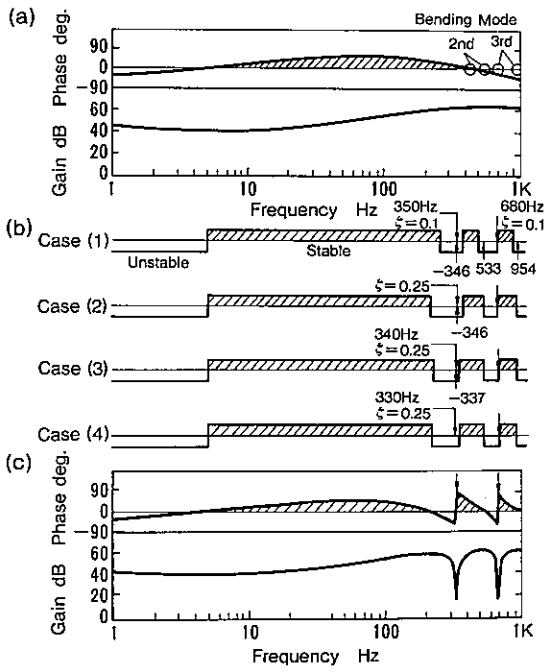

Fig.10 Stabilization of High Frequency Modes (Notch filter)

The horizontal axis is for rotational speed, against which the change in amplitude is shown. Unbalance quantities are shown in the figure. From this example, it is deduced that although the peak of the first bending mode appears around 170 rps, amplitude can be held at a low level by adjusting the value of tracking cross stiffness.

6.5 Frequency Response Analysis

Lastly Fig.13 shows a complete round of transfer characteristics obtained for the global system comprising the rotor and control circuit system. The figure shows the open loop characteristics of the lower rotor shaft. The horizontal axis is for frequency, as a function of which the change in gain and phase is shown. This example is for rotor speed of 0 rps. Generally, in a gain curve, the peak of the resonant point represents the eigenmode when the electromagnetic bearing is free, while the peak of the antiresonant point does so when the bearing is pin-fixed.

Fig.14 shows the open loop characteristics for rotor speed of 300 rps. Since these two examples are for the forward vibration, the position of the gain peak is moving toward the higher frequencies as the rotational speed increases.

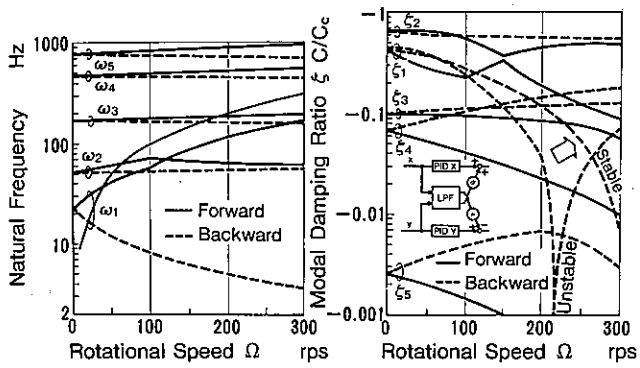

Fig.11 Stability Analysis (LPF + Cross Stiffness)

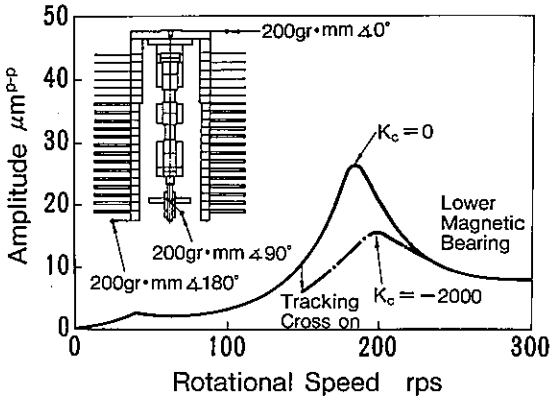

Fig.12 Unbalance Response and Cross Coupling Effect (Tracking filter + Cross Stiffness)

7. CONCLUSIONS

The above contents is summarized as follow.

(1) For the turning vibration of a rotor, forward transfer function G ($j\omega$) and backward transfer function G($-j\omega$) were introduced in the electronic circuit, and a differential euqation was established to couple the rotor and the electronic circuit.

(2) It is possible to analyze a cross circuit and tracking/tuning type circuit by expressing the transfer function G(s) of electronic circuit with a complex number.

(3) A force may be input at any desired point because the rotor system and electronic circuit system are meshed and assigned with nodal points by the finite element method. Further, output points may be freely changed to obtain transfer characteristics, because a sensor can be installed on any desired point.

(4) Stability analysis, unbalance response analysis and frequency response analysis were explained using examples.

8. REFERENCES

[1] O. Matsushita, et al 2;
Trans. of JSME Vol 48, No. 431C, (1982), p. 925 (in Japanese)

[2] O. Matsushita, et al 2;
Trans. of JSME Vol 47, No. 418C, (1981), p. 727 (in Japanese)

[3] O. Matsushita and M. Ida;
Trans. of JSME Vol 50, No. 452C, (1984), p. 626 (in Japanese)

[4] H. Saito;
Mechanical Vibration in Engineering, chapter 8, Yokendo (1982) (in Japanese)

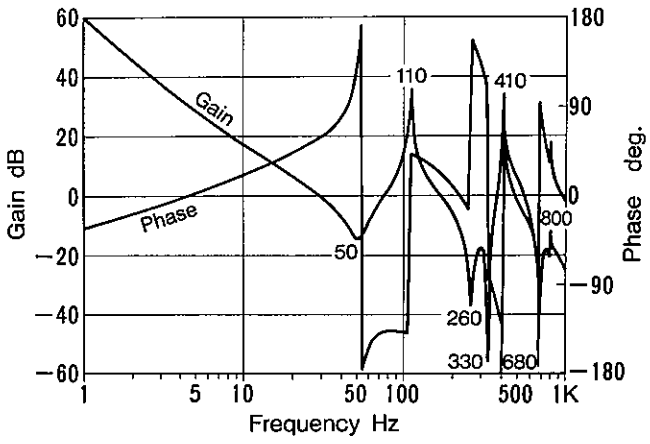

Fig.13 Overall transfer function (Lower X) 0rps

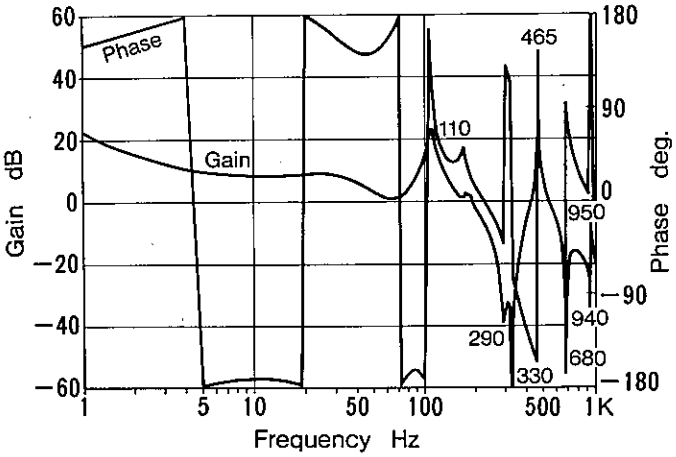

Fig.14 Overall transfer function (Lower X) 300rps

2nd International Symposium on Magnetic Beaing
July 12-14, 1990, Tokyo, Japan

Vibration Control of Magnetically Suspended Flexible Rotor by the Use of Optimal Regulator

S.AKISHITA* T.MORIMURA* S.HAMAGUCHI**

*Department of Mechanical Engineering, Ritsumeikan University,
Kita-ku, Kyoto 603, Japan
**NTN Corp. Iwata, Shizuoka 438, Japan

Abstract This paper proposes the application expansion of frequency shaped regulator to the vibration control of the flexible rotor supported by magnetic bearings. The dynamics of the flexible rotor is modeled as axi-symmetric slender shaft with FEM. The design method of the regulator containing the second order pre-filter of low-pass property is described applying the plant model of the flexible rotor and the radial magnetic bearings. The practical aspect of designing is examined for a flexible slender rotor of total length $520mm$. The regulator derived from the rotor model containing only two rigid-body modes proves effective for the vibration control of the rotor. The influence of the sampling rate of the controller and of the cut-off frequency of the filter are examined by the use of computer simulation.

1. INTRODUCTION

The use of magnetic suspension is increasing in its various forms with its proven high level of reliability, negligible maintenance and low energy consumption. The benefits come from the non-contact support which results in negligibly small friction and low vibration level of the supported body. Its use spreads from the high speed rail way vehicle to the rotational machinery. One of the most attractive advantages of the magnetic suspension is the applicability to the vibration control of the flexible suspended structure. The control system concerned with maintaining a floating gap is also applied to the vibration suppression. Modern machinery is apt to decrease of its weight and accordingly the stiffness. On the other hand the moving speed of the machinery consistently increases. These trends often result in the increase of the control band-width and the decrease of the natural frequency of the structure. Incidentally we are forced to solve the problem of the resonance between the structure and the control system.

In order to support a flexible rotor statbly by magnetic bearing, the suppressing of higher mode vibration else than two rigid-body mode is needed, although only four pairs of actuators are installed in magnetic suspension systems. This is a typical problem of spill-over avoidance in flexible structure. Direct feedback control[1] where colocated sensor signals are fed-back to actuators have been utilized. In a magnetic suspension system direct position feedback causes the positive spring and direct velocity feedback causes the damping effect. The design method of control systems concerns with assignment of the velocity feedback gains to the flexible vibration mode. The utilization of the pseudo inverse was proposed to determine the gain matrix to the excessive degrees of the mode[2,3].

A flexible rotor has other problems, the first of which is the variation of the natural frequencies with the rotational speed and the second of which is the estimation errors of those. One of reasonable and practical means to cope with the problems is the utilization of the controller which has low-pass property. Recently the design method of the frequency shaped optimal regulator was developed[4,5] and its application to flexible space structures was proposed[6]. The authors propose the expansion of its application to the flexible rotor suspended by magnetic bearing. The optimal regulator is designed to stabilize the two rigid-body modes which have the natural frequencies of null and its accurate mass property. For suppressing the flexible mode whirl which is not modeled at designing, the low-pass property of the the regulator is made use of.

In section 2 the modelling of the magnetic bearing and flexible rotor is described. The non-rotational model of the rotor is supposed. But we treat four-axis control type magnetic bearing as the model. Finite Element Method

(FEM) is adopted to represent the dynamics of the flexible rotor for its broad applicability. In section 3 the design method of the regulator is described, where multi-input multi-output control systems are supposed. In section 4 the practical aspect of the designing are designed; cut-off frequency in the filter and sampling rate in the digital controller. These are examined with computer simulation. The adequacy of the conroller designing is approved.

2. MODELLING

As mentioned above a 4-axis control type magnetic bearing is supposed in the paper. A schematical cross sectional view of the radical magnetic bearing is shown in Fig.1. One axis contorol magnet comprises a pair of coil-sand iron cores. The rotor center is displaced at x from its equilibrium position. The gaps in the left pole and the right pole are ξ_l and ξ_r respectivel. The atractive forces f_l,f_r generated in both sides are represented respectively by the currents i_l,i_r and the gaps as follows,

$$f_l = 0.5k_L(i_l/\xi_l)^2, \qquad f_r = 0.5k_L(i_r/\xi_r)^2 \tag{1}$$

$$k_l = \frac{\mu_0}{2}NA \tag{2}$$

where μ_0 is the magnetic permeability of free space , N the turn number in the coil and A the surface area in the pole. The common coefficient k_L is assumed between both electro-magnets . As the gaps at the equilibrium position are common such as $\xi_l = \xi_r = \xi_0$, the non-equilibrium gaps ξ_l and ξ_r are represented as follows,

$$\xi_l = \xi_0 + x, \qquad \xi_r = \xi_0 - x \tag{3}$$

Then the currents in both gaps are assumed as in the following equations.

$$i_l = i_0 + x, \qquad i_r = i_0 - x \tag{4}$$

where i_0 is the common bias current between both coils. The currents are meaningful only when they are positive. The resultant force F composed of f_l and f_r are deduced as follows,

$$F = -f_l + f_r = -\frac{k_L}{2}\left(\frac{i_0+i}{\xi_0+x}\right)^2 + \frac{k_L}{2}\left(\frac{i_0-i}{\xi_0-x}\right)^2 \tag{5}$$

The coil currents i_l,i_r are governed with the input voltages v_l,v_r across the coil by the following relations

$$\begin{cases} K_{cl}v_l = (i_l - i_0)R_{cl} + \frac{d}{dt}(L_l i_l) \\ K_{cr}v_r = (i_r - i_0)R_{cr} + \frac{d}{dt}(L_r i_r) \end{cases} \tag{6}$$

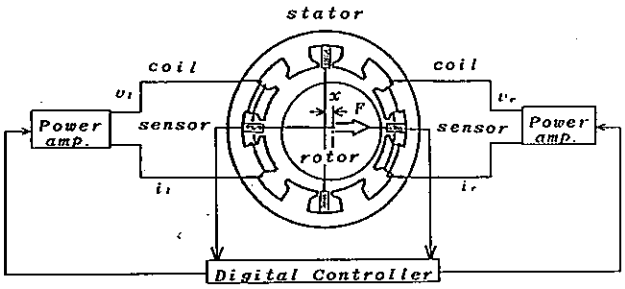

Fig.1 Cross sectional view of radial magnetic bearing

where

$$L_l = k_L/\xi_l, \qquad L_r = k_L/\xi_r \tag{7}$$

and, K_{cl} and K_{cr} are the voltage gains in the power amplifiers, R_{cl} and R_{cr} the resistances in both side coils. When the common voltage gains in the power amplifiers and the common resistances in the coils are assumed as,

$$K_c = K_{cl} = K_{cr} \tag{8}$$

$$R_c = R_{cl} = R_{cr} \tag{9}$$

Equation(6) is approximated as in the following, after the linearized expansion of ξ_l, ξ_r, i_l and i_l around their equilibrium conditions are introduced.

$$\begin{cases} K_c v_l = & R_c i & + \frac{k_L}{\xi_0}\dot{i} - \frac{k_L i_0}{\xi_0^2}\dot{x} \\ K_c v_r = & -R_c i & - \frac{k_L}{\xi_0}\dot{i} + \frac{k_L i_0}{\xi_0^2}\dot{x} \end{cases} \tag{10}$$

As v_l and v_r are correlated with each other, single variable v represents both variables as follows,

$$v = v_l = -v_r \tag{11}$$

when the coil current lag time, $T_0 = k_l/\xi_0 R_c$ is sufficiently short compared with the other dynamical characteristic time, we can simplify Eq.(10) as follows,

$$i = (K_c/R_c)v + (k_{Li}/R_c)\dot{x} \tag{12}$$

where k_{Li} is defined as follows,

$$k_{Li} = k_L(i_0/{\xi_0}^2) \tag{13}$$

The resultant force F can be approximated by using the similar linearization as follows,

$$F = -2k_{Li}i + 2k_{Lx}x \tag{14}$$

where k_{Lx} is defined as follows,

$$k_{Lx} = k_L({i_0}^2/{\xi_0}^3) \tag{15}$$

The bending motion of a flexible rotor is described by utilizing FEM. An axi-symmetric rotor is devided into n

components. The center point of i-th component is on $P(x_i, y_i)$ as shown in Fig.2. We assume that y_i is time-invariant. x_i means the radial displacement and it is represented as follows,

$$x_i = x_c + y_i\theta + w_i \tag{16}$$

where x_c is the displacement of the center of the gravity of the rotor, θ is the tilting angle of the rigid body mode, and w_i is defined as follows,

$$w = [x_c, \theta, w_1, w_2, \cdots, w_n]^T \tag{17}$$

The equation of the rotor motion is represented by the following,

$$M\ddot{w} + Kw = B^{'}f \tag{18}$$

where M and K are the mass matrix and the stiffness matrix respectively. We should note that the dynamics of rotation is not considered in this paper. f is the force vector composed of the magnetic forces f_u, f_l at the upper bearing and the lower bearing respectively , as shown in the following equation.

$$f = [f_u, f_l]^T \tag{19}$$

Then, matrix $B^{'}$ is represented as follows,

$$B'^T = \begin{matrix} \\ \\ \end{matrix} \begin{matrix} & & & & (i_u) & & (i_l) & \\ \end{matrix} \begin{bmatrix} 1 & y_u & \cdots & 1 & \cdots & 0 & \cdots \\ 1 & y_l & \cdots & 0 & \cdots & 1 & \cdots \end{bmatrix} \tag{20}$$

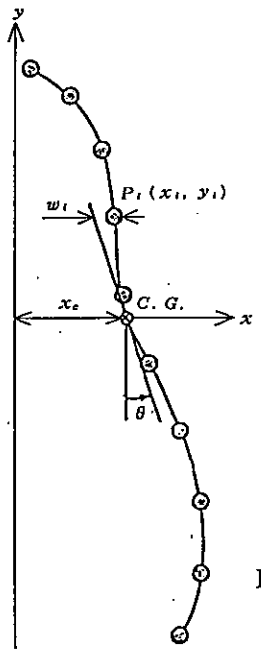

Fig.2 FEM model of flexible rotor

where y_u and y_l mean the y coordinate of the upper bearing and the lower bearing respectively, and they are on i_u component and on i_l component respectively. We transfer variable w to q with transfer matrix P as follows,

$$w = Pq \tag{21}$$

Then Eq.(18) is transferred to the decoupled equation as follows,

$$\ddot{q} + Lq = B_1 f \tag{22}$$

$$\begin{cases} L = diag.(0, 0, w_1^2, w_2^2, \cdots, w_n^2) \\ B_1 = P^T B^{'} \end{cases} \tag{23}$$

Eq.(22) is applied to the computer simulation reserving the non-linearity in f_u and f_l represented by Eq.(5). But for designing the controller the linearly approximated equations, Eq.(12) and Eq.(14), are introduced. Then, Eq.(22) is transformed to the standard equation of the state retaining m flexible mode variables as follows,

$$\dot{x} = Ax + Bu \tag{24}$$

x is the state variable redefined as follows,

$$x = [x_c, \theta, q_1, \cdots, q_m, \dot{x_c}, \dot{\theta}, \dot{q_1}, \cdots, \dot{q_m}]^T \tag{25}$$

u is the input variable composed of the input voltages of the power amplifiers as follows,

$$u = [v_u, v_l]^T \tag{26}$$

Matrix A and B are rearranged as follows,

$$A = \begin{bmatrix} 0_m & \vdots & I_m \\ \cdots & \cdot & \cdots \\ A_1 & \vdots & A_2 \end{bmatrix} \tag{27}$$

$$A_1 = L_m + 2k_{Lx}\Phi B_{1m}^T$$
$$A_2 = (-2k_{Li}^2/R_c)\Phi B_{1m}$$

$$\Phi^T = \begin{bmatrix} P_{u1} & P_{u2}, & \cdots & , P_{um} \\ P_{l1} & P_{l2}, & \cdots & , P_{lm} \end{bmatrix} \tag{28}$$

$$B = -\frac{2k_{Li}K_c}{R_C}\begin{bmatrix} 0 \\ \cdots \\ B_{1m} \end{bmatrix} \tag{29}$$

where Φ is the mode shape matrix at magnetic bearings. The outputs of the system are the displacements of the center of i_u-th component and i_l-th component, as the colocation of the sensors and the actuators are assumed. The output equation is represented as follows,

$$y = Cx \tag{30}$$

$$C = \left[\Phi^T \ \vdots \ 0 \right] \tag{31}$$

3. CONTROL BY THE OPTIMAL REGULATOR

Imagine that the equilibrium of the flexible rotor suspension breaks down by some disturbance. Optimal regulator is utilized as the controller to restore the equilibrium and to maintain the stability of rotor suspension. When a plant model is represented by Eqs.(24) and (30), the following performance index J made up of an integral of quadrant forms is introduced.

$$J = \int_0^\infty [x^T C^T C x + u^T R^T R u] dt \tag{32}$$

On designing the conventional regulator R is time- invariant matrix independent upon angular frequency. The system input u is determined as $u = -kx$ so that the index J may be minimized. As R decreases, the higher gain and the frequency band-width pertains the controller. But if the model becomes obscure especially at high frequency range, the control system tends to unstable. For flexible rotor suspension systems some mode frequencies increase with the rotational speed. In order to preserve the robustness of the controller from the high-frequency uncertainty in the system model, we apply the optimal regulator reulting from frequency-shaped weight matrix. Equation (32) is transformed by using Perseval's theorem as follows,

$$J = \frac{1}{2\pi} \int_{-\infty}^{+\infty} \left[||Cx(i\omega)||^2 + ||Ru(i\omega)||^2 \right] d\omega \tag{33}$$

While C is assumed as time-invariant in the paper, R is treated as frequency-dependent as follows,

$$R^{-1}(i\omega) = \begin{bmatrix} r_{11}^{-1}(i\omega) & 0 \\ 0 & r_{22}^{-1}(i\omega) \end{bmatrix} \tag{34}$$

where $r_{11}^{-1}(i\omega)$ and $r_{22}^{-1}(i\omega)$ are defined as follows,

$$\begin{cases} r_{11}^{-1}(i\omega) = \omega_{01}^2/(s^2 + 2\zeta_{01}\omega_{01}s + \omega_{01}^2) \\ r_{22}^{-1}(i\omega) = \omega_{02}^2/(s^2 + 2\zeta_{02}\omega_{02}s + \omega_{02}^2) \end{cases} \tag{35}$$

$r_{11}^{-1}(i\omega)$ and $r_{22}^{-1}(i\omega)$ represent the low-pass property of 2nd order filter. ω_{01} and ω_{02} are the cut-off frequencies for u_l and u_r respectively. We introduce $v(i\omega)$ repersented as follows,

$$v(i\omega) = R(i\omega)u(i\omega) \tag{36}$$

From Eq.(34) it can be inferred that $R^{-1}(i\omega)$ represents the transfer matrix of low pass filter. Therefore, $v(i\omega)$ and $u(i\omega)$ are the input and output of low-pass pre-filter respectively, as shown in Fig.3(a). New state variable z is introduced to represent the internal description of the pre-filter as follows,

$$\dot{z} = A_F z + B_F v \tag{37}$$

$$u = C_F z \tag{38}$$

$$z = [z_1, z_2, \dot{z}_1, \dot{z}_2] \tag{39}$$

where A_F and B_F are represented as follows,

$$A_F = \begin{bmatrix} 0 & \vdots & I \\ \cdots & \cdot & \cdots \\ -D_1 & \vdots & -2G \end{bmatrix} \tag{40}$$

$$\begin{cases} C_1 = diag.(\zeta_{01}\omega_{01}, \zeta_{02}\omega_{02}) \\ D_1 = diag.(\omega_{01}^2, \omega_{02}^2) \end{cases}$$

$$B_F = \begin{bmatrix} 0 \\ \cdots \\ D_1 \end{bmatrix} \ (41), \qquad C_F^T = \begin{bmatrix} I \\ \cdots \\ 0 \end{bmatrix} \ (42)$$

In order to construct the closed-loop of the extended system shown in Fig.3(a), we introduce the extended state variable $\bar{x}$ as follows,

$$\bar{x}^T = \left[x^T \ \vdots \ z^T \right] \tag{43}$$

The state equation of the extended system is represented as follows,

$$\dot{\bar{x}} = \bar{A}\bar{x} + \bar{B}v \tag{44}$$

where $\bar{A}$ and $\bar{B}$ are represented as follows,

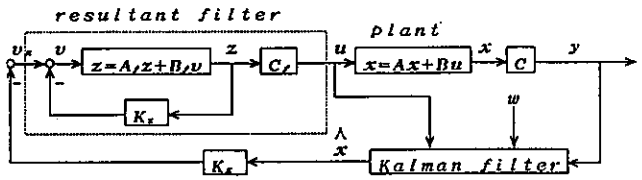

(a) extended system with prefilter

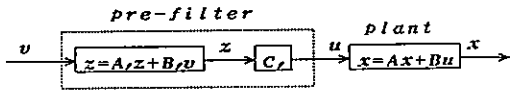

(b) closed-loop of frequency shaped regulator

Fig.3 Block diagram

$$\bar{A} = \begin{bmatrix} A & \vdots & BC_F \\ \cdots & \cdot & \cdots \\ 0 & \vdots & A_F \end{bmatrix} \quad (45), \qquad \bar{B} = \begin{bmatrix} 0 \\ \cdots \\ 0 \end{bmatrix} \quad (46)$$

Introducing the output matrix $\bar{C}$, which is time-invariant, as follows,

$$\bar{C} = \begin{bmatrix} C & \vdots & 0 \end{bmatrix} \quad (47)$$

the output equation of the extended system is represented as follows,

$$\bar{y} = \bar{C}\bar{x} \quad (48)$$

We can rearrange Eq.(33) for the extended system with new variables as follows

$$J = \frac{1}{2\pi}\int_0^\infty [||\bar{C}\bar{x}(i\omega)||^2 + ||v(i\omega)||^2]d\omega \quad (49)$$

after applying Parseval's theorem again, J is rewritten in time-domain as follows,

$$J = \int_0^\infty [\, \bar{x}^T\bar{C}^T\bar{C}\bar{x} + v^2 \,]dt \quad (50)$$

Since $\bar{x}$ and v are related with time-invariant weighting matrix($\bar{C}^T\bar{C}$ and I), the feedback gain can be determined with conventional design method for regulators as follows,

$$v = -\bar{B}^T P\bar{x} = -K_x x - K_z z \quad (51)$$

where P is determined from Ricatti's equation shown as follows,

$$\bar{A}^T P + P\bar{A} - P\bar{B}\bar{B}^T P + \bar{C}^T\bar{C} = 0 \quad (52)$$

As the controllability and observability of A, B and matrices are assumed for plant, the extended systems of $\bar{A}$, $\bar{B}$ and $\bar{C}$ can be stabilized.Then closed-loop of the frequency shaped regulator is composed as shown in block diagram of Fig.3(b). As the reduced oder model is applied for the plant, the output of the model contain the residual error w. Therefore Kalman filter is applied to estimate the state variable $\hat{x}$.

4. VIBRATION CONTROL ON FLEXIBLE ROTOR

We are discussing the practical aspect of the controller designing. The object is schematically shown in Fig.4. The slender rotor, which has a large disc in the midst, is suspended by an axial magnetic bearing and is supported radially by four radial magnetic bearings; the two at the upper end and other two at the lower position.

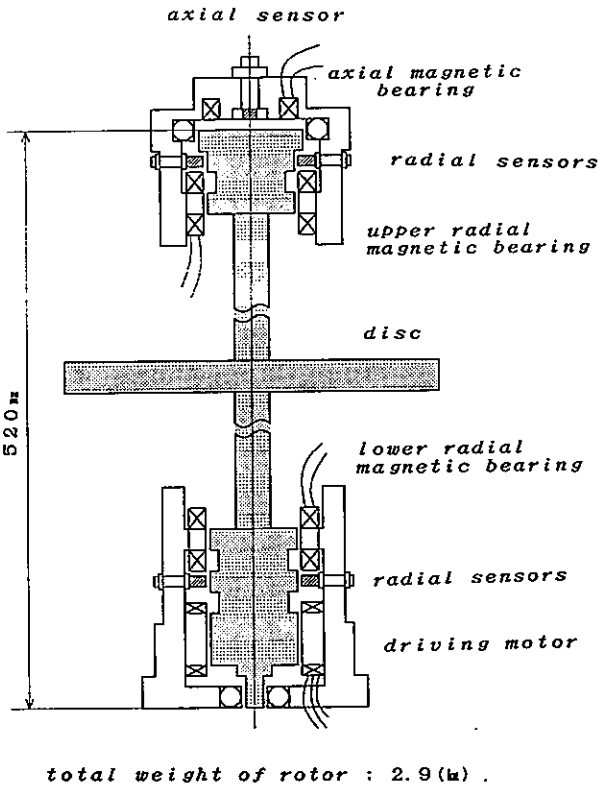

Fig.4 Schmatical cross-sectional view of 4-axis controlled magnetic bearing and suspended flexible rotor

The total length of rotor is about $520mm$ and its weight is about $3.0kg$ including a large disc. The rotor is modeled with FEM. The computational results of mode shape are shown in Fig.5. The first natural frequency of bending is $52Hz$. As the rotor is divided into 15 components, totally 15 eigen frequencies and eigen vectors are derived. But taking their significance and accuracy into consideration, first four modes are reserved at the computer simulation.

First designing of the frequency shaped regulator is executed by using the flexible rotor dynamics model which has two-rigid body modes and first two flexible modes. In case of the low-pass filter of $\omega_{01} = \omega_{02} = 251.3$ ($f_0 = 40Hz$) and $\zeta_{01} = \zeta_{02} = 0.5$ matrix $\bar{A}$, $\bar{B}$ and $\bar{C}$ are shown as in Appendix.The gap length $\xi_0 = 0.5\ mm$ and the bias current of the coil $i_0 = 0.5\ amp.$ are assumed for the magnetic bearing. Applying these matricies, gain matrix K of the regulator for extended systems are derived by using MATLAB toolbox as follows,

$$K_x = \begin{bmatrix} 63130 & -83420 & 2019 & 165.3 \\ 56810 & 47160 & -176.6 & 373.8 \\ 566.4 & -728.7 & 12.46 & -0.1210 \\ 653.7 & 521.4 & -11.50 & 0.2828 \end{bmatrix}$$

$$K_z = \begin{bmatrix} 1.219 & -0.0203 & 0.0034 & -0.00005 \\ -0.0202 & 0.9000 & -0.00005 & 0.0027 \end{bmatrix} \quad (53)$$

The pole locations of the closed loop for the plant are derived from the eigen values of matrix $(A - BK_x)$ as shown in table.1.

$$\begin{cases} -1.269e-02 \pm 1.553e+03\ i \\ -1.794e-02 \pm 3.065e+02\ i \\ -2.386e+02 \\ -8.816e+01 \\ -1.605e+02 \\ -1.134e+02 \end{cases}$$

table.1

The adequacy of the regulator is proven with the computer simulation as shown in Fig.6 (a). The intial condition on the simulation is given, where the center of the rotor is displaced by $0.15mm$ (conically) and the input voltage is zero. On the simulation the sampling rate of the controller including the pre-filter can be given else than the simulation time division of Runge-Kutta solver. In this case the controller sampling rate $\Delta T = 0.5\ msec$ is assumed. Fig.6 (b) shows the variation of the input voltage of the upper electro-magnets. At the start of the simulation $x = 0.15\ mm$ and then the rotor is applied the attracting force to increase the displacement, while the input voltage of the electro-magnet does not rise. The rotor moves to the direction where the displacement enlarges till the input-voltage rises sufficiently and the restoring force rises at the pair of electro-magnets. After the controller works effectively the rotor is settled down at the equilibrium point within about 0.05 *msec*.

Further designing of the regulator is tried on the basis of simplest rotor dynamic model that contains only two rigid-body modes. The derived gain matrix K_x for regulator is shown as follows,

$$K_x = \begin{bmatrix} 63120 & -83400 & 566.6 & -728.9 \\ 56811 & 47160 & 653.6 & 521.5 \end{bmatrix} \quad (54)$$

where the same low-pass filter as the above is assumed. Comparing the gain matrix with that shown in Eq.(53) we find that the components for the rigid-body mode state variables are almost common between both gain matrices.

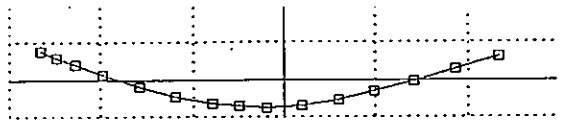

(a) 1st mode; 52 Hz

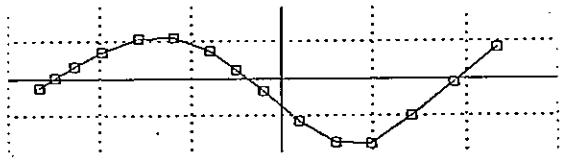

(b) 2st mode; 247 Hz

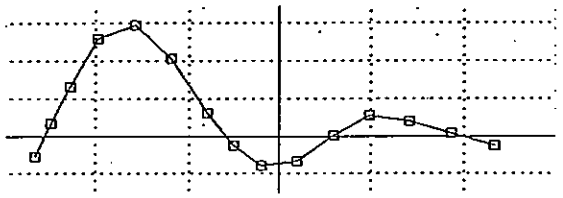

(c) 3st mode; 553 Hz

Fig.5 Mode shape of flexible rotor (FEM)

On the other hand, as the longer sampling rate in the controller is favourable, the computer simulation is excuted for the controller of the gain matrix of Eq.(54) assuming the sampling rate $\Delta T = 2\ msec$. We can find from Fig.7 that the stabilized rotor motion is assured though the settling time elongates compared with the case shown in Fig.6 (a). The influence of the filter cut-off frequency is interesting. The simulation result is shown in Fig.8 for cut-off frequency $f_0 = 25\ Hz$ and the same sampling rate. The rotor motion is stabilized not only for the initial displacement but also for the disturbace of 80 Hz imposed on $t = 0.20\ sec$ during one fouth of its period. We should add that for the longer sampling rate $\Delta T = 3\ msec$, the controller is effective. As the cut-off frequency f_0 decreases, the lag time at the input voltage rise increases and finally the rotor fails in restoring the equilibrium condition. A typical sample for the case of $f_0 = 10\ Hz$ is shown in Fig.9 (a) (b).

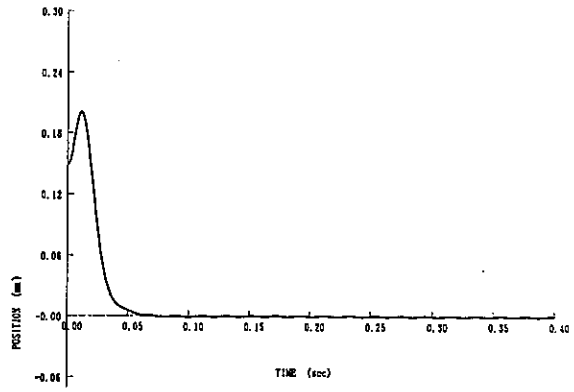

(a)rotor displacement

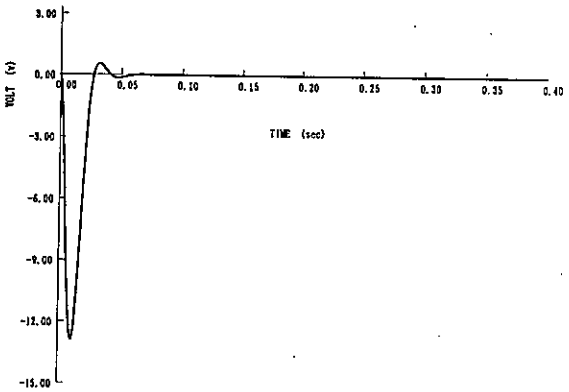

(b)input voltage

Fig.6 Vibration control by the regulator
$f_0 = 40\ Hz, \quad \Delta T = 0.5\ msec$

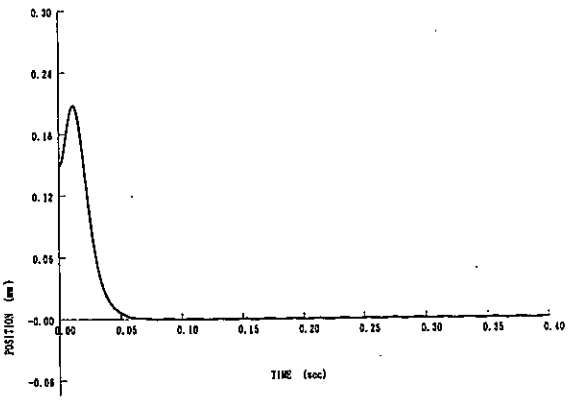

Fig.7 Vibration control by the regulator designed on the simplest model; rotor displacement
$f_0 = 40\ Hz, \quad \Delta T = 2.0\ msec$

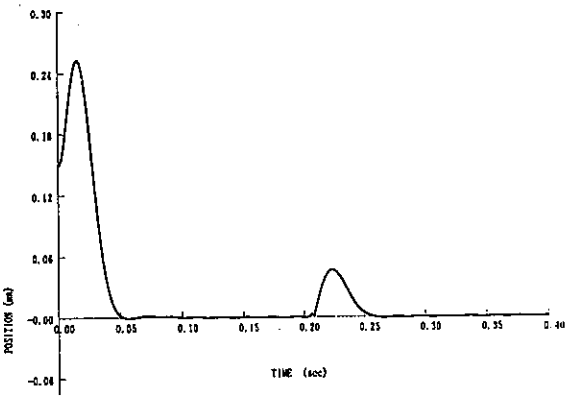

Fig.8 Vibration control by the regulator; rotor displacement
$f_0 = 25\ Hz, \Delta T = 2.0\ msec$

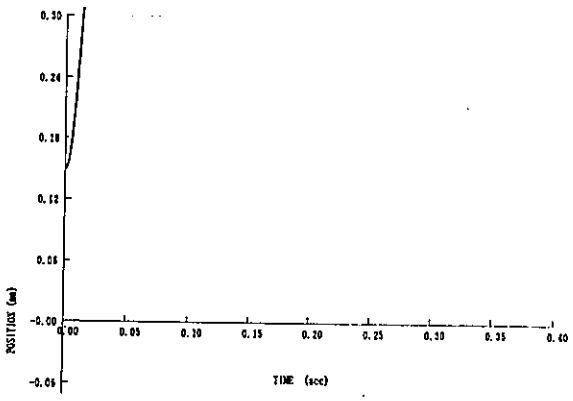

(a) rotor displacement

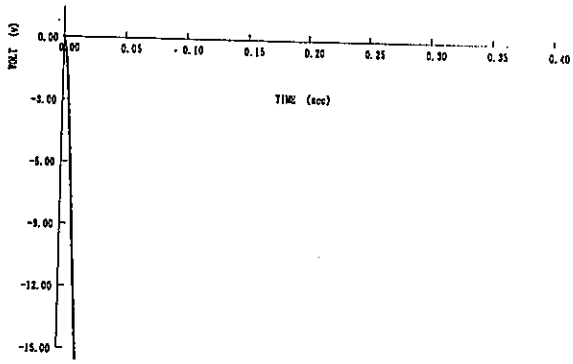

(b) input voltage

Fig.9 Vibration control by the regulator;
$f_0 = 10\ Hz, \Delta T = 2.0\ msec$

5. CONCLUSION

The effectiveness of the regulator containing the pre-filter of low pass property was verified for suppressing the vibration of the flexible rotor supported by magnetic bearings by using computer simulation. The regulator was derived from the rotor model containing only two rigid-body modes. The influences of the controller sampling rate and of the cut-off frequency of the pre-filter were examined. We can conclude that the frequency shaped regulator is applicable for controlling the flexible rotor support by magnetic bearigs, even if the accurate dynamic models of the flexible modes are not accessible. The regulator applicability will be verified on the experiment of the systems at near future.

REFERENCE

1. M.J.Balas, "Feed-back Control of Flexible System ", IEEE Transactions on Automatic Control, Vol.AC-23, No.4, pp.673, 1978
2. J.R.Salm, "Active Electromagnetic Suspension of an Elastic Rotor; Modelling, Control and Experimental Results ", Transactions of the ASME, Journal of Vibration, Acoustics, Stress and Reliability in Design", Vol.110, pp.493, 1988.
3. S.Akishita and K.Hayashi, "Vibration Control on Magnetically Suspended Flexible Beam ", the 1990 ASME Computers in Engineering Meeting in Boston, (to appear).
4. N.K.Gupta, "Frequency-Shaped Cost Functionals: Extension of Linear-Quadratic-Gaussian Design Methods ", Journal of Guidance and Control, Vol.3, No.6, pp.529, 1980.
5. B.D.O.Anderson and D.L.Mingori, "Use of Frequency Dependence in Linear Quadratic Control Problems to Frequency-Shape Robustness ", Journal of Guidance and Control, Vol.8, No.3, pp.447, 1985.
6. T.Kida, M.Ikeda and I.Yamaguchi, "Optimal Regulator with Low-Pass Property and Its Application to LSS Control ", Transactions of the Society of Instrument and Control Engineers, Vol.25, No.4, pp.448, 1989, (in Japanese).

APPENDIX

$$\bar{A} = \begin{bmatrix}
0.0 & 0.0 & 0.0 & 0.0 & 1.0 & 0.0 & 0.0 & 0.0 & 0.0 & 0.0 & 0.0 & 0.0 \\
0.0 & 0.0 & 0.0 & 0.0 & 0.0 & 1.0 & 0.0 & 0.0 & 0.0 & 0.0 & 0.0 & 0.0 \\
0.0 & 0.0 & 0.0 & 0.0 & 0.0 & 0.0 & 1.0 & 0.0 & 0.0 & 0.0 & 0.0 & 0.0 \\
0.0 & 0.0 & 0.0 & 0.0 & 0.0 & 0.0 & 0.0 & 1.0 & 0.0 & 0.0 & 0.0 & 0.0 \\
8974 & -2214 & 818.5 & 465.0 & -4.395 & 1.084 & -0.401 & -0.228 & 0.227 & 0.227 & 0.0 & 0.0 \\
-2203 & 10650 & -1267 & 786.6 & 1.079 & -5.217 & 0.621 & -0.385 & -0.297 & 0.186 & 0.0 & 0.0 \\
409.1 & -634.1 & -93910 & -26.31 & -0.200 & 0.311 & -0.046 & 0.013 & 0.023 & -0.002 & 0.0 & 0.0 \\
232.4 & 393.1 & -26.31 & -2412300 & -0.114 & -0.192 & 0.013 & -0.026 & -0.0049 & 0.017 & 0.0 & 0.0 \\
0.0 & 0.0 & 0.0 & 0.0 & 0.0 & 0.0 & 0.0 & 0.0 & 0.0 & 0.0 & 1.0 & 0.0 \\
0.0 & 0.0 & 0.0 & 0.0 & 0.0 & 0.0 & 0.0 & 0.0 & 0.0 & 0.0 & 0.0 & 1.0 \\
0.0 & 0.0 & 0.0 & 0.0 & 0.0 & 0.0 & 0.0 & 0.0 & -63170 & 0.0 & -251.3 & 0.0 \\
0.0 & 0.0 & 0.0 & 0.0 & 0.0 & 0.0 & 0.0 & 0.0 & 0.0 & -63170 & 0.0 & -251.3
\end{bmatrix}$$

$$\bar{B} = \begin{bmatrix}
0.0 & 0.0 \\
0.0 & 0.0 \\
0.0 & 0.0 \\
0.0 & 0.0 \\
0.0 & 0.0 \\
0.0 & 0.0 \\
0.0 & 0.0 \\
0.0 & 0.0 \\
0.0 & 0.0 \\
0.0 & 0.0 \\
63165 & 0.0 \\
0.0 & 63165
\end{bmatrix}, \quad \bar{C}^T = \begin{bmatrix}
0.5803 & 0.5803 \\
-0.7592 & 0.4729 \\
0.1179 & -0.0121 \\
-0.0248 & 0.0850 \\
0.0 & 0.0 \\
0.0 & 0.0 \\
0.0 & 0.0 \\
0.0 & 0.0 \\
0.0 & 0.0 \\
0.0 & 0.0 \\
0.0 & 0.0 \\
0.0 & 0.0
\end{bmatrix}$$

2nd International Symposium on Magnetic Beaing
July 12-14, 1990, Tokyo, Japan

Active Vibration Control of Flexible Rotor for High Order Critical Speeds using Magnetic Bearings

K. Nonami and H. Yamaguchi

Fuculty of Engineering, Chiba University
1-33 Yayoi-cho,Chiba 260, Japan

Abstract

Experimental reseach tests were performed by means of active magnetic bearings to actively control the rotor vibrations of a very flexible rotor mounted on ball bearings. The purpose of this test is to verify the efficiency of magnetic bearing for higher order critical speeds. Therefore, we have used a slender shaft without balancing. We have located two magnetic bearings between two conventional bearings. The direct output feedback control is realized by a digital controller of DSP. Also we have used variable feedback gains and on-off control for large amplitudes. Though it was impossible to pass the some critical speeds without magnetic bearings, we can pass four critical speeds with safety when magnetic bearings are working.

1.Introduction

Active vibration control of flexible rotors can be divided into two types on the basis of the actuators as shown in Fig.1. Type 1 uses electromagnetic actuators or magnetic bearings that apply control forces to a rotating shaft and do not contact the shaft. Type 2 uses linear actuators that contact conventional bearing housings.

For type 1 controls a flexible rotor is supported by conventional bearings, and magnetic bearings or electromagnetic actuators are used only for active vibration control. Let us briefly survey the literature for type 1 controls. Burrows and Sahinkaya(1987,1988) and Redmond et al.(1985) have shown the results of active vibration control at the first critical speed with digital controllers. Allaire et al.(1986) and Kasarda et al.(1988) investigated the efficiency of active vibration control at the first critical speed by varying the location of the magnetic bearing. Bradfield et al. (1986) and Nagai et al.(1986) have tried active digital vibration control of rotating-shaft flexural vibration at the first bending mode. Bradfield et al.(1989) have done a programmable electromagnetic force control using variable feedback gains for the first critical speed. Nikolajsen et al.(1979) have presented experimental active vibration control data of a marine transmission shaft that correlate very well with theoretical data. Matsushita et al.(1987) studied liquid stabilization of unstable rotors. Most of these controls use type 1 actuators to apply control forces and are therefore limited in their ability to control higher order vibration modes. Note that all of these papers address active control at the first critical speed. It is of interest to provide active control not only at the first critical speed but also the higher order critical speeds. However we can not see the reports up to this time that the resonances at higher order critical speeds are well controlled.

Several investigators have done research in active vibration control with type 2 actuators. Stanway et al.(1981,1984) considered controllability and conducted a simulation by using state feedback. Moore et al.(1980) and Lewis et al.(1982) used transfer functions to analyze a control system and discussed the effect of velocity feedback based on an experimental study with horn speakers. Nonami has presented the experimental active control results of a Jeffcott rotor with an optimal regulator(1985) and the active control of a multibearing-disk rotor from simulations and experiments by means of quasi-modal control(1986,1988a,1988b). Also Nonami et al. have recently presented excellent data of unbalance force cancellation using feedforward control(1989a) and active vibration control of flexible rotor with eight critical speeds by direct output feedback control(1989b). Ulbrich (1986, 1987) and Fuerst et al.(1988) have evaluated the efficiency of various control rules by using a test rotor on actively controlled supports. Palazzoro et al.(1988, 1989) demonstrated active vibration control by using piezoelectric actuators to apply control forces to bearing housings.

Most papers on type 2 actuators describe the characteristics of vibration control near the second critical speed and higher order modes and show effective vibration control of the higher order modes. Type 2 actuators are more effective in controlling higher order modes because two actuators are used (one at each bearing housing) whereas only one type 1 actuator (magnetic bearing), located between the two conventional bearings, is ordinarily used. Also type 2 actuators generally have greater force capability than type 1. Therefore the higher order modes can be controlled. Generally speaking, electrodynamic force actuators(type 2 actuators) are superior to the electromagnets of magnetic bearings as actuators for vibration control because it is easier to generate the desired control force with type 2 actuators. Also, type 2 actuators are not plagued with the eddy current loss and residual magnetism inherent in magnetic bearings. This enables simpler control system design. A major drawback of the type 2 actuator is the possible coupling of motion when the actuators are mounted at 90° to each other. Hence the motion must be uncoupled by providing a link between the bearing housing and the actuator. This link must have very high longitudinal stiffness and very low lateral stiffness. Also the actuator is larger than magnetic bearing in general. The ideal concept for active control is a flexible rotor supported by only actively controlled magnetic bearings because this concept employs the advantages of both types.

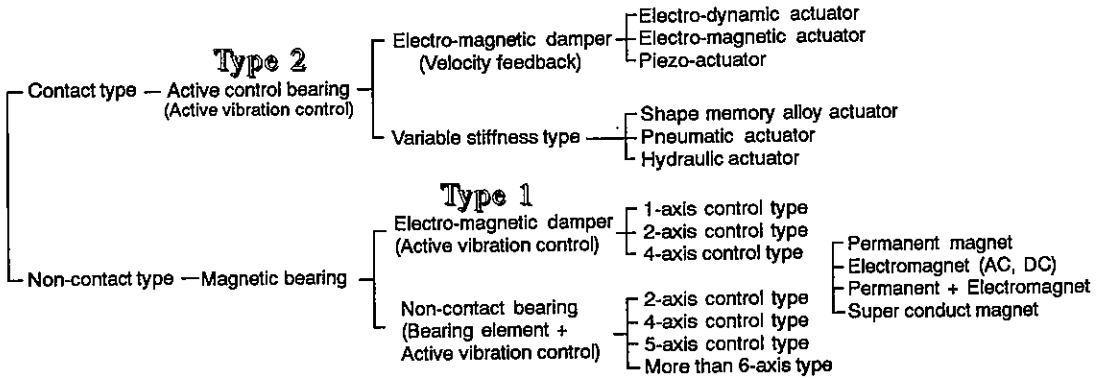

Fig.1 Classification of rotor control method based on control device

The purpose of this study is to verify the capability of magnetic bearing as active control actuator for higher order bending modes. Therefore, we have used a slender and very flexible shaft without balancing supported by ball bearings which has four bending critical speeds under 100 Hz. We have located two magnetic bearings between the two conventional ball bearings. It is difficult to realize a control system with full-state feedback for a flexible rotor that takes into account the higher order modes. Therefore we must utilize a control system with direct output feedback for magnetic bearings. The direct output feedback control is realized by a digital controller of DSP. Also we have used variable feedback gains depending on rotating speeds and have used on-off control algorithm for very large amplitudes. As the results, the active vibration control efficiency has been experimentally verified.

2. Test Rig

The test rig used for the active control experiments is schematically shown in Fig.2. The flexible steel shaft is 10 mm in diameter and 940 mm long and has nine disks of 67 mm diameter. Each disk is 20 mm thick and each mass is 0.5 kg. The total mass of the flexible rotor is approximately 5 kg. The shaft is supported by 10 mm single row, deep-groove ball bearings. The bearing span is 800 mm. The shaft is connected to the high frequency driving motor of 1.5 kW by a flexible coupling. Two active magnetic bearings located between two ball bearings apply control forces to the shaft. The gap between the electromagnets and the disk is about 1.5 mm. The touch down bearings protect in an emergency when the amplitudes exceed about 1.2 mm. The shaft displacements measured by optical sensors are measured as close as possible to the magnetic bearings. These signals are the inputs for the digital controller consisted of DSP through 8 channel analog-digital converter. After the computation of control signals based on the algorithm of Fig.5, the output signals from the DSP is supplied to the magnetic bearings through 8 channel digital-analog converter and power amplifiers.

3. Experimental Modal Analysis and FEM Analysis

An experimental modal analysis of the flexible rotor system was performed with a two channel FFT analyzer. Figure 3 shows one of transfer function when two magnetic bearings are working. Figure 4 shows the mode shapes

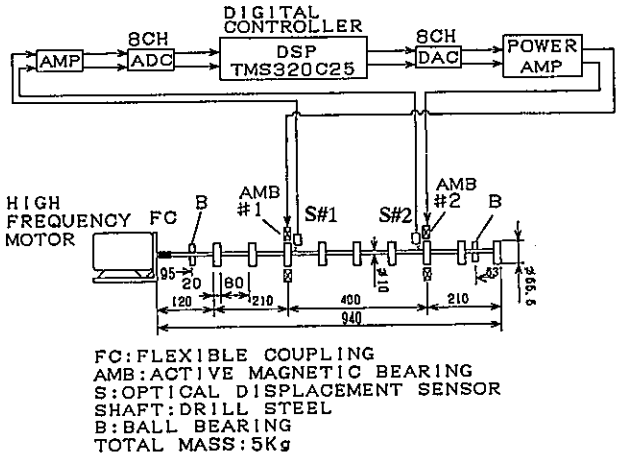

Fig.2 Schematic diagram of test rig

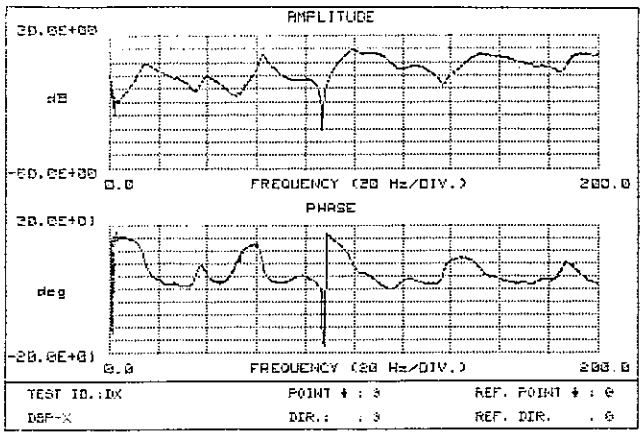

Fig.3 One example of transfer fuction of test rotor with control using AMB #1 and #2 by FFT analyzer

based on experimental FFT analysis. Figure 3 and 4 indicate that there are four natural frequencies under 100Hz. The mode shapes are very simple because the laboratory test rotor is supported as the simple support or hinged support at near both end in addition to two magnetic bearings. From FEM analysis using a mathematical model of Fig.2, the first bending mode of the flexible rotor supported by only conventional bearings is 10.0 Hz, the second is 37.0 Hz, the third is 66.2 Hz, the fourth is 85.5 Hz and the fifth is 117.0 Hz. On the other hand, the natural frequencies in the case of the rotor controlled by two magnetic bearings are shown in Fig.4. Two cases with and without magnetic bearings are almost similar concerning their natural frequencies except the first mode. Also these mode shapes are shown in Fig.4. These analytically determined natural frequencies and mode shapes are very close to the experimentally determined modal frequencies and mode shapes.

4. Control Strategy

It is predicted that the unbalance responses become large because the test rotor is very slender and long shaft. Of course, it is difficult to take a fine balancing for this shaft on account of same reasons. Therefore, we have to think the controller limitter which means the following devise. The moment the maximum deflection in magnetic bearings exceeds some threshold of amplitudes, one of two face to face electromagnets is shut down because the other side of electromagnet immediately recovers the shaft to the stable equilibrium. As soon as the shaft deflection becomes smaller than the threshold amplitude, the electromagnet recovers as the actuator. This concept is based on that the large amplitudes have a strong nonlinearity in magnetic bearings. So, not only the digital linear controller can not carry out such nonlinear control, but also the threat remains as a possibility of a generation for a self-excited vibration caused by the contact between the shaft and the touch down bearing. Figure 5 shows the above mentioned algorithm of a judge by comparison with the threshold amplitude.

One more important thing is to realize the variable feedback gains depending rotating speed. The test rotor has four bending critical speeds under 100 Hz. This gives a hint that four kinds of optimal feedback gains exist for each mode taking into account the saturation of digital controller. It is so called an adaptive algorithm. We have experimentally searched for the optimal feedback gains by means of the experimental FFT analysis and the test run. We selected the three turning speeds for four group of gains and their gains

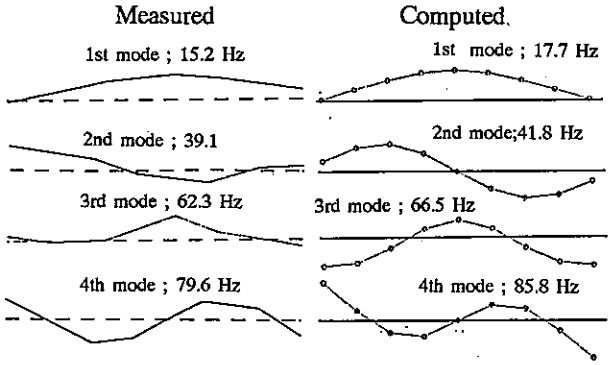

Fig.4 Measured mode shapes and computed mode shapes of of test rotor with control using AMB #1 and #2

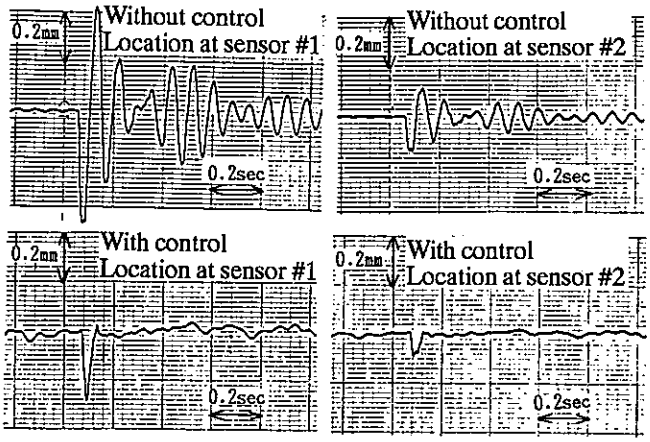

Fig.6 Impulse responses with and without control at sensor locations for the horizontal direction

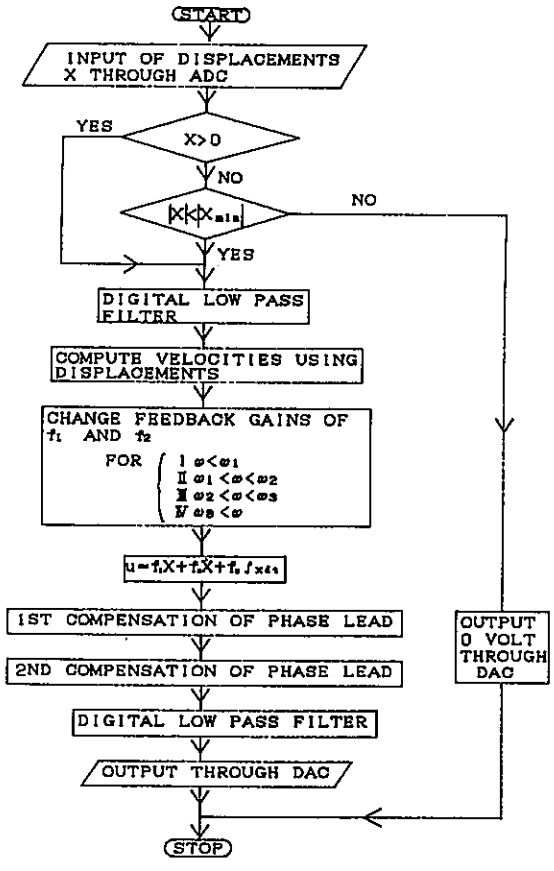

Fig.5 Flow chart of control algoritm to execute in DSP controller

are constant up to the next turning speed. The whole algorithm consists of some digital filters based on PID and phase compensations. This is shown in Fig.5.

We used DSP control to realize the algorithm shown in Fig.5. This DSP chip is TMS320C25 and 40 MHz for clock. The analog-digital converter of 12 bit has a capability of parallel eight channels samples and holds at the same time. The sampling frequency is 200 kHz for each channel. On the other hand, the digital -analog converter of 14 bit has a capability of eight channels outputs simultaneously. This sampling time is 5 μsec. As the result, it is very faster than another DSP chip. In our experiments, the sampling time is 250 μsec to execute the algorithm in Fig.5 for eight channels.

5. Experiments by Means of DSP

Figure 6 shows the impulse responses at locations of two sensors without control and with control using active magnetic bearings #1 and #2. In the case of no control, the responses at two locations are modulated and so complicated. This is caused by the beat of two adjacent natural frequencies between the first bending for the horizontal direction and the first bending for the vertical direction. In the case of control, the amplitudes are immediately reduced to zero within half period. However the small vibrations can be observed near the equilibrium because the velocity feedback gains are so high. The responses are very well in general.

Figure 7 shows the unbalance responses at the two measuring stations, namely two sensor locations of Fig.2 from 0 to 100 Hz for the horizontal and vertical directions. The data are for no control, active control using only AMB #2 and active control using AMB #1 & #2. The data were measured on the condition that the rotating speed was automatically increased with 1 Hz/sec for the acceleration rate. So, it seems that theses data are the unbalance responses in the case of steady state. The unbalance responses without control are big amplitudes because the shaft has big unbalances. As the necessary consequency, the shaft contacts with the touch down bearings. We observed the violent vibration and the rubbing vibration caused by hitting against the touch down bearings at all critical speeds up to 100 Hz. In particular, when the shaft passes through the first critical speed, it was impossible to

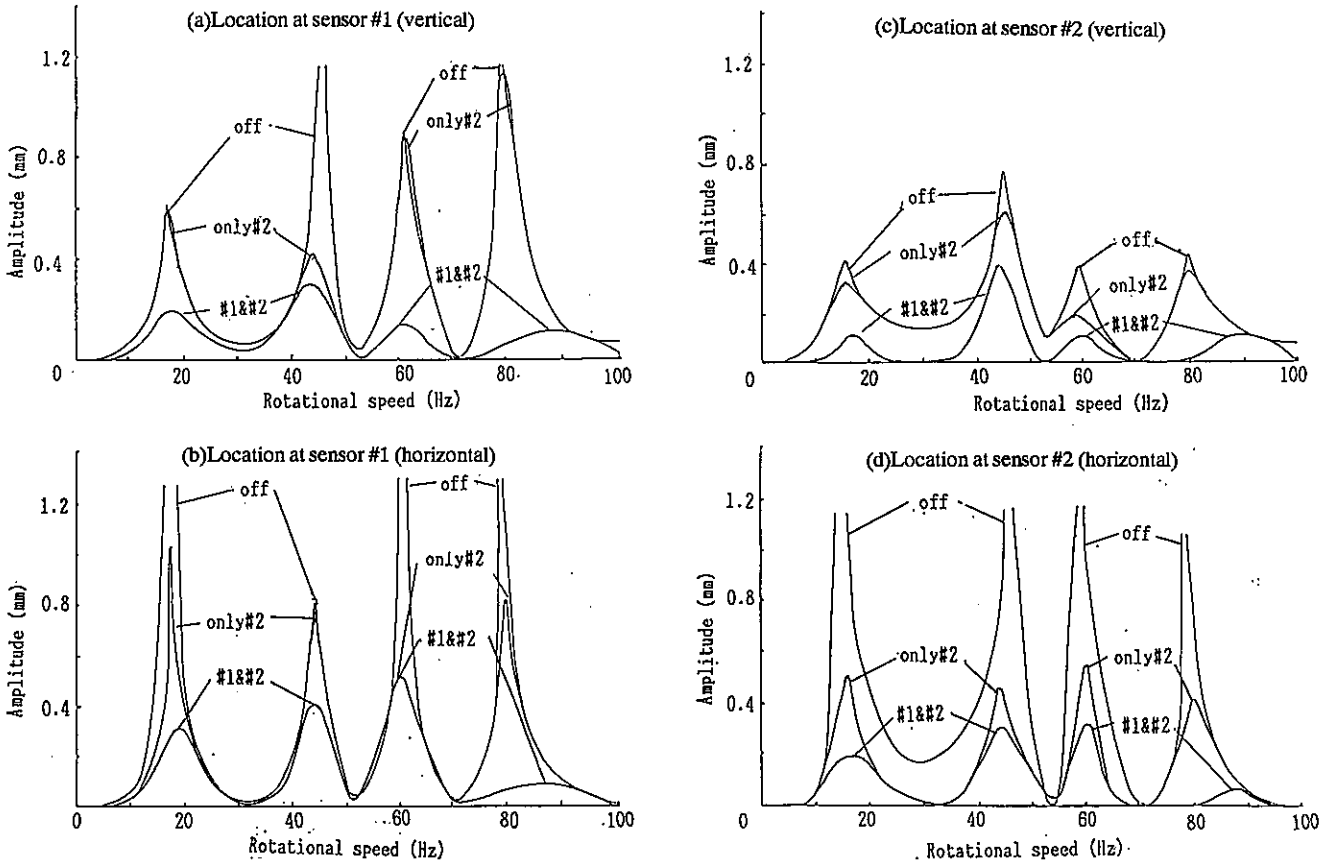

Fig.7 Measured unbalance responses at sensor locations in three cases, namely without control, with control using only AMB #2 and with control using AMB #1 and #2

automatically increase the rotating speed in many cases. Also it was sometimes impossible to pass the fourth critical speed.

In contrast to the case of no control, it is very easy to pass with safety at the every critical speed and it is possible to reduce under the considerable small amplitude in transition through critical speeds in the case of active control using AMB #1 & #2. It was confirmed varying the threshold amplitude of X_{min} that the efficiency of the controller limiter which means on-off switching. This control strategy is so useful for active vibration control of large amplitudes like a nonlinear behavior. Also variable feedback gains are better than constant feedback gains on the point of view for optimization of each mode. The resonance peaks still exist and do not disappear entirely until now. These results do not signify the limitation of AMB. It is sure that we can get more good data near future because the total maximum current of the power source is at the highest 1.5 A including bias currents when total eight electromagnets are working. It is considered that electromagnetic forces are essentially effective for small vibration near the equilibrium. Therefore, the control efficiency might be increased for a fine balanced rotor when the same digital algorithm would be applied.

In the previous discussion, two AMB(#1 & #2) were used for active vibration control. Now, we examine the vibration control effect when only AMB #2 was used for control. Also Fig.7 shows the experimental data. The responses in this case are of course worse than that in the case that AMB #1 & #2 are working regarding vibration control efficiency. This is due to the simple reason of the insufficiency of control forces comparing with strong unbalance forces. Although AMB #2 was working in cases of the previous and the present, the resonance amplitudes are influenced by the control of AMB #1 as shown in Fig.7 (c),(d). This means that the dynamic characteristics with active control in the left side of AMB #1 and the right side of AMB #2 interact with each other. and that vibration control is improved by the superposition.

6. Conclusions

The active vibration control for higher order bending modes, namely up to fourth bending mode, have been tried by means of DSP control. The control strategy with variable feedback gains for small amplitudes and on-off control for large amplitudes have been applied to very slender shaft without balancing. From the experiments, it was impossible for the test rotor to pass the first and the fourth critical speeds without magnetic bearing. By contrast, we can pass four critical speeds with safety using magnetic bearing.

References

Allaire,P.E., Humphris,R.R., and Kelm,R.D.,1986,
"Dynamics of a flexible rotor in magnetic bearings"
Rotordynamic Instability problems in High-Performance Turbomachinery -1986,NASA CP-2443,pp.419-430.

Bradfield,C.D., Roberts,J.B., and Karunendiran,S.,1986,
"Performance of an electromagnetic bearing for the vibration control of a super critical shaft"
Rotordynamic Instability Problems in High-Performance Turbomachinery - 1986,NASA CP-2443,pp.431-460.

Bradfield,C.D.,Roberts,J.B., and Karunendiran,S.,1989,
"A programmable electromagnetic bearing for vibration control of a flexible shaft",Rotating Machinery Dynamics, Proceedings of the 12th biennial ASME Conference on Mechanical Vibration and Noise,ASME ,Vol 18-1,pp.335-343

Burrows,C.R.and Sahinkaya,M.N.,and Clements,S.,1987,
"Electromagnetic control of oil-film supported rotor using sparse measurements", Rotating Machinery Dynamics, Proceedings of the 11th biennial ASME Conference on Mechanical Vibration and Noise,ASME,Vol.1,PP.127-132

Burrows,C.R.Sahinkaya,M.N.,1988,
"Control strategies for use with magnetic bearings"
Vibration in Rotating Machinery,i.Mech. E. Conf., C273/88,pp.23-32.

Furst,S.and Ulbrich,H.,1988,
"An active support system for rotors with oil-film bearings.",Vibration in Rotating Machinery,I.Mech.E. Conf.C261/88,pp.61-68.

Huckerbridge,A.A. and Lawrence,c.,1987,
"Identification of structural interface characteristics using component mode synthesis,"
Modal Testing and Analysis,Proceedings of the Eleventh Biennial Conference on Mechanical Vibration and Noise,ASME,pp.121-129.

Kasarda,M.E.F.,Allaire,P.E.,Humphris,R.r.,and Barrett ,L.E.,1988,
"A magnetic damper for first mode vibration reduction in multimass flexible rotors,"
Rotordynamic Instability Problems in High-Performance Turbomachinery-1988,NASA CP-3026,pp.353-372.

Lewis,D.W.,Moore,J.W.,Bradley,P.L.,and Allaire,P.E., 1982,
"Vibration limiting of rotors by feedback control,"
Rotordynamic Instability Problems in High-Performance Turbomachinery-1982,NASA CP-2250,pp.434-436

Matsushita,O.,Tagami,M., Yomeyama,M.Saitou,I., Nagoata,A.,and Aizawa,M.,1987,
"Stabilization by electromagnetic damper for contained liquid-inducedrotor vibration,"
Nippon Kikai Gakkai Ronbunshu,C Hen(Trans. JSME),Vol.53,No.496,pp.2453-2458.

Moor J.W.,Lewis,D.W.,and Heinzaman,J.,1980,
"Feasibility of active feedback control of rotordynamic instability,"Rotordynamic Instability Problems in High-Performance Turbomachinary -1980,NASA CP-2133,pp.467-476.

Nagai,B., Okada,Y.,Matsuda,K.,and Kibune,K.,1986,
"Digital control of electro-magnetic damper for rotating machinery,"
Int. Conf. on Rotordynamics,Tokyo,pp.415-419.

Nikolajsen,J.L.,Holmes, R.,and Gondhalekar,V.,1979,
"Investigation of an electromagnetic damper for vibration control of a transmission shaft,"
Proc.I.Mech.E.(London),Vol.193,pp.331-336.

Nonami,K.,1985,
"Vibration control of rotorshaft systems by active control bearings,"ASME Paper 85-DET-126

Nonami,K. and Fleming,D.P.,1986,
"Qusai-model vibration control by means of active control bearings,"Int.Conf.on Rotordynamics, Tokyo, pp.429-436.

Nonami,K.,1988a,
"Active vibration control of flexible rotor supported by active control bearings,Part1,"
Nippon Kikai Gakkai Ronbunshu,C Hen(Trans.JSME), Vol.54,No.449,pp.579-586.

Nonami,K.,Kawamata,s. and Hotate,M.,1988b,

"Active vibration control of flexible rotor supported by active control bearings,Part2,"
Nippon Kikai Gakkai Ronbunshu,C Hen(Trans.JSME), Vol.54,No.501,pp.1073-1078

Nonami,K.,Kawamata,S.,1989a,
"Feedforward control to unbalance force cancellation for flexible rotor systems",Proceedings of the international symposium on advanced computer for dynamics and design,pp.297-302.

Nonami,K.,Dirusso,E. and Fleming,D.P.,1989b,
"Active vibration control for flexible rotor by optimal direct-output feedback control",Rotating Machinery Dynamics,Proceedings of the 12th biennial ASME Conference on Mechanical Vibration and Noise,ASME,Vol.18-1,pp.327-334.

Palazzolo,a.b.,Kascak,A.F.,Lin,R.R.,Montague,G., and Alexander,R.M.,1988,
"Piezoelectric pushers for active vibration control of rotating machinery", 5th Workshop on Rotordynamic Instability Problems in High-Performance Turbomachinery.

Palazzolo,A.B.,Lin,R.R.,Kascak,A.F.,Montague,J.,and Alexander,R.M.,1989,
"Test and theory for piezoelectric actuator-active vibration control for rotating machinery",Rotating Machinery Dynamics,Proceedings of the 12th biennial ASME Conference on Mechanical Vibration and Noise,ASME,Vol.18-1,pp.367-374.

Redmond,I.,MeLean,R.F., and Burrows,C.R.,1985,
"Vibration control of flexible rotors,"
ASME Paper85-DET-127.

Stanway,R. and Burrows,C.R.,1981,
"Active vibration control of a flexibility mounted journal bearings,"
Journal of Dynamic Systems, Measurement and Control, Vol.103,No.4,pp.383-388

Stanway,R. and O`Reilly,j.,1984,
"State-variable feedback control of rotor -bearing suspension systems,"
Vibration in Rotating Machinery,I.Mech.E. Conf.,pp.515-524.

Ulbrich,H.,1986,
"Dynamik und Regelung von Rotorsystemen,"
Forschr.-Ber.VDI-Z, Reihe ll,Nr.86.

Ulbrich,H,.1987
"Control of flexible rotors by active elements,"
Rotating Machinery Dynamics;Proceedings of the Eleventh Biennial ASME Conference on Mechanical Vibration and Noise,Vol.1,pp.191-196.

2nd International Symposium on Magnetic Beaing
July 12-14, 1990, Tokyo, Japan

VIBRATION CONTROL OF A LARGE TURBOGENERATOR BY ELECTROMAGNETIC DAMPERS

CHAN HEW WAI C.
Electricité de France. Direction des Etudes et Recherches
1 av. du Général de Gaulle
92141 Clamart - FRANCE

Abstract

The passing through critical speeds of rotating machines with long shafts may often lead to vibratory problems. In such cases, one solution would be to add damping on the shaft line during running through the critical speeds in order to reduce vibrations. These additional dampings can result from active electromagnetic devices. The Research and Development Department at Electricité de France has demonstrated the feasability of such an attempt. For this particular case, a test bench has been developed and a 10,000 daN load capacity electromagnetic damper was studied. After the promising results obtained, we have undertaken new works in order to improve the load capacity and the reliability of the electromagnetic damper. Our ultimate aim is to prove that this solution may be applied to a large 900 Mwe turbogenerator in operation.

1. Introduction

Today, Electricité de France (EDF) operates an important number of machines for electricity production. These machines with long shafts often operate above several critical speeds. These machines were designed using two different technologies. The first consists on supporting each rotor by two hydrodynamic bearings and in the second, each rotor is supported by only one bearing. In this case, the shafts may sometimes show high levels of vibrations during the running through certain critical speeds due to little damping offered by fluid-film bearings. The Research and Development Department at EDF has been interested in this problem for many years and has proposed an interesting solution which consists on adding one or many electromagnetic dampers for active vibration control on the machines under consideration.
Several papers have reported the use of electromagnetic forces to dampen vibrations, but only in laboratory or for small-size machines.
Nikolajsen et al. [1] were the pioneers who have demonstrated the effectiveness of a controlled magnetic damper to reduce vibration in a long transmission shaft.
Burrows and Sahinkoya [2,3] used an electromagnetic damper to a laboratory rotor supported by fluid film bearings.
Recently, Allaire et al. [4] have developed and tested a magnetic device used as a bearing or a damper for vibration reduction in a multimass flexible rotor.

The first works have lead us in designing and constructing a prototype of a large size damper. So, an experimental bench to test the electromagnetic damper was developed. In that time, its load capacity was defined to 10,000 daN. Tests conducted have shown that the electromagnetic damper met the requirements of design specifications.
The main results were reported at the 1987 ASME Conference [5] and at the first International Symposium on Magnetic Bearings in Zurich [6].
Today, taking these promising results obtained into account , we deal with the industrialization phase, including some major changes.
Indeed, in normal cases, the load capacity of 10,000 daN is sufficient to significantly reduce vibration during running through the most difficult critical speeds on the aimed machine. However, the requirements with respect to machine operating conditions and reliability are such at EDF that it is better to increase the damper load capacity to 30,000 daN to take into account exceptional unbalances. This excess load capacity of three times is required for the worst case unbalance distribution estimated on the existing machine. But, the dimensional constraints are unchanged. So, the design of the future magnetic damper components was guided by three major concerns : load capacity, size and reliability.
The purpose of this paper is to report on new studies which have been undertaken in order to improve the damper load capacity and the complete device reliability.

2. Magnets Design

The first damper tested is described in Fig.1. It included 6 poles with 4 magnetic axis. It only covered the upper 270° of the rotor. It was an "incomplete" damper.

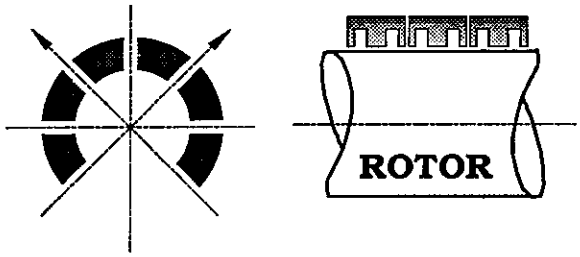

6 poles of 45° each 3 E - shaped magnets per pole

Fig.1 First magnetic damper working principle.

Each 45° pole contained 3 independant E-shaped magnets. Each of the 18 power amplifiers which drived electromagnet operated on 160 V DC with a maximum current of 50 A. Thus, each pole was to have provide 7,000 daN in order to develop 10,000 daN rotating force. The nominal air gap was 2 mm. The magnet sheets used were in silicon iron.
The tests conducted showed the effectiveness of such a device; even if this " incomplete " damper did not work in the best conditions.
But, in order to take exceptional unbalances into account, it is necessary to increase the damper load capacity to 30,000 daN and the air gap to 3 mm to avoid any possible contact. These represent the new design constraints.
So, the first phase of the study consisted in determining by numerical calculations using Finite Elements Method (FEM) the load capacity limit of the former electromagnets.
Firstly, these preliminary computations have shown that with the present E-shaped electromagnets with silicon iron sheets, it is impossible to reach the desired rotating force of 30,000 daN. Secondly, they also demonstrated that the use of an "incomplete" damper led to the same result.
So, further calculations with various material sheets, but with the same shape, have been made. Figure 2 shows the first magnetization curves of the candidate materials.

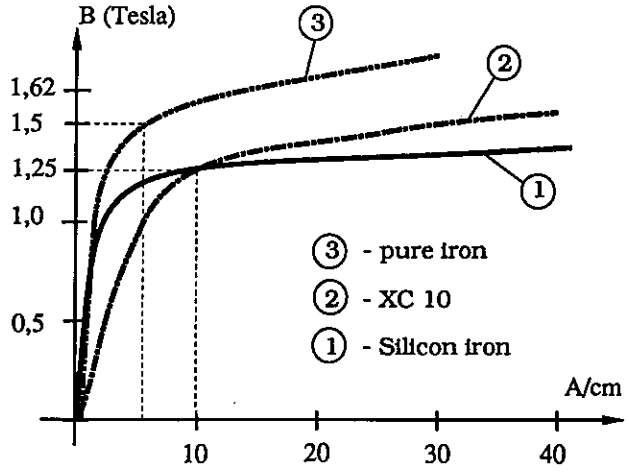

Fig.2 First magnetization curves for different materials.

The main results obtained with the E-shaped magnets are indicated in table 3 according to the nature of sheets used.

Nature of Sheets	One Magnet Load Capacity (daN)	Amplitude of the Rotating Force (daN)
Silicon Iron Presently used	2,225	13,350
XC 10	2,805	16,830
Pure Iron	3,972	23,830

Table 3. Theoretical rotating force amplitude for a 360° damper with E-shaped magnets according to different sheets.

Furthermore, these computations reveal that E-shaped magnets does not represent the optimum. Indeed, Fig.4 shows one induction calculation with this magnet design.

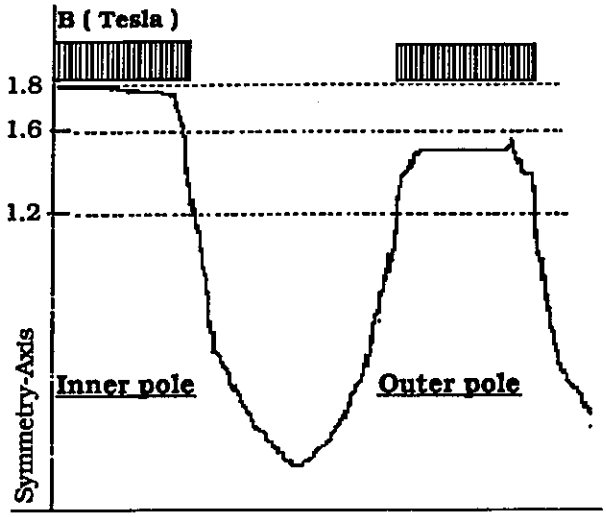

Fig.4 One flux density calculation with E-shaped magnet.

It can be seen that the outer pole induction is clearly smaller than it is under the inner pole. All other calculations made with this magnet shape give similar results.
Tests in order to equalize the two inductions have been carried out. A 80% surface reduction of the outer pole has been made and an unequal coil turns distribution tested (the outer pole had twice as much turns as the inner). In all cases, results have been disappointing for the equality of the two inductions have never been obtained.
Thus, further calculations with U-shaped magnets have been realized. These enable changes due to magnet shape to be evaluated, the other parameters being unchanged.

Nature of Sheets	One Magnet Load Capacity (daN)	Amplitude of the Rotating Force (daN)
XC 10	6,070	36,422
Pure Iron	6,198	37,188

Table 5. Theoretical rotating force amplitude for a 360° damper with U-shaped magnets according to different sheets.

Table 5 summarizes the main results obtained with U-shaped magnets with different sheets.
In fact, in the same outside dimensions, U-shaped magnets give a 20% active surface increase: less coils are used.

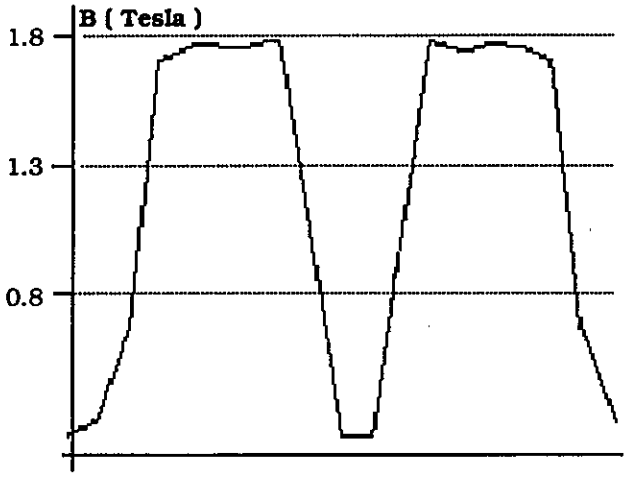

Fig. 6 Flux density calculation with U-shaped magnet.

Fig.6 shows the good flux density symmetry within the two poles. As an electromagnet magnetic force is proportional to the square of the flux density, this explains the significant gain obtained with this magnet shape.

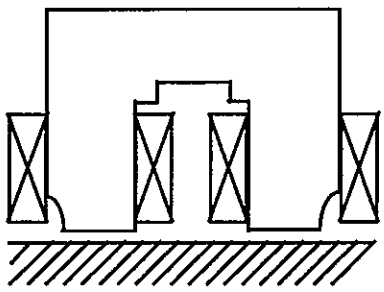

Fig.7 The adopted U-shaped magnet.

This, along with the development of a new power amplifier of 30 KVA, indicates that it is theorecally possible to have access to the value of 30,000 daN on condition to have a full damper which covers the 360° of the rotor. Tests on real scale will confirm these results.

3. Power amplifier

With the former damper, power amplifiers of 8 KVA were used and were sufficient in order to develop 10,000 daN rotating force at 17 Hz with a 2 mm nominal air gap.

As the new goal is the 30,000 daN rotating force obtention with 3 mm air gap, the development of a power amplifier of 30 KVA has been undertaken.

The specifications submitted to the Société de Mécanique Magnétique (S.2.M), the damper manufacturer, contained the following stipulations :

- Reactive power : 30 KVA,
- Load inductance : 200 mH.
- Phase displacement : 5° at 17 Hz with 200 mH maximum.
- The flux feedback control is required.

The amplifier is designed to provide the reactive power of an electromagnet to the future damper of 30,000 daN in order to obtain a rotating force as $F = Fo + Fo \sin (wt)$. The maximum force $Fmax = 2Fo$ must correspond to the maximum current value. For that, the amplifier must be able to supply a 60 A 17 Hz current without phase displacement of the flux feedback control.

4. First tests

Before the manufacturing of the second damper model, it was interesting to verify the calculations results and the new 30 KVA amplifier performances. So, a real scale model of the U-shaped magnet was constructed.

The new amplifier was developed and tested with this representative inductive load. The main results are displayed in Figs.8,9 and 10.

Fig.8 represents the induction and the electromagnet force as a function of the current. The attained force with a 60 A current is about 6,400 daN. It means that the damper rotating force using these magnets will be 38,400 daN (6,400x3x2). The air gap is 3 mm.

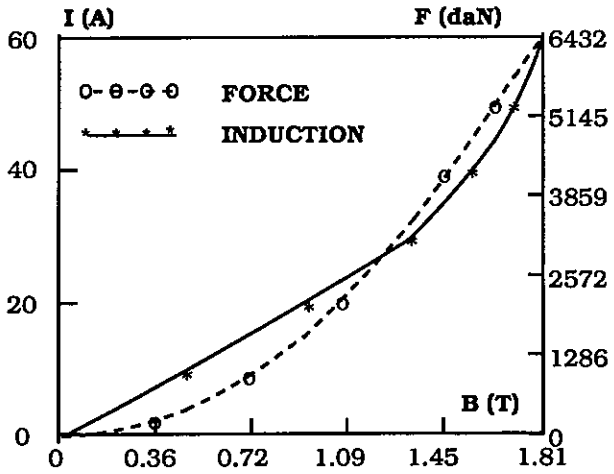

Fig.8 Force and flux density curves of the tested U-shaped magnet as a function of the current. Air gap is 3 mm.

The electromagnet force is proportional to the square of the flux measured by the flux measurement coil. For this reason, the reference force signal first passes through a linearizer. The linearizer output becomes the flux feedback control reference. The electromagnet is therefore in force drived.

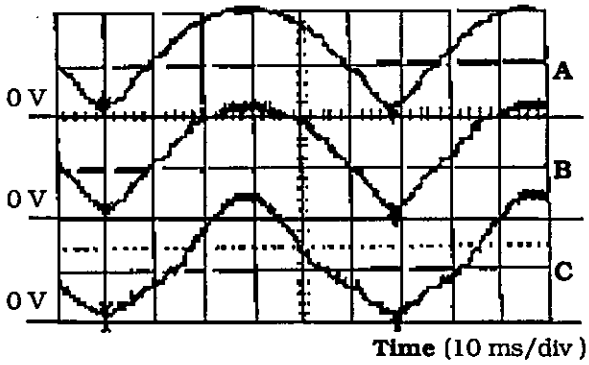

A - Flux Reference (5 V / div)
B - Flux (5 V / div)
C - Current (30 A / div)

Fig.9 Amplifier results at 17 Hz during force modulation tests.

The amplifier results during force modulation tests are indicated in Figs.9 and 10.

It appears in Fig.9 that the amplifier modulates with the real load a force at 17 Hz without significant difference in phase between the flux reference and

the flux itself. Note the difference between flux and current due to magnetic iron saturation flux density.

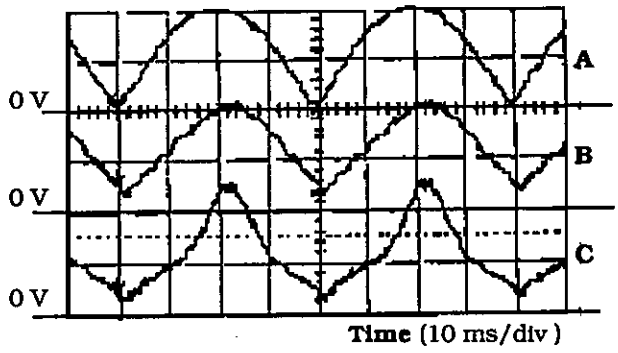

A - Flux Reference (5 V / div)
B - Flux (5 V / div)
C - Current (30 A / div)

Fig. 10 Amplifier results at 25 Hz during force modulation tests.

The results at 25 Hz are presented in Fig.10. The amplifier shows voltage saturation and the current increases with its maximum slope. So, a phase displacement in flux appears.

Thus, we can say that the experimental results of the U-shaped magnet driven by the new 30 KVA amplifier are completely in accordance with theoretical predictions.

5. Digital control

Reliability is our major concern. In order to improve the complete device reliability, a digital control has been studied and developed. The digital control is based on a DSP card with a Texas Instruments microprocessor (TMS320C25).

This card, VMEbus compatible, includes 64 Kbytes dual port RAM for exchanges with the control processor (Motorola 68000), I/O auxiliary ports for information transferts with the A/D and D/A converters, a DMA controller for I/O data transferts.

Sensor signal acquisition card is composed by a synchronous demodulator, analog anti-aliasing filter, sample and hold circuit and a 12 bits A/D converter. The amplifiers are driven by 13 bits D/A converters (see Fig.11).

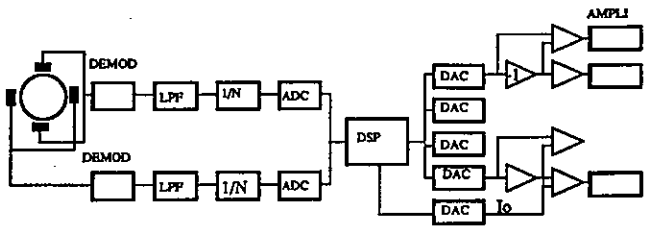

Fig.11 Block diagram of the digital control.

Displacement probes measure rotor motions. These primary signals pass through a run-out suppression block. A large bandwith phase correction network composed mainly by a filtered derivation function ensures a 90° phase lead in the range of 4 to 20 Hz. In this way, we create a damping force due to a velocity feedback.
In order to obtain a high damping coefficient without damaging stability, a tracking filter is used. Such a filter (synchronized with the rotating speed) is in fact a pure numerical integrator which bandwith is adjusted to have an adequate response of the machine. Its function is to reduce the output signal to zero. So, its gain is nearly "infinite". That means the damping value is very high and constant whatever the frequency.
The sine and cosine signals which synchronize the tracking filter are issued from a sin/cos table stored on the DSP card. A key phaser, along with a Phase Locked Loop (PLL), enables the right sinus and cosinus values to be obtained. Finally, a coefficients weighting circuit guides the right signal to its corresponding amplifier (see Fig.12).

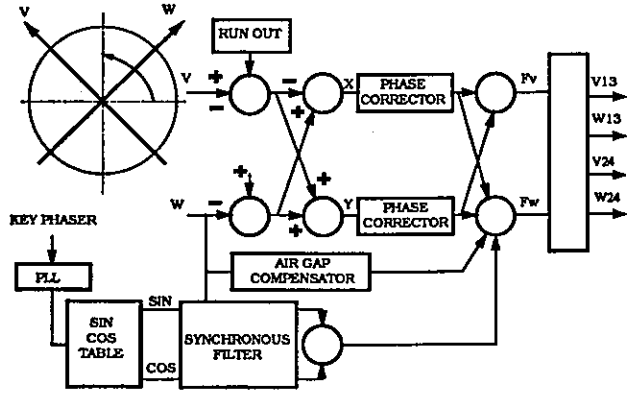

Fig.12 Digital control system.

This digital control scheme has been realized and tested with the former damper of 10,000 daN.

6. Main results

Typical results when the digital control operates are presented in Figs.13, 14, 15 and 16. The flexible rotor used must pass a bending critical speed at about 16.4 Hz, up to a nominal speed of 20 Hz.

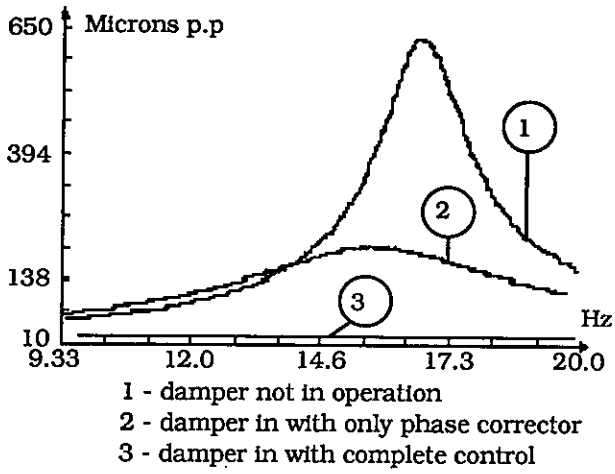

Fig.13 Vertical rotor vibrations according to different damping coefficients. (unbalance=0,10 m.kg)

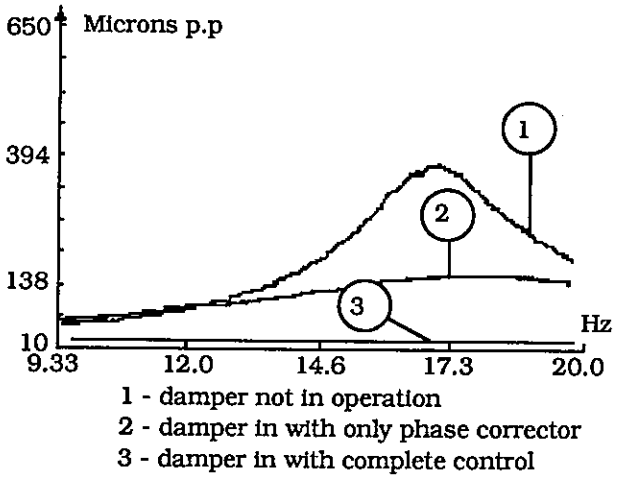

Fig.14 Horizontal rotor vibrations according to different damping coefficients. (unbalance=0,10 m.kg)

Figures 13 and 14 indicate rotor vertical and horizontal vibrations with a residual unbalance mass of approximately 0,10 m.kg during deceleration for different damping values provided by the electromagnetic damper.
Firstly, it can be seen that the rotor's critical speed does not shift when the damper is operating, and secondly, that vibrations are well damped when it is running through the critical speed.
Therefore the electromagnetic damper well fulfills its damper function (stiffness is practically equal to zero). This first damper was designed to provide a rotating force of 10,000 daN at 17 Hz. To verify these figures, tests were conducted on the test bench by applying unbalance masses up to 8,6 m.kg which represent a rotating force of about 10,000 daN at 17 Hz.

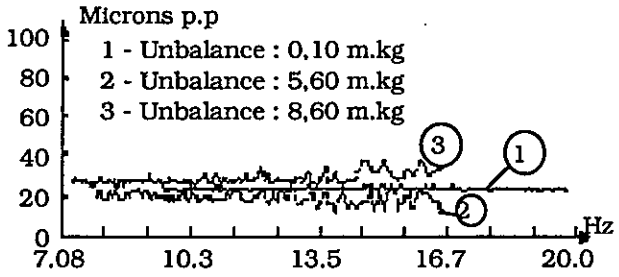

Fig.15 Vertical rotor vibrations with the complete digital control according to different unbalances.

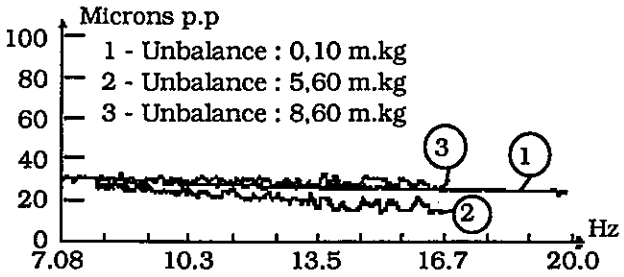

Fig.16 Horizontal rotor vibrations with the complete digital control according to different unbalances.

Figures 15 and 16 show these tests results. The rotor vibrations are practically constant(30 microns peak to peak) whatever the unbalance masses. These residual vibrations correspond to inevitable errors issued

from the run-out suppression block.
That demonstrates the great efficiency of the damper and shows the high damping coefficient it can deliver.
These very interesting results have already been observed with the former analog controlled damper. The main change is the fact that the digital control gives better results with a very high degree of stability.

7. Conclusion

The results observed during different tests on the U-shaped magnet driven by the new 30 KVA amplifier allow us to say that the 30,000 daN rotating force will be obtained without any major problem.
The new amplifier in question gives complete satisfaction.
The digital control used is consistent with the expectations. Tests conducted on it show that it is possible to effectively dampen the rotor vibrations with a high damping coefficient without damaging the stability.
The digital control will certainly be implemented on the industrial prototype. Indeed, it will improve the reliability and will make easier the damper setup, specially on site. Also, it allows, if necessary, the implementation of special functions, not easily available in analog circuits, in order to optimize the rotating force modulus. Here, the expected gain is about 20 %.
These works have represented the components feasability studies (magnet, amplifier, digital control scheme). The next step consists on realizing and testing the complete second damper model with these previous components. These tests are necessary in order to define the design specifications of the industrial device.
Our ultimate goal is to design and realize an industrial prototype damper which should be mounted on site to an existing 900 Mwe turbogenerator set in operation.

References

1. NIKOLAJSEN J.L., HOLMES R., GONDHALEKAR V.,"Investigation of an Electromagnetic Damper for Vibration Control of a Transmission Shaft," IMechE, 1979, pp. 331-336.

2. BURROWS C.R., SAHINKAYA, N., and CLEMENTS, S.,"Electromagnetic Control of Oil-Film Supported Rotors Using Sparse Measurements," Rotating Machinery Dynamics, ASME Publication, September 27-30, 1987, pp.127-132.

3. BURROWS C.R., SAHINKAYA, N., TRAXLER, A., and SCHWEITZER, G.,"Design and Application of a Magnetic Bearing for Vibration Control and Stabilization of a Flexible Rotor," Magnetic Bearings Symposium, June 6-8, 1988, pp. 159-168.

4. ALLAIRE, P.E., KASARDA, M.E.F., HUMPHRIS, R.R., AND D.W. LEWIS,"Vibration Reduction in a Multimass Flexible Rotor Using a Midspan Magnetic Damper," Magnetic Bearings Symposium, June 6-8, 1988, pp. 149-158.

5. CHAN HEW WAI, C., MOREL, J., "Application of an Active Magnetic Bearing for Vibration Control Near Critical Speeds in Large Rotating Machines," ASME Publication, September 27-30, 1987, pp.151-157.

6. CHAN HEW WAI, C., MOREL, J., "The Electromagnetic Damper- Towards a First Large-Scale Industrial Application," Magnetic Bearings Symposium, June 6-8, 1988, pp. 189-198.

2nd International Symposium on Magnetic Beaing
July 12-14, 1990, Tokyo, Japan

THE CONTROL OF PROPELLER-INDUCED VIBRATIONS IN SHIP TRANSMISSION SHAFTS

J DARLING and C R BURROWS

School of Mechanical Engineering, University of Bath, Bath, UK

Abstract

The fluctuating force generated by a ship's propeller leads to axial and radial vibrations which are subsequently transmitted to the hull. The simulation study presented here demonstrates how a tuneable vibration absorber utilizing a magnetic thrust bearing and inertial mass employed in parallel with a hydrodynamic thrust bearing can reduce propeller drive shaft axial vibrations. The sensitivity to controller errors and the influence of vibration absorber mass are examined. It is shown that a practical device using well proven magnetic actuation techniques could be developed.

The variable stiffness and damping characteristics of hydrodynamic thrust bearings mean that a fixed parameter closed loop controller will not perform well at all operating conditions. It is argued that the use of self tuning or model-reference type of closed-loop adaptive control is impractical. An open-loop speed-dependent control strategy is developed. This is inherently stable but may increase vibration amplitudes at frequencies other than the propeller passage frequency.

1. Introduction

One of the principal causes of vibration in a ship is the fluctuating axial force generated by the propeller or propulsor. Generally, this force comprises a steady load superimposed with a fluctuating component at the blade passage frequency [1]. This periodic force is a direct result of the non uniform wake of the hull and the clearance between the propulsor and the hull. Although the harmonic content of the thrust load may be reduced by good design it cannot be eliminated. As a result, alternative methods of vibration reduction have been investigated and some have been applied to sea going vessels.

Acoustic resonator devices and 'vibration absorber' mass/spring/damper systems are presently employed on sea going vessels. These passive devices which are tuned to a single frequency attenuate vibration at a specific operating condition [2] but are of little benefit at other operating conditions. This limitation in passive devices has led to work in the field of magnetic bearings [3, 4]. These devices, which are now available in both radial support and axial thrust form, may be controlled actively, responding rapidly to transducer and microprocessor signals.

Magnetic bearings have been applied both theoretically and experimentally to flexible rotors. Whilst most researchers have used collocation to effectively replace the passive squeeze film damper device with a system which can be tuned [4] others have applied more sophisticated techniques which aim to reduce shaft vibration throughout its length. It has been shown that the changing stiffness and damping coefficients of hydrodynamic support bearings can lead to instability in a closed loop multiple input system. As a result Burrows and Sahinkaya have used an open loop adaptive control strategy to minimize radial vibration in a flexible rotor [5].

The application of magnetic thrust bearings is in its infancy. Lewis and Allaire [6] have shown theoretically that a magnetic thrust bearing installed in parallel with the existing hydrodynamic thrust bearing on a ship can reduce vibration over certain frequency ranges. In this work a magnetic bearing acting directly between the thrust bearing housing and hull was employed in order to generate a negative stiffness which when combined with the thrust bearing stiffness reduced the transmission of force from the propeller to the hull. The consequences of changing stiffness and damping on system stability and vibration attenuation are noted as are the restrictions imposed by limited shaft motion and limited magnetic bearing negative stiffness.

This study considers the forces transmitted to the hull of a vessel in a typical uncontrolled thrust bearing/shaft/propulsor system. This simplified linearised axial vibration model is used for comparison purposes. Following this, a tuned vibration absorber utilising a magnetic thrust bearing is included in the theoretical model. The effects of absorber mass and thrust bearing damping on vibration attenuation and absorber mass amplitude are established at a number of operating conditions and a means of implementing the system is proposed.

2 Shaft Axial Vibration Model

A schematic diagram of the thrust bearing, shaft and propulsor system is shown in figure 1. A tilting pad

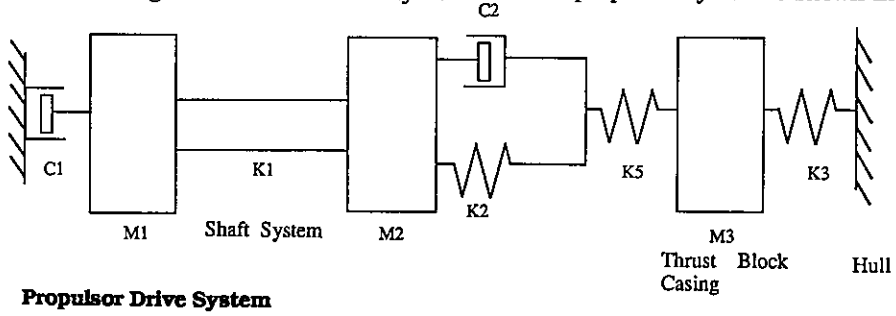

Figure 1. Propulsor Drive System

double acting thrust bearing carries both the primary and fluctuating loads and is mounted via a flexible element to the hull. The thrust bearing is modelled as a fixed mass with a linearised stiffness and damping coefficient. The stiffness was split into two components in series. A constant stiffness accounted for the thrust block structure and a variable stiffness accounted for the fluid element. Since the evaluation of the thrust bearing parameters was not the primary objective of this paper, and since both stiffness and damping are known to be complicated functions of speed, load and operating temperature the numerical values used in this work were obtained experimentally.

The hull of the vessel is assumed to be fixed since its mass is significantly larger than that of the shaft/propulsor system. An extensive finite element analysis of the shaft, main hull and local structure members as carried out by Fujii and Tanida [7] was not thought to be appropriate in this simplified model. The shaft itself is modelled as two fixed masses. At the thrust bearing end an element of the shaft mass is combined with the coupling whilst at the other end the remaining shaft mass is combined with that of the propulsor. Data concerning the shaft mass, stiffness and damping were typical for the given application.

A set of simultaneous differential equations describing the motion of each of the mass elements was developed and analysed in the frequency domain using fixed stiffness and damping parameters.

Three operating speeds and a range of hydrostatic loads were considered in this work (Table 1). The results of figures 2a and 2b demonstrate that the shaft mass/spring/damper combination operating at a rotational speed of 24 rev/min is below its lowest natural frequency throughout the range of operating conditions and the transmitted force is slightly higher than the fluctuating applied force between 100N and 150N. The lowest resonant frequency of the standard system (based on the highest speed and highest load operating condition) was 17Hz.

Speed (rev/min)	Steady Load (kN)	Film Stiffness K2 (MN/m)	Film Damping C2 (MNs/m)
10	13	15.3	10.6
18	42	64.0	21.6
24	75	130.8	34.0
10	1413	16200.0	5670.0
18	1442	12500.0	2260.0
24	1475	11300.0	1460.0

Table 1. Thrust bearing film stiffness and damping

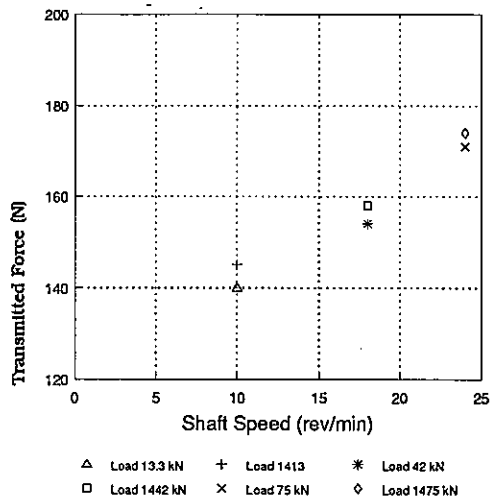

Figure 2a. Force Transmitted to Hull

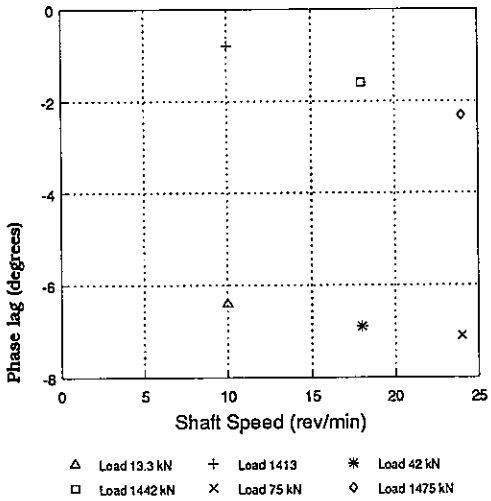

Figure 2b. Phase of Transmitted Force

3 The Active Vibration Absorber

If the vibration generated by the propeller and transmitted to the hull were always at one frequency this effect could be countered by attaching a vibration absorber [1] to the thrust block casing represented by mass M_3 in Fig.1. In variable speed machines the absorber can still be effective if damping is introduced in parallel with the absorber spring [2]. An alternative to this classical approach is to use an active vibration absorber instead of a passive mass, spring, damper system. With this approach the absorber can be tuned to be effective in a range of frequencies.

One possibility is to couple the thrust block casing mass M_3 to an auxiliary mass M_4 as shown in Fig.3. by using an electro-magnetic actuator. A magnetic actuator, or bearing in open-loop is essentially unstable because the force of attraction decreases with increasing relative displacement, but with position feedback the magnetic actuator is equivalent to a spring. By varying the feedback gain this is equivalent to having a spring of variable stiffness. This stiffness can be controlled to minimise the

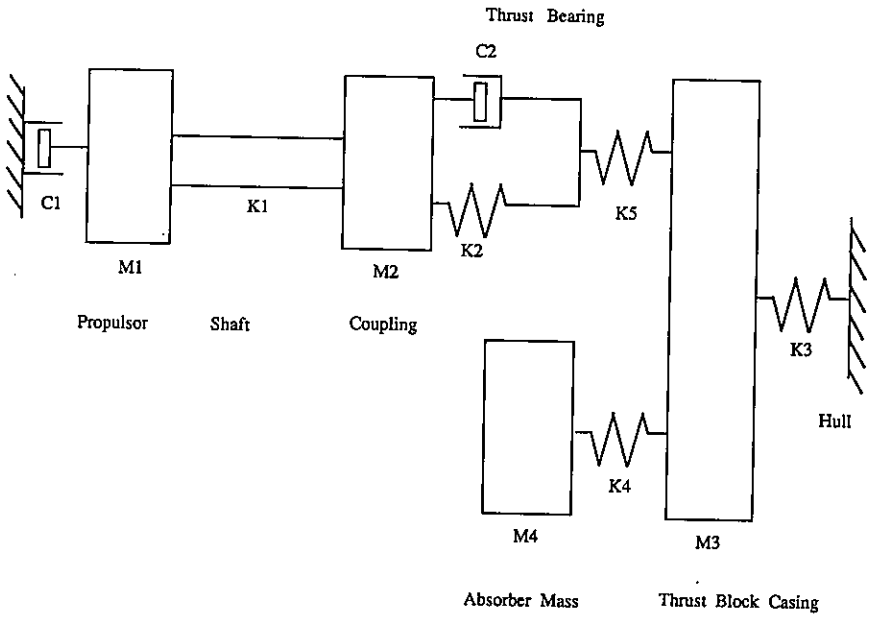

Figure 3. Propulsor Drive with Mass/Spring Vibration Absorber

vibration at a given (variable) operating speed of the propellor. If the actuator is also controlled by a signal proportional to the relative velocity of masses M_3 and M_4 the effect is equivalent to introducing a damping force between the masses. Thus by using velocity feedback around the magnetic actuator and varying the gain this is equivalent to introducing a variable dashpot between the masses.

If an active vibration absorber is used the gain values need to vary automatically as a function of motor speed in order to minimise the vibrations transmitted to the hull. If system parameters do not change with time and are a simple function of rotor speed the appropriate gain settings could be selected by a scheduling process. In practice it is necessary to develop a strategy to select the gain on-line to account for short-term and long-term variations in parameter values. This is discussed later.

Before parameter values were specified the magnitude of the control force required from a magnetic actuator was unknown. The specification of a propulsor variable force component of between 100N and 150N was such that this can easily be met using current technology. This figure was based on measurements taken from a typical large vessel.

3.1 Undamped Active Vibration Absorber In this study the methods for achieving on-line control of the magnetic actuator are not developed. The work is confined to determining the reduction in transmitted forces that can be achieved over a range of operating conditions. The emphasis is on examining the feasibility of achieving a reduction in transmitted force with an auxiliary mass value which would be acceptable in a sea going vessel. Thus the effect of different mass values is considered. In addition it is inevitable that there will be tuning errors in the magnetic actuator control system. Both of these variables are examined in figure 4. It is clear that the system is very sensitive to errors, a 1% error is sufficient to raise the transmitted force to its original level. However, the system is less sensitive if a large absorber mass is used. A 10 tonne reaction mass would reduce the transmitted force by 70% even if the tuning error was a great as ±0.5%. Although a mass of this size would be difficult to support on low friction bearings it should be appreciated that the volume of steel would be little more than $1m^3$.

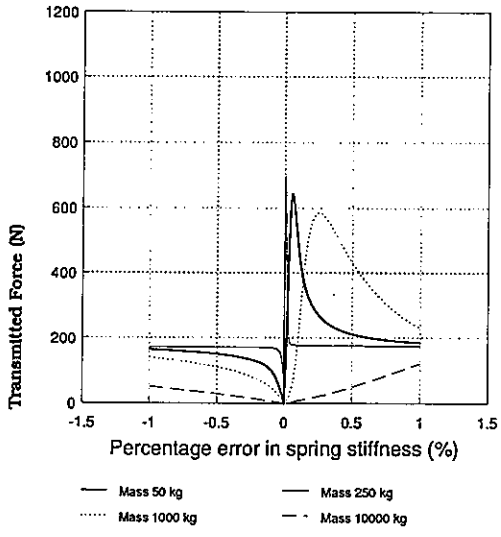

Figure 4. Influence of vibration absorber spring stiffness error on force transmitted to hull

The amplitude of the vibration absorber mass is an important aspect in the design of a magnetic device. The maximum allowable amplitude of vibration is typically less than $1mm$. The results of figure 5 show that a vibration absorber mass of over 70 Kg is necessary to reduce the amplitude to acceptable levels.

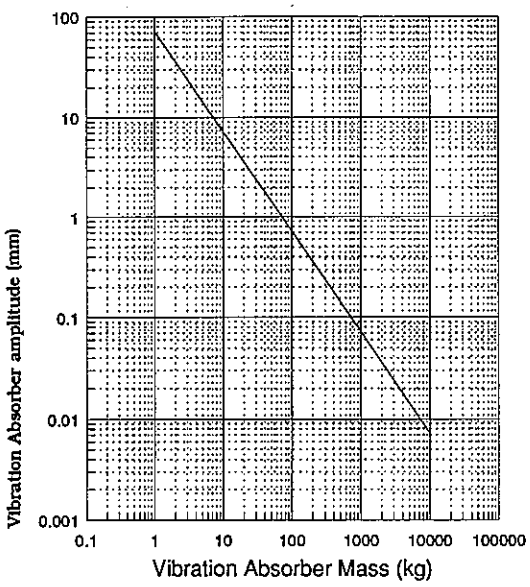

Figure 5. Vibration Absorber Mass and Amplitude

The problem of tuning errors and speed changes might be overcome by switching off the magnetic device if the exciting frequency fell below the tuned frequency. This would avoid the problem of force amplification but would be difficult to implement in a real system since the switch from force cancellation to force amplification is very sudden. In addition, the degree of force cancellation would vary from excellent to poor depending on if the system was operating above or below its tuned frequency.

3.2 Damped Absorber (Magnetically tuned mass/spring/damper)

In order to reduce the system sensitivity to speed changes and errors in tuning a magnetic damper in parallel with the magnetic spring was added (figure 6). The damping was introduced into the equations of motion and the computer model modified accordingly.

The introduction of damping into the magnetic vibration absorber has two effects. First, it is no longer possible to cancel completely the force transmitted to the hull, even with an 'ideal' system [2]. The degree of force attenuation is dependent on the level of damping and the accuracy of tuning. Secondly, the vibration absorber sensitivity to speed changes is reduced. Although this is of benefit the maximum attenuation that may be achieved with a damped device is much reduced (figure 7).

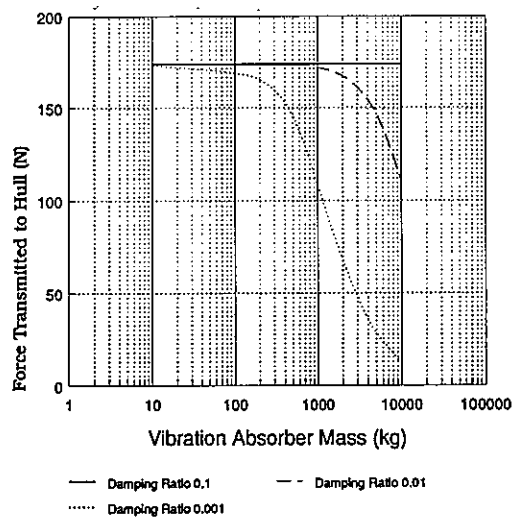

Figure 7. Influence of Mass and Damping on Force Transmitted to Hull

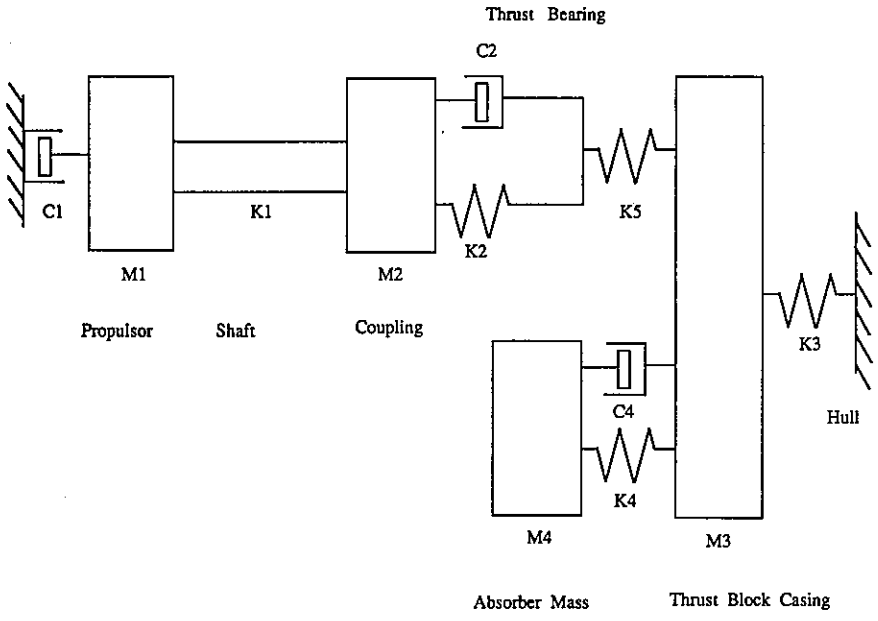

Figure 6. Propulsor Drive with Mass/Spring Damper Vibration Absorber

For example, a 1 tonne vibration absorber with active damping providing a damping ratio of 0.01 would raise the transmission of force to within 65% of the standard vessel.

Alternative mounting positions for an active device were modelled as above but as before the system was very sensitive to tuning errors.

4. The limitations of a magnetically tuned vibration absorber

The use of a magnetic actuator as a tunable mass/spring/damper vibration absorber clearly has limitations. In effect the tunable passive device is subject to the same problems as a simple mass/spring/damper. In this application, the sensitivity of the system to speed changes either requires unacceptably accurate tuning from the magnetic actuator or a large absorber reaction mass. Clearly, this approach is not acceptable and an adaptive vibration controller reacting to the system parameters is necessary. Once again, the magnetic actuator would generate a force which was reacted against a free mass. The size of the reacting mass required in an adaptive device would be no greater than that necessary in the device investigated above. A reaction mass of 250 Kg would have an amplitude of less than 1 mm if used to cancel a 7 Hz fluctuating force of between 100N and 150N at the propulsor. In this case the actuator force would no longer be a function of the mass position and velocity but would be dependent on transducer signals from elsewhere in the vessel.

5. Alternative control strategies

As noted earlier, the use of localised feedback of position and velocity which causes a magnetic actuator to behave like a controllable spring and dashpot unnecessarily restricts the capabilities of these devices. The primary reason for using collocation of the sensors and actuators [8] referred to by some authors as decentralized control [9] is that it avoids the problem of instability associated with the use of state feedback to assign the eigenvalues in a multivariable system. This problem will become manifest if the simple model used in Fig.1 is made more representative of the physical system by modelling the shaft by a larger number of mass/spring elements, and by examining the effect of coupling between the radial and axial motion. Thus four state variables will not be sufficient to model the system. In order to achieve eigenvalue assignment to arbitrarily determined locations it is necessary to measure or estimate all of the state variables. This requirement, coupled with the possibility of the closed-loop system becoming unstable explains why other workers have adopted a very simple control philosophy. By using local feedback and causing the magnetic actuator to act like a spring and damper the possibility of instability is avoided. This is at the cost of an improved performance attainable by utilising the full capability of the magnetic actuator.

These problems can be overcome by using an open-loop adaptive control strategy developed by Burrows and Sahinkaya [5] for the control of the synchronous vibration of an unbalanced rotor. As well as avoiding problems associated with stability the technique in its developed form [10] allows the control action to minimise rotor vibrations without prior knowledge of system parameters. This is of prime importance in the application considered here where the bearing stiffness and damping properties vary with speed and temperature etc.

This approach employs the full capability of magnetic actuation compared with the more restricted approach adopted in many applications reported in the literature.

The open-loop adaptive algorithm uses measurements of rotor displacement distributed along the shaft. Any measurement at a critical shaft location can be weighted in the performance index which assesses the effectiveness of the control action. The object is to control the amplitude and phase of the force applied by the magnetic actuator to minimise the performance index or cost function which typically is the sum of squares of displacement. The results presented in [10] show how effective this strategy is. Sahinkaya and Burrows have shown elsewhere [11] how it can be combined with local feedback to achieve various design goals. In summary, if more complex control strategies are used it is clear that it will be possible to significantly reduce the force transmissibility compared with the simple tuned absorber discussed earlier.

It may be possible to extend this approach and control subharmonic and multiple harmonic vibration in addition to that at the blade passage frequency.

6. Conclusions

This study has shown that the use of electro-magnetics for vibration isolation in a ship at the blade passage is feasible using an absorber mass of acceptable magnitude.

In order to achieve acceptable performance over a range of operating conditions it is necessary to employ the full capability of magnetic actuators and not restrict their use to tunable spring and damper elements. This collocation of the sensors and actuators is not capable of achieving the required reduction in transmissibility.

7. References

[1] LEWIS, D W, ALLAIRE, P E and THOMAS, P W
Active magnetic control of oscillatory axial shaft vibration in ship transmission systems. Part 1: System natural frequencies and laboratory scale model. Tribol Trans V32 n2 Apr 1989 pp 170-178.

[2] DEN HARTOG
Mechanical Vibrations, Fourth Edition, McGraw Hill Book Co, 1956.

[3] SCHWEITZER, G and ULBRICH, H
Magnetic bearings - A novel type of suspension. IMechE Conf Vibrations in rotating machinery, 1980.

[4] CHAN, H W and MOREL, J
Application of an active magnetic bearing to vibration control near critical speeds in large rotating machines, ASME 11th Biennial Conf on Mech Vib and Noise, Boston, Mass, 1987. DE-Vol-2, pp 151-158.

[5] BURROWS, C R and SAHINKAYA, M N
Vibration control of multi-mode rotor bearing systems. Proc of the Royal Soc, Lond, Vol.A386, pp 77-94, 1983.

[6] LEWIS, D W and ALLAIRE PE
Control of oscillating transmitted forces in axial-thrust bearings with a secondary magnetic bearing. ASLE Trans v 30 n1 Jan 1987 pp 1-10 ISSN:0569-8197, 1987.

[7] FUJII, K and TANIDA, K
Ship vibration diagnosis system - 2. Vibration response analysis and its application. I.H.I. Engineering Review 16, 1, pp 14-20 (1983).

[8] SALM, J and SCHWEITZER, G
Modelling and control of a flexible rotor with magnetic bearings. IMechE Conf on Vibration in Rotating Machinery, York, C277/84.

[9] BLEULER, H and SCHWEITZER, G
Decentralized Control, Applied Control and Identification Symp. IASTED, Copenhagen, 1983.

[10] BURROWS, C R, SAHINKAYA, M N and CLEMENTS, S. Active vibration control of flexible rotors - an experimental and theoretical study. Proc Royal Soc, London, 1989. A422, pp 123-146.

[11] BURROWS, C R, SAHINKAYA, M N and CLEMENTS, S. Electromagnetic control of oil-film supported rotors using sparse measurements. Trans ASME Journal of Vibs, Acoustic, Stress and Reliability in Design. July 1988. Vol.110, pp 295-299.

2nd International Symposium on Magnetic Beaing
July 12-14, 1990, Tokyo, Japan

PERMANENT MAGNET BIASED MAGNETIC BEARINGS – DESIGN, CONSTRUCTION AND TESTING

Christopher K. Sortore, Engineer, Aura Systems, El Segundo, CA 90245
Paul E. Allaire, Assistant Dean and Professor, Mech. & Aero. Engr., Univ. of Virginia, Charlottesville, VA 22901
Eric H. Maslen, Graduate Research Assistant, Mech. & Aero. Engr., Univ. of Virginia, Charlottesville, VA 22901
Robert R. Humphris, Research Professor, Mech. & Aero. Engr., Univ. of Virginia, Charlottesville, VA 22901
Phil A. Studer, Private Consultant, Magnetic Concepts, Silver Spring, MD 20901

Abstract

Magnetic bearings may have the steady state bias flux supplied either from electromagnet coil currents or from permanent magnets. In the second case, the active control flux is provided by electromagnetic coils. The permanent magnet bias design provides advantages of minimum power consumption, smaller size and weight compared to the all electromagnetic design. This paper outlines the theoretical analysis of permanent magnet biased magnetic bearings. Further, it describes the construction and testing of a set of these bearings in a high speed rotor test rig. The bearings were tested in a rotor in several ways, including white noise excitation (non–rotating) and unbalance response (rotating) up to 23,000 rpm. Theoretical and measured results are compared. The power consumption of the original liquid lubricated bearings was 3,000 watts while the all electromagnetic design was approximately 500 watts. The permanent magnet biased design was measured at 207 watts (total power).

Nomenclature

a	area	F	Laplace trans. force
f	force vector	H	mag. field strength
g	air gap length	I	current
k_{eq}	equiv. stiffness	J	current density
k_i	actuator gain	N	no. of wire turns
k_x	bearing stiffness	W	energy
l	mag. path length	$\underline{\nabla}$	gradient operator
s	Laplace variable	μ_o	mag. permeability of free space
$\underline{s}$	position		
v	volume	μ_r	rel. permeability
B	mag. induction	$\underline{\nabla}$	gradient operator

1. Introduction

Magnetic bearings have advanced to the point of being able to offer several different varieties of advantages to rotating machinery manufacturers and users. The use of permanent magnets, in conjunction with electromagnets, provides one appealing option which strongly reduces the power required to operate magnetic bearings. Power consumption reduction of at least an order of magnitude is expected over conventional bearings.

Studer [1] discussed the use of magnetic bearings for space use in an energy storage flywheel. Many other researchers, such as Murakami, et. al [2], Heimbold [3], and Eisenhaure [4], to cite only a few, have explored the use of magnetic bearings in space. Work on flexible shaft rotating machines has been reported by Allaire et. al [5, 6]. Keith et. al [7] and Yates et. al [8] developed a digital control systems for magnetic bearings in high speed rotating machines.

Permanent magnets have been successfully employed in passive magnetic bearings by Yonnet [9] and Okuda et. al [10]. These bearings have the advantage of eliminating the weight and complexity of the electromagnetic components of the combination bearings. However, these bearings have low damping characteristics and the dynamic stability is less than required in some situations as reported by Arai [11].

Two early patents were obtained by Studer [12,13] on the use of permanent magnets in magnetic bearings. These patents have useful concepts similar to those employed in the bearings discussed in this paper. Wilson and Studer [14] have applied the permanent magnet bias concept to linear motion bearings. Ohkami et. al [15] have performed some interesting comparative studies of magnetic bearings which use permanent magnet biasing. Tsuchiya et. al [16] studies the stability of a high speed rotor suspended in magnetic bearings. Meeks [17] has performed a comparison of various magnetic bearing design approaches and concludes that combining actively controlled electromagnets with permanent magnets results in a superior magnetic bearing in terms of size, weight and power consumption.

This work describes the design, construction and testing of a set of magnetic bearings using this concept [18]. Both permanent magnets and electromagnets are used in a configuration which effectively provides the necessary flux in the appropriate air gaps, while simultaneously keeping the undesirable power losses to a minimum. The design includes two radial bearings and a thrust bearing.

2. Magnetic Bearings

The first bearing discussed is the radial bearing. It operates at one end of the high speed rotor (described later) and controls radial forces only. Two views of this bearing are shown in Figure 1. Appendix A presents an analysis of a simplified magnetic circuit with a permanent magnet providing the bias flux. Four axially magnetized arc segments are positioned circumferentially adjacent to the rotor. The bias flux generated by the permanent magnets passes down the laminated stator pole leg, through the working air gap, axially along the shaft, then returns to the permanent magnet via a radial bias pole piece. The active control generated by the coils also passes down the stator pole leg and through the working air gap.

The return path for the active (control) flux is different. It flows circumferentially around the stator, as shown in Figure 1. This design thus requires only four poles and four coils, in contrast to the all electromagnetic designs. Appendix A gives a discussion of the theory associated with the bearing design. Additionally, the coils for each bearing axis are connected in series. This means that the bearing control system requires only five current amplifier channels rather than the ten required of the all electromagnetic design.

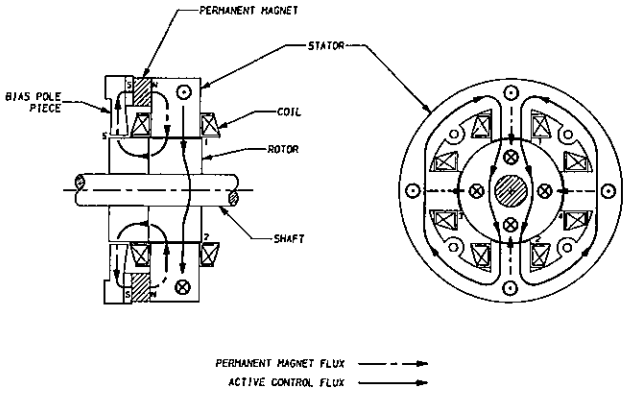

Fig. 1 Radial Magnetic Bearing Flux Paths

The combination radial/thrust bearing is illustrated in Fig. 2. The radial portion of the bearing is very similar to the radial bearing at the other end. However, the thrust bearing has a unique magnetic flux path design. The permanent magnet bias flux passing along the shaft splits equally between the two thrust poles before returning to the permanent magnet. A single active (control) coil produces a magnetic flux, in the shape of a toroid, which adds or subtracts to the bias flux in the working air gaps between the thrust disk and the thrust poles.

The bearings designed for this project are different from all electromagnetic bearing designs in that they employ both permanent magnets and electromagnets. Permanent magnets generate the bias flux in the working air gaps and electromagnets are used to modulate this flux.

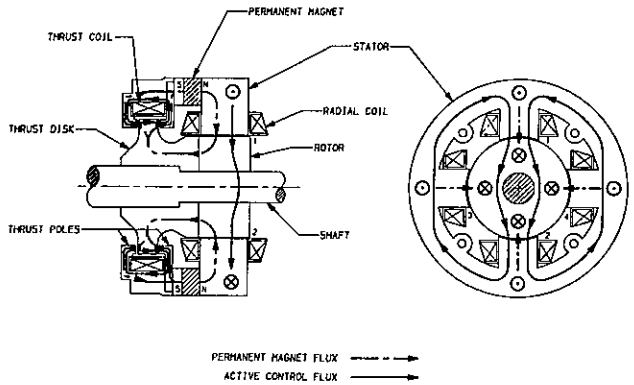

Fig. 2 Combination Radial/Thrust Magnetic Bearing Flux Paths

The purpose of establishing a bias flux in the working air gaps is to linearize the governing force equation of the magnetic actuator. The bias flux is a nominal flux density about which the control flux is varied. If a bias flux of zero is used (only one opposing actuator is operated at a time), then the force generated by the actuator on the rotor follows a quadratic force law, i.e., the force will be proportional to the square of the flux density in the air gaps. Consequently, the force slew rate will be zero when the rotor is in the nominal balanced position and the transient response will be adversely effected. If, however, the bearing fluxes are modulated about a non–zero bias flux, (with opposing actuators symmetrically perturbed) it is easily shown that the force becomes linearly related to the control flux. The following section demonstrates this important relation.

3. Bearing Forces

The force generated by a magnetic bearing on an object suspended in its field is a function of the geometry of the magnetic circuit and the magnetic induction in its air gaps. For simple magnetic circuits, this function is also quite simple. In the classic bearing geometry where an object is suspended between two opposing horseshoes, the force acting on the suspended body is given by the simple relation

$$f = \frac{A_g}{\mu_o}(B_1^2 - B_2^2) \tag{1}$$

If these two flux densities are perturbed symmetrically about some fixed point, then the resulting force is linear in the perturbation flux. That is if

$$B_1 = B_{bias} + B_{pert} \tag{2}$$

and

$$B_2 = B_{bias} - B_{pert} \tag{3}$$

then the net force is given by

$$f = 4\,\frac{A_g}{\mu_o}\,B_{bias}\,B_{pert} \tag{4}$$

Equation (4) illustrates the linearizing effect of a bias flux. An important fact concerning this bias flux is that it is to be held constant: modulation of the bearing force is accomplished by modulating a superimposed perturbation or control flux.

The purpose of introducing permanent magnets into a magnetic bearing circuit is to establish this bias flux without using any energy. The trick is to do this without requiring the control flux to pass through the permanent magnets, which have a low permeability.

The various magnetic circuits which have been devised to accomplish this combination of permanent magnet biasing and electromagnet perturbation tend to be more complicated than the simple opposing horseshoe scheme described above, with the result that the equations governing their generated forces are more complicated than (1). One method for determining the operating equations is based on studying the variation of the magnetic energy in the circuit as the supported object

is moved. Appendix A outlines such a method. The main result of the energy analysis is that the force in any given direction is approximated by

$$f_x \cong \frac{\partial}{\partial x}\left[\frac{1}{2\mu_o}\sum_{i=1}^{gaps} B_i^2 v_i\right] \tag{5}$$

Although the actual operating equations are more complicated than (1), they retain the main result that the operation of the bearing is linearized by prebiasing the air gaps to a fixed level and then perturbing them symmetrically.

4. Open Loop Stiffness and Actuator Gain

The force generated by a magnetic bearing is generally described by an equation which is linear in the control current but is most likely nonlinear in the displacement of the supported object. For the purpose of studying the stability and dynamic performance of the closed loop system, a linearized actuator mathematical model of the magnetic bearing is required. The bearing force acting in the x direction is expanded in a truncated Taylor series as

$$f_x(x,i_c) = f_x\Big|_{\substack{x=0\\ i_c=I_o}} + \frac{\partial f_x}{\partial x}\Big|_{\substack{x=0\\ i_c=I_o}} x + \frac{\partial f_x}{\partial i_c}\Big|_{\substack{x=0\\ i_c=I_o}} (i_c - I_o) \tag{6}$$

where I_o is the nominal control current required to hold the object suspended at x=0. In the absence of body forces and with a perfectly balanced circuit, this current will usually be zero. Since I_o is the current required to suspend the object at x=0, the net force acting on the object is

$$f_{x_{net}} \cong \frac{\partial f_x}{\partial x}\Big|_{\substack{x=0\\ i_c=I_o}} x + \frac{\partial f_x}{\partial i_c}\Big|_{\substack{x=0\\ i_c=I_o}} (i_c - I_o) \tag{7}$$

The linearized actuator properties are identified from (7) as

$$K_x \equiv -\frac{\partial f_x}{\partial x}\Big|_{\substack{x=0\\ i_c=I_o}} \quad \text{and} \quad K_i \equiv \frac{\partial f_x}{\partial i_c}\Big|_{\substack{x=0\\ i_c=I_o}} \tag{8}$$

The minus sign in the definition of K_x is introduced so that this term can be described as a stiffness. In the absence of a feedback loop, the stiffness of the support is entirely governed by K_x, so this term is referred to as the open loop stiffness. K_x is negative, indicating the open loop instability of magnetic suspensions. K_i relates the actuator force to the control current, so it is called the actuator gain.

Similar expressions can be obtained for each of the other two orthogonal directions. For a radial bearing, the axial properties are usually very weak and are ignored, and, likewise for a thrust bearing, the radial components are typically ignored.

5. Control System

The control circuitry is the key to any stable magnetic bearing system. This segment detects the motion of the shaft, determines the necessary control force and then supplies a current to the appropriate electromagnet to generate this force. Four distinct components make up the magnetic bearing system: 1) the magnetic actuators, 2) the position probes and associated conditioning circuitry, 3) analog proportional–integral–derivative (PID) controllers and 4) transconductance power amplifiers.

The actuator of the magnetic bearing is comprised of coils, iron stator pole pieces, permanent magnets and the rotor. The position probes are eddy current induction sensors and their output signals pass through coordinate transformation circuits to the analog controller, which contains the PID compensation network. The output of this compensator drives the transconductance power amplifier. This amplifier supplies the necessary current to the various coils, which produce the required magnetic fluxes and forces for stable operation of the bearing.

The operational behavior of the control electronics may then be combined with the dynamics of the bearing–rotor system to form the overall closed–loop control system. Figure 3 shows a block diagram of such a system. The characteristics of the position sensor, PID analog controller and the power amplifier are all combined in the complex transfer function, $G_c(s)$, of the feedback controller. This transfer function, $G_c(s)$, relates the rotor position to the actuator current. From the block diagram, the approximate closed–loop transfer function is determined to be

$$\frac{X(s)}{F_x(s)} = \frac{1}{ms^2 + K_x + K_i G_c(s)}$$

where m is the effective mass of the rotor.

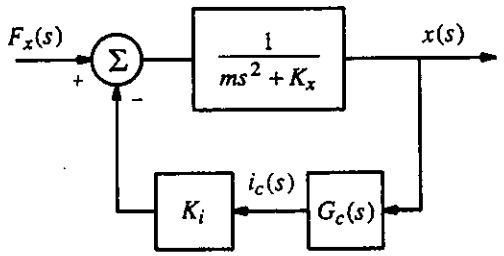

Fig. 3 Closed Loop Magnetic Bearing Control System

6. Prototype Bearing Construction

The four–pole radial bearing stator, shown in Figures 1 and 2, is designed to be identical for both bearings. The stators and rotors are constructed of a silicon–iron lamination material of 0.18 mm (0.007 inches) thickness. Each rotor and stator consists of

approximately 100 laminations, which were glued together using a two part activator/resin adhesive. The final shapes were machined by wire EDM (electric discharge machining). The bearing stators have an outside diameter of approximately 10.6 cm (3.0 inches) with an axial length of 1.8 cm (0.7 inches). The outside diameter of the laminated rotor is 3.8 cm (1.5 inches). Thrust bearing components were machined from soft magnet iron. The high energy permanent magnets, made from a Neodymium–Iron–Boron alloy, have a maximum energy product of 2.4 x 10^5 T–Amps/m (30 MG–Oe). The bearings support a shaft weighing approximately 1.68 kG (3.7 lbm).

7. Load Capacity

Results of measurements of the maximum load applied to the shaft, before it falls out of support, are plotted as a function of the controller proportional gain, K_p, in Figure 4. For these measurements the force was applied to the shaft by hanging weights and a pulley system constructed such that the force was acting in the appropriate direction, i.e. along the bearing axes.

The variation of the maximum load at lower proportional gains is actually a measure of the stability threshold of the system. As noted earlier, the open loop stiffness, K_x, is defined at a nominal operating point, i.e. rotor position deviation and control current are equal to zero. However, as the bearing is loaded with a static force, the steady state current begins to increase and it can be shown that K_x is a function of the operating point of the control current. In other words, as the control current increases, K_x also increases and thus increasing the proportional gain has the effect of compensating for this increase in K_x and consequently improving the stability of the system.

Therefore, measurements made at the higher proportional gains represent a more accurate indication of the actual load capacity of the bearing, whereby sufficient stability is provided so that magnetic saturation of the pole structures is achieved. The maximum predicted loads shown in Figure 4 are calculated using a saturation flux density value.

8. Equivalent Bearing Stiffness and Damping

Results of measurements of the equivalent stiffness of the radial and thrust bearings are shown in Figure 5. A constant force, ΔF, was applied and the displacement, Δx, of the shaft was noted while the controller integrators were switched off. The stiffnesses may then be easily found from $K_{eq} = \Delta F/\Delta K$. A linear regression, performed on the measured data, indicated a very good correlation to predicted values. It should be noted that the proportional gain, K_p, has a direct effect on the stiffness of the bearings, as previously demonstrated by Humphris, et al. [19].

Relative damping in the bearings was investigated by analyzing the frequency response of the rotor to injected white noise. Noise composed of all frequencies of interest was injected into the power amplifier of the appropriate axis under study and a Fast Fourier Transform (FFT) was performed on the sensor output of that axis. A typical frequency response, composed of 100 averages, is shown in Figure 6 for the turbine–end radial bearing as the controller derivative gain, K_r, is varied. As expected [19], this derivative gain variation had a direct effect on the damping in the bearing. The first large peak represents the first two modes of shaft vibration, as they are very close together in frequency and essentially indistinguishable. The frequency of the observed second peak is actually the third mode of shaft vibration and the third small peak near 60,000 rpm is the fourth mode. Note that the derivative gain variation strongly affects the first two modes, has a smaller effect on the third mode and virtually no influence on the amplitude of vibration of the fourth mode.

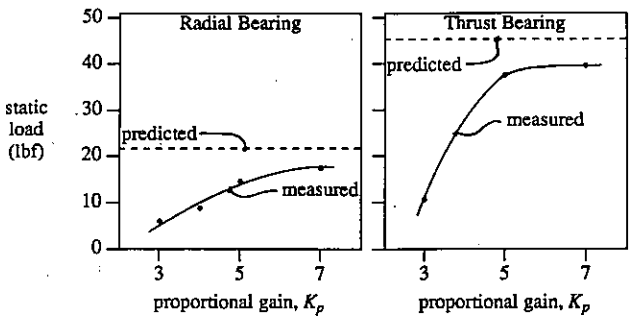

Fig. 4 Load Capacity versus Proportional Gain Setting

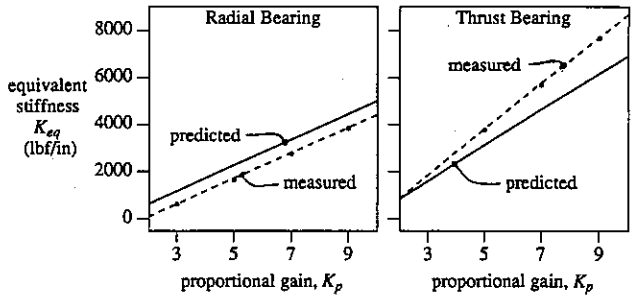

Fig. 5 Equivalent Bearing Stiffness versus Proportional Gain Settings

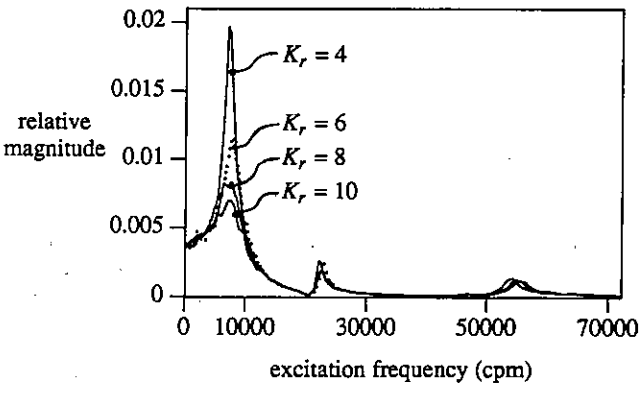

Fig. 6 Frequency Response to White Noise

9. Critical Speeds and Rotor Response

The frequency response due to white noise indicates the approximate damped critical speeds of the flexible shaft supported in magnetic bearings. However, these values represent the zero speed natural frequencies. The effects of gyroscopic stiffening due to attached disks would not be included. With the shaft rotating, the observed critical speeds would be higher, as expected, since the natural frequency is given by $\omega_n = \sqrt{k/m}$, where k is the system stiffness and m is the modal mass of the rotor. Actual run–up vibration magnitude and phase information for rotor speeds up to approximately 23,000 rpm is shown in Figure 7. High vibration levels at the onset of the third critical mode prevented operation at higher speeds. As noted in Figure 7, the first vibration mode is observed as approximately 10,000 rpm and the second at approximately 13,000 rpm.

10. Power Consumption

Finally, several power measurements on the overall magnetic bearing system were made with a wattmeter. The total power consumption for this bearing with its supporting electronics was 207 watts. This measurement represents a significant improvement over the approximately 500 watts of total power consumed by a comparable magnetic bearing using no permanent magnets.

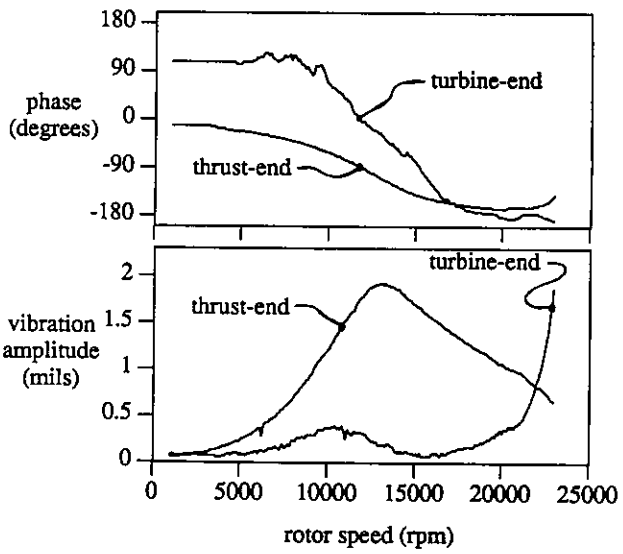

Fig. 7 Rotor Runup Response

11. Conclusions

The brief theory which was presented in this paper established the basic electromagnetic and mechanical relationships necessary to develop a set of permanent magnet biased magnetic bearings. The design involved both radial and thrust bearings. The availability of newer rare–earth high energy permanent magnets made it possible to effectively provide the necessary bias fluxes in the bearing.

The bearings and rotor were successfully constructed and operated. A number of tests and experiments were performed on the bearing–rotor system. The tests consisted of load capacity, stiffness and damping measurements. The results proved to be very positive in that the theoretical predictions and the observed performance matched reasonably well, giving credibility to the models which were used to perform the analysis. Of particular interest for this study was the measured power consumption of the bearings. It clearly demonstrates that the use of permanent magnets can improve the operating efficiency of an active magnetic bearing, in this case by a factor of 2.5.

It was successfully observed and demonstrated that these bearings have strong potential for future use as efficient, reliable bearings. However, further research and developed is required in the areas of controls, magnetic materials and actuator design before it is possible to install them into a useful industrial application.

References

1. Studer, P. A., "Magnetic Bearings for Instruments in the Space Environment," NASA Technical Memorandum 78048, 1978.

2. Murakami, C., A. Nakajima, S. Akishita, M. Inoue and K. Yabu'Uchi, "A Magnetically Suspended Flywheel for Attitude Control of Satellites," Mitsubishi Denki Giho (Japan), Vol. 58, No. 3, pp. 26–30, 1984.

3. Heimbold, G., "Impact of Magnetic Bearing Rotor Design on Satellite Nutational Stability," Journal of Guidance Control Dynamics, Vol. 7, No. 3, pp. 279–285, 1984.

4. Eisenhaure, D., "Inertial Energy Storage for Satellites," NASA Conference Publication 2346, pp. 101–116, 1984.

5. Allaire, P. E., R. R. Humphris and L. E. Barrett, "Critical Speeds and Unbalance Response of a Flexible Rotor in Magnetic Bearings," Presented at the European Turbomachinery Symposium, Brunel, The University of West London, October 1986.

6. Allaire, P. E., R. R. Humphris and R. D. Kelm, "Magnetic Bearings for Vibration Reduction and Failure Prevention," Proceedings of the 40th Meeting of Mechanical Failures Prevention Group, National Bureau of Standards, Gaithersburg, MD, April 1985.

7. Keith, F. J., R. D. Williams, P. E. Allaire and R. M. Schafer, "Digital Control of Magnetic Bearings Supporting a Multimass Flexible Rotor," Presented at the Magnetic Suspension Technology Workshop, Hampton, VA, February 1988.

8. Yates, S. W. and R. D. Williams, "A Fault–Tolerant Multiprocessor Controller for Magnetic Bearings," IEEE Micro, pp. 6–17, August 1988.

9. Yonnet, J.–P., "Passive Magnetic Bearings Made Only with Permanent Rings," Proc. 6th Int'l Workshop on Rare Earth–Cobalt Permanent Magnets and Their Applications, pp. 203–212, 1982.

10. Okuda, H. T., K. Abukawa, and M. Ito, "Characteristics of Permanent Magnet Bearings," Hitachi Research Laboratory, Hitachi Ltd., Japan, 1984.

11. Arai, J., "Dynamic Stability of a Passive Magnetic Suspension With an Eight–Pole Stator," Bulletin JSME, Vol. 27, No. 229, pp. 1506–1512, 1984.

12. Studer, P. A., NASA, **Magnetic Bearing**, Patent 3865442, Patent Application 100637, February 1975.

13. Studer, P. A., NASA, **Linear Magnetic Bearing**, Patent 4387935, Patent Application 214361, Dec. 1980.

14. Wilson, M. and P. A. Studer, "Linear Magnetic Bearings," Presented at the Int'l Workshop on Rare Earth–Cobalt Magnets and Their Applications, Roanoke, VA, June 1981.

15. Ohkami, Y., O. Okamato, T. Kida, C. Murakami, A. Nakajima, S. Hagihara and K. Yabuuchi, "A Comparison Study of Various Types of Magnetic Bearings Utilizing Permanent Magnets," Presented at the Int'l Workshop on Rare Earth–Cobalt Magnets and Their Applications, Roanoke, VA, June 1981.

16. Tsuchiya, K. and M. Inoue, A. Nakajima, Y. Ohkami, and C. Murakami, "On Stability of Magnetically Suspended Rotor at High Rotational Speed," Presented at the Aerospace Sciences Meeting, Reno, NV, January 1989.

17. Meeks, C., "Trends in Magnetic Bearing Design," Paper presented at Naval Sea Systems Command Magnetic Bearing Forum, Washington, D.C., July 1989.

18. Sortore, C. K., P. E. Allaire, E. H. Maslen, R. R. Humphris, and P. A. Studer, "Design of Permanent Magnet Biased Magnetic Bearings for a Flexible Rotor," presented at the 44th MFPG Meeting, Virginia Beach, VA, April 2–5, 1990.

19. Humphris, R. R., R. D. Kelm, D. W. Lewis and P. E. Allaire, "Effect of Control Algorithms on Magnetic Journal Bearing Properties," Journal of Engr. for Gas Turbines and Power, Vol. 108, October 1986.

20. Hebbale, K., "A Theoretical Model for the Study of Nonlinear Dynamics of Magnetic Bearings," Master of Science Thesis, Cornell University, January 1985.

Appendix A. Energy Derivation of Bearing Forces

The force generated by magnetic actuators is determined by the sensitivity of the flux density in the circuit to variations in position of the supported structure. This description of the magnetic effect is useful in analyzing the behavior of complex magnetic circuits such as permanent magnet biased actuators. A variety of researchers have employed such an analysis, producing results identical to those based on simpler approaches for simple magnetic circuits [7,18,20]. The analysis is based on a conventional energy variation argument: the magnetic circuit will tend toward a configuration which minimizes its potential energy. The mechanism which produces this tendency is called a "force". Thus, if the magnetic circuit is lossless so that the magnetic energy represents a potential function, the force is described by

$$\underline{f} \equiv -\nabla W_m \tag{A.1}$$

where W_m is the total energy contained in the magnetic field generated by the magnetic circuit and the gradient operator is with respect to configuration space. If the position of the supported structure relative to the magnetic circuit is

$$\underline{s} = x\,\underline{i} + y\,\underline{j} + z\,\underline{k} \tag{A.2}$$

then the force acting on the structure is

$$\underline{f} \equiv -\left\{ \frac{\partial}{\partial x} W_m\,\underline{i} + \frac{\partial}{\partial y} W_m\,\underline{j} + \frac{\partial}{\partial z} W_m\,\underline{k} \right\} \tag{A.3}$$

For the general, nonlinear magnetic circuit, the total energy required to take the field distribution from some nominal state, B_o and H_o, to some other state, B and H is

$$W_m = -\int_{\infty} \int_{B_o}^{B} \underline{H} \cdot d\underline{B}\, dv \tag{A.4}$$

The volume integral is computed over all of space. Assume that the induction, $\underline{B}$, is an explicit function of the variable x which partially describes the position of the supported object and the change from the initial state to some other state is caused entirely by varying x. Then

$$\begin{aligned} f_x\Big|_{H=H_o,B=B_o} &= \frac{\partial}{\partial x} \int_{\infty} \int_{B_o}^{B} \underline{H} \cdot d\underline{B}\, dv \\ &= \frac{\partial}{\partial x} \int_{\infty} \int_{x_o}^{x} \underline{H} \cdot \frac{\partial}{\partial x}\underline{B}\, dx\, dv \end{aligned} \tag{A.5}$$

or,

$$\begin{aligned} f_x = &\int_{\infty} \underline{H_o} \cdot \frac{\partial}{\partial x}\underline{B}\Big|_{H=H_o,B=B_o} dv \\ &+ \frac{\partial}{\partial x} \int_{\infty} \underline{H_o} \cdot \underline{B_o}\, dv \end{aligned} \tag{A.6}$$

Similar expressions describe the forces in the y and z directions. Equation (A.6) forms the basis for computing the forces in the fairly complicated magnetic circuits which comprise permanent magnet biased magnetic bearings.

For design purposes, it will be convenient to compute the forces using a crude finite element method, where it is assumed that the magnetic flux is confined to the physical structure of the magnetic circuit and simply

described air gap volumes. In making this assumption, leakage and fringing effects are neglected. These effects can be included in a more detailed analysis where some estimate of the shape of finite fringing and leakage volumes is determined and added into the circuit description as paths parallel to those passing through the structure. Such refinements improve the accuracy of the performance prediction, but complicate the analysis and tend to obscure the design dependent effects which are to be illustrated. With these limitations in mind, the integral over all space of (A.6) can be written as a sum over the various components of the circuit.

In the air gaps, the relationship between $\underline{H}$ and $\underline{B}$ is linear:

$$\underline{B}_{gap} = \mu_o \underline{H}_{gap} \tag{A.7}$$

Similarly, if the magnetic induction in the iron stays well below the saturation level, the relationship in the iron is similar, scaled by a large (~5000) relative permeability, μ_r:

$$\underline{B}_{iron} = \mu_o \mu_r \underline{H}_{iron} \tag{A.8}$$

The relationship between $\underline{B}$ and $\underline{H}$ in the permanent magnets is quite nonlinear, but it does have the property that $\underline{B}$ and $\underline{H}$ are parallel with opposite sense.

If it is further assumed that each of the components can be broken into a set of sections throughout whose volumes the induction is fairly constant, then (A.6) becomes

$$f_x = \frac{1}{2\mu_o}\sum_{i=1}^{gaps}\frac{\partial}{\partial x}\left\{B_i^2 v_i\right\} + \frac{1}{2\mu_o}\sum_{i=1}^{legs}\frac{1}{\mu_{r_i}} v_i \frac{\partial}{\partial x} B_i^2 + \sum_{i=1}^{magnets} H_i v_i \frac{\partial}{\partial x} B_i \tag{A.9}$$

where the volumes of the iron and permanent magnets have been assumed to be fixed. The scalars B_i and H_i have replaced the corresponding vector quantities because, if the field varies slowly in time, then the two vectors are always parallel: in the iron and air gaps, the vectors point in the same direction whereas in the permanent magnet, they point in opposite directions.

For a well designed magnetic circuit, the flux density in the permanent magnets will be fairly independent of the position of the supported object. Further, the length of the iron paths will be substantially less than μ_r times the length of the air gaps, so (A.9) is dominated by the first term. Neglecting the less significant terms and interchanging the order of summation and differentiation produces

$$f_x \cong \frac{\partial}{\partial x}\frac{1}{2\mu_o}\sum_{i=1}^{gaps} B_i^2 v_i \tag{A.10}$$

The magnetic induction, B, in the air gaps is found from Ampere's circuital law:

$$\oint \underline{H}\cdot d\underline{l} = \iint \underline{J}\cdot d\underline{a} \tag{A.11}$$

which states that the line integral of the magnetic field strength around any closed path is equal to the integral over the enclosed area of the current density in that area. For magnetic circuits whose fields are modulated by winding wire coils around various legs of the circuit and applying currents to these legs, the area integral simply becomes a measure of the total current linked by the path of the line integral. Thus,

$$\oint \underline{H}\cdot d\underline{l} = NI \tag{A.12}$$

where N is the number of wire turns enclosed by the path and I is the current in the wire.

Equation (A.12) can be discretized for the crude finite element approach of this discussion if it is assumed that each element of the magnetic circuit has a characteristic length in the direction of $\underline{H}$ and a characteristic area normal to $\underline{H}$. In this manner, each closed path in the magnetic circuit is governed by

$$\sum_{i=1}^{n} H_i l_i = NI \tag{A.13}$$

where n is the number of elements in the path. If each path contains p iron legs, a air gaps, and m permanent magnets, then (A.13) can be broken into

$$\frac{1}{\mu_o\mu_r}\sum_{i=1}^{p} B_i l_i + \frac{1}{\mu_o}\sum_{i=1}^{a} B_i l_i - \sum_{i=1}^{m} H_i l_i = NI \tag{A.14}$$

Note that the sense of the integral path and the H vector are opposite in the permanent magnets, hence the minus sign preceding the permanent magnet term in (A.14). Further simplification is possible if, consistent with (A.10), the loss in the iron due to finite μ_r is neglected. This produces

$$\frac{1}{\mu_o}\sum_{i=1}^{a} B_i l_i = \sum_{i=1}^{m} H_i l_i + NI \tag{A.15}$$

One further relation is generally required to compute the induction in the gaps. This is Maxwell's divergence theorem which states that

$$\underline{\nabla}\cdot\underline{B} = 0 \tag{A.16}$$

This means that there are no sources or sinks of induction. Practically, it implies that the total flux, Φ, at any node of the magnetic circuit is zero. The flux, Φ, is simply the integral of $\underline{B}\cdot d\underline{a}$ over any surface. In the analysis presented here, it is assumed that $\underline{B}$ is uniform

across any given crossection of the circuit taken normal to $\underline{B}$. Thus, for a fixed element of the circuit,

$$\Phi_i = B_i A_i \qquad (A.17)$$

For a node of the circuit connected to e elements, (A.16) implies

$$\sum_{i=1}^{e} \Phi_i = 0 \qquad (A.18)$$

where the sense of Φ_i is taken relative to the node: flux into the node is taken as positive while flux out of the node is taken as negative.

Equations (A.15) and (A.18) together with the nonlinear B–H relationship for any permanent magnets in the circuit, define a complete set of governing equations for the inductions in each of the circuit elements. The nonlinear nature of the permanent magnets requires an iterative solution for the resulting network equation, but the solution is generally fairly easy to obtain. Once the inductions have been computed, equation (A.10) can be evaluated for each direction to determine the bearing forces.

As an example, consider the magnetic circuit of Figure A.1.

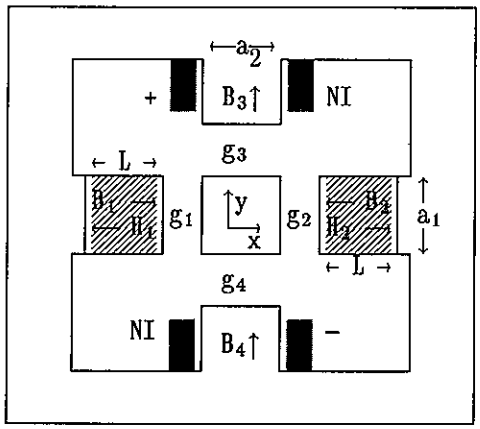

Figure A.1: simple magnetic circuit

The position of the suspended object is given by (x,y). The air gaps have lengths g_1, g_2, g_3, and g_4 given by

$$g_1 = g_a + x\,;\ g_2 = g_a - x\,;\ g_3 = g_b - y\,;\ g_4 = g_b + y$$

Permanent magnets are indicated by the shaded regions ▨ and wire coils are indicated by ▮. The coils have N turns and the current direction is such that a positive I in either of the coils will tend to produce positive B_3 and B_4.

Three independent loop paths can be found to produce via (A.15) the equations

$$B_3 g_3/\mu_0 + B_4 g_4/\mu_0 = 2NI \qquad (A.19)$$

$$B_1 g_1 + B_2 g_2 = LH_1 - LH_2 \qquad (A.20)$$

$$B_1 g_1/\mu_0 + B_3 g_3/\mu_0 = LH_1 + NI \qquad (A.21)$$

Equation (A.18) gives, for the fluxes entering the supported object,

$$B_1 a_1 + B_4 a_2 - B_2 a_1 - B_3 a_2 = 0 \qquad (A.22)$$

These equations may be summarized by

$$\begin{bmatrix} a_1 & -a_1 & -a_2 & a_2 \\ g_1 & g_2 & 0 & 0 \\ g_1 & 0 & g_3 & 0 \\ 0 & 0 & g_3 & g_4 \end{bmatrix} \begin{Bmatrix} B_1 \\ B_2 \\ B_3 \\ B_4 \end{Bmatrix} = \begin{Bmatrix} 0 \\ \mu_0 L(H_1 - H_2) \\ \mu_0(LH_1 + NI) \\ 2\mu_0 NI \end{Bmatrix} \qquad (A.23)$$

subject to

$$B_1 = f(H_1) \qquad (A.24)$$

$$B_2 = f(H_2) \qquad (A.25)$$

where these latter two functions describe the magnetization curve for the permanent magnet material.

These last three equations must be solved iteratively because of the nonlinearity of (A.24) and (A.25): these functions will typically be specified by an empirical magnetization curve. A symbolic solution to (A.23) was generated using MACSYMA. The resulting expressions were substituted into (A.10) and the forces in the x and y directions were computed to be

$$f_x\big|_{x=0,y=0} = \mu_0 \frac{a_1 a_2 (H_2^2 - H_1^2) L^2}{2 g_a (g_a + g_b)} \qquad (A.26)$$

$$f_y\big|_{x=0,y=0} = \mu_0 \frac{a_1 a_2 (H_1 + H_2) LNI}{g_b (a_1 g_b + a_2 g_a)} \qquad (A.27)$$

The force in the x direction is independent of the coil current. If $H_1 = H_2$, f_x is zero when the object is centered. The force in the y direction is linear in the current, I. Equation (A.27) illustrates that the magnetization force of the permanent magnets determines the effectiveness of variations in I.

Acknowledgements

The authors would like to thank the Center for Computer Aided Engineering of the Center for Innovative Technology of the Commonwealth of Virginia for partial support of this work. This work was based on research supported in part by a National Science Foundation Graduate Fellowship. Any opinions, findings, conclusions or recommendations expressed in this publication are those of the authors and do not necessarily reflect the views of the National Science Foundation.

2nd International Symposium on Magnetic Beaing
July 12-14, 1990, Tokyo, Japan

SINGLE AXIS ACTIVE MAGNETIC BEARING SYSTEM WITH MECHANICAL DAMPERS FOR HIGH SPEED ROTOR

M.MIKI, Y.TANAKA, Y.YAMAGUCHI, T.ISHIZAWA and A.YAMAMURA

Development Dept., Nippon Ferrofluidics Corp., 1-2-1, Makuharihongo, Chiba-shi, 281, Japan

Abstract

We realized a single axis active magnetic bearing system for high speed rotor(60,000rpm) by applying mechanical dampers. Test machine's rotor is M = 0.76 kg, I_z = 4.3 $\times 10^{-4}$ kgm^2, and $I_x = I_y = 1.8 \times 10^{-3}$ kgm^2. Naturally, this system is mounting position free. Though we have well known eddy current damper and oil damper, the mechanical damper that we developed is a simple and unique one. In this paper, we show that a single axis active magnetic bearing system with the mechanical dampers has good features if the system parameters are selected systematically and carefully. Furthermore, the dynamic behavior of rotor suspended by this magnetic bearing system is analyzed and test result of this system is shown.

1. Introduction

Though magnetic bearings are known from forty years ago, very limited number of products have been developed so far. The majority of application is of special order products used in scientific application or space development[1]. In recent years, the magnetic bearing for wafer transfer-machine is developed in semiconductor manufacturing industry which are also of special order products[2]. The turbo molecular pump is only one exception that succeeded in mass production[3]. However,its share in the entire market is as low as approximately 10 %.

It is true that magnetic bearings have many distinctive features which are not attained by ordinary ball bearing. However, practical application of these bearings is greatly hindered by the fact that production cost is very high and that size of the circuit and structure is too big.

The most important matter to make these magnetic bearings popular is [How to design small size and low cost magnetic bearings without loosing original features of those].

Currently, we developed a single axis active magnetic bearing which satisfied the purpose said above. This is equipped with a simple and unique mechanical damper made of viscoelastic material, (though we have well known eddy current damper and oil damper[4][5].)

The following four features are distinctive:

1) It has enough stability from 0rpm till ultra high speed rotation(60,000rpm) like five axes active magnetic bearing.
2) It has sufficient spring constant in every direction for mounting position free.
3) Power consumption of the magnetic bearing is very small.
4) It is small sized and low cost magnetic bearing.

This system seems best suited for such an application in which a rotor is simply turned at high speed such as a chopper, pump, and compressor.

2. Character

The character of this magnetic bearing system is shown below.

1) Character of rotor

Mass of rotor	0.76 Kg
Moment of inertia of rotor (Z is rotational axis)	I_z= 4.3×10^{-4}Kgm^2 I_x=I_y=1.8×10^{-3}Kgm^2
Rotational speed	60,000rpm

2) Charactor of magnetic bearing

Structure	Two passive radial magnetic bearings with mechanical damper and One active axial magnetic bearing
Steady current of Axial magnets	0~0.2 A
Resonance points	
Toransrational mode	50 Hz
Tilting mode	57 Hz

3) Motor

High frequency induction motor	Max. 150 W
Run-up time (60,000rpm)	2 min.

4) Size

Structure $\phi 100 \times 180$mm
(Circuit-box $250 \times 130 \times 430$mm)

3. Entire construction

Single axis active magnetic bearing system with mechanical dampers is shown fig.1. The rotor is supported by passive radial magnetic bearings A and B, and by active axial magnetic bearing C. Acceleration up to 60,000 rpm is driven by means of a high frequency induction motor D.

With passive magnetic bearing A, three permanent magnets are provided at both rotor side and stator side on the concentric circle, and they are repulsing each other. This sort of magnetic bearing is stable in radial direction and is unstable in axial direction. Three permanent magnets are magnetized in axial direction and are laminated in the order of NS, SN, NS.

The stator which holds permanent magnets of passive magnetic bearing A acts as mechanical damper X and moves freely in radial direction only. With this configuration, a viscoelastic material 1 is put between main stator and movable stator 2. When the rotor is vibrated in radial direction, mechanical damper X is vibrated in radial direction, and its energy is absorbed by viscoelastic material 1 to damp vibration of the rotor.

Passive magnetic bearing B is basically identical with magnetic bearing A. One of differences is such that stator portion is divided into two segments of fixed part and moving damper part Y. Rotor side holds three permanent magnets, fixed part of stater side holds two and moving damper part Y holds one. Two permanent magnets are provided on both rotor side and fixed part on the concentric circle so that they may repulse each other with a similar manner as observed with magnetic bearing A. This sort of bearing is stable in radial direction and unstable in axial direction. Permanent magnets remained at rotor side and at moving damper part Y absorb each other in axial direction. This moving damper Y is of mechanical damper and can move in radial direction only. When the rotor is vibrated in radial direction, it is vibrated according to permanent magnet force, and its energy is absorbed by viscoelastic material 3 put between main stator and movable stator 4 with a similar manner as observed with mechanical damper A.

Active axial magnetic bearing C consists of two axial electromagnets 5 of similar configuration, an armature disk 6, an axial position sensor 7, and an electromagnetic control circuit(not shown fig.1). As for axial direction damping, amplitude and phase of electromagnetic force is being controlled.

Since bias magnetic flux is applied to the axial direction electromagnet by the permanent magnet, little electric current should be flowed through the electromagnetic coils in steady state.

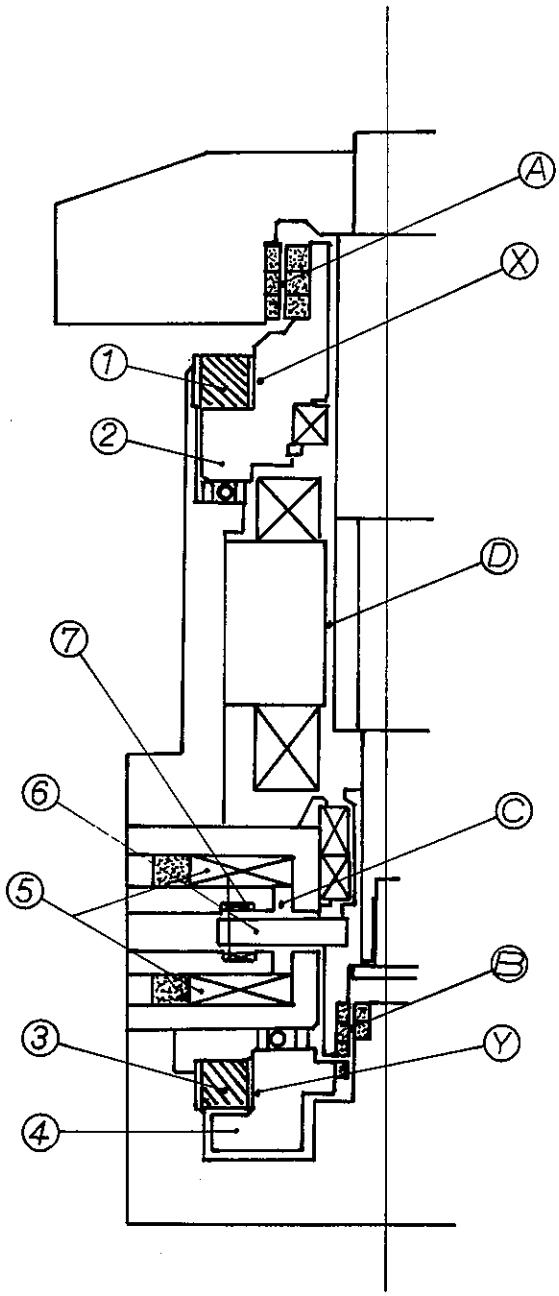

Fig.1 Entire construction of single axis active magnetic bearing system with mechanical dampers

4. Modeling and numerical calculation

4.1 Radial equations of motion

It is discussed only radial motions because main theme in this paper is passive radial magnetic bearings with mechanical dampers.

A model shown which is considered in this in-

vestigation is shown fig.2. Principal axes of coordinates are X, Y, Z, θ_X, θ_Y, and θ_Z. Coordinates at points A and B are X_a, Y_a, X_b, and Y_b. Definition of each parameter is shown in Table 1.

The following assumptions are made.

1) Displacement in θ_x and θ_Y direction is smaller than L_a and L_b respectively.
2) Movement of the damper is limited to a plane perpendicular to the axis of rotation.
3) Gravity acts in the direction of -X.
4) The rotor is rigid.

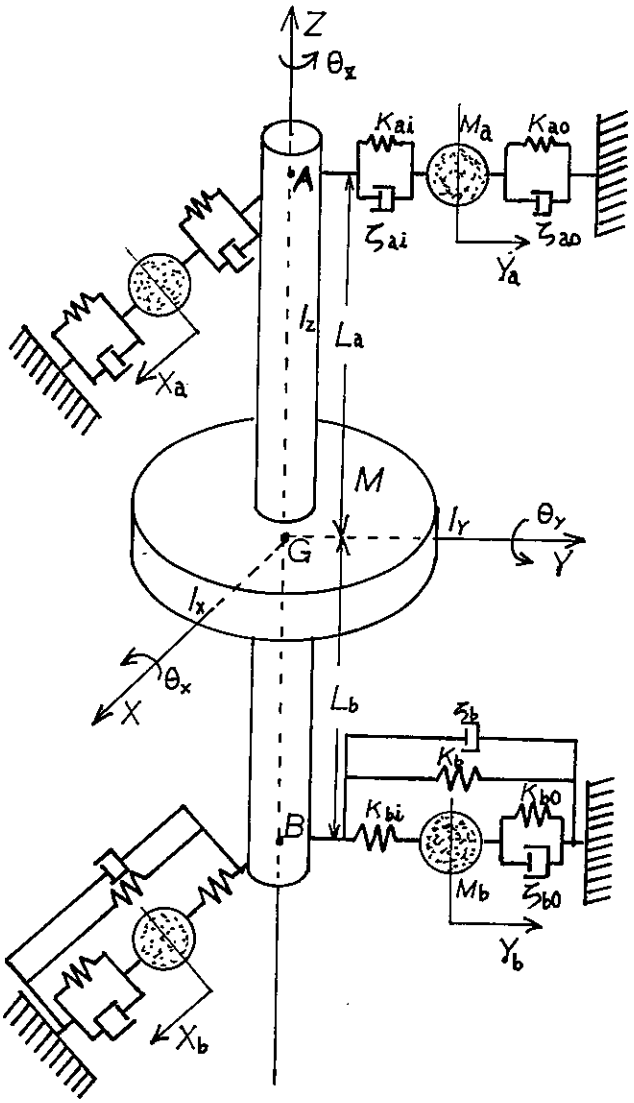

Fig.2 A model of passive radial magnetic bearings with mechanical dampers

Symbol	Definition
M	Mass of rotor
I_z	Moment of inertia of rotor (z, x, and y direction)
I_x I_y	
L_a	Distance between center of gravity and point A or B
L_b	
K_{ai}	Spring constant at point A i:Inside o:Outside
K_{ao}	
ζ_{ai}	Damping coefficient at point A i:Inside o:Outside
ζ_{ao}	
M_a	Mass of damper A
K_b	Spring constant at point B :Directly coupled with stator i:Inside o:Outside
K_{bi}	
K_{bo}	
ζ_b	Damping coefficient at point B :Directly coupled with stator o:Outside
ζ_{bo}	
M_b	Mass of damper B
ω	Rotor angular speed
g	Acceleration of gravity

Table 1 Definition of parameters

Radial equations of motion are as follows.

(1)

$$MX'' = -Mg - X(K_{ai}+K_b+K_{bi}) - \theta_y(L_aK_{ai} - L_b(K_b+K_{bi})) + X_aK_{ai} + X_bK_{bi} + 2\zeta_{ai}(K_{ai}ML_b/(L_a+L_b))^{1/2}(-X' - \theta_y'L_a + X_a') + 2\zeta_{bi}(K_bML_a/(L_a+L_b))^{1/2}(-X' + \theta_y'L_b)$$

(2)

$$MY'' = -Y(K_{ai}+K_b+K_{bi}) + \theta_x(L_aK_{ai} - L_b(K_b+K_{bi})) + Y_aK_{ai} + Y_bK_{bi} + 2\zeta_{ai}(K_{ai}ML_b/(L_a+L_b))^{1/2}(-Y' + \theta_x'L_a + Y_a') + 2\zeta_{bi}(K_bML_a/(L_a+L_b))^{1/2}(-Y' - \theta_x'L_b)$$

(3)

$$I_y\theta_y'' = -X\,(L_aK_{ai} - L_b\,(K_b + K_{bi})) - \theta_y\,(L_a^2K_{ai} + L_b^2\,(K_b + K_{bi})) + X_aL_aK_{ai} - X_bL_bK_{bi} + I_z\omega\,\theta_x' + 2\zeta_{ai}\,(K_{ai}ML_b/(L_a + L_b))^{1/2}\,(-X' - \theta_y'L_a + X_a')\,L_a - 2\zeta_{bi}\,(K_bML_a/(L_a + L_b))^{1/2}\,(-X' + \theta_y'L_b)\,L_b$$

(4)

$$I_x\theta_x'' = -Y\,(L_aK_{ai} - L_b\,(K_b + K_{bi})) - \theta_x\,(L_a^2K_{ai} + L_b^2\,(K_b + K_{bi})) - Y_aL_aK_{ai} + Y_bL_bK_{bi} - I_z\omega\,\theta_y' - 2\zeta_{ai}\,(K_{ai}ML_b/(L_a + L_b))^{1/2}\,(-Y' + \theta_x'L_a + Y_a')\,L_a + 2\zeta_{bi}\,(K_bML_a/(L_a + L_b))^{1/2}\,(-Y' + \theta_x'L_b)\,L_b$$

(5)

$$M_aX_a'' = -M_ag - X_a\,(K_{ao} + K_{ai}) - X_a'2\zeta_{ao}\,(M_aK_{ao})^{1/2} + \theta_yL_aK_{ai} + XK_{ai} - 2\zeta_{ai}\,(K_{ai}ML_b/(L_a + L_b))^{1/2}\,(-X' - \theta_y'L_a + X_a')$$

(6)

$$M_aY_a'' = -Y_a\,(K_{ao} + K_{ai}) - Y_a'2\zeta_{ao}\,(M_aK_{ao})^{1/2} - \theta_xL_aK_{ai} + YK_{ai} - 2\zeta_{ai}\,(K_{ai}ML_b/(L_a + L_b))^{1/2}\,(-Y' + \theta_x'L_a + Y_a')$$

(7)

$$M_bX_b'' = -M_bg - X_b\,(K_{bo} + K_{bi}) - X_b'2\zeta_{bo}\,(M_bK_{bo})^{1/2} - \theta_yL_bK_{bi} + XK_{bi}$$

(8)

$$M_bY_b'' = -Y_b\,(K_{bo} + K_{bi}) - Y_b'2\zeta_{bo}\,(M_bK_{bo})^{1/2} + \theta_xL_bK_{bi} + YK_{bi}$$

4.2 Numerical calculation

Dynamic characteristics of the rotor are studied by numerical calculation using equations of motion obtained in 4.1.

The result from numerical calculations is shown below.

1) If spring constants of force supporting rotor are determined by maintaining the relation of $L_b/L_a = K_{ai}/(K_b + K_{bi})$, spring constants of force supporting rotor are nearly equal to those of force supporting damper, and mass of damper is nearly equal to effective mass of rotor respectively, damping capacity of the system becomes optimum.
2) The limit of rotational speed depends on the amount of decrease in resonance frequency and damping capacity of tilting mode due to gyro effect when rotational speed increases.

An example of caliculation is shown in fig.3.

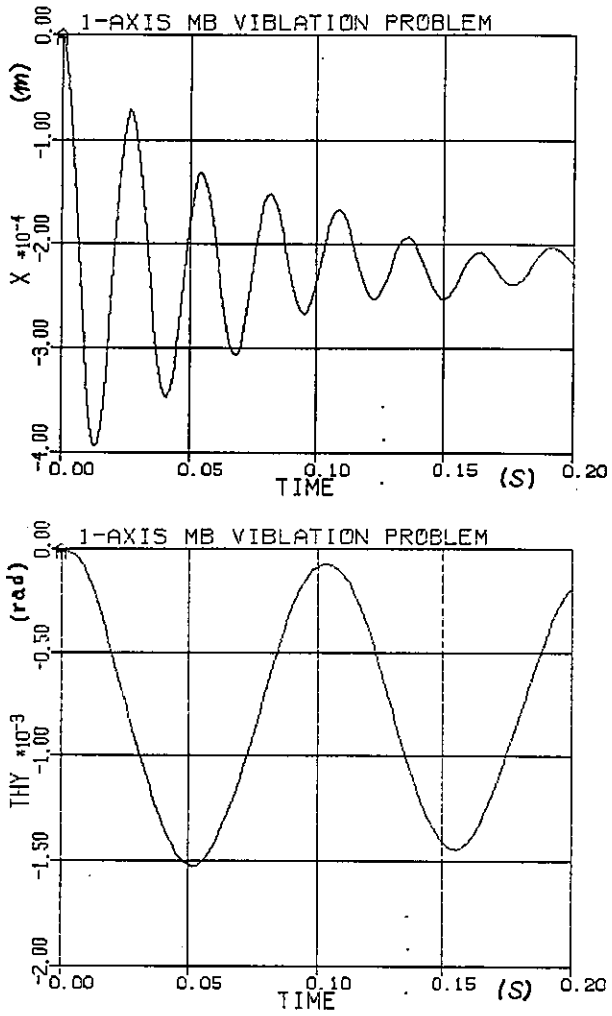

Fig.3 Rotor's motions of X and θ_Y direction at $\zeta_{ao}=0.14$, $\zeta_{bo}=0.14$, $\zeta_{ai}=0.01$, $\zeta_b=0.01$, and $\omega = 2\pi \times 10^3$ rad/s

5. Test result

In order to confirm the effect of mechanical damper, we compared real rotor's motion with the result of numerical calculation by using the parameters that were measured. (Only spring constants of the force of permanent magnets are designed values.[6])

As is shown in fig. 4a and 4b, similarity between two viblation-forms is pretty good.

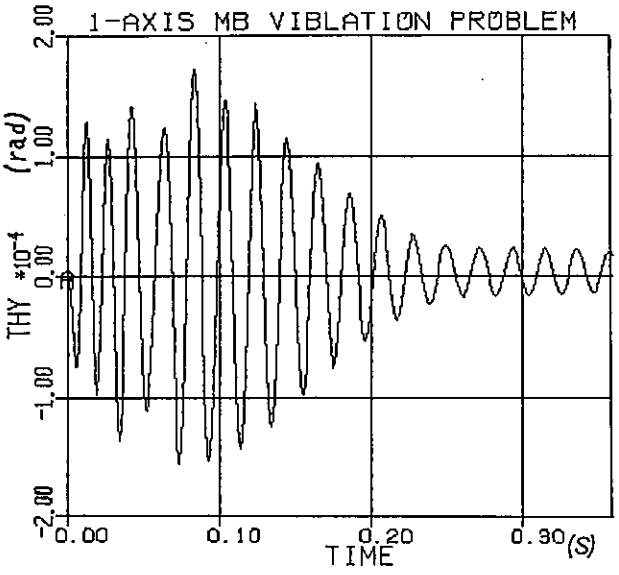

Fig.4a Rotor's motion of θ_y direction in calculation at $\zeta_{ao}=0.11$, $\zeta_{bo}=0.11$, $\zeta_{ai}=0.01$, $\zeta_b=0.01$, $K_{ai}=6.5\times10^4$ N/m, $K_b=K_{bi}=1.2\times10^4$ N/m, $K_{ao}=2.2\times10^4$ N/m, $K_{bo}=7.2\times10^4$ N/m and $\omega=0$

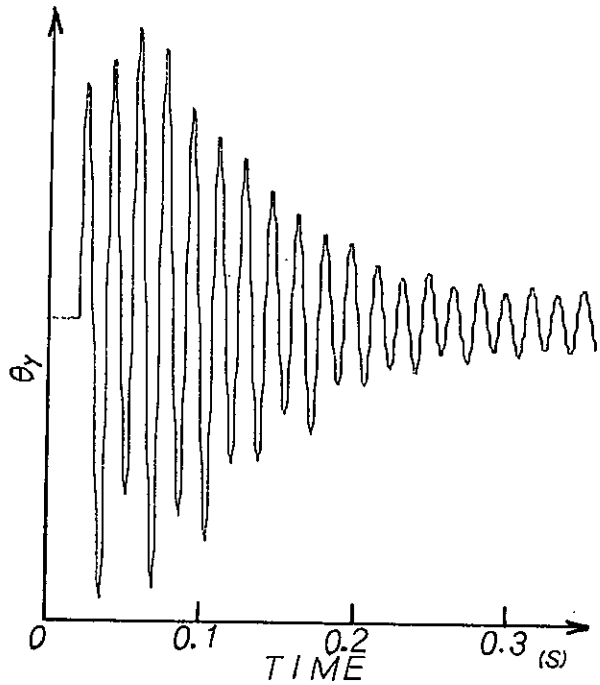

Fig.4b Rotor's motion of θ_y direction in measurement

6. Conclusions

It has become clear that we can design a mechanical damper optimumly by using the model mentioned above and selecting the parameters systematically and carefully, though most of people have considered tuning in mechanical damper is very difficult. And we think this method is one of the answers for designing small size and low cost magnetic bearing without loosing original features of it.

7. References

[1] MURAKAMI,C : Development Activity on Magnetic Bearings for Space Use in National Aerospace Laboratory of Japan. Proc 6th Int Workshop Rare Earth Cobalt Perm Magnets Their Appl. '82 P.227-235

[2] AZUKIZAWA,T., et al.: A Linear Induction Motor Control System for Magnetically Levitated Carrier System. Proceedings of International Conference on Maglev and Linear Drives '86

[3] ISHIZAWA,T et al.: Ionics '85 Vol.11 No.9 P.23-30

[4] P.ANSTETT et al.: The Very First Satellite to Use Magnetic Bearing Wheels. 33rd Congress of the IAF. '82-331

[5] J.W.BEAMS: Magnetic Bearings. Automotive Engineers Congress Detroit '64 Soc. Automotive Engrs, P.13-17

[6] J.P. YONNET: Analytical Calculation of Magnetic Bearings. 5th Int Workshop on Rare Earth Cobalt Perm Magnets and their Appl. '81 P.189-251

2nd International Symposium on Magnetic Beaing
July 12-14, 1990, Tokyo, Japan

USING HIGH-SPEED ELECTROSPINDLES WITH ACTIVE MAGNETIC BEARINGS FOR BORING OF NON-CIRCULAR SHAPES

Bernd MÖLLER

GMN Georg Müller Nürnberg AG, Nürnberg, West Germany

Abstract
For boring of non-circular shapes the active magnetic bearings of a high-speed work spindle can be used as an actuator to generate the required deflections of the tool. For a profitable boring process with good surface finish high cutting speeds need to be reached. The resulting rotational speed of the tool requires a fast radial movement of the spindle shaft for boring of non-circular shapes. Here the spindle cannot follow the reference signals without delay. A phase lag between displacement and rotation of the tool causes deviations from the predetermined shape. For this reason transfer functions and physical limitations of the spindle have to be taken into account to attain precise manufacturing.

1. Introduction

Main targets of research and development in the field of cutting technologies are the increase of flexibility in mass production, higher automation level in small-lot fabrication and the reduction of time for manufacturing. One aspect is the decrease of essential operating time: To raise the chip removal rate, higher cutting force or speed is needed. Due to the limited load capacity and stiffness of machine, tool and workpiece, increasing the cutting speed is a better solution than using high cutting forces [5,6]. Therefore the availability of rapid work spindles with high stiffness and power is fundamental to the use of high-speed cutting in industrial production. The demand for small cutting forces is very important in fine machining, because a high accuracy of the workpiece is reached only if deflections of tool and workpiece due to cutting action are low [2].

High-speed spindles with ball bearings are a good choice for many applications, but when best performance is needed active magnetic bearings have advantages compared to other bearing types due to low friction, high stiffness and big shaft diameter. Work spindles with active magnetic bearings are mainly used for milling and grinding, when high cutting speed and power is recommended [1,3,7].

A disadvantage lies in high expenditures for spindles with active magnetic bearings. The expenditure however, can be justified in using its additional capabilities: Inherent control signals are helpful in process monitoring and control without additional sensors. Furthermore it is possible to apply reference signals of the servo loops for radial and axial movement of the shaft within the air gap of bearings. This is sometimes used to increase accuracy of workpieces: Machining offsets are compensated by static displacement of the tool [4].

The final shape of a workpiece is determined by tool movement and tool geometry. Due to the higher flexibility there is a tendency to replace special purpose machine tools with specific tool geometries by numerically controlled machines with standard tools. Turning and boring in general is used for circular parts. For manufacturing of non-circular shapes are manufactured by modulating the rotation of the work spindle with an additional movement. For a profitable boring process with good surface finish, high cutting speeds should be reached. The resulting spindle speed requires a fast radial movement of the actuator for boring of non-circular shapes.

Using an electrospindle with active magnetic bearings as an actuator has the following advantages:

- Point of application of force and deflection measurement is close to the process.
- Combination of bearing and actuating functions.
- No wear or fatigue even at high frequencies.
- Low moving mass.
- Easy control of magnetic forces.

Applications of non-circular bores are found - for example - in piston engines: Holes for the gudgeon pin in a piston sometimes need to have an oval shape with a deviation from circle of about 50µm at bore diameters between 20 and 30mm. Generally bore bars with a high ratio of length to diameter have to be used for manufacturing. Due to the vibration behavior of these tools, additional damping is recommended to achieve chatter-free cutting.

2. Bore geometry and cutting edge movement

A special feature of the boring process is the generation of workpiece shape with a single cutting edge similar to turning. The cutting edge is fixed at the end of a rotating bar (radius r_{ko} from tool center line) generating a circular hole when using pure axial feed. Non-circular shapes are generated with additional radial movement $\mathbf{r_o}$ as function of tool rotation. The resulting orbital movement $\mathbf{r_t}$ of the cutting edge can be described by (Fig. 1):

$$\mathbf{r_t} = \mathbf{r_o} + \mathbf{r_k} \qquad (1)$$

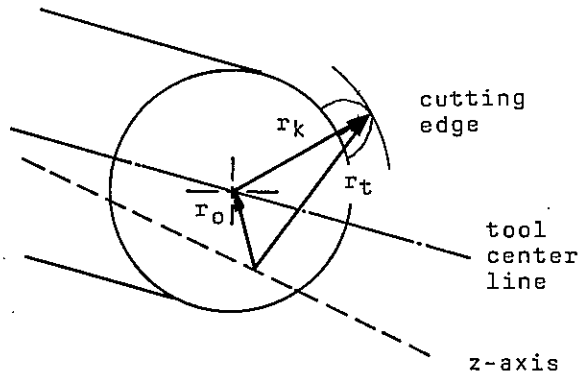

Fig. 1 Vector diagram of tool movement.

In a fixed system of coordinates:

$$x_t = x_o(\phi) + r_{ko} \cdot \cos(\phi) \qquad (2)$$

$$y_t = y_o(\phi) + r_{ko} \cdot \sin(\phi) \qquad (3)$$

$$\phi = \Omega \cdot t = 2 \cdot \pi \cdot f_n \cdot t \qquad (4)$$

If the non-circularity is small compared to the mean bore diameter (e.g. 1%), radial movement of the tool center line $\mathbf{r_o}$ is much smaller than the radius r_{ko} of the tool and it is possible to neglect movements x_c normal to vector $\mathbf{r_k}$. Only the infeed movement x_p changes the bore shape. The non-circularity r_d - i.e. the deviation from circle - can be described in polar coordinates:

$$r_d \approx x_p = x_o(\phi) \cdot \cos(\phi) + y_o(\phi) \cdot \sin(\phi) \qquad (5)$$

The orbit of cutting edge results from a modulation of tool deflection and rotation. Only a very short section of the hole is manufactured at every turn. For producing a predefined non-circularity the radial movement has to be repeated periodically.

Assuming sinusoidal deflections various shapes are possible using different amplitudes and frequencies. A specific frequency relation between rotation and deflection results in a characteristic shape of the bore. Fig. 2 shows the orbit of the tool lip for a number of revolutions up to repetition of the contour. This point is reached when rotation and deflection of tool have both finished an integer multiple (n_n and n_a) of periods. Therefore a rational ratio between deflection frequency f_a and rotational frequency f_n is required:

$$f_a / f_n = n_a / n_n \qquad n_a, n_n \in \mathbf{N} \qquad (6)$$

The period of repetition is:

$$T = n_n / f_n \qquad (7)$$

To attain a low surface roughness the repetition time T should be kept as low as possible. Therefore a high rotational speed f_n together with a small number of revolutions n_n per repetition cycle should be attained. For practical use three cases are of special interest:

The deflection frequency f_a is

A) an integer fraction ($n_a = 1$) of
B) direct synchroneous ($n_a = 1$; $n_n = 1$) to
C) an integer multiple ($n_n = 1$) of rotational frequency f_n.

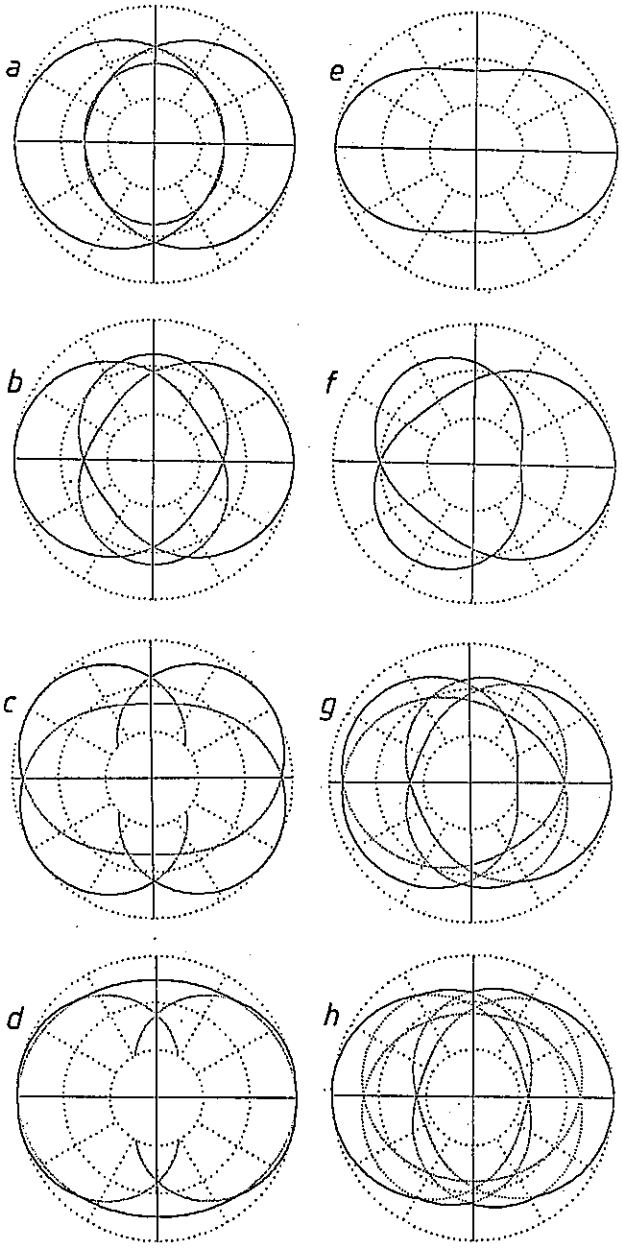

Fig. 2 Examples: Tool lip movement as deviation from circle; $|x_{o1}/y_{o1}|=4$

	a	b	c	d	e	f	g	h
x_{o1}/y_{o1}	++	+-	--	-+	+-	+-	+-	+-
f_n/f_a	3	3	3	3	1	2	4	5

To describe rotational processes it is often favourable to use complex numbers instead of two-dimensional vectors. The formulation for the tool rotation in this case is:

$$r_k = r_{ko} \cdot e^{j \cdot \phi} = r_{ko} \cdot e^{j \cdot \Omega \cdot t} \quad (8)$$

The cutting edge movement results from a transformation of the tool deflection into rotating coordinates:

$$r_t = (r_k + r_o) \cdot e^{-j \cdot \phi} \quad (9)$$

$$r_t = r_{ko} + r_o \cdot e^{-j \cdot \phi} \quad (10)$$

The deviaton of cutting edge movement from circle is:

$$x_p = \mathrm{Re}\ \{ r_t - r_{ko} \} \quad (11)$$

$$x_p = \mathrm{Re}\ \{ r_o \cdot e^{-j \cdot \phi} \} \quad (12)$$

Non-sinusoidal but periodic deflections r_o of the tool are described by Fourier series:

$$r_o(t) = \sum_{i=-\infty}^{+\infty} r_{oi} \cdot e^{j \cdot i \cdot \phi} \quad (13)$$

$$\phi = 2 \cdot \pi \cdot f_a \cdot t \quad (14)$$

The complex coefficients r_{oi} build up the discrete spectrum of the tool centre movement. Using the frequency domain for signal description has several advantages:

- Periodic signals are signified by discrete spectra, digital processing is easy.
- The process has low-pass characteristic, only a few coefficients are needed.
- Easy compensation of dynamic responses of transfer elements by multiplication of signal spectra and frequency responses.
- Transformation from rotating to fixed coordinates and vice versa is acomplished by shifting the signal spectra.

3. Requirements on process control

High rotational speeds of the tool require fast radial movements of the spindle shaft for boring of non-circular shapes. Due to the dynamic response of the active magnetic bearings the spindle cannot follow the reference signal without delay. On the other hand a phase lag between displacement and rotation of the tool causes deviations from the predetermined shape. For this reason transfer functions have to be taken into account to attain precise manufacturing.

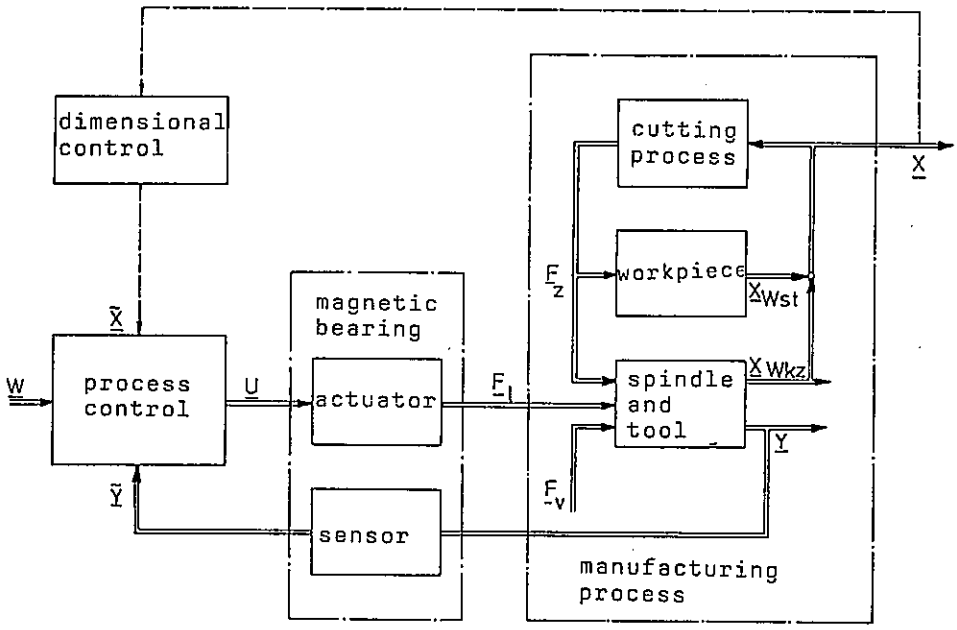

Fig. 3 Principal structure of process control.

Fig. 3 shows the principal structure of the non-circular boring process using a spindle with active magnetic bearings. The process control has to generate appropriate commands for the actuator to achieve the necessary tool movement. Main tasks of the process control are:

- Stability of control loops and sufficient damping of modes
- Suppression of disturbances and para meter variations
- Appropriate reaction on command signals

Main causes for disturbances and parameter variations of the boring process and the resulting requirements on the process control are:

- Determinable discrete changes:
  Variation of technological parameters like tool change, different workpieces, cutting speed, feedrate etc. Disturbance variable compensation or approach in mass production is possible.
- Undeterminable discrete changes:
  Variation of overmeasure or material properties of workpiece without a priori knowledge. Robust control is required.
- Slow changes with time:
  Tool wear and change of temperature. Robust control and compensation by dimensional control is recommended.
- Cutting path dependent changes:
  Changing forces due to first or interrupted cut etc. require a good stiffness for low and high frequencies.

Some of the requirements on the process control are contradictionary, so that a compromise has to be found especially in single loop controls. For an independent design of command and disturbance response two degrees of freedom in the control loop are required. Fig. 4 shows a simple example: Stability and good characteristic behavior is achieved by the feedback control whereas the feedforward control acts as a compensation filter to attain an appropriate command response. Due to the low pass characteristic of the compliance response it is not possible to realize a proportional relation between a transient command signal and the controlled quantity because a non ergodic compensation filter would be required. In this application the command signals are assumed to be periodic. Here a non ergodic response can be changed to ergodic behavior by shifting the signal one period. The same applies if the bore shape is changed as function of axial feed, because this variation is very slow compared to the frequencies of deflection movement.

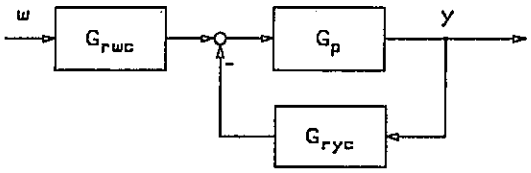

Fig. 4 Single-variable control with two degrees of freedom
G_{ryc}: Feedback controller,
G_{rwc}: Feedforward controller
G_p : Process.

Due to the use of periodic command signals the compensation filter is quite simple: Only a few discrete frequencies have to be processed. The linearity of the process is an important assumption for a proper use of the compensation filter. When limitations of the actuator are reached compensation does not work any more.

Amplitude and frequency of tool movement is restricted by physical limitations of the actuator - e.g. the active magnetic bearing. The major limitations are given by:

- Maximum static displacement
- Moving mass
- Maximum forces of the actuator
- Maximum slew rate of forces.

Fig. 5 shows the maximum amplitudes of an actuator with these limitations. For generating oscillating movements there is a quadratic increase of forces with frequency for a constant amplitude. At high frequencies the most important limitation is given by the slew rate of forces due to the maximum speed of energy exchange in the actuator.

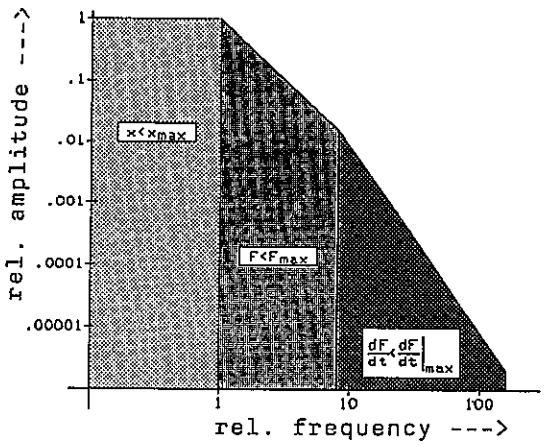

Fig. 5 Maximum amplitude of an actuator as function of frequency

4. Test results

A special machine tool for boring tests was developed at the *Institute of Cutting Technology and Machine Tools of TH Darmstadt*. The machine is equipped with a *S2M* electrospindle, type *B20/500*. Maximum rotational speed is 30000/min. One axial and two radial bearings are used to control the spindle shaft in five axis of motion. The control of translational and tilting motion is decoupled. Only the tilting modes are used for deflecting the tool, because forces of inertia are lower and maximum tool deflection is bigger compared to the translational motion. But this deflection mode has a disadvantage: Due to gyroscopic effects the tilting axes are coupled and the command response is speed dependent.

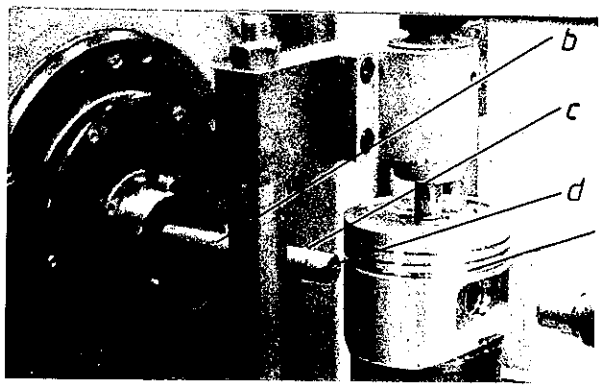

Fig. 6 Experimental set-up for non-circular boring.
(Ref.: *PTW, TH Darmstadt*)

For the conception of the boring machine the special demands of the process had to be considered. To avoid big resonance amplitudes due to the high frequency of forces, the machine frame is made of polymer concrete. Bore bars with a high ratio of length to diameter (e.g. length 100mm, diameter 18mm) were used for manufacturing tests (Fig. 6). In this case even carbide bars do not provide sufficient dynamic stiffness of the tool, additional damping is required to attain chatter-free cutting. With a mechanical vibration absorber fixed at the tip of the bore bar, it was possible to keep out-of-round less than 1µm when boring circular holes at high speeds (e.g. 22500 rpm, see Fig. 7). Using a low feed per revolution good surface roughness (e.g. Ra = 0.2µm) is possible.

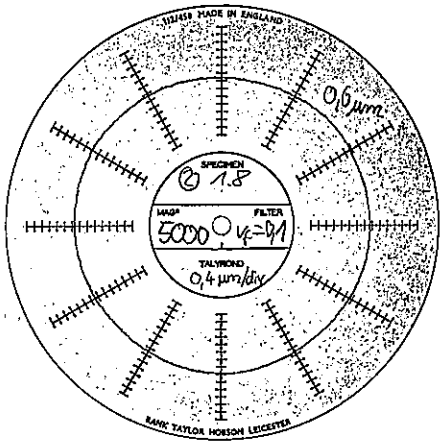

Fig. 7 Out-of-round of a circular bore. (feed rate: 100mm/min; rotational speed: 22500/min)

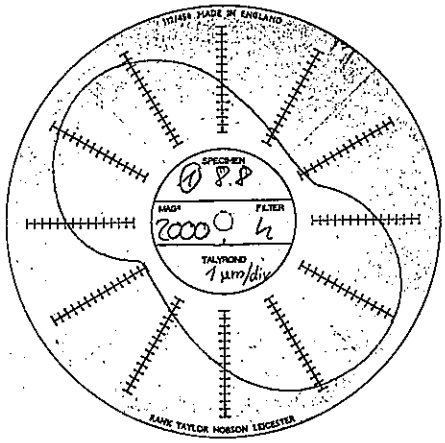

Fig. 9 Geometric distortion due to phase offset.

For generation and adaption of the periodic command functions required for non-circular boring, a function generator on the basis of a real-time computer with *VME*-Bus (Processor *MC68020*) was developed. An important feature of this system is the use of a special function generator card, with the capability for a fast output of periodic signals without loading the main processor (Fig. 8). The main processor handles the different control functions and computes the time series from Fourier coefficients (inverse FFT).

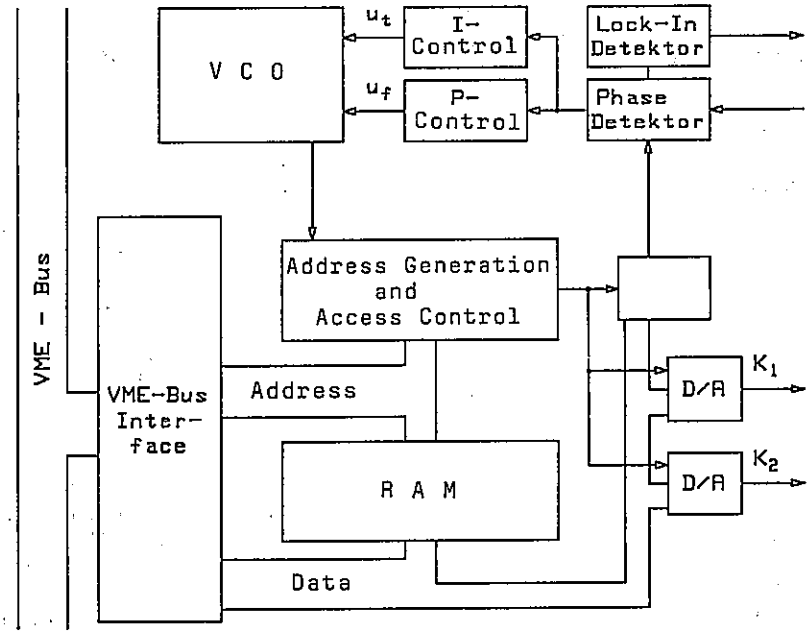

Fig. 8 Block diagram of function generator

For generating the proper shape of the bore with a single cutting edge - in contradiction to grinding - an exact phase relation between rotation and deflection movement is required. Geometric distortions are caused by constant phase offsets (see Fig. 9) as well as beat frequencies due to asynchroneous deflection (Fig. 10). A phase locked loop is used for sychronisation of the control signals with spindle rotation.

When using synchroneous deflection ($f_a = f_n$) at high rotational frequencies, amplitude is limited due to the maximum slew rate of bearing forces, i.e. the rating of power amplifiers. In this case the maximum ovality for boring at rotational speeds higher than 20000/min was less than 20µm. A bigger ovality is attainable when reducing rotational speed of the spindle or using a deflection frequency with an integer fraction of rotational frequency. In both cases surface roughness increases, if the feed rate is not reduced. A good compromise was found in manufacturing approximate elliptical shapes with a frequency ratio of one to three (Fig. 11). The frequency of deflection movement is still well above the rigid body modes determined by the feedback control of the magnetic bearings.

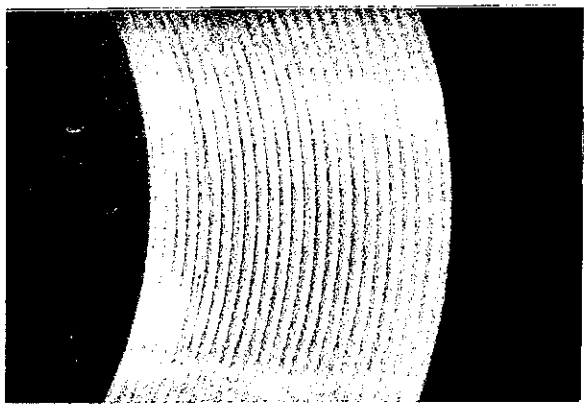

Fig. 10 Bore surface structure due to frequency offset.

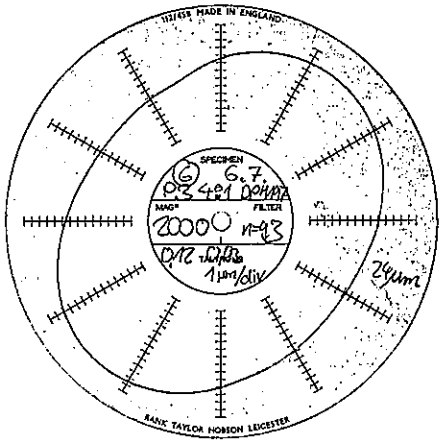

Fig. 11 Non-circular bore ($f_e = f_n/3$, $y_{o1} = -x_{o1}/4$, $f_n = 22500/min$).

For approaching and maintaining the predetermined shape of the bore, adaption of the command signals to compensate for variations of process response is necessary. In the adaption process the following steps are carried out:

1. Calculate required tool movement (Fourier coefficients) for manufacturing the predetermined shape.
2. Measure frequency response of spindle.
3. Process command signals (compensation filter).
4. Measure actual movement, compare with set values and adapt compensation filter.
5. Repeat Pt. 3 and 4 to minimize deviation.
6. Manufacture first workpiece and measure frequency response in process.
7. Adapt command signals to the actual response.
8. Repeat manufacturing and correction of command signals until actual shape is sufficient.
9. Check workpiece shape and tool movement for variations to maintain workpiece quality by adaption of command signals.

In many cases the predetermined shape is approached when manufacturing the second workpiece. For a lot with identical technological parameters reproducability in general is good without continued adaption. This applies even to intermediate retooling or switching-off, if the initial status of the machine tool is properly reconstructed.

5. Conclusions

It was proved by extensive tests that it is possible to manufacture non-circular shapes with very good accuracy and surface quality at high rotational speeds using a work spindle with active magnetic bearings as an actuator. The deflection frequencies were well above the rigid body modes determined by the active magnetic bearing. Phase offsets between rotation and deflection movement were minimized by an adaptable compensation filter. The major limitation of the process was given by the maximum deflection amplitude and frequency of the spindle: For a sufficient feed rate together with low surface roughness high frequencies are required. Here the slew rate of acceleration due to spindle mass and rating of power amplifiers limits the deflection amplitude.

The original conception of the electrospindle used for the manufacturing tests was high-power milling at fast cutting speeds. With a spindle designed for the special demands of non-circular boring, range of application could be extended significantly. For the use in industrial production integration of spindle and process control is necessary to attain easy operation of the manufacturing process. Automatic processing of command signals from reference shape and adaption to parameter variations is required. Programming should reach a level comparable to numerical controls (CNC).

References

[1] *Arnold, W.*: Beitrag zur Entwicklung und Einsatz aktiv magnetgelagerter Hochgeschwindigkeits-Fräs(„)spindeln. Hanser München Wien 1985

[2] *Kaufeld, M.*: Hochgeschwindigkeitsfräsen und Fertigungsgenauigkeit dünnwandiger Werkstücke aus Leichtmetallguß. Hanser München Wien 1987

[3] Möller, B.: Spindle Systems for high-speed Machine Tools. NSC-DFG Joint Symposium on Precision and High-speed Manufacturing Technology, Tainan, Taiwan (ROC) 1990
[4] N.N.: Bearbeitungszeiten werden um das 5-fache gesenkt. S2M magazine Nr.5 (1988), St-Marcel (F)
[5] Scherer, J.: Hochgeschwindigkeitsfräsen von Aluminiumlegierungen. Hanser München Wien 1984
[6] Schulz, H.: Hochgeschwindigkeitsfräsen metallischer und nichtmetallischer Werkstoffe. Hanser München Wien 1989
[7] Siegwart, R.; Traxler, A.: Möglichkeiten und Grenzen schneller Aktuatoren am Beispiel einer magnetisch gelagerten Hochgeschwindigkeits-Frässpindel. VDI Bericht 787, VDI-Verlag Düsseldorf 1989

2nd International Symposium on Magnetic Beaing
July 12-14, 1990, Tokyo, Japan

DESIGN AND PERFORMANCE OF A HIGH SPEED MILLING SPINDLE IN DIGITALLY CONTROLLED ACTIVE MAGNETIC BEARINGS

R. SIEGWART[1], R. LARSONNEUR[1], A. TRAXLER[2]

[1]Institute of Robotics, Swiss Federal Institute of Technology (ETH), 8092 Zurich, Switzerland
[2]MECOS TRAXLER AG, CH-8400 Winterthur, Switzerland

ABSTRACT

High Speed Cutting (HSC) finds increasing industrial interest due to its capability of drastically reducing production times. HSC uses up to ten times higher cutting speeds and allows greatly improved metal removal capacity. Furthermore, cutting forces are lower and surface quality is better than in the conventional cutting process. Active magnetic bearings (AMB) allow much higher surface speeds than conventional ball bearings and are therefore perfectly suitable for HSC applications. After a short introduction into HSC this paper describes the overall design of a magnetically suspended milling spindle with a power of 35 kW at 40'000 rpm and a cutting force of 1000 N. Mechanical spindle design and related problems such as material strength and rotor stiffness are investigated. "Conditioning" of the AMB rotor system in terms of *observability* and *controllability* is discussed. Linear and nonlinear characteristics of the *electro-magnetic actuator* (bearing magnet and power amplifier as one unit) are described. Digital controller layout is based on a layout method (*SPOC-D*) for *structurally predefined* discrete-time control systems. This method optimizes feedback parameters of arbitrary *low order* control schemes for *high order* plants. Results of milling tests are presented, showing the advantages of AMBs in HSC technology.

1. INTRODUCTION

Experiments performed at different research centers since the late seventies showed that the cutting process of materials such as aluminum and plastic can be substantially improved by increasing the cutting speed [1,2]. Based on these results, a new cutting technology, the *High Speed Cutting* (HSC), was developed and introduced into industrial applications during the past decade.

The main advantages of High Speed Cutting are:

- higher relative cutting volume
- lower cutting time
- lower cutting forces
- reduced loading of cutting tool and cutting machine
- reduced tendency for chattering
- less warming of the work piece as the removed chip carries more heat
- lower production cost

Despite of the high standard already reached in HSC technology, considerable research is still going on, particularly aimed at increasing cutting speeds and at optimizing the whole cutting process. Therefore, a clear trend towards milling spindles reaching higher rotational speeds, needing less maintenance and showing additional features such as *"in-process-control"* is discernible [3,4,5].

Active magnetic bearings (AMB) seem to be a very suitable tool for the challenging application of HSC. However, high demands are placed on actuator, controller and rotor design. The great potential of AMB technology in this field has been shown by the first analog-control AMB milling spindle developed by *S2M* in cooperation with the *Technical University of Darmstadt* [6].

2. MILLING SPINDLE DESIGN

2.1 HSC Milling Spindle Requirements

For almost all technically interesting HSC operations, tools with diameters between 10 and 60 mm and ISO 40 tool holders are used. To date, conventional ball bearing milling spindles with ISO 40 tool-holders can reach rotational speeds ranging from 15'000 to 20'000 rpm at a maximum cutting power up to 30 kW. However, *optimal* cutting speed can most often not be reached using conventional milling spindles due to the limited surface speed of the ball bearings. This is especially the case for small tool diameters. By using the latest *ceramic bearing* technology, a 20 to 30% increase in maximum rotational speed is possible, but life time of such bearings is limited to a few thousands of hours at best.

For a further important step towards higher rotational speeds using ISO 40 tool holders, electro-magnetic bearings seem to be the only feasible solution. Apart from the higher rotational speed, AMBs feature long lifetime due to the complete lack of mechanical wear. In addition, by using the force and displacement signals available in an AMB system, new insights into the whole cutting process can be obtained.

2.2 Overall Design Concept

The AMB milling spindle (figure 1) described in this paper was developed at the *Swiss Federal Institute of Technology (ETH)* and built in cooperation with the milling spindle manufacturer *IBAG Zürich AG* specialized in HSC technology [7]. The spindle design features the following characteristics:

- maximum rotational speed: 40'000 rpm
- maximum cutting power: 35 kW
- maximum cutting force: 1000 N
- integrated ISO 40 tool change system
- digital control using a DSP

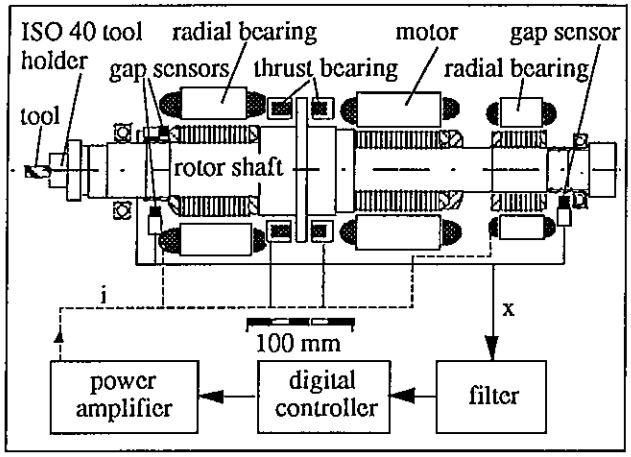

Figure 1: AMB milling spindle system

In order to find an optimal solution for the demanding task of developing an AMB high speed milling spindle, special emphasis was put on mechanical rotor design (high static and dynamic stiffness of the rotor shaft), on AMB actuators (bearing and power amplifier) and on digital control.

2.3 Mechanical Rotor Design

In order to cope with the static and dynamic cutting forces on the one hand and to reduce vibration effects on the other hand, the spindle rotor must be made as stiff as possible. The consequence of this basic design rule is a *short rotor* with a shaft diameter as *large* as possible. Therefore, due to centrifugal forces, the rotor elements are stressed up to their mechanical limits given by the material strength.

In order to reduce eddy current and hysteresis loss, motor and magnetic bearing elements consist of soft magnetic iron sheets which have to be *shrink-fitted* on to the rotor core. These lamination sheets do not increase rotor stiffness; they only add mass to the rotor core and, therefore, lead to decreased natural frequencies of the bending modes. Hence, from the stiffness point of view, the inner diameter of motor and bearing lamination sheets must be made as large as possible.

From the material exploitation point of view, however, thicker lamination sheets would allow higher surface speeds, since reference stress at the inner edge of the lamination sheets increases with the inner sheet diameter [8].

Figure 2 shows the speed dependency of radial and reference stress at the inner edge of the lamination sheets (front bearing). The material strength of the soft magnetic iron ranges near 400 N/mm^2.

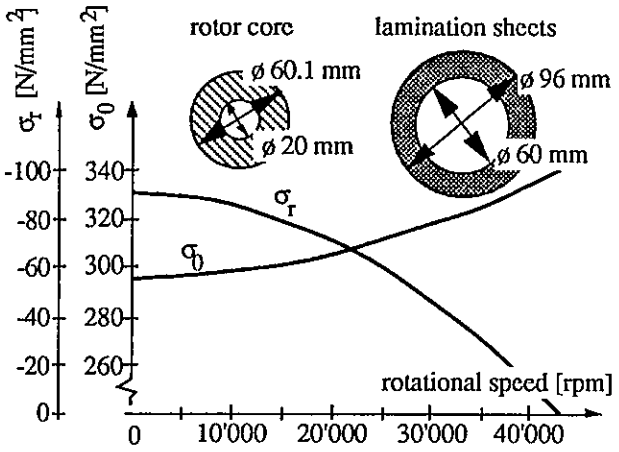

Figure 2: Radial stress σ_r at the contact between rotor core and lamination sheets and maximum reference stress σ_0 at the inner edge of the lamination sheets for the front radial bearing

The mechanical design of the AMB spindle rotor (figures 1 and 3) was dominated be the following constraints:

- highest possible yield strength for motor and bearing lamination sheets
- highest possible motor power and bearing forces
- ISO 40 tool system
- maximum rotational speed below first bending mode
- easy assembly of the whole spindle unit

The eigenfrequencies and corresponding mode shapes of the relevant first two bending modes are plotted in figure 3.

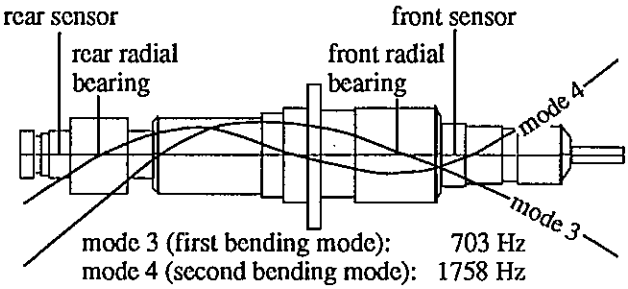

Figure 3: Eigenfrequencies and corresponding mode shapes of the AMB milling spindle

As it can be concluded from figure 3, the first elastic bending mode is very close to the maximum rotational speed (666 Hz) and must therefore be considered the most critical element of the rotor design. This also shows that further investigations must be made for future

applications, especially in the field of high speed motor elements featuring both high power and high mechanical stiffness.

2.4 Conditioning of an AMB Rotor in Terms of Observability and Controllability

Active magnetic bearings can be considered elements suitable for *supplying* energy *to* or for *removing* energy *from* the supported rotor. The "energy space" of the rotor can be subdivided into its different modes of motion, and the performance of energy transfer to or from these modes is represented by the so-called *controllability* and *observability* properties.

Generally, a non-turning rotor in AMBs can be described by the following set of linear differential equations in modal space (vector x of order n):

$$\ddot{x} + \mathrm{diag}(2\delta_i)\,\dot{x} + \mathrm{diag}(\omega_i^2)\,x = \tilde{B}\,u\,; \quad i = 1...n$$
$$y = \tilde{C}\,x \qquad (1)$$

$\tilde{B}$: control matrix
$\tilde{C}$: measurement matrix
δ_i: modal damping coefficients
ω_i: eigenfrequencies

We assume that the rotor is suspended with a very low stiffness ($\omega_{1,2} << \omega_3 \ldots \omega_n$) and that all eigenmodes show low damping δ_i, so that the open-loop system is stable. These assumptions have no relevant effect on controllability and observability but facilitate discussion of the system properties.

For the rotor system described by (1) the following state space description can be derived:

$$\dot{z} = A\,z + B\,u$$
$$y = C \cdot z \qquad (2)$$
$$z = \begin{bmatrix} x \\ \mathrm{diag}(1/\omega_i)\dot{x} \end{bmatrix}$$
$$A = \begin{bmatrix} \varnothing & \mathrm{diag}(\omega_i) \\ -\mathrm{diag}(\omega_i) & -\mathrm{diag}(2\,\delta_i) \end{bmatrix}$$
$$B = \begin{bmatrix} \varnothing \\ \mathrm{diag}(\frac{1}{\omega_i})\,\tilde{B} \end{bmatrix}\;;\quad C = \begin{bmatrix} \tilde{C} & \varnothing \end{bmatrix}$$

The symbols used in (2) are:

z: state vector of modes and scaled velocity (order 2n)
y: measured displacement
A: system matrix of weakly supported rotor
B: influence matrix of bearing forces
C: measurement matrix

For a system described by (2) with A being a stable matrix one can define the *observability gramian* W_o and the *controllability gramian* W_c [9,10] as follows:

$$W_o = \int_0^\infty e^{A^T t}\,C^T\,C\,e^{At}\,dt = U\,\Sigma_o^2\,U^T$$
$$W_c = \int_0^\infty e^{At}\,B\,B^T\,e^{A^T t}\,dt = V\,\Sigma_c^2\,V^T$$
$$U = [u_1 \ldots\ldots u_{2n}]\;;\; U^T U = I\;;\; \Sigma_o^2 = \mathrm{diag}(\sigma_{oi}^2)\;;\; i = 1...2n$$
$$V = [v_1 \ldots\ldots v_{2n}]\;;\; V^T V = I\;;\; \Sigma_c^2 = \mathrm{diag}(\sigma_{ci}^2)\;;\; i = 1...2n \qquad (3)$$

The quadratic form η_o

$$\eta_o = z_0^T W_o z_0 \qquad (4a)$$

represents the total signal "energy" (L^2 norm) seen at the system output due to the initial state z_0, whereas η_c

$$\eta_c = z^T W_c^{-1} z \qquad (4b)$$

denotes the minimum control energy required to reach the state z [17]. Expressions (4a) and (4b) are quantitative measures for observability and controllability of the state vector z. Eigenvectors u_i and v_i in (3) denote observable and controllable directions with associated energy σ_{oi}^2 for the observability gramian and σ_{ci}^2 for the controllability gramian.

The so-called *condition numbers* κ_o and κ_c given by

$$\kappa_o = \frac{\sigma_{o\max}^2}{\sigma_{o\min}^2}\;;\quad \kappa_c = \frac{\sigma_{c\max}^2}{\sigma_{c\min}^2} \qquad (5)$$

are quantitative numbers to determine the observability and controllability properties of the rotor system. High condition numbers correspond to a poor conditioning.

For a rotor system in modal state space description (2) the eigenvectors of the observability and controllability gramians u_i and v_i are equal to the i-th (normalized) eigenvector of the system matrix A. Therefore the singular values σ_{oi}^2 and σ_{ci}^2 are equal to the signal energy η_o and the control energy η_c respectively for an assumed unit initial state in direction of the i-th eigenmode. Moreover, for small modal damping coefficients δ_i, the singular values are directly proportional to the inverse of the damping δ_i.

Figures 4 and 5 show the singular values σ_{oi}^2 and σ_{ci}^2 of the observability and controllability gramians related to the eigenmodes of the milling spindle rotor (modes 1 and 2 are the rigid body modes). The singular values for front and rear bearings are plotted individually to show the influence of each single magnetic bearing on the total observability and controllability status. For example, mode 4 is very

poorly observable but quite well controllable from the front bearing, a fact which is also reflected by the mode shapes of the milling spindle rotor (figure 3).

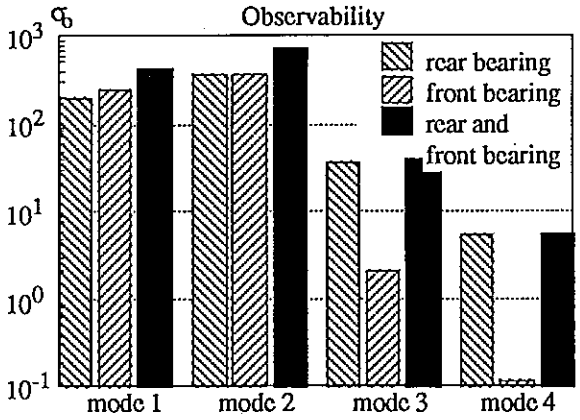

Figure 4: Observability of the AMB milling spindle rotor

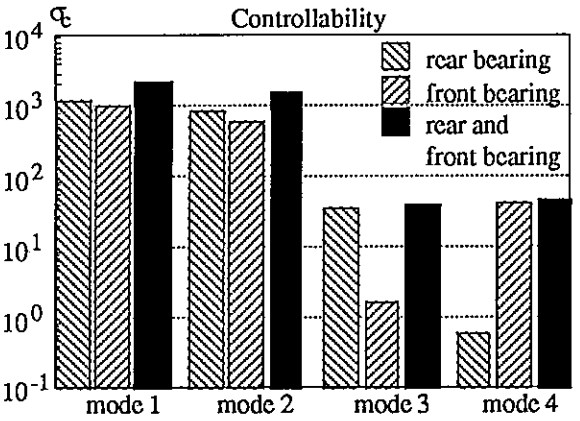

Figure 5: Controllability of the AMB milling spindle rotor

The gramians are also a useful tool for model reduction [16]: (stable) eigenmodes with very poor observability *and* controllability can be neglected.

For both observability and controllability one can find the corresponding condition numbers for the milling spindle rotor applying expression (5):

$\kappa_o = 150$
$\kappa_c = 70$

Observability of the milling spindle rotor is poorer than controllability. This is particularly caused by the 2nd elastic eigenmode (4th mode) which shows a *vibration node* near the front sensor location. It is therefore useful to *cut off* the sensor signal between the third and forth mode by means of an appropriate low pass filter.

Although controllability of the milling spindle rotor is rather good, the effectiveness of tuning for the higher modes will be decreased by the limited bandwidth of the AMB actuator. This is investigated in the next section.

3. AMB ACTUATOR LAYOUT

3.1 Dynamic Bearing Force

The force-current-displacement relationship of the magnetic bearing force F produced by a pair of opposing electro-magnetic coils using current control (figure 6) is given by the following well known expression:

$$F = k\left[\left(\frac{i_0+i_x}{s-x}\right)^2 - \left(\frac{i_0-i_x}{s+x}\right)^2\right] \tag{6}$$

The constant k depends on the bearing design parameters, i_0 is the the nominal current (pre-magnetization), i_x is the control current, s is the nominal air gap and x is the rotor displacement from the unstable nominal equilibrium position.

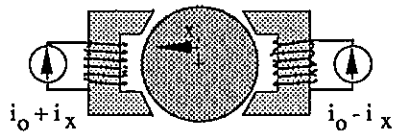

Figure 6: AMB current control

Since coil resistance can be neglected, one can obtain for the related coil voltages u^+ and u^-:

$$u^+ = k_\Delta k \frac{\partial}{\partial t}\left(\frac{i_0+i_x}{s-x}\right);\quad u^- = k_\Delta k \frac{\partial}{\partial t}\left(\frac{i_0-i_x}{s+x}\right) \tag{7}$$

The constant $k_\Delta \approx 1$ is a correction term which takes into consideration the permeability of the iron and possible geometric properties [11].

In order to describe the bearing force dynamics, the time-derivative of the bearing force given by (6) can be formulated using expression (7):

$$\frac{\partial F}{\partial t} = \frac{2}{k_\Delta}\left[\left(\frac{i_0+i_x}{s-x}\right)u^+ - \left(\frac{i_0-i_x}{s+x}\right)u^-\right] \tag{8}$$

Hence, the maximum dynamic bearing force near the nominal rotor position (x = 0) can be derived from (8):

$$\frac{\partial F}{\partial t} \approx 2\,\frac{i_0\, u_{max}}{s} \tag{9}$$

$$u^+ = u_{max};\ u^- = -u_{min};\ k_\Delta \approx 1$$

With a nominal current i_0 being equal to the half maximum current i_{max}, the following relation between power P of the power amplifier and bearing force dynamics is obtained:

$$\frac{\partial F}{\partial t} = \frac{i_{max}\, u_{max}}{s} = \frac{P}{s} \tag{10}$$

Assuming the dynamic bearing force to be sinusoidal with frequency f and amplitude F_0, equation (10) can also be written as:

$$F_{0_{max}} = \frac{1}{2\pi f}\frac{P}{s} \tag{11}$$

Expressions (10) and (11) are rather simple and helpful relations for the design of an AMB actuator. This is shown along with the milling spindle example in the following section.

3.2 Actuator Layout for the Milling Spindle

As mentioned in section 2.2 a maximum static cutting force of 1000 N must be realizable with the AMB milling spindle. In addition, bearing forces must cover a wide dynamic range in order to achieve the required stiffness and damping up to the first elastic bending mode.

The related maximum bearing forces are around 1000 N for the rear bearing and 2000 N for the front bearing. Assuming an AMB actuator bandwidth up to 1 kHz (first bending mode is located at 703 Hz), i.e. providing the maximum bearing force over this whole frequency range, the required amplifier power can be calculated by application of expression (11):

$P_{max} = 2.4$ kVA (rear bearing)
$P_{max} = 4.8$ kVA (front bearing)

These required amplifier powers are quite large, and to date, such amplifiers are not available on the market. Therefore, new switched type power amplifiers with a maximum current of 8 A, a voltage of 310 V and a switching rate of 100 kHz were developed. Thus, a power of 2.5 kVA per bearing channel is achieved, only matching the requirements of the rear bearing. However, since controllability of the first elastic bending mode is much better for the rear than for the front magnetic bearing (figure 5), sufficient damping should be provided using the mentioned power amplifier and an appropriate control algorithm (section 4).

3.3 Nonlinear Model of the AMB Actuator

Power amplifiers are rather often the most limiting component in an AMB system. Because of their low loss, switched amplifiers using current control are most commonly used for AMB systems, especially in the case of high power applications. Besides current control, other possibilities such as voltage or flux control are possible which, for some applications, can improve AMB performance [12,13,14].

Figure 7 shows a schematic diagram of the AMB actuator including bearing coil and nonlinear amplifier logic.

Coil voltage u is determined by the (generally small) coil resistance R_{cu}, the current i and the switched amplifier voltage u_{out}:

$$u = u_{out} - R_{cu}\, i \tag{12}$$

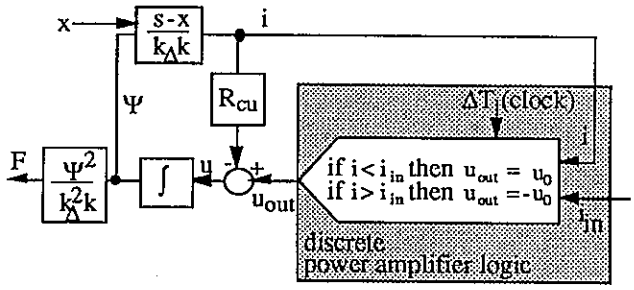

Figure 7: Schematic diagram of the AMB actuator including one bearing coil and switched power amplifier with current control

By integrating the coil voltage over time one obtains the flux linkages Ψ:

$$\Psi = N\,\Phi = \int u\, dt \tag{13}$$

Coil inductivity L can be derived from (13) using the definition $\Psi = L\, i$ (see also figure 7):

$$i = \frac{\Psi}{L} = \frac{(s-x)}{k_\Delta k}\,\Psi \tag{14}$$

$$L = \frac{k_\Delta k}{(s-x)} \tag{15}$$

By introducing Ψ in expression (6) for only one bearing coil, the AMB force can be expressed by the flux linkage and the AMB constants k and k_Δ:

$$F = \frac{1}{k_\Delta^2 k}\,\Psi^2 \tag{16}$$

Simulations with this nonlinear AMB actuator model for the milling spindle are shown in section 5 and compared with a standard linear model. The behavior of the electromagnetic coil is simulated as a continuous-time system, whereas the logic of the switched power amplifier must be considered as a discrete-time system (figure 7).

4. Discrete-Time Controller Layout

A typical property of AMB systems is that only very few system states, most often two displacement signals in each movement plane, are measurable. Thus, especially in the case of flexible rotor structures, the plant order is much higher than the number of output signals available.

A well-known control theoretical consequence resulting from too few output signals being available on the one hand, and from the necessity of achieving enough damping up to high frequencies on the other hand, is that an observer-based state feedback should be implemented in order to include the full system dynamics. However, in case of digital control, such *high order* controller structures will

require a high number of necessary computations, so that only *low sampling rates* can be achieved. Consequently, simpler *low order* discrete-time dynamic output schemes must be provided, which, despite of their low order, take into account the *full dynamics* of the high order plant.

Many layout techniques for discrete-time low order controllers presently available are based on *quasi-continuous approximations* of well-known continuous-time low order control schemes. This approach rather often results in unsatisfactory dynamic behavior of the closed-loop system and, in some cases, may even lead to *instability*.

For the AMB milling spindle the so-called SPOC-D controller layout method was applied (Structure-Predefined Optimal Control for Discrete Systems). This method was first presented in [15]; its detailed description can be found in [8]. The basic properties of the layout method can be summarized as follows:

Order and structure of the discrete-time controller for the nominal high order plant model are predefined *prior* to the controller layout. This predefinition can be made *freely* according to *practical needs*. In the subsequent controller layout, a parameter optimization is performed taking into account the dynamics of the high order plant as well as those of the low order controller.

In addition, the SPOC-D method allows to include control parameter interdependencies *directly* into the optimization process in order to achieve system properties such as

- specific static magnetic bearing stiffness
- specific frequency domain behavior of a decentralized feedback path (gain and phase at a given frequency, noise rejection at high frequencies for robustness, etc.)

Figure 8 illustrates the decentralized controller performance achieved using SPOC-D. The optimized controller transfer function (curve 2) is compared with a discrete-time PD approximation (curve 1). The traditional PD approximated controller shows high gain at high frequencies and, therefore, generates noise. For the SPOC-D optimized controller, the conditions of low noise at high frequencies as well as of the static bearing stiffness were included as additional control parameter interdependencies in the optimization process. Furthermore, the optimized controller features better phase lead in the frequency mid-range. Both, low noise and better phase lead provide an additional amount of robustness for the AMB milling spindle.

The eigenvalues of the closed-loop system with SPOC-D optimized controller are:

- $\lambda_1 =$ -48 ± 133 Hz (rigid body mode)
- $\lambda_2 =$ -174 ± 333 Hz (rigid body mode)
- $\lambda_3 =$ -151 ± 812 Hz (1st bending mode)
- $\lambda_4 =$ -5 ± 1753 Hz (2nd bending mode)

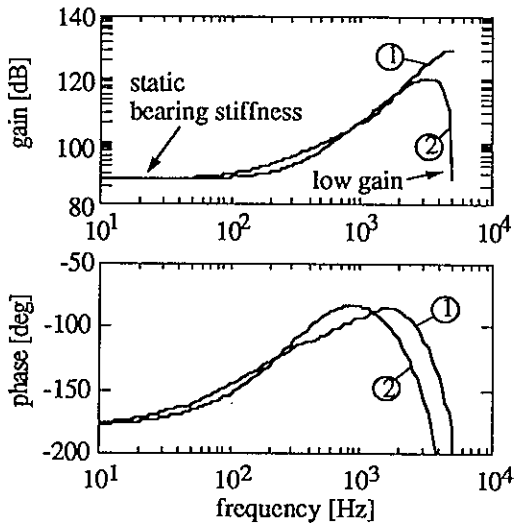

Figure 8: Bode plots of third order decentralized PD controller (1) and of SPOC-D optimized controller (2) with same order

Damping of the two rigid body modes and of the first bending mode are satisfactory, whereas the damping of the second bending mode turns out to be rather small. This is caused by the limited controller and actuator bandwidths and by the poor controllability and observability of the 2nd bending mode using decentralized feedback. However, additional damping of this mode, not included in the model description, is provided by the material's internal damping.

5. RESULTS

Owing to a rotor design which reaches the material strength limits, to the switched power amplifier, to the high sampling rate achieved with a DSP and to the SPOC-D optimized decentralized controller, a HSC milling spindle in AMBs was realized [7]. Compared with conventional ball bearing HSC milling spindles with same cutting power, the rotational speed was doubled, so that lower cutting forces, a higher metal removal rate and optimal surfaces on the work piece could be reached.

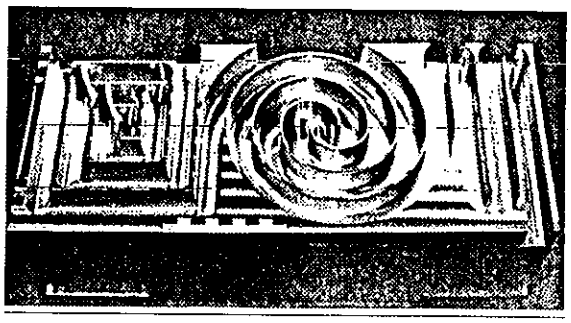

Figure 9: Integral aluminum work piece with straps of 2 mm thickness and of 27 mm height

Figure 9 shows a typical HSC work piece, cut with a miller of 20 mm diameter at cutting speed of 2300 m/min. The whole cutting process took 72 seconds. A cutting speed of over 6000 m/min and a removal rate of more than 1600 cm^3/min were reached applying different tools.

In figure 10 the dynamic compliance of the AMB milling spindle is compared with a conventional milling spindle featuring the same *related cutting force* K_v. The related cutting force K_v is a comparative value for an average cutting force and can be defined as follows:

$$K_v = \frac{\text{cutting power}}{\text{rotational speed} \cdot \text{tool holder diameter}} \qquad (17)$$

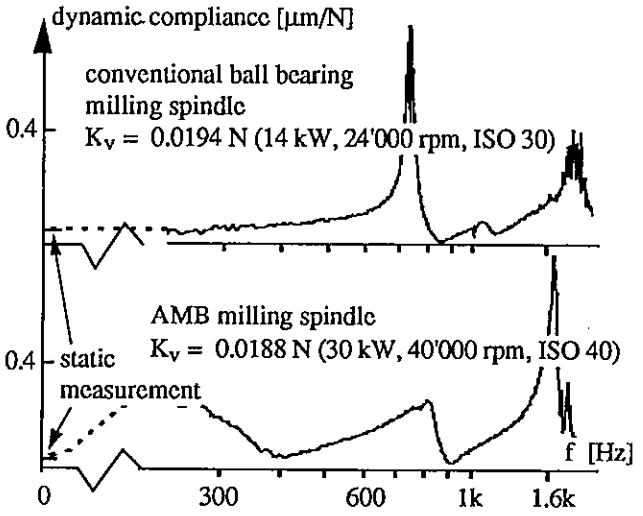

Figure 10: Measured spindle compliance at the tool for a conventional and for the AMB milling spindle

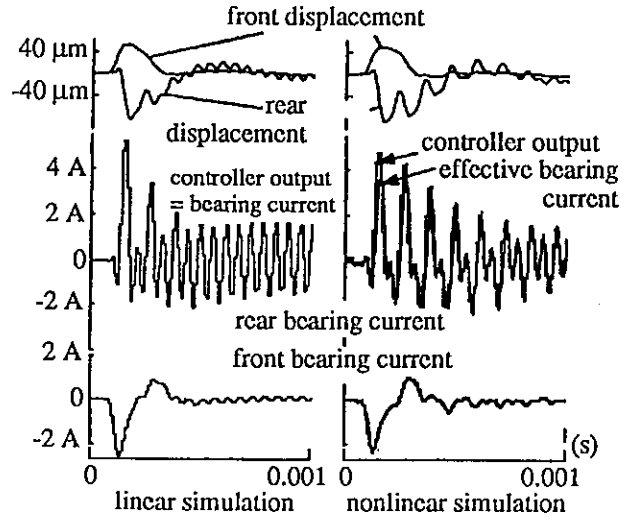

Figure 11: Linear and nonlinear simulations of the system behavior to a force impact at AMB spindle tool

In the low frequency range (50 - 300 Hz) the AMB spindle shows a higher compliance, i.e. a lower dynamic stiffness, than the conventional one. However, this does not affect the cutting process since cutting forces mainly contain higher frequency components. Figure 10 also demonstrates that damping of the first bending mode is much higher for the AMB spindle than for the conventional one, thus, excitations even in the frequency range of the 1st bending mode can be tolerated. Although both AMB and conventional milling spindle have the same related cutting force K_v, the AMB spindle features a cutting power and a rotational speed which are about *twice as high* as for the conventional milling spindle.

Simulations of the AMB system response to a force impact at the spindle tool are shown in figure 11. Power amplifier nonlinearities described in section 3.3 are *included*. Correspondence with measured signals (figure 12) is very good, which points out the precise model worked out for the AMB spindle, especially taking into account the nonlinear amplifier dynamics. Damping reduction of the nonlinear model compared with the linear counterpart is caused by the limited dynamic range of the power amplifier (dynamic current saturation).

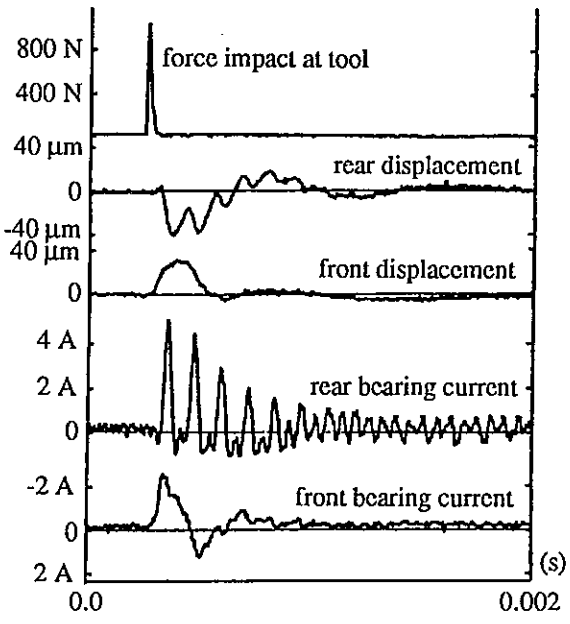

Figure 12: Measured system response to a force impact at AMB spindle tool

6. CONCLUSION

The AMB milling spindle prototype described in this paper has proven the feasibility of contactless support for HSC milling spindles by means of digitally controlled electromagnetic bearings.

The yielded results could be achieved thanks to the introduction of a digital signal processor (DSP) and thanks to a new discrete-time controller layout method in conjunction with a realistic model of the whole system. Furthermore, a specifically developed switched power amplifier and a sophisticated stiff rotor construction have contributed to the good overall performance of the AMB milling spindle system.

Nevertheless, future investigations must be made in the fields of motor elements for high rotational speed and of low cost solutions for power amplifier and digital control systems. New "in-process-control" features based on digital control systems have to be implemented in order to optimize the whole cutting process and thus to create highly automated and reliable systems.

REFERENCES

[1] STEINMETZ E. (Editor): Hochgeschwindigkeitsfräsen von metallischen und nichtmetallischen Werkstoffen, Technische Mitteilungen, vol. 17, 1983

[2] TLUSTY J.: Dynamics of High-Speed Milling, Journal of Engineering for Industry, vol. 108, 1986

[3] GALLIST R.: Hochgeschwindigkeitszerspanung - Entwicklung bis zum Jahr 2000, Technica, 2/1988

[4] SCHULZ H.: Die Vorteile des Hochgeschwindigkeitsfräsens, Technica, 26/1988

[5] VANN C. and M. CUTKOSKY: Closing the Loop in CAD/CAM Integration, proceedings of the USA-Japan Symposium on Flexible Automation, Minneapolis, Minnesota, July 1988

[6] ARNOLD W.: Beitrag zu Entwicklung und Einsatz aktiv magnetgelagerter Hochgeschwindigkeits-Fräs(„)spindeln, Thesis TH Darmstadt, 1985

[7] SIEGWART R.: Aktive magnetische Lagerung einer Hochleistungs-Frässpindel mit digitaler Regelung, Thesis ETH No. 8962, Zurich, 1989

[8] LARSONNEUR R.: Design and Control of Active Magnetic Bearing Systems for High Speed Rotation, Thesis ETH No. 9140, Zurich, 1990

[9] BOYD S.: Multivariable System Theory, lecture notes EE364, Stanford, 1990

[10] MOORE B.C.: Principal component analysis in linear systems: Controllability, observability and model reduction, IEEE Transactions on Automatic Control, 2/1981

[11] SIEGWART R. and A. TRAXLER: Möglichkeiten und Grenzen schneller Aktuatoren am Beispiel einer magnetisch gelagerten Hochgeschwindigkeits-Frässpindel, VDI-Berichte Nr. 787, 1989

[12] VISCHER D.: Sensorlose und spannungsgesteuerte Magnetlager, Thesis ETH No. 8665, Zurich, 1988

[13] VISCHER D. and H. BLEULER: A New Approach to Sensorless and Voltage Controlled AMBs Based on Network Theory Concepts, paper submitted to the 2nd International Symposium on Magnetic Bearings, Tokyo, July 1990

[14] ZLATNIK D. and A. TRAXLER: Cost-Effective Implementation of Active Magnetic Bearings, paper submitted to the 2nd International Symposium on Magnetic Bearings, Tokyo, July 1990

[15] LARSONNEUR R. and R. HERZOG: Optimal Design of Structure Predefined Discrete Control for Rotors in Magnetic Bearings (SPOC-D), 1st International Symposium on Magnetic Bearings, Zurich, June 1988

[16] WILLIAMS T.: Closed-Form Grammians and Model Reduction for Flexible Space Structures, IEEE Transactions on Automatic Control, 3/1990

[17] GLOVER K.: All optimal Hankel norm approximations of linear multivariable systems and their L^{∞}-error bounds, Int. J. Control, vol. 39, 6/1984

2nd International Symposium on Magnetic Beaing
July 12-14, 1990, Tokyo, Japan

MONITORING AND ACTUATING FUNCTION OF THE INTERNAL GRINDING SPINDLE WITH MAGNETIC BEARING

Masato OTA, Sigenori ANDO, Jin-ichiro OSHIMA

SEIKO SEIKO Co.,Ltd. Narashinoshi, Chiba 275, JAPAN

Abstract

Ultra-high speed (180,000rpm) internal grinding spindle with active magnetic bearing (AMB) was manufactured slightly modified from our licensor's original model. Grinding accuracy with AMB spindle was confirmed better than with conventional ball bearing spindle,thanks to the vibration-free AMB operation. Beside the accuracy,using shaft location sensor signal and bearing control current, the moments of the grinding wheel touches against the work piece and against the dresser diamond are detected. The force adaptive control was performed using bearing current monitoring and shaft retreat motion with AMB as an actuator. These functions decrease grinding idle time and improve grinding quality.

1. Introduction

The machine tool shaft speed has further been advanced to improve processing efficiency. The machine tools with adaptive control and a self-diagnosis function have been developed to maintain high-accuracy processing for a long time. An active magnetic bearing spindle (AMB) can be an effective element to realize these functions.

The electromagnet and sensor which are the elements of the magnetic bearing provides various information related to processing phenomena. Further, the utilization of the actuating function which is the essential function of the electromagnet enables the improvement of the processing accuracy and the reduction of the processing time.

Presently, the mainstream bearing for the wheel spindle for an internal grinding machine is a rolling bearing but the vibration due to the rolling motion mechanism and due to the unbalance of the rotor limits the processing accuracy. The magnetic bearing, however, generates only very low vibrations even at a high speed revolution because of its being non-contact bearing and its automatic balance function[1]. From this viewpoint, the magnetic bearing has excellent characteristics as the spindle bearing for machine tools.

The following describes the experiment results on the monitoring and actuating function of the five-axis control type magnetic bearing spindle.

2. Structure of five-axis control type magnetic bearing spindle

Figure 1 shows its structure. It is composed of a radial electromagnet, axial electromagnet and displacement sensor corresponding to that. The revolution drive is made by a built-in high frequency motor. The air gap at the bearing portion is 200 μm on its radius. A auxiliary bearing is mounted on both end of the shaft to protect the magnetic bearing when power failure . The air gap of the auxiliary bearing shall be half of the magnetic bearing gap and it is designed so that the auxiliary bearing will not touch the rotor at its normal operation.

3. Monitoring function

One of the characteristics of the active magnetic bearing (AMB) is a monitoring function. Observing the output of the built-in displacement sensor used for control and the control current of the electromagnet enables to know what is happening the processing phenomena (grinding force, tool abrasion, etc.). The monitoring function when the AMB spindle is used in the internal grinding machine is described below.

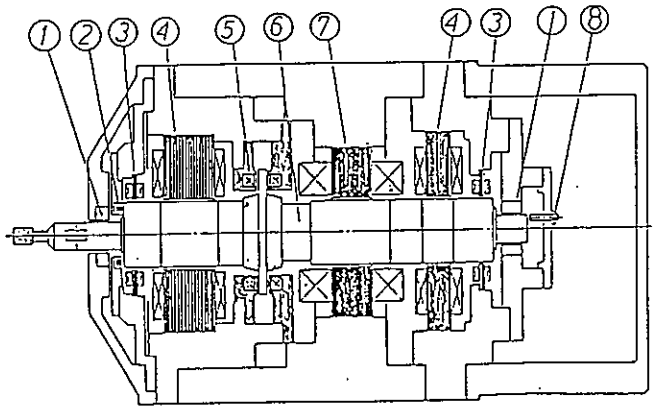

Figure 1 The Structure of The Spindle

3.1 Gap elimination

For the purpose of reducing the idle time in processing and preventing a work piece damage from collision with grinding wheel , gap elimination is employed. Detecting the touch of the work piece with the wheel, the controller of the mechanical system changes the feed from quick approach to rough grinding speed. When the control current of the electromagnet reaches a preset value, it is fed back to the infeed system of the machine to change the feed speed. The results of this experiment are described in Item 5.

3.2 Truing force

In order to maintain the grindability of the wheel , a truing operation with a sharp diamond dresser is carried out. If the diamond dresser becomes dull, the surface of the grinding wheel which has been trued loses grindability. This lower grindability wheel increases the grinding force. The increase of the grinding force increases the elastic deformation in the tool system, the work piece and its holding system and decreases the processing accuracy. Therefore, it is important for maintaining the stable processing accuracy to obtain the information on the sharpness of the diamond dresser.

Figure 2 shows the examples of the truing force monitored by the AMB control current in the cases where the sharpness of a single-point diamond dresser was changed. In these experiment examples a force as minute as 0.1 N could be measured.

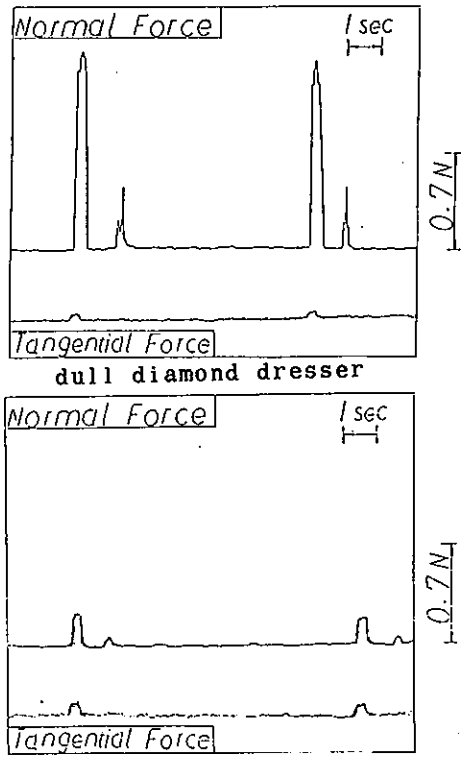

Figure 2 Truing force

3.3 Grinding force monitoring

We can detect the bearing force by monitoring the current of the bearing coil. In principle, the force applied on the AMB is proportional to the squared value of the coil current if the bearing gap is kept constant.

Before monitoring, we confirmed that the relation between the coil current and the bearing force was within 5% from linearity, in the 20 N force range.

In Figure 3, the upper chart was obtained from the input power signal of the driving motor. Each peak shows the power consumption of a work piece.

Simultaneously obtained with power, the charts at the middle and bottom show the coil current of the bearing located in the infeed direction of the grinding wheel and the bearing at right angles to the infeed. The middle and the bottom chart therefore show two components; normal grinding forces and grinding forces tangential to the wheel.

From Figure 3, we can see that the bearing current chart picks up very sharply, quickly reaches its peak, then varies around the peak with some repetitive motions. These motions correspond to the grinding process explained in the table below.

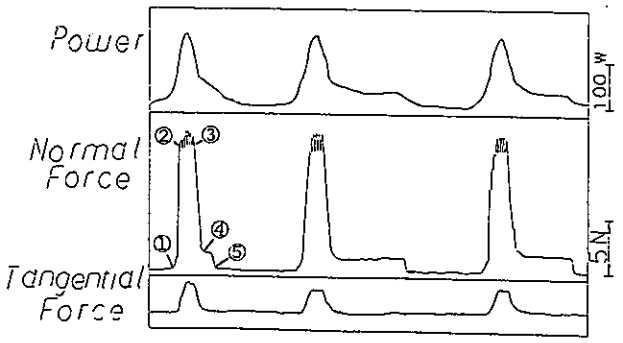

Figure 3 Grinding force

Thus, the bearing current monitoring is a much better method for watching the grinding process than is motor power monitoring. The reason is that the AMB system reacts very quickly to the load. For instance, current response to the load is in the order of ms and the AMB system's control bandwidth is close to 1 kHz in the case of this spindle.
However, the motor power monitor cannot detect the transient energy exhaustion of the rotor's spin at the early stage of wheel contact against the work piece.

From the viewpoint of the grinding process monitoring, the bearing current represents force variation faithfully and tells us what happens during grinding operation better than power monitoring does.

Spot Number in Figure-3	Situation	Grinding Process
~ ①	Non-Contact Wheel to Work	Air Cut (Quick Approach to the Work Piece)
①	Initial Contact	Start of Grinding
① ~ ②	Transient State	Pile Up Accumulation (note 1)
② ~ ③	Steady State (Periodical Variation)	Rough Grinding (note 2) (Synchronized with Wheel Oscilation)
③ ~ ④	Transient State	Rough to Finish (Accumiulation Decrement)
④ ~ ⑤	Steady State	Finish Grinding (note 3)
⑤	Release Contact	Wheel Retreate

Note 1 : Accumulation = Radial unground amount (Infeed - Removed) ≒ Elastic Deformation

Note 2 : Stock is removed efficiently

Note 3 : Surface Smoothing Process

Table Situation and Grinding Process

To confirm the detection sensitivity of the force on the bearing by the coil current, a wheel Truing force was applied by a single-point diamond tool and the depth of the Truing cut was 0.01 mm.
Under this condition, 1.5 N normal force was measured, and 0.1 N sensitivity can be seen in Figure 2.

3.4 Rotor behavior motion

Against the grinding force, the wheel spindle deflects and the shaft rotating center moves dynamically. This dynamic shaft movement is observed through the shaft location sensor signal.

Figure 4, (a) and (b), shows the spectrum of the sensor signal. The frequency of the highest peak is the spindle's rotation frequency, this peak means that the rotor is rotating around its inertial axis without vibration due to imbalance, as described before.

Figure 4(a) was obtained at the rough grinding stage. On higher side of the frequency of rotation, several small peaks can be seen on the bending resonance and harmonics of the shaft rotation frequency. On the lower frequency side of the shaft rotation, there are some levels of component but on unspecified frequencies.

These lower frequency components are probably caused by remaining geometric error of the work piece being ground, and these levels diminish gradually until the end of the grinding process.
Figure 4(b) shows the spectrum of the fine grinding process. We can see that there are fewer lower frequency components and no resonance frequency.

Thus, shaft behavior tells us in real time what is happening in the grinding process. We can see whether shape error on the work piece is being corrected and whether there is any grinding chatter.

4. Actuator function

4.1 High-speed respondency

Figure 5 shows the Lissajous' figure of the radial sensor output whenthe rotor spindle is excited by inputting a sinusoidal wave signal to the control circuit of the radial electromagnet. The right side shows the Lissajous' figure at a normal revolution and the left side shows that at 100-Hz excitation. These experiment results show that the rotor shaft can be moved at a high speed with a basic revolution accuracy maintained.

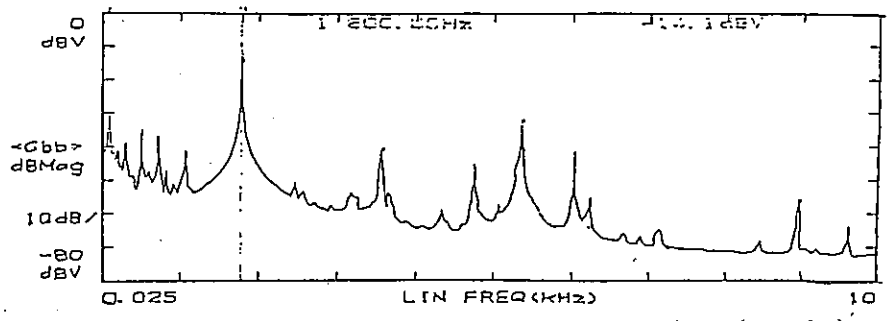

Figure 4 (a) Shaft Motion Spectrum at Rough Grinding (Example)

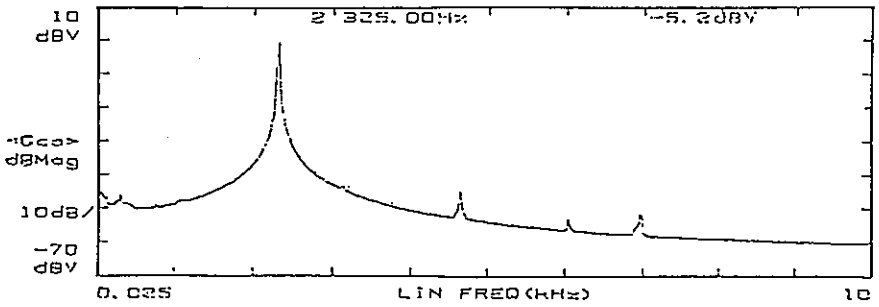

Figure 4 (b) Shaft Motion Spectrum at Finish Grinding

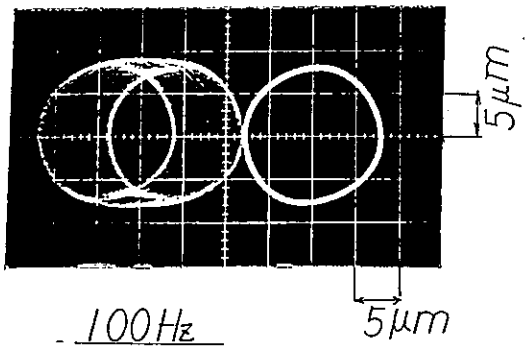

Figure 5 Lissajous'figure

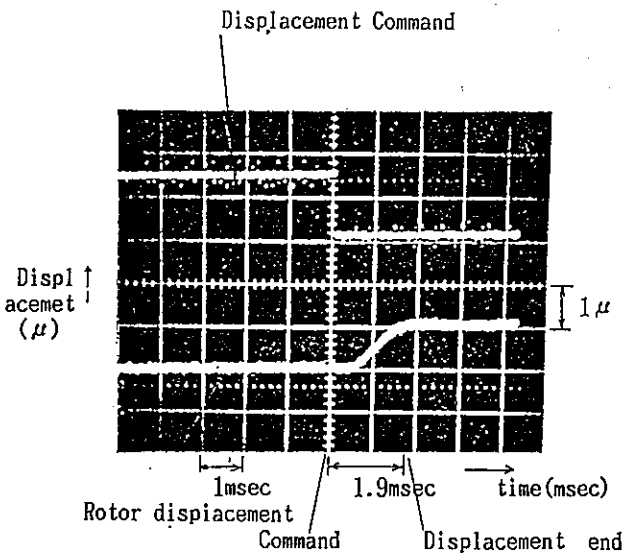

Figure 6 Rotor Displacement Respondency

Figure 6 shows the experiment data on a step response.

4.2 Retreat motion

For improving the efficiency of the grinding process with the internal grinding machine by reducing idle time, the infeed table is retracted in the opposite direction temporarily between the rough grinding process. The idle time can be reduced by changing the large grinding force at the time of rough grinding to the small one as quickly as possible.

Usually, the infeed table with a system in which a hydraulic drive or servomotor is combined with a ball screw. The response delay of the hydraulic pressure or motor, which is scores tens of m sec., can be reduced to several m sec. by displacing the rotor of the magnetic bearing spindle.

Moreover, the response delay of the wheel disengagement with work piece at grinding finish greatly affects the dimension and accuracy of a work piece. In the same way, the displacement of the grinding spindle rotor at the time of grinding finish enables to lessen the disengagement delay and to stabilize the dimension and accuracy. This function is very important to a machine which is used for mass production.

5. Constant grinding force control

Constant grinding force control is a kind of adaptive control constraint . It decreases and stabilizes the deviation of the processing accuracy due to the change of the sharpness of the wheel by controlling the feed speed so that the grinding force may be constant. As a result, the idle time caused by the grinding stock removal variation is minimized and the efficiency is improved.

Figure 7 shows the block diagram of the constant grinding force control. The feed speed is controlled so that the control current of the electromagnet during the grinding processing may be a preset value.

Figure 8 shows the example of the experiment on the constant grinding force control. The position of the infeed table, dimension of a work piece and two components of the grinding force (Fn, Ft) are shown there.

The gap elimination and the retreat motion which displaces the rotor shaft at a point where the rough grinding speed is changed into the fine grinding are carried out there by utilizing the output signal of the electromagnet control current.

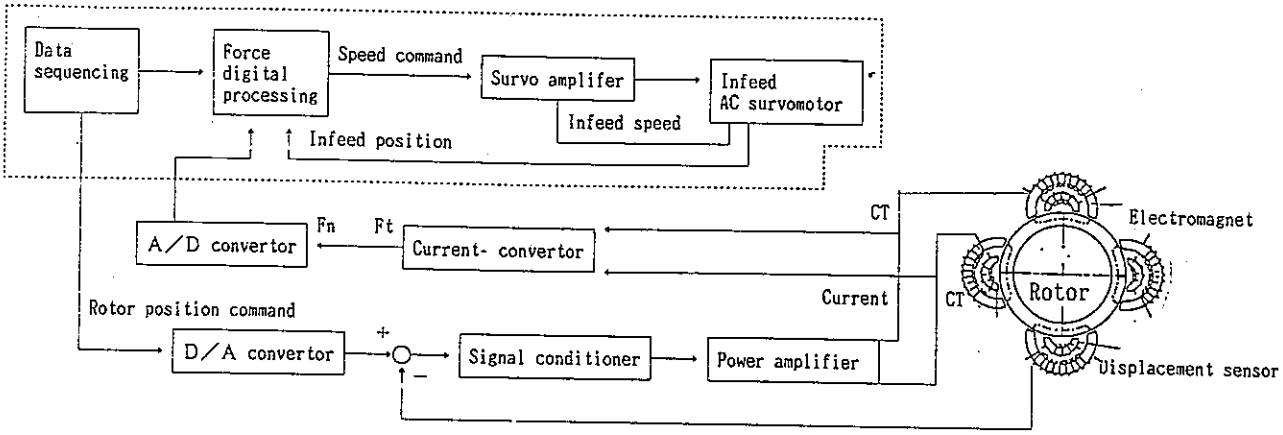

Fig 7. Block Diagram of Constant Force Control

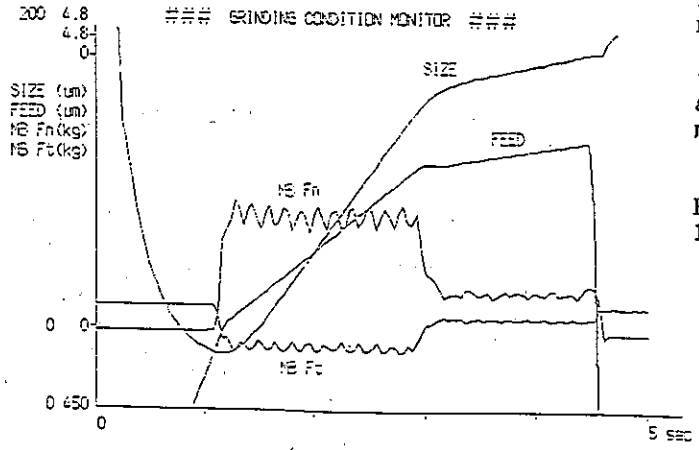

Figure 8 Grinding condition monitor

6. Conclusion

We confirmed the effectiveness of the monitoring and actuating functions in the experiment in which the active magnetic bearing was applied to the grinding wheel spindle for the internal grinding machine.

Because the AMB spindle functions as a high-speed and high-accuracy actuator and can make infeed motions after moving the rotor shaft which is revolving parallel or slantingly, it has a good chance of realizing a cylindricity or roundness control of a work piece easily.

Moreover, we are quite confident of that it will become an effective element in realizing an intelligent machine enabling adaptive control, tool life anticipation, processing quality stabilization and failure prediction based on the monitored processing conditions.

Reference

1) French patent 2 336 602

2nd International Symposium on Magnetic Beaing
July 12-14, 1990, Tokyo, Japan

SWITCHING AMPLIFIER DESIGN FOR MAGNETIC BEARINGS

F. J. KEITH*, E. H. MASLEN**, R. R. HUMPHRIS**, R. D. WILLIAMS*

*Department of Electrical Engineering, **Department of Mechanical and Aerospace Engineering
University of Virginia, School of Engineering and Applied Science, Charlottesville, VA 22901, U.S.A.

Abstract

Magnetic bearings incorporating linear feedback generally require an efficient transconductance power amplifier having a fairly broad bandwidth. The design evolution of an asynchronous switching amplification scheme which employs a novel control algorithm is presented. This design yields low harmonic distortion, excellent stability, good immunity to short-pulse failure and high efficiency.

In conjunction with the need for true transconductance behavior, the highly inductive loads inherent in magnetic bearing applications impose specialized demands which are not well met by conventional amplifiers. Adequate force slew rate requires large power supply voltage overhead which produces prohibitively low efficiency in linear (non-switching) amplifiers. Further, the variable nature of the load impedence renders precompensated open-loop schemes unsuitable.

These difficulties can be overcome by using a switching amplifier in a high gain current feedback loop. The high loop gain required to minimize error and provide wide bandwidth precludes the use of pulse width modulation (PWM) suggesting, instead, simpler bang-bang approaches.

Both hysteresis and sample-hold configurations were investigated and found to have significant shortcomings in this application. In particular, hysteresis amplifiers suffer from short-pulse susceptibility leading to low efficiency or output device failure. The sample-hold scheme provides excellent short-pulse immunity but produces fairly severe harmonic distortion, especially at low signal amplitudes.

A novel control algorithm, designated Minimum Pulse Width (MPW), is proposed. This approach is asynchronous as in the case of hysteretic control, yet imposes a restriction on the minimum pulse width delivered to the output devices. The resulting performance combines the low distortion of a hysteresis amplifier and the short-pulse immunity of sample-hold schemes. Experimental results are presented to support this claim.

Introduction

Active magnetic bearings generate a force on the supported structure which is generally modeled as functionally related to the electric current in the electromagnet coils. In class A applications, opposing electromagnets are prebiased (either with a bias current or with permanent magnets) and the force generated is essentially proportional to a perturbation current applied to both opposing magnets [1-4]. In class B operation, only one of an opposing pair of magnets is activated at a time and the force is related to the square of the current [2]. The underlying assumption in control schemes developed for either of these two modes of operation is that the current in the electromagnet coils of the bearing can be controlled explicitly. Such control defines the operation of a transconductance power amplifier: the amplifier drives a current through a load which is proportional (over the bandwidth) to a command signal. Since the command signal is typically a voltage, the amplifier generates a current which is proportional to an applied voltage, hence the term transconductance.

Design of such an amplifier poses several interesting challenges. Traditional power amplifiers are usually not well suited for this application, as they typically provide an output *voltage* proportional to an input voltage. If the impedence presented by the magnetic bearing coils were fixed, then some sort of precompensation might permit true transconductance behavior over some bandwidth. Generally, the impedance of a magnetic bearing coil is a strong function of the operating conditions, rendering precompensation ineffective. For this reason, true transconductance behavior can only be achieved through a high gain current feedback loop around the load.

In addition to the need for explicit transconductance behavior, amplifiers used in magnetic bearing applications must posess sufficient voltage overhead to provide adequate current slewing (and thus bearing force slewing) capability. Given a particular force slew rate requirement for a bearing, the necessary supply voltage can be calulated from the nominal coil inductance and actuator gain [5]. The required supply voltage will typically be well in excess of the voltage needed merely to provide the coil bias current.

Early amplifier design at the University of Virginia involved the design and construction of a linear transconductance amplifier (see figure 1 for a simplified schematic of the output stage). This amplifier was designed to operate small experimental test rigs one of which exhibited $L_{coil} \approx 150$ mH (at nominal gap) and $R_{coil} \approx 20\ \Omega$. This rig is typically operated with bias currents of ≈ 500 mA from a supply voltage of 100 VDC. Under these conditions, approximately 10 VDC appears across the coil, and roughly 90 VDC across the output MOSFET (leading to coil and amplifier dissipations of 5 and 45 W, respectively). Using the typical actuator gain for this rig ($\approx$ 125 lbf/A) and the calculated maximum current slew rate (667 A/sec) yields an approximate force slew rate limit of $\approx$ 83,000 lbf/sec. Subsequent bearing designs have been revised to bring the coil inductance into the 1-15 mH range and the coil resistance down to 1-10 Ω, thus permitting the use of higher current, lower voltage amplifiers to achieve the same force slew rates [6].

The principal drawback of linear amplifiers is that they are very inefficient, a characteristic further exacerbated by the high voltage overhead requirements imposed by magnetic bearing applications. The linear amp discussed above, for example, operates at approximately 10% efficiency and

dissipates roughly 450 W (45W × 10 channels) while operating a fairly small experimental rig. Clearly, such losses would be intolerable in higher power applications. For this reason, and because linear amplifiers must be tuned to the specific load to ensure stability of the current feedback loop, it was concluded that switching amplifiers might provide a better approach.

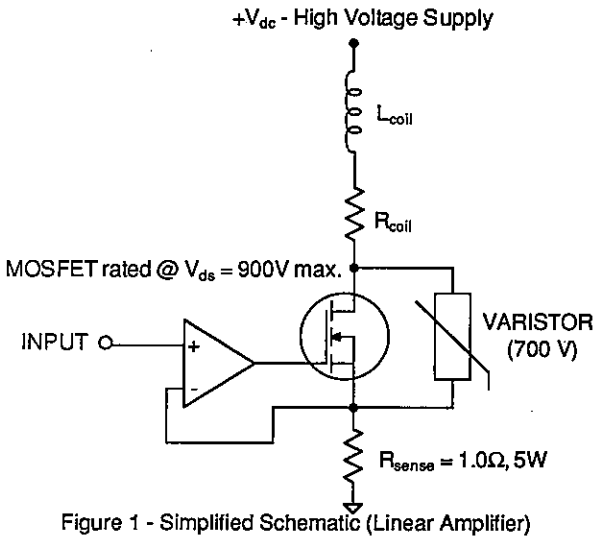

Figure 1 - Simplified Schematic (Linear Amplifier)

Switching Amplifiers - General Characteristics

Switching power amplifiers are distinguished from the more conventional linear power amplifiers in that the output voltage, rather than being continuously variable over some wide range, is restricted to two fixed levels. The purpose of this restriction is to minimize power losses in the output devices, which are generally some kind of transistor. Linear amplifiers, on the other hand, achieve a variable output voltage by controlling the resistance of the output transistors which are in series with the load between a fixed power supply and ground. Thus, at any output voltage intermediate between the power supply voltage and ground, the output transistors must dissipate power resistively.

Switching power amplifiers avoid this power dissipation by only operating the output transistors in a saturated "on" (low resistance) state or an "off" (very high resistance) state. Power dissipation in these amplifiers occurs primarily while the transistors are switching from one state to the other, with some power also being dissipated in the "on" state due to the non-zero on-resistance of the transistors. Because most of the power dissipation in these amplifiers occurs during the state transitions, the efficiency relies on keeping the switching rate below some threshold which depends upon the switching characteristics of the output transistors.

By switching the output stage at rates in excess of the required amplifier bandwidth (typical switching rates are 10-100 kHz) and varying the duty cycle of the output waveform, it is possible to create an output signal which combines the desired low frequency component with a higher frequency noise component. The nonlinear compensator in figure 2 regulates this switching; the form of compensation greatly effects the performance of the overall circuit. For example, a direct connection between the error amplifier and the output stage (i.e., the nonlinear compensator is a straight wire) results in a linear amplifier since the error signal will force the output devices to operate in their linear operating region. To achieve the efficiency potential of switching amplifiers, the nonlinear compensator must *restrict* the rate at which the output devices switch. Although the noise output components move to higher frequency bands as the switching rate of the amplifier is increased, this action progressively degrades its efficiency (in the limit, as the switching rate approaches infinity, the efficiency converges to that of a linear amplifier, since attempts at rapid switching yield operation in the linear region). Lower switching rates, while introducing more low frequency noise, generally dissipate less heat and result in more efficient operation. While switching amplifiers generally radiate significantly higher levels of EMI/RFI emissions than equivalently rated linear amplifiers, their efficiency can easily be an order of magnitude greater. The central design issue for a switching transconductance amplifier then becomes: given the requirements imposed above (load insensitivity, explicit control of coil current, efficiency, etc.), how does one determine the manner in which the output stage should be switched to achieve robust, high bandwidth, low distortion operation?

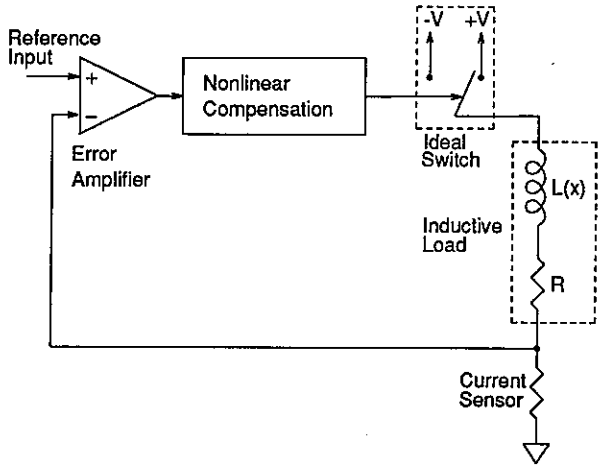

Figure 2 - Block Diagram of Generic Closed-Loop Transconductance Amplifier

The most widely used switching power amplifier is the Pulse Width Modulated, or PWM, amplifier. This amplifier is a voltage-to-voltage amplifier, generally employing no feedback. The linearization scheme employed in PWM amplifiers is to rapidly switch the voltage applied to the load between two fixed levels, V_1 and V_2, in such a way that the average voltage across the load is equal to the desired voltage. This is usually accomplished by comparing the input voltage to a high frequency triangle wave of fixed amplitude and frequency. As long as the reference triangle wave is smaller than the input voltage, the output devices are switched to apply V_1 ($V_1 > V_2$) to the load. When the reference triangle wave rises above the input voltage, the output devices are switched to apply V_2 to the load. In this manner, the duty cycle of the output pulse train is modulated to provide an average output voltage proportional to the command signal. All subsequent references to "PWM amplifiers" in this

paper are to the type of PWM amplifier described in this paragraph.

One common approach to the transconductance design problem is to precompensate a traditional PWM power amplifier so that the output current is proportional to the input voltage over some range of frequencies [7]. Such a configuration, shown in figure 3, has the advantage that its primary component, the PWM power amplifier, is readily available in the commercial market, and often includes the necessary precompensation circuitry [8]. However, the precompensation circuit in the open-loop PWM solution must be tuned to the load impedence - a troubling constraint, given that the coil characteristics of magnetic bearings are typically ill-defined and when, in addition, the coil impedence changes with the gap between the magnetic bearing pole pieces and rotor laminations.

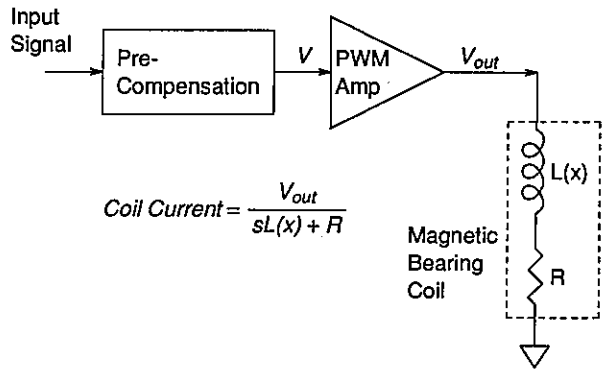

Figure 3 - Open-Loop PWM Transconductance Amplifier

The same PWM amplifier can be used to produce a transconductance amplifier in the configuration of figure 2. However, this scheme still has a number of drawbacks. Operation of a PWM amplifier in its continuous region imposes restrictions on the maximum voltage slew rate that can be applied to its input (see figure 4). This, in turn, restricts the amount of gain which can be employed in the feedback loop, which reduces both the low frequency accuracy and bandwidth of the amplifier. Increasing the error amplifier gain (or increasing the gain of the *linear* compensation block in figure 4) can reduce this error, but such action tends to present large, rapidly-changing voltages to the PWM generator. These input voltages will tend to saturate the PWM amplifier at either zero percent duty cycle (off) or 100 percent duty cycle (on) during each period of the PWM reference triangle wave. As the gain of the error amplifier is made large, the PWM amplifier begins to operate as a simple sample and hold device: it ceases to switch during its sampling interval, remaining either "on" or "off" for each entire interval.

Bang-Bang Algorithms - Sample/Hold and Hysteresis

This sample and hold behavior is not necessarily undesirable, but it can be accomplished with far simpler circuitry than that of a PWM amplifier. A simpler approach to building a switching transconductance amplifier for driving inductive loads is a "bang-bang" control system with a fixed sampling rate [9, 10]. This scheme involves driving the output transistors directly with the current comparator signal: when the output current is larger than the requested current,

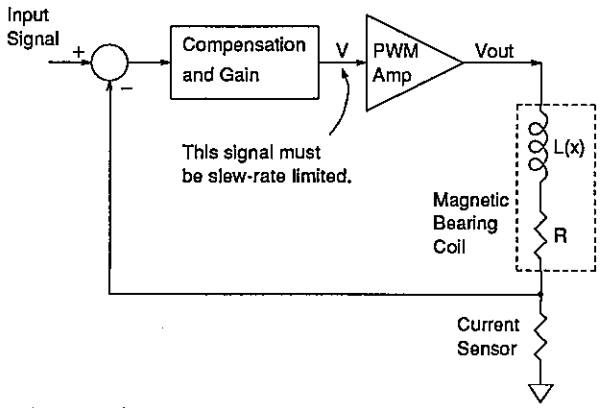

Figure 4 - Closed-Loop PWM Transconductance Amplifier

the output transistors switch the output voltage to its "low" value; when the output current is smaller than the requested current, the output transistors switch the output voltage to its "high" value. In order to restrict the switching to a rate which provides high efficiency, a sample-and-hold device is inserted between the comparator and the output stage. This device is driven by a periodic clock. At the beginning of each clock period, the sample-and-hold device transfers the state of the comparator to the output devices. This state is then retained for the remainder of the clock period. In this manner, the maximum switching rate is fixed by the clock (see figure 5). The *D flip-flop* shown in figure 5 is logic circuit which performs the sample/hold action on discrete binary signals.

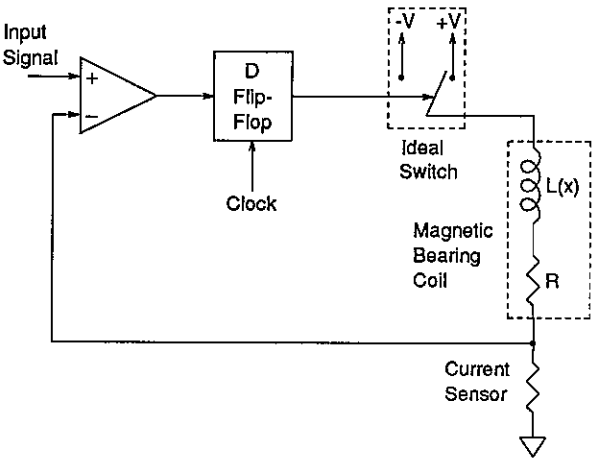

Figure 5 - Sample/Hold Configuration

Fixed sampling rate control can be implemented with a fairly simple circuit, giving it a substantial advantage over PWM control. Its primary drawback is that, because the switching instants are fixed by the clock, it tends to produce significant harmonic distortion. It also exhibits a deadband rendering it very insensitive to small signals.

Figure 6 presents simulated and measured time response data for the sample/hold configuration. The simulated data was generated by digital computer with idealized models for the comparator, current sensing, output switch, and series inductive/resitive load. The measured response was captured

with a digital storage oscilloscope.

Casual inspection of figure 6 reveals discrepancies between the simulated and measured responses. These differences result from characteristics of the experimental setup which remain unmodelled in the simulation: nonidealities of the output devices driving the load, and asymmetric propagation delays generated by the control circuitry in the power output modules [11]. The simulation program models the IGBT output devices used for these experiments as ideal switches, a model which ignores the static voltage drop and poor high frequency dynamic performance of the transistors (for example, the manufacturer of the devices used here recommends that they be switched no faster than 20 kHz; our sample/hold controller switches at 62.5 kHz). The greatest contributor to the discrepancy, however, is the asymmetric propagation delay between control pulse and output device response. Close inspection of the sample/hold waveform reveals that, while the *average* sample period is 16 μS (as it should be), the amplifier often generates successive pulses of, for example, 13 μS and 19 μS. Such behavior, not accounted for in the simulation, significantly alters the operating characteristics of the sample/hold amplifier. This behavior, though, is uniquely a function of the particular output modules employed here and is not intrinsic to the sample/hold algorithm. In any event, both the simulated and measured responses display the substantial distortion typical of sample/hold operation.

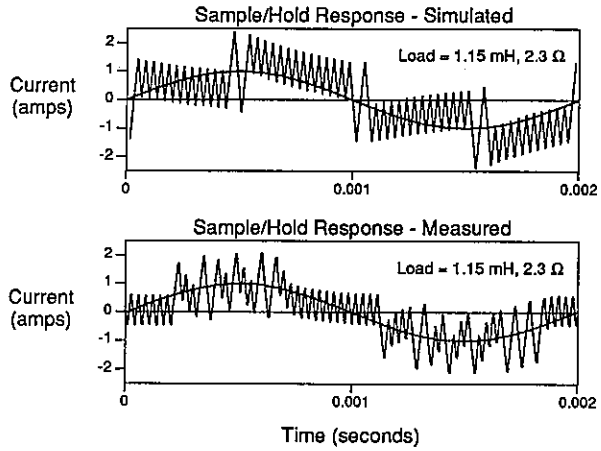

Figure 6 - Time Responses (Sample/Hold)

The decision-making capability of the sample/hold amplifier can be significantly improved if these decisions are allowed to occur in an asychronous manner. Rather than fixing each switching instant with an impartial clock, the load response should determine each switching instant directly. At the same time, the switching rate needs to remain restricted. One method of achieving such behavior is to add a small amount of hysteresis to the comparator so that rather than switching to a positive state precisely when the current error becomes positive and switching to a negative state precisely when the error becomes negative, the positive transition is delayed until the error reaches some threshold value, $+\varepsilon$, and the negative transition is delayed until the error reaches another threshold, $-\varepsilon$. When the amplifier is driving an inductive load, these voltage thresholds yield a time delay due to the integrating effect of the load. Thus, a fixed period sample/hold device is apparently not required to control the maximum switching rate: the output of the hysteretic comparator can drive the output devices directly with no intervening logic.

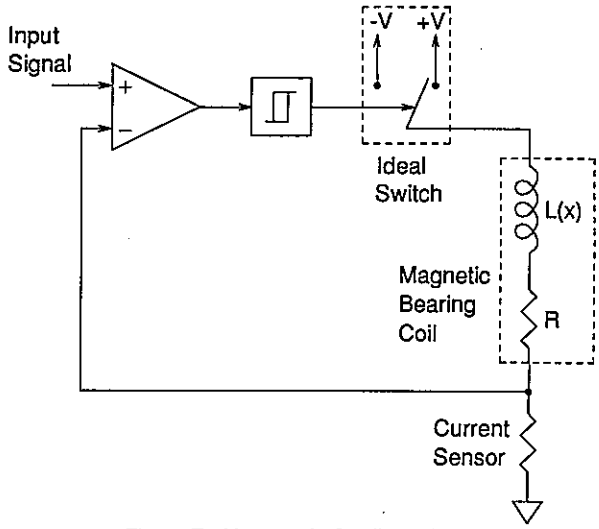

Figure 7 - Hysteresis Configuration

The circuit required to implement hysteretic control is even simpler than that required for fixed sampling rate control, dispensing with the clock and the sample-and-hold device at the expense of only a few resistors needed to produce the desired hysteresis. The absence of a fixed sampling rate results in an asychronous configuration which exhibits greatly reduced harmonic and crossover distortion (note the tight tracking and low distortion of the simulated response in figure 8). The most apparent drawback to this design is that the switching rate will depend not only on the amount of hysteresis designed into the circuit, but also on the load impedance and the power supply voltages. Consequently, the amplifier must, to some extent, be tuned to the load in order to ensure that the switching rate does not exceed the maximum allowed by the output stage while remaining high enough to yield good bandwidth. A more insidious problem inherent in hysteretic control is that it can produce very short control pulses if the reference signal changes rapidly [12]. This is particularly a problem in the presence of noise in the reference signal. In the simple analysis, short control pulses will only seem to degrade the efficiency of the amplifier, but if the output stage is an H-bridge, short pulses may cause device failure. (Some commercial H-bridge power devices have short pulse detection circuits to avoid this: short pulses will cause the output device to turn off [11].)

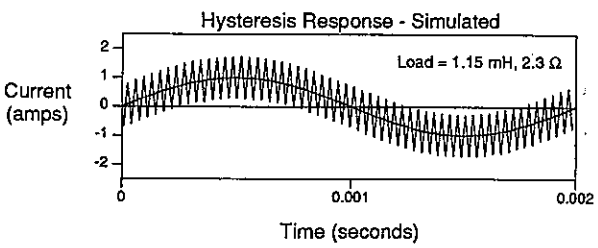

Figure 8 - Time Response (Hysteresis)

It is instructive to compare the distortion characteristics of the sample/hold and hysteresis amplifiers. Figures 9 and 10 show simulated waveform reconstructions obtained by performing a Fourier analysis over 20 cycles of amplifier response to a sine wave excitation and then summing the first 12 harmonics. The resulting waveforms confirm what might be expected from inspection of the time response plots: namely, that the hysteresis algorithm introduces much less distortion than the sample/hold approach does. These results also illustrate that, as the amplitude of the reference input signal is reduced, the distortion characteristics of *both* types of amplifier grow worse. However, even for the 1 amp experiment (figure 10), the hysteresis amplifier generates less than 1 percent THD, and the reconstructed waveform is virtually indistinguishable from the reference input. (It should be pointed out that, all else being equal, increasing the load inductance will improve the distortion characteristics of any of these control schemes). Clearly, an algorithm which embodies the distortion characteristics of the hysteresis approach yet does not demonstrate its shortcomings offers significant improvements over the sample/hold design.

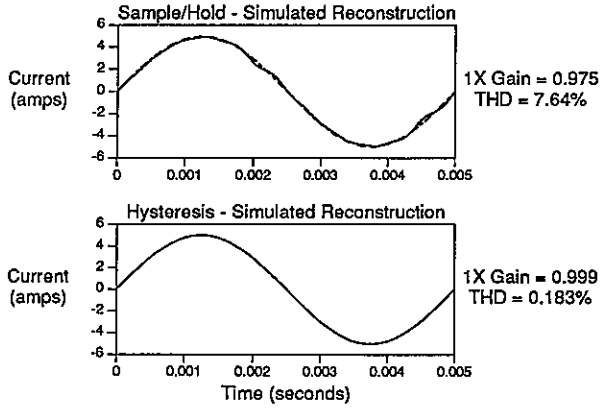

Figure 9 - Reconstructed Waveforms (5 Amp peak)

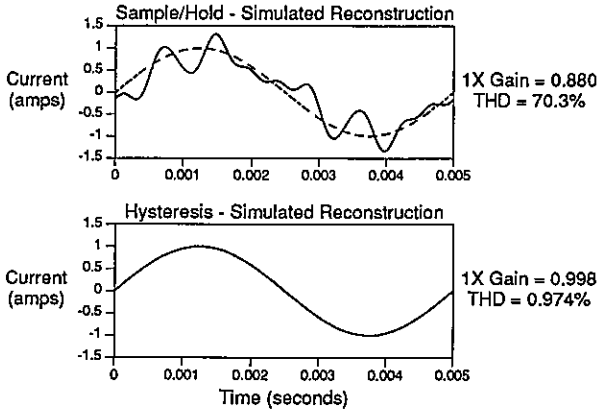

Figure 10 - Reconstructed Waveforms (1 Amp peak)

Minimum Pulse Width Configuration

The Minimum Pulse Width power amplifier, hereafter referred to as the MPW amplifier, is intended to achieve the high efficiency of a switching amplifier without some of the drawbacks of prior designs such as high complexity, high distortion and short pulse fault susceptibility.

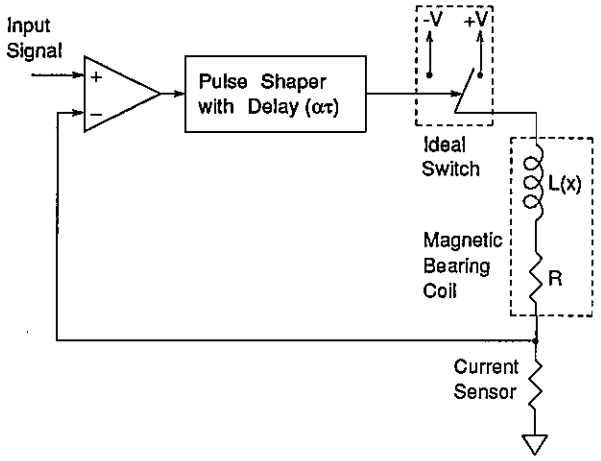

Figure 11 - MPW Configuration

The primary shortcoming of hysteresis control is its short pulse susceptibility. One solution to this problem is to insert a pulse shaping circuit after the hysteresis element which either strips short pulses out of the pulse train or stretches them to an acceptable length. While this would eliminate the short pulse problem, it suggests a further simplification. Since the primary objective of the hysteresis is to produce finite length pulse, but the same function is also provided by the pulse shaping circuit, the hysteresis is now unnecessary. These considerations lead directly to the design of the minimum pulse width amplifier.

The MPW amplifier is constructed in the same basic configuration as the previously mentioned sample/hold and hysteresis schemes (see figure 11). However, the nonlinear compensator consists of simple digital logic which keeps the pulse width of the control signal applied to the output device greater than some fixed minimum. The operation of this pulse shaper can be summarized as follows. Each incoming pulse is delayed by a period of $\alpha\tau$ where α is a fixed number ranging between zero and one while τ is the minimum permissible pulse width. At the end of the time delay interval, if the pulse shaper detects that the incoming pulse has ended (the incoming pulse width was less than $\alpha\tau$) then the pulse is not transmitted. Thus, pulses of duration less than $\alpha\tau$ are stripped from the pulse train. On the other hand, if the pulse has not ended prior to $\alpha\tau$, it is transmitted to the output of the pulse shaper and the output state is retained for a duration of at least τ. In this manner, pulses of duration greater than τ are delayed by a period $\alpha\tau$, but otherwise are not modified. Pulses of duration less than τ but greater than $\alpha\tau$ are also delayed by $\alpha\tau$ but, in addition, are extended to a duration of τ. This behavior is summarized in figure 12.

The primary differences between this design and the previous techniques are:

1.) in a fixed sampling rate controller, switching can only occur at the clock edge; with MPW, the transition can occur anytime up to within the minimum pulse period of the last transition.
2.) in a fixed sampling rate controller, the control pulse period must be an integer multiple of the clock period; MPW permits control pulse periods to vary continuously

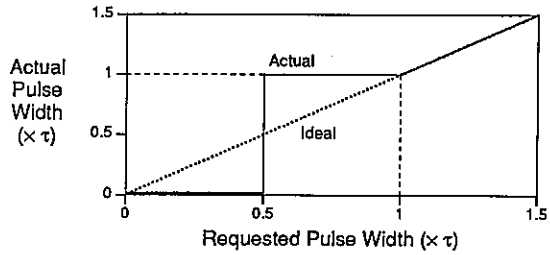

Figure 12 - Pulse Width Transfer Function ($\alpha = 0.5$)

from the fixed minimum period to infinity.

3.) in a fixed sampling rate controller, control pulses emanating from the comparator are always extended to the nearest integer multiple of the clock period; MPW extends only those pulses which are between one half the fixed minimum pulse width and equal to the fixed minimum (shorter pulses are discarded and longer pulses are not altered).

4.) fixed sampling rate control does not explicitly introduce a time delay between the control pulse emanating from the comparator and that delivered to the output device, but a time delay is implicit since this control scheme always extends the preceding pulse; MPW introduces a fixed time delay equal to one half the minimum pulse width ($\alpha = 0.5$).

5.) hysteretic control does not explicitly restrict the minimum pulse width seen by the output devices; this restriction is one of the motivating characteristics of MPW control.

6.) the switching times in a fixed sampling rate controller are determined by a regular clock (i.e., a synchronous configuration); the MPW configuration has no clock and operates aynchronously.

The objective in stripping off short pulses rather than extending them to the minimum pulse width is to eliminate a small signal deadband which results from always extending them (see figure 13 for simulated time responses which show the effect of increasing the "strip off" threshold from 0 to 0.5τ, where τ is the minimum pulse width allowed). Short pulse detection cannot be accomplished without observing the first $\alpha\tau$ portion of the pulse. This necessarily implies a time delay of $\alpha\tau$; however, choosing $\alpha = 0.5$ eliminates the deadband and minimizes harmonic and crossover distortion. It is important to realize that there is no advantage to increasing α beyond 0.5τ; in fact, such action merely reduces the bandwidth of the amplifier (by increasing the delay in the feedback loop) and moderately increases the THD seen in the output signal (see figures 14 and 15 for plots of typical 1X (fundamental) gain and THD versus α). Introduction of the α delay in the feedback loop has the additional effect of increasing the amplitude of the output switching noise, which is the predominant reason for the increased THD beyond $\alpha = 0.5$ (this increase in output noise is evident in the plots of figure 13).

Figure 16 shows the simulated and measured waveforms for the MPW amplifier. Note that the agreement between simulation and measurement is much better than in the case of the sample and hold scheme. This reflects the fact that the asynchronous nature of the MPW control scheme renders it much less sensitive to the asymmetric propagation

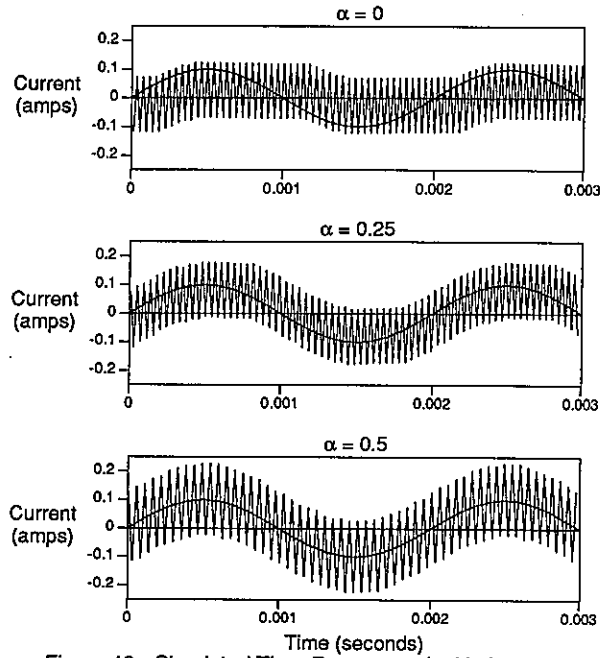

Figure 13 - Simulated Time Responses for Various α

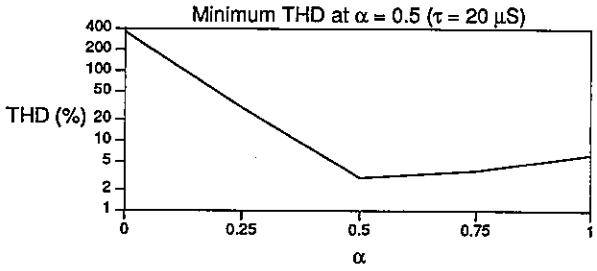

Figure 14 - Total Harmonic Distortion versus α

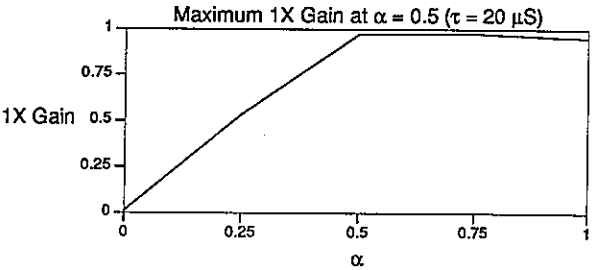

Figure 15 - Fundamental Gain versus α

delay in the output devices.

The MPW time response of figure 16 can be compared to the hysteresis time response shown in figure 17, where the hysteresis level has been adjusted to give approximately the same noise level in the two waveforms. The excellent agreement between these traces supports the argument that the MPW configuration provides most of the advantages of hysteresis control. This agreement is even more evident in comparing the filtered responses shown in figures 18 and 19. As before, the simulated waveforms are reconstructed by adding

the first twelve harmonic responses as determined by Fourier analysis. This removes the switching noise while retaining the most significant distortion characteristics. The similarity of the fine structure in figure 19 is particularly striking.

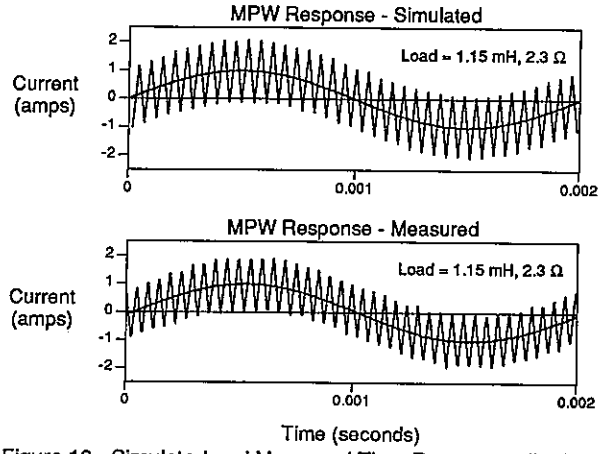

Figure 16 - Simulated and Measured Time Responses (MPW)

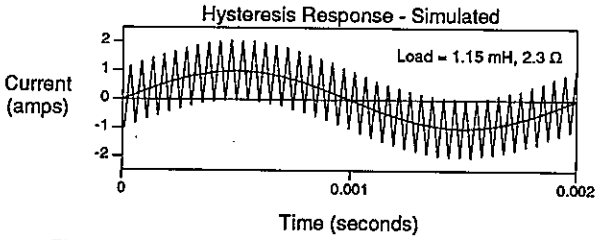

Figure 17 - Simulated Time Response (Hysteresis)

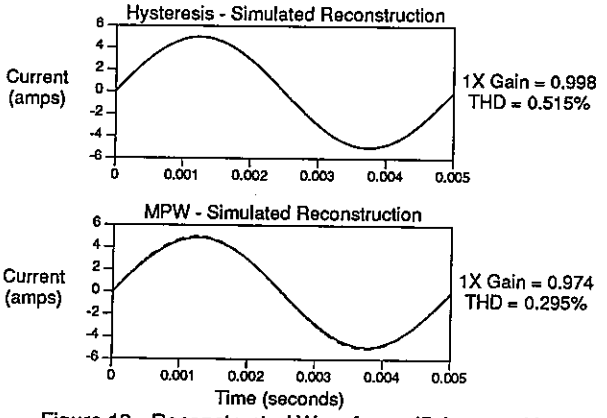

Figure 18 - Reconstructed Waveforms (5 Amp peak)

Additional Experimental Results

With any amplifier, especially one destined for application in a closed-loop control system, the frequency response is a performance index of interest. Figure 20 shows responses for the MPW amplifier under the following conditions: 100 mV, 2 V or 8 V (peak) sine wave input, swept from 100 Hz to 25.6 kHz; 1.15 mH, 2.3 Ω load; V_{supply} = 100 VDC; amplifier gain is 1 A/V. Note that the effective bandwidth of the amplifier depends on the excitation amplitude: as this value is increased from 2 V to 8 V (peak), the

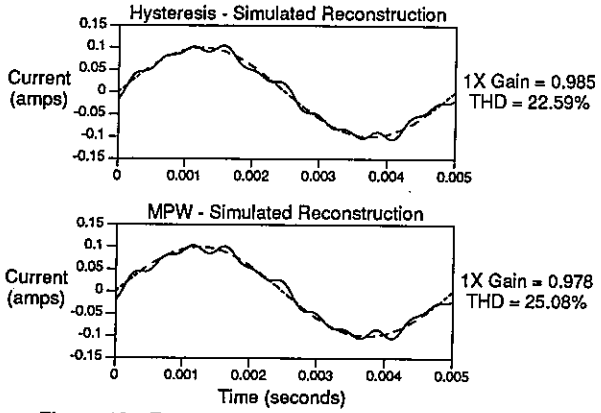

Figure 19 - Reconstructed Waveforms (100 mA peak)

"break point" in the response curve is reduced from approximately 7 kHz to about 1.8 kHz. This amplitude dependence is characteristic of systems experiencing nonlinear limiting; here, operation of the amplifier beyond the break point incurs transconductance errors as the slew rate limits of this particular supply voltage/load inductance combination are exceeded. Slew rate limiting is discussed extensively in [4], [5] and [13].

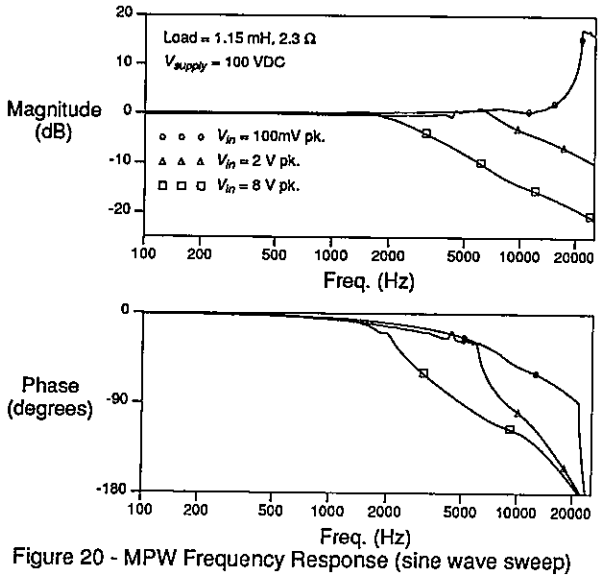

Figure 20 - MPW Frequency Response (sine wave sweep)

Two additional properties of the MPW amplifier should be noted. First, it is important to realize that the break point in the frequency response curve is *not* the same as the "-3 dB" point often referred to in linear system analysis (note that the phase response of the MPW amplifier is not -45 degrees at the break point as would be expected for a linear system). Also, significant aliasing is observed for the low amplitude curve at frequencies higher than ≈ 20 kHz (this behavior is manifested as an apparent increase in gain for these frequencies). Since this amplifier is a sampled-data system, Shannon's sampling theorem [14, 15] states that operation above the Nyquist frequency (defined as 0.5 × sampling rate) will result in aliasing. With a minimum pulse width of 23

μS, the effective maximum switching rate of this MPW amplifier is ≈ 44 kHz, which implies a Nyquist frequency of ≈ 22 kHz. Typically, devices of this sort are considered to have usable bandwidths no wider than one half of the Nyquist frequency.

Conclusions

The results presented in this paper successfully establish the viability of a new type of switching transconductance amplifier, the Minimum Pulse Width amplifier. These results demonstrate attainment of the stated design goal of low harmonic distortion, and by design the MPW amplifier is fundamentally immune to short-pulse failure. With no particular precautions or tuning performed, an amplifier of this design has been operated successfully with loads varying from 1-200 mH, thus demonstrating its insensitivity to load variations.

Earlier approaches to the transconductance amplifier design problem were investigated. Open-loop schemes employing conventional PWM voltage-to-voltage amplifiers exhibited a high degree of sensitivity to the load impedence and required tuning to achieve transconductance behavior. Introducing current feedback around such a PWM amplifier reduced this load sensitivity, but the closed-loop configuration was still unnecessarily complex and suffered from low frequency accuracy and bandwidth limitation problems.

Two bang-bang control schemes (sample/hold and hysteresis) were considered. Both of these configurations overcame the complexity problems associated with conventional PWM amplifiers, but each presented different limitations. The sample/hold design produced significant harmonic distortion and exhibited a deadband which rendered it insensitive to small signals. The hysteresis demonstrated very low distortion behavior, but suffered from short-pulse susceptibility which could potentially degrade efficiency and destroy output devices during normal operation.

The Minimum Pulse Width (MPW) design was presented. Simulated and measured results from the MPW amplifier confirm that it overcomes both the harmonic distortion problem of the sample/hold approach and the short-pulse susceptibility problem of the hysteresis configuration. Measured frequency response data for the MPW amplifier was presented; this data demonstrated the amplitude dependence expected for a system experiencing slew rate limiting and the aliasing characteristic of sampled-data systems operated above their Nyquist frequency.

References

[1] Hebbale, K., "A Theoretical Model for the Study of Nonlinear Dynamics of Magnetic Bearings," Cornell University Thesis, January 1985.

[2] Bleuler, H., "Decentralized Control of Magnetic Rotor Bearing Systems," Ph.D. Dissertation, Swiss Federal Institute of Technology, ETH report number 7573, Zurich, Switzerland, 1984.

[3] Humphris, R. R., R. D. Kelm, D. W. Lewis and P. E. Allaire, "Effect of Control Algorithms on Magnetic Bearing Journal Properties," Journal of Engineering for Gas Turbines and Power, Vol. 108, October 1986.

[4] Keith, F. J., "Digital Control System Design for Active Magnetic Bearings," M. S. Thesis, University of Virginia, May, 1988.

[5] Maslen, E., P. Hermann, M. Scott and R. R. Humphris, "Practical Limits to the Performance of Magnetic Bearings: Peak Force, Slew Rate, and Displacement Sensitivity," ASME Journal of Tribology, Vol. 111, April 1989, pp. 331-336.

[6] Maslen, E. H., P. E. Allaire, M. A. Scott, "Magnetic Bearing Design for a High Speed Rotor," Proceedings of the First International Symposium on Magnetic Bearings, ETH Zurich, Switzerland, June 6-8, 1988, pp. 137-146.

[7] Lorenz, R. D., and D. B. Lawson, "Performance of Feed Forward Current Regulators for Field Oriented Induction Machine Controller," Conf. Rec., 1986 Annual Mtg. IEEE Ind. Appl. Soc., pp. 99-105.

[8] Copley Controls Corp. Selection Guide, "PWM Servo Amplifiers."

[9] Kheraluwala, M. and D. M. Divan, "Delta Modulation Strategies for Resonant Link Inverters," PESC 87, Conf. Records, pp. 271-278.

[10] Lorenz, R. D. and D. M. Divan, "Dynamic Analysis and Experimental Evaluation of Delta Modulators for Field Oriented AC Machine Current Regulators," IEEE - IAS Annual Conference Records, 1987.

[11] General Electric Data Sheet, "GS105 GESmart MODULE Half-Bridge Switch Motor Driver."

[12] Brod, D. M. and D. W. Novotny, "Current Control of VSI-PWM Inverters," IEEE Transactions on Industry Applications, Vol. IA-21, No. 4, May/June 1985, pp. 562-570.

[13] Gibson, J. E., *Nonlinear Automatic Control*, McGraw-Hill Book Company, Inc., 1963.

[14] Oppenheim, A. V. and Schafer, R. W., *Digital Signal Processing*, Prentice-Hall, Inc., 1975.

[15] Kuo, B. C., *Digital Control Systems*, Holt, Rinehart and Winston, Inc., 1980.

2nd International Symposium on Magnetic Beaing
July 12-14, 1990, Tokyo, Japan

PROBLEMS, SOLUTIONS AND APPLICATIONS IN THE DEVELOPMENT OF A WIDE BAND POWER AMPLIFIER FOR MAGNETIC BEARINGS

T.BARDAS*, T.HARRIS*, C.OLEKSUK*, G.EISENBART**, J.GEERLIGS**

*NOVA CORPORATION OF ALBERTA
**NOVA HUSKY RESEARCH CORPORATION

Abstract

This paper describes the development of a power amplifier for magnetic bearings capable of switching 50 A and 160 V DC at 40 kHz. Magnetic bearing amplifiers for large industrial equipment require high power handling capacity to control bearing current. In order to reduce power losses, the amplifiers need to be switching. A high clock rate in the amplifier is desirable to reduce distortion in the bearing current but causes increases in the amplifier power losses. The operation of a switching amplifier is described as well as the limitations of the components. The testing results of the amplifier are discussed.

1. Introduction

NOVA Corporation of Alberta currently operates 13 gas compressors ranging in size from 3,800 kW to 21,000 kW that utilize magnetic bearings. The magnetic bearings used in NOVA's compressors have been supplied by Magnetic Bearings Incorporated and operate using an attractive principle. The current in the bearings is used to create a magnetic field between the rotor and stator elements. The current and, therefore, the bearing force is controlled by a switching regulator commonly called a power amplifier.

With an eye towards the future and machines with more flexible rotors operating at higher speeds, NOVA saw the need for a more efficient and effective amplifier. NOVA, therefore, commissioned the development of such an amplifier to its research arm NOVA HUSKY Research Corporation. The amplifier was to have the same power output as the present amplifiers (50 A x 160 V) but the switching speed was to be more than doubled from 17 Khz to 40 Khz. The amplifier cooling was to be forced ambient air only.

2. Power Output Requirements for Power Amplifiers

An important characteristic in determining whether an active magnetic bearing can modulate a dynamic load is the rate at which force can be changed in the bearing. Assuming dynamic forces on a shaft to be sinusoidal in nature, higher force change rates result from larger forces or higher frequencies. If the actual rate of force change exceeds the bearing's maximum force change rate, the bearing will be unable to control the load and is, therefore, force slew rate limited. The sum of the dynamic and static forces on the bearing may be below the bearing's static capacity but the bearing current cannot be changed fast enough to access the unused capacity. On an actual machine, the current wave form becomes triangular in nature when the bearing is force slew rate limited.

The parameters that control the rate of force change in a bearing, can be found by multiplying the partial derivative of force with respect to current, by the derivative of current with respect to time. (see Appendix 'A').

$$\frac{dF}{dt} = \frac{\partial F}{\partial i_b}\frac{di_b}{dt} = \frac{i_b V_b}{g} \qquad (1)$$

The maximum rate of force change in a bearing is governed by the gap in the bearing and by the power applied to the bearing by the power amplifier and is unrelated to the size of the bearing. In practice reducing the air gap does not change the bearing force response because halving the air gap in a given radial bearing also halves the static current needed to levitate the shaft. The only methods to improve the bearings force response are to increase the voltage driving the coil or the static operating current. The static operating current

can be increased by reducing the number of turns or by increasing the static load with an opposing magnetic bearing. In either case the amplifier must be able to deliver the necessary current at the required voltage in order to make the bearing response satisfactory.

In NOVA's compressor stations the D.C. back-up power for the station is provided by stationary batteries that float at 132 V. The cost and space requirements for a separate battery bank outweigh the benefits of operating the bearing at a higher voltage. The air gap in the radial bearing is usually about 5.1×10^{-4}m while the levitating current is about 20 amps. From equation (1) this results in a maximum rate of force change of 5.2×10^{6} N/sec.

The maximum actual rate of force change for an unbalance is:

$$\frac{dF}{dt} = \frac{2\pi n F_{peak}}{60} \qquad (2)$$

Therefore, a typical radial bearing operating at 10,000 rpm could produce the force change rate developed from a 4,945 N peak unbalance force. This only becomes a limitation if the bearing has capacity for unbalance loads greater than 4,945 N peak.

3. Switching vs. Linear Amplifiers

In order to control the field in a magnetic bearing, regulation of current to the bearing by an amplifier is necessary. The simplest choice for current control is a linear amplifier consisting of a transistor in series with the bearing coil as shown in Fig. 1. The bearing current is varied by changing the voltage drop across the regulating transistor. A current feedback loop is used to regulate the voltage drop across the transistor. This approach has been used successfully in magnetic bearings but leads to high heat dissipation in the amplifier when large static or dynamic load capacities are required.

The power needed by a linear amplifier is determined by the supply voltage and the current in the bearing.

$$P_q = V_s i_b = i_b (V_t + V_b) \qquad (3)$$

The heat dissipated in a linear amplifier is determined by the voltage drop across the transistor and the current. The ability of the bearing, to respond to force change is determined by the additional voltage above steady state that can be placed across the bearing coil. The additional voltage that can be placed across the coil is the voltage drop across the transistor. Therefore the ability of the bearing to regulate dynamic loads is directly related to the power losses of the amplifier.

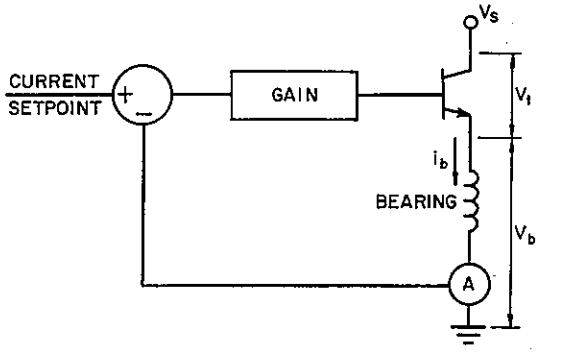

FIGURE 1
LINEAR POWER AMPLIFIER

As an example, a typical quadrant in a radial bearing used in a gas compressor requires 20 amps to levitate the shaft. The amplifier is powered by 130 V and the coil resistance is about 0.3 ohm. The steady state voltage drop across the coil would be 6 V and the drop across the transistor would be 124 V. The power required for this axis, in levitating the shaft, would be 2,600 W of which 2,480 W is lost in the power amplifier.

A compressor normally has 4 active radial bearing quadrants which would result in nearly 10 kW of power being required for amplifier losses. While the 10 kW may be insignificant in terms of energy compared to the compressor, it represents a significant problem for cooling the amplifiers to a temperature at which the regulating transistors can survive.

The alternative to a linear amplifier is a switching amplifier. The simplest possibility is as shown in Fig. 2. When the current required is below set point the switch is connected to the voltage supply. The current would then rise at a rate of

V_b/L_b until it reached the desired level, when the switch would close shorting the coil. The voltage across the coil would reverse and the current would continue. The rate of current decay would be determined by the L/R time constant of the coil and the bearing current. Normally, this would result in an unacceptable length of time to reduce to the current and the bearing force due to the low resistance in the loop.

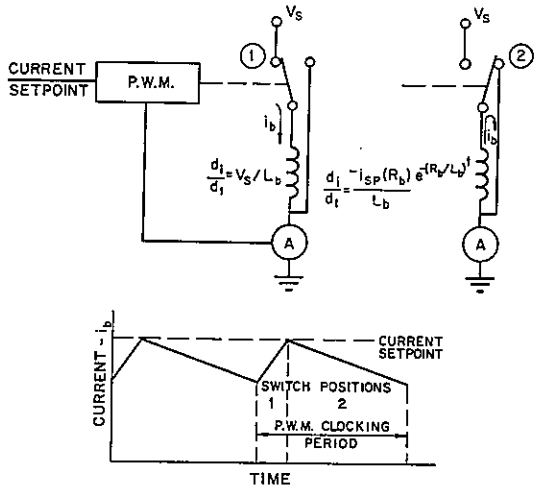

FIGURE 2
SINGLE SWITCH SWITCHING AMPLIFIER

An additional resistor could be added in the closing loop to decrease the L/R time constant to make the rate of current decay equal to the current rise for a given operating current. This results in the resistor being sized to produce the same voltage drop as the voltage supply. With equal rise and decay rates a duty cycle of 50% is required in order to maintain the selected operating current. Half of the time the bearing receives energy from the power supply, the other half the bearing supplies energy to the flyback resistor. The bearing axis losses would then be:

$$P_q = i_b^2 R_b + \frac{V_b i_b}{2} \qquad (4)$$

The power losses in a bearing quadrant using the previous example would be 1420 W with 1300 W being lost in the flyback resistor. The amplifier loses are still high and the current decay rate varies with the bearing current.

The ideal situation is if the energy lost in the fly back resistor could be fed back in to the power supply. The energy could then be reused in the next switch cycle when the current in the bearing is being increased. This can be accomplished by a circuit shown in Fig 3. The supply voltage is applied when switches 1 and 4 are closed and switches 2 and 3 are opened. The current increases at a rate of V_b/L_b. When switches 2 and 3 are closed and switches 1 and 4 are opened, the voltage across the coil reverses and the current flows from the coil back to the power supply. The current decreases at rate of V_b/L_b. The power supply must be able to accept the current from the bearing or high coil voltage will result. A capacitor across the power supply serves this purpose. The amplifier is really a switch that transfers energy back and forth between an inductor and a capacitor.

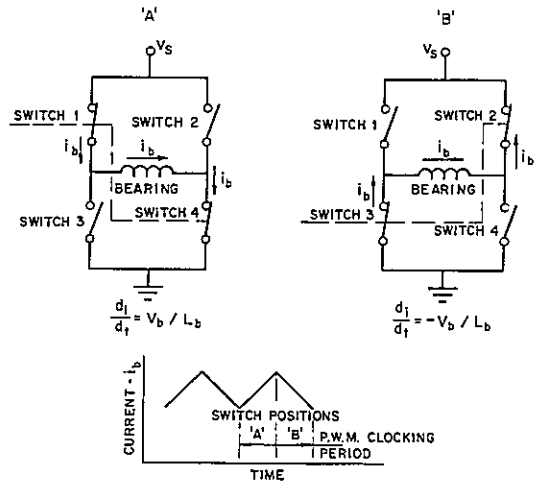

FIGURE 3
FOUR SWITCH SWITCHING AMPLIFIER

The drawback of using a switching amplifier is the distortion introduced into the bearing current. At a constant current level the peak to peak value of the ripple current is given by the following:

$$i_r = \frac{V_b}{2L_b f_{pwm}} \qquad (5)$$

The amount of ripple, therefore, depends on the size of bearing and the switching frequency. In small machines the switching frequency must be increased to reduce the ripple to an acceptable amount.

The amplifier losses are restricted to resistive losses across the switches and the losses during switching. By proper design these losses can be made a fraction of the product of voltage and current regulated by the amplifier. This is the design challenge.

4. Operation of a Switching Amplifier

The switching amplifier (Fig. 4) consists of two transistor switches and two diodes arranged to form an H-bridge with the bearing coil. The two transistors form one pair of switches that allow energy to be increased in the bearing. The diodes form the other pair of switches that allow energy to be reduced in the bearing. The transistors are the only switches that have to be actively controlled. The diodes are passive switches that become conducting whenever the coil voltage becomes greater than the supply voltage. This guarantees the current direction in the bearing and that the coil will not become open circuited. The high resulting voltages could destroy components.

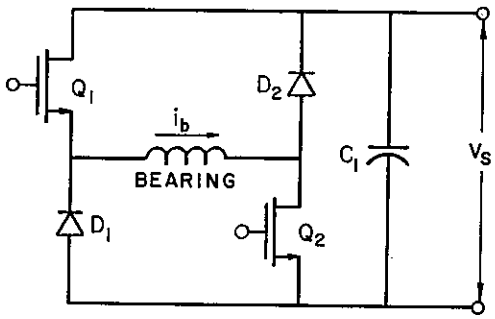

FIGURE 4

SWITCHING AMPLIFIER SCHEMATIC

The switching of the amplifier is controlled by a pulse width modulator. The pulse width modulator (PWM) can be controlled using either current or flux feedback. The pulse frequency of the PWM, therefore, controls the maximum switching rate of the amplifier. During operation at any constant current, the amplifier duty cycle is nearly 50%. When the coil current is increasing the duty cycle increases.

Regulation of the flux density in the bearing is achieved by switching energy between the capacitor and the bearing coil. This results in the highly efficient nature of switching amplifiers, as compared to linear amplifier which regulates by dissipating energy in the form of heat.

The capacitor sees an alternating current equal to the switching frequency of the amplifier. The peak value of the alternating current, equals the bearing current. The inductance of the power supply cable prevents most of the switching current from being seen at the power supply. The current from the power supply is mainly D.C. and is determined by the power losses in the bearing and amplifier.

5. Power Losses in Switching Amplifiers

The power losses in the amplifier can be divided into two categories, static and dynamic. The static losses are caused by the resistance of the transistors and the capacitor and the forward biased voltage drop of the diodes. These losses are related to the square of the bearing current in the case of resistance and directly to the current in the diodes. The static power losses can be minimized by choosing metal oxide semi-conductor field effect transistors (MOSFET) with low resistances. In the case of the diodes the voltage drop is fixed if silicon diodes are used.

The dynamic losses result from the fact that the transistor switches do not start and stop conducting current instantaneously. When one of the transistor switches turns on, the full supply voltage is across the device. The voltage remains until the transistor resistance is low enough to allow it to conduct the full bearing current at which time the the voltage drop is determined by the transistor resistance. A similar situation occurs when the transistor turns off. The dynamic losses are related to the bearing current and the switching frequency of the amplifier. In order to minimize the switching losses in the amplifier, the transistor switches must be selected to switch as quickly as possible. As a result MOSFET transistors were selected.

6. Limitation of Amplifier Components

According to initial calculations, power losses of less than 150 W were attainable. Actual

measurements of a breadboarded switch, however, proved that dynamic losses were greater than expected. In order to keep these losses low at the 40 kHz switching rate, the switching time had to be kept to a minimum. Unfortunately very little information was available about high speed, high voltage and high current switching problems and the initial tests were not encouraging due to high heat dissipation. The development of the switch was further aggravated by severe oscillations which could not be suppressed by means of dampening. Contrary to the expectations of high efficiency when using fast recovery diodes and MOSFET switches, the limitations of such devices and their undesirable interactions were observed. These are explained in connection with problems encountered during the development.

The immunity of MOSFET's to thermal second-breakdown failures gives them an advantage over bipolar transistors. Yet they still run the risk of avalanche breakdown as do bipolar devices. The avalanche breakdown can be traced to the turning on and off of the parasitic bipolar transistor which is an inherent feature of each MOSFET device (Fig. 5). The voltage limit of the parasitic transistor is its base-collector junction breakdown voltage. Its base-emitter resistance, temperature and D.C. current gain (h_{FE}) determine the current level at which the breakdown occurs. In the MOSFET's parasitic transistor, the base and emitter terminals are shorted together on the die, to yield the least base-emitter resistance (R_{BE}). The base to emitter resistance together with the collector-base junction capacitance (C_{CB}) determine the MOSFET's drain to source dV/dt. A positive transition of the drain to source voltage causes flow of current through the C_{CB} which corresponds to the rate of the voltage rise. The resulting voltage drop across the R_{BE} can reach a point, at which the parasitic transistor turns on. This undesirable turn on or switchback, interferes with the normal circuit operation of the MOSFET and can possibly destroy it.

Maximum dV_{DS}/dt information is not yet specified on MOSFET data sheets. The high rate of voltage rise between the drain and the source of the MOSFET can only occur during the off-

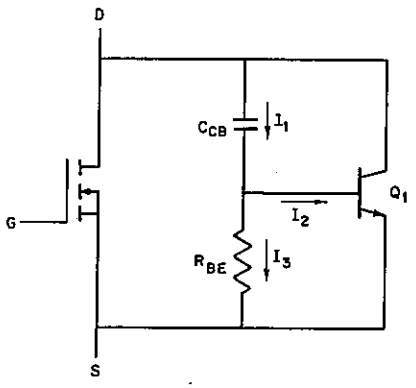

FIGURE 5
EQUIVALENT MOSFET SWITCH SCHEMATIC WITH THE INHERENT BIPOLAR TRANSISTOR

switching of an inductive load. Such is not the case with the H-bridge switch, since the fast recovery rectifiers effectively clamp the bearing magnet to the supply. In spite of that, some parasitic inductances associated with the H-bridge switch cause severe voltage spikes. In order to reduce the effects of parasitic inductances, interconnections must be as short as possible within the switch.

Data sheets of the MOSFET used, however, list a maximum allowed rate of change of current at turn off (di/dt). The value of di/dt depends on the drain to source voltage. For the 160 V supply voltage, a maximum of 10 A/ns can be read. Actual measurements have shown a rate of 1 A/ns under maximum load conditions. The maximum rate of current change might have drastically increased during critical conditions outlined in the test result section.

Another limiting factor of the MOSFET is its breakdown voltage limit. As the breakdown voltage increases, the transistor's on-resistance goes up exponentially. In addition to the supply voltage a reasonable safety margin must be added for the handling of voltage surges. For the 160 V supply, a 400 V MOSFET device was considered adequate.

The switching speed of a MOSFET device is determined by the travel time of the majority carriers, the gate capacitance, the transistor's package inductance, the internal gate resistance and the driver impedance. The delay at turn on is due to the length of time it takes for the gate

voltage to rise to the threshold level, where the device begins to conduct. As the gate to source voltage increases above the threshold level, the drain to source voltage is falling and the Miller effect takes place while a large increase in capacitance occurs. After the drain voltage drops to its final "on value", the gate to source voltage begins to increase again and no Miller effect takes place. A typical characteristic of the drain-source voltage versus the gate charge is shown in Fig. 6. Particularly critical is the time during the drain to source voltage drop during which severe oscillations were observed. A quick charging of the gate through a low impedance drive circuit seemed to be an easy solution. Unfortunately, the MOSFET power module has no internal Zener diode protection and the maximum gate to source voltage is only 20 V. It is, therefore, important to select devices with short duration of drain to source voltage drop.

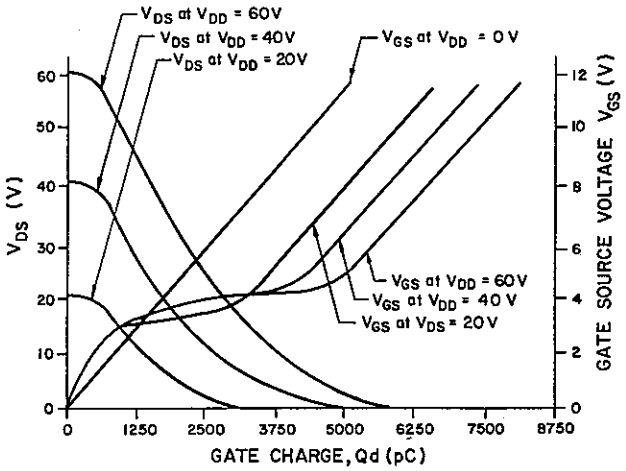

FIGURE 6

DRAIN-SOURCE VOLTAGE VERSUS GATE CHARGE

The reverse recovery time (t_{rr}) of the 4-bridge rectifier has been singled out as the main cause of the circuit oscillations. During the reverse recovery time, diodes continue to conduct in the reversed voltage direction. The current is determined by only the external resistance in the diode circuit. The reverse recovery time should be as short as possible because during that period, both rectifiers of the switch represent a short in the respective leg of the H-bridge. The fast recovery rectifiers used in the bridge have a trr of 50 n sec. The mechanism of circuit oscillations can be explained by means of the H-bridge diagram into which parasitic capacitances and stray inductances have been added as shown in Fig. 7. In the diagram C_s represents the capacitance associated with the rectifier. Its value is rather variable and dependent on the state of the device. In this instance it is considered to be in the "off" state. L_s is the stray inductance representing the wiring and the lead inductance of the rectifier. Cgd is the gate to drain capacitance of the MOSFET and it too is variable according to the state of the device. To simplify the discussion, the other stray inductances and parasitic capacitances at the various MOSFET leads are not shown. A series resonant circuit is formed by C_s and L_s in each leg of the bridge. Whenever it is excited by a pulse, the circuit will ring at its natural frequency. Without further intervention, the decay time of the oscillations can be many microseconds. At the MOSFET turn off, this oscillation barely occurs because the diodes switch to their "on" state and C_s is effectively removed thus preventing the energy exchange with L_s. At the MOSFET turn on, however, the effect of the resonant circuit is dramatic and potentially destructive. Within less than 100 nanoseconds the MOSFET carries its full rated current and the

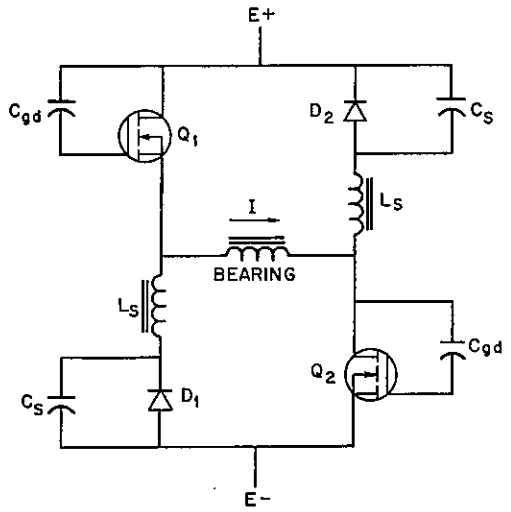

FIGURE 7

H-BRIDGE WITH STRAY COMPONENTS

rectifier begins its turn off. At this time, the drain voltage is still high and within 50 nanoseconds after the load current has been taken up by the MOSFET, the reverse recovery charge of the rectifier collapses. The energy in the stray inductance is now exchanged with the parasitic capacitance C_s in an oscillatory fashion at frequencies of 60 to 150 megahertz. With little damping, very large voltage oscillations are present at the drain which is coupled into the gate through the gate to drain capacitance Cgd. The net result is increased power dissipation in the MOSFET as well as large voltage swings at the gate which can destroy the device.

Thus our concerns were concentrated on the basic H-bridge circuit. The problems were further aggravated by circuits external to the power amplifier. The power supply by necessity is some distance away from the amplifier and is connected with long cable runs. These cables have inherent inductances, that are rather large, in the hundreds of microhenries range. As far as the switching problems in the bridge are concerned, the net result is the same as was caused by the stray inductances inside the bridge but on a larger scale. In addition, since the full load current reverses polarity every half cycle, these cables would have to be inordinately large if more than one amplifier was in use. For this reason, an electrolytic capacitor bypasses the supply bus bar in each amplifier. Unfortunately, electrolytic capacitors for higher voltage ratings have poor characteristics in regard to the series inductance (ESL) and the series resistance (ESR). The ESL figure limits the applicability of electrolytic capacitors for high di/dt demands, whereas the ESR value determines ohmic losses at a given ripple current.

These are all problems due to inherent characteristics of components. Solution of these becomes the key to a successful design.

Measurements taken during the laboratory tests of the amplifier is recorded on diagrams shown in Fig. 8. The oscillograms of the output voltages, which were measured between the load terminals and the ground, verified the switching speed. The barely visible voltage spikes are within a safe operating limit of the semiconductor components.

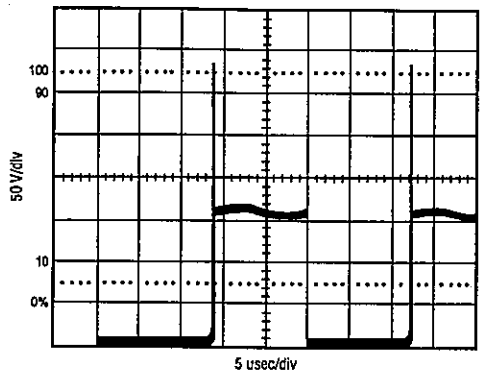

FIGURE 8
Amplifier Load Terminal 1 to Ground Voltage

7. Design and Layout of the Power Amplifier

Performance criteria of the power amplifier was achieved by a careful selection of components as well as efficient layout and mounting of all parts. The design goal was for a high speed H-bridge switch that could be operated with air cooling. Because at least ten amplifiers are used in the typical magnetic bearing installations, physical size considerations were important. Cabinet space is always at a premium. Fortunately, compact size coincides with the electrical considerations to reduce stray inductance through minimal conductor lengths.

Once the appropriate heat sink was selected, all the electrical components were fitted to the mounting surface of the heat sink. Efficient MOSFET's were selected and mounted directly on the heat sink, then interconnected by heavy bus bars. For ease of mounting, power modules were preferred to flat pack housing. Rectifier diodes are mounted to the heat sink on a heavy L bracket. A printed circuit board, carrying all remaining components is positioned on top of the bus bars. The arrangement features short, low inductance paths among all components. An example of optimization is the connection between the gate driver chips and gates of the power MOSFET's. In this instance, an excess length of only 10 mm would cause a 60% increase in spurious noise

on the gate signal in spite of the fact that the drivers can source or sink 6 A.

Effective dampening of oscillations has been achieved by RC snubbers as well as losses of ferrite cores which are coupled to the conductors of the bridge. Dampening by ferrite has some negative effect on the stray inductances which create voltage spikes, so care must be made in the application.

A pulse width modulated signal at the output of the controller is sent onto a fibre optic cable through a fibre optic transmitter. The cable carries the signal to a fibre optic receiver at the amplifier and appropriate drivers control the gates of the MOSFET switches. The fibre optic signal transmission avoids any potential noise pick-up due to EMI effects caused by high dv/dt or due to the number of amplifiers in use.

8. Amplifier Performance Results

The original specifications for the development of the amplifier called for operation at a 40 kHz switching rate with the power dissipation of less than 150 W at a maximum load of 50 A and 160 VDC. The switching rate and load capability were fully satisfied. The heat dissipation spec was not met.

At the present time, available power measurement equipment revealed a power loss of approximately 200 W at a room temperature of 21°C. The corresponding efficiency amounts to 97.5%. An increase of efficiency is expected at a lower switching rate of 17 kHz, however, it was not yet confirmed by measurements. Although heat dissipation is higher than specified the amplifier is still suitable for air cooled cabinet design.

Ruggedness of the amplifier has been proven by breaker trips under short circuit conditions, which did not cause any deterioration of performance. The design is, therefore, considered suitable for industrial service.

Measurements taken during the laboratory tests of the amplifier are recorded on diagrams shown in Fig. 8 and 9. The oscillograms of the output voltages, which were measured between the load terminals and ground verified the switching speed. The barely visible voltage spikes are within the safe operating limit of the semiconductor components.

Actual modulation of the switching pulses occur in the magnetic bearing controller. The modulating circuitry contains a minor feedback loop and a pulse width modulator as shown in Fig. 9. The minor feedback loop maintains the bearing current or magnetic flux in proportion to the PID control signal by means of the pulse width modulator. Operation of the arrangement is apparent from the diagram in Fig. 10. The bearing current wave form shows the 40 kHz triangular switching ripple which is superimposed on a 500 Hz sine wave with a DC offset.

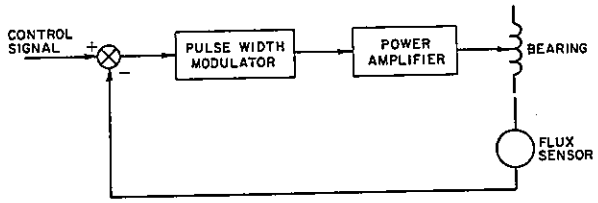

FIGURE 9
BLOCK DIAGRAM OF THE PULSE WIDTH MODULATING CIRCUIT

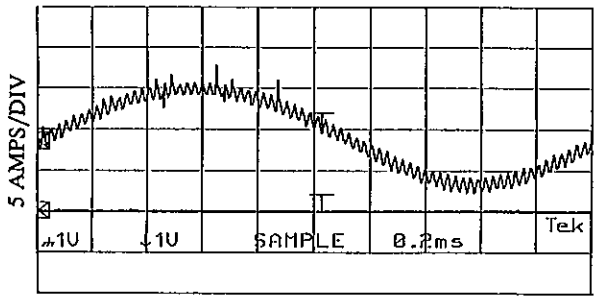

FIGURE 10
CURRENT IN A 0.4 mH LOAD
DRIVEN BY POWER AMPLIFIER

References

[1] MASLEN, E., et al., "Pratical Limits to the Performance of Magnetic Bearings: Peak Force, Slew Rate, and Displacement Sensitivity, "Journal of Tribology, Vol.111, April 1989, pp.331-336

[2] MILLMAN, J., Micro-Electronics Digital and Analog Circuits and Systems, New York, McGraw Hill, 1979 ,pp.52-54

[3] MACOMBER, L., "Compute Thermal Resistance-The Key to Computer-Grade Capacitor Ripple," Electronic Design, Vol.12, June 1979, pp.80-83
[4] SEVERNS, R., "MOSFET Rise to New Levels of Power", Electronics, May 1980, pp.145-149
[5] LABERKRACK, J., Linear/Switch Mode Voltage Handbook, Motorola, 1982, pp.81

Nomenclature

Symbol		Meaning
i_b	=	current in bearing quadrant coil
g	=	air gap between bearing stator and rotor
f_{pwm}	=	frequency of pulse with modulator
F_b	=	force produced by bearing axis on rotor
F_{peak}	=	peak dynamic force
L_b	=	inductance of bearing
n	=	shaft speed (rpm)
N	=	number of turns in bearing quadrant
P_q	=	power loss in a bearing quadrant including amplifier losses
R_b	=	resistance of bearing quadrant coil
V_b	=	voltage applied across bearing quadrant coil
V_s	=	voltage of power supply
V_t	=	voltage across transistor

Appendix A

The rate of force change in a bearing can be determined in the following manner.The force in a bearing is given by the following equation as long as the reluctance of the core is small compared to the air gap.

$$F = \frac{A\mu_0(Ni_b)^2}{4g^2} \qquad (A1)$$

The partial derivative of bearing force with respect to current becomes;

$$\frac{\partial f}{\partial i_b} = \frac{A\mu_0 N^2 i_b}{2g^2} \qquad (A2)$$

The rate of current change in the bearing is determined by the voltage across the bearing coil and the inductance of the bearing.

$$\frac{di}{dt} = \frac{V_b}{L_b} \qquad (A3)$$

If the reluctance of the core material is again neglected, the inductance of the bearing is:

$$L_b = \frac{N^2\mu_0 A}{2g} \qquad (A4)$$

Combining equation (A3) with (A4) and mulptiplying by equation (A2) yields the bearing force rate change:

$$\frac{dF}{dt} = \frac{\partial F}{\partial i_b}\frac{di_b}{dt} = \frac{i_b V_b}{g}$$

2nd International Symposium on Magnetic Beaing
July 12-14, 1990, Tokyo, Japan

COST-EFFECTIVE IMPLEMENTATION OF ACTIVE MAGNETIC BEARINGS

D. ZLATNIK and A. TRAXLER

Institute for Robotics, ETH Zürich, CH-8092 Zurich, Switzerland.

Abstract

A low-cost implementation of an active magnetic bearing (AMB) is achieved, using cheap Hall-effect sensors instead of displacement sensors, centralized digital control and signal processing on a single microcomputer, a modular structure using commercial components and in some cases, eliminating the need for a thrust bearing. Together with cost effectiveness the performance and overall reliability due to simplicity, are kept. An AMB for a crystal growth process was successfully integrated with the constraint of a wide gap between rotor and stator.

1. Introduction

The active magnetic bearing (AMB) as an inherently unstable plant requires feedback control. Possible approaches are feeding back the measured rotor displacement, flux, current or voltage, to produce controlled electromagnetic forces, acting on the rotor [5].

In most of the existing implementations of AMB's, a separate displacement measurement system ist used, which is expensive relatively to the overall system cost, because of high-quality "clean" measurement which is not always necessary and may even reject useful information [1].

In certain applications as in crystal-growth described later, system and environmental constrains force the mechanical design to allow a free axial movement of the rotor for handling, i.e. no axial bearing, and a wide gap between rotor and stator. An earlier work [2] describes an electro-permanent magnetic bearing for a similar application. In that approach, permanent magnets supply a passive axial stiffness, so an extra active axial bearing is also eliminated. The limitation of this approach is that the rotor axial degree of freedom is not controlled and not actively damped.

In this work we describe an AMB system for controlling the rotor's five degrees of freedom, using only radial AMB's and very cheap Hall-effect sensors for rotor position control. Following a brief description of the system concept, the mechanical construction, the displacement measurement and the control are described with simplified formulations. Finally an implementation of the AMB for a crystal growth process is presented.

2. System concept

An industrial or commercial product should be designed to be *functional, reliable, low-cost* and *adaptable within its environment.*

Reliability is based on simplicity and in AMB it is mainly achieved by use of reliable power-amplifiers and converting measurement signal processing and control realized in complex analog electronics, into software algorithms. A microcomputer, centralizing control and system operation, enables an on-line monitoring and diagnostics to predict or detect failure and apply emergency procedures.

Adaptation within the environment regards mainly to functionality inside a large-scale plant of identical units and noise problematics due to high current switching (fig. 1). A large-scale plant requires compatibility with the communication network for operational commands and monitoring done by the plant supervisor. Noise is reduced, using shielding and grounding to be effective in protecting both the system and the environment.

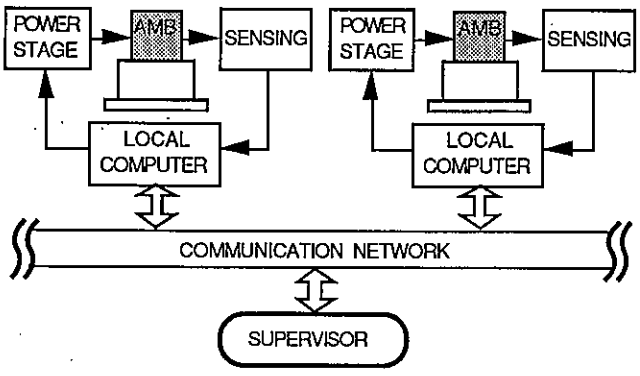

Fig. 1: *Large scale system*

The system operates in discrete "stable" states like STOP, FLOAT, ROTATE, CALIBRATE, DIAGNOSE. For example, ROTATE can be performed only if FLOAT is succesfull. Each of the states can be reached via the supervisor, through the communication network upon request or through an emergency procedure.

3. Mechanical setup of the AMB system.

The mechanical layout uf the AMB system includes two radial AMBs, **A** and **B** as described in fig. 2. Each bearing includes four electro-magnets. The rotor is held vertically by these bearings which apply both, radial and axial force components. The two bearings control five degrees of freedom of the rotor The rotation about the **Z** axis is controlled by a motor drive..

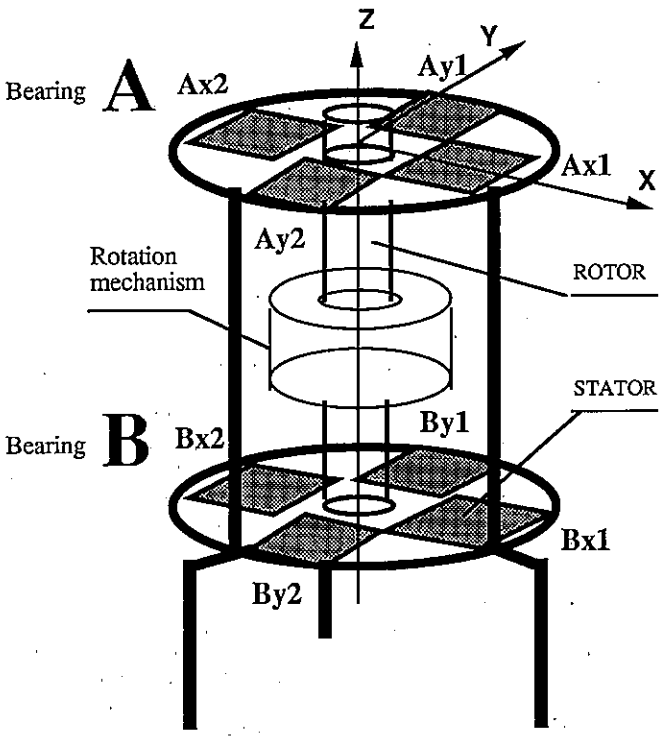

Fig. 2: *Mechanical setup of AMB System*

The cross-section of one electromagnet-pair is shown in fig. 3. The magnets are driven by the currents i_1 and i_2 and produce a magnetic flux in the U-shaped core. The flux-path is closed by an iron core attached to the rotor. The force, generated by the magnets can be separated into a radial and an axial component.

The currents through the coils of the magnets are generated by power amplifiers. The current in each coil is combined of two components, i_v, premagnetization current, also generating the axial force component, and i_x, the control current to control the radial force.

Based on the configuration of fig. 3, the total airgap g(x,z) can be expressed as

$$g(x,z) \cong x_0 \pm x + \sqrt{(x_0 \pm x)^2 + (z_0 \pm z)^2} \qquad (3.1)$$

where the sign of x regards to the left and right electromagnets, and the sign of z is general.

With the driving currents

$$i_1 = A_i\,(U_v + U_x) = i_v + i_x \qquad (3.2)$$

and

$$i_2 = A_i\,(U_v - U_x) = i_v - i_x \qquad (3.3)$$

the linearization in the working point $(i_x,i_v,x,z) = (0,i_{vo},0,0)$ leads to the force components

$$F_x \cong 2\left(K_i i_x + K_x x\right) + K_z z \qquad (3.4)$$

$$F_z \cong 2\left(F_0 + K_i i_v - K_z z\right) \qquad (3.5)$$

where F_x can be controlled with the control current i_x and the axial force F_z has to be controlled with the premagnetization current i_v which is therefore not constant as usual in AMB's. The constants K_i, K_x and K_z depends on i_{vo}.

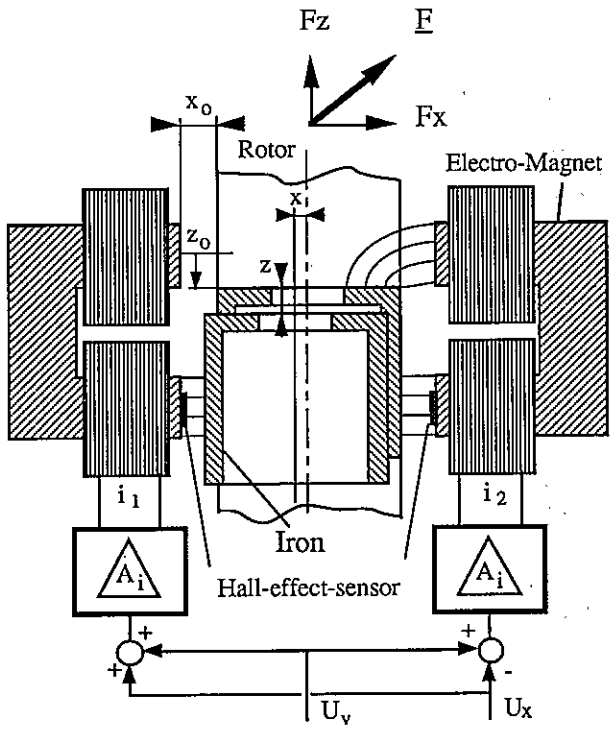

Fig. 3: *AMB pair cross-section and current drive*

In general, a complete layout includes two AMB's, controlling five degrees of freedom of the rotor. Depending on the application, the rotor can be mounted vertically or horizontally as shown in fig. 4. In the horizontal setup, the rotor cores are mounted to produce opposite controlled axial forces and in the vertical setup, they produce summed controlled axial forces, carrying the rotor weight.

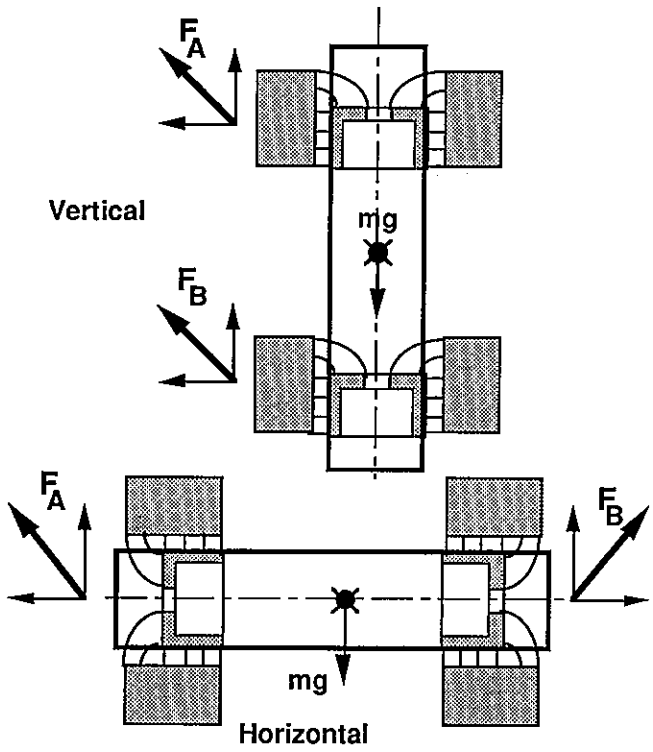

Fig. 4: *Vertical and horizontal constructions.*

4. Displacement measurement using Hall-effect sensors

The measurement of rotor displacement in an AMB is used in the closed-loop control to stabilize the rotor and to achieve the required stiffness. The displacement can be measured directly by using any kind of commercial gauge based on inductance, capacitance or optics. These gauges achieve good performance for small ranges and gaps. They occupy relatively large space and require dedicated electronics which increase the cost.

We here describe an alternative possibility, using Hall-effect sensors. They actually measure the flux density, which depends on the rotor displacement and the ampere-turns in the magnet coils. They show sufficient sensitivity for measurements on magnetic bearings with a large gap and a small displacement-range. By combining a differential scheme with two sensors, it is possible to measure both axial and radial displacements.

On the design of the sensor layout and the signal conditioning we achieve the following:

- High sensitivity of the sensor output relative to the measured displacement.
- Low sensitivity of the sensor output relative to the coupled variables, i.e. the current in the stator coils and sensor positioning.
- Decoupled measurements of the displacements in the axial and radial directions.

The principle scheme in fig. 3 shows two Hall-effect sensors which are placed on each lower pole of the electro-magnets where the measurement sensitivity to rotor movements is high and where stray effects are lower than on the upper poles. In fact the measurement of the flux density $\boldsymbol{B}$, at the lower pole, is not sensitive to the position of the sensor on the pole.

The output of the two Hall-effect sensors is sensitive to both axial and radial rotor displacements and is not sensitive to the rotation of the rotor.

Driving a hall-effect-sensor with a constant current i_h and placing the sensor in a magnetic field $\boldsymbol{B}$, the output voltage V_h generated by a Hall-effect sensor is proportional to the product of the flux density $\boldsymbol{B}$ and the current i_h.

In the magnets, the relation between ampere turns Θ and magnetic field strength H is given by the equation

$$\Theta = i\,n = \int_s \vec{H}\,ds = H_{fe} L_{fe} + H_g g_{(x,z)} \qquad (4.1)$$

where L_{fe} ist the length of the flux path in the iron and g is the length of the flux path in the airgap. The same relation expressed by the flux density $\boldsymbol{B}$ is

$$\Theta = i\,n = \frac{B}{\mu_o}\left(\frac{L_{fe}}{\mu_r} + g(x,z)\right) \qquad (4.2)$$

Since the relative permability of the iron is $\mu_r >> 1$, equation (4.2) can be simplified by the approximation

$$\Theta = i\,n = \frac{B}{\mu_o} g(x,z) \qquad (4.3)$$

Using (4.3) to express the flux density $\boldsymbol{B}$ for each side of the rotor leads to the equations

$$B_1 = n\,\mu_o\left(\frac{i_1}{g(+x,\pm z)}\right),\quad B_2 = n\,\mu_o\left(\frac{i_2}{g(-x,\pm z)}\right) \qquad (4.4)$$

Measuring B_1 and B_2 with the hall sensors we get the signals U_{h1} and U_{h2}. We replace B_1 and B_2 in (4.4) by the measured signals and we build the sum and the difference of these signals. Linearization of this relation in the working point $(i_x, i_v, x, z) = (0, i_{v0}, 0, 0)$ leads to the expressions for the displacement in radial and axial direction:

$$\hat{x} = C_x i_x + C_R\left(U_{h1} - U_{h2}\right) \qquad (4.5)$$

$$\hat{z} = C_v i_v + C_A\left(U_{h1} + U_{h2}\right) + C_0 \qquad (4.6)$$

where the coefficients C depends on the working point. The radial displacement signal mainly depends on the difference of the Hall-sensor signals and the axial displacement signal depends on the sum.

The design of an analog electronics circuit or a software signal processing to compute the equations (4.5) and (4.6) is relatively simple. Fig. 5 shows the block diagram of a

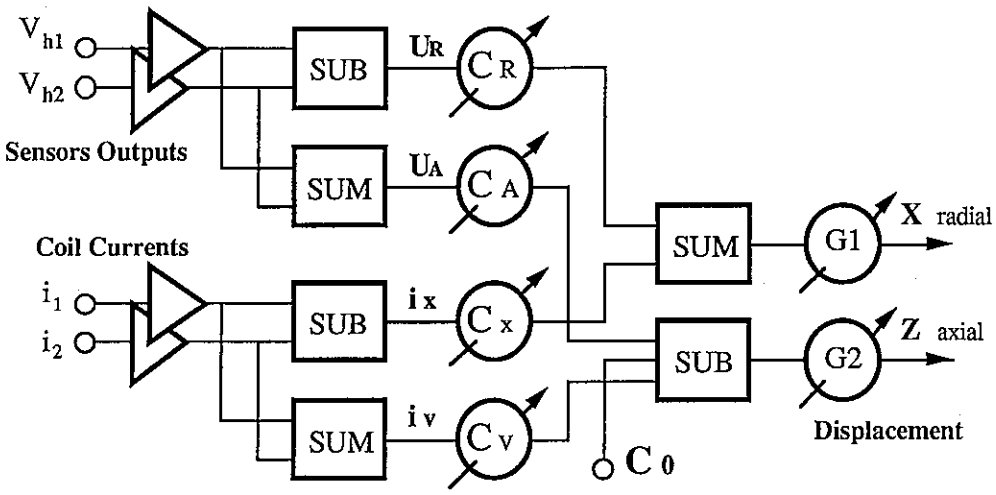

Fig. 5: *Sensors signal-conditioning*

realization which was built, using low cost operational amplifiers. The test results showed a high resolution and sufficient linearity. The cross-coupling between axial and radial displacements was approximately 5 %. A software realization even simplifies the tuning procedure of the coefficients.

5. Dynamic model and control concept.

Fig. 6 shows the functional blocks and the signal flow.of the closed-loop system, based on the flux density measurement. It can be seen that observing the rotor position is possible due to the mutual interaction of ***current, flux*** and ***position*** in the plant.

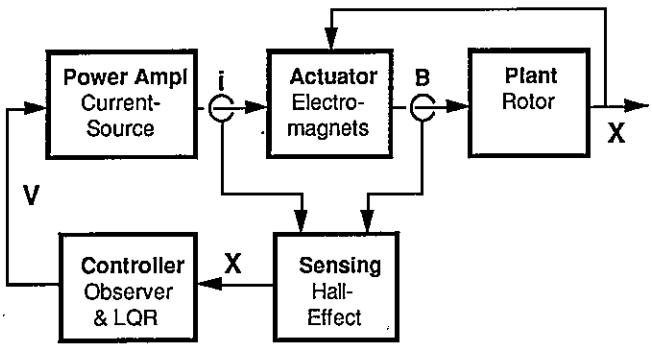

Fig. 6: *Principle control scheme*

For the dynamic model of the rotor, the coordinate system was defined as shown in fig. 7. The floating rotor as a free rigid-body has six degrees of freedom; three rotations (α,β,γ), and three translations (x,y,z). f_a and f_b are the forces of the two AMB's. The equations of motion have the well known form

$$M\ddot{\bar{s}} + P\dot{\bar{s}} + Q\bar{s} = N\bar{f} + V\bar{I} \qquad (5.1)$$

with $\bar{s} = (\alpha,x,\beta,y,\gamma,z)^T$

where M, P and Q are the coefficients of the autonomous rotor. **f** and **I** are vectors of the bearing and the load forces and moments.

Neglecting moments about the rotor axis Z_R, the forces acting on the rotor are the bearing controlled forces f_a and f_b and the rotor weight mg. Each of the bearing forces can be separated into radial and axial components. The axial components are used to compensate the rotor weight and to control the axial position of the rotor. The radial components are used to control the radial position of the rotor.

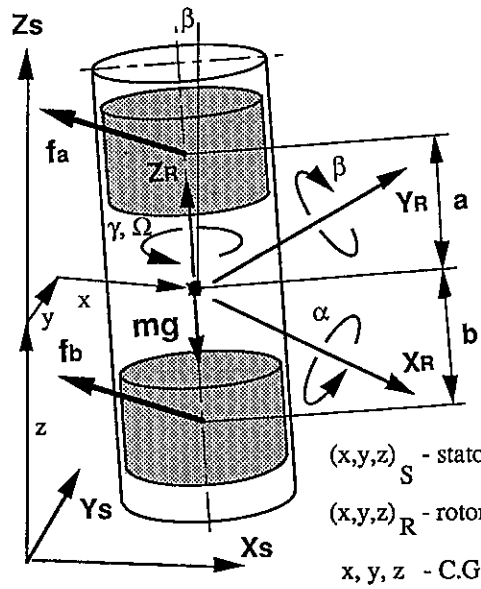

$(x,y,z)_S$ - stator coordinates.

$(x,y,z)_R$ - rotor coordinates.

x, y, z - C.G. transl. move.

Xa,Xb - measured position.

Fig. 7: *Rotor coordinates system*

The linear state-space model of the plant is developed, based on the model in [3]. Since radial and axial forces are decoupled, the model can be developed separately for the axial and radial directions.

In the radial direction for example, neglecting rotational harmonics, the dynamic model can be expressed with the state equations

$$\dot{\bar{x}} = \mathbf{A}\,\bar{x} + \mathbf{B}\,\bar{u} \qquad (5.5)$$

$$\bar{y} = \mathbf{C}\,\bar{x} \qquad (5.6)$$

With the state vector

$$\bar{x} = \left(x_a\ x_b\ y_a\ y_b\ \dot{x}_a\ \dot{x}_b\ \dot{y}_a\ \dot{y}_b\right)^T \qquad (5.7)$$

and the control vector

$$\bar{u} = \left(i_{xa}\ i_{xb}\ i_{ya}\ i_{yb}\right)^T \qquad (5.8)$$

With the dynamic model, the feedback controller can be designed to achieve the required performance, defined by the specifications. Since the observed variables are the rotor position, any of the existing and classical approaches can be adapted. One of these is based on the linear quadratic optimal regulator LQR, supplied with the full state, partly generated by a reduced order observer for the rotor position derivatives. Existing software packages can easily generate the observer and controller parameters based on the given model, and perform time simulation.

6. Computer Hardware and Software

A single board computer, based on a general purpose processor like Motorola MC680xx or based on a digital signal processor (DSP), is used. The processor is supported by input/output peripherals like D/A converters, A/D converters, parallel-port, communication device and timer. The structure of the computer system is shown in fig. 8.

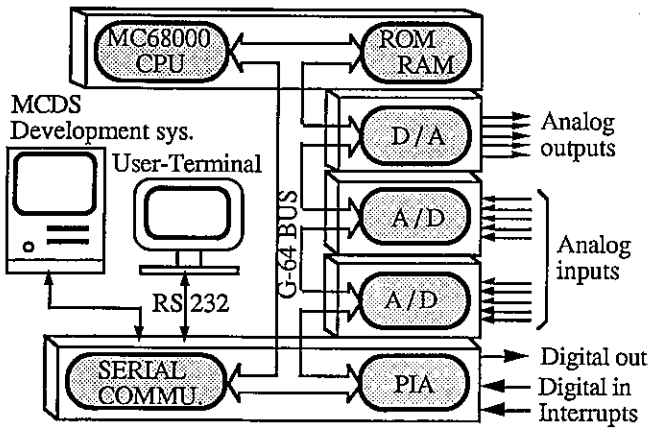

Fig. 8: *Structure of the omputer system*

The software is written in an high level language (Modula-2, C-language, etc.) on a personal computer using an appropriate development system. It is recommended to program the control equation in assembler to get a time optimale code and therefore a fast sampling rate. The object code is compiled and then down-loaded into the target system for execution.

The software is related to the hierarchy shown in fig. 9. Necessary procedures are imported to higher levels, from the low levels. The module '**Address**' holds the control-words locations of the complete hardware like: Timer, Serial-ports, A/D and D/A. modules.

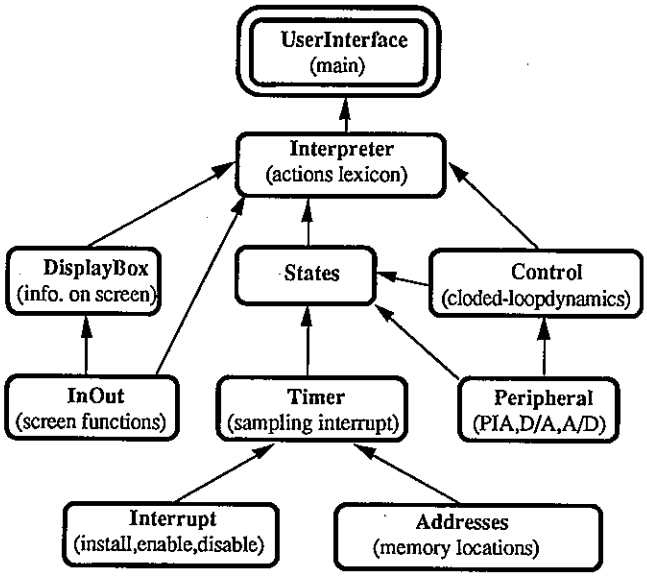

Fig. 9: *Software modules*

The modules '**Interrupt**', '**Timer**' and '**Peripheral**' are used to interact with the hardware, using a simple command format. The module '**Interrupt**' includes procedures to install, enable and disable interrupts. The module '**Timer**' includes procedures to start the timer with an externally defined time base and to stopp the timer. The timer interrupts the control process and defines the sampling rate.

The module '**Peripheral**' includes procedures which allow the use of analog and digital input/output ports with simple, single commands. E.g. this includes the control of each bit in the two eight bit parallel ports and each channel in the two A/D converters and in the D/A converter.

The module '**Control**' includes procedures to sample the rotor position signals, to transmit the current contol signals and to compute the closed-loop control algorithm, using imported procedures from the hardware level.

The module '**States**' contains procedures which select the requested system states mentioned in chapter 2.

The module **'Interpreter'** translates the user commands and executes them using procedures to read data from the terminal and display data on the screen. Tis procedures are imported from **'InOut'** and **'DisplayBox'**. The module **'UserInterface'** interacts with the user through a normal text terminal.

6. Implementation example: An AMB for a crystal-growth process.

The AMB system with the Hall-effect sensors ist suitable to support the rotor of a crystal-growth system. Fig. 10 shows a layout of the crystal-growth system. The crystal, fixed at the lower end of the rotor has to be pulled out of the melted metal or silicone. While pulling the crystal, the rotor has to be turned slowly to ensure a regular growth of the crystal.

The AMB suspension is carried vertically by an electro-mechanical actuator. The rotor is isolated inside a quartz tube, positioned and controlled in both axial and radial directions under special environmental conditions such as highly corrosive atmosphere and high temperature. For this kind of application which needs a very big airgap between rotor and magnets, the AMB with the hall-effect sensors are suitable

The important properties of this magnetic-bearing are a sufficient stiffness with a relatively large gap between rotor and stator, no separate axial bearing and a relatively low-cost realization.

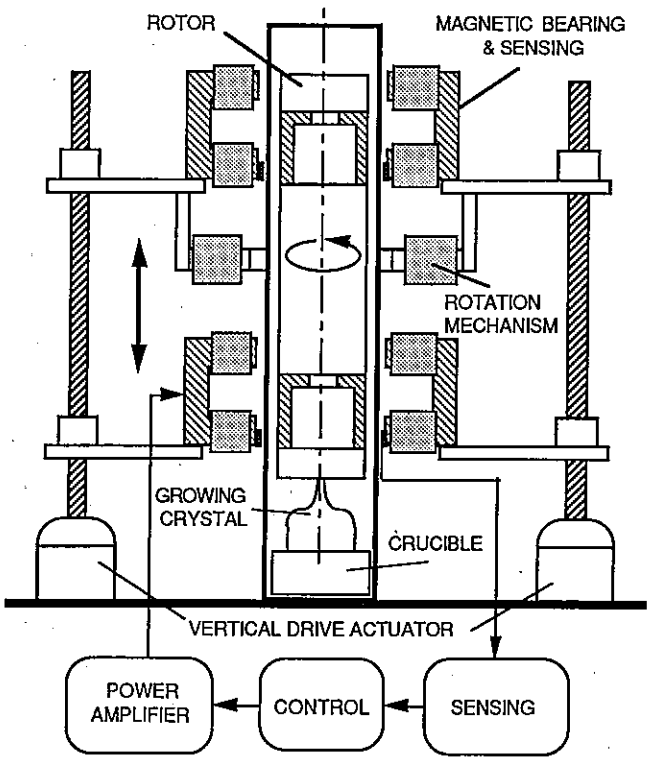

Fig. 10: *Construction layout of a crystal-growth system.*

The laboratory set-up which was designed, built and tested at the Institute for Robotics at ETH Zurich is shown in fig. 11. The system was realized, based on the preceding chapters. It performs satisfactory. Since in this application the rotation speed is very low, the velocity dependent coefficients of the plant model (in (5.5)) are neglected and the controller is decentralized, i.e. similar for all four radial directions.

The important characteristics are:

Mechanical:	Rotor dimensions:	Ø 80 x 600 L mm.
		Rotor weight: 3.5 Kg.
		Radial Gap: 17 mm.
Electrical:	Modular Switching Power Amplifiers 150 V x 15 A peak.	
Measurement:	Hall-sensors:	KSY 10 (Siemens)
	Signal conditioning:	Analog electronics.
Control:	Local LQR control with reduced order observer. Sampling frequency: 350 Hz.	
	Hardware:	MC 68000,Single-Board Computer
	Software:	Modula-2

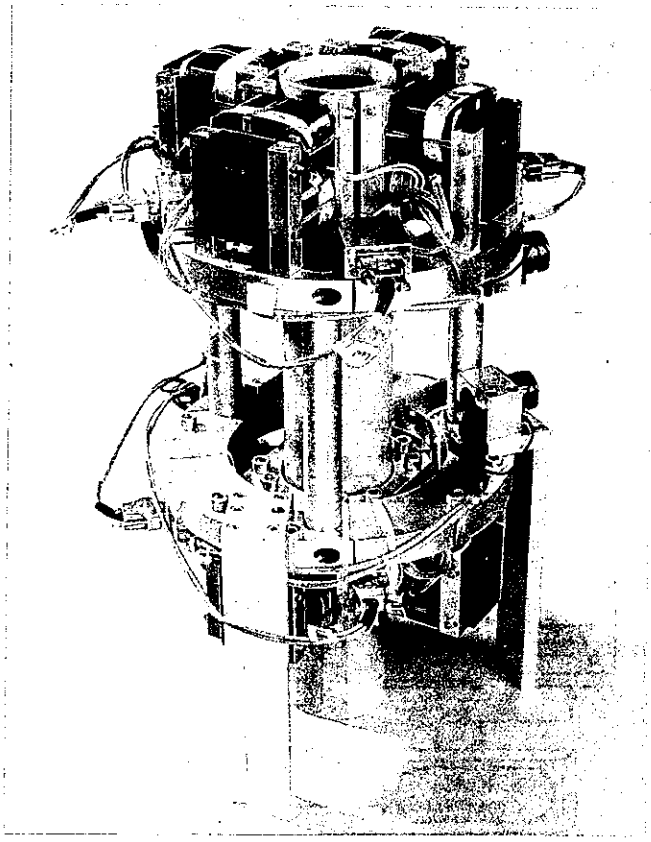

Fig. 11: *Laboratory set-up for AMB for the crystal-growth system.*

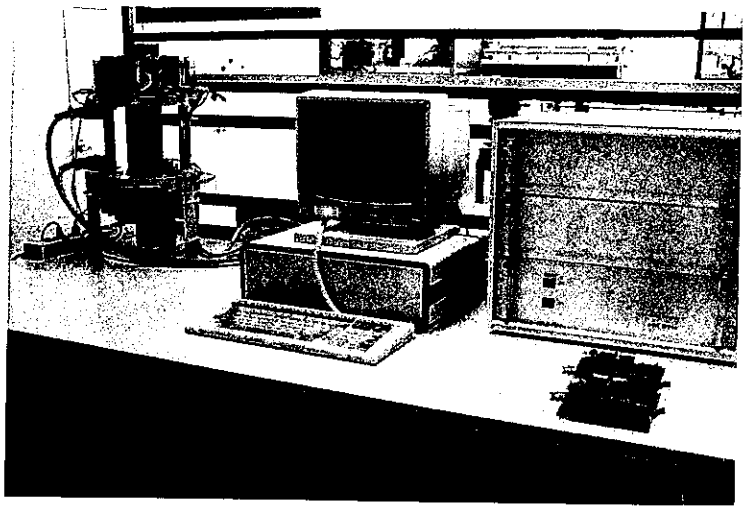

Fig. 12: *Laboratory set-up for AMB for the crystal-growth system.(Magnetic bearings,computer system and power amplifiers)*

7. Conclusions

A new way of using Hall-sensors to measure the rotor displacement in Active Magnetic Bearings was developed and tested. This measurement system shows good performance especially with a wide airgap It is simple and can be implemented at extremely low-costs.

A special setup of rotor and stator allows positioning and control of the rotor in both axial and radial directions *without* a a separate axial bearing.

A modular architecture of the computer system together with modular software and modular power amplifiers enables a straight forward and short time integration.

A laboratory setup of AMB for a crystal growth process was built and tested with satisfactory performance.

References:

[1] Schweitzer, G., H. Bleuler, A. Traxler, D. Vischer, D. Zlatnik: New Concepts for Low-Cost Mechatronics; Magnetic Bearing Example. Second IFAC Symposium on Low-Cost Automation, Milano, November 1989.

[2] Boden, K.: Wide-Gap, Electro-Permanent Magnetic Bearing System with Radial Transmission of Radial and Axial Forces. Proc. of the first Int. Symposium on Magnetic Bearings ETH Zurich, June 1988, Springer Verlag., 1989.

[3] Bleuler, H.: Decentralized control of a Magnetic Rotor Bearing System. Diss. ETH Nr. 7573, Zürich 1984.

[4] Traxler A.: Eigenschaften und Auslegung von berührungsfreien elektromagnetischen Lagern. Diss. ETH Nr. 7851, Zürich, 1985.

[5] Vischer, D.: Sensorlose und spannungsgesteuerte Magnetlager, Diss. ETH Nr. 8665, Zürich, 1988.

2nd International Symposium on Magnetic Beaing
July 12-14, 1990, Tokyo, Japan

IRON LOSSES AND WINDY LOSSES OF HIGH ROTATIONAL SPEED ROTOR SUSPENDED BY MAGNETIC BEARINGS

H. UEYAMA AND Y. FUJIMOTO
ELECTORONICS DEPARTMENT, R&D CENTER, KOYO SEIKO CO.,LTD.

Abstract

The power losses of a rotor suspended by magnetic bearings are lower than that by conventional ball bearings, slide bearings and so on. This merit comes from no mechanical contact which is unique characteristic of magnetic bearings. The power losses of magnetic bearings consist of iron losses (the sum total of eddy current losses and hysterisis losses) and windy losses (due to the friction between the rotor surface and the air). In the high rotational speed region, the power losses tend to increase and must be considered when we design the rotor system. We can easily estimate the sum total of power losses by the free deceleration characteristics of the rotor and separate between iron losses and windy ones by the comparison between the results in the vacuum and in the air.

In this paper, we try to derive the equation of iron losses based on the results of deceleration experiment for some softferromagnetic materials (2 different thickness of silicon steel, amorphous alloy and so on) and for several steady state currents in the vacuum (1×10^{-3} torr). As to windy losses, on the other hand, we try to compare the experimental results with the theoretical ones from the view point of hydrodynamics.

1. Introduction

Recently, magnetic bearing systems are under investigation about applications for industrial machines, i. e., internal grinding spindle, milling spindle, etc. These small, high rotating rotors must be designed to have large diameters and short length to set its 1st resonant bending mode frequencies high enough to nominal rotational speeds. But some problems written below will follow.

1) Burst or destruction of the parts; motor rotor, armature of magnetic bearings.
2) Shortage of output power of motor reduced by rotational power losses.

To overcome these problems,

A) Spinning burst test of the parts made of especially soft ferromagnetic materials.
B) Development of excellent performance motor; high peripheral speed, high power.
C) Grasp of the power losses in the state of highspeed rotation of magnetically suspended rotor and feed back to rotor design.

are necessary.

In this paper, dealing with term C), characteristics of iron losses of several ferromagnetic materials and of windy losses of several rotors are reported.

2. Experimental equipment

Each spindle we experimented is suspended by 5-axis active controlled, D.C.-type magnetic bearings. The experimental equipment (Fig. 1) and pole arrangement of radial magnetic bearings (Fig.2) are shown. In these experiments, the spindles are set perpendicularly only.

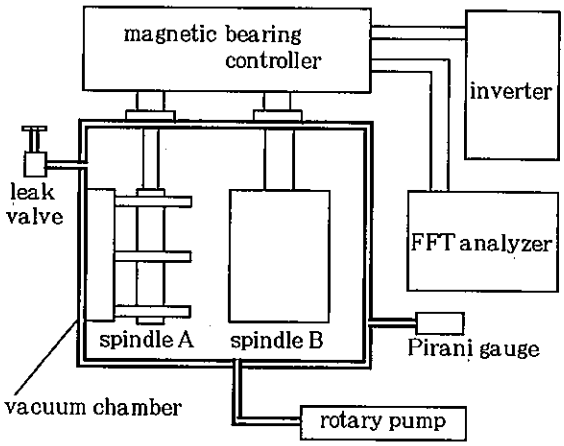

Fig. 1 experimental equipment

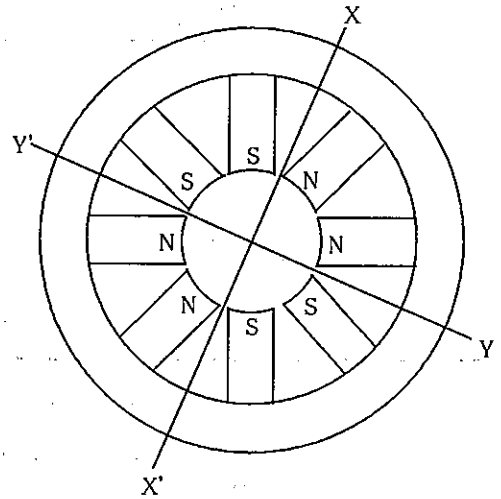

Fig. 2 pole arrangement of radial magnetic bearings

The values of rotational losses are calculated from the characteristics of free deceleration of rotor by the following manner.

Accelerating the rotor to nominal rotational speed by highfrequency induction motor built in the spindle, we cut off the input power of the motor, and the rotational speed is measured by FFT by means of processing the signal of displacement sensor that the magnetic bearings itself have, while the rotor is decelerating without any load. The power losses are obtained by the following equation.

$$W_{(N)} = 1/\Delta T/2 \cdot Iz \cdot (N1^2 - N2^2) \cdot (\pi/30)^2 \quad \text{——(1)}$$

N : rotational speed $N(rpm) = (N1 + N2)/2$
ΔT : deceleration interval of N1 to N2
Iz : polar inertial moment of rotor around rotational axis

When the iron losses W_I for several Io (steady state currents) of radial magnetic bearings are measured, the pressure in the chamber is reduced below 1×10^{-3} torr by rotary pump to be uneffected by hydraulic friction. So the windy losses $W_{W(N)}$ can be estimated by the next equation.

$$W_{W(N)} = W_{(N,Io)} - W_{I(N,Io)} \quad \text{——————} \quad (2)$$

Although W_I was measured for several steady state currents of axial magnetic bearing, any dependence on the currents was not found in the deceleration characteristics. So the iron loss of axial magnetic bearing is recongnized little enough to be ignored.

3. Materials for rotor armature of magnetic bearings

Table.1 shows the materials of rotor armature of radial magnetic bearings experimented for W_I and their characteristics.

Table.2

No.	material	thickness (mm)	tensile strength (kg/mm^2)	resistance ($\mu\Omega$-cm)	insulator
1	silicon steel	0.35	53	49	inorganic
2	↑	0.10	49	52	↑
3	amorphous (Fe)	0.03	>200	130	——
4	maraging steel	0.05	185	52	oxide

Amorphous alloy is ordinarily used for core of high frequency transformer after magnetic annealing. This heat treatment will better its magnetic characteristics, especially permability. But its mechanical characteristics, especially toughness, will be impaired. It is not practical for shrink fitting to use annealled amorphous alloy. So the rotor of amorphous alloy was used and laminated without the heat treatment and insulation too.

On the other hand, maraging steel has high tensile strength and toughness and is used for the rotor of centrifuge. It is easy to suppose that this material brings about huge hysterisis losses, because it is half hard feromagnetic material. To obtain higher rotational performance, this test was attempted.

4. Rotors

All of the rotors experimented are 3 types with the same rotor diameter at radial magnetic bearings. The shapes of the rotors and combinations with armature materials are shown in Table.2.

Table.2

No.	shapes	material	Iz	housing
A	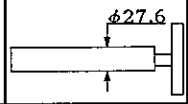	1	1127 ($gr\text{-}cm^2$)	block type
B	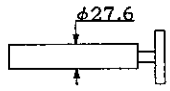	1 2	888 ($gr\text{-}cm^2$)	enclosed type
C	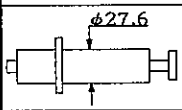	1 2 3 4	625 ($gr\text{-}cm^2$)	enclosed type

5. Iron losses

Iron losses (W_I) can be measured directly by the deceleration characteristic in the vacuum. The experimental results of W_I are shown in Fig.3 – 6.

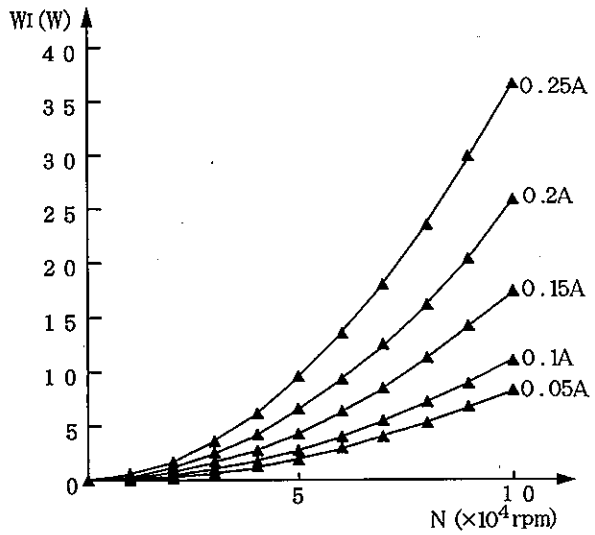

Fig.3 W_I of Silicon steel (t=0.35)

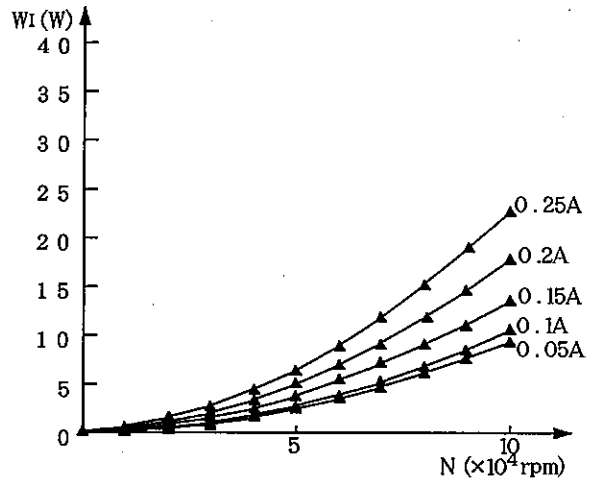

Fig. 4 WI of Silicon steel (t = 0.1)

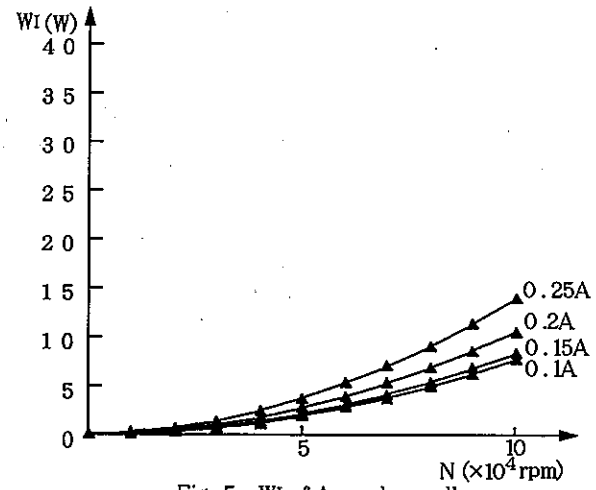

Fig. 5 WI of Amorphous alloy

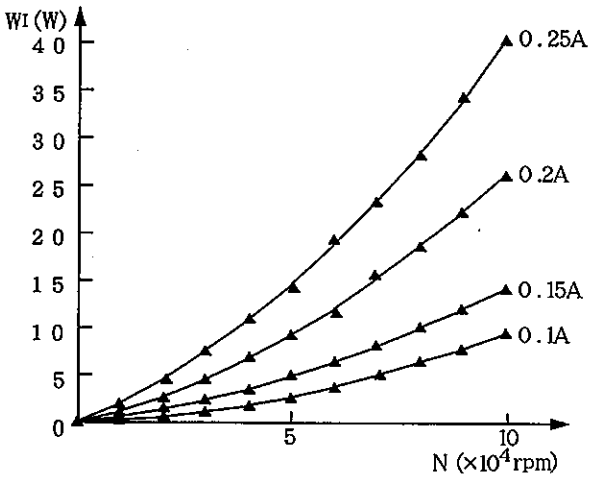

Fig. 6 WI of Maraging steel

Generally speaking, iron losses can be given of the sum total of hysterisis losses (W_h) and eddy current losses(W_e). The former is in proportional to frequency (f), and the latter is in proportional to f^2. So we assume that W_I can be presented by the following equation.

$$W_I = W_h + W_e = H \cdot N + E \cdot N^2 \quad \text{——————————} \quad (3)$$

H : hysterisis coefficient
E : eddy current coefficient

The coefficient H and E, can be obtained for each steady state current Io from Fig.3–6 are drawn in Fig.7,8.

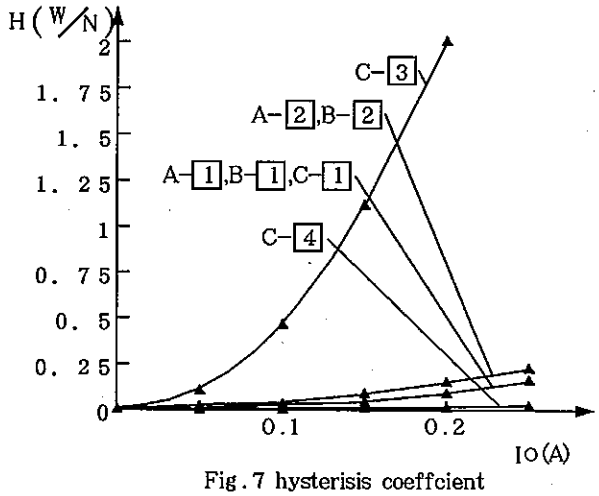

Fig. 7 hysterisis coeffcient

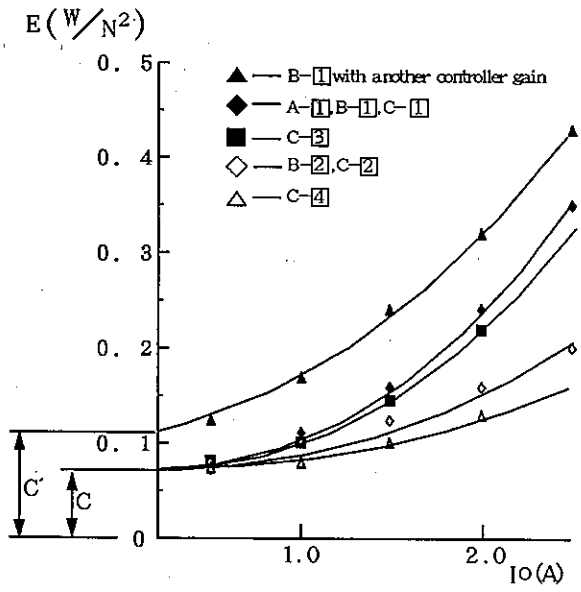

Fig. 8 eddy current coefficient

Judging from these diagrams, it can be said that H and E are in proportional to Io^2, however E includes offset term C. Synthesizing these results, the following experimental equation is obtained.

$$W_I = h \cdot Io^2 N + (e \cdot Io^2 + C) \cdot N^2 \quad \text{——————} \quad (4)$$

Table. 3 shows h and e for each material. Being expected before, the high value of h for [4] shows huge W_h. On the other hand, it is noticeable that h and e for [3] are about 1/3 for conventional [1].

Table. 3

material No.	$h(W/N \cdot A^2)$	$e(W/N^2 \cdot A^2)$
[1]	2.5	4.0
[2]	3.8	2.3
[3]	0.8	1.5
[4]	51.0	3.8

Offset C has a certain relation to control gain, because in case of higher control gain of radial bearings is set, offset C increase to C'. C maybe depend on control current ΔI. However, we can't recongnize such offset for H. The reason of it can be supposed that the control current ΔI for stabilizing the rotor has little effect on H, because it only increases the hysterisis of the minor loop. But ΔI usually includes higher frequency components, so it may has much contribution on W_e.

By the way, the values of H and E for the case of A-[1] (A spindle and [1]- rotor), B-[1] and C-[1] are nearly equal unintentionally, also B-[2] and C-[2] too. It is quite natural for A and B, because they have same radial magnetic bearings. Examining into the reason, we found that the following relation happened to be formed for B spindle and C spindle.

$$L_A N_A^2 = L_B N_B^2 \fallingdotseq L_C N_C^2 \quad \text{——————} \quad (5)$$

L_I : total lamination width of radial magnetic bearings
N_I : number of winding turns for each radial magnet
I : shows Ispindle

Eq.(5) means that the steady state attractive force Fo of each spindle coincides, because...

$$F_O \propto S \cdot B_g^2 \propto (D_i \cdot L_i) N_i^2 \cdot I_O^2 \quad \text{——————} \quad (6)$$

S : attractive area
Di : diameter of radial magnetic bearings
B_g : magnetic flux density at the air gap

In short, for the same armature material, the coefficient H and E are in proportional to Fo.

hence

$$W_I = \overline{h} \cdot F_O \cdot N + (\overline{e} \cdot F_O + C) \cdot N^2 \quad \text{——————} \quad (7)$$

Furthermore,

$$W_I = \overline{h} \cdot \Sigma F \cdot N + (\overline{e} \cdot \Sigma F + C) \cdot N^2 \quad \text{——————} \quad (8)$$

here,

$$\Sigma F = \sum_j \sum_k F_{jk} \quad \text{——————} \quad (9)$$

$j = X, Y$
$k = 1, 1', 2, 2'$

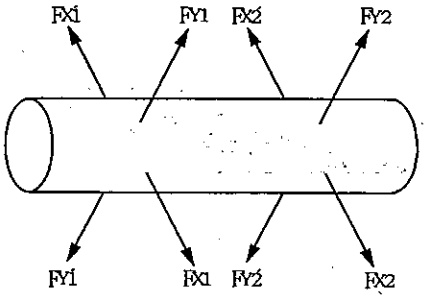

Fig. 9 configuration of magnetic forces

6. Windy losses

Windy losses can be estimated by subtracting W_I from W; total rotational losses obtained from deceleration characteristics in the air.

$$W_W = W - W_I = W_{(Io)} - W_{I(Io)} \quad \text{——————} \quad (10)$$

The windy losses of B spindle for several Io are shown in Fig. 11. The values of windy losses, naturally independent of Io, coincide with each other, meaning that the measurement and the separation has enough precision.

Now, the rotational friction losses of cyliynder or disc in the infinite yessel can be described by useing Karman's coefficient of the resisting moment Cf.[3]

for cylinder

$$W_{W_1} = \pi \rho / g \times \omega^2 \times (D/2)^4 \times l \times C_{f1} \times 1.027 \times N \quad \text{——} \quad (11)$$

for disc

$$W_{W_2} = \rho / 2g \times \omega^2 \times (D/2)^5 \times C_{f2} \times 1.027 \times N \quad \text{——} \quad (12)$$

here

$$C_{f1} = \begin{cases} 1.728 \times Re_1^{-0.5} & \text{(for laminar flow)} \\ 0.072 \times Re_1^{-0.2} & \text{(for turbulent flow)} \end{cases}$$

$$C_{f2} = \begin{cases} 1.935 \times Re_2^{-0.5} & \text{(for laminar flow)} \\ 0.072 \times Re_2^{-0.2} & \text{(for turbulent flow)} \end{cases}$$

$Re_1 = 2\pi r_1^2 \omega / \nu$
; peripheral Reynolds number for cylinder
$Re_2 = r_2^2 \omega / \nu$
; peripheral Reynolds number for disc
r_1 ; radius of cylinder
r_2 ; radius of disc
$\nu = 1.501 \times 10^{-5} (m^2/s)$
; coefficient of kinetic viscosity of the air

ω ; angular velocity of cylinder or disc
$\rho = 1.2(kg/m^3)$; density of the air at 20°C
$g = 9.8(m/sec^2)$; gravitational acceleration
$N = \omega \cdot (30/\pi)$; rotational speed in rpm

Substituting the constants and coefficients into eq. (11), (12) and rearranging, the following equation for the total windy losses can be obtained.

$$Ww \fallingdotseq (4.43\times10^{-8}\times\Sigma D_1^3 l + 1.006\times10^{-8}\times\Sigma D_2^4) N^{2.5} \text{ (W)}$$
(for laminar flow) —— (13)

D1 ; diameter of cylinder (mm)
l ; length of cylinder (mm)
D2 ; diameter of disc (mm)
N ; rotational speed ($\times10^4$rpm)

The first term of eq. (13) describes Ww for the cylinder part of rotor, and the second term for the disc part.
Rec (critical Reynolds number) at which transition to turbulent flow occurs is about 5×10^5. For the region above Rec, eq. (13) must be changed into the following equation.

$$Ww \fallingdotseq (4.435\times10^{-8}\times\Sigma D_1^3 l + 1.006\times10^{-8}\times\Sigma D_2^4) N^{2.5}$$
(for laminar flow)
+
$$(7.89\times10^{-8}\times\Sigma D_1^{3.6} l + 8.849\times10^{-10}\times\Sigma D_2^{4.6}) N^{2.8}$$
(for turbulent flow)
—— (14)

Calculated results from eq. (13) and (14) are compared with the experimental ones in Fig.11. Eq. (13) is correct only in the region $N < 20000$ rpm. Eq. (14) is also correct in the region $N < 60000$ rpm.
Furthermore, considering the clearance between rotor and surrounding electro-magnets that have smooth inner surface molded by epoxy regin, not in the infinite vessel, the flow can be thought as Couette flow. [4]
With the assumption that Couette flow may occur, the coefficient of the resisting moment becomes

$$C_f = 0.00759\, R\omega^{-0.24}$$
$$= 0.00759\, (r_m \cdot \delta \cdot \omega/\nu)^{-0.24} \quad \text{—— (15)}$$

$r_m = (r_i + r_o)/2$
$\delta = (r_i - r_o)$; gap
r_i ; inner radius of electro-magnet
r_o ; outer radius of rotor

and

$$Ww \fallingdotseq (4.435\times10^{-8}\times\Sigma D_1^3 l + 1.006\times10^{-8}\times\Sigma D_2^4) N^{2.5}$$
(for laminar flow)
+
$$(7.89\times10^{-8}\times\Sigma D_1^{3.6} l + 8.849\times10^{-10}\times\Sigma D_2^{4.6}) N^{2.8}$$
(for turbulent flow)
+
$$1.2893\times10^{-9}\,\Sigma D_1^{3.76} l \cdot N^{2.76}$$
(for Couette flow at cylinder)
—— (16)

The estimated values by eq. (16) explain the experimental results very well.
In the case of A spindle, because the housing is separated block type, the windy losses tend to fit the turbulent flow, as shown in Fig.10.

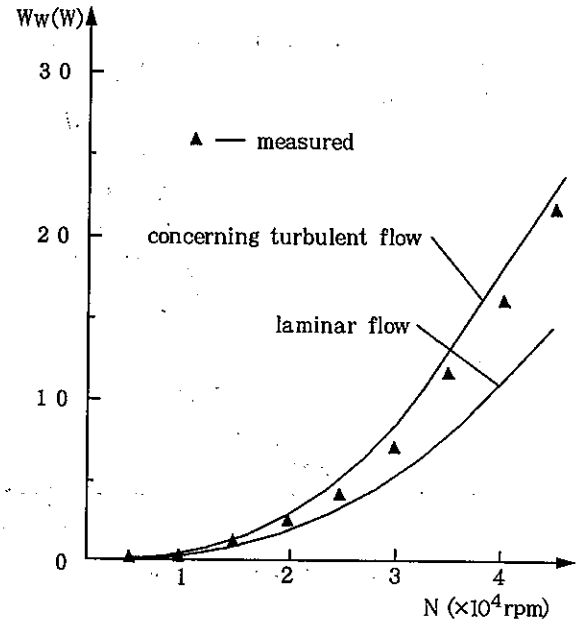

Fig. 10 Ww of spindle A

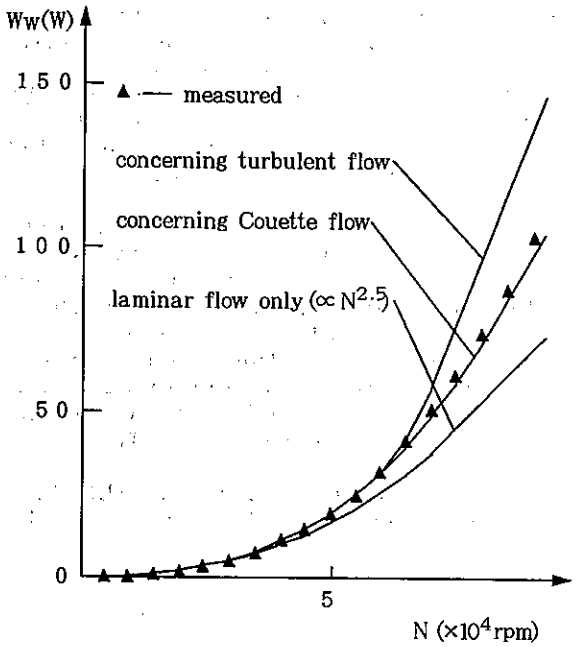

Fig. 11 Ww of spindle B

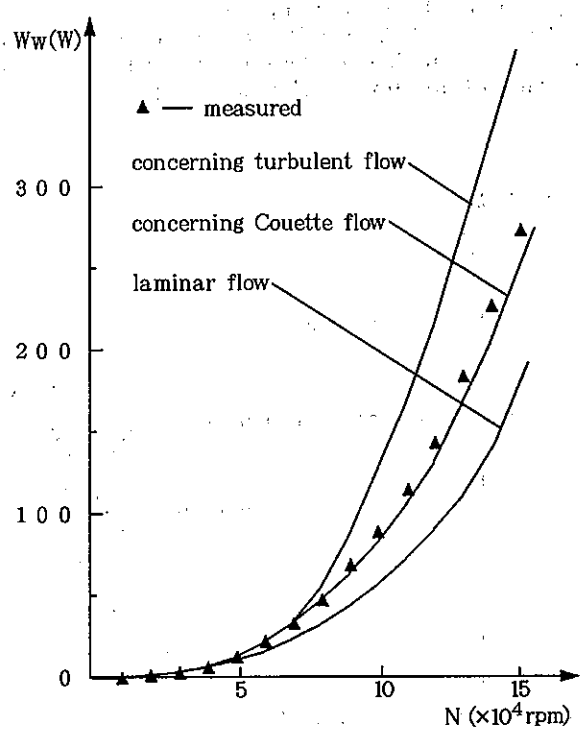

Fig. 12 Ww of spindle C

7. Summary

Following aspect about iron losses and windy losses of high rotational speed rotor suspended by magnetic bearings is obtained.

1. With the assumption of experimental eq. (3) about W_I, eq. (4) that has control-term C in the term being in proportional to N^2.
2. The values of coefficient h and e^2 that have relation to hysterisis losses and eddy current losses respectively, being included by eq. (4) are decided experimentally.

Furthermore,

3. Eq. (8), more genelarized form, is offered.
4. About windy losses, the comparison with theoretical value, from the view point of hydrodynamics, of laminar or turbulent flow and experimental value is achieved.
5. It is shown that, for the cylinder part of rotor having little clearance to housing, the experimental value is precisely explained with the assumption of Couette flow.

We express our thanks to AICHI STEEL CO,. LTD. for offering maraging steel and its technical supports.

References:

[1] T, HIGUCHI. et al : Experimental Estimation of Rotational Losses of Magnetic Bearings. Spring conference of Precision, P86 – 87, (1988)

[2] H, MATSUMURA. et al : Characteristics of Friction on Magnetic Bearings. T.IEE Japan, Vol.108D, No.5, P462–468, (1988)

[3] T.von.Karman : z.f.Angew.Math.u.Mech., Bd. 1, S.223 (1921)

[4] Y, YAMADA. et al. : Frictional Drag Active on the Inner Cylinder in Rotaing Cylinder when Outer Cylinder Rotates: Bulletin of Nagoya Institute of Technology, Vol. 19, P203 – 215, (1967)

2nd International Symposium on Magnetic Beaing
July 12-14, 1990, Tokyo, Japan

EXTREME PRECISION MAGNETIC BEARINGS FOR LINEAR AND ROTARY APPLICATIONS

David B. Eisenhaure*, James R. Downer*, Richard L. Hockney*, Bruce G. Johnson*,
Vijay Gondhalekar*, Michael Gerver*, Kathleen Misovec*, Monique Gaffney*, Alex Slocum**
*SatCon Technology Corporation, 12 Emily Street, Cambridge, MA 02176 USA
**Massachusetts Institute of Technology, Civil Engineering, Cambridge, MA 02139

Abstract

SatCon Technology Corporation is developing magnetic bearings and suspensions for a number of linear and rotary applications which require positioning accuracies considerably higher than those obtainable with passive mechanical bearings. These applications, which include instrument bearings, magneto-optical data storage, tunneling microscope slides, and machine tool spindles require positioning accuracies as high as 10^{-6} mm over a broad frequency range in the presence of environmental disturbances. Obtaining these levels of precision in active magnetic bearings requires new developments in sensor, actuator, and control subsystems. Substantial technology advances have occurred during the last decade that have an appreciable impact on the performance and feasibility of magnetic bearings for precise positioning applications. These advances in technology include improvements in sensors, magnetic materials, improved semiconductor power electronics, improved digital electronics, and better control system technology. This paper compares and contrasts the design approaches for major magnetic bearing subsystems in these applications that SatCon currently has under development. The achievable resolution is shown to be determined by position measurement accuracy, suspension gain, suspension bandwidth, internal component noise, and external disturbance force levels. Expected external disturbance force levels from ground motion, air currents, and acoustic effects are projected. Given the expected disturbance force levels, measurement accuracy, and required controller performance, magnetic suspensions and bearings can be developed which will provide positioning accuracies better than the 10^{-6} mm (ten Angstroms) required.

1. Introduction

In the sensor area precision positioning requires sensors with high precision, wide bandwidth, and low noise. Optical interferometric sensors currently provide accuracies approaching the 10^{-6} mm requirement and are expected to substantially exceed this figure in the near future. Precision inductive and capacitive sensors although not as precise as optical sensors, provide simple low-cost measurements which have sufficient precision for less demanding applications.

The need in the actuator area is for high specific-performance designs having wide bandwidth and good plant characteristics. In its various designs, SatCon is employing biased/-unbiased electromagnet, electrodynamic, and superconducting actuators. Superconducting actuators have the highest performance potential, widest bandwidth, and have good plant characteristics with minimal high frequency dynamics. Superconductors allow the construction of magnetic devices 10 or more times lighter than conventional magnetics, and the recent development of high temperature superconducting material holds much promise for the future. Advances have taken place in magnetic steels, amorphides, and permanent magnets, all of which contribute to improved electromagnet and electrodynamic actuators. In the magnetic steel area, materials such as vanadium permendur allow operating flux densities exceeding two Tesla. In the area of amorphides, materials such as Met-Glas allow high-frequency, low-loss operation. Permanent magnet materials such as samarium-cobalt and neodymium-iron have energy products approaching 40 MGOe and allow lightweight, high-efficiency magnetic designs.

In the control-system area, techniques to efficiently handle multi-input/multi-output, non-linear systems and time-varying systems with wide-bandwidth environmental disturbances are needed. SatCon's approaches for handling multi-input/output systems include linear-quadratic-Gaussian-control, loop-transfer-recovery, disturbance accommodating control, and model-reference-control techniques. In systems where non-linear effects are significant we have employed sliding-mode or variable structure, time-delay, and non-linear-quadratic-Gaussian-control methods. Adaptive control techniques such as self-tuning regulation are readily adapted to time-varying systems and those with uncertain parameters. SatCon has made particular advances in the application of sliding mode and disturbance accommodating control to precision magnetic bearings.

2. MIT/SatCon Magnetically Suspended Linear Slide

Current designs of precision machines such as wafer steppers and diamond turning machines are generally performance limited by mechanical contact between moving parts, misalignment between actuators and bearings, stability of air bearings, and/or attainable temperature control. An example of a system which uses magnetic suspensions to obtain extreme precision by eliminating or reducing many of these problems is the Atomic Resolution Measuring Machine being developed by SatCon and MIT. This system is depicted in Figure 1. The baseline slide has approximate envelope dimensions of 12 inches by 6 inches by 2 inches. This baseline slide would have a weight in Earth's gravity of ten pounds. In this paper the baseline ARMM will be used as a conceptual model to examine the issues associated with extreme precision magnetic bearing and suspension design. The analysis assumes that the slide dynamics are beyond the bandwidth of the magnetic bearing and will not be a factor in the suspension's performance.

The baseline magnetic suspension block diagram is shown in Figure 2. The principle of operation of a magnetic suspension system is quite simple: the position of the suspended slide is measured and the control system regulates the current to an electromagnet by a gain the slide at the desired location. A simple control system might be characterized by a gain (stiffness) which relates errors in position to applied magnetic force and a bandwidth which

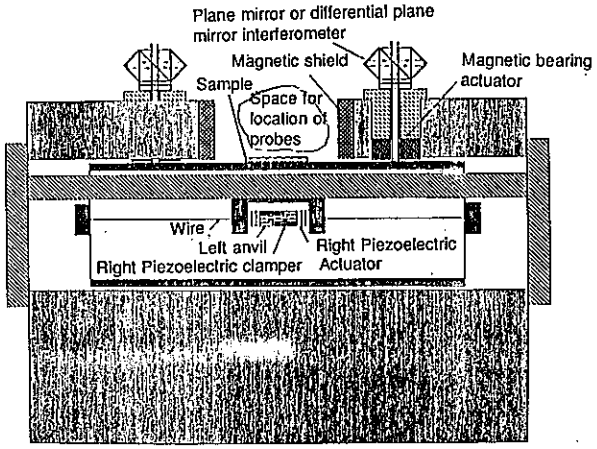

Figure 1. Cutaway side view of Atomic Resolution Measuring Machine (ARMM)

indicates the frequency range over which the magnetic force may be applied. In addition to gain and bandwidth, the control system would require electronic compensation for stable operation. Magnetic suspensions generally have unstable plant characteristics which lead to a minimum required system bandwidth for stability of about 10 Hz for many suspensions. Maximum achievable bandwidths could range from 100 Hz for a simple attractive system to 40 KHz or higher for systems implemented with ferrite or voice coil actuators. As with all position control servos, accuracy is determined by position measurement accuracy, controller gain, controller bandwidth, internal component noise. and external disturbance forces acting on the suspended slide. The remainder of this paper examines in detail the control system options together with the sensor and actuator characteristics required to achieve extremely high positioning precision.

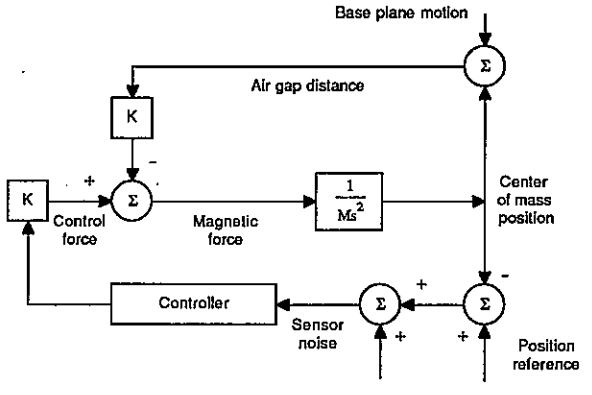

Figure 2. Basic Magnetic Suspension Block Diagram

3. Control System Developments

Satcon's efforts in the control area have been directed at developing both hardware and control algorithm solutions to the problem of precision motion control with electromagnetic actuators in the presence of environmental and internal disturbances. Over the past two years, significant advances have been made in applying nonlinear control algorithms to the nonlinear attraction force electromagnetic suspensions and using disturbance accommodating control theory to reduce vibrations in magnetic bearing systems. The use of these advanced control algorithms has been made possible by advances in digital signal processing hardware.

In many of our rotor systems, magnetic bearings have been chosen because of their capability to reduce vibration and noise. One advantage of magnetic bearings in reducing vibration, of course, is their non-contacting nature. Since they are actively controlled, the dynamics of the bearing can be tailored to both reduce transmitted vibrations and to attenuate vibrations of the machinery base. Like all actively controlled systems, however, actively controlled magnetic bearings can amplify sensor and electrical noise. As discussed below, these sensor noise effects can become the dominant noise source in precision applications where the environment is relatively quiet.

One of the most promising areas for increased performance by actively controlled magnetic bearings is reducing the synchronous vibrations produced by rotor mass unbalance. In magnetic bearing systems, these mass unbalance effects are seen as additive output disturbances in the feedback loop. The mass unbalance disturbance are seen primarily as a sinusoidal error at the synchronous frequency. At SatCon, we are developing controllers using Disturbance Accommodating Control (DAC) theory to reject these mass unbalance effects and allow the rotor to spin about its principal axis at all rotational speeds.

Disturbance accommodating control theory applies to systems with disturbances that have a waveform structure. Consequently, reducing the synchronous vibrations of rotating systems is a good application for DAC theory because the disturbances possess a waveform structure. As

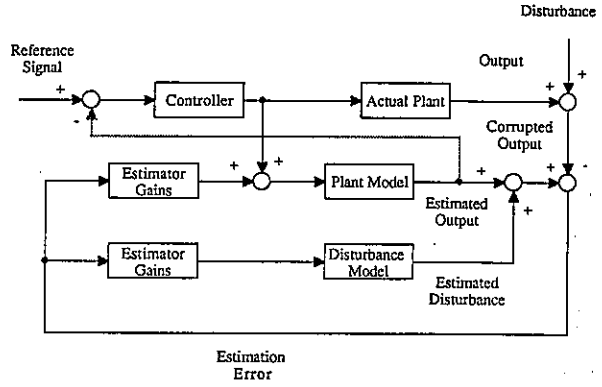

Figure 3. Disturbance Accommodating Control Block Diagram

can be seen in Figure 3, the DAC controller uses both a plant and disturbance model in the estimator, allowing accurate estimates of both the plant states and the disturbance. DAC theory is being used at SatCon to develop control/estimation schemes that enable the rotor to spin about its center of mass, in the presence of either synchronous magnetic unbalance disturbances or the measurement error (mass unbalance) disturbances. Our simulation results show excellent rejection of either disturbance at the synchronous frequency, thereby reducing the production of vibrations by the rotating system. We are currently constructing a 80 kg , 3600 rpm magnetically suspended rotor testbed that will use the DAC controller.

In the last two years, we have been investigating the use of various nonlinear control algorithms with the inherently nonlinear actuators that conventional attraction force electromagnetic bearings represent. These have included sliding mode or variable structure, time-delay, and nonlinear quadratic Gaussian methods. We have found that these nonlinear controllers have significant performance advantages over more conventional controllers at the cost of increased design, analysis, and implementation complexity.

We have implemented a sliding mode controller on a three-degree-of-freedom precision pointing and tracking testbed. This testbed uses attraction force electromagnet to slew a isolated mass through a desired trajectory. The control algorithm must provide the proper slew forces in the presence of experimentally controlled vibrations applied to the stators of the actuators. The goal is to minimize the tracking error in the presence of these vibrations.

As shown in Figure 4, the sliding mode controller uses measured gap information to invert the nonlinear force/current/gap relation of the actuators. Additional feedback loops guarantee stability in the presence of bounded disturbances and modelling error. This rather complicated block diagram illustrates the structure of the sliding mode controller. An actuator produces a control force which changes the inertial position of the tracking body (plant). Vibration disturbances can change the magnetic gap, which also changes the control force and thus there is a path between vibration disturbance and inertial position. The sliding mode controller has the potential to achiever better performance than the linear controller because it has a structure that directly compensates for this vibration path. More specifically, an estimation scheme produces estimated gaps and the controller uses a nonlinear model of the plant to counteract the effect of the vibration disturbance. The controller also uses estimated position and velocities to calculate control currents that are similar to a PD type of controller but are calculated to insure stability in the presence of the effect of bounded modelling uncertainty and disturbances. our research has shown that in order to achieve performance advantages over linear controllers, the sliding mode controller depends heavily on a good inertial measurement and estimation as well as highly accurate plant models.

Figure 5. shows the performance of this controller compared to more conventional linear controllers. We were interested in assessing the performance of the nonlinear sliding mode control approach to: a linear phase lead controller and a

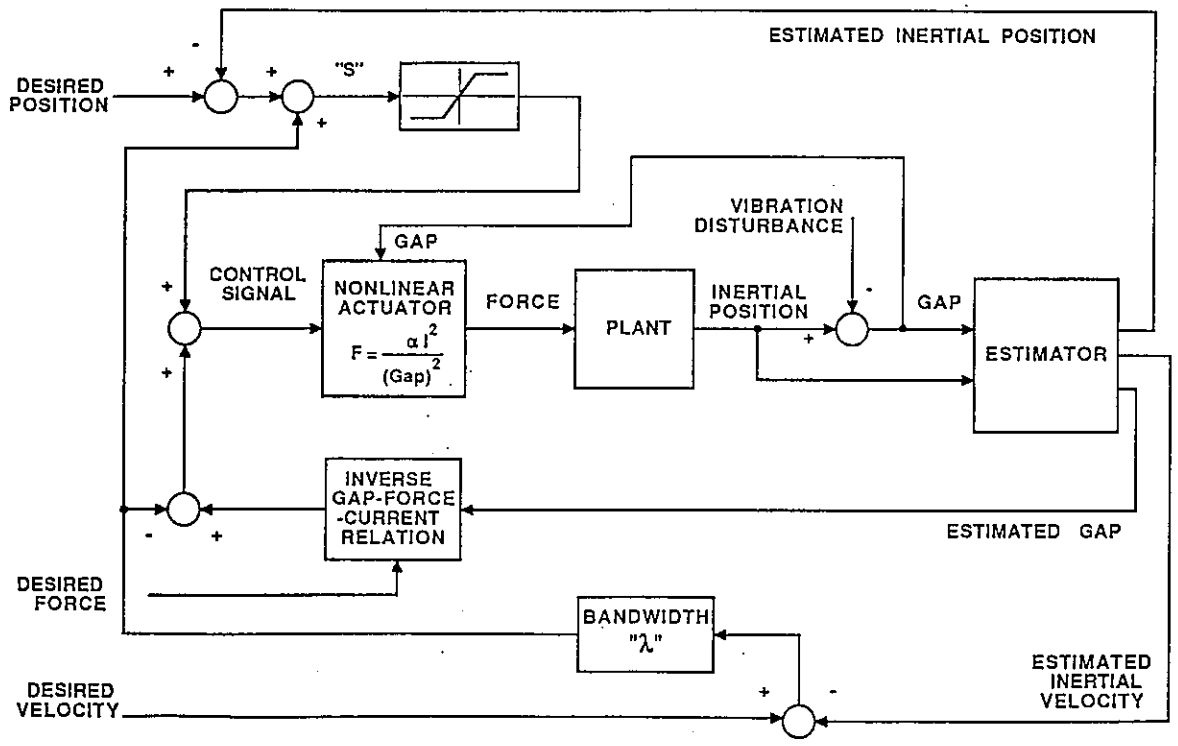

Figure 4. Sliding Mode Control Block Diagram

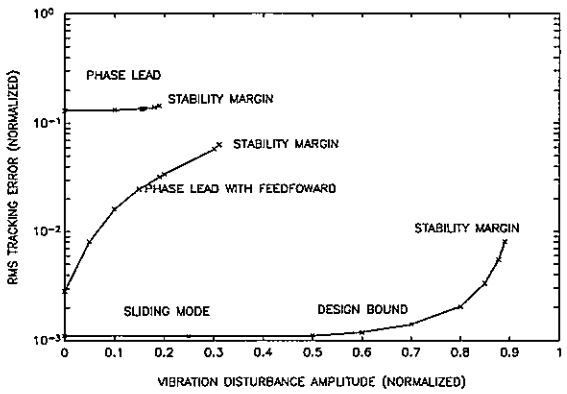

Figure 5. Sliding Mode Control Tracking Air vs Vibration Amplitude

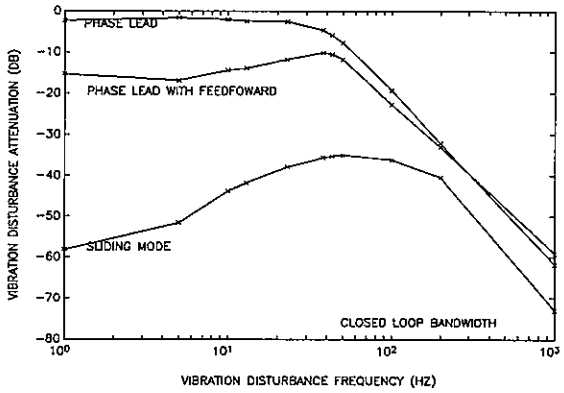

Figure 6. Sliding Mode Control Vibration Isolation vs Frequency

phase lead with a feedforward term. This plot is based on simulations of a tracking maneuver in the presence of a vibration disturbance for these three controllers. The performance measure of RMS tracking error is plotted, vs the vibration disturbance amplitude. The sliding mode controller achieves better tracking performance by at least an order of magnitude. The sliding mode controller also has higher stability margins than the more conventional control approaches. The stability margin is reached when the tracking error is high enough to cause the magnetic gaps to go to zero. The sliding mode controller in these simulations is designed for the maximum disturbance amplitude shown in the figure. An even higher stability margin could be obtained by increasing the design bound at the expense of higher tracking error.

Another performance measure to use to assess the potential of sliding mode control in comparison to more conventional linearized control approaches is vibration disturbance attenuation shown in figure 6.. This is a measure of how much disturbance energy is being transmitted to the tracking body. This plot shows vibration disturbance attenuation vs vibration disturbance frequency. The sliding mode controller achieves better disturbance attenuation that the phase lead or the phase lead with feedforward approaches. We were particularly interested in performance near the closed loop bandwidth. Better linear controllers can be designed for disturbances below the bandwidth, but all linear controllers have a limited attenuation capability when the disturbances are near the system bandwidth. This is due to fundamental physical considerations and the structure of the controller. For these simulations, analysis indicated this limiting performance value to be around -9 dB for the linearized approaches. The plot shows that this limitation is accurate for the linear controller and that the sliding mode controller, because of its different structure, is not limited to this performance value. It is achieving about -40 dB at disturbance frequencies near the closed loop bandwidth.

As mentioned earlier, the use of these advanced control algorithm is predicated on high performance, low cost digital signal processors. The advances made in digital signal processors and associated software development tools have gone a long way towards reducing the cost in real terms of implementing complex signal conditioning and digital control algorithms. When applied to the control of precision magnetic bearings where fairly complex algorithms are implemented, the number crunching capability per dollar delivered by the DSPs is very rewarding.

However there is an inherent limitation, at least currently at the low cost end, of the signal resolution delivered by interface electronics, principally the digital to analogue convertors. The expanding digital audio market has promoted low cost 16 bit convertors which give a resolution approaching 15 ppm. Moderate cost 20-22 bit convertors may be expected in the near future which will be adequate to deliver a 1 ppm signal resolution at the signal input end of the digital signal processor.

A very important advantage offered by digital signal processors is the ability to easily implementing error correction logic to the incoming measurement data stream from the A/D convertors. This of course relieves to a certain extent the burden and cost of designing linear and environmentally insensitive sensors. The extra computational effort for error correction itself is usually small, however the quality of correction depends on the error modelling and extra information, such as temperature, made available to the model. The influence on the cost of the "total" sensor system is more from the hardware associated with obtaining this extra information.

Floating point arithmetic DSPs and the available development tools have gone a long way towards elevating the programmers task by eliminating scaling as with integer math DSPs. However quantization noise generated by the finite precision imposed by the finite word length architecture can become a serious impediment when implementing signal processing or control algorithms requiring a large number of mathematical operations on the raw data. Specialized large word length machines which retain full precision of any arithmetic operation by using integer math and dynamically expanding the word length may become a necessity for an extreme precise implementation of control algorithms. However this type of machines are not likely to be available at the low cost end.

SatCon's implementation of the sliding mode control algorithm mentioned above is based on a integer math DSP utilizing 12 bit signal inputs an a 32 bit internal number precision. Although routines were developed for higher precision math these were not used in view of the low precision available on the raw data and the inherent execution time penalties. Currently the control of a superconducting magnet large angle magnetic suspension is being implemented on a floating point DSP. The application is numerically intensive as a result of the large number of geometrical transforms involved in the signal processing stage and is expected to fully utilize the floating point capability of the TMS320C30 selected for the implementation.

4. Position Measurement

The fundamental requirements for sensors which measure the position of the suspended object are that they be non-contacting, and capable of sensing the total dynamic range of motion, typically twice the magnetic air-gap or about 1 mm. The basic sensor types applicable to this task are capacitive, inductive, eddy-current and photo-electric where the latter category includes both the diffuse-reflective type and interferometers. Ultra-precision positioning requires levels of stability and resolution that eliminate the diffuse-reflective in all applications and inductive sensors in many applications. The sensitivity of the diffuse-reflective sensor to both surface finish and contaminants make its use inappropriate. In the case of the inductive sensor, changes in the incremental permeability of the target material due to the variations in ambient magnetic field make nanometer resolution impossible for sensors co-located with the actuators. Interferometers capable of 1 mm dynamic range routinely provide nanometer resolution and stability, but are physically large, require a mirrored surface, and cost approximately $10,000 per channel. Thus, achieving nanometer resolution with either the eddy-current or capacitive sensors would greatly reduce both system cost and complexity. In addition, since both these techniques effectively average information over a relatively large surface area, microscopic surface-finish features are unimportant.

Capacitive position sensors measure the capacitance of the air-gap between the sensor electrode and the target. Eddy-current sensors measure the loss in the target material induced by the time-varying magnetic field created by the probe.

Both sensors perform best with a non-magnetic metallic target, and are extremely linear over a specified range. Both also employ measurement electronics which measure the impedance of the sensor: $x_c = j\ _oC$ for the capacitive and loss resistance for the eddy-current. This then involves the measurement of both voltage and current for both types. First order calculations indicate the combined resolution achievable with these two measurements is one part in 10^5, indicating 10 nm is a reasonable goal.

The stability of measurements made with the capacitive and eddy-current sensors is predominantly influenced by the temperature sensitivity of the physical property used in the measurement process. Both the dielectric constant of air and the resistivity of aluminum have a temperature coefficient of about 0.5%/°C, which indicates a required temperature stability on the order of 10^{-3}°C. This requirement can be reduced significantly by employing two identical sensors in a bridge configuration, where variations in thermal gradients will become the predominant error source. Since temperature gradient control is necessary for many aspects of these ultra-precision applications, such techniques as virtual-zero-power suspension or constant power actuators will be used in any event as discussed previously.

4.1 Theoretical Limits on Sensor Precision

We have examined the limitations on the precision of capacitive, inductive, and eddy current sensors imposed by the following fundamental sources of noise: 1) thermal noise, sometimes called Johnson noise, whose magnitude is given by the Nyquist theorem; 2) Barkausen events in ferromagnetic materials, which cause the B-H curve, and hence the permeability, to be slightly different, in a random way, on each cycle, introducing noise in inductive sensors, 3) the Heisenberg uncertainty principle of quantum mechanics, which limits the precision by which energy (and hence potential) can be measured if the measurement is done in a finite time; and 4) the finite charge of an electron, which limits the precision to which current can be measured in a finite time. The limitations on precision imposed by these sources of noise have been compared with the limitations of 15 ppm or 1 ppm imposed by the digital to analog converters, in order to determine when these other sources of noise might impose more severe limitations than the digital electronics, and in order to see at what point one would run into these limitations if the resolution of the electronics is further improved in the future.

Any type of sensor has a characteristic length d representing the range over which it has a linear response. In the case of the inductive and eddy current sensors, d is the largest dimension of the coil, whether length or diameter, and in the case of capacitive sensors d is the gap distance. Within the linear range, the uncertainty in position Δx is related to the uncertainty in voltage ΔV for inductive sensors by

$$\Delta x = d\ \Delta V / I_c L \omega \qquad (1)$$

where I_c is the current in the coil, L is the inductance of the coil, and ω is the frequency with which the probe is being excited. For eddy current sensors

$$\Delta x = d\ \Delta V / I_r R_{eddy} \qquad (2)$$

where

$$R_{eddy} = L\omega(1 + \rho_r/\mu_r \omega d^2)^{-1} \qquad (3)$$

is the part of the resistive impedance of the coil due to the current induced in the rotor. For capacitive sensors,

$$\Delta x = d\ \Delta V\ \omega C / I_c \qquad (4)$$

where C is the capacitance.

The contribution to ΔV from the digital electronics is

$$\Delta V_{digit} = 1.5 \times 10^{-5} V \text{ or } 10^{-6} V \qquad (5)$$

where $V = I_c(R_{wire} + i/\omega C)$ for capacitive sensors (with R_{wire} being the resistance of the lead wires attached to the sensor), $V = I_c(R_{coil} + R_{eddy} + iL\omega)$ for eddy current sensors (with R_{coil} being the coil resistance), and $V = I_c(R_{coil} + R_{eddy} + R_{hys} + iL\omega)$ for inductive coils. Here R_{hys} is the part of the resistive impedance of the coil due to hysteresis in the rotor

$$R_{hys} \simeq (I_c \nu \omega \mu_0^3/3\pi\mu_r^3)(1 + \mu_r \omega d^2/\rho_r)^{-1/2} \quad (6)$$

where μ_r and ρ_r are the permeability and resistivity of the rotor, and $\nu \equiv d\mu/dH$ is between 10 and 100 times μ_r^2/B_s for most materials, B_s being the saturation magnetization. Equation (6) is valid at low ω, but falls off at high ω, especially above 10^6, because domain walls cannot respond so quickly to changes in magnetic field.

The other sources of noise depend on the time τ over which the measurement is taken, being greater for shorter τ. The maximum possible τ is the response time needed to stabilize the rotor, and is generally some fraction of the rotation period, say 1 msec for a 10,000 rpm rotor. Depending on the method used for taking the measurements, τ may be much shorter than this, increasing the noise level. This is especially important for quantum and finite electron charge noise, where there are long term correlations. With thermal and Barkhausen noise, there are no long term correlations, and taking one measurement over a long time is equivalent to averaging many measurements of shorter duration with the same total time.

In estimating the magnitude of different sources of noise, it will be convenient to use approximate expressions for the resistance, inductance and capacitance of the sensors. For inductive and eddy current sensors, it will be advantageous to make the resistance of the coil as low as possible for a given d, and this means that the length, outer radius, and thickness should all be of order d. Then

$$R_{coil} \simeq N^2 \rho_c / d \quad (7)$$

$$L \simeq N^2 \mu_0 d \quad (8)$$

where N is the number of turns, ρ_c is the coil resistivity, and μ_0 is the permeability of free space. Equation (7) is valid if the wire thickness $w \propto d/N^{1/2}$ is less than the skin depth $\delta_c = (\rho_c/\mu_0\omega)^{1/2}$, i.e. if $\omega < NR_{coil}/L$, otherwise the resistance is increased by a factor of about w/δ_c. The capacitance of a capacitive sensor is

$$C \simeq \epsilon_0 A/d \quad (9)$$

where $\epsilon_0 = 8.85 \times 10^{-12}$ farads per meter is the permittivity of free space, and A is the area of the capacitor plates. The lead resistance is

$$R_{wire} \simeq \rho_w l_w / A_w \quad (10)$$

where the wire length l_w must be much greater than $A^{1/2}$, the cross-sectional area of the wire A_w must be less than A, and ρ_w is the wire resistivity. There is also a practical upper limit on $A^{1/2}/d$. Two other useful quantities are the maximum current density J_{max}, above which a coil or lead wire will melt, and E_{max}, the electric field at which breakdown will occur in a capacitive sensor. For copper at room temperature

$$J_{max} \simeq 4 \times 10^6 \text{ A/m}^2 \quad (11)$$

and a typical value for breakdown is

$$E_{max} \simeq 10^7 \text{ volts per meter} \quad (12)$$

For any reasonable values of the parameters, inductive and eddy current sensors are limited by J_{max},

$$I < J_{max} d^2 \quad (13)$$

and capacitive sensors are limited by E_{max}

$$I < E_{max} \omega \epsilon_0 A \quad (14)$$

although capacitive sensors could be limited by current density in the lead wires, if their cross-sectional area A_w is much less than A.

At frequencies well below kT/h, which is in the infrared at room temperature, and well below the collision frequency of electrons in the sensor, which is also in the infrared for copper, thermal noise in the voltage of a circuit has a flat frequency spectrum[8]

$$S(\omega) = kTR \quad (15)$$

where k is Boltzmann's constant, T is the temperature, R is the resistance of the circuit, and $S(\omega)d\omega$ is the average square of the voltage between ω and $\omega + d\omega$. If we wish to measure a signal at frequency ω, and take a time τ to make the measurement, then only the noise between $\omega - \tau$ and $\omega + \tau$ will interfere with the measurement, and the smallest signal (or change in signal) that can be detected will be

$$\Delta V_{thermal} \simeq (kTR/\tau)^{1/2} \quad (16)$$

Barkhausen events in a ferromagnetic material are sudden changes in magnetization that occur in a small volume v_B as H is changed, due to the sudden freeing of a domain boundary from a pinning site. "Sudden" means in about a microsecond; Barkhausen events do not occur at frequencies greater than about 10^6 Hz. They cause noise in an inductive sensor because they occur randomly, not repeating their pattern from cycle to cycle. The change in voltage in the coil associated with a single Barkhausen event in the rotor is

$$V_B \simeq \nu \omega I_c^2 N^2 (v_0/d_3)(\mu_0/\mu_r)^3(1 + \mu_r \omega d^2/\rho_r) \quad (17)$$

In deriving Eq. (17), we assumed that $(\mu_0/\mu_r)(1+d^2/\delta_r^2)^{1/2} \ll 1$, which is always satisfied for $\omega < 10^6$ Hz and $d < 1$ cm. (A safe assumption, since for $\omega > 10^6$ Hz, Barkhausen events do not take place at all.) The parameter ν appearing in Eq. (17) is defined after Eq. (6), and v_0 is the average volume over which the magnetization reverses direction in a Barkhausen event occurring at the steepest part of the B-H curve. (At lower H, the volume is proportional to H^2.) Bozorth[9] quotes average values of 10^{-15} m^3 for iron, 5×10^{-14} m^3 for 50 Permalloy, and a maximum value of 4×10^{-12} m^3, corresponding perhaps to an average value of 10^{-12} m^3, for silicon steel. The situation is somewhat complicated by the fact that if H is changed very slowly, one Barkhausen event can give rise to another, eventually resulting in a cascade of thousands of individual events, which cause a change in voltage thousands

of times greater than indicated by Eq. (17). However, this process seems to require on the order of a millisecond for each event induced, so at frequencies greater than about 10^3 Hz there should be no clustering of Barkhausen events, and Eq. (17) should be correct. If, as seems reasonable, Barkhausen events are correlated within a cycle, but uncorrelated (or substantially uncorrelated) one cycle to the next, then after averaging over a time τ several cycles long, the uncertainty in voltage due to Barkhausen events will be

$$\Delta V_{Bark} \simeq (\omega\tau)^{-1/2} V_B \qquad (18)$$

According to Heisenberg's uncertainty principle, the uncertainty in the energy in a measurement done over a time τ must be greater than h/τ, where $h = 6.6 \times 10^{-34}$ joule-sec is Planck's constant. The quantum mechanical uncertainty in a measurement of voltage, which is energy per charge, would therefore be

$$\Delta V_{QM} = h/e\tau \qquad (19)$$

This is the voltage associated with changing the magnetic flux by one quantum of flux, h/e, during a time τ; another way of stating this is that it is impossible to measure changes in flux of less than h/e, one flux quantum. Naively one might think that the uncertainty would be

$$\Delta V_{QM} \simeq h\omega/\pi e \qquad (20)$$

which corresponds to a change in flux of one quantum in half a wave period, and that averaging over a time τ much longer than a wave period would result in an uncertainty of

$$\Delta V_{QM} \simeq h\omega^{3/2}\tau^{1/2}/\pi^{3/2}e \qquad (21)$$

If the AC potential were determined by making independent measurements of the DC potential at each half wave period, and then averaging them, then the quantum uncertainty would indeed be given by Eq. (21). However, in principle it ought to be possible to make a single measurement of AC potential over many wave periods, in which case Eq. (19) would apply.

The finite electron charge $e = 1.6 \times 10^{-19}$ coulombs means that changes of current smaller than e/τ cannot be measured in a time τ. The uncertainty in voltage associated with this is

$$\Delta V_{elec}/V = e/\tau I \qquad (22)$$

This expression ought to be appropriate even for τ much longer than a wave period, since electrons are conserved, and if the current is a lower than it should be, say, during one half of a cycle, because of finite electron charge, then it ought to compensate for this in the next half cycle; the total uncertainty in charge after any number of cycles should not be greater than e.

Applying Eqs. (5), (16), (18), (19), and (22) to a typical room temperature copper inductive sensor with d = 1 cm, τ = 1 msec, $\omega = 10^4$ sec^{-1}, V = 1 volt, N = 2000, and a ferromagnetic rotor with $\rho_s = 5 \times 10^{-7}$ ohm-meters, $\mu_r = 1000\mu_0$, $v_0 = 10^{-14}$ m^3, $v = 10\mu_r^2/B_s$, B_s = 1 tesla, and $\Delta V_{digit}/V = 1.5 \times 10^{-5}$, we find

$$\delta_r \simeq 0.2 \text{ mm} \ll d, \quad \delta_c \simeq 1.2 \text{ mm} > d/N^{1/2},$$
$$R_{coil} \simeq 6\Omega, \quad R_{hys} = 6 \times 10^{-15}\Omega, \quad R_{eddy} \simeq 400\Omega,$$
$$\Delta V_{digit} \simeq 1.5 \times 10^{-5} \text{ volts},$$
$$\Delta V_{thermal} \simeq 1.5 \times 10^{-7} \text{ volts},$$
$$\Delta V_{Bark} \simeq 5 \times 10^{-15} \text{ volts},$$
$$\Delta V_{QM} \simeq 4 \times 10^{-12} \text{ volts},$$
$$\Delta V_{elec} \simeq 8 \times 10^{-14} \text{ volts}$$

The only thing that comes close to the digital noise is the thermal noise, and that could be reduced, relative to the digital noise, by increasing the voltage or decreasing the number of turns. Eventually the current density limit J_{max} would be reached, at which point

$$\Delta V_{thermal}/V \simeq (kT\rho_c)^{1/2}\tau^{-1/2}\mu_0^{-1}d^{-7/2}J_{max}^{-1}\omega^{-1} \simeq 5 \times 10^{-11} \qquad (33)$$

At this current density $\Delta V_{Bark}/V$ would increase to 1.5×10^{-11}, almost up to $\Delta V_{thermal}/V$, but far less than $\Delta V_{digit}/V$. $\Delta V_{thermal}$ could be reduced further by increasing ω, but then ΔV_{Bark} would become greater than $\Delta V_{thermal}$. The result would be essentially the same (but without Barkhausen noise) for an eddy current sensor, assuming the same parameters but with $\mu_r = \mu_0$.

We conclude that for inductive and eddy current sensors with d ≃ 1 cm, digital noise is the limiting factor, with no other source of noise coming close if the sensor is properly designed, that is if it has high enough current density and frequency (high enough flux). If it is designed with too low a flux, thermal noise could become a limited factor.

The thermal noise at the current density limit scales like $d^{-7/2}$, so if d were an order of magnitude or two smaller, as it might be in some highly miniaturized future application, thermal noise will be the limiting factor even at the current limit.

Quantum noise is negligible for inductive and eddy current sensors, if we assume that a measurement can be made over a full millisecond without "collapsing the wave function", so to speak. If the method of measurement in fact takes much less than a millisecond, even if many measurements are averaged over a millisecond, then quantum noise would be much greater, and could be the limiting factor. In particular quantum noise could exceed thermal noise if τ were small noise, since quantum noise scales like τ^{-1} while thermal noise scales like $\tau^{-1/2}$. This can happen more easily in cryogenic situations, where thermal noise will be lower, both because kT is lower and because J_{max} could be greater.

For a capacitive sensor with d = 1 mm, A = 1 cm^2, V = 1000 volts, R_{wire} = 1 mΩ, $\omega = 10^6$ sec^{-1}, τ = 1 msec, we find

$$C = 1 \text{ pf}, \quad I = 1 \text{ mA},$$
$$\Delta V_{digit} \simeq 15 \text{ mV or } 1 \text{ mV},$$
$$\Delta V_{thermal} \simeq 6 \times 10^{-11} \text{ volts},$$
$$\Delta V_{QM} \simeq 4 \times 10^{-12} \text{ volts},$$
$$\Delta V_{elec} \simeq 1.6 \times 10^{-13} \text{ volts}$$

All sources of noise other than digital noise are negligible in this case, and will be negligible for a capacitive sensor with parameters anywhere near these ones. In possible future applications with extremely small d, for example in nanotechnology, and with voltage limited by breakdown, ΔV_{elec} will eventually dominate; this would happen sooner if τ were very small.

5. Conclusions

SatCon believes that magnetic bearings and suspensions have tremendous potential for the development of extreme precision positioning systems. We believe that this technology will have a tremendous impact over the next decade in the development of a new generation of machinery for industrial and scientific applications in both terrestrial and space environment. The factors that determine achievable resolution for a magnetically suspended system are position measurement accuracy, controller bandwidth, controller gain internal noise, and external disturbance forces. Laser interferometers are expected to be available in the near future with resolutions exceeding one Angstrom and adequate accuracy for a one Angstrom resolution suspension application. Capacitive and eddy current sensors can approach these resolutions with reduced volume and cost. Based on these considerations, the authors believe that a magnetically suspended systems having resolutions in the one to 100 Angstrom can be developed using state-of-the-art and near-state-of-the-art technology.

6. Bibliography

1. Binnig, G. and H. Rohrer: Scanning Electron Microscopy. Helvitica Physica Acta, Vol. 55, pp.726-735(1982).
2. Lindsey, K. and P. Steuart: NPL Nanosurf 2: A Sub-nanometer Accuracy Stylus-based Surface Texture and Profile Measuring System with a Wide Range and Low Environmental Susceptibility. 4th Int. Precision Engr. Sem. Cransfield Inst. of Tech., U.K., p.15(11-14 May 1987).
3. Donaldson, R. and S. Patterson: Design and Construction of a Large Vertical-Axis Diamond Turning Machine. SPIE's 27th Annual International Technical Symposium and Instrument Display (21-26 August 1983).
4. Moore, W.: Foundations of Mechanical Accuracy. The Moore Special Tool Company. Bridgeport, Connecticut, pp.24-28(1970).
5. Biesterbos, J., et al: A Submicron I-Line Wafer Stepper. Solid State Technology, pp.73-76(1987).
6. Nuhn, M.; Yao, S.; Avrit, B.: I-Line Wafer Stepper Used for Low Volume Production of 0.5 Micrometer GaAs Integrated Circuits. Solid State Technology, pp.81-84(1987).
7. Berthold, J.; Jacobs, S.; Norton, M.: Dimensional Stability of Fused Silica, Invar, and Several Ultra-low Thermal Expansion Materials. Metrologia 13, pp.9-16(1977).
8. Reif, F.: Fundamentals of Statistical and Thermal Physics. McGraw-Hill, pp.587-594(1965).
9. Bozorth, Richard M.: Ferromagnetism. Van Nostrand, New York. pp.524-532(1951).

2nd International Symposium on Magnetic Beaing
July 12-14, 1990, Tokyo, Japan

PERFORMANCE OF THE ACTIVE MAGNETIC BEARINGS*

Zhong CAI† Zuming ZHANG‡ Hongbin ZHAO†
†Department of Engineering Physics, Tsinghua University, Beijing, P.R. China
‡Beijing Management Institute of Machinery Industry, Beijing, P.R. China

Abstract The digital controllers of active magnetic bearings system (AMB) are designed. The performance of the controllers are measured and analyzed. The stability is an essential feature for a closed loop control system. By adjusting the magnitude and phase characteristics of the controllers, a stable close-loop control systems are obtained. The step disturbance forces are applied to the system and the responses of system in different conditions are measured and the system stability is optimized by modifying the properties of the controllers. The optimal controllers can attenuate the vibration of the rotor effectively and have large stable range. Some problems of the digital controllers are discussed. The structure of the magnetic bearing system is analyzed for improving the stiffness and the damping of the rotor.

Introduction

The active magnetic bearings system is a closed loop control system. For this system, the stability is an essential feature. By adjusting the magnitude and phase characteristics of the controllers, a stable closed loop control system can be obtained. But it may be difficult to obtain a system with a wide stable range.

For a magnetic bearing, the stiffness and dynamic range are also important features. High stiffness may make AMB system unstable, while low stiffness may make it unable to suspend the rotor. Some tradeoffs should be made to decide these features.

There are two approaches to implement the AMB controller. One is analog approach, the other is digital approach. The later approach is suitable for adaptive or optimal control because its properties can be changed easily by modifying its software. Therefore, it is an approach which makes the design of controller easier.

Experimental System

Figure 1 shows the axial AMB system. It is independent of the radial AMB system and can be considered as a single degree of freedom system. It is relatively easy to study the performance by changing the control parameters.

The closed loop control system consists of an eddy-current displacement sensors, magnitude and phase controller, power amplifiers, bias coils and control coils. For the digital approach, the controllers are implemented with real-time FIR, IIR filters and other software packages in the digital signal processing (DSP) system, which consists of a personal computer and a TMS320 development system.

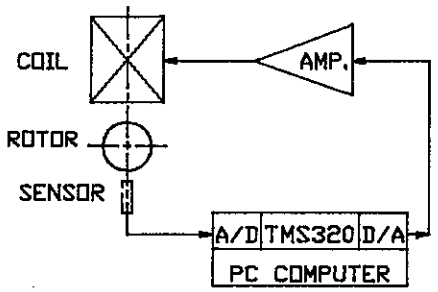

Figure 1: Axial AMB System

The bias coil and control coil are separated and the number of the bias coil turns is more than that of the control coil turns. In this case, the bias coil needs less current to suspend a given weight. In addition, the control coil has less inductance to decrease the phase-lag caused by large coil inductance.

The eddy-current displacement sensor is mounted at the center of the coils, a short axial distance away from the shaft. In the linear range, the output of the sensor, which is produced by a analog circuit, is a DC voltage proportional to the position offset of the shaft. Its reference point (zero-output point) and sensitivity can be changed easily.

The offset signal is sent to the controller which possesses of two parallel paths. These paths allow for the proportional gain and the velocity adjustment, which affect the stiffness and damping of the AMB system, respectively. In our experiments, the controller is implemented both with analog circuits and with a digital

*Supported by the National Natural Science Fundation of China

signal processing system. As shown in Figure 1 DSP system consists of a TMS320 microprocessor, which can perform an addition or multiplication operation in a 200ns instruction cycle. The TMS320 also includes some special instructions for fast implementation of sum-of-products computations encountered in digital filtering calculations.

The filters programs are sent to TMS320 from a PC computer. When a signal is sampled by the AD converter, an interrupt signal make the filter programs execute. The result is sent to DA converter. The output of DSP system has a DC component and noise, whose frequency is proportional to the sample rate of DSP system. In order to filter the high frequency noise, a low pass filter with small time constant is used before the signal is sent to the power amplifier. The effect of the low pass filter to the performance of the system can be ignored, because the small time constant causes a large pole point. The power amplifier is used as control coil driver, which can control the position of the rotor, as well as position adjustment.

Digital Controller Performance

The design of the analog controllers is relatively familiar to most of designers and have been implemented in many laboratories. In this paper, we focus to the design of digital controllers.

A digital PID controller is used. The proportional path is used to adjust the stiffness, the differentiator is used to adjust the damping of the rotor and the low pass digital filter with certain gain is used to adjust the total stiffness and damping. The transfer function of this controller is given by

$$G(z) = \frac{K_I}{z - e^{-\tau/\tau_I}}\left(K_P + \frac{K_D(z-1)}{\tau_D(z - e^{-\tau/\tau_D})}\right)$$

where τ is the sampling interval, τ_D and τ_I are the time constants of the integrator and the differentiator, K_I, K_D are the gains of them, respectively. The K_P is the gain of the proportional path.

A software package called Digital Filter Design Package (DFDP) is available to design the digital filters. The designed filters are FIR filters, which can be described generally as:

$$y(n) = \sum_{i=0}^{N-1} h(i)x(n-i)$$

where $h(i)$ are the coefficients of the filters, $x(n-i)$ and $y(n)$ is the inputs and outputs, N is the taps of the filters. It is a advantage of the FIR filters that it can be easily designed as a filter with linear phase response. Compared with IIR filter, this advantage makes

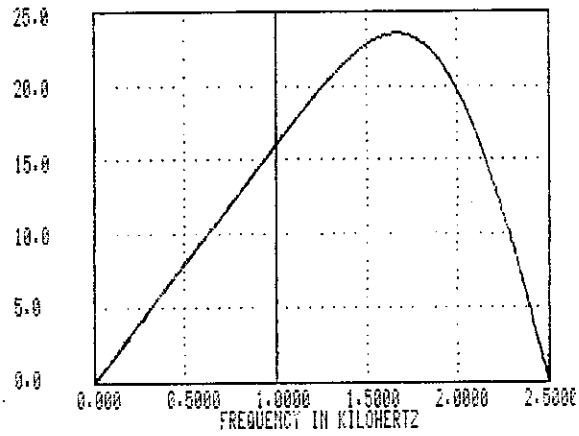

Figure 2: Magnitude Response of Differentiator

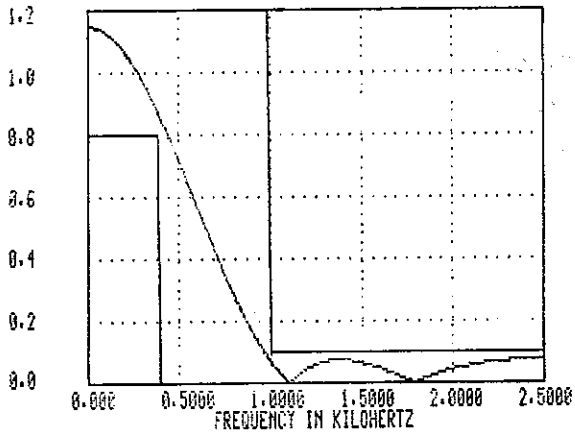

Figure 3: Magnitude Response of Low-pass Filter

it relatively easy to handle the phase response. For a linear phase response FIR filter, the phase response can be given as follow.

For even unit impulse response filter:

$$\phi(\omega) = -\frac{N-1}{2}\omega$$

For odd unit impulse response filter (such as differentiator):

$$\phi(\omega) = \frac{\pi}{2} - \frac{N-1}{2}\omega$$

We can see that the larger the taps N is, the larger the phase lag is. And a N taps FIR filter needs N times of multiplication, addition and memory access, respectively, which also will increase the phase lag of the filter. In order to reduce the phase lag, the filters with smaller taps are used.

The characteristics of the differentiator and the low pass filter used to construct the controller are shown

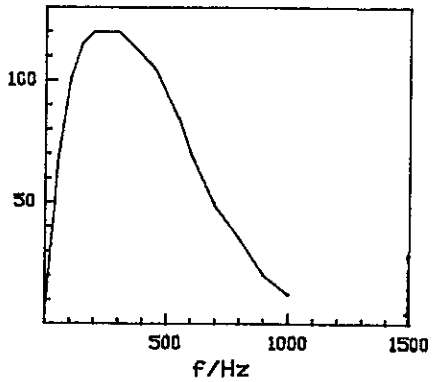

Figure 4: Open Loop Frequency Response of Controller

in Figure 2 and Figure 3. In a constructed controller, the characteristics can be changed easily by altering the results of proportional path, the differentiator and the low pass filter respectively. Left shifting the results of proportional path or low pass filter in memory will increase the stiffness of the rotor, while left shifting the results of the differentiator will increase the damping of the rotor. But this method has its limitations: the results only can be increased or decreased with the factor of two and the shifting operation may cause the results overflow or underflow.

The open loop frequency responses of the controller are measured. The results are shown in Figure 4. The controller has a phase lead of 30° at 20Hz, which is the resonance frequency of the rotor in axial direction. It can be seen that the magnitude of controller remains high at high frequency. Because the magnetic bearing system has the effect of low pass filter in the closed loop system, the magnitude at high frequency will be reduced. The step response of the system with different stiffness and damping are shown in Figure 5. Under the maximum damping of this controller, the DC gain can be changed from 8.9dB through 16.2dB.

Another controller without low pass filter, which has a phase lead of 60° at 20Hz, is designed. Compared with the previous controller, it has larger damping at the resonance frequency. Under the maximum damping of this controller, its DC gain can be changed from 6.8dB through 18.1dB. It is obvious that the controller with larger phase lead has a larger range of stability and the stiffness can also be larger.

Analysis of Stiffness and Structure

For a magnetic bearing system shown in Figure 6, we assume that the motion range of the rotor near the reference position is small and the magnetic flux level is well below the saturation in the core material and the

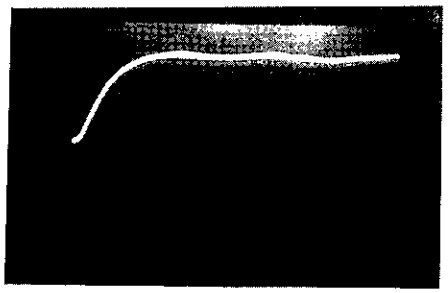

(a). small damping

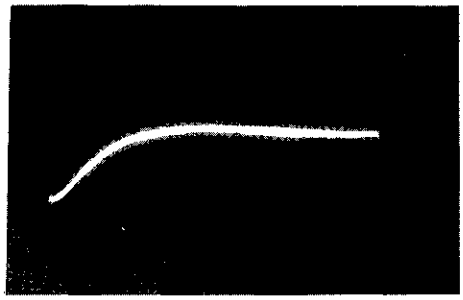

(b). large damping

Figure 5: Step Response of Closed Loop System

fringing and leakage of the magnetic flux are neglected. According to the assumptions, the linearized analysis can be used.

As shown in Figure 6, the magnet force exerted on the rotor at a distance z is,

$$f = \frac{\mu_0 A(n_0 i_0 + ni)^2}{4z^2}$$

where μ_0 is permeability of free space, A is area of magnetic pole, $n_0 i_0$ is magnetomotive force of bias coil, ni is magnetomotive force of control coil.

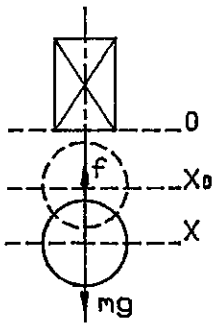

Figure 6: Magnetic Bearing System

At distance z, there is an increment Δz of z_0, then the current in the control coil is,

$$i = k_i \Delta z$$

where k_i is a coefficient dealt with displacement sensitivity of the rotor. The total force exerted on rotor is,

$$\Delta f = f - mg$$

At distance z_0, the electromagnetic force is,

$$f_0 = \frac{\mu_0 A n_0^2 i_0^2}{4 z_0^2} = mg$$

So, at distance z, the total force is, ($\Delta z \ll z_0$)

$$\begin{aligned} \Delta f &= f - mg = f - f_0 \\ &= \frac{\mu_0 A (n_0 i_0 + ni)^2}{4 z^2} - \frac{\mu_0 A n_0^2 i_0^2}{4 z_0^2} \\ &\doteq \left(\frac{\mu_0 A n_0 i_0 n k_i}{2 z_0^2} - \frac{\mu_0 A n_0^2 i_0^2}{2 z_0^3} \right) \Delta z \end{aligned} \tag{1}$$

The axial stiffness K of the rotor is,

$$K = K_p - K_n = \frac{\Delta f}{\Delta z}$$

where, the K_p is positive stiffness,

$$K_p = \frac{\mu_0 A n_0 i_0 n k_i}{2 z_0^2}$$

the K_n is negative stiffness,

$$K_n = \frac{\mu_0 A n_0^2 i_0^2}{2 z_0^3}$$

The positive stiffness is the effect of control coil and the negative stiffness is the effect of bias coil, which has a negative effect to the stability of the system. It is essential to overcome the negative stiffness by increasing the positive stiffness. Defining

$$z_m = \frac{n_0 i_0}{n k_i}$$

At the position $z > z_m$, we have

$$K_p > K_n$$

So, if the rotor is at the position $z < z_m$, it will have a negative stiffness and move toward the magnet out of control. To avoid this case, we keep the rotor at a distance $z > z_m$ away from the electromagnet on the condition that the rotor is in the linear range of the system.

From Eq.(1), we can see that the stiffness of the rotor can be increased by increasing the reference distance z_0, but the power for suspending the rotor also will be increased and may cause the saturation of the core material. Also, increasing the control coil turns n has the drawback of increasing the coil inductance. So, the most effective way to increase the stiffness is to increase the coefficient k_i on the condition that the system is stable. This result can also be used in other magnetic bearing system of permanent magnets with attractive force.

Conclusions

Analog and digital controllers of the AMB system are designed and constructed. To improve the performance, different kinds of real-time control programs which have different magnitude and phase response are used. The characteristics of the controllers are measured and analyzed. The controllers with large phase lead at resonance frequency of rotor have relatively large range of stability. Hence, stiffness of the rotor can be changed in large range. The maximum stiffness of the rotor also can be increased. This is very important for improving the performance of the AMB system.

The structure of the magnetic bearing system is also discussed in this paper. Within the minimum suspension distance, the rotor will be out of control and moves toward the magnet. The minimum distance is proportional to the magnetomotive force of bias coil and inversely proportional to the control coil turns and the displacement sensitivity of the control system. The method to avoid this case is to keep the position of the rotor at a distance larger than the minimum suspension distance.

References

1. Humphris,R.R., Allaire,P.E., et al, "Effect of Control Algorithms on Magnetic Journal Bearing Properties," J. of Eng. for Gas Turbines and Power, Vol.108, No.4, pp.624-632 (1986)

2. Kanemitsu,Y., Ohsawa, M. and Watanabe,K., "Active Control of a Flexible Rotor by an Active Bearing," Proc. of the 1st. Intern. Symp., ETH Zurich, Switzerland, pp.367-380 (1988)

3. Bleuler,H., "Controlling Magnetic Bearing Systems with a Digital Signal Processor," Proc. of the 1st. Intern. Symp., ETH Zurich, Switzerland, pp.381-390 (1988)

4. Okada,Y., Nagai,B. and Shimane,T., "Digital Control of Magnetic Bearing with Rotationally Synchronized Interruption,"Proc. of the 1st. Intern. Symp., ETH Zurich, Switzerland, pp.357-364 (1988)

5. Larsonneur,R., Herzog,R., "Optimal Design of Structure Predefined Discrete Control for Rotor in Magnetic Bearings", Proc. of the 1st. Intern. Symp., ETH Zurich, Switzerland, pp.347-356 (1988)

6. Matsushita,O., Bleuler,H., Sugaya,T. and Kaneko,R., "Modeling for Flexible Mechanical Systems", Proc. of the 1st. Intern. Symp., ETH Zurich, Switzerland, pp.337-346 (1988)

2nd International Symposium on Magnetic Beaing
July 12-14, 1990, Tokyo, Japan

Application of Periodic Learning Control with Inverse Transfer Function Compensation in Totally Active Magnetic Bearings

T.HIGUCHI*, M.OTSUKA*, T.MIZUNO**, T.IDE***

*Institute of Industrial Science, University of Tokyo;
7-22-1, Roppongi, Minato-ku, Tokyo 106
**Faculty of Engineering, Saitama University; Shimo-Okubo Urawa 338
***Fuji Heavy Industries Ltd.; 3-9-6, Osawa, Mitaka, Tokyo 181, Japan

Abstract

Rotating machinery has two vibration problems caused by mass imbalance of a rigid rotor --- whirling motion of the rotor and vibration of the housing. In order to solve these problems in magnetic bearings, the authors propose to apply periodic learning control (**PLC**) with inverse transfer function compensation (**ITFC**), which can deal with periodic disturbances. In order to suppress the whirling motion, the PLC with the ITFC calculates compensatory inputs added to force control signals from the sampled rotor displacement. In order to reduce the vibration of the housing, the PLC with ITFC calculates compensatory inputs added to force control signals from the sampled force control signals. The implementation of the PLC with ITFC is easily accomplished by adding a digital controller, which consists of a personal computer, an A/D converter, and four D/A converters, to a conventional analog PID-controller. The authors have carried out several experiments by applying the PLC with ITFC to obtain the following results: (1) Translational and tilting whirling motions are reduced from about $\pm 3\mu m$ to $\pm 1\mu m$, and from about $\pm 80\mu rad$ to $\pm 20\mu rad$, respectively, at the rotor speed of *51,000rpm* (*850rps*); (2) Vibration of the housing of a magnetic bearing spindle is reduced from about $\pm 0.6G$ to $\pm 0.1G$ in average at the rotor speed of *57,000rpm* (*950rps*).

1. Introduction

Rotating machinery has two major vibration problems caused by mass imbalance of a rigid rotor. One is whirling motion of the rotor. The other is vibration transmitted to the housing of the machine. Magnetic bearings can solve these problems by controlling the forces of electromagnets.

The whirling motion of the rotor can be suppressed by providing the forces of electromagnets which counteract the disturbance forces arising from the imbalance. Several control laws based on this concept have been developed([1],[2], for example). Based on the same concept, the authors propose to apply periodic learning control (**PLC**) with inverse transfer function compensation (**ITFC**) in magnetic bearings to suppress the whirling motion.

The vibration of the housing can be reduced by making the axis of rotation coincide with the principal axis of inertia[3]. When the axis of rotation coincides with the principal axis of inertia, attractive forces of electromagnets do not fluctuate. The authors proposed control schemes to reduce those fluctuations of the forces of electromagnets which are synchronous with the rotation of the rotor[4]. However, it is generally difficult to measure the forces of electromagnets. On the other hand, it is easy to measure coil-currents of electromagnets. When the coil-currents do not fluctuate, the forces of electromagnets fluctuate very little, because the difference between the geometrical axis of the rotor and the principal axis of inertia is generally small. Thus, reducing the fluctuations of coil-currents have a good effect to reduce the vibration of the housing. The authors propose to apply the PLC with ITFC in magnetic bearings in order to reduce the fluctuations of coil-currents, aiming at the reduction of the vibration of the housing.

2. Periodic Learning Control (PLC) with Inverse Transfer Function Compensation (ITFC)

Disturbances to rotating machinery contain periodic and repetitive components. The period is the time for one rotation. Periodic learning control (PLC) can make periodic output errors converge to zero by repeatedly adding the errors in the last period into the control input in the next period[5][6][7].

Fig.1 shows a block diagram of the PLC with the ITFC we propose to apply[7][8]. Let us now explain the PLC with ITFC of one degree of freedom for the sake of brevity. While the filter F(s) is not always necessary for the basic form of the PLC with the ITFC, F(s) is employed here in order to deal only with the fundamental component of the output error E(s).

Symbol $\hat{}$ added to $G^{-1}(s)$ denotes that $G^{-1}(s)$ may have some errors. Providing that R(s)=0, the output error of the n^{th} repetition is given by

$$En(s) = -G(s)\cdot\{1-\hat{G}^{-1}(s)F(s)G(s)\}^{n}\cdot W(s) \quad . \quad (1)$$

The output error converges to zero when the following equation is satisfied:

$$| 1-\hat{G}^{-1}(s)F(s)G(s) | < 1 \quad . \quad (2)$$

Because the filter F(s) extracts only the component synchronous with the rotation, eq.(2) yields;

$$| 1-\hat{G}^{-1}(j\omega)G(j\omega) | < 1 \quad . \quad (3)$$

If eq.(3) is satisfied at the angular velocity ω of the rotor, the error converges to zero.

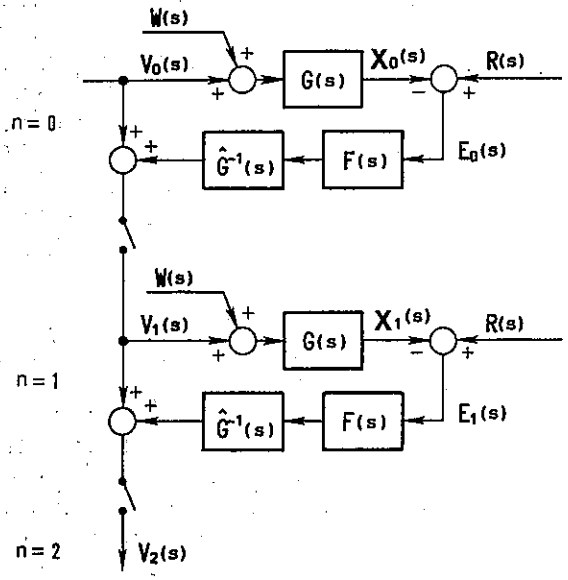

Fig.1 Block Diagram of Periodic Learning Control with Inverse Transfer Function Compensation
X(s): output of the controlled system
V(s): compensatory input ($V_0(s)=0$)
R(s): periodic reference input
E(s): output error of the controlled system; = R(s)-X(s)
G(s): closed loop transfer function of the controlled system, where X(s)= G(s)V(s).
F(s): filter which extracts only the fundamental component of the system.
W(s): periodic disturbance
n: repetitive number of periodic learning control
(All subscripts denote the repetitive number.)

3. Application of PLC with ITFC in Magnetic Bearings

Fig.2 shows a structure of a control system. As mentioned in chapter 2, the PLC with the ITFC is applied in order to make the output errors of the controlled system converge to zero. The controlled system corresponds to a closed loop system which consists of magnetic bearings and a PID-controller in Fig.2. The PID-controller stabilizes translational motion (x,y,z) and tilting motion (θ_x,θ_y) of the rotor, respectively; Such a control scheme is called central control. The definition of coordinate is shown in Fig.3. A symbol u_k (current control signal) in Fig.2 represents a signal of control force in the k direction (k=x,y,z,θ_x,θ_y). Coil-current in each electromagnet is determined from these current control signals through geometrical conversion[1].

The **PL-controller** shown in Fig.2, which consists of a personal computer, an A/D converter, and four D/A converters, is added to the controlled system to carry out the PLC with the ITFC. The PL-controller samples the output errors of the controlled system, carries out the calculation of F(s) and $\hat{G}^{-1}(s)$ (See Fig.1), and adds the compensatory inputs to the current control signals. The reference inputs to the controlled system are treated as zero in this paper.

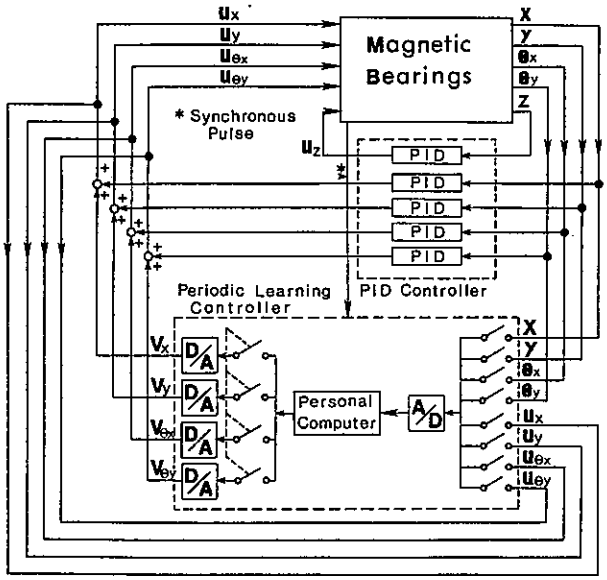

Fig.2 Diagram of Control System
u_k: current control signal in the k direction (k=x,y,z,θ_x,θ_y)
v_k: compensatory signal in the k direction (k=x,y,θ_x,θ_y)

Because the PLC with ITFC makes the output errors of the controlled system converge to zero, what is treated as the output determines the effect of the PLC with ITFC. When the rotor displacement is treated as the output, the PLC with ITFC suppresses the whirling motion. When the fluctuations of current control signals are treated as the output, the PLC with the ITFC reduces the fluctuations of coil-currents.

As the authors proposed in [4], the PLC with the ITFC can reduce the vibration of the housing by treating the fluctuations of the forces of electromagnets as the output.

Applying the PLC with the ITFC in magnetic bearings has some good properties[8]: 1)The PLC with the ITFC makes the output errors converge to zero even when parameters of the controlled system are not accurately identified. 2)The implementation of the PLC with the ITFC is easily accomplished by adding a digital controller to a conventional (analog) PID-controller. 3)The PLC with the ITFC does not affect the stability of magnetic bearings at all.

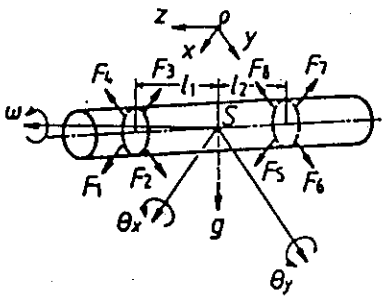

Fig.3 Coordinate System and Forces Acting on the Rotor

4. Suppression of Whirling Motion

The authors carried out an experiment to suppress the whirling motion at the rotor speed 850rps (51,000rpm). A section view of the magnetic bearing spindle used in the experiment is shown in Fig.4. It consists of eight radial electromagnets, four radial gap sensors, two axial electromagnets, an axial gap sensor, a motor-stator, and a rotor.

Here we define symbols used to explain a procedure of the PLC with the ITFC to suppress the whirling motion.

n : repetitive number of the PLC

$\mathbf{x}(t) = [x, y, \theta_x, \theta_y]^T$: rotor displacement

$\mathbf{x}^*(t) = [x^*, y^*, \theta_x^*, \theta_y^*]^T$: component of x with the same frequency as the rotor speed

$\mathbf{v}(t) = [v_x, v_y, v_{\theta x}, v_{\theta y}]^T$: compensatory input to suppress the whirling motion

T_f^{-1} : 4-4 complex matrix that represents characteristics of the inverse transfer function $G^{-1}(s)$ at the rotor speed, f(rps)

The structure of T_f^{-1} is as follows:

$T_f^{-1} = (c_{LM})$, $c_{LM} = a_{LM}\exp(j \cdot p_{LM})$ (L,M=1,..,4).

T_f^{-1} is calculated from Tf obtained by another experiment, where each term of x(t) (the output of the controlled system) is measured when a sinusoidal test signal is given to each term of v(t) (the compensatory input)[9]. This experiment is carried out when the rotor is not rotating. (T_f^{-1} can also be calculated from parameters of the controlled system[8].)

The procedure of the PLC with the ITFC to suppress the whirling motion is as follows:

[n.1] Compensation with $\mathbf{v}_n$ begins. $\mathbf{v}_n$ is given to the controlled system through four D/A converters every 10μs.

[n.2] $\mathbf{x}_n$ is sampled by the A/D converter every 10μs throughout one rotation at least. [n.2] is carried out when steady-state response can be observed.

[n.3] $\mathbf{x}_n^*$ is calculated by means of Fourier series expansion. [n.3] corresponds to F(s) in Fig.1.

[n.4] $\mathbf{x}_n^*$ is multiplied by T_f^{-1} from the left side. [n.4] corresponds to $\hat{G}^{-1}(s)$ in Fig.1.

[n.5] The next compensatory input $\mathbf{v}_{n+1}$ is calculated by the following equation:

$$\mathbf{v}_{n+1} = - \sum_{k=0}^{n} T_f^{-1} \mathbf{x}_k^* \quad .$$

A set of fluctuations of x,..,θ_y denoted with n=0 in Fig.5 (a) is whirling motion before the PL-controller works [0.1], where the brackets [.] correspond to those in the procedure of the PLC with the ITFC above. The personal computer calculates synchronous components of the sampled data [0.3]:

$$\mathbf{x}_0^* = \begin{bmatrix} 2.4\cos(2\pi ft+162\text{deg}) \ (\mu\text{m}) \\ 1.7\cos(2\pi ft-118\text{deg}) \ (\mu\text{m}) \\ 63\cos(2\pi ft-49\text{deg}) \ (\mu\text{rad}) \\ 82\cos(2\pi ft-137\text{deg}) \ (\mu\text{rad}) \end{bmatrix} .$$

Phase angle is defined as an angle from the rotor-fixed reference. The PL-controller obtains the position of this reference of angle as a pulse per rotation. Next, $\mathbf{v}_1$ is calculated according to [0.4] and [0.5].

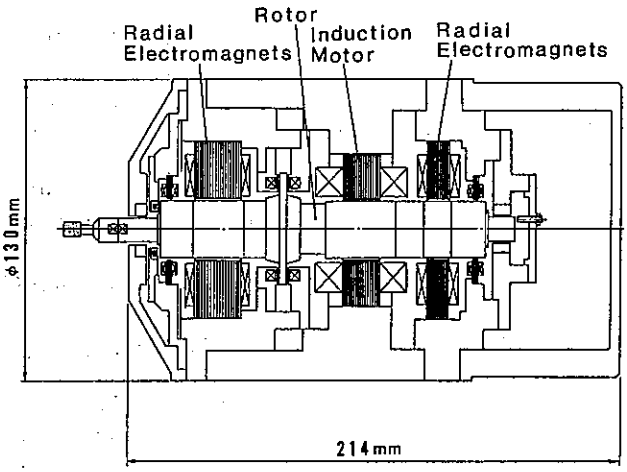

Fig.4 Cross Section of Magnetic Bearing Spindle
(Manufactured by Seiko Seiki Co., Ltd. , Japan)

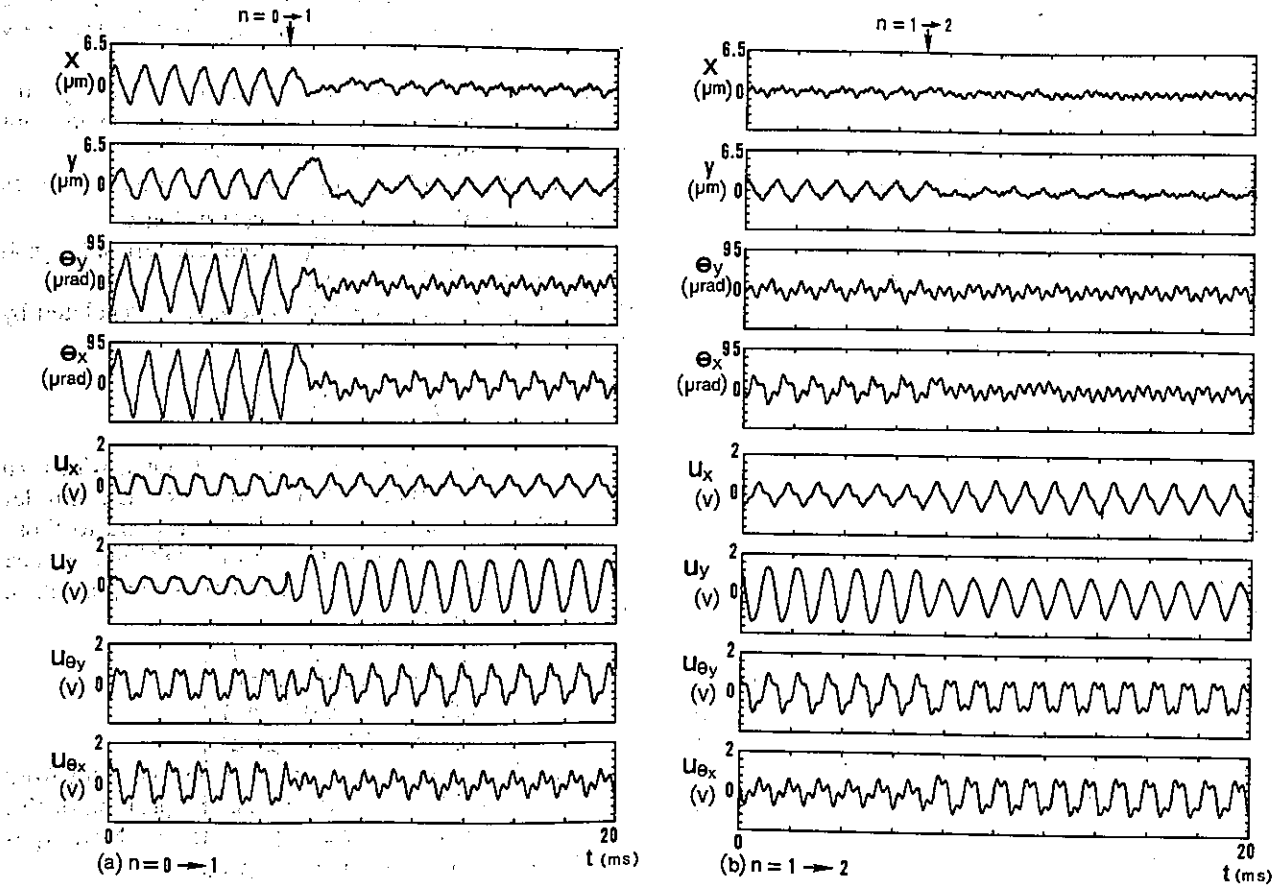

Fig.5 Suppression of Whirling Motion by PLC with ITFC (850rps).
$x,..,\theta_y$: rotor displacement , $u_x,..,u_{\theta y}$: force control signals , n: repetitive number of the PLC

"n=0→1" in Fig.5 (a) denotes the time when the compensation with v_1 begins [1.1]. The v_1 is given continuously through four D/A converters every 10μs. The figure shows that the residual whirling motion is not negligible. This estimation implies that the T_f^{-1} has some errors. In order to reduce this residual whirling motion, the PLC with the ITFC proceeds to [1.2],.,[1.5].

"n=1→2" in Fig.5 (b) denotes the time when compensatory input changes form v_1 to v_2 [2.1]. The figure shows that the whirling motion becomes smaller after this change. Fig.6 shows that the component of x at 850Hz is reduced very well. On the other hand, the other components are not affected because only the component synchronous with the rotation is extracted in the procedure [n.3]. Fig.7 shows that suppressing the whirling motion does not result in the reduction of the housing vibration. In the experiment, the vibrations are measured at a band which fixes the housing on the base.

In the next chapter, it is shown that the reduction of the housing vibration can be realized by another application of the PLC with the ITFC.

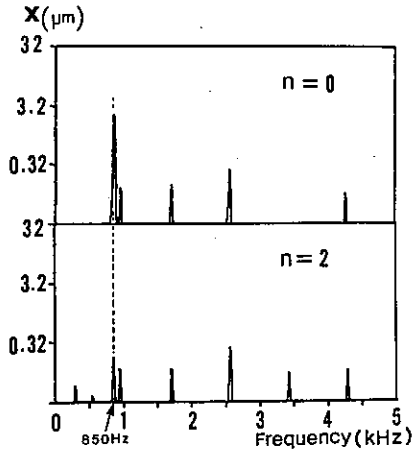

Fig.6 Comparison of Whirling Motions in Frequency Domain with and without Suppression of Whirling Motion
n : repetitive number of periodic learning control

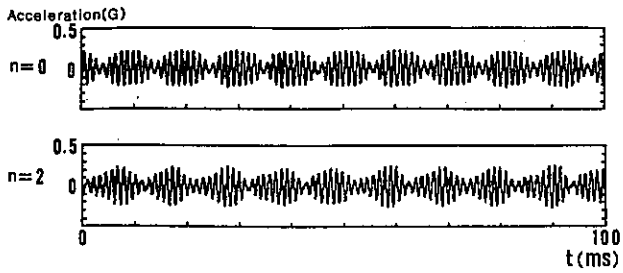

Fig.7 Comparison of Vibrations of Spindle Housing with and without Suppression of Whirling Motion
n : repetitive number of periodic learning control

5. Reduction of fluctuations of coil-currents in electromagnets

The vibration of the housing is usually undesirable because it is transmitted to the environment. Thus, to reduce the vibration of the housing is as important as to suppress the whirling motion.

The authors apply the PLC with the ITFC in order to reduce synchronous fluctuations of coil-currents of electromagnets, aiming at the reduction of the vibration of the housing.

The PLC with the ITFC to reduce the fluctuation of coil-currents has a procedure similar to the procedure for the suppression of the whirling motion. While the rotor displacement is treated as the output of the controlled system for the suppression of the whirling motion, the current control signals are treated as the output for the reductions of fluctuations of coil-currents. As T_f^{-1} is introduced for the suppression of the whirling motion, a 4-4 complex matrix S_f^{-1} which represents the characteristics of the inverse transfer function of the controlled system at the rotor speed is introduced. S_f^{-1} is calculated from S_f obtained by an experiment similar to the experiment carried out for T_f.

The procedure of the PLC with the ITFC to reduce the fluctuations of current control signals is as follows:

[n.1] Compensation with $\mathbf{v}_n$ begins. $\mathbf{v}_n$ is given to the controlled system through four D/A converters every 10μs.
[n.2] $\mathbf{u}_n$ is sampled by the A/D converter every 10μs throughout one rotation at least. [n.2] is carried out when steady-state response can be observed.
[n.3] $\mathbf{u}_n^*$, which is the component of $\mathbf{u}_n$ with the same frequency as the rotor speed, is calculated by means of Fourier series expansion.
[n.4] $\mathbf{u}_n^*$ is multiplied by S_f^{-1} from the left side.
[n.5] The next compensatory input $\mathbf{v}_{n+1}$ is calculated by the following equation:

$$\mathbf{v}_{n+1} = - \sum_{k=0}^{n} S_f^{-1} \mathbf{u}_k^* \quad .$$

The experiment was carried out at the rotor speed of 950rps (57,000rpm). Fig.8 (a) shows that the first trial (n=1) of the PLC with the ITFC reduces the fluctuations of the current control signals and the vibration of the housing. Transient vibration did not disappeared in Fig.8 (a). The steady-state vibration when n=1 is shown in Fig.8 (b). This figure shows that the PLC with the ITFC drastically reduces the vibration of the housing. Fig.9 shows that only the synchronous fluctuation of current control signal u_x and only the synchronous vibration of the housing are reduced.

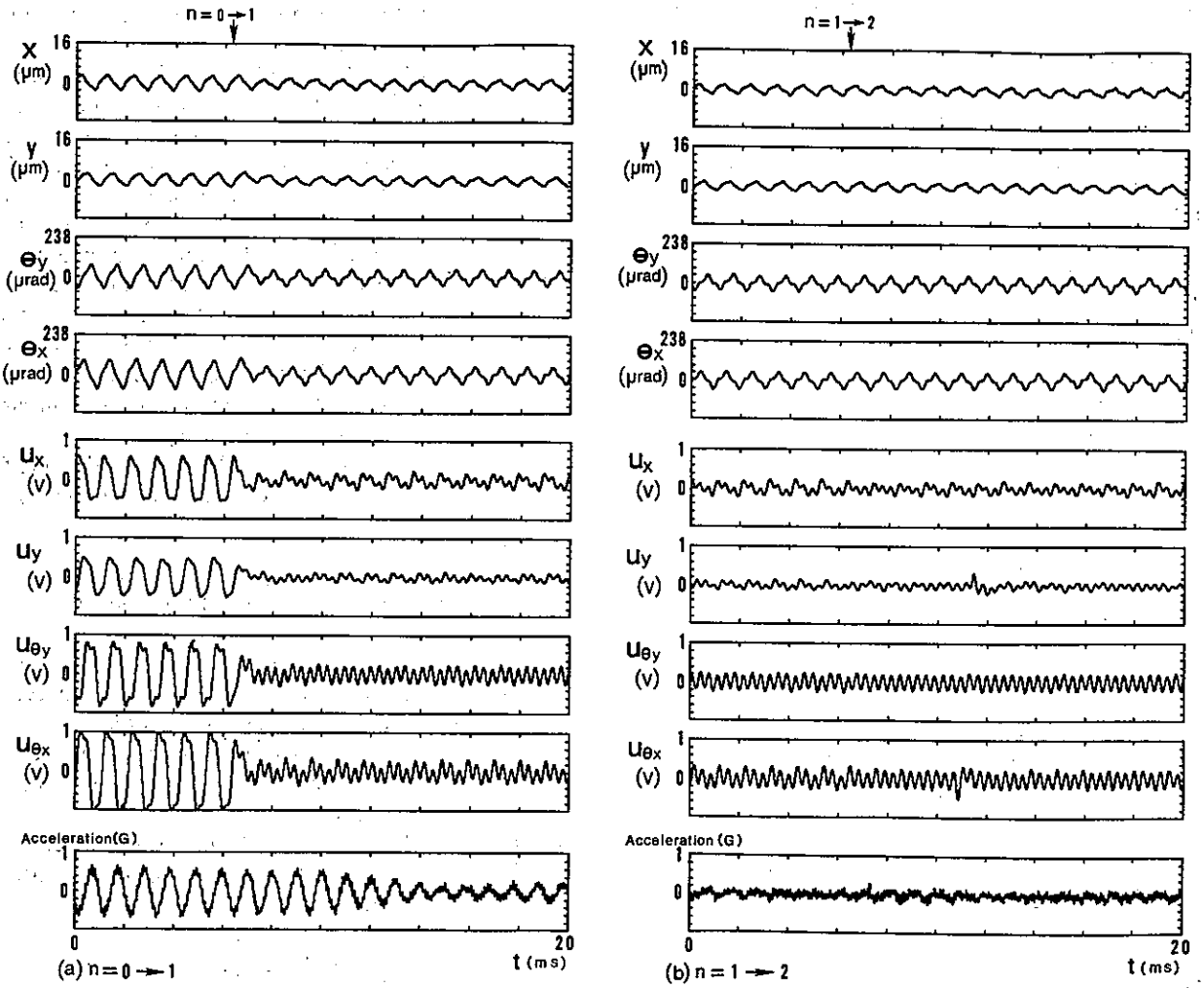

Fig.8 Reduction of Fluctuations of Current Control Signals, and Reduction of Vibration of Housing (950rps).
The accelerometer was attached to the metal band that fixes the spindle housing to the base.
x_y, θ_y: rotor displacement , $u_x, u_{\theta y}$: force control signals , n: repetitive number of the PLC

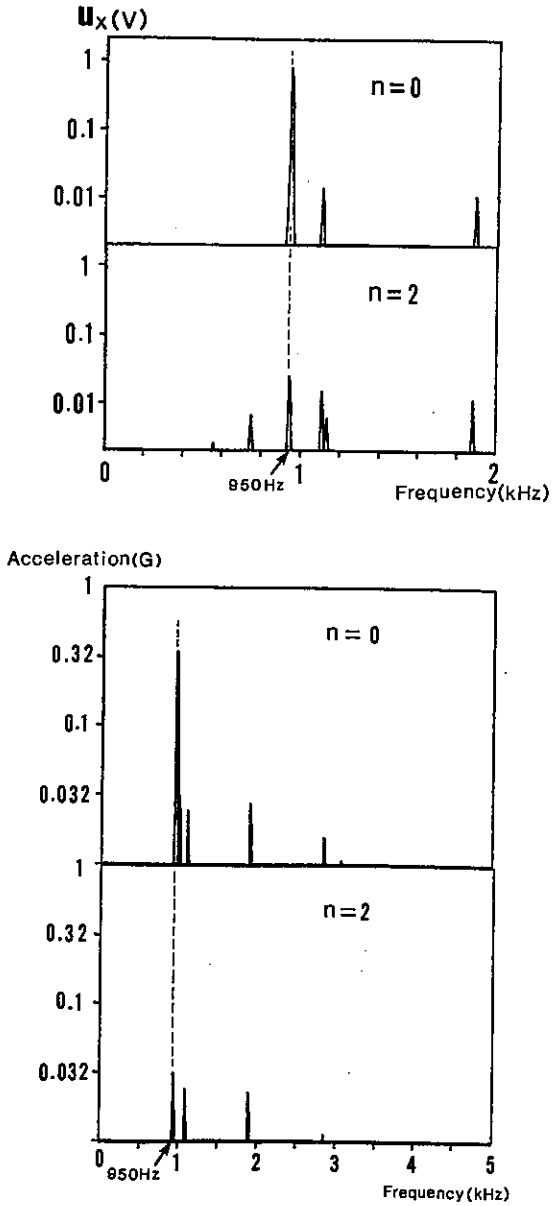

Fig.9 Fluctuation of Current Control Signal and Vibration of Spindle Housing in Frequency Domain

6. Applications and Future Prospects

In this paper, the authors have applied the PLC with the ITFC in the magnetic bearings stabilized by central control. The PLC with the ITFC can be applied also in the magnetic bearings stabilized by decentralized control in order to suppress the whirling motion and to reduce the vibration of the housing. The authors will report about this in [10].

Machine tools are subject to periodic disturbances such as cutting resistance. The PLC with ITFC can be applied in the magnetic bearings for machine tools because the PLC with ITFC can also compensate for periodic disturbances other than those caused by the mass imbalance.

The authors proposed the basic idea of two other applications of the PLC with ITFC to reduce the vibration of the housing. One is the PLC with ITFC which reduces the fluctuations of the forces of electromagnets[4]. This will effectively reduce the vibration of the housing even if the difference between the geometrical axis of the rotor and the principal axis of inertia is relatively large. The other is the PLC with ITFC in which compensatory inputs are added not to the current control signals but to sensor-outputs[11]. The amplitudes and the phase-angles of the compensatory inputs in this application vary very little even if the rotational speed changes. Therefore, the reduction of the vibration of the housing will be easily accomplished with this improved application when the rotor speed is increasing or decreasing.

The authors are aiming to carry out experiments to demonstrate the effects of the applications mentioned in this chapter.

7. Conclusion

The authors proposed to apply the PLC with the ITFC in magnetic bearings for solving the vibration problems. The implementation of the PLC with ITFC is easily accomplished by adding a digital controller to a conventional controller. The experiments were carried out to demonstrate that the PLC with the ITFC can suppress the whirling motion or can reduce the vibration of the housing. The results of the experiments are as follows: (1) Translational and tilting whirling motions are reduced from about $\pm 3\mu m$ to $\pm 1\mu m$, and from about $\pm 80\mu rad$ to $\pm 20\mu rad$, respectively, at the rotor speed of *51,000rpm* (*850rps*); (2) The vibration of the housing of the magnetic bearing spindle is reduced from about $\pm 0.6G$ to $\pm 0.1G$ in average at the rotor speed of *57,000rpm* (*950rps*).

Acknowledgment

We would like to thank Mr.M.Ota, Mr.S.Ando, and Mr.T.Kawashima of Seiko Seiki Co.,Ltd. for their continuous support and for allowing us to use their magnetic bearing spindle and their controller.

References

[1]MIZUNO,T. HIGUCHI,T.: Compensation for Unbalance in Magnetic Bearing Systems; Trans. SICE, Vol.20, No.12, pp.1095-1101 (1984).

[2]MATSUMURA,F. FUJITA,M. OIDA,C.: A Design of Robust Servo Controllers for an Unbalance Vibration in Magnetic Bearing Systems; Proc. of 1st Int. Symposium of Magnetic Bearings, pp.319-326 (1988).

[3]HABERMANN,H. BRUNET,M.: The Active Magnetic Bearing Enables Optimum Control of Machine Vibrations; ASME, Int. Gas Turbine Conf. No.84-GT-221 (1985).

[4]HIGUCHI,T. MIZUNO,T. OTSUKA,M.: Application of Periodic Learning Control Method to Magnetic Bearings; Linear-Drive, IEE-JPN, LD-89-48, pp.37-46 ('89-11).

[5]INOUE,T. et al: High Accuracy Control for Magnet Power Supply of Proton Synchrotron in Recurrent Operation; Trans. IEE-JPN, Vol.100-C, No.7, pp.234-240 (1980).

[6]KAWAMURA,S. MIYAZAKI,F. ARIMOTO,S.: System Theoretic Study on Learning Control Method; Trans. SICE, Vol.21, No.5, pp.445-450 (1985).

[7]HIGUCHI,T. YAMAGUCHI,T.: The Non-Circular Profile Machining by a Lathe with Numerical Controlled Electro-Hydraulic Servo-Mechanism; Proc. 6th Int. Conf. on Production Engineering Osaka 1987, JSPE.

[8]HIGUCHI,T. MIZUNO,T. OTSUKA,M.: Compensation for Mass Imbalance Using Periodic Learning Control Method in Magnetic Bearing System; Trans. ISCIE, Vol.3, No.5, pp.147-153 (1990).

[9]HIGUCHI,T. MIZUNO,T. OTSUKA,M.: Reduction of Fluctuations of Coil-Currents Using Periodic Learning Control in Totally Active Magnetic Bearings; Proc. JSPE, Spring-1990, pp.73-74.

[10]Authors: Compensation for Mass Imbalance Using Periodic Learning Control in Magnetic Bearings--- Support without Vibration by Modification of Sensor Output; Proc. JSPE, Autumn-1990, (to be published).

[11]OTSUKA,M. HIGUCHI,T. MIZUNO,T.; Comparison of Magnetic Bearing Control Systems for Rotation around Principal Axis of Inertia;Proc. 2nd Sympo. on Electromagnetic Force, IEE-JPN (1990-6), pp.414-419.

2nd International Symposium on Magnetic Beaing
July 12-14, 1990, Tokyo, Japan

REAL TIME BALANCING OF A FLEXIBLE ROTOR SUPPORTED BY MAGNETIC BEARING

Y. KANEMITSU , M. OHSAWA , K. WATANABE
EBARA RESEARCH CO.,LTD.
2-1 Hon Fujisawa 4-chome, Fujisawa-shi , 251 , JAPAN

Abstract

In this paper, the validity of a digital compensator of 5-axis magnetic bearing with a DSP for levitating a flexible rotor was confirmed by rotation test of the rotor operating beyond the bending natural frequencies of rotor.

After that, a real time balancing system was made, in which the digital compensator board with DSP for levitatig the rotor were employed and synchronous correction signals for balancing were synthesized by the DSP board to add to compensation signal and to cancel initial unbalance in the rotor. In a real time balancing test by using the combination of the analog and digital boards,the initial shaft vibration disappeared below the 1st bending critical speed. In another test, rotor vibration was suppressed under one tenth of initial value by the real time balancing using the digital compensator.

1 Introduction

A magnetic bearing which uses DC magnets and proxmity sensors measuring relative displacement between rotor and stator regulates magnet coil current to keep journal position constant and suppress rotor vibration. However it is difficult to make loop gain of it's controller larger because of the occurence of unstable vibration of levitated rotor, so that the shaft vibration caused by unbalance in rotor remains.

We have made a five axis active magnetic bearing as an experiment and controlled it by using an analog circuit and a digital IIR filter circuit as compensator in order to levitate a flexible rotor[1].

A digital compensator is suitable for adaptive or optimal control of a magnetic bearing because the properties of the compensator can be easily changed by modification of it's software. Real time balancing test of the rotor is carried out by using the digital compensator. The effective coefficient method is employed for the balancing, where effictive coefficient between a control signal from the compensator and sensor output is automatically estimated by a host personal computer.

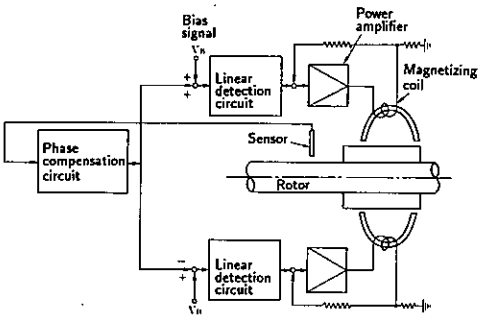

Fig.1 Block diagram of the rotor-AMB system

2 Test apparatus

2.1 Configuration of controller

Each axis of the active magnetic bearing(AMB) is regulated individually and it's controller is made up of a shift circuit of a displacement signal, a compensation circuit, two driver circuit and two power amplifiers. The block diagram of the system is shown in fig.1.

2.2 Rotor

Fig.2 shows a test apparatus for attesting the ability of the analog compensator and the digital compensator to levitate and balance a flexible rotor. The shaft is 531mm in length, and 26mm in maximum diameter. A induction motor rotor

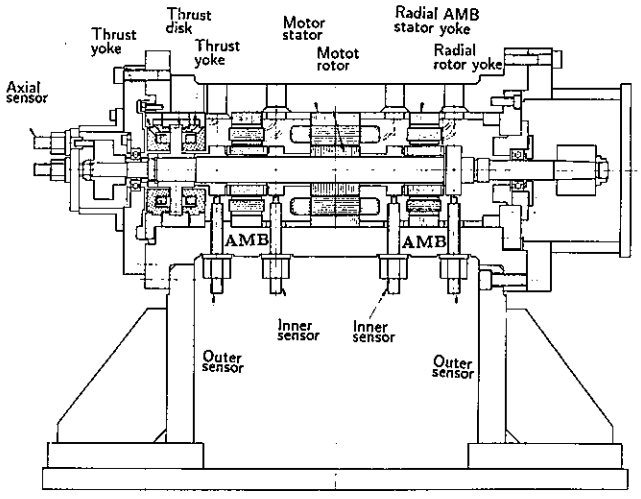

Fig.2 Test apparatus

is located in the middle of the shaft and two radial magnetic bearing(RMB) are situated on both sides of the motor rotor. A thrust magnetic bearing(TMB) is located at left end of shaft. Eddy current type proximity sensors with two mounting holes are prepared for the RMB sensors at both sides of the bearing, but inner sensors are used in tests. The natural frequencies and modes of the tested rotor was measured in a free-free condition and the measured results are presented in fig.3. The 1st and 2nd natural frequencies of the rotor were 290Hz and 690Hz, but in the real-time balancing test the 1st and 2nd natural frequencies became 340Hz and 760Hz respectively, because of modifying shapes of an unbalance disk attached at right end of the shaft and a sensor disk attached at left end of the shaft between rotation tests and balancing tests for the purpose to get a synchronous reference sine wave.

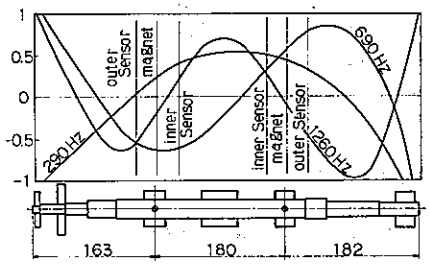

Fig.3 Natural frequencies and modes

2.3 Control using with analog compensator

For an analog compensator, a compensation circuit(A) containing a low-pass filter at high-frequencies and ones(B) without it were made and their measured transfer functions are as shown in fig.4.

In case of the rotation test using the analog compensator(A), the rotor reached 32,000rpm, but 1st natural vibration occured at this speed.

Fig.5 shows results of a rotating test using the compensator(B) which has a larger phase-lead than compensator(A) as shown in fig.4. The rotating speed reached 40,000rpm by compensator(B) without unstable vibration because of the increase in phase-lead. Maximum rotating speed in a series of ratating tests is 40,000rpm which is just below the second bending critical speed of 42,000rpm. As each test has no rigid mode resonance, and small resonance of 1st bending mode, we proved that the analog compensator has sufficient damping action in these frequency ranges.

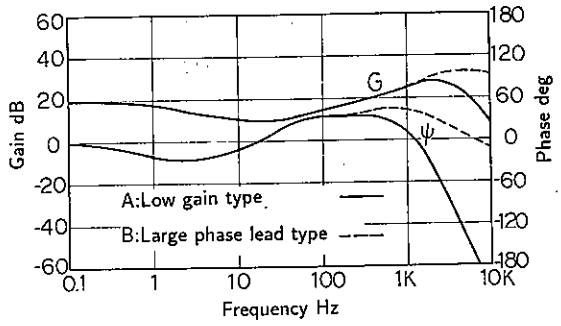

Fig.4 Transfer functions of analog compensators

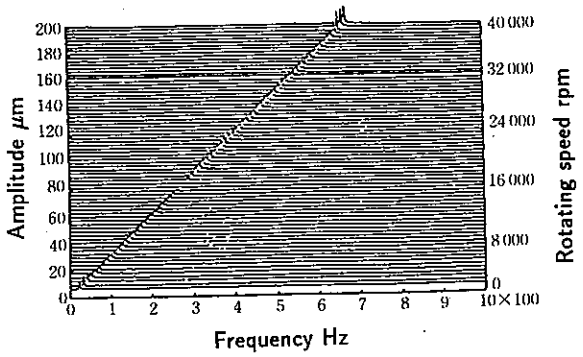

Fig.5 Waterfall diagram of rotating test
[with analog compensator(B)]

2.4 Digital compensator with DSP

Based on an analog compensator(B) where the speed was raised beyond the 1st bending natural frequency of the rotor, an digital IIR filter compensator was prepared. The analog compensator must have parts on board changed when it is necessary to change their filter characteristics. With digital compensators, their filter characteristics are altered by changing contents of a filter coefficient memory. Therefore an optimal or adaptive control may be realized if it is possible to change the memory contents during operation.

When the transfer fanction G(s) on s-plane is given, the transfer function D(z) on z-plane is found by the bilinear transformation[2,3] expressed below.

$$D(z) = G(s)|_{s=\frac{2(1-z^{-1})}{\Delta T(1+z^{-1})}} \tag{1}$$

Where ΔT is the sampling period. As the relation between input $X(z)$ and output $Y(z)$ of n stages 2nd order IIR filter can be expressed as follows,

$$\frac{Y(z)}{X(z)} = D(z) = \prod^{n} \frac{b_0 + b_1 z^{-1} + b_2 z^{-2}}{1 + a_1 z^{-1} + a_2 z^{-2}} \tag{2}$$

The filter output $Y(z)$ can be found by calculating the output of each stages sequentially. The output $u(n)$ of each stage at $t = n\Delta T$ is found as follows:

$$\begin{aligned} u(n) &= b_0 e(n) + b_1 e(n-1) + b_2 e(n-2) \\ &\quad -a_1 u(n-1) - a_2 u(n-2) \end{aligned} \tag{3}$$

Fig.6 shows a block diagram of the digital compensator. A digital signal processor(DSP TI/TMS320C25) is used to implement the IIR filter type compensator which carrys out the equation(3). With this DSP, a high-speed 12-bit A/D con-

verter, of which conversion time is 2μsec, and three 12-bit D/A converters were used to make 3 compensators consisting of 7 stages 2nd-order IIR filters. The sampling frequency is 4000Hz for each axis (12kHz in total) at an instruction time of 125ns. A host personal computer(HPC) controls transference of data between the DSP and the HPC through a programmable peripheral interface (PPI μPD71055) and estimates unbalance of the rotor. The AMB system with this filter shown in fig.7 converts analog signals from the proximity sensors to digital signals by the A/D converter and stores them in the data memory on the DSP board . It also changes the compensated digital signals to analog signal for output by the D/A converter.

A comparison between transfer functions of analog and digital filter are shown in Fig.8. An IIR filter(1) is designed to have the same properties as the analog compensator(B) and an IIR filter(2) has an additional 2nd order phase lag-lead stage. The gain G of IIR filter(1) agrees with the analog compensator up to 700Hz. Beyond this frequency, however, the gain of filter(1) increases and fall abruptly beyond a certain frequency. In order to attain an adequate phase lead at 1st and 2nd bending natural frequencies of the rotor, another IIR filter(2) was made by adding a 2nd order phase lag-lead stage to the IIR filter(1).

2.5 Control using digital compensator

With the IIR filter(2) whose phase for the range including the natural frequencies of the rotor is advanced sufficiently as shown in fig.8, a waterfall diagram of radial vibration in the rotation test was attained as shown in fig.9. As the result the response is fully damped even at the bending critical speed 18,000 rpm. This means that the vibration of the rotor is fully controllable by means of the phase compensation. With this filter the speed was raised to 28,000rpm.

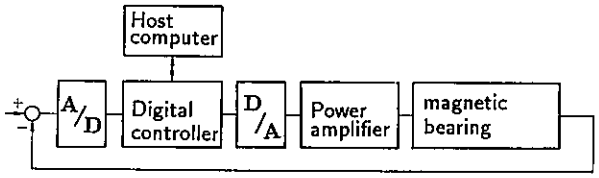

Fig.7 AMB system with the digital compensator

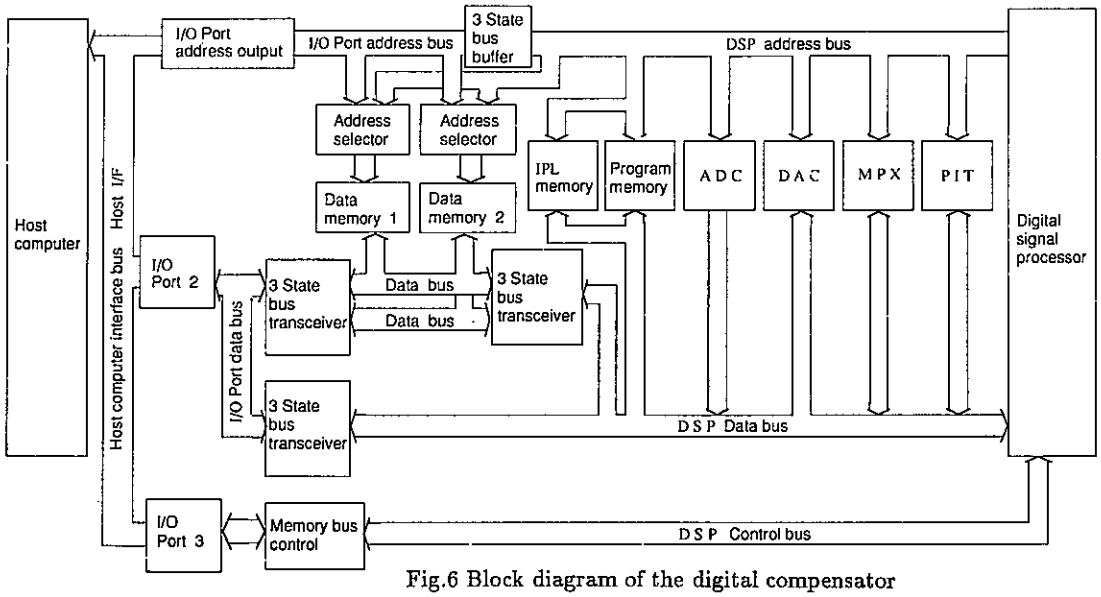

Fig.6 Block diagram of the digital compensator

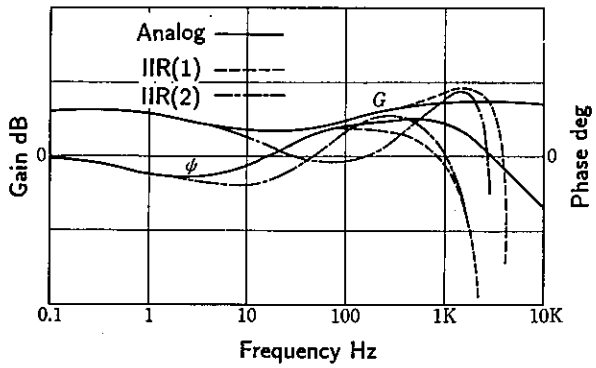

Fig.8 Comparison between the transfer function of analog and digital filters

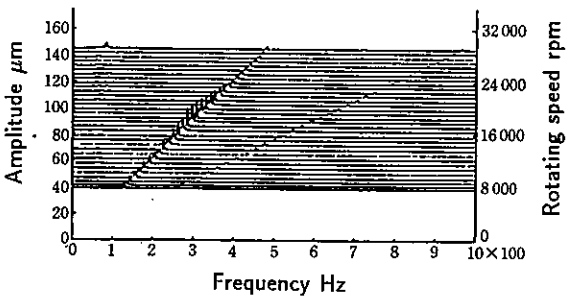

Fig.9 Waterfall diagram [with IIR filter(2)]

3 Method of real time balancing

In fig.10 which shows a block diagram of AMB-rotor system whirled by disturbance from mass unbalance, we attempt to suppress the vibration caused by unbalance disturbance $Fux(, Fuy)$ by adding a correction signal $Wx(, Wy)$, which synchronizes with rotating speed, to the compensation signal for levitating the rotor at an entrance of power amplifier in the way that the correction signal cancels the unbalance disturbance.

If we know a transfer function between synchronous correction signal and sensor output $G(s) = X/W_x$, we can easily get control input W_x by dividing sensor output by the transfer function $G(s)$. But it is very difficult to measure the transfer function at rotating frequency during rotation by a serbo analyser owing to the existance of synchronous vibration by unbalance.

Therefore we attempt to balance the rotor in almost the same way as so-called "effective coefficient method" employed in the field of balancing turbomachinery rotor as follows:

1. Trial inputs W_{xj}, W_{yj} meeting following equations are added to output signals of orthogonal compensators in the DSP according to a command from the HPC on the basis of the reference sine wave made by a eccentric disk attached at left end of the rotor.

$$W_{xj} = -W_j \cos(n\omega\Delta T + \theta_j) \tag{4}$$

$$W_{yj} = -W_j \cos(n\omega\Delta T + \theta_j + \pi/2) \tag{5}$$

where j is bearing number and ΔT is sampling period (1/4,000 sec).

2. Initial sensor outputs X_{k0}, Y_{k0}(k is sensor number) without the trial inputs and sensor outputs X_{kj}, Y_{kj} with the trial inputs W_{xj}, W_{yj} are written into memory on the DSP once and transfered from the DSP memory to the HPC memory.

3. Effective coefficients $a_{11} \ldots a_{42}$ between the trial inputs W_{xj}, W_{yj} and sensor outputs X_{kj}, Y_{kj} are calculated by the HPC as follows:

$$a_{1j} = \frac{\hat{X}_{1j}\exp(i\theta_{x1j}) - \hat{X}_{10}\exp(i\theta_{x10})}{\hat{W}_j \exp(i\theta_j)} \tag{6}$$

$$\vdots$$

$$a_{4j} = \frac{\hat{Y}_{2j}\exp(i\theta_{y2j}) - \hat{Y}_{20}\exp(i\theta_{y20})}{\hat{W}_j \exp(i\theta_j)} \tag{7}$$

where $\hat{X}_j, \theta_j$ are amplitude and phase of X_j respectively.

4. Amplitude W_j and phase θ_j of correction inputs W_{xj}, W_{yj} to correct the unbalance of rotor are estimated by the method of least squares and sent back to the DSP. Replacing a correction input vector $\mathbf{W}$, a initial sensor output vector $\mathbf{X}$,an effective coefficients matrix $\mathbf{A}$ and a residual vector $\mathbf{E}$ as follows:

$$\mathbf{W} = -[W_1 \exp(i\theta_1), W_2 \exp(i\theta_2)]^T \tag{8}$$

$$\mathbf{X} = [\hat{X}_{10}\exp(i\theta_{x10}), \hat{Y}_{10}\exp(i\theta_{y10}), \hat{X}_{20}\exp(i\theta_{x20}), \hat{Y}_{20}\exp(i\theta_{y20})]^T \tag{9}$$

$$\mathbf{A} = \begin{bmatrix} a_{11} & a_{12} \\ \vdots & \vdots \\ a_{41} & a_{42} \end{bmatrix} \tag{10}$$

$$\mathbf{E} = \mathbf{X} - \mathbf{A}\mathbf{W} \tag{11}$$

We obtain the correction input vector $\mathbf{W}$ on condition that $\mathbf{E}^T\mathbf{E}$ is minimized as follows:

$$\mathbf{W} = -(\mathbf{A}^T\mathbf{A})^{-1}\mathbf{A}\mathbf{X} \tag{12}$$

5. Synchronous correction inputs W_{xj}, W_{yj} to correct the unbalance are added to output signal of each compensator in the same way as 1..

First, the trial input Wx is added at output of compensator of each bearing controller and sensor output is measured . The measured signal is transfered from the DSP memory to the HPC while the rotor is rotating . A effective coefficient between the input W_x and the sensor output signal X is calculated by the HPC and amplitude and phase of correction signal W_x are determined .

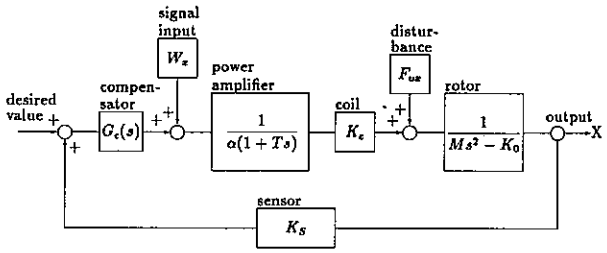

Fig.10 Block diagram of real time balance system of rotor levitated by AMB and whirled by unbalance

4 Method to make correction signals

Fig.11 shows a block diagram for explaining how to make the correction signals to compensate the unbalance of rotor by the DSP board and the HPC.

A procedure to make the signals is as follows:

1. The proximity sensor measures motion of the eccentric rotating disk attached at the left end of shaft and produces a reference sine wave. We employ phases between the vibration waveform the reference sine wave in the calculation of the effective coefficients to minimize a measurement error of phase.

2. A pulse signal per shaft rotation to trigger A/D conversion on is formed from the reference sine wave.

3. The number of system clock pulses(4MHz) during a rotation is counted by a PIT(Programmable Interval Timer, μPD71054) of which trigger signal is the pulse signal and is written in the data memory on the DSP board.

4. At the same time, the reference sine signal and the shaft vibrations are sequentially converted to digital signals by

the A/D converter, whose sampling frequency is 4KHz per channel, and 512 sampling data of each signal are kept in the memory.

5. The HPC communicates with the DSP board and reads the sampled data and the PIT data.

6. The HPC calculates fourier coefficients a, b of synchronous component with rotation of shaft as follows:

$$a = \frac{1}{256}\sum_{i=0}^{511} X(i)\cos(i\omega\Delta T) \tag{13}$$

$$b = \frac{1}{256}\sum_{i=0}^{511} X(i)\sin(i\omega\Delta T) \tag{14}$$

$$A = \sqrt{a^2+b^2}, \theta = \arctan(-b/a) \tag{15}$$

where $X(i), \omega, \Delta T, A$ and θ are sampled data, rotating speed, sampling period, amplitude and phase.

7. The calculated phases of shaft vibrations are corrected by subtracting the phase of the reference sine wave from them.

8. The synchronous correction inputs W_{xj}, W_{yj} to correct the unbalance calculated by the method based on the foregoing paragraph

9. The HPC communicates with the DSP board and writes the amplitude A and phase θ of synchronous correction input in the DSP memory.

10. A map of cosine values of each 2 degrees is prepared in the DSP memory beforehand.

11. The PIT measures a rotation period T and lapse time t from a last trigger pulse and the DSP calculates signal phases ψ_x, ψ_y of W_x, W_y based on the above-mentioned data as follows:

$$\psi_x = (\frac{2\pi t}{T} + \theta)\frac{180}{\pi} \tag{16}$$

$$\psi_y = (\frac{2\pi t}{T} + \theta)\frac{180}{\pi} + 90 \tag{17}$$

12. The correction values W_x, W_y are calculated by seeing the above-mentioned map of cosine values as follows:

$$W_x = A\cos\psi_x \tag{18}$$

$$W_y = A\cos\psi_y \tag{19}$$

13. The correction signals W_x, W_y are put out by the 12-bit D/A converters.

14. The process 11-13 are repeated every sampling.

Some waveforms of X and Y direction synthesized in the process 1-13 are shown in fig.12. In the case of low rotating speed, the synthesized waveform is smooth sine wave. But on the other hand the waveform becomes steped form of the sampling period 4000Hz when rotating speed is relatively high.

At first we employed the analog compensator for levitating the rotor and DSP board for balancing respectively. Secondly we used the DSP board for levitating and balancing the rotor.

5 Result of real time balancing

Fig.13 shows a system block diagram where we employed the analog compensator for levitating the rotor and DSP board for balancing respectively. Each of three known unbalances(3.2 , 4.5 , 27.9mmgr) is attached to the right end disk to change the unlabance of rotor and the rotor is raised to a prescrived speed. After that the real time balancing circuit was turned on and off sequentially and rotor vibrations at sensors of AMB were measured by FFT analyser and shown in fig.14-fig.18.

In fig.14, ordinate, abscissa and tilted co-ordinate represent amplitude of shaft vibration, frequency and time respectively when a smallest unbalance was attached and real time balancing was performed. At 10,000rpm initial synchronous vibration of 5μm almost vanished when the switch of the balancing circuit was on and again appeared when it was off. Vibration components except the synchronous vibration were not affected by this operation of the balancing. Waveforms of correction input and shaft vibration at 10,000rpm are shown

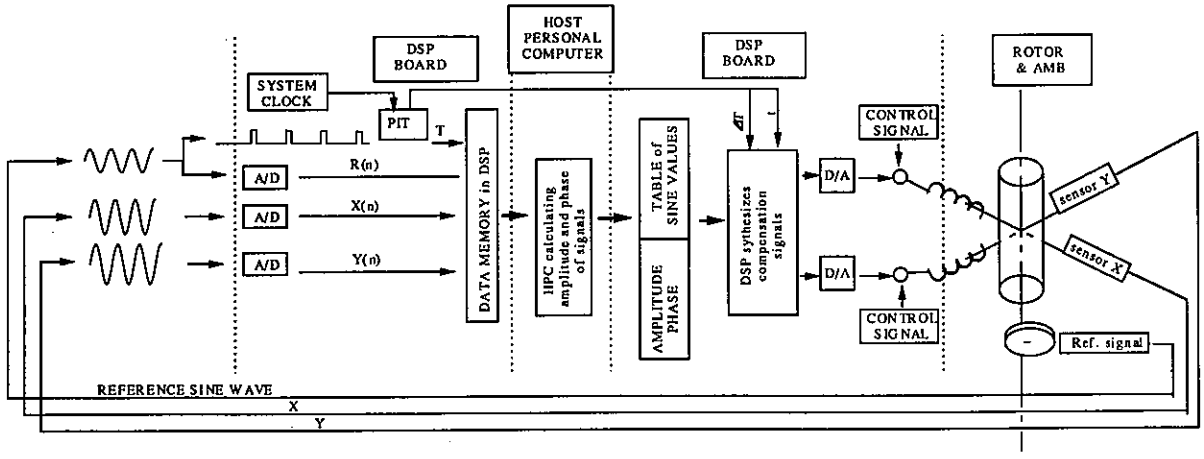

Fig.11 A block diagram for explaining how to make the correction signals

in fig.15. This figure shows that the correction input made by the DSP has the same period as the shaft vibration under balancing.

Near 1st bending critical speed(21,000rpm), initial vibration of 10μm decreases to 2μm under balancing in fig.14(b). Fig.16 shows waveforms of correction input and shaft vibration at 1st bending critical speed(21,240rpm). The correction input waveform becomes steped form of a sampling period ΔT because of high rotating speed.

Under executing the real time balance, initial vibration of 6μm decreases merely to 4μm at 30,000rpm and initial vibration does not change at 40,000rpm in fig.14(c)(d). Because impedance of the magnetizing coil of AMB bacomes large and the coil current are restricted to flow as the rotating speed increases, it is essential for improving the ability of the balancing to make the electric power source of the AMB larger or to make the coil impedance smaller .

Fig.17,18 show shaft vibration response where the attached unbalance became larger. The initial vibration remains at 21,000rpm in the case of 4.5mmgr, and the shaft vibration does not decrease at 15,000rpm in the case of 27.9mmgr. If we prepared a larger power source for the AMB, a large initial unbalance of rotor would be balanced even at high speed by the proposed method.

Next,we levitated and balanced the rotor only by the DSP board. A system block diagram in this case is shown in fig.19 and waveforms of shaft vibration and control signal at 10,000rpm is presented in fig.20.

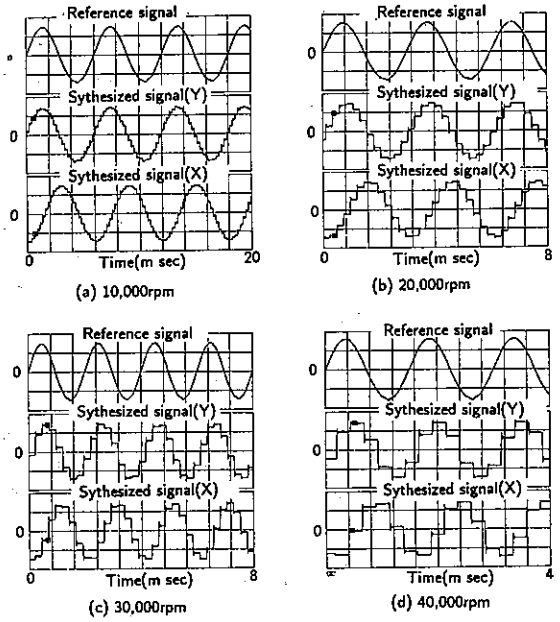

Fig.12 Synthesized waveform by DSP board

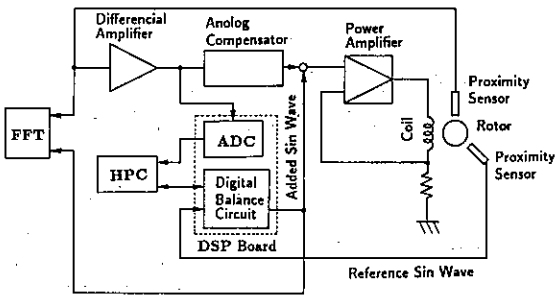

Fig.13 Block diagram of a hybrid system with an analog compensator and a digital balancing board

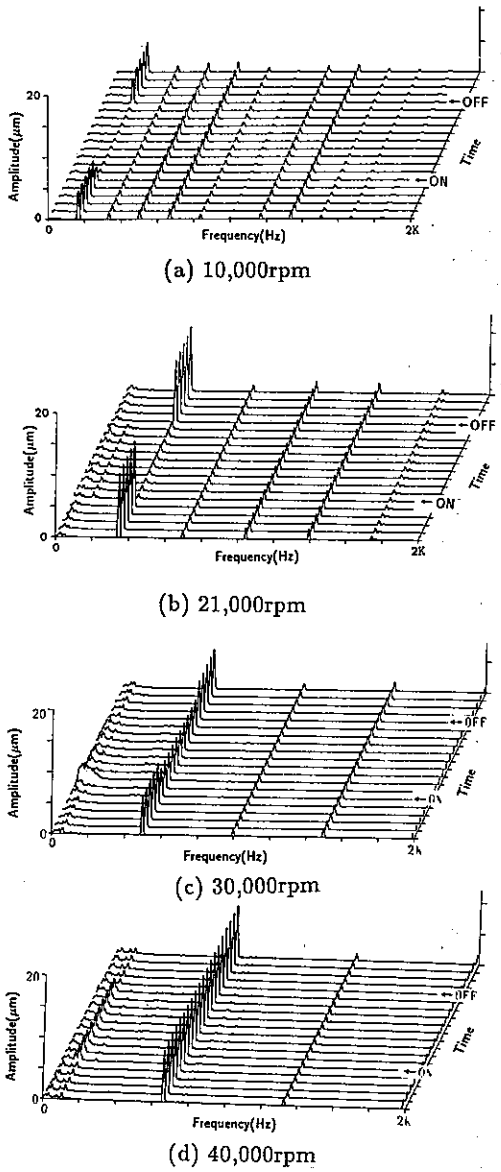

Fig.14 Waterfall diagrams of shaft vibration under balancing (unbalance=3.2mmgr)

According this test result, the shaft vibration under executing real time balance is one fifth of the vibration before balancing and the control signal supplied to the power amplifier under balancing is larger than that before balancing .

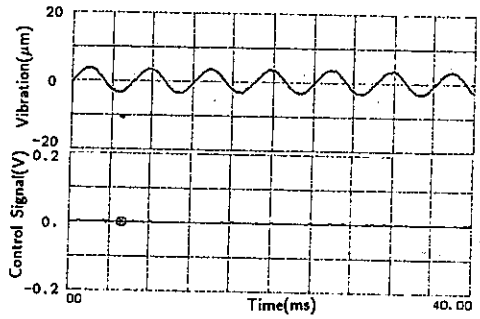

(a) before balancing

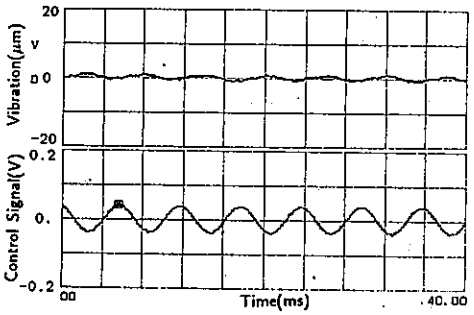

(b) under balancing

Fig.15 Waveforms of correction input and shaft vibration at 10,000rpm

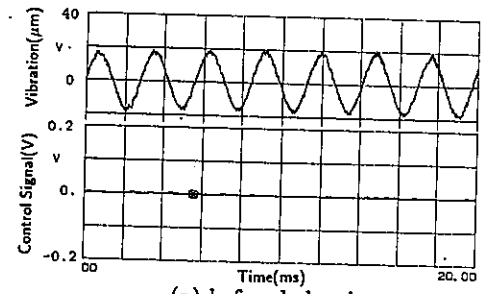

(a) before balancing

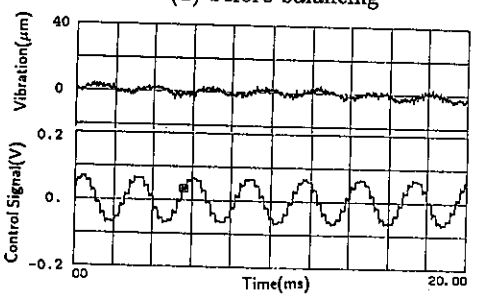

(b) under balancing

Fig.16 Waveforms of correction input and shaft vibration at 1st bending critical speed(21,240rpm)

From this test it become clear that the active magnetic bearing with digital controller is powerful actuator for balancing, especialy in the case that unbalance of a rotor changes while running.

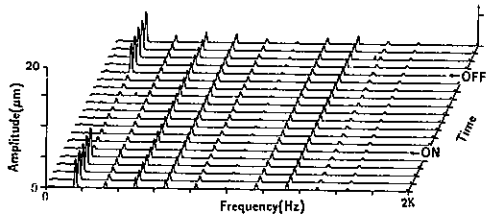

(a) 10,000rpm

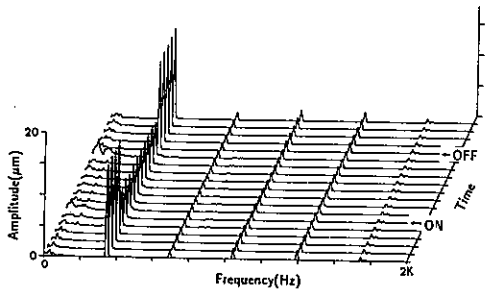

(b) 21,000rpm

Fig.17 Waterfall diagrams of shaft vibration under balancing (unbalance=4.5mmgr)

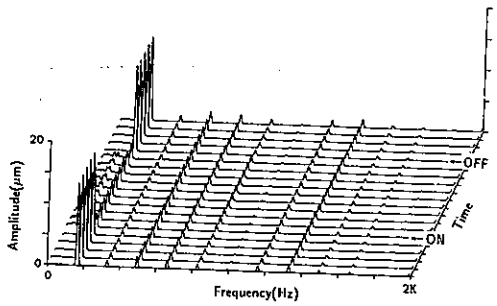

(a) 10,000rpm

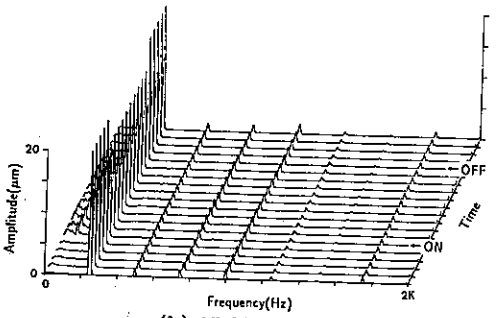

(b) 15,000rpm

Fig.18 Waterfall diagrams of shaft vibration under balancing (unbalance=27.9mmgr)

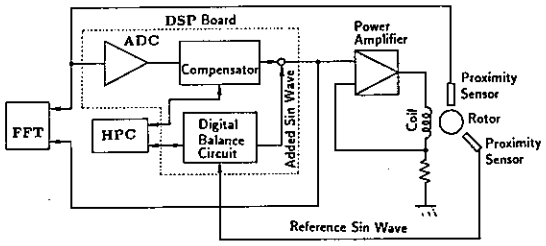

Fig.19 Block diagram of a system with DSP board for levitatig and balancing

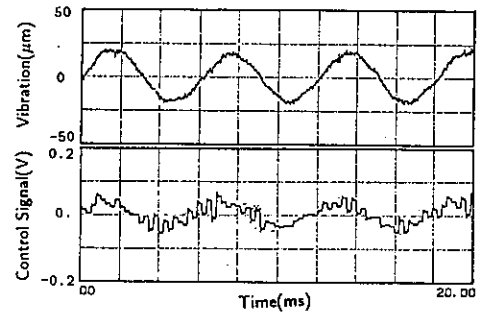

(a) before balancing

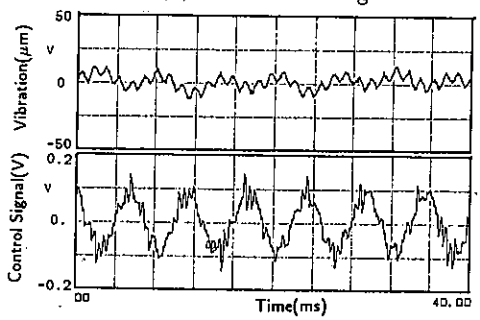

(b) under balancing

Fig.20 Waveforms of correction input and shaft vibration at 10,000rpm

6 Conclusion

We have made a real time balancing system in which the digital compensator board with DSP for levitatig the rotor are employed and synchronous correction signals for balancing are synthesized by the DSP board to add to compensation signal for levitation and to cancel initial unbalance in the rotor. In a real time balancing test by using the combination of the analog compensator and digital boards, the initial shaft vibration disappeared below the 1st bending critical speed.

In another test using only DSP board for levitating and balancing the rotor, the initial vibration was balanced by the DSP system at 10,000rpm.

7 References

[1] Kanemitsu,Y.,Ohsawa,M.,Watanabe,K. *Active Control of a Flexible Rotor by an Active Magnetic Bearing* Proc. 1st International Sympsium on Magnetic Bearings pp367-380(1988)

[2] Slivinsky,C.,Borniski,J. *Digital Signal Applications with TMS320 family* (Texas Instruments) pp689-724(1986)

[3] Kido,K. *Introduction to Digital Signal Processing* (in japanese) pp183-189 Maruzen(1985)

8 Nomenclature

a_{ij}	effective coefficient
$\mathbf{A}$	effective coefficient matrix
$D(z)$	transfer function on z-plane
$\mathbf{E}$	residual vector
F_{ux}, F_{uy}	unbalance disturbance
$G(s)$	transfer function on s-plane
j	actuater number
k	sensor number
ΔT	sampling period
W_x, W_y	correction input
T	rotating period
$\mathbf{W}$	correction input vector
X, Y	relative displacement
$\mathbf{X}$	initial vibration vector
θ	phase
ψ_x, ψ_y	phase of correction input
ω	rotating speed

2nd International Symposium on Magnetic Beaing
July 12-14, 1990, Tokyo, Japan

Modeling and Control of Magnetic Bearing Systems Achieving a Rotation Around the Axis of Inertia

Fumio Matsumura, Masayuki Fujita, and Kenji Okawa.
Dept. of Electrical and Computer Eng., Kanazawa University
2-40-20 Kodatsuno, Kanazawa 920, Japan

Abstract

This paper deals with the problem of an unbalance vibration in magnetic bearings. A rigorous modeling of a magnetic bearing system to achieve a rotation of the rotor around its axis of inertia is made. Then, an effective control scheme is proposed based on the state-space approach. The objective of the control scheme is to construct a controller which preserve internal stability and reject the disturbances. To solve this problem, output regulator with internal stability are introduced. The effectiveness of the proposed controller is demonstrated by a numerical example.

1. Introduction

Magnetic bearing systems have become practical in many industrial fields and numbers of studies for magnetic bearing systems have been reported. Especially, active control type magnetic bearing systems have been studied because of their several attractive features.

On the other hand, two critical problem exist in a application of the magnetic bearing systems. One is the problem of the interference caused by gyroscopic effect and the other is the problem of the vibration caused by the unbalance on the rotor. We deal with the latter problem.

In this paper, to solve this problem, a rotation of the rotor around the inertial axis is considered. First, a rigorous modeling of a magnetic bearing system in which the rotation of the rotor is on its axis of inertia is developed. Next, an effective control scheme is proposed based on the state-space approach. Finally, the effectiveness of the proposed controller is demonstrated by a numerical example.

2. Modeling

In this section, we derive the state equation of a magnetic bearing system in which the rotation of the rotor is on its inertial axis with the following assumptions:
(1) The rotor is rigid body.
(2) The unbalance is in the radial direction only.
(3) The unbalance is arbitraryly small such that the rotor rotates around the axis of inertia within a region that nonlinearity is negligible.
In this study, our interest is concerned in the relatively small motion about the equilibrium point and in the control problem of the radial direction.

Unbalance

The coordinates of the rotor X_r, Y_r, Z_r , called inertial axes, are set as shown in Fig. 1. ε is the distance between the center and the center of mass of the rotor, and τ is the angle of the inertial axis to the geometrical axis X_f. Fig. 2 shows the relationship between the coordinates of the stator and the rotor. The position of the center and the center of mass of the rotor are given as $F(x_f, y_f, z_f)$ and $G(x_r, y_r, z_r)$, respectively. When the rotor rotates around the inertial axis inclining at an angle of τ, the following equations hold in the relationship between the center and the center of mass and in the relationship between the geometric axis and the inertial axis, respectively.

$$\begin{bmatrix} y_f \\ z_f \end{bmatrix} = \begin{bmatrix} y_r \\ z_r \end{bmatrix} + \begin{bmatrix} \varepsilon\cos(\phi+\kappa) \\ \varepsilon\sin(\phi+\kappa) \end{bmatrix} \tag{1}$$

$$\begin{bmatrix} \theta_f \\ \psi_f \end{bmatrix} = \begin{bmatrix} \theta_r \\ \psi_r \end{bmatrix} + \begin{bmatrix} \tau\cos(\phi+\lambda) \\ \tau\sin(\phi+\lambda) \end{bmatrix} , \tag{2}$$

where κ and λ are initial value. These two equa-

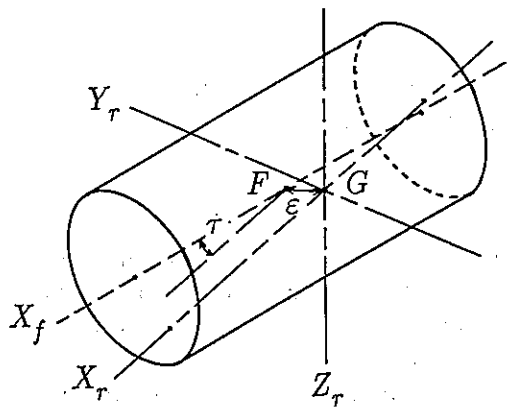

Fig.1 Coordinates of rotor

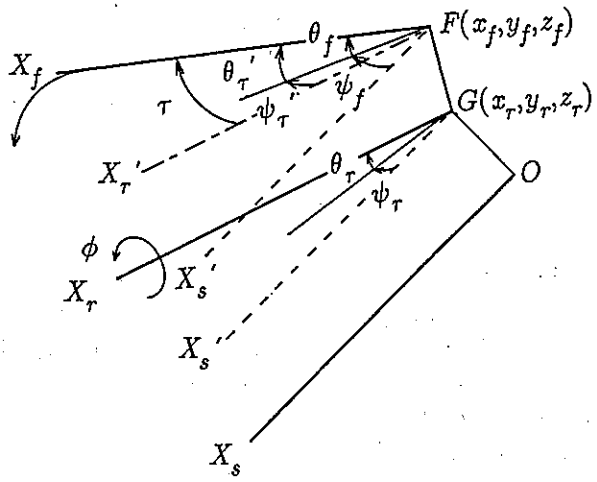

Fig.2 Relation between coordinates of stator and rotor

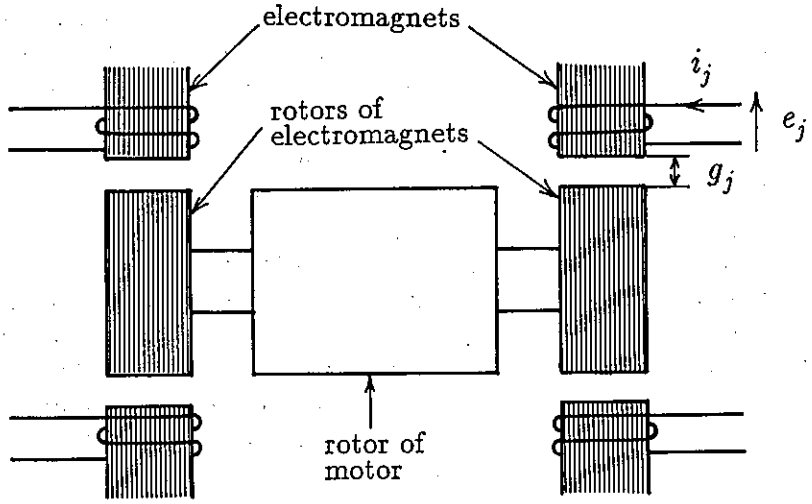

Fig.3 Structure and variables of magnetic bearing systems

tions are arranged in a vector form by writing

$$x_f = x_r + w. \tag{3}$$

where

$$x_f = \begin{bmatrix} y_f \\ z_f \\ \theta_f \\ \psi_f \end{bmatrix}, \quad x_r = \begin{bmatrix} y_r \\ z_r \\ \theta_r \\ \psi_r \end{bmatrix}, \quad w = \begin{bmatrix} \varepsilon\cos(pt+\kappa) \\ \varepsilon\sin(pt+\kappa) \\ \tau\cos(pt+\lambda) \\ \tau\sin(pt+\lambda) \end{bmatrix}.$$

Equations of Motion

The dynamical equations of the magnetic bearing systems in which the unbalance of the rotor is taken into consideration are given as follows

$$m\begin{bmatrix}\ddot{y}_r\\ \ddot{z}_r\end{bmatrix}=\alpha\begin{bmatrix}y_f\\ z_f\end{bmatrix}+\begin{bmatrix}f_{l3}-f_{l4}+f_{r3}-f_{r4}\\ f_{l2}-f_{l1}+f_{r2}-f_{r1}+mg\end{bmatrix}+\begin{bmatrix}f_{dy}\\ f_{dz}\end{bmatrix}+\alpha l_m\begin{bmatrix}-\psi_f\\ \theta_f\end{bmatrix} \quad (4)$$

$$J_y\begin{bmatrix}\ddot{\theta}_r\\ \ddot{\psi}_r\end{bmatrix}=pJ_x\begin{bmatrix}0 & -1\\ 1 & 0\end{bmatrix}\begin{bmatrix}\dot{\theta}_r\\ \dot{\psi}_r\end{bmatrix}+\begin{bmatrix}(f_{l1}-f_{l2})\,l_l-(f_{r1}-f_{r2})\,l_r\\ (f_{l3}-f_{l4})\,l_l-(f_{r3}-f_{r4})\,l_r\end{bmatrix}$$
$$+l_f\begin{bmatrix}-f_{dz}\\ f_{dy}\end{bmatrix}+\alpha l_m\begin{bmatrix}z_f\\ -y_f\end{bmatrix}+\alpha l_m{}^2\begin{bmatrix}\theta_f\\ \psi_f\end{bmatrix} \quad (5)$$

m : mass of the rotor
p : rotational speed of the rotor
J_x : moment of inertia about X_r
J_y : moment of inertia about Y_r or Z_r
l_r, l_l : length between the center of mass and the point of the force by the radial electromagnet of the right or left hand
f_{ri}, f_{li} : attractive force by each electromagnet of the right or left hand, i = 1 ~ 4
α : coefficient of the attractive force by the induction motor due to the shift of the rotor in the radial direction

Dynamical Equations in Electromagnet

Fig.3 shows the principle of the magnetic bearing systems. We use subscripts ri (i=1 ~ 4) , li (i=1 ~ 4) to denote each electromagnet. Letter e_j (j=ri or li) represents the voltage applied to each electromagnet. Similarly, i_j and g_j denote the current flowing into each electromagnet coil and the gap length between the rotor and each electromagnet, respectively. Using a linearization, the forces applied on the rotor by each electromagnet are written as follows in a matrix form in terms of the vector g_f and the vector i.

$$f = C_2g_f+C_3i = C_2C_1x_f+C_3i \quad (6)$$

where $g_f=[\,g_{l1}'\ g_{r1}'\ g_{l3}'\ g_{r3}'\,]^T$, $i=[\,i_{l1}'\ i_{r1}'\ i_{l3}'\ i_{r3}'\,]^T$, where letters with a prime denote a variation about the equilibrium point (cf.appendix).
Substituting (3) into (6) yields

$$f = C_2C_1x_r+C_3i+C_2C_1w. \quad (7)$$

In an electrical circuit including the electromagnet coil, the following dynamical equation holds.

$$\frac{d}{dt}i=-\frac{R}{L}Ii+\frac{1}{L}Ie \quad (8)$$

where

$$e=[\,e_{l1}'\ e_{r1}'\ e_{l3}'\ e_{r3}'\,]^T,$$

R :resistance of the electromagnet coil
L :inductance of the electromagnet coil

State Equation

Substituting (3), (7) and (8) into (4), we obtain

$$\begin{bmatrix}\dot{x}_r\\ \ddot{x}_r\\ \dot{i}\end{bmatrix}=\begin{bmatrix}0 & I & 0\\ A_1+B_1C_2C_1 & A_2P_1 & B_1C_3\\ 0 & 0 & (-R/L)I\end{bmatrix}\begin{bmatrix}x_r\\ \dot{x}_r\\ i\end{bmatrix}$$
$$+\begin{bmatrix}0\\ 0\\ (1/L)I\end{bmatrix}e+\begin{bmatrix}0\\ A_1+B_1C_2C_1\\ 0\end{bmatrix}w \quad (9)$$

(cf.appendix). Applying the coordinate transformation

$$g_r = C_1x_r \quad (10)$$

to the system (9) leads to

$$\dot{x}=\begin{bmatrix}0 & I & 0\\ C_1(A_1+B_1C_2C_1)C_1^{-1} & C_1A_2P_1C_1^{-1} & C_1B_1C_3\\ 0 & 0 & (-R/L)I\end{bmatrix}x$$
$$+\begin{bmatrix}0\\ 0\\ (1/L)I\end{bmatrix}e+\begin{bmatrix}0\\ C_1(A_1+B_1C_2C_1)\\ 0\end{bmatrix}w_1. \quad (11)$$

Since variables $g_f, \dot{g}_f, i$ can be measured, the output equation is given as follows.

$$y=\begin{bmatrix}I & 0 & 0\\ 0 & I & 0\\ 0 & 0 & I\end{bmatrix}\begin{bmatrix}g_r\\ \dot{g}_r\\ i\end{bmatrix}+\begin{bmatrix}C_{10}\\ C_{10}P_1\\ 0\end{bmatrix}w \quad (12)$$

These equations show that sinusoidal disturbances w_1 due to (caused by) the unbalance of the rotor affect the system dynamics and measured outputs. These disturbances can be described as the output of the autonomous system,

$$\dot{w}_1=P_1w=\begin{bmatrix}0 & -p & 0 & 0\\ p & 0 & 0 & 0\\ 0 & 0 & 0 & -p\\ 0 & 0 & p & 0\end{bmatrix}w\ ,\quad w(0)=\begin{bmatrix}\varepsilon\cos\kappa\\ \varepsilon\sin\kappa\\ \tau\cos\lambda\\ \tau\sin\lambda\end{bmatrix}. \quad (13)$$

3. Problem Statement

The system is described as the following equations.

$$\dot{x}=A(p)x+Bu+E_1w \quad (14)$$

$$\dot{w}=P_1(p)w_1 \quad (15)$$

$$y = C_1x+C_2(p)w \tag{16}$$

$$z = D_1x \tag{17}$$

where x is the state variable, u is the control input,
w is the disturbance, y is the measured output, and z is the controlled output. Matrices $A(p),P_1(p),C_2(p)$ have terms which increase in proportion to the angular velocity p. Our objective is to construct a controller which preserve internal stability and reject the disturbances ($z(t)\to 0$ as $t\to\infty$) at any rotational speed in the presence of uncertain initial conditions. To solve this problem, we introduce so-called " output regulator with internal stability " theory [1].

4. Design of Control System

Output Regulator with Internal Stability

The control system has the feedback configuration and the feedforward configuration. The control input is given by

$$u = K_1x+K_2w \ . \tag{18}$$

The feedback input K_1x provides an internal stability and the feedforward input K_2w provides an output regulation. Design procedure of this control law is composed of following three steps [2].
<step1>The system is stabilized by the state feedback. <step2>A feedforward input which cancels
the influence from the disturbance to the state to be controlled is computed. <step3>An observer is introduced to estimate unmeasurable state variables and disturbances. Then x,w in (18) are replaced by output of the observer.

$$u = K_1\hat{x}+K_2\hat{w} \tag{19}$$

Implementation

We construct a controller according to above-mentioned procedure. <step1>At any rotational speed the system (14) is stabilized by using the quadratic stabilization technique. This technique is effective to the variation due to gyroscopic effect.

$A(p)+K_1B$ is stable.

<step2> The feedforward input to achieve a asymptotic disturbance rejection at any rotational speed is computed as follows.
The eigenvalue of $P_1(p)$ and the eigenvector corresponding to each eigenvalue are computed.

$$\lambda_1 = \lambda_3 = jp \ , \ \lambda_2 = \lambda_4 = -jp \ ,$$

$$t_1 = \begin{bmatrix}1\\ j\\ 0\\ 0\end{bmatrix} \ , \ t_2 = \begin{bmatrix}1\\ -j\\ 0\\ 0\end{bmatrix} \ , \ t_3 = \begin{bmatrix}0\\ 0\\ 1\\ j\end{bmatrix} \ , \ t_4 = \begin{bmatrix}0\\ 0\\ 1\\ -j\end{bmatrix} \ .$$

For each λ_i,t_i , let (f_i, g_i) be a pair of vectors satisfying

$$\begin{bmatrix}\lambda_iI-A & B\\ D_1 & 0\end{bmatrix}\begin{bmatrix}f_i\\ g_i\end{bmatrix} = \begin{bmatrix}E_1\\ 0\end{bmatrix}t_i \tag{20}$$

Let

$$K_2 = -UT^{-1} \ .$$

where

$$U = [\ g_1 \ \ g_2 \ \ g_3 \ \ g_4\ ]$$

Calculating K_2 for the variation of the rotational speed, let K_2 be a function of p. Resulting feedforward gain matrix K_2 makes the transfer function from $w(0)$ to z zero.

$$T(s,p) = D_1\{sI-(A(p)+BK_1)\}^{-1}(E_1+BK_2)(sI-P_1(p))^{-1} \tag{21}$$
$$= 0$$

Minimal Order Observer

<step3> In this system, a part of the state variables of the system and the disturbances to the system can't be measured. Therefore, we employ a minimal oder observer to estimate these variables. The observer is designed for the following augmented system.

$$\begin{bmatrix}\dot{x}\\ \dot{w}\end{bmatrix} = \begin{bmatrix}A(p) & E_1\\ 0 & P_1(p)\end{bmatrix}\begin{bmatrix}x\\ w\end{bmatrix} + \begin{bmatrix}B\\ 0\end{bmatrix}u = A_c(p)x_c+B_cu \tag{22}$$

$$y = \begin{bmatrix}C_1 & C_2(p)\end{bmatrix}\begin{bmatrix}x\\ w_1\end{bmatrix} = C_c(p)x_c \tag{23}$$

Observability of the pair $(C_c(p), A_c(p))$ is guaranteed except for the case $p=0$. Hence, we restrict the rotational speed within a reasonable range. The minimal order observer is given,

$$\dot{\xi} = A(p)\xi+K_o(p)y \ , \tag{24}$$

$$\hat{x}_c = D(p)\xi+H(p)y \ , \tag{25}$$

where

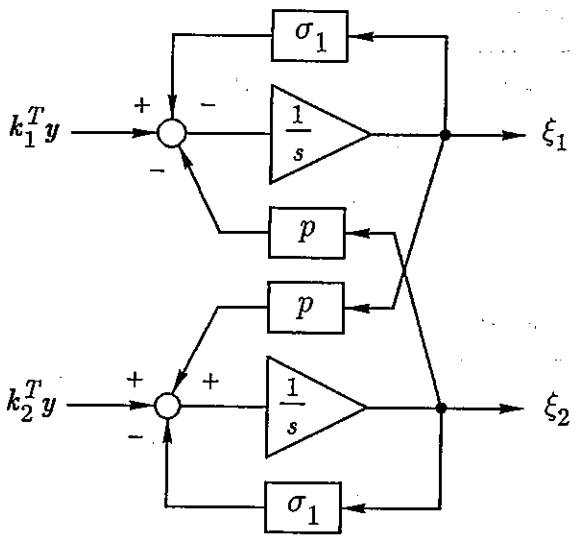

Fig.4 Internal model of sinusoidal disturbances

$$A(p) = P_1(p) - LE_3(p) \ ,$$

$$K_o(p) = A(p)L - LA(p) \ , \quad B = -LB = 0$$

$$D(p) = \begin{bmatrix} C_1 \\ C_1P_1(p) \\ 0 \\ I_4 \end{bmatrix} \ , \quad H(p) = \begin{bmatrix} I_4 + C_1L \\ I_4 + C_1P_1(p)L \\ I_4 \\ L \end{bmatrix} \ .$$

The observer is determined by specifying the observer gain matrix L . In specifying L , we use the turn over method to stabilize the observer at any rotational speed (except for $p=0$).

$A(p)$ is stable.

In this case, the resultant observer has an internal model of the disturbances as shown in Fig. 4. With the output of the above-designed observer, the control input is given as

$$u = K_1\hat{x} + K_2(p)\hat{w} \tag{26}$$

From (24),(25) and (26) such synthesis is achieved by the dynamical output feedback configuration.

5. Property of Composite System

We show that the proposed control system (24),(25) and (26) indeed preserves the internal stability and rejects the disturbances. Arrangement of (14),(24),(25) and (26) gives the following composite system.

$$\begin{bmatrix} \dot{x} \\ \dot{e} \end{bmatrix} = \begin{bmatrix} A(p)+BK_1 & -BK_1C_2(p)+BK_2(p)C_1 \\ 0 & A(p) \end{bmatrix} \begin{bmatrix} x \\ e \end{bmatrix} + \begin{bmatrix} E_1+BK_2(p) \\ 0 \end{bmatrix} w_1 \tag{27}$$

$$\dot{w} = P_1(p)w \tag{28}$$

where e is an error vector of the observer. If $w_1 = 0$ in (27), the composite system is asymptotically stable since $A(p)+BK_1$ and $A(p)$ are stable at any rotational speed.

Laplace transforms of (17),(27) and (28) lead the following equation.

$$\begin{aligned} Z(s) &= D_1X(s) \\ &= D_1\{sI-(A+BK_1)\}^{-1}x(0) \\ &\quad + D_1\{sI-(A+BK_1)\}^{-1}(-BK_1C_2+BK_2(p))(sI-A)^{-1}e(0) \\ &\quad + D_1\{sI-(A+BK_1)\}^{-1}(E_1+BK_2(p))(sI-P_1)^{-1}w(0) \end{aligned} \tag{29}$$

where $x(0), e(0), w(0)$ express the initial value of each variable. Since $A(p)+BK_1$ and $A(p)$ are stable at any rotational speed, the first term and the second term of right side asymptotically approach to zero. Moreover, the third term is zero (see <step2>). Hence,

$$z(\infty) = 0$$

Therefore, effectiveness of the proposed controller is confirmed.

6. Numerical Example

Above-developed control scheme is applied for 4-axis active control type magnetic bearing system. Parameters of this system are given in Table 1,2. The system behavior is discussed for the variation of the rotational speed from 0rpm to 10000rpm.

<step1> The system is stabilized within 10000rpm by the quadratic stabilization method. Then,

$$K_1 = \begin{bmatrix} 1.635e5 & -9.474e2 & 0 & 0 & 6.752e2 & -5.29 \\ -9.474e2 & 1.635e5 & 0 & 0 & -5.29 & 6.752e3 \\ 0 & 0 & 6.735e4 & -6.526e2 & 0 & 0 \\ 0 & 0 & -6.526e2 & 6.735e4 & 0 & 0 \end{bmatrix}$$

$$* \begin{bmatrix} 0 & 0 & -1.42e2 & 9.953e-1 & 0 & 0 \\ 0 & 0 & 9.953e-1 & -1.42e2 & 0 & 0 \\ 4.474e2 & -7.805 & 0 & 0 & -8.945e1 & 1.152 \\ -7.805 & 4.474e2 & 0 & 0 & 1.152 & -8.945e1 \end{bmatrix}$$

Table 1 Parameters of rotor

item	letter	value	unit
Mass of rotor	m	1.39×10^{1}	kg
Moment of inertia about X_r	J_x	1.348×10^{-2}	kg ·m^2
Moment of inertia about Y_r	J_y	2.326×10^{-1}	kg ·m^2
Length	$l_r(l_l)$	1.3×10^{-1}	m

Table 2 Parameter of electromagnet

item	letter	value	unit
attractive force	F_{l1}	9.09×10	N
	F_{l2}	2.20×10	N
	F_{l3}	2.20×10	N
	F_{l4}	2.20×10	N
	F_{r1}	9.09×10	N
	F_{r2}	2.20×10	N
	F_{r3}	2.20×10	N
	F_{r4}	2.20×10	N
coil current	I_{l1}	6.3×10^{-1}	A
	I_{l2}	3.1×10^{-1}	A
	I_{l3}	3.1×10^{-1}	A
	I_{l4}	3.1×10^{-1}	A
	I_{r1}	6.3×10^{-1}	A
	I_{r2}	3.1×10^{-1}	A
	I_{r3}	3.1×10^{-1}	A
	I_{r4}	3.1×10^{-1}	A
gap length	W	5.5×10^{-4}	m
Resistance of coil	R	1.47×10	Ω
Inductance of coil	L	2.85×10^{-1}	H

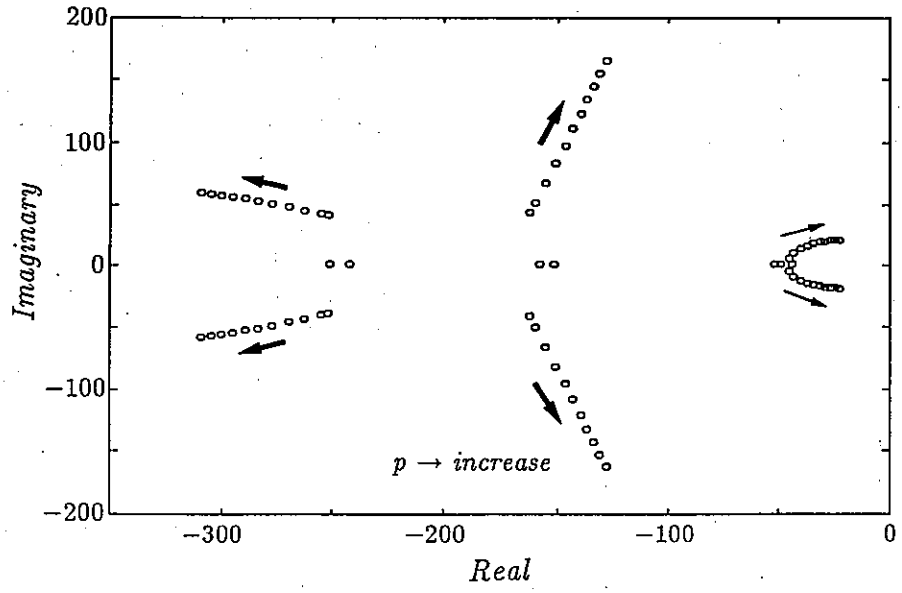

Fig.5 Root locus of closed loop system

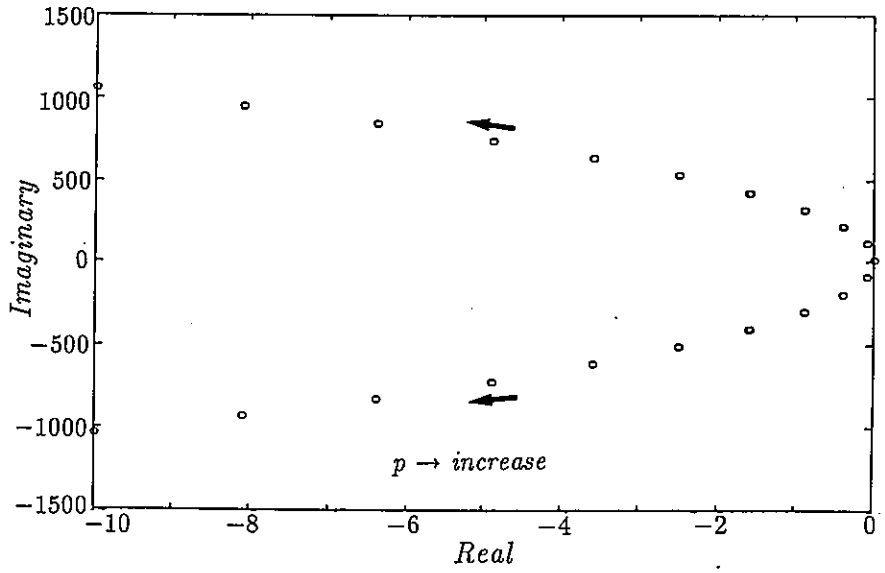

Fig.6 Root locus of observer

Fig. 5 shows the root locus of closed-loop system for the change of the rotational speed. Obviously, closed-loop system is stable at any rotational speed. <step2> Computation result of the feedforward gain is as follows.

$$K_1(p) = \begin{bmatrix} 2.718e2\times p & 1.504e5 & -1.93e4 & 3.535e1\times p \\ 2.718e2\times p & 1.485e5 & 1.955e4 & -3.535e1\times p \\ -5.22e4 & 1.606e2\times p & -2.089e1\times p & -8.476e3 \\ -5.22e4 & 1.606e2\times p & 2.089e1\times p & 8.476e3 \end{bmatrix}$$

$$= \begin{bmatrix} 0 & 2.718e2 & 3.535e1 & 0 \\ 0 & 2.718e2 & -3.535e1 & 0 \\ -1.606e2 & 0 & 0 & -2.089e1 \\ -1.606e2 & 0 & 0 & 2.089e1 \end{bmatrix} \begin{bmatrix} 0 & -p & 0 & 0 \\ p & 0 & 0 & 0 \\ 0 & 0 & 0 & -p \\ 0 & 0 & p & 0 \end{bmatrix}$$

$$+ \begin{bmatrix} 0 & 1.504e5 & -1.93e4 & 0 \\ 0 & 1.485e5 & 1.955e4 & 0 \\ -5.22e4 & 0 & 0 & -8.476e3 \\ -5.22e4 & 0 & 0 & 8.476e3 \end{bmatrix}$$

The gain matrix $K_2(p)$ has elements which are in proportion to the rotational speed.

<step3> Fig. 6 shows the root locus of the observer corresponding to the change of the rotational speed. The observer is stabilized at 10000rpm. In this case, poles of P is turned over against the axis $\mathrm{Re}\lambda=-5$. It can be seen that the system is stable except for $p=0$.

7. Conclusion

The modeling of a magnetic bearing system to achieve the rotation around its axis of inertia was developed. Then, based on the state-space approach, we proposed an effective control scheme for this problem. This problem was solved by using output regulator with internal stability theory. Constructing the dynamical output feedback controller, it has been shown that the unbalance compensation was achieved in a wide range of rotational speed.

8. References

[1]O.A.Sebakhy and W.M.Whonham:"A Design Procedure for Linear Multivariable Regulators" Automatica,12,467(1976)

[2]H.Kimura:"Observer-based Regulator Synthesis" Osaka University Technical Report, 85-4 (1985)

appendix

$$A_1 = \begin{bmatrix} \alpha/m & 0 & 0 & -\alpha l_m/m \\ 0 & \alpha/m & \alpha l_m/m & 0 \\ 0 & \alpha l_m/J_y & \alpha l_m^2/J_y & 0 \\ -\alpha l_m/J_y & 0 & 0 & \alpha l_m^2/J_y \end{bmatrix},$$

$$A_2 = \begin{bmatrix} 0 & 0 & 0 & 0 \\ 0 & 0 & 0 & 0 \\ 0 & 0 & J_x/J_y & 0 \\ 0 & 0 & 0 & J_x/J_y \end{bmatrix}, \quad P_1 = \begin{bmatrix} 0 & -p & 0 & 0 \\ p & 0 & 0 & 0 \\ 0 & 0 & 0 & -p \\ 0 & 0 & p & 0 \end{bmatrix},$$

$$B_1 = \begin{bmatrix} 0 & 0 & 1/m & 1/m \\ -1/m & -1/m & 0 & 0 \\ l_l/J_y & -l_r/J_y & 0 & 0 \\ 0 & 0 & l_l/J_y & -l_r/J_y \end{bmatrix},$$

$$C_1 = \begin{bmatrix} 0 & 1 & -l_l & 0 \\ 0 & 1 & l_r & 0 \\ -1 & 0 & 0 & -l_l \\ -1 & 0 & 0 & l_r \end{bmatrix}$$

$$C_2 = -\frac{2}{W} diag\left[F_{l1}+F_{l2}\,,\, F_{r1}+F_{r2}\,,\, F_{l3}+F_{l4}\,,\, F_{r3}+F_{r4} \right]$$

$$C_3 = 2\,diag\left[\left(\frac{F_{l1}}{I_{l1}}+\frac{F_{l2}}{I_{l2}}\right), \left(\frac{F_{r1}}{I_{r1}}+\frac{F_{r2}}{I_{r2}}\right), \left(\frac{F_{l3}}{I_{l3}}+\frac{F_{l4}}{I_{l4}}\right), \left(\frac{F_{r3}}{I_{r3}}+\frac{F_{r4}}{I_{r4}}\right) \right]$$

2nd International Symposium on Magnetic Beaing
July 12-14, 1990, Tokyo, Japan

DESIGN of MAGNETIC BEARING CONTROLLERS BASED ON DISTURBANCE ESTIMATION

T.MIZUNO* and T.HIGUCHI**

*Faculty of Engineering, Saitama University, Shimo-Okubo Urawa 338, Japan
**Institute of Industrial Science,The University of Tokyo, Minato-ku, Tokyo 106, Japan

Abstract

In order to minimize AC power dissipation in the electromagnet or vibratory force transmitted to the base through the bearing, two control methods are presented which use disturbance estimation generated by the observer for unbalance. One is designed to eliminate periodic component from control input asymptotically. By using this method, even an unbalance rotor can be suspended stably with fixed exciting current. The other is designed to eliminate oscillatory component from bearing force. This method enables the rotor to rotate about its principal axis. Another control method is presented which feeds back rate-plus-displacements of the center of mass and the principal axis of rotor. Such signals are obtained by compensating synchronous observatory disturbances by using the output of the observer. It is shown that the three control methods are equivalent if the bias magnetic flux is null.

1. Introduction

An unbalance on a rotor causes whirling motions of the rotor and alternating forces of the bearings in rotating machines. The authors have shown a magnetic bearing control system in which an unbalanced rotor can be suspended without whirling[1]. The concept of designing the control system was that the effects of unbalance were estimated by an observer and canceled by the electromagnetic forces of the bearing. With the control method applied, the position of the rotor can be maintained at the desired position with high precision. However, it is suitable for some machines to minimize the variation of exciting currents or vibratory force transmitted to the base through the bearing. In this paper, control methods are presented which can eliminate stationary alternating components from exciting currents or electromagnetic forces and keep them constant by using the output of the observer. Another control method is presented which feeds back the estimated signals of the displacement of the principal axis; such signals are obtained by compensating synchronous observatory disturbances by use of the output of the observer. It will be shown that the proposed three control methods are equivalent when the bias magnetic flux is null. Effectiveness of the proposed control methods are verified by simulation.

2. Modeling

A model, which is used for investigation of a typical totally active magnetic bearing system dynamics, is shown in **Fig.1**. Since the rotor is treated as a rigid body in this paper, it has six degrees of freedom of motion. In order to keep the rotor rotating about an fixed axis, the magnetic bearing has to control five degrees of freedom of motion. The eight electromagnets, which are numbered as ①,...,⑧ in **Fig.1**, are used to control two translational motions and two rotational motions in the radial directions. The two electromagnets which are numbered as ⑨, ⑩ are used to control one translational motion in the axial direction.

To derive the equations of motion, a coordinate frame O-xyz fixed in space is defined as shown in **Fig.2**; the origin O corresponds to the center of the rotor S in the desired position and z-axis corresponds to its rotating axis.

The attractive force of the n^{th} magnet is represented as F_n. The directions of $F_1,\ldots,F_8$ are also shown in **Fig.2**. For small motions about the stationary, F_n can be approximated by a linear relation:

$$F_n=F_0-Gd_n+Hi_n \quad n=1,\ldots,8 \qquad (1)$$

where

F_0:stationary force

G,H:coefficients of the linearized model of the magnet

i_n:incremental current flowing through the winding

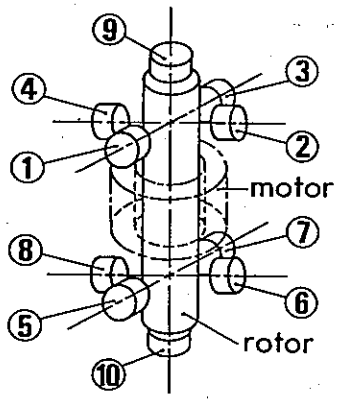

Fig.1 Model of a totally active magnetic bearing (①- ⑩ : electromagnets)

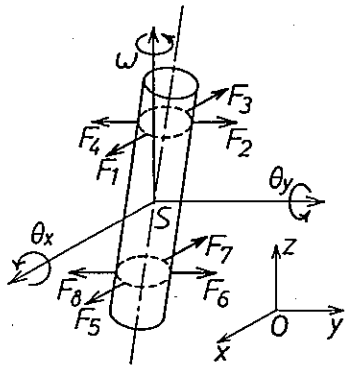

Fig.2 Coordinate axes and forces acting on the rotor

d_n:incremental gap between the rotor and the magnet

Each d_n is determined by the translational and rotational displacements of rotor.

When the rotor is driven to rotate at a constant speed ω, the equations of motion in the radial directions are given by[1]

$$\left.\begin{aligned} m\ddot{x}_s-4Gx_s&=H(i_1-i_3+i_5-i_7)+m\varepsilon\omega^2\cos(\omega t+\alpha)\\ m\ddot{y}_s-4Gy_s&=H(i_2-i_4+i_6-i_8)+m\varepsilon\omega^2\sin(\omega t+\alpha)\\ I_r\ddot{\theta}_x+I_a\omega\dot{\theta}_y-4Gl^2\theta_x&\\ =H(-i_2+i_4+i_6-i_8)l+(I_r-I_a)\tau\omega^2\cos(\omega t+\beta)&\\ I_r\ddot{\theta}_y-I_a\omega\dot{\theta}_x-4Gl^2\theta_y&\\ =H(i_1-i_3-i_5+i_7)l+(I_r-I_a)\tau\omega^2\sin(\omega t+\beta)& \end{aligned}\right\}(2)$$

where

m:mass of the rotor

I_a, I_r:polar and transverse mass moments of inertia of the rotor

l:distance between the center of the rotor and the magnets

α, β:parameters on angular location of static and dynamic unbalance

ε:eccentricity of the rotor (amount of static unbalance)

τ:angle between the rotational axis and the principal axis (amount of dynamic unbalance)

x_s, y_s:displacements of the rotor center S in x and y directions

θ_x, θ_y:angular displacements of rotor axis about x and y axes

It is clear from eq.(2) that the total system can be divided into two subsystems; one is related to translation and the other is related to rotation. In each subsystem the dynamics is expressed in the form[1,3]:

$$\dot{\mathbf{x}}(t)=\mathbf{A}\mathbf{x}(t)+\mathbf{B}\mathbf{u}(t)+\mathbf{D}\mathbf{w}(t) \tag{3}$$

$$\dot{\mathbf{w}}(t)=\mathbf{E}\mathbf{w}(t) \tag{4}$$

where

Table 1 Variables and Coefficients in each subsystem

symbol	subsystem related to translation	subsystem related to rotation
x_1	x_s	θ_x
x_2	y_s	θ_y
u_1	$i_1-i_3+i_5-i_7$	$-i_2+i_4+i_6-i_8$
u_2	$i_2-i_4+i_6-i_8$	$i_1-i_3-i_5+i_7$
w_1	$\varepsilon\omega^2\cos(\omega t+\alpha)$	$(1-c)\tau\omega^2\cos(\omega t+\beta)$
w_2	$\varepsilon\omega^2\sin(\omega t+\alpha)$	$(1-c)\tau\omega^2\sin(\omega t+\beta)$
a	$4G/m$	$4Gl^2/I_r$
b	H/m	Hl/I_r
c	0	I_a/I_r

$$\mathbf{x}=[x_1\ \dot{x}_1\ x_2\ \dot{x}_2]^T,\quad \mathbf{u}=[u_1\ u_2]^T,\quad \mathbf{w}=[w_1\ w_2]^T$$

$$A=\begin{bmatrix}0 & 1 & 0 & 0\\ a & 0 & 0 & c\omega\\ 0 & 0 & 0 & 1\\ 0 & -c\omega & a & 0\end{bmatrix}\quad B=\begin{bmatrix}0 & 0\\ b & 0\\ 0 & 0\\ 0 & b\end{bmatrix}\quad D=\begin{bmatrix}0 & 0\\ 1 & 0\\ 0 & 0\\ 0 & 1\end{bmatrix}$$

$$E=\begin{bmatrix}0 & -\omega\\ \omega & 0\end{bmatrix}$$

The variables and coefficients are defined as shown in **Table 1**.

It is remarked that the effects of unbalance are considered to be exogenous disturbances to the system

$$\dot{\mathbf{x}}(t)=\mathbf{A}\mathbf{x}(t)+\mathbf{B}\mathbf{u}(t) \tag{5}$$

and the disturbance model has the state form given by eq.(4).

3. Disturbance Estimation

Since it is difficult to measure the effects of unbalance $\mathbf{w}(t)$ in real time, we will construct an observer which asymptotically generates the disturbance state $\mathbf{w}(t)$ from measurable signals $\mathbf{x}(t)$ and $\mathbf{u}(t)$; later we will use the estimation for regulation control or disturbance compensation control.

According to the theory of observers, a minimal-order observer, which estimates $\mathbf{w}(t)$, is given by

$$\dot{\mathbf{z}}(t)=(\mathbf{E}-\mathbf{VD})\mathbf{z}(t)+(-\mathbf{VA}+\mathbf{EV}-\mathbf{VDV})\mathbf{x}(t)-\mathbf{VBu}(t) \tag{6}$$

$$\hat{\mathbf{w}}(t)=\mathbf{z}(t)+\mathbf{V}\mathbf{x}(t) \tag{7}$$

where

$$\mathbf{z}=[z_1,\ z_2]^T,\quad \hat{\mathbf{w}}=[\hat{w}_1,\ \hat{w}_2]^T$$

$$V=\begin{bmatrix} 0 & \sigma & 0 & \nu \\ 0 & -\nu & 0 & \sigma \end{bmatrix}$$

For convergence the parameter σ must satisfy

$$\sigma > 0 \tag{8}$$

4. Control Laws

In this chapter we will construct a control system in which the exciting currents or the attractive forces of the magnets converge to their set-point values although an unbalanced rotor is suspended stably. Another control method is also presented which feeds back the estimated signals on the motions of the center of mass and the principal axis instead of the center of configuration and the geometrical center axis.

Define complex variables as

$$\left.\begin{aligned} x&=x_1+jx_2 \\ u&=u_1+ju_2 \\ w&=w_1+jw_2 \\ z&=z_1+jz_2 \\ \hat{w}&=\hat{w}_1+j\hat{w}_2 \end{aligned}\right\} \tag{9}$$

and denote each Laplace-transformed variable by the capital. Since this paper focuses on stationary states, we will ignore initial conditions $\mathbf{x}(0)$ and $\mathbf{z}(0)$. Then by using these variables the dynamics of the control system is written as

$$X(s)=\frac{1}{t_o(s)}(bU(s)+W(s)) \tag{10}$$

$$W(s)=\frac{w(0)}{s-j\omega} \tag{11}$$

$$\hat{W}(s)=\frac{\sigma-j\nu}{s+\sigma-j(\omega+\nu)}W(s) \tag{12}$$

where the polynomial $t_o(s)$ is defined as

$$t_o(s)=s^2-jc\omega s-a \tag{13}$$

The initial condition w(0) can be represented as

$$w(0)=X_e\omega^2 \tag{14}$$

where

$$X_e=\varepsilon e^{j\alpha} \tag{15}$$

in the subsystem related to translation, and

$$X_e=(1-c)\tau e^{j\beta} \tag{16}$$

in the subsystem related to rotation. Moreover, we define f(t) as

$$f(t)=ax(t)+bu(t) \tag{17}$$

and x_b as

$$x_b(t)=x(t)-X_e e^{j\omega t} \tag{18}$$

or

$$X_b(s)=X(s)-\frac{W(s)}{t_n(j\omega)} \tag{19}$$

where

$$t_n(s)=s^2-jc\omega s \tag{20}$$

The variable f(t) represents force or moment acting on the rotor and $x_b(t)$ represents displacement of the center of mass or angular displacement of the principal axis.

For convenience we define [X] for a Laplace-transformed variable X(s) as the coefficient of $(s-j\omega)^{-1}$ when we expand X(s) into partial fraction form. If X(s) has $j\omega$ as a simple pole, [X] is given by

$$[X]=\lim_{s\to j\omega}(s-j\omega)X(s) \tag{21}$$

This quantity represents the amplitude and phase of sinusoidally varying component of x(t).

4.1 Current Regulation Control If control input u(t) becomes null in each of the subsystems related to translation and rotation, the exciting currents of magnets will be automatically kept constant. Thus, in the following we treat the control input u(t) as a variable to be regulated.

The control strategy is to decompose the control u(t) into two parts,

$$u(t)=u_x(t)+u_w(t) \tag{22}$$

where $u_x(t)$ and $u_w(t)$ are chosen to stabilize a closed-loop system (5) and to eliminate sinusoidally varying component from the control input itself, respectively.

We give u_x in an linear feedback form[2]:

$$U_x(s)=-k(s)X(s) \tag{23}$$

where

$$k(s)=p_v s+(p_d-jp_c) \tag{24}$$

The feedback coefficients p_d, p_v and p_c are selected to satisfy the stability conditions:

$$(s1)(bp_d-a)bp_v+bp_c c\omega>0 \tag{25}$$

$$(s2)(bp_d-a)(bp_v)^2-(bp_c)^2+bp_v bp_c c\omega>0 \tag{26}$$

Next, we determine $u_w(t)$ as follows. First, we will find $U_w(s)$ such that

$$U(s)=0 \tag{27}$$

From eqs.(22) and (24), U(s) is written as

$$U(s)=-k(s)X(s)+Uw(s) \tag{28}$$

Substitution of eq.(10) into eq.(28) yields

$$U(s)=\frac{1}{t_c(s)}(-k(s)W(s)+t_o(s)U_w(s)) \tag{29}$$

Hence, the solution of eq.(27) is

$$U_w(s)=\frac{k(s)}{t_o(s)}W(s) \tag{30}$$

Second, replace W(s) by the estimate $\hat{W}(s)$ in the control law (30) as

$$U_w(s)=\frac{k(s)}{t_o(s)}\hat{W}(s) \tag{31}$$

From eqs.(12), (29) and (31),

$$U(s)=-\frac{k(s)(s-j\omega)}{t_c(s)(s+\sigma-j(\omega+\nu))}W(s)$$

$$=-\frac{k(s)w(0)}{t_c(s)(s+\sigma-j(\omega+\nu))} \tag{32}$$

and from eq.(10) and (32),

$$X(s)=\frac{(s-j\omega)W(s)}{t_c(s)(s+\sigma-j(\omega+\nu))}+\frac{(\sigma-j\nu)W(s)}{t_o(s)(s+\sigma-j(\omega+\nu))} \tag{33}$$

Using eq.(32) to compute [U] yields

$$[U]=0 \tag{34}$$

Thus, the control input u(t) converges to zero. However, the second term in the right-hand side in eq.(33) shows that the closed-loop system falls into instability.

Third, in order to recover stability, we replace $t_o(s)$ by $t_o(j\omega)$ in the control law (31) as

$$U_w(s)=\frac{k(s)}{t_o(j\omega)}\hat{W}(s) \tag{35}$$

Then, substitution of eq.(35) into eq.(29) leads

$$U(s)=-k(s)\cdot\frac{(\sigma-j\nu)t_o(s)-(s+\sigma-j(\omega+\nu))t_o(j\omega)}{t_c(s)(s+\sigma-j(\omega+\nu))t_o(j\omega)}W(s) \tag{36}$$

Hence,

$$[U]=0 \tag{37}$$

From eqs.(10),(12),(29) and (35),

$$X(s)=[1+\frac{bk(s)(\sigma-j\nu)}{t_o(j\omega)(s+\sigma-j(\omega+\nu))}]\frac{W(s)}{t_c(s)} \tag{38}$$

This equation reveals that the rotor remains stably suspended and yields

$$[X]=-\frac{w(0)}{(1-c)\omega^2+a} \tag{39}$$

As a result, we can realize a stable suspension with asymptotical elimination of the sinusoidally varying component from the exciting currents by determining the control input as

$$U(s)=-k(s)(X(s)-\frac{\hat{W}(s)}{t_o(j\omega)}) \tag{40}$$

Then, the stationary components of f(t) and $x_b(t)$ are obtained as follows:

$$[F]=\frac{-aw(0)}{(1-c)\omega^2+a} \tag{41}$$

$$[X_b]=(\frac{1}{(1-c)\omega^2}-\frac{1}{(1-c)\omega^2+a})w(0) \tag{42}$$

In a magnetic bearing instrument using permanent magnet to provide the bias magnetic flux, DC power dissipation in the coil can be reduced to zero for steady load by the virtually zero power system[5]. In contrast with this, the proposed current regulation control enables zero AC power dissipation under periodically changing load due to unbalance.

4.2 Force Regulation Control If f(t) converges to zero in each subsystem, the electromagnetic forces will come to constant values. Thus, in the following we treat f(t) as a variable to be regulated.

From eqs.(9) and (17),

$$X(s)=\frac{1}{t_n(s)}(F(s)+W(s)) \tag{43}$$

From eqs.(17), (28) and (43),

$$F(s)=\frac{1}{t_n(s)}[(a-bk(s))W(s)+bt_n(s)U_w(s)] \tag{44}$$

This implies that F(s) becomes null if $U_w(s)$ is given by

$$U_w(s)=(k(s)-\frac{a}{b})\frac{W(s)}{t_n(s)} \tag{45}$$

We replace W(s) by $\hat{W}(s)$ to realize the control law (45) and $t_n(s)$ by $t_n(j\omega)$ not to lose internal stability:

$$U_w(s)=(k(s)-\frac{a}{b})\frac{\hat{W}(s)}{t_n(j\omega)} \tag{46}$$

Then F(s) is

$$F(s)=\frac{(bk(s)-a)}{t_c(s)}[\frac{(\sigma-j\nu)t_n(s)}{(s+\sigma-j(\omega+\nu))t_n(j\omega)}-1]W(s) \tag{47}$$

Hence,

$$[F]=0 \tag{48}$$

When the control input is given by eq.(46), the displacement X(s) and control input U(s) are obtained as follows:

$$X(s)=[\frac{(bk(s)-a)(\sigma-j\nu)}{t_n(j\omega)(s+\sigma-j(\omega+\nu))}+1]\frac{W(s)}{t_c(s)} \tag{49}$$

$$U(s)=[(k(s)-\frac{a}{b})\frac{(\sigma-j\nu)t_o(s)}{s+\sigma-j(\omega+\nu)t_n(j\omega)}-k(s)]\frac{W(s)}{t_c(s)} \tag{50}$$

Hence,

$$[X]=\frac{w(0)}{t_n(j\omega)}=X_e \tag{51}$$

$$[U]=-\frac{aw(0)}{bt_n(j\omega)} \tag{52}$$

From eq.(51),

$$[X_b]=0 \tag{53}$$

This implies that the rotor rotates about its the principal axis and the state of "automatic balancing"[4] is realized when force regulation control is applied.

4.3 Observatory disturbance compensation

We can design control system based upon a model that describes the motions of the gravity center and the principal axis instead of the geometrical center and axis. The motions, however, cannot be measured directly by the position sensors built in the magnetic bearing instrument. In this case the signals generated by the position sensors are considered to contain a sinusoidal disturbance due to configuration error. This observatory disturbance can be asymptotically eliminated by using the output of observer as

$$\hat{X}_b(s)=X(s)-\frac{\hat{W}(s)}{t_n(j\omega)} \tag{54}$$

We determine the control input to stabilize the motions of gravity center and principal axis by feedback compensation such as

$$U(s)=-k(s)\hat{X}_b(s) \tag{55}$$

Then, displacement X(s), control input U(s) and control force F(s) are obtained as follows:

$$X(s)=\frac{1}{t_c(s)}[\frac{bk(s)(\sigma-j\nu)}{t_n(j\omega)(s+\sigma-j(\omega+\nu))}+1]W(s) \tag{56}$$

$$U(s)=\frac{k(s)}{t_c(s)}[\frac{t_o(s)(\sigma-j\nu)}{t_n(j\omega)(s+\sigma-j(\omega+\nu))}-1]W(s) \tag{57}$$

$$F(s)=[a-bk(s)(1-\frac{t_n(s)(\sigma-j\nu)}{t_n(j\omega)(s+\sigma-j(\omega+\nu))})]\frac{W(s)}{t_c(s)} \tag{58}$$

Hence,

$$[X]=(1+\frac{a}{t_c(j\omega)})\frac{w(0)}{t_n(j\omega)} \tag{59}$$

$$[U]=-k(j\omega)\frac{aw(0)}{t_c(j\omega)t_n(j\omega)} \tag{60}$$

$$[F]=\frac{aw(0)}{t_c(j\omega)} \tag{61}$$

From (19) and (59),

$$[X_b]=\frac{aw(0)}{t_c(j\omega)t_n(j\omega)} \tag{62}$$

In this control system the rotor does not rotate around its principal axis and both the exciting current and bearing force vary sinusoidally unless the parameter a is equal to zero.

4.4 Comparison of the control methods Using real-valued variables the control input is given

Table 2 Data for numarical simulation

controlled object		designed controller	
a	1.00	p_d	2.73
b	1.00	p_v	2.34
c	0.02	p_c	0
ω	1.00	σ	0.25
X_e	0.98+j0	ν	0
		z(0)	0

by

$$\mathbf{u}(t)=\mathbf{P}_1\mathbf{x}(t)+\mathbf{P}_2\hat{\mathbf{w}}(t) \tag{63}$$

where $\mathbf{P}_1$ is

$$\mathbf{P}_1=-\begin{bmatrix} p_d & p_v & -p_c & 0 \\ p_c & 0 & p_d & p_v \end{bmatrix} \tag{64}$$

and $\mathbf{P}_2$ is

(1)current regulation control

$$\mathbf{P}_2=\frac{1}{(1-c)\omega^2+a}\begin{bmatrix} p_d & -\omega p_v+p_c \\ \omega p_v-p_c & p_d \end{bmatrix} \tag{65}$$

(2)force regulation control

$$\mathbf{P}_2=\frac{1}{(1-c)\omega^2}\begin{bmatrix} p_d\frac{a}{b} & -\omega p_v+p_c \\ \omega p_v-p_c & p_d\frac{a}{b} \end{bmatrix} \tag{66}$$

(3)observatory disturbance compensation

$$\mathbf{P}_2=\frac{1}{(1-c)\omega^2}\begin{bmatrix} p_d & -\omega p_v+p_c \\ \omega p_v-p_c & p_d \end{bmatrix} \tag{67}$$

It is clear from eqs.(65),(66) and (67) that the above mentioned three control methods are identical if the parameter a equals zero. This parameter represents the degree of instability caused by the bias magnetic field that provides a linear control force-current characteristics. We can realize a magnetic bearing with zero-bias field by compensating nonlinearity of the characteristics. Then, an unbalanced rotor can be suspended stably with fixed exciting currents and bearing forces.

5. Numerical Simulation and Analysis on Frequency Characteristics

To confirm the effectiveness of the proposed control methods, several numerical simulations are carried out. The values of the parameters used in the simulations are listed in **Table 2**;

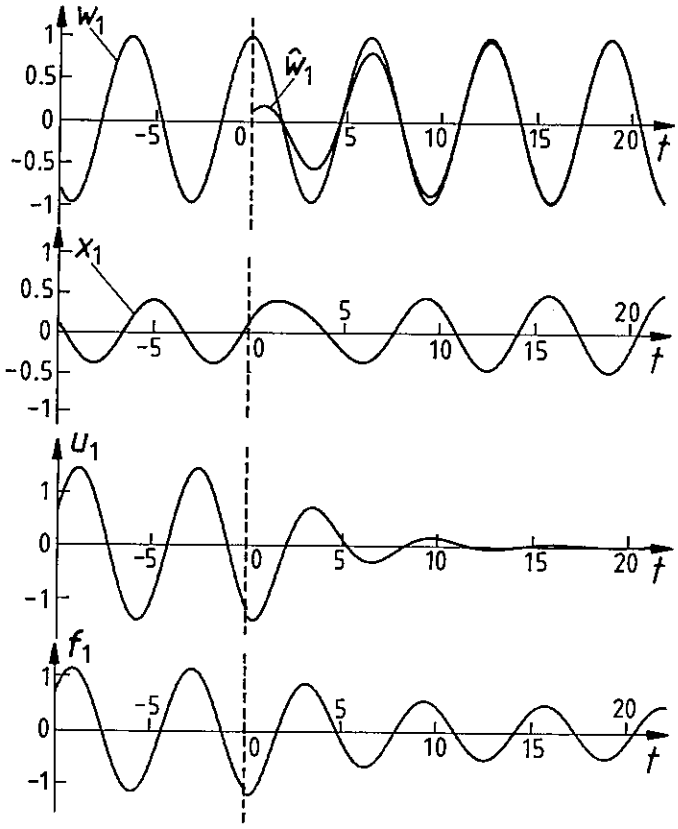

Fig.3 Response when the current regulation control is applied at t=0

they represent normalized values that are obtained by describing the system equation by dimensionless variables[1,2,3].

Figures 3 and **4** show responses when the current regulation control and the force regulation control are applied; each regulation control start at t=0 and the stationary response of the system using the simple feedback control

$$\mathbf{u}(t)=\mathbf{P}_1\mathbf{x}(t) \tag{68}$$

is shown for t<0. Figure 3 shows that with the convergence of estimation sinusoidally varying component of control input disappears in the current regulation control system. The same is said of bearing force in the force regulation system (Fig.4).

Next, we show several numerical studies on the performance of the system using the simple feedback control or using alternatively the current regulation control and the force regulation control in add to (68). We design the controllers for ω=1.0 (**case a**) and 2.0 (**case b**). Other design parameters pd, pv, pc, σ and ν are set to be same as used in the simulation.

The amplitudes of displacement, control input and bearing force at each rotational speed are shown in **Fig.5** (case a) and **Fig.6** (case b);

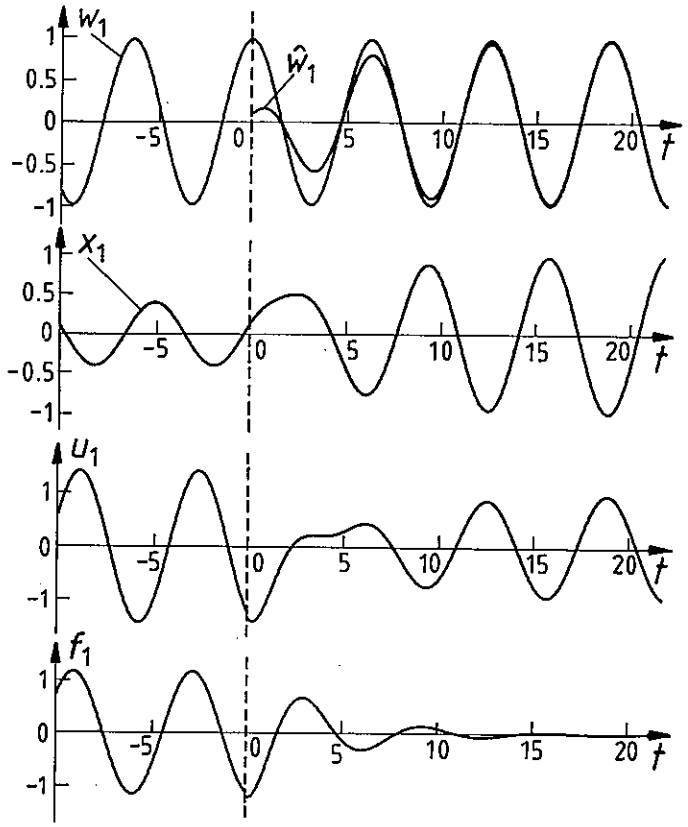

Fig.4 Response when the force regulation control is applied at t=0

it is to be remarked that in both cases the parameters of controller are fixed although the rotational speed changes. We can see again that at the designed frequency control input and bearing force become null in the current and force regulation control systems, respectively. It is seen that the performance of the system using the current regulation control becomes very similar to that of the system using the force regulation control when they are designed for a high rotational speed.

6. Conclusions

The possibility of suspending a rotor without any synchronous variation in the exciting current or bearing force in a magnetic bearing has been shown. Whereas the virtually zero power system enables zero DC power dissipation in the coil under steady load, the proposed current regulation control enables zero AC power dissipation under periodically changing load due to unbalance. When the force regulation control is applied, the rotor is rotating about its inertial axis. When the bias magnetic field can be reduced to zero, the exciting current and force of electromagnet are to be regulated at the same time. In this case the observatory compensation control yields the same result.

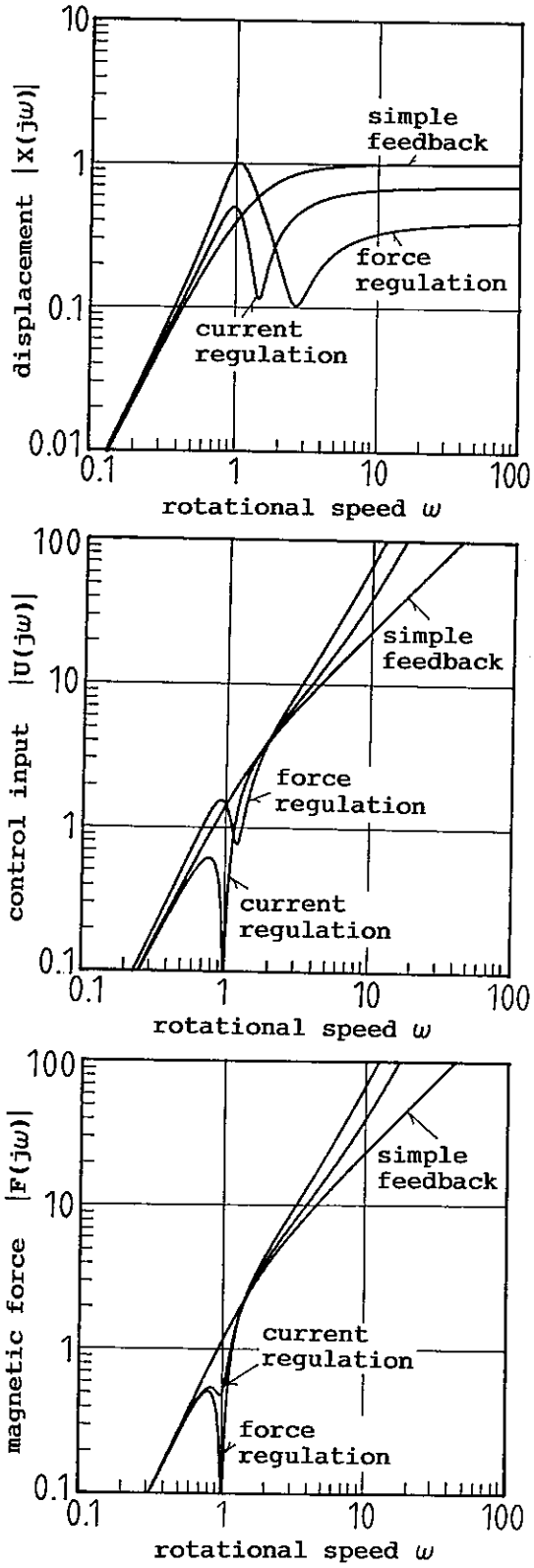

Fig.5 Unbalance responses; current regulation and force regulation controllers are designed for ω=1.0

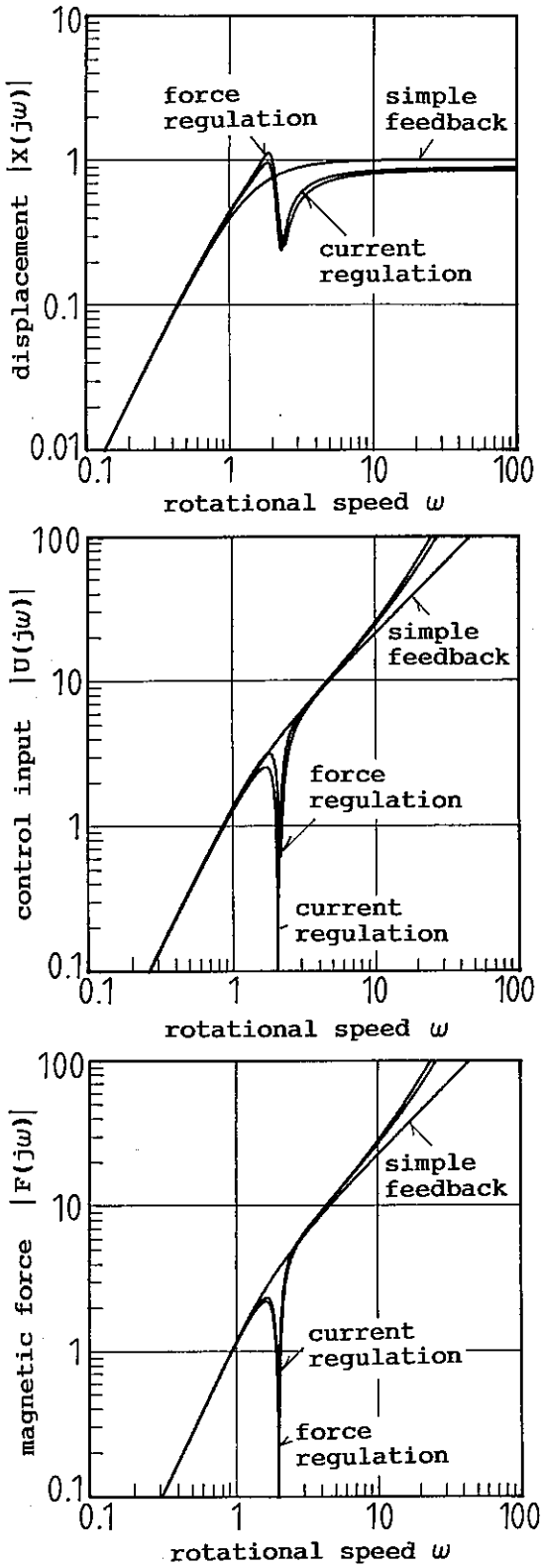

Fig.6 Unbalance responses; current regulation and force regulation controllers are designed for ω=2.0

Since we have shown the control methods based on the same state equation and observer that was used in our previous works, it will be possible to apply the developed methods of analysis on parameter variations and modification of the structure of controller[3].

References

[1]Mizuno, T. and Higuchi, T.: Compensation for Unbalance in Magnetic Bearing System (in Japanese), Trans. Society of Instrument and Control Engineers, Vol.20, No.12, pp.1095-1101(1984).

[2]Mizuno, T. and Higuchi, T.: Design of the Control System of Totally Active Magnetic Bearings ---Structures of the Optimal Regulator---, Proceedings, 1st International Symposium on Design and Synthesis, Tokyo(1984).

[3]Mizuno, T. and Higuchi, T.: Structure of Magnetic Bearing Control System for Compensating Unbalance Force, Dynamics of Controlled Mechanical Systems (G.Schweitzer and M.Mansour eds.), pp.135-146, Springer-Verlag (1989).

[4]Habermann, H. and Brunet, M.: The Active Magnetic Bearing Enables Optimum Control of Machine Vibrations, ASME International Gas Turbine Conference, 85-GT-221(1985).

[5]Henrikson, C.H.: Magnetically Suspended Momentum Wheels for Spacecraft Stabilization, AIAA Paper No.74-128, Washington, D.C.(1974)

2nd International Symposium on Magnetic Beaing
July 12-14, 1990, Tokyo, Japan

A DECOMPOSITION OF THE JEFFCOTT ROTOR

D. FERMENTAL, E. CUSSON, P. LAROCCA
The Charles Stark Draper Laboratory, Inc.
555 Technology Square, Cambridge, MA, USA

Abstract

This report provides a novel representation of a magnetically suspended rotor consisting of a single inertia, supported on a massless shaft exhibiting stiffness and damping (the Jeffcott model). The state variables are chosen in a way that allows the plant to be transformed into subsections. These subsections independently account for translation, rotation and bending. The report also derives observability and controllability matrices for the Jeffcott rotor.

1 Introduction

This effort provides representations of a magnetically levitated rotor consisting of an inertia on a shaft. The inertia is not centered and the magnetic forces act on the shaft ends where the system sensors are also located. The study, which extends the work of Johnson[1] and McCallum[2] includes two plant models. In one model the shaft is rigid. In the second, the Jeffcott model, the shaft bends. In both, the shaft is taken as massless, which allows the second model to be treated as an embellishment of the first. The development assumes an isotropic shaft with internal damping only. The result is a plant that becomes unstable, and remains so, above the first critical speed, a spin rate corresponding to the undamped natural frequency of plant translational oscillations when the spin rate is zero.

The plant equations used for the Jeffcott model are identical to those derived in McCallum[2]. However, the plant state vector is defined in a different way. The equations account for both translation and rotation of the shaft and include gyroscopic effects.

Unlike the work of McCallum, it is assumed in this document that the magnetic bearings are compensated. This is justified since the gap compensation must be part of a design effort in any case. Here, it is assumed local feedback at each bearing removes the position dependence, and thus, the negative stiffness element associated with bearing magnetic field.

Johnson[1], considering translational motion only, showed that the Jeffcott model is both controllable and observable at all spin rates. McCallum[2] extended this result to include radial rotation and its associated gyroscopic effects, but provides no determinant for either the controllability matrix or the observability matrix. These are supplied in closed form in this report.

2 Model References

Initially the equations are cast to include linearized terms that represent uncompensated magnetic bearings. Later it will be assumed that the bearings are compensated, and the magnetic terms will be dropped from the analysis.

The rotor is taken to be an inertia on a shaft supported at its ends. The inertia is at a distance, L1, from the leftmost support, and a distance, L2, from the rightmost support. Figure 1 presents a side view and shows vertical forces. Horizontal forces can be shown in a like manner. Axial motion is not considered.

The spin axis of the rotor is taken to be along the X axis with clockwise spin being a positive angular rotation, ω_x. Vertical motion is along the Y axis, and horizontal motion is along the Z axis. The yaw angle, ξ_1, is about the Y axis, and the pitch angle, ξ_2, is about the Z axis.

In Figure 2 the spring constant for the magnetic bearing at bearing 1 in the vertical direction is -Ky1 and the vertical force, Fsy1, acting on the shaft satifies

$$Fsy1 = Fy1 + Ky1 * Y1$$

where Y1 is the vertical displacement of the shaft end, and Fy1 is a plant input. Note that the force on the shaft due to the bias field Ky1*Y1 increases with displacement. The forces Fsy2, Fsz1 and Fsz2 are similar in form.

The spring, dashpot combination (K1,B1) is used to model the shaft stiffness and damping between the inertia and the leftmost support, while the combination (K2,B2) models the other section. Since both stiffness and damping are inversely proportional to length they can be expressed as a ratio

$$\frac{K1}{B1} = \frac{K2}{B2} = S_o.$$

Figure 2 shows the spring-dashpot combination for the shaft at the leftmost support from the rear. The couplet (Y1,Z1) defines the position of the shaft while (Ys1,Zs1) is the end of the shaft without bending. If the pitch angle is small.

$$Ys1 = Yr - L1 * \xi_2$$

The difference Ys1 - Y1 is due to the deflection of the shaft and is represented by the variable DY1. DY2, DZ1, and DZ2 are defined in a similar manner. The inertia of the plant about the X axis, is J_a. The inertia about the Y axis and the Z axis, is J_r. It is assumed in the analysis that the pitch and yaw angles are sufficiently small and that the values of J_a and J_r are independent of plant motion.

3 The Jeffcott Model

From Fig. 1 the forces acting on the rotor in the vertical direction are Fsy1 and Fsy2. These forces tend to move the rotor both in translation and rotation. The equations for the translation motion, neglecting gravity is

$$Fsy1 + Fsy2 = \ddot{M} * Yr$$

where M is the rotor mass. The equation for the rotational motion is

$$L2 * Fsy2 - L1 * Fsy1 = Jr * \ddot{\xi}_2 - Ja * \omega_x * \dot{\xi}_1$$

where $Ja * \omega_x * \dot{\xi}_1$ is the gyroscopic torque caused by changing the yaw angle as the rotor spins about the X axis with angular velocity ω_x. If the rotor is balanced the equations can be written as

$$\begin{aligned}
\ddot{Y}_r &= \frac{(Ky1 + Ky2) * Yr}{M} - \frac{(L1 * Ky1 - L2 * Ky2) * \xi_2}{M} \\
&\quad + \frac{Fy1 + Fy2}{M} \\
\ddot{Z}_r &= \frac{(Kz1 + Kz2) * Zr}{M} + \frac{(L1 * Kz1 - L2 * Kz2) * \xi_1}{M} \\
&\quad + \frac{Fz1 + Fz2}{M} \\
\ddot{\xi}_2 &= \frac{(L1^2 * Ky1 + L2^2 * Ky2) * \xi_2}{Jr} \\
&\quad - \frac{(L1 * Ky1 - L2 * Ky2) * Yr}{Jr} \\
&\quad \frac{-L1 * Fy1 + L2 * Fy2 + Ja * \omega_x * \dot{\xi}_1}{Jr} \\
\ddot{\xi}_1 &= \frac{(L1^2 * Kz1 + L2^2 * Kz2) * \xi_1}{Jr} \\
&\quad + \frac{(L1 * Kz1 - L2 * Kz2) * Zr}{Jr} \\
&\quad + \frac{L1 * Fz1 - L2 * Fz2 - Ja * \omega_x * \dot{\xi}_2}{Jr}.
\end{aligned}$$

These equations coupled with

$$Y1 = Yr - L1 * \xi_2; \quad Y2 = Yr + L2 * \xi_2$$

$$Z1 = Yr + L1 * \xi_1; \quad Z2 = Yr - L2 * \xi_1$$

describe the rigid plant. The state variables are

$$[Y_r, \xi_2, Z_r, \xi_1, \dot{Y}_r, \dot{\xi}_2, \dot{Z}_r, \dot{\xi}_1].$$

Figure 2 shows the deflection of the shaft as seen from the leftmost support or bearing 1. The force acting to bend the shaft, Fs1, is the vector sum of Fsy1 and Fsz1. The deflection of the shaft at the bearing, DR1, satisfies

$$Fs1 = K1 * DR1 + B1 * \dot{DR1}.$$

The forces, Fsy1, and, Fsz1, can be written as

$$Fsy1 = K1 * Cos(\theta) * DR1 + B1 * Cos(\theta) * \dot{DR1}$$

$$Fsz1 = K1 * Sin(\theta) * DR1 - B1 * Sin(\theta) * \dot{DR1}.$$

Since,

$$\begin{aligned} DY1 &= Cos(\theta) * DR1 \\ DZ1 &= Sin(\theta) * DR1 \\ D\dot{Y}1 &= Cos(\theta) * D\dot{R}1 - \omega_x * Sin(\theta) * DR1 \\ D\dot{Z}1 &= Sin(\theta) * D\dot{R}1 - \omega_x * Cos(\theta) * DR1 \end{aligned}$$

we can write the force equations as

$$\begin{aligned} Fsy1 &= K1 * DY1 + B1 * (D\dot{Y}1 + \omega_x * DZ1) \\ Fsz1 &= K1 * DZ1 + B1 * (D\dot{Z}1 - \omega_x * DY1) \\ Fsy2 &= K1 * DY2 + B1 * (D\dot{Y}2 + \omega_x * DZ2) \\ Fsz2 &= K1 * DZ2 + B1 * (D\dot{Z}2 + \omega_x * DY2). \end{aligned}$$

Crandall[3] speaks of the cross terms in these equations as being quasi— gyroscopic. They provide the mechanism for coupling energy from the rotor spin into rotation of the shaft deflection, the shaft whirl.

These results can be recast as equations for the additional state variables [DY1, DZ1, DY2, DZ2] thus,

$$D\dot{Y}1 = \frac{Fy1}{B1} + \frac{Ky1 * Y1}{B1} - S_o * DY1 - \omega_x * DZ1$$

$$D\dot{Z}1 = \frac{Fz1}{B1} + \frac{Kz1 * Z1}{B1} - S_o * DZ1 - \omega_x * DY1$$

$$D\dot{Y}2 = \frac{Fy2}{B2} + \frac{Ky2 * Y2}{B1} - S_o * DY2 + \omega_x * DZ2$$

$$D\dot{Z}1 = \frac{Fz2}{B2} + \frac{Kz2 * Z2}{B2} - S_o * DZ2 + \omega_x * DY2.$$

The state vector $[\mathbf{x}]^t$ for a shaft with bending can now be defined as

$$[Y_r, \xi_2, Z_r, \xi_1, \dot{Y}_r, \dot{\xi}_2, \dot{Z}_r, \dot{\xi}_1, D_{Y1}, D_{Z1}, D_{Y2}, D_{Z2}].$$

With no mass imbalance, the forces acting on the rotor are

$$Fsy1 = Fy1 + Ky1 * Y1; \quad Fsy2 = Fy2 + Ky2 * Y2$$

$$Fsz1 = Fz1 + Kz1 * Z1; \quad Fsz2 = Fz2 + Kz2 * Z2.$$

For compensated bearings, bearings with drives so designed that forces on the shaft due to the end positions are removed by local feedback, the stiffness constants [Ky1, Ky2, Kz1, Kz2] are zero and the plant input vector is defined as

$$[\mathbf{u}]^t = [F_{Y1}, F_{Z1}, F_{Y2}, F_{Z2}]$$

The output vector is defined as

$$[\mathbf{y}]^t = [Y_1, Y_2, Z_1, Z_2].$$

where

$$Y1 = Y_r - L1 * \xi_2 + DY1; \quad Y2 = Y_r + L2 * \xi_2 + DY2$$

$$Z1 = Z_r + L1 * \xi_1 + DZ1; \quad Z2 = Z_r - L2 * \xi_1 + DZ2.$$

$$\begin{aligned} \dot{Y}1 &= \frac{K1 * Y_r}{B1} + \dot{Y}_r + \omega_x * (Z_r + L1 * \xi_1 - Z1) \\ &\quad - \frac{K1 * L1 * \xi_2}{B1} - L1 * \dot{\xi}_2 \\ &\quad + \frac{(Ky1 - K1) * Y1}{B1} + \frac{Fy1}{B1} \\ \dot{Y}2 &= \frac{K2 * Y_r}{B2} + \dot{Y}_r + \omega_x * (Z_r - L2 * \xi_1 - Z2) \\ &\quad + \frac{K2 * L2 * \xi_2}{B2} + L2 * \dot{\xi}_2 \\ &\quad + \frac{(Ky2 - K2) * Y2}{B2} + \frac{Fy2}{B2} \\ \dot{Z}1 &= \frac{K1 * Z_r}{B1} + \dot{Z}_r + \omega_x * (-Y_r + L1 * \xi_2 + Z2) \\ &\quad + \frac{K1 * L1 * \dot{\xi}_1}{B1} + L1 * \dot{\xi}_1 \\ &\quad + + \frac{(Kz1 - K1) * Z1}{B1} \frac{Fz1}{B1} \\ \dot{Z}2 &= \frac{K2 * Z_r}{B2} + \dot{Z}_r + \omega_x * (-Y_r - L2 * \xi_2 + Y2) \\ &\quad - \frac{K2 * L2 * \dot{\xi}_1}{B2} - L2 * \dot{\xi}_1 \\ &\quad + \frac{(Kz2 - K2) * Z2}{B2} + \frac{Fz2}{B2} \end{aligned}$$

The translational forces are

$$Fy_r = Fsy2 + Fsy2; \quad Fz_r = Fsz1 + Fsz2$$

and the torques are

$$\begin{aligned} Te2 &= -L1 * Fsy1 + L2 * Fsy2 \\ Te1 &= L1 * Fsz1 - L2 * Fsz2. \end{aligned}$$

These results completely describe the Jeffcott model with internal damping. Fig. 3 shows a Block diagram of the model. The subsection for bending, translational and rotation can be easily identified.

4 Normalization

The model is normalized in the following way. Let

$$\begin{aligned} \text{1 unit of length} &= \text{L1 meters} \\ \text{1 unit of time} &= \tfrac{1}{S_n} \text{ seconds} \\ \text{1 unit of mass} &= M \text{ kg} \end{aligned}$$

Therefore,

1 unit of force = M*L1*S_0^2 newtons.

The damping factor associated with the shaft between the mass and bearing 1 is B1. It's normalized value is $\frac{1}{v}$ where

$$\frac{1}{v} = \frac{B1}{M * S_0}.$$

Since $\frac{K1}{B1} = S_0$, where K1 is the stiffness constant for the same shaft section, the normalized value of K1 is $\frac{1}{v}$ as well. The inertia, Jr, in normalized terms becomes

$$\frac{1}{m} = \frac{Jr}{M*L1^2}.$$

To complete the normalization, three other ratios are required

$$\begin{aligned} \mathrm{r} &= \frac{L2}{L1} = \frac{K2}{K1}\,\frac{B2}{B1} \\ \mathrm{w} &= \frac{\omega_x}{S_0} \\ a &= \frac{Ja}{Jr} * \mathrm{w}. \end{aligned}$$

For the system equations in the standard state space form

$$\begin{aligned} \dot{\mathbf{x}} &= A\mathbf{x} + B\mathbf{u} \\ \mathbf{y} &= C\mathbf{x} + D\mathbf{u}. \end{aligned}$$

The normalized plant matrices are:

$$[A] =$$

$$\begin{bmatrix} 0 & 0 & 0 & 0 & 1 & 0 & 0 & 0 & 0 & 0 & 0 & 0 \\ 0 & 0 & 0 & 0 & 0 & 1 & 0 & 0 & 0 & 0 & 0 & 0 \\ 0 & 0 & 0 & 0 & 0 & 0 & 1 & 0 & 0 & 0 & 0 & 0 \\ 0 & 0 & 0 & 0 & 0 & 0 & 0 & 1 & 0 & 0 & 0 & 0 \\ 0 & 0 & 0 & 0 & 0 & 0 & 0 & 0 & 0 & 0 & 0 & 0 \\ 0 & 0 & 0 & 0 & 0 & 0 & 0 & a & 0 & 0 & 0 & 0 \\ 0 & 0 & 0 & 0 & 0 & 0 & 0 & 0 & 0 & 0 & 0 & 0 \\ 0 & 0 & 0 & 0 & 0 & -a & 0 & 0 & 0 & 0 & 0 & 0 \\ 0 & 0 & 0 & 0 & 0 & 0 & 0 & 0 & -1 & -w & 0 & 0 \\ 0 & 0 & 0 & 0 & 0 & 0 & 0 & 0 & w & -1 & 0 & 0 \\ 0 & 0 & 0 & 0 & 0 & 0 & 0 & 0 & 0 & 0 & -1 & -w \\ 0 & 0 & 0 & 0 & 0 & 0 & 0 & 0 & 0 & 0 & w & -1 \end{bmatrix}$$

$$[B] =$$

$$\begin{bmatrix} 0 & 0 & 0 & 0 \\ 0 & 0 & 0 & 0 \\ 0 & 0 & 0 & 0 \\ 0 & 0 & 0 & 0 \\ 1 & 0 & 1 & 0 \\ -m & 0 & mr & 0 \\ 0 & 1 & 0 & 1 \\ 0 & m & 0 & mr \\ v & 0 & 0 & 0 \\ 0 & v & 0 & 0 \\ 0 & 0 & rv & 0 \\ 0 & 0 & 0 & rv \end{bmatrix}$$

$$[C] =$$

$$\begin{bmatrix} 1 & -1 & 0 & 0 & 0 & 0 & 0 & 0 & 1 & 0 & 0 & 0 \\ 1 & r & 0 & 0 & 0 & 0 & 0 & 0 & 0 & 1 & 0 & 0 \\ 0 & 0 & 1 & 1 & 0 & 0 & 0 & 0 & 0 & 0 & 1 & 0 \\ 0 & 0 & 1 & -r & 0 & 0 & 0 & 0 & 0 & 0 & 0 & 1 \end{bmatrix}$$

$$[D] =$$

$$\begin{bmatrix} 0 & 0 & 0 & 0 \\ 0 & 0 & 0 & 0 \\ 0 & 0 & 0 & 0 \\ 0 & 0 & 0 & 0 \\ 0 & 0 & 0 & 0 \\ 0 & 0 & 0 & 0 \\ 0 & 0 & 0 & 0 \\ 0 & 0 & 0 & 0 \end{bmatrix}$$

5 Controllability

The system controllability matrix is

$$[C_n] = [B][A * B][A^2 * B].$$

In normalized form it is equal to

$$\begin{bmatrix}
0 & 0 & 0 & 0 & 1 & 0 & 1 & 0 & 0 & 0 & 0 & 0 \\
0 & 0 & 0 & 0 & -m & 0 & mr & 0 & 0 & am & 0 & -amr \\
0 & 0 & 0 & 0 & 0 & 1 & 0 & 1 & 0 & 0 & 0 & 0 \\
0 & 0 & 0 & 0 & 0 & m & 0 & -mr & am & 0 & -amr & 0 \\
1 & 0 & 1 & 0 & 0 & 0 & 0 & 0 & 0 & 0 & 0 & 0 \\
-m & 0 & mr & 0 & 0 & am & 0 & -amr & a^2m & 0 & -a^2m & 0 \\
0 & 1 & 0 & 1 & 0 & 0 & 0 & 0 & 0 & 0 & 0 & 0 \\
0 & m & 0 & -mr & am & 0 & -amr & 0 & 0 & a^2m & 0 & a^2m \\
v & 0 & 0 & 0 & -v & -vw & 0 & 0 & -v^2 & -v^2w & 0 & 0 \\
0 & v & 0 & 0 & vw & -v & 0 & 0 & v^2w & -v^2 & 0 & 0 \\
0 & 0 & rv & 0 & 0 & 0 & -rv & -rvw & 0 & 0 & -rv^2 & -rv^2w \\
0 & 0 & 0 & rv & 0 & 0 & rvw & -rv & 0 & 0 & rv^2w & -v^2
\end{bmatrix}$$

and

$$det[C_n] = (mv(r+1))^4 * r^2 * (1+w^2)^3 * (1+(w-a)^2).$$

Thus, det$[C_n]$ is positive, and the plant is controllable, for all choices of plant parameters, except r = -1. This simply means the plant requires two separate bearings to be controllable.

6 Observability

The observability matrix is

$$[O_b] = [[C][C * B][CB^2]]^t.$$

In normalized coefficients $[O_b]$ =

$$\begin{bmatrix}
1 & -1 & 0 & 0 & 0 & 0 & 0 & 0 & 1 & 0 & 0 & 0 \\
1 & r & 0 & 0 & 0 & 0 & 0 & 0 & 0 & 1 & 0 & 0 \\
0 & 0 & 1 & 1 & 0 & 0 & 1 & 0 & 0 & 0 & 1 & 0 \\
0 & 0 & 1 & -r & 0 & 0 & 0 & 1 & 0 & 0 & 0 & 1 \\
0 & 0 & 0 & 0 & 1 & -1 & 0 & 0 & -1 & -w & 0 & 0 \\
0 & 0 & 0 & 0 & 1 & r & 0 & 0 & w & -1 & 0 & 0 \\
0 & 0 & 0 & 0 & 0 & 0 & 1 & 1 & 0 & 0 & -1 & -w \\
0 & 0 & 0 & 0 & 0 & 0 & 1 & -r & 0 & 0 & w & -1 \\
0 & 0 & 0 & 0 & 0 & 0 & 0 & -a & (1-w^2) & 2w & 0 & 0 \\
0 & 0 & 0 & 0 & 0 & 0 & 0 & ar & -2w & (1-w^2) & 0 & 0 \\
0 & 0 & 0 & 0 & 0 & -a & 0 & 0 & 0 & 0 & (1-w^2) & 2w \\
0 & 0 & 0 & 0 & 0 & -ar & 0 & 0 & 0 & 0 & -2w & (1-w^2)
\end{bmatrix}$$

and

$$det[O_b] = (r+1)^2 * (w^2+1)^2 * [(r+1)^2 * (w^2+1)^2 + a^2 * (w*(r-1)+(r+1))^2].$$

Thus, det$[O_b]$ is positive and the plant is observable for all choices of plant parameters, except again r = -1.

7 Conclusion

The observability and controllability matrix for the Jeffcott model shows that the system is both observable and controllable for all rotation speeds. The model can be been decomposed into a translational, rotational and bending subsection. An attractive feature of this model is, independent control laws can be designed for each subsection and filtering requirements can be tailored to meet their particular needs.

References

[1] Johnson B. G., Active Control of a Flexible Rotor, S.M. Theses, Massachusetts Institute of Technology, September 1986, CSDL-T-864.

[2] McCallum D. C. Dynamic Modelling and Control of a Magnetic Bearing-Suspended Rotor System, S.M. Thesis, Massachusetts Institute of Technology, May 1988, CSDL-T-995.

[3] Crandall S. H., Physical Explanations of the Destabilizing Effect of Damping in Rotating Parts, Rotordynamic Instability Problems in High Performance Turbomachinery, NASA CP 2133, May 1980.

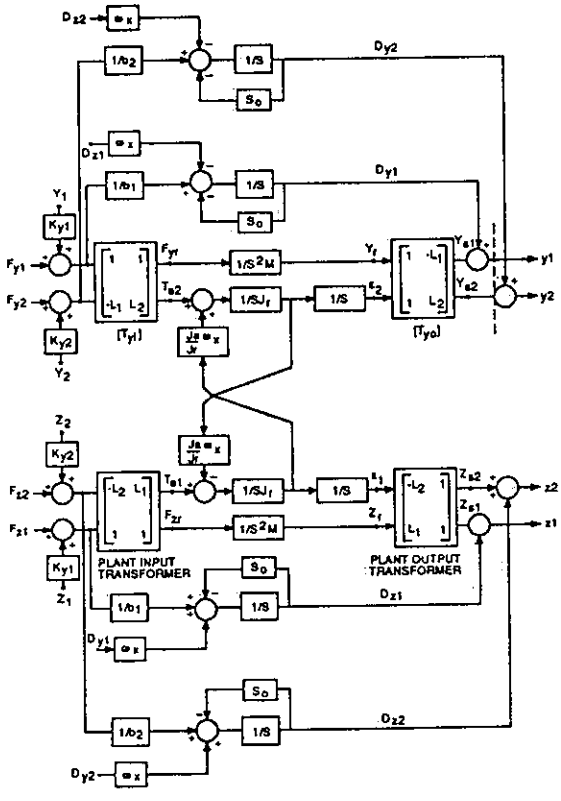

Figure 3. Block diagram of the Jeffcott rotor.

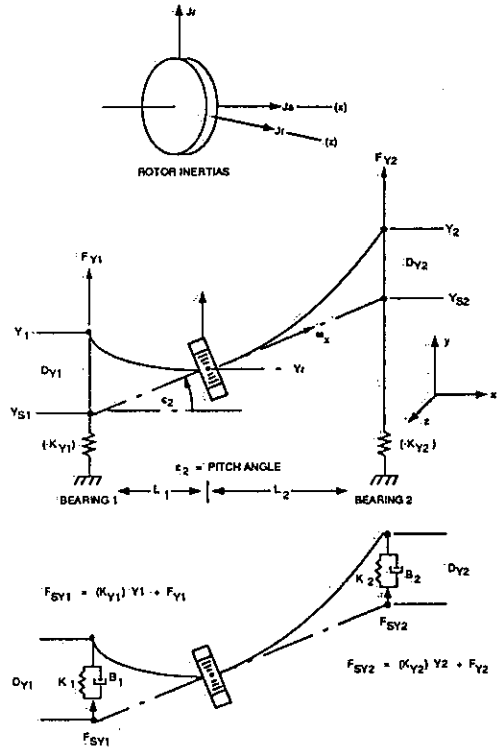

Figure 1. Side view of the Jeffcott Model showing references.

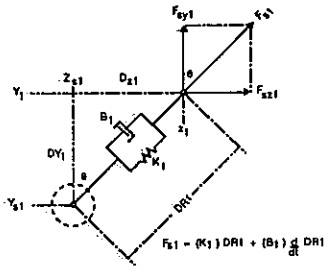

Figure 2. The spring-dashpot combination at the leftmost support.

2nd International Symposium on Magnetic Beaing
July 12-14, 1990, Tokyo, Japan

PERFORMANCE COMPARISON BETWEEN CENTRALIZED AND DECENTRALIZED CONTROL OF THE JEFFCOTT ROTOR

P. LAROCCA, D. FERMENTAL, E. CUSSON
The Charles Stark Draper Laboratory, Inc.
555 Technology Square, Cambridge, MA, USA

Abstract

Decentralized control is a typical strategy for controlling a rotating shaft/rotor using magnetic bearing actuators. It is often chosen for its simplicity of design and ease of implementation in analog circuitry. However, in high performance systems where high bandwidth is required, decentralized control may not be appropriate. This paper numerically analyzes the decentralized control of a Jeffcott rotor and shows that system bandwidth decreases as rotor rotational velocity increases. The paper then compares the performance of a centralized and a decentralized controllerto illustrate that the higher bandwidth achieved using centralized control has significant performance advantages over decentralized control.

1. Introduction

Decentralized control of magnetic bearing systems has been the subject of much research in both the commercial and academic communities. A review of magnetic bearing literature reveals that decentralized control exhibits adequate performance while being simple in design and implementation [1,2]. Most applications concern fixed platform land based rotating systems whose primary disturbances are gravity and mass unbalance loading. In such applications, high system bandwidth is not required to maintain stability and special means are used to allow operation beyond shaft critical speeds.

This paper addresses the bandwidth limitations imposed by using decentralized control and suggests that for systems operating in a moving platform environment with a dynamic disturbance envelope, such as a high performance jet engine, decentralized control may not meet performance requirements.

Numerical analysis is used to determine closed loop bandwidth of a system which consists of a rotating shaft/rotor with a four axis radial control scheme, each axis having a position and velocity sensor and P-D controller. The individual controllers are decoupled (i.e. decentralized control).

The rotor model used is the Jeffcott rotor. In this model, the rotor is taken to be a mass exhibiting inertia attached to a massless shaft characterized by stiffness and damping. The Jeffcott model is both controllable and observable for all rotational rates. The magnetic bearing actuators are assumed to be linear force devices and are not considered in the analysis. Mass unbalance and gravity are also ignored.

A decentralized controller has eight feedback gains, a number that is insufficient to independently place the twelve plant poles. This paper uses numerical methods to show that at high plant rotation rates, stable decentralized control dictates low control gains and, as a result, severely limits the allowed system bandwidth.

Since the Jeffcott rotor is both controllable and observable, a centralized control scheme will allow unrestricted system bandwidth via independent pole placement. This implies that any desired performance can theoretically be achieved. Since the system poles can be placed at any desired location, the problem of critical speeds does not arise.

The paper first presents the Jeffcott rotor model in a normalized state space form. Normalization allows the plant to be characterized by five independent ratios. A decentralized feedback gain matrix [G] is introduced and the closed loop system

is formed. Decentralized control requires velocity sensors or velocity estimators. The $[G]$ matrix is combined with the feedforward $[D]$ matrix, created by the velocity sensors, to form a new $[g]$ matrix which is combined with the $[A, B, C]$ system matrices to complete the closed loop system. In order to facilitate calculations, the rotor is taken as a sphere at the center of a massless rod and, because of symmetry, the four P-D controllers are assumed to be identical.

The numerical analysis consists of calculating stability regions of decentralized control gains for various rotational operating speeds. The results show that as the rotational rate increases, the stability region decreases and that the gains are limited to a region of lower values. As a consequence of the reduced gains, system bandwidth decreases with increasing rotational velocity. This conclusion is supported by bandwidth estimations from closed loop pole locations.

A performance comparison is made between a decentralized controller and a centralized, optimal full state feedback controller. The comparison is based on step response and disturbance rejection simulations done under identical operating conditions.

2 Jeffcott Rotor Model

To generalize results, the Jeffcott rotor model is expressed in normalized form. That is, it is expressed in terms of dimensionless ratios and therefore made dimensionless. The model is presented in state space form, and no derivation is included. For a Lagrangian based derivation, see [3], for a Newtonian based derivation, see [4].

The Jeffcott model consists of a rotor on a flexible shaft which is characterized by stiffness and damping terms. The magnetic bearing actuators are not considered and the Jeffcott model accepts force inputs. The plant can be described in twelve states. Four states describe the rotor positions and velocities in the Y-Z plane, the X-axis is the axis of rotation. Four states describe pitch and yaw angle and rates and the remaining four states describe the amount of bending a shaft has incurred. Figure 1 illustrates this concept for the Y-axis.In the figure, Y_r defines the Y-axis rotor position, ξ_2 defines the pitch angle, Y_1 represents the Y-axis position sensor output at bearing 1. The Y_1 position is comprised of two parts, Y_{S1} which represents the position of an stiff shaft deflection, and D_{Y1} which represents the amount that the shaft has bent on the left side of the rotor. ω_x is the rotational velocity about the X-axis.

The complete set of system matrices in normalized form appear in Appendix A. The plant state vector is defined as $[\mathbf{x}]^t =$

$$[Y_r, \xi_2, Z_r, \xi_1, \dot{Y}_r, \dot{\xi}_2, \dot{Z}_r, \dot{\xi}_1, D_{Y1}, D_{Z1}, D_{Y2}, D_{Z2}].$$

The plant input vector is defined as

$$[\mathbf{u}]^t = [F_{Y1}, F_{Z1}, F_{Y2}, F_{Z2}]$$

and the state output vector,shaft position and velocity information at each bearing, is defined as

$$[\mathbf{y}]^t = [Y_1, Z_1, Y_2, Z_2, \dot{Y}_1, \dot{Z}_1, \dot{Y}_2, \dot{Z}_2].$$

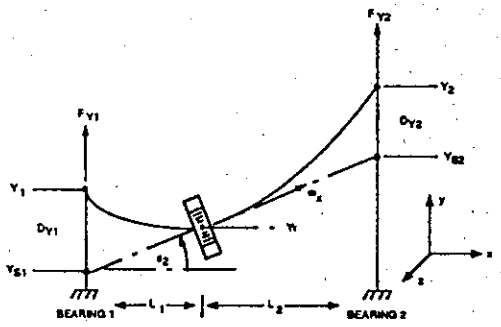

Figure 1: Flexible Shaft Definitions

The model is normalized by defining basic system units as follows:

1 unit of length	=	L1 meters
1 unit of time	=	$\frac{1}{S_0}$ seconds
1 unit of mass	=	M kg

where L1 is the distance from magnetic bearing 1 to the rotor center, M is the mass of the rotor, and S_0 is the ratio of shaft stiffness to damping in sec^{-1}. Using these as basic units, a unit of force can now be defined as

1 unit of force = $M^*L1^*S_0^2$ newtons.

The damping factor associated with the shaft between the mass and bearing 1 is $B1$. Its normalized value is $\frac{1}{v}$ and is defined as

$$\frac{1}{v} = \frac{B1/M}{S_0}.$$

Since $(B1/K1) = S_0$, where $K1$ is the shaft stiffness constant for the same shaft section, the normalized value of $K1$ is $\frac{1}{v}$ as well. The radial inertia of the rotor, Jr, has the normalized value $\frac{1}{m}$ with

$$\frac{1}{m} = \frac{Jr}{M*L1^2}.$$

and to complete the normalization, three other ratios are defined as

$$\begin{aligned} r &= \frac{L2}{L1} = \frac{B2}{B1}\,\frac{K2}{K1} \\ w &= \frac{\omega_x}{S_0} \\ a &= \frac{Ja}{Jr} * w \end{aligned}$$

where $\omega_x$is the angular velocity of the rotor and Ja is the axial rotor inertia.

To provide meaning to these normalizations, we will present a set of plant parameters in standard MKS units and their normalized equivalents in Table 1. to them:

Parameter	Physical units	Normalized units
Mass M	100 Kg	1
Shaft stiffness K1	$4 \times 10^8\ \frac{Newton}{meter}$	1/100
Shaft damping B1	$2000\ \frac{Newton-sec}{meter}$	1/100
Length L1	1 $meters$	1
Inertia Jr	1 $Kg - meter^2$	1/100
S_0 = K1/B1	2000 sec^{-1}	1

Table 1. Plant Parameters

3 Numerical Analysis

The system equations in standard state space form are

$$\begin{aligned} \dot{\mathbf{x}} &= A\,\mathbf{x} + B\,\mathbf{u} \\ \mathbf{y} &= C\,\mathbf{x} + D\,\mathbf{u} \\ \mathbf{u} &= -G\,\mathbf{y} \end{aligned}$$

with A, B, C and D given in the Appendix and normalized G being

$$\begin{bmatrix} G11 & 0 & 0 & 0 & G21 & 0 & 0 & 0 \\ 0 & G11 & 0 & 0 & 0 & G21 & 0 & 0 \\ 0 & 0 & G12 & 0 & 0 & 0 & G22 & 0 \\ 0 & 0 & 0 & G12 & 0 & 0 & 0 & G22 \end{bmatrix}.$$

We assume the plant is completely symmetric so that $G11 = G12$ and $G21 = G22$.

The feedforward matrix D and the feedback matrix G can be combined to form a single feedback matrix g as follows. Substituting in for $\mathbf{y}$, $\mathbf{u}$ becomes

$$\mathbf{u} = -\,GC\,\mathbf{x} - GD\,\mathbf{u}.$$

Solving for $\mathbf{u}$ yields

$$\mathbf{u} = -\,[\mathrm{I} + GD]^{-1}\,GC\,\mathbf{x}.$$

That is

$$\begin{aligned} \mathbf{u} &= -\,gC\,\mathbf{x} \text{ where} \\ g &= -\,[\mathrm{I} + GD]^{-1}\,G. \end{aligned}$$

Thus the system can be modeled with the four matrices $[A]$, $[B]$, $[C]$, $[g]$, and the closed loop system matrix becomes

$$A_{cl} = A - BgC,$$

where g is

$$\begin{bmatrix} g1 & 0 & 0 & 0 & g2 & 0 & 0 & 0 \\ 0 & g1 & 0 & 0 & 0 & g2 & 0 & 0 \\ 0 & 0 & g1 & 0 & 0 & 0 & g2 & 0 \\ 0 & 0 & 0 & g1 & 0 & 0 & 0 & g2 \end{bmatrix}.$$

For the plant parameters of Table 1 and with $r = 1$ and with $a = w$, so that, $m = 100$, $v = 100$, numerical analysis was used to determine the stability region of the gains $g1$ and $g2$ as a function of the normalized rotational velocity, w.

The objective of the analysis is to determine, for a given w, the range of gains over which the system is stable and to determine the maximum achievable bandwidth for that w. Bandwidth can be defined in many ways. Here, however, for all w there is a pole pair closer to the origin than any other system pole, and it is reasonable to take for the system bandwidth the real part of these poles, since the inverse of this is a measure of system settling time.

The stability of the closed loop system was tested for the logarithmically spaced gain vectors

$[g1(i), g2(j)]$ in the range of 10^{-5} to 10^{3}. This was done for selected values of w. Figure 2 shows the composite stability regions in the $(g1, g2)$ plane. As the figure shows, the stability region is a maximum at small w, and becomes progressively smaller as w increases. Further, the gains are limited to lower values. This suggests the system bandwidth must decrease for increasing w. The bandwidth results are summarized in Table 2 which contains the w of interest, the maximum bandwidth at that rate, and the gains which created that bandwidth. Note that the table is in scaled units.

w	$g1$	$g2$	Bandwidth
0.01	1000	1000	4.92×10^{-1}
0.02	1000	1000	4.87×10^{-1}
0.03	1000	1000	1.57×10^{-1}
0.04	1.00	8.90×10^{-1}	7.08×10^{-2}
0.05	1.00	8.90×10^{-1}	6.26×10^{-2}
0.06	1.00	8.90×10^{-1}	4.73×10^{-2}
0.07	4.13×10^{-4}	8.49×10^{-3}	4.55×10^{-2}
0.08	4.13×10^{-4}	8.49×10^{-3}	4.55×10^{-2}
0.09	4.13×10^{-4}	8.49×10^{-3}	4.54×10^{-2}
0.10	4.13×10^{-4}	8.49×10^{-3}	4.54×10^{-2}
0.14	4.13×10^{-4}	8.49×10^{-3}	4.54×10^{-2}
0.20	4.13×10^{-4}	8.49×10^{-3}	4.52×10^{-2}
0.30	4.13×10^{-4}	8.49×10^{-3}	4.52×10^{-2}
0.40	4.13×10^{-4}	8.49×10^{-3}	4.52×10^{-2}
0.50	4.13×10^{-4}	8.49×10^{-3}	4.52×10^{-2}

Table 2. Decentralized Control Summary

To provide meaning to the scaled units, w = .01 rads/pseudoseconds (psec) corresponds to 20 rads/sec or a 3.18 Hz rotational rate and the bandwidth of .49 rads/psec correspond to 980 rads/sec or a 156 Hz bandwidth. At w = .1 rads/psec, a 31.8 Hz rotational rate the system bandwidth falls to .0454 rads/psec or 14.5 Hz bandwidth. Clearly, as the rotational velocity increases, the system bandwidth decreases. It must do so for decentralized control.

4 Performance Comparison

In order to illustrate the consequence of bandwidth limitations imposed by decentralized control, a comparison of performance will be made using both centralized and decentralized controllers operating on the same plant under the same test conditions. Step

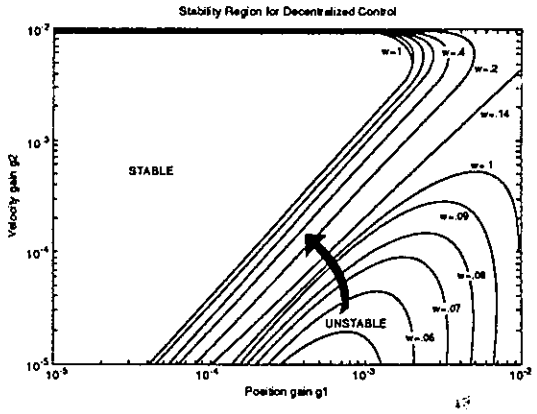

Figure 2: Composite stability regions

response simulations are typically used as performance measures in control system evaluations and were used here. Additionally, d.c. disturbance simulations were run to illustrate the rejection properties of both controllers.

The simulations were run using the normalized system, so time is expressed in pseudoseconds (psec) where 1 psec = 1/2000 sec. For the tests, the rotational velocity of the rotor was set at $\sqrt{.02}$ or .141 rads/psec. This corresponds to the plant resonant frequency, where $\omega_r^2 = 2K1/M$, or $w^2 = 2/v$. The gains for the decentralized controller are such that they provide the maximum possible bandwidth for a stable configuration. The gains used are $g_{position} = 4.132 \times 10^{-4}$ and $g_{velocity} = 8.49 \times 10^{-3}$. The decentralized closed loop bandwidth is dictated by the pole pair at $-0.0454 \pm 0.0666j$.

The centralized control system used is an optimal state feedback controller. Centralized control has additional degrees of control freedom which allows for complete and independent pole placement. Therefore, the resulting closed loop bandwidth is not limited, and can be made any value desired. For the purpose of comparison, it was made to be approximately 6 times the closed loop bandwidth of the maximum decentralized controller bandwidth. The centralized control closed loop bandwidth is dictated by the pole pair at $-0.2869 \pm 0.2754j$.

Figure 3 contains the closed loop frequency re-

sponses of the centralized and decentralized systems. The loop is measured from position command input to rotor position output. It clearly illustrates the increased bandwidth afforded by using a centralized control system.

A step response simulation of the two systems is shown in Figure 4. The command input is a step of 1.27×10^{-4} meters (5 mils) of rotor position in the Y axis. The time, in pseudoseconds, represents .1 seconds. The centralized controller response is close to ten times faster, with much less over-shoot. Figure 5 contains the rotor position when a d.c. disturbance to simulate gravity is applied. Again the centralized controller dramatically out-performs the decentralized controller. The time of response is much faster, but more importantly, the magnitude of the rotor displacement is 100 times less in the centralized control response. The decentralized control rotor may have exceeded its hard stop limit just from the application of gravity. In a jet engine application, the disturbance envelope can include load at up to ten times gravity [5] and clearly, a limited bandwidth decentralized control strategy is not adequate.

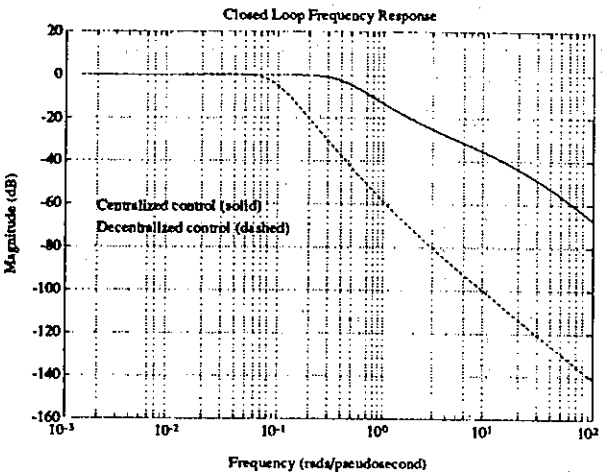

Figure 3: Closed loop frequency responses

5 Conclusion

A normalized version of the Jeffcott Rotor model was presented. Stability regions for decentralized control were determined as a function of rotor rotational velocity. From those stability regions, the maximum closed loop system bandwidth design was found, and the bandwidth and the associated decentralized controller gains were noted. It was shown that as the rotational velocity increased, the maximum bandwidth achievable decreased due to a decrease in the stability region of the decentralized control gains to lower and lower values. To quantify the lower bandwidth forced by the use of decentralized control, a high bandwidth, centralized control system was designed using optimal full state feedback techniques and a performance comparison between the two control systems was done under identical operating conditions. The centralized controller clearly has significant performance advantages over the decentralized controller in both step response and disturbance rejection tests.

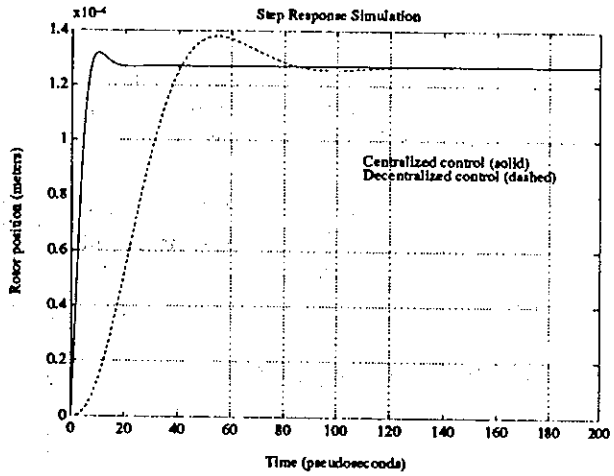

Figure 4: System step responses

References

[1] Schweitzer, G. and A. Traxler. **Design of Magnetic Bearings.** Proceedings of the International Symposium on Design and Synthesis, Tokyo, Japan, July, 1984.

[2] Blueler, H. and G. Schweitzer. **Dynamics of a Magnetically Suspended Rotor with Decentralized Control.** Applied Control and Iden-

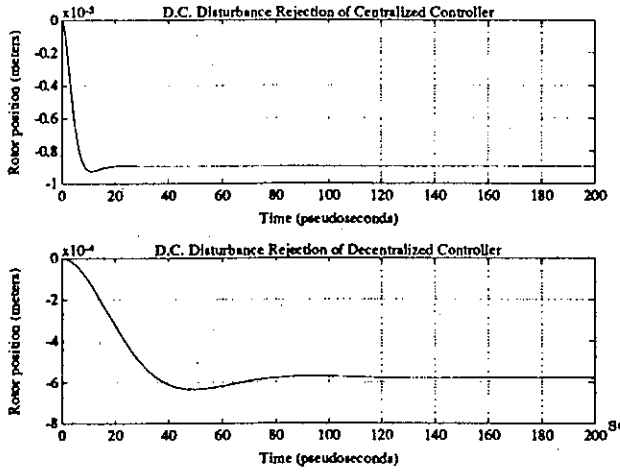

Figure 5: Gravity application responses

tification Symposium of the IASTED, Copenhagen, June,1983.

[3] McCallum, D. **Dynamic Modelling and Control of a Magnetic Bearing — Suspended Rotor System**, MIT SM Thesis, May, 1988.

[4] Fermental, D., P. LaRocca, and E. Cusson. **The Jeffcott Rotor: It's Decomposition and Control.** C.S. Draper Lab Report CSDL-P-2920, February, 1990.

[5] Pratt and Whitney Co. report FR-18022.

Appendix A

This appendix contains the system matrices in normalized form. The system is in the standard state space form

$$\dot{\mathbf{x}} = A\,\mathbf{x} + B\,\mathbf{u}$$
$$\mathbf{y} = C\,\mathbf{x} + D\,\mathbf{u}.$$

The state vector is defined as

$$[\mathbf{x}]^t = [Y_r, \xi_2, Z_r, \xi_1, \dot{Y}_r, \dot{\xi}_2, \dot{Z}_r, \dot{\xi}_1, D_{Y1}, D_{Z1}, D_{Y2}, D_{Z2}],$$

and the A matrix is

$$\begin{bmatrix}
0 & 0 & 0 & 0 & 1 & 0 & 0 & 0 & 0 & 0 & 0 & 0 \\
0 & 0 & 0 & 0 & 0 & 1 & 0 & 0 & 0 & 0 & 0 & 0 \\
0 & 0 & 0 & 0 & 0 & 0 & 1 & 0 & 0 & 0 & 0 & 0 \\
0 & 0 & 0 & 0 & 0 & 0 & 0 & 1 & 0 & 0 & 0 & 0 \\
0 & 0 & 0 & 0 & 0 & 0 & 0 & 0 & 0 & 0 & 0 & 0 \\
0 & 0 & 0 & 0 & 0 & 0 & 0 & a & 0 & 0 & 0 & 0 \\
0 & 0 & 0 & 0 & 0 & 0 & 0 & 0 & 0 & 0 & 0 & 0 \\
0 & 0 & 0 & 0 & 0 & -a & 0 & 0 & 0 & 0 & 0 & 0 \\
0 & 0 & 0 & 0 & 0 & 0 & 0 & 0 & -1 & -w & 0 & 0 \\
0 & 0 & 0 & 0 & 0 & 0 & 0 & 0 & w & -1 & 0 & 0 \\
0 & 0 & 0 & 0 & 0 & 0 & 0 & 0 & 0 & 0 & -1 & -w \\
0 & 0 & 0 & 0 & 0 & 0 & 0 & 0 & 0 & 0 & w & -1
\end{bmatrix}$$

The input vector is defined as

$$[\mathbf{u}]^t = [F_{Y1}, F_{Z1}, F_{Y2}, F_{Z2}]$$

so that [B] is

$$\begin{bmatrix}
0 & 0 & 0 & 0 \\
0 & 0 & 0 & 0 \\
0 & 0 & 0 & 0 \\
0 & 0 & 0 & 0 \\
1 & 0 & 1 & 0 \\
-m & 0 & mr & 0 \\
0 & 1 & 0 & 1 \\
0 & m & 0 & mr \\
v & 0 & 0 & 0 \\
0 & v & 0 & 0 \\
0 & 0 & rv & 0 \\
0 & 0 & 0 & rv
\end{bmatrix}$$

The state output vector, shaft position and velocity information at the magnetic bearings, is defined as

$$[\mathbf{y}]^t = [Y_1, Z_1, Y_2, Z_2, \dot{Y}_1, \dot{Z}_1, \dot{Y}_2, \dot{Z}_2],$$

so the [C] matrix is

$$\begin{bmatrix}
1 & -1 & 0 & 0 & 0 & 0 & 0 & 0 & 1 & 0 & 0 & 0 \\
0 & 0 & 1 & 1 & 0 & 0 & 0 & 0 & 0 & 1 & 0 & 0 \\
1 & r & 0 & 0 & 0 & 0 & 0 & 0 & 0 & 0 & 1 & 0 \\
0 & 0 & 1 & -r & 0 & 0 & 0 & 0 & 0 & 0 & 0 & 1 \\
0 & 0 & 0 & 0 & 1 & -1 & 0 & 0 & -1 & -w & 0 & 0 \\
0 & 0 & 0 & 0 & 0 & 0 & 1 & 1 & w & -1 & 0 & 0 \\
0 & 0 & 0 & 0 & 1 & r & 0 & 0 & 0 & 0 & -1 & -w \\
0 & 0 & 0 & 0 & 0 & 0 & 1 & -r & 0 & 0 & w & -1
\end{bmatrix}$$

and the [D] matrix is

$$\begin{bmatrix}
0 & 0 & 0 & 0 \\
0 & 0 & 0 & 0 \\
0 & 0 & 0 & 0 \\
0 & 0 & 0 & 0 \\
v & 0 & 0 & 0 \\
0 & v & 0 & 0 \\
0 & 0 & rv & 0 \\
0 & 0 & 0 & rv
\end{bmatrix}$$

2nd International Symposium on Magnetic Beaing
July 12-14, 1990, Tokyo, Japan

A NEW APPROACH TO SENSORLESS AND VOLTAGE CONTROLLED AMBs BASED ON NETWORK THEORY CONCEPTS

DIETER VISCHER*), HANNES BLEULER*)

*) Dr., Institute of Robotics , Swiss Federal Institute of Technology (ETH), 8092 Zurich, Switzerland

Abstract

Active magnetic bearings (AMBs) as actuators operate not only in the direction from the amplifier to the bearing magnet and then to the rotor, but also in the **opposite direction,** from the rotor back to the amplifier. In this paper, such effects are not dismissed as deviation from the ideal, but are used to **improve** the design of the sensing system. The AMB is interpreted as a **two-port** converting electrical (current & voltage) into mechanical values (force & velocity) and vice versa. This is the basis for assessing some unconventional control schemes including **voltage control** and the **"sensorless" bearing.** By this term, we would like to designate a rotor-bearing model with bearing voltage as input and bearing current as output, using no specific sensing hardware. It can be shown that such a system is observable and controllable. The paper presents a short discussion of the fundamental AMB equations in the new context. An **example** of a sensorless bearing realized at our laboratory illustrates the **practical feasibility** of this new approach to AMB modelling and control.

1. Introduction

The "classical" modelling of control plants is often based on idealized unidirectional signal-flow representations. Looking at the energy transmissions inside a system, however, it can be seen that some elements such as actuators and amplifiers are actually of a **bidirectional** nature.

Methods based on measuring the airgap dependent inductance e.g. by means of some high frequency modulation or pulsing are known and have been patented since many years (/Sit 67/, /Schef 75/ and others), but they do not seem to have evolved beyond experimental setups.

In this paper we would like to take the entirely different approach of using the **controllability and observability** of the AMB-plant with **voltage input and current output.** First feasibility tests have been made in 1987 /Vi 88/ and a current project at our Institute aims at improving the practical performance.

We concentrate here on AMBs with a pair of two opposite electromagnets as shown in fig. 1 since this is the most common setup for rotor bearings. The main results of this paper are nevertheless also applicable to the one-sided case of magnetically levitated vehicles or special rotor designs using gravity or combinations with passive magnetic bearings.

Flux-sensing also fits nicely into the framework of this work. Flux control shares many advantages with voltage control. Practical results have been obtained at our Institute. They are described in the contribution "Cost-Effective Implementation of AMB" by Zlatnik and Traxler /Zl 90/, at this same symposium. Here we therefore concentrate on voltage-controlled and sensorless bearings and we will not discuss flux sensing.

2. The Basic AMB-Equations

The basic AMB equations are obtained from Maxwell's laws. This derivation is not shown here. Secondary effects such as stray fields and saturation are neglected. Furthermore, it is assumed, that the complete energy of the magnetic field is concentrated in the active airgap, the flux in the iron core is neglected. Fig. 1 shows the actuator considered:

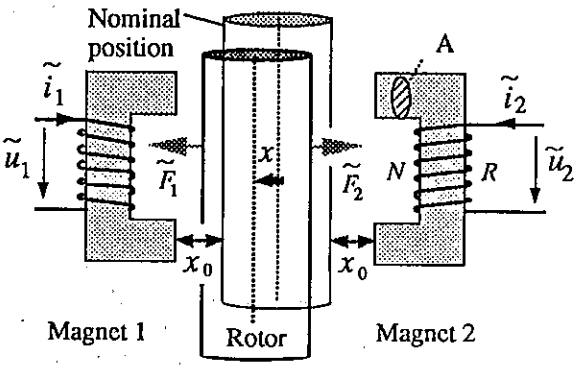

Fig.1 Notations for a two-sided actuator with one mechanical degree of freedom, the rotor displacement x . A displacement to the left is defined positive, for x=0 the air gaps are x_0. More symbols are listed in table 1 on the next page.

The equations relevant for control layout are obtained from a linearization for the operating point, by defining constant operating-point (or nominal) values (subscript zero) and variable components (subscript one or two, indicating the left or right magnet of fig.1).

Operating point
x_0 : Nominal airgap i_0 : Nominal (or premagnetisation) current
Variables
$\tilde{i}_1 = i_0 + i_1$ $\quad \tilde{i}_2 = i_0 + i_2$ Currents in coil 1 and 2 (Corresponding relations for forces & voltages)
Basic bearing constants:
N : Number of Windings A : Iron Cross Section R : Copper Resistance
Secondary bearing constants:
$L = NA\,\mu_0/2x_0$: inductance at x= const.= 0 $k_i = L\,i_0/x_0$: Force-current factor $k_s = k_i\,i_0/x_0$: Force-displacement factor

Table 1: Notations ($\mu_0 = 1.257 \cdot 10^{-6}$Vs/Am)

With the assumptions stated before, the linearized relation of force F_1 and voltage u_1 can be found as

$$\frac{dF_1}{dt} = \frac{i_0}{x_0}(u_1 - Ri_1) \tag{1}$$

A second basic equation relates current change to voltage in the coil and displacement velocity:

$$\frac{di_1}{dt} = \frac{1}{L}u_1 - \frac{R}{L}i_1 - \frac{i_0}{x_0}\dot{x} \tag{2}$$

The more familiar relation (3) can be obtained by substituting the integral of (1) into the integral of (2)

$$F_1 = k_i\, i_1 + k_s\, x \tag{3}$$

These equations are valid only for the linearized components of force, voltage and current as defined in table 1.

Equation (2) describing the coil voltage is of minor importance when the classical current control scheme is used. In the present paper however, it provides the basis for voltage controlled AMBs and the sensorless bearing through the voltage induced by rotor motion in the magnetic field. The constant k_i not only relates the force to the current but also appears with the contribution of the rotor velocity $\dot{x}$ to the voltage u_1 . Its dimension is [N/A] = [Vs/m].

3. The AMB as a Two-Port

The AMB can be interpreted as a *two-port* converting electrical variables (current i_1 & voltage u_1) into mechanical ones (force F_1 & velocity $\dot{x}$) **and vice versa.** Equations (1) and (2) can be summarized in a transfer matrix. At the same time, we transform to the Laplace domain where differentiation is replaced by the Laplace variable s. For simplicity, variable names are kept the same as in the time domain.

$$\begin{bmatrix} F_1 \\ \dot{x} \end{bmatrix} = \begin{bmatrix} \frac{i_0}{x_0}\frac{1}{s} & -\frac{i_0}{x_0}\frac{R}{s} \\ \frac{1}{k_i} & -\frac{x_0 s}{i_0} - \frac{R}{k_i} \end{bmatrix} \begin{bmatrix} u_1 \\ i_1 \end{bmatrix} \tag{4}$$

Fig. 2 gives an *equivalent circuit* for the AMB two-port. It consists of a resistance R, an inductance L and an idealized "basic AMB two port".

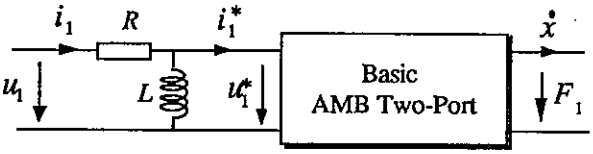

Fig. 2 The AMB as two-port: Equivalent circuit. The mechanical variables can be interpreted as electrical ones according to the classical analogy force-voltage and current-velocity.

If the mechanical variables force and velocity are interpreted as electrical ones according to the classical (i.e. force-voltage and velocity-current analogy), this AMB-two-port becomes equivalent to an ideal transformer with an s-dependent constant. Its transfer matrix is

$$\begin{bmatrix} F_1 \\ \dot{x} \end{bmatrix} = \begin{bmatrix} \frac{i_0}{x_0}\frac{1}{s} & 0 \\ 0 & -\frac{x_0 s}{i_0} \end{bmatrix} \begin{bmatrix} u_1^* \\ i_1^* \end{bmatrix} \tag{5}$$

The sign follows from the definition of the positive directions at the output of the two-port. The basic AMB is *lossless*, it has the property of converting the entire electrical power into mechanical power *and vice versa*:

$$i_1^* \cdot u_1^* = -F_1 \cdot \dot{x} \tag{6}$$

As opposed to other two-ports such as dc-motors and transformers, the basic AMB transfer matrix is a function of the Laplace variable s.

Two-ports are often operated as actuator and sensor. A dc–motor, for instance, is basically controlled by means of the current and can then be interpreted as a "torque-source". Sometimes it is used as a "velocity-source" employing voltage control. According to the two-port concept, the dc-motor may also serve as velocity or torque-sensor, as actually realized in some applications

The AMB also can be operated as actuator, sensor or both, actuator and sensor, at the same time. It can not only serve as velocity sensor like the dc-motor, but it has the additional possibility of operating as a position sensor. From equation (5) it can be seen, that the rotor deflection x_1 is proportional to the current i_1^* of the basic AMB 2-port.

$$x = -\frac{x_0}{i_0}\, i_1^* \qquad (7)$$

Therefore current i_1 must contain somehow the information on the displacement x. Current is easily measured and this is actually implemented for almost any practical AMB system, be it only to protect the amplifier from overcurrent. From this fact, the idea of the feasibility of a "sensorless" bearing was derived.

4. State-Space Model

The complete state-space model for the actuator-bearing-rotor system includes at least two mechanical states (velocity and displacement). In addition, each electro magnet contributes one state variable to the model. In the case of two-sided actuators (fig. 1), two state variables, e.g. the currents in the coils, are necessary for each mechanical degree of freedom to completely describe the behavior of the open loop system.

Fig. 3 shows the state-space model for such a system, including Newton's law

$$m\,\ddot{x} = F_1 - F_2 = \tilde{F}_1 - \tilde{F}_2 \qquad (8)$$

where m is the equivalent rotor mass effective at the actuator.

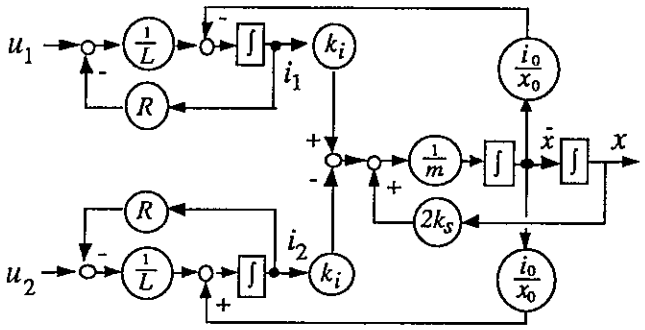

Fig. 3 ***Linearized state-space model for one mechanical degree of freedom and two coils*** *according to fig. 1. The two currents (i_1, i_2,) in each coil of the bearing, rotor velocity $\dot{x}$ and deflection x are used as state variables. This model's observability from the current measurements alone is the basis for a practical sensorless bearing system. Currents are measured in the amplifiers and can be used as controller inputs, voltages as plant inputs.*

The MIMO-system (**Multiple Input Multiple Output**) shown in fig.3 is observable from the current measurements (i_1, i_2) alone. Using the voltage inputs (u_1, u_2), it is also controllable. This means that **measuring the rotor displacement x is not needed** for control.

This has been demonstrated in practical setups by Vischer and in a student project of our Institute /JV 90/. A patent /VTB 88/ has been applied. Some possibilities for control layout making use of the results above are now elaborated.

5. Transformations of the State-Space Model and Transfer Functions

The state space model shown in fig. 3 is used to design a bearing control with voltage instead of current as input variable. This will be called "voltage control". Voltage control has been investigated thoroughly by many authors /Ul 84/, often in the context of maglev vehicles (e.g. /Jay 81/, /Br 80/)

The system of fig. 3 is observable if at least two of the three outputs (i_1, i_2, x) are available to the controller. The following two cases, both of which have some advantages for AMB applications, will be examined further:

- voltage control combined with three measurements (i_1, i_2 and x)
- voltage control combined with the current measurements only (sensorless bearing)

One way to control the above systems is to implement a Luenberger observer and a state feedback controller. The full state-feedback matrix has 8 coefficients (2 inputs, 4 states). Some additional control parameters are used for the Luenberger observer. Such controllers were built and tested at our institute. A voltage controlled AMB with and without sensor was realized as described above (see also section 8 on experiments).

As we deal only with a single mechanical degree of freedom, we seek to simplify this controller. It is possible to describe the plant (fig. 3) as a set of two SISO-systems (Single Input Single Output), as shown in fig. 4. If the four values (i_1+i_2), x, $\dot{x}$ and $\ddot{x}$ (or force, see e.g. /GC 77/ or /GMM 77/) are used as state variables instead of i_1, i_2, x and $\dot{x}$, the MIMO-system can be replaced by a 3rd order and a first order SISO-system.

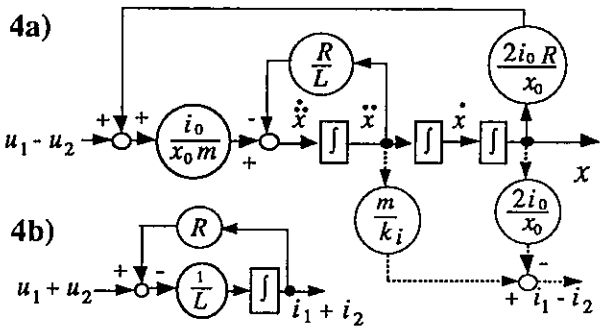

Fig. 4 Transformed state-space model for the system of fig. 3. This choice of state variables produces two decoupled subsystems, fig. 4a (with states x, $\dot{x}$ and $\ddot{x}$) and fig. 4b with the single state variable (i_1+i_2,)

Fig. 4a shows that the rotor movement only depends on the difference between the two input voltages u_1 and u_2, whereas the sum of the currents i_1+i_2 is only a function of the sum u_1+u_2.

The transfer function of the first subsystem (fig. 4a) is

$$x = \frac{\frac{i_0}{m\,x_0}}{s^3 + \frac{R}{L}s^2 - \frac{2\,R\,i_0^2}{m\,x_0^2}} (u_1 - u_2) \tag{9}$$

This subsystem is a triple integrator for $R=0$ (R is the copper resistance). The parameter R destabilizes this open-loop system.

The transfer function of the 2nd subsystem (fig. 4b) is

$$(i_1 + i_2) = \frac{1/L}{s + R/L} (u_1 + u_2) \tag{10}$$

which is a stable first order system independent of the rotor movement.

In fig. 4, the current difference (i_1-i_2) it is shown to be a difference of state variables. Acceleration as state variable can be replaced by (i_1-i_2). The transfer function (11) from input (u_1+u_2) to output (i_1-i_2) nicely shows the operation principle of the sensorless bearing.

$$(i_1 - i_2) = \frac{\frac{1}{L}s^2 - \frac{2\,i_0^2}{m\,x_0^2}}{s^3 + \frac{R}{L}s^2 - \frac{2\,R\,i_0^2}{m\,x_0^2}} (u_1 - u_2) \tag{11}$$

Fig. 5 shows the corresponding simple state-space model.

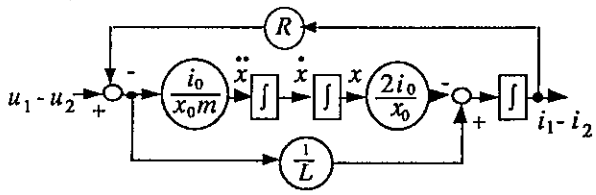

*Fig. 5 **Transformed state-space model of the SISO-plant of fig.4b for sensorless operation.** (State variables: (i_1-i_2), x and ẋ) This system together with the subsystem of fig.4b leads to a simple linear controller.*

The transfer functions (9) & (11) are of full order, therefore it can be deduced that the voltage controlled AMB-plant is observable and controllable from the measurements (i_1+i_2) and x *or* (i_1-i_2).

Since the subsystem (fig. 4b) is stable, it is sufficient to control the SISO-system (fig. 4a) characterized by equation (11). Again, this has been experimentally verified. However, a simple controller (proportional feedback, see section 7.1) for the subsystem (fig 4b) enhances the performance of the entire system.

6. Multiple Mechanical Degrees of Freedom

The extension to a full order system with multiple mechanical degrees of freedom is straightforward. As before, each pair of opposing electro magnets is separated into two subsystems. The subsystems (fig 4b) are independent of the mechanical system.

The influence from one mechanical degree of freedom to another acts just like an **additional force input** at the corresponding summation points in figures 3 4 or 5. Decentralization, i.e. the implementation of local feedback based on a complete model, is feasible in most practical cases /Bl 84/, with the obvious implications on the model order used for analysis. With such a layout approach, the on-line computing power requirements grow only proportional to the number of control channels.

In many cases, it is even possible to simplify one step further and to base control layout itself on a decentralized model, which brings us back to the simple models described in sections 4 and 5.

7. Control

Given a state-space model of the sensorless AMB as shown in fig 1 and knowing that the system is observable and controllable, an appropriate control can be found in a straightforward manner. There is a large number of publications on AMB control. A representative choice can be found in this symposium and in /Sch 88/. Results often can be combined with concepts presented here. Some specific control features relevant in the context of this paper are now shortly treated.

7.1 Operational Point Controller

It is again assumed that two opposite magnets with separate coils, as shown in fig.1 are used for each degree of freedom. The current and voltage sums and differences used as state variables in fig. 4 are

$$\tilde{i}_1 + \tilde{i}_2 = 2\,i_0 + i_1 + i_2 \quad \text{and} \quad \tilde{i}_1 - \tilde{i}_2 = i_1 - i_2$$
$$\tilde{u}_1 + \tilde{u}_2 = 2\,u_0 + u_1 + u_2 \quad \text{and} \quad \tilde{u}_1 - \tilde{u}_2 = u_1 - u_2 \tag{12}$$

Using (12), a control law for the subsystem of fig. 4b can be found as

$$\frac{\tilde{u}_1 + \tilde{u}_2}{2} = P\left(i_{0_{des}} - \frac{\tilde{i}_1 + \tilde{i}_2}{2}\right) \tag{13}$$

where i_{0des} is the desired premagnetisation or nominal current and P a proportional feedback. Since this servo has the property of controlling the premagnetisation current to a desired value, we refer to it as "operational point controller ".

It has been stated before that the two SISO-systems fig.4a & fig.4b are independent of each other, which allows for a separate control design for each of those subsystems. The

analysis was based on the *linearized* AMB model. However, only a *high* proportional feedback of the working point controller can guarantee the linearization to be accurate since equation (3) is only valid close to the working point.

Fig.6 shows how to connect the amplifiers to the controller taking advantage of the state-space representation of section 5 (fig. 4).

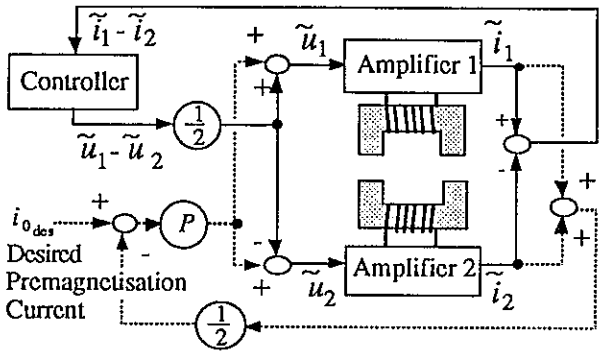

Fig.6 Working point controller connections for the voltage controlled bearing

The purpose of the working point controller can be summarized as follows:

- It improves the accuracy of linearization.
- It simplifies control by reducing plant order and the number of inputs. Single degree of freedom mechanical models become SISO.

7.2 Voltage-Controlled Bearings

A variety of measurement combinations is possible.

From a measurement of displacement x and (i_1-i_2), the acceleration (or force) can be obtained with a simple summation. A similar result can be obtained with flux measurement (/Vi 88/, /VTB 88/, /ZT 90/).

Measuring just x, a PD^2 is the most simple control necessary for the third order system.

The sensorless bearing is of course the most spectacular output variable combination. The simplest possible linear controller for the sensorless bearing is

$$i_1 - i_2 = \frac{b_2 s^2 + b_1 s + b_0}{a_1 s + a_0} u_1 - u_2 \qquad (14)$$

In practice, we did not try this simple controller, but we used a state feedback with observer as described in sections 5 and 8.

7.3 The Voltage-Controlled AMB Compared to the Classical Current-Control

Strictly speaking the term "current-controlled bearing" designates a special voltage-controlled bearing consisting of two current controllers as inner loops and a position control as outer loop. As magnet current in reality is a state variable (eq. (2)), the dynamics of the inner control loop is usually neglected for treatment of the outer loop with current as plant-input. The transfer function of the plant of this outer loop, a simple current controlled AMB, is

$$x = \frac{k_i}{m} \frac{1}{s^2 - p^2} i_1 - i_2 \qquad (15)$$

where $p = \sqrt{\frac{m}{2k_s}}$

The current controlled AMB has the *advantage* of being independent from copper resistance. Furthermore its transfer function is of 2nd order whereas the voltage controlled bearing is a 3rd order system .

The open-loop plant with current input has however the *disadvantage* of being "strongly unstable" (pole at $+p$). The plant with voltage input is also unstable, but to a lesser degree. The root-locus plot (fig. 7) shows the poles of the open-loop 3rd order plant (fig. 4a or eq.(9) and (11)) as a function of the copper resistance R.

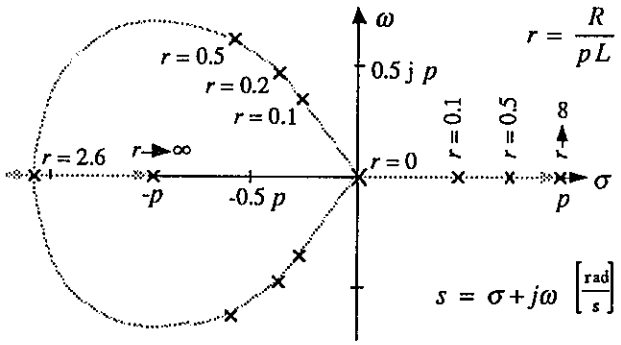

*Fig. 7 **Poles of the 3rd-order plant as function of copper resistance R.** The normalized copper resistance r is typically in the range of 0.5% to 5%. This leads to 3 open-loop poles closer to the origin than for the 2nd-order plant of eq. (15).*

It can thus be expected that a voltage-controlled AMB is at least theoretically easier to stabilize and less sensitive to noise and time lag than a current controlled one. A quantitative analysis of this statement and a more detailed comparison of voltage and current controlled bearings is given in /Vi 88/.

8. Experiments

In practice, the sensorless bearing is difficult to realize and sensitive to parameter uncertainties. We did not yet achieve a high stiffness. One way to operate it, is to build a Luenberger observer (with i_1 and i_2 as inputs) for the system of 4th order according to fig. 3 and to check it against a position measurement. A state feedback can then be implemented

and sensorless operation is achieved by switching position feedback from the measured signal to the estimated one.

For an experimental rotor with linear (not switched) power amplifiers, this was implemented in /JV 90/ on a signal processor with a sampling time of 120 µsecs. With a robust but not very stiff state feedback, it could then successfully be switched from the measured displacement to the estimated one. Measured step responses in both operation modes are shown below:

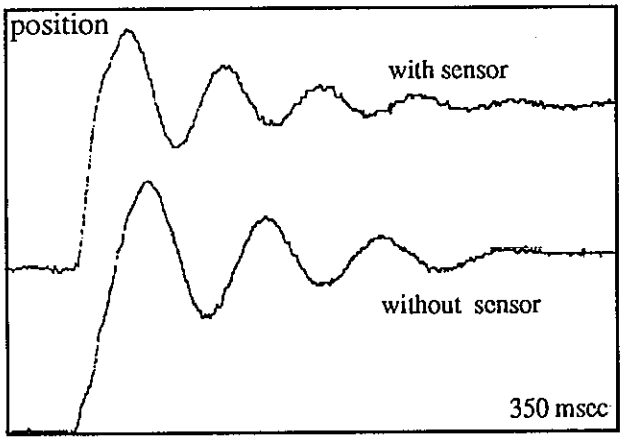

Fig. 8: Measured step responses (peak amplitude about 0.2 mm) of an AMB system with state feedback and position measurement on the top curve, with sensorless operation from a Luenberger observer and current measurements only on the bottom curve. The state feedback is the same in both cases. However, the observer is very sensitive to the copper resistance of the coil.

9. Conclusions

The AMB actuator is regarded as a two port in the framework of network theory. This leads us to reconsider the choices for state, input and output variables of the AMB system. Results including voltage control, flux control (in /ZT 90/) and a sensorless bearing are presented.

Voltage control might be promising for many applications, as advantages are clearly indicated by theory. The sensorless control scheme using the observability of the AMB-actuator with voltage input and current output has been implemented experimentally. Although this particular type of bearing does not yet have very good performance, it could eventually be improved and used in some low-cost applications.

The general trend is towards an increase in control software sophistication (higher order, observer) with the advantage of making better use of the hardware.

Further research is needed in all domains in the scope of this contribution.

10. References

/Sit 67/ James L. **Sitomer** & M. D. **Leis**: "Time Sharing Pulsed Rebalancing System" U.S. Pat. Nr. 3,508,444, 1970

/Schef 75/ **Scheffer**, D., **Guse**, R.: Elektromagnetische Lagerungseinrichtung. Deutsche Patentschrift Nr. 25 37 597, Anmelder: Firma Padana AG (Zug, CH), Inst. für Textiltechnik Stuttgart, Reutlingen, 23. 8. 1975.

/Vi 88/ Dieter **Vischer** "Sensorlose und Spannungsgesteuerte Magnetlager", Doctor Thesis Nr. 8665, ETH Zürich, 1988

/Zl 90/ D. **Zlatnik** and A. **Traxler** "Cost-Effective Implementation of AMB" 2nd Int. Symp. on Magnetic bearings, Tokyo, 1990

/JV 90/ P. **Jordil**, F. **Volery**: "Régulation d'un palier magnétique sans senseur de position" Student's diploma project, Feb. 1990, Inst. for Robotics, ETH Zürich

/VTB 88/ **Vischer, Traxler, Bleuler** "Magnetlager", patent application Nr. P 3937687.7, 13.Nov.89, Germany

/Ul 84/ H. **Ulbrich**, E. **Anton**: "Theory and Application of Magnetic Bearings with Integrated Displacement and Velocity Sensors", The Inst. of Mech. Eng., C299/84, Cambridge 1984

/Jay 81/ Bhalchandra Vinayak **Jayawant** "Electromagnetic levitation and suspension techniques" London, Arnold, 1981

/Br 80/ **Breinl**, W.: Entwurf eines unempfindlichen Tragregelsystems für ein Magnetschwebefahrzeug. Fortschrittbericht der VDI-Zeitschriften, Reihe 8, Nr. 34, München, 1980.

/GC 77/ **Gottzein**, E., **Crämer**, W.: Critical Evaluation of Multivariable Control Techniques based on MAGLEV Vehicle Design. IFAC Symposium on Multivariable Technological Systems, Canada, July 1977.

/GMM 77/ **Gottzein**, E., **M iller** L., **M eisinger**, R.: Magnetic Suspension Control System for High Speed Ground Transportation Vehicles. World Electrical Congress, Moscow, June 1977.

/Bl 84/ H. **Bleuler**: "Decentralized Control of Magnetic Bearing Systems", Doctor thesis no 7573, ETH Zürich 84

/Sch 88/ G. **Schweitzer**, ed.: Magnetic Bearings. Proceedings of the First International Symposium, Springer-Verlag, ETH Zürich, June 6-8 1988

2nd International Symposium on Magnetic Beaing
July 12-14, 1990, Tokyo, Japan

A DESIGN METHOD OF A DYNAMIC COMPENSATOR OF CONICAL MODES FOR MAGNETIC BEARINGS OF A RIGID SPINNING ROTOR

Chikara MURAKAMI

Faculty of Aerospace Engineering, Tokyo Metropolitan Institute of Technology,
6-6 Asahigaoka, Hino-shi, Tokyo 191, Japan

Abstract

A design method of a dynamic compensator for magnetic bearings levitating a spinning rigid rotor is proposed. The basic control concept is to move not the rotor directly but the angular momentum vector. The control strategy is to move the angular momentum vector to the spinning axis for nutation suppression and to move the vector to the central position of the stator for precession suppression. It is necessary to estimate the angular momentum vector. An easy estimation method is presented here without using complex observer system or rate signals. A block diagram of the tootal system including the dynamic compenstor clarifies physical meaning of the cross-feedback. Approximate analytic eigen values of the total system are obtained using complex number variables. Several simulation examples are given, showing validity of the approximate analytic solutions.

Introduction

There are two conical modes in whirling motion of rigid spinning bodies supported by active magnetic bearings. They are a low frequency (backward) mode and a high frequency (forward) one. The control strategy is to move the angular momentum vector, H, of the rotor to the central axis of the stator or desired rotor position for suppression of the former mode and to the spinning axis for suppression of the latter one. Therefore, it is necessary to obtain signals of H position or rate signals of tilting angles of the rotor to control any mode. In this paper, an easy method for estimation of H without using complex observer system or rate signals is proposed, and a simple method for construction of a dynamic compensator for suppression of both modes from a standpoint of physical meaning are presented. Approximate analytical eigen values of the total system including the dynamic compensator are also presented. Simulation examples verify effectiveness of above-mentioned method. These concepts may suggest some new control methods of flexible spinning rotors.

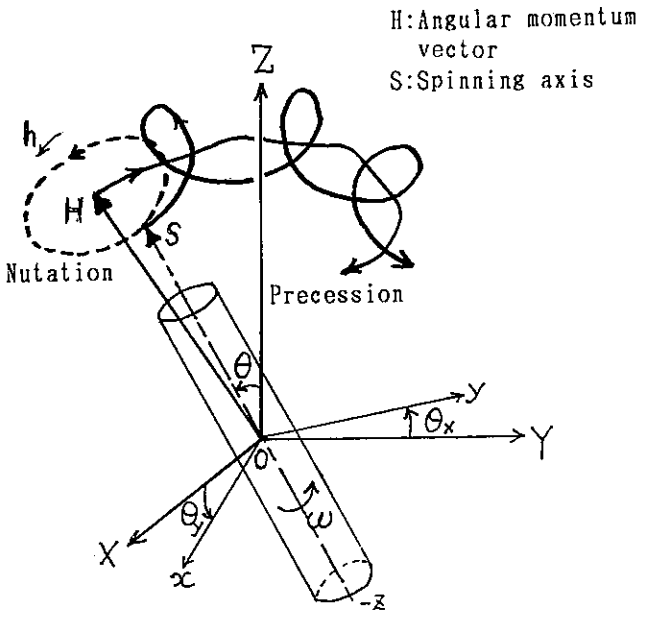

Fig. 1 Nutation, precession, coordinate system and notation

1. Outline of conical motions

H of the axi-symmetrical spinning rotor (the rotor, in the following) is governed by the following simple equation:

$$dH/dt=T \qquad (1)$$

where T is extermal or control torques. Therefore, H is easily controllable by T. However, H is invisible, instead, position of the rotor or the spinning axis, S, is visible and sensed by gap sensors. Generally, in magnetic bearings, T contains at least restoring torque which is negative and proportional to small tilt angle, θ, of S, i.e. $T=-K\theta$, where K is restoring coefficient. When H is near to S, direction of the restoring torque is clockwise as seen in Figure 1. In the field of satellite control, motion of H is called precession, whereas motion of S around H is called nutation. Generally, S draws a cone or a circle when we see the motion from headside of H.

The cone angle ν is decided by S and H at each instant, where only H is directly moved by T. Rotational speed of S around H or nutational angular velocity seen from stator-side, h, is independent of magnitude of ν when ν is small. h and ν are expressed as follows:

$$h = \sigma \omega \tag{2}$$

where σ is moment of inertia ratio (I_s/I_d) of the rotor with spinning speed ω (Ref. [1]), and

$$\nu = \tan^{-1}(I_d \theta' / I_s \omega) \fallingdotseq \theta'/h \tag{3}$$

where ' means 1st order time derivative. Note that nutation is always anti-clockwise, whereas precession is clockwise in case of magnetic bearings, anti-clockwise in case of a top on the ground where restoring torque is negative.

From above-mentioned characteristics, the control strategy is easily derived:

(1) For suppression of nutation, H should be moved to S.

(2) For suppression of precession, H should be moved to the central position.

In order to do these, we must know H position.

2. Equations of motion

Let O-XYZ be an inertia coordinate system whose origin O coincides with center of mass of the rotor, and Z-axis is parallel to the central axis of the stator. For convinience of expressing the spinning axis S, let's adopt a moving but non-spinning coodinate system, o-xyz, whose origin o and z-axis coincide with center of mass and spinning axis S of the rotor, respectively. Of course, x and y axes are not fixed to the rotor but always near the X and Y axes, respectively (see Fig. 1).

Small tilt angle θ is decomposed to θ_x and θ_y, and expressed as a complex number :

$$\underline{\theta} = \theta_x + i\theta_y \qquad (i=\sqrt{(-1)}) \tag{4}$$

In the following, complex numbers are expressed by underlined characters, and " means 2nd order time derivatives. Using Eq. (4), Eq. (1) becomes

$$\underline{\theta}'' - i h \underline{\theta}' + k \underline{\theta} = \underline{T} \tag{5}$$

where $k = K/I_d$ and $\underline{T} = (T_x + iT_y)/I_d$.
In case of high speed and $\underline{T}=0$, we get two approximate eigen values:

$+ i h$ (high freq. or N mode)

$- i k/h$ (low freq. or P mode)

N and P stand for nutation and precession, respectively. Note that, though, motions of H include both modes, they comprize almost P mode alone (Ref. [1]).

In order to visualize attitude of S and H, we define a complex number plane Z=1 on which real and imaginary axes are parallel to X and Y axes, respectively. S and H are the positions where they cross the plane. Then S is expressed as :

$$\underline{S} = \theta_y - i\theta_x = -i\underline{\theta}. \tag{6}$$

Using Eq. (3), we get

$$\underline{H} - \underline{S} = \underline{\theta}'/h \tag{7}$$

3. Estimation of H

We can estimate approximate $\underline{H}$, $\underline{H_e}$, from $\underline{S}$ using low pass filter (LPF) by eliminating high frequency mode, N mode. In this paper, only a first order LPF is used. Its transfer function F, whose time constant is τ, is :

$$F = (1+\tau s)^{-1} \tag{8}$$

At first, operate F to $\underline{S_s}$, a Laplace transformed variable of $\underline{S}$. Here, we choose the breaking frequeacy, $1/\tau$, as follows:

$$k/h < 1/\tau \ll h. \tag{9}$$

Phase lag angle α of LPF at P mode is

$$\alpha = \tan^{-1}(\tau k/h) \tag{10}$$

Using α, we can get more accurate $\underline{H_e}$, whose Laplace transformed value is $\underline{H_{es}}$, by clockwise rotation by α ;

$$\underline{H_{es}} = e^{-i\alpha} F \underline{S_s} \tag{11}$$

Sometimes, gain correction may be required.

4. Feedback torque for stabilization

Required Laplace transformed feedback torque divided by I_d, $\underline{T_s}$, for suppressing two modes is expressed as follows:

$$\begin{aligned} \underline{T_s} &= -K_p \underline{H_{es}} - K_n(\underline{H_{es}} - \underline{S_s}) \\ &= -(K_p + K_n)\underline{H_{es}} + K_n \underline{S_s} \\ &= -K_{pn}\underline{H_{es}} + K_n \underline{S_s} \end{aligned} \tag{12}$$

where $K_{pn} = K_p + K_n$ (13)

K_{pn} may include gain correction for $\underline{H_{es}}$ estimation. K_p and K_n are feedback gain for P and N modes suppression, respectively. Using Eq. (6) and Eq. (11), Eq. (13) becomes :

$$\underline{T_s} = (-K_{pn} e^{-i\alpha} F + K_n)(-i\underline{\theta_s}) \tag{14}$$

where $\underline{\theta_s}$ is Laplace transformed variable of $\underline{\theta}$. Clearly, Eq. (14) expresses the inter-axis cross coupling feedback (or simply, cross feedback).

5. Compensated system and eigen values

Through Laplace transformation of Eq. (5), and using Eq. (14), we get the following 3rd order characteristic equation :

$$\tau s^3+(1-i\tau h)s^2+[\tau k+i(\tau K_n-h)]s +k-K_{np}\sin\alpha+i(K_n-K_{pn}\cos\alpha)=0 \quad (15)$$

Under the condition of Ineq. (9) and small region of K_n and K_p, approximate eigen values of three modes, λ_n, λ_p and λ_τ (τ mode) are :

$$\lambda_n=-(K_n/h)+i\,h\,(1-K_n/(\tau h^3)) \quad (16)$$

$$\lambda_p=-(K_p+ik)/(h-\tau K_n) \quad (17)$$

$$\lambda_\tau=-(1/\tau)+((K_p+K_n)/h)-(\tau K_pK_n/h^2) +i[\tau k(K_p+K_n)/h^2] \quad (18)$$

From Eqs. (16) and (17), it is clear that the compensation or the cross feedback gives N and P mode dampings which are proportional to K_n and K_p, respectively. And these results show validity of control law, Eq. (12), derived from standpoint of dynamics. Eqs. (17) and (18) show that restoring coefficient, k, has no effect on damping but effects for increasing vibratory frequencies, though indispensable to stability at low rotation speed. In Eq. (17), it is required for stability that denominator be positive :

$$h > \tau K_n \quad (19)$$

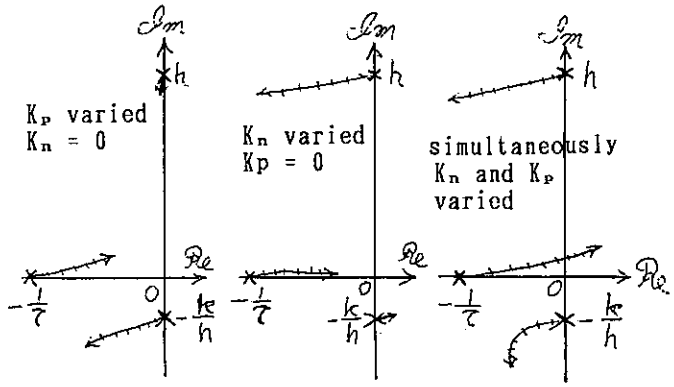

Fig. 2 Root loci of compensated system

Inequality (19) gives some restrictions on τ and K_n at low ratation speed. The second term of Eq. (18) shows that too large K_n and K_p may introduce instability in τ mode at low rotation speed. In any case, we should pay attentions to variation of rotation speed.

Figure 2 shows root loci where K_p and/or K_n increase from zero to some high values in a numerical example shown in the next chapter.

A block diagram of the compensated total system is shown in Fig. 3, where F, $e^{-i\alpha}$ and cross-feedback are described concretely.

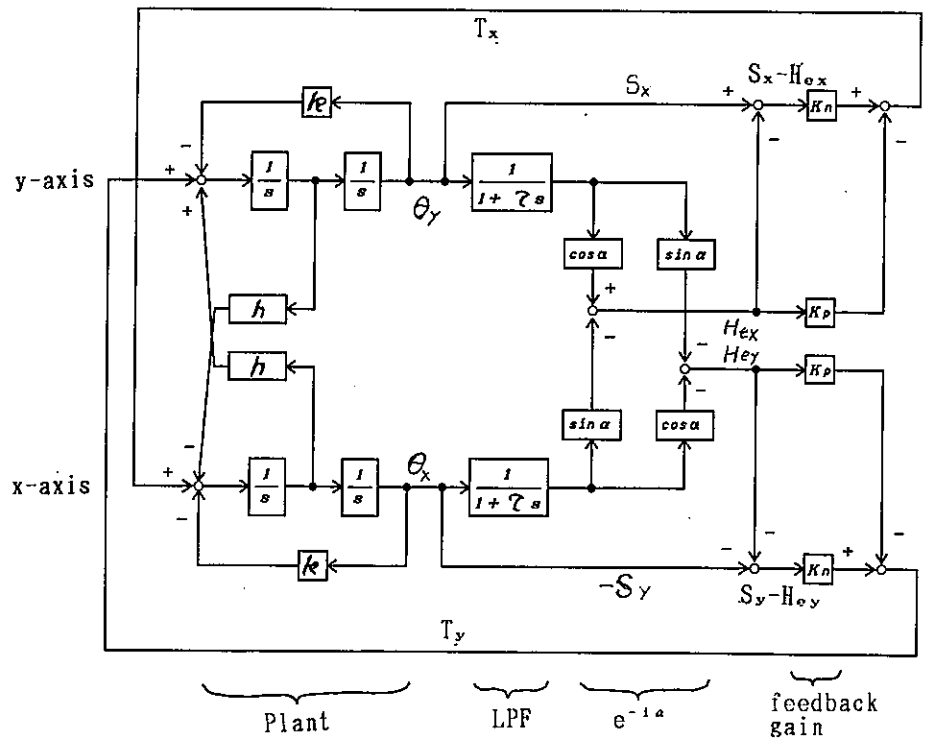

Fig. 3 Block diagram of compensated total system

6. Numerical simulation examples

The following model was used and run by computer: $\sigma = l_s/l_d = 0.5$, $h = \sigma\omega = 1000$[rad/s], $k = 1.51\times10^5$[s^{-2}], $\tau = 2.73$[ms], $1/\tau = 366$[rad/s], $\alpha = 22.4$[deg], $k/h = 151$[rad/s].

Figure 4 is a case of no control ($K_p = K_n = 0$). Of cource, there is neither divergence nor convergence. In addition to loci of S and H, a locus of the signal passed through the LP F is shown by dotted line where some gain reduction is observed and measured value of phase lag angle, α, is 25[deg].

Several cases with K_p and/or K_n are simulated. Results are the same as Fig. 2.

In Fig. 5, two gains have non-zero values ($K_n = K_p = 1.58\times10^5$[$s^{-2}$]). Both modes decay rapidly. At the beginning of the H motion, H goes outside. This comes from a mistake where zero was given as the initial value of LPF, indicating H_e is at the origin, therefore, H was moved to S direction.

Effects of α correction is difficult to estimate by analytical solution. Here, root loci of the above-mentioned model when α is varied are shown in Figs. 6 , 7 and 8 . Effect on P mode is shown is Fig. 6 where the nominal value is on the best position. Effect on N mode is shown in Fig. 7 where the nominal value is on not so good position, but the negative real part is almost the same as P mode, therefore, it is unnecessary to change. Figure 8 is the case of τ mode, where the nominal value position has quite large magnitude of negative real part. Again, therefore, it is needless to change. In this example, α correction brings about 30% increase of damping of both N and P modes.

It is interesting to note that phase adjustment can be attained by geometrical rotation of signals on the rotating plane.

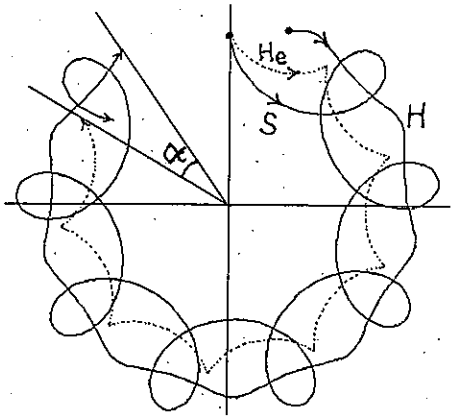

Fig. 4 Loci of S, H and H_e of uncontrolled system

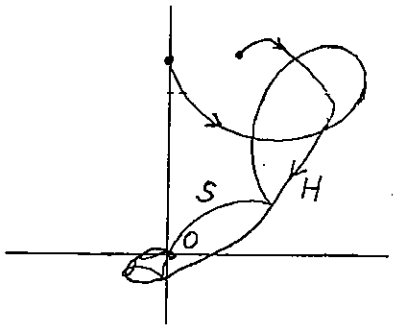

Fig. 5 Loci of S and H of controlled system

Reference

[1] "Magnetic Bearings" (Proceedings of 1st international symposium on magnetic bearings) Springer Verlag, 1989, pp. 311~318.

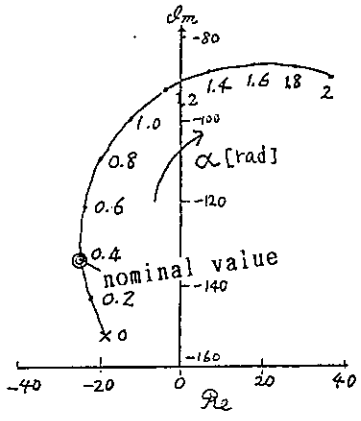

Fig. 6 Root locus of P mode

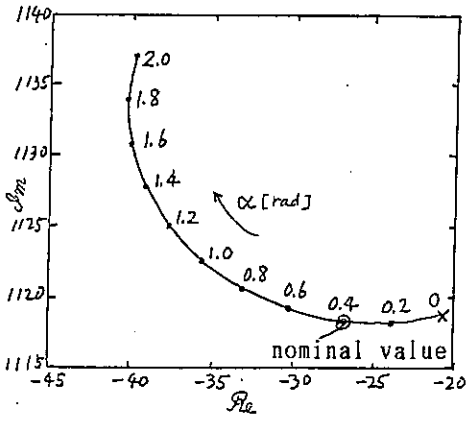

Fig. 7 Root locus of N mode

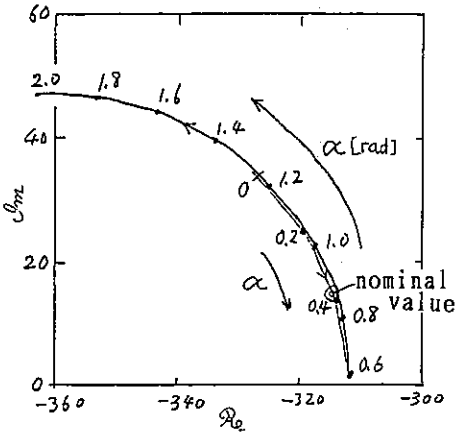

Fig. 8 Root locus of τ mode

2nd International Symposium on Magnetic Beaing
July 12-14, 1990, Tokyo, Japan

LINEAR COMPENSATION FOR MAGNETIC BEARINGS

SEI ISHIDA

Yaskawa Electric,Laboratory,Yahata-nishi,Kitakyushu 806,Japan

Abstract

By employing magnetic attraction and feedback control of the rotor's levitating position, active magnetic bearings can suspend rotors without mechanical contact. However, magnetic attraction has a significant non-linear relationship vis-a-vis the air gap between the rotor and the electromagnet, and vis-a-vis the current which flows in the electromagnet. Also, the dynamic characteristics of magnetic attraction are influenced by the air gap. Therefore, in the presents of an external force, both the levitating position and current vary too greatly to obtain stable status. To solve this problem, the author proposes some compensation methods to compensate for the electromagnet's non-linear characteristics within the linear system.

1. Introduction

For recent mechanical systems, smaller size, lighter weight, higher speed, and higher accuracy have been required. Magnetic bearings are suitable to meet those requirements. A magnetic bearing suspends a rotor without mechanical contact by employing magnetic force. Since no other media are required, magnetic bearings can be used under special conditions such as high or low temperature, high pressure, or vacuum. They are used for turbo molecular pumps or machine tool spindles since they remain clean and free from wear, and maintenance is not necessary[1,..,6]. Also it is possible to use the active magnetic bearings at speeds which exceed the rotor bending mode's critical speed, since these bearings have variable bearing stiffness[7,8]. While the active magnetic bearings have the above-mentioned features, their magnetic attraction has significant non-linear characteristics. Generally, a control system was supposed to be a linear system, assuming that the air gaps and electromagnets' currents would vary slightly. Since most designs were based on this theory, it is often the case that a rotor would not stop vibrating once it exceeded the linear range.

Some ideas to compensate for non-linearity of the electromagnet have been considered[9,10,11]. Untill now, compensation has been required in order to compensate for non-linearity over a wide range of air gaps, without using a sensor except in the case where a displacement sensor was used for magnetic bearings.

In this paper, first of all, I will propose three methods to compensate for the stationary non-linearity of electromagnet. These three methods are called "bias method" (B method), "square root method" (R method), and "combination method" (C method), respectively[12]. These methods compensate for the proportional relationship between a command signal given by a magnetic bearing controller and the force acting on the rotor even if the air gap between the rotor and electromagnet is changed. Also, they have the function of holding constant the loop gain in the control system.

Next, a method to compensate for the dynamic non-linearity of electromagnet will be described. In this method, dynamic characteristics between a command signal given by a magnetic bearing controller and the force acting on the rotor are compensated for, i.e., they are kept constant, even if the air gap between the rotor and electromagnet is changed. Also, a function to hold constant the initial stability of the control system is available using this method.

Typical experiments of two stationary linearizing methods will be explained below.

2. Ordinary Methods

Fig.1 shows a model diagram of a push-pull type radial magnetic bearing. In this figure, a pair of electromagnets are provided in a vertical axis.

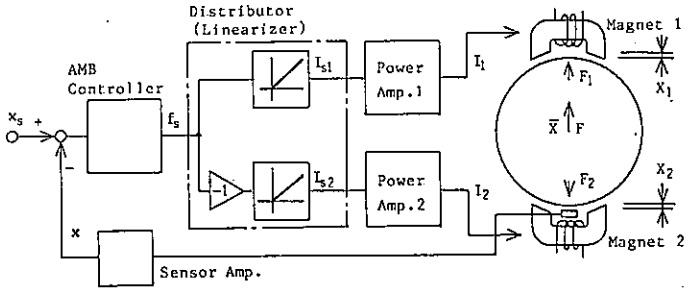

Fig.1 Magnetic Bearing Control Model

A control system is also shown in the same axis. However, in actuality, the identical magnets and control systems are provided in the horizontal axis as well. Magnetic attraction is generated by current supplied from a power amplifier to levitate a rotor in the center. The following equations are given for electromagnet 1(Subindex is omitted).

$$Rm=\frac{1}{A}\left(\frac{l}{\mu}+\frac{2X}{\mu_o}\right) \quad (1)$$

$$NI=Rm\Phi \quad (2)$$

$$F=\frac{\Phi^2}{\mu_o A} \quad (3)$$

F:attractive force
Φ:magnetic flux
N:number of coil turns
I:elecrtromagnet coil current
A:elecrtromagnet core area
Rm:magnetic reluctance
X:air gap
l:magnet core path length
μ_o:air permeability
μ:magnet core permeability

According to the above three equations, the relation between attractive force F, air gap X and current I will be as shown in Equation (4).

$$F=K\left(\frac{I}{X+X_{oo}}\right)^2 \quad (4)$$

$$X_{oo}=l\mu_o/2\mu,\ K=\mu_o AN^2/4$$

X_{oo} is equivalent to the air gap, and it is determined by the magnet core path length(l). As such, X_{oo} is a constant determined by I. Since magnet core permeability is much greater than that of air, the Equation (4) can be approximated as follows:

$$F=K\left(\frac{I}{X}\right)^2 \quad (5)$$

In this equation, it is shown that the magnet has typical non-linear characteristics since its attractive force is in inverse proportion to the squared air gap. If both the gap and current change by dX and dI around a value X_o and I_o, and both are squared so as to be closely approximated, then this system can be considered as a linear system as shown in Equation (6).

$$F=K\frac{I_o^2}{X_o^2}\left(1+\frac{2}{I_o}dI+\frac{2}{X_o}dX\right) \quad (6)$$

Since power amplifier current has an equation $I_1=K_1 I_{s1}$ (K_1 : power amplifier conversion coefficient, I_{s1} : current command), there is no proportional relation except the linear relation between current command and attractive force. However, the relationship expressed by Equation (6) is not valid if either the air gap or current is changed greatly.

There have been some simple methods to compensate for non-linear characteristics of an electromagnet. Fig.2 shows one of these methods, in which bias is simply added to the distributor output stage shown in Fig.1. This method is called the ordinary bias method (OB method). In this configuration, there are these relations.

$I_1=K_1 I_{s1}$, $I_{s1}=f_o+f_s$
$I_2=K_1 I_{s2}$, $I_{s2}=f_o-f_s$
$F_1=K\left(\frac{I_1}{X_1}\right)^2$, $F_2=K\left(\frac{I_2}{X_2}\right)^2$
$X_1=X_o-\overline{X}$, $X_2=X_o+\overline{X}$
$F=F_1-F_2$
f_o:bias
f_s:controller command signal
X_o:air gap in the center position
$\overline{X}$:deviation from X_o

Equation (7) is obtained from the above equations.

$$F=KK_1^2\left[\frac{(f_o+f_s)^2}{X_1^2}-\frac{(f_o-f_s)^2}{X_2^2}\right]$$
$$=4KK_1^2\frac{f_o^2}{X_o^2}\left(\frac{f_s}{f_o}+\frac{X}{X_o}\right) \quad (7)$$

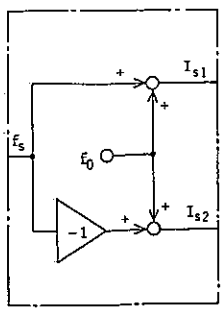

Fig.2 OB Method

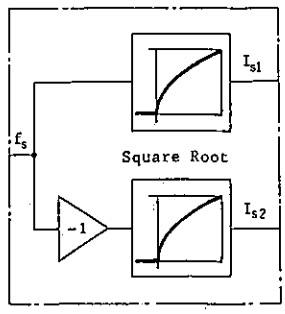

Fig.3 OR Method

When the value of $\overline{X}$ is close to 0, controller command signal fs and resultant force F acting on the rotor have a proportional relation by which a linear system is obtained. However, in this method, the linear relation cannot hold if a rotor deviates from the center position. In this OB method, bias f_o can be added by a distributor as shown in Fig.2. Another way to produce the same effect using the same OB method is to wind another coil around an electromagnet to apply constant current. Both methods have the same characteristics.

Fig.3 shows the second ordinary method, where a square root circuit is employed in the output stage of the distributor shown in Fig.1. This method is called the ordinary root method (OR method). In this method, Equation (8) is obtained as follows:

$$I_{s1}=\sqrt{f_s}\ (0=<f_s),\quad I_{s2}=\sqrt{-f_s}\ (f_s<0)$$
$$F=KK_i^2\frac{f_s}{X_1^2}\quad (0=<f_s)$$
$$F=KK_i^2\frac{f_s}{X_2^2}\quad (f_s<0) \qquad (8)$$

According to these equations, it can be seen that controller command fs and force F acting on the rotor have a proportional relation only when the rotor is levitating in the center. However, when the rotor deviates from the center, linearity is lost and stability will be reduced even in OB method.

As described above, when the two ordinary linearizing methods are used, controller command fs and force F acting on the rotor have a proportional relation only when the rotor is located in the center. It is possible to design and obtain (by using linear control system theory) a stable control system. However, when the rotor deviates a great deal from the center, linearity is lost and stable control is not available. Therefore, while a rotor is moving normally around the center, the stable control status could be retained. However, when large vibration is generated by external force or at startup, normal operation is very diffcult to achieve.

3.Proposed Methods

3.1 Bias Method (B Method)

Fig.4 shows the first method proposed in this paper. This method improves upon the OB method. A multiplier is provided in the output stage of the distributor shown in Fig.2. The most remarkable feature of this method is that a command signal added to the bias f_o is multiplied by another, separate signal which corresponds to the air gap between the electromagnet and the rotor. This air gap signal γ_1 or γ_2 is obtained by adding/subtracting a displacement sensor signal γ (which detects rotor deviation $\overline{X}$) to/from signal γ_o corresponding to air gap X_o in the center position.
The two power amplifier commands are :

$$I_{s1}=\gamma_1(f_o+f_s),\quad I_{s2}=\gamma_2(f_o-f_s)$$

When the displacement sensor's sensing factor is k_P, two air gap signals are

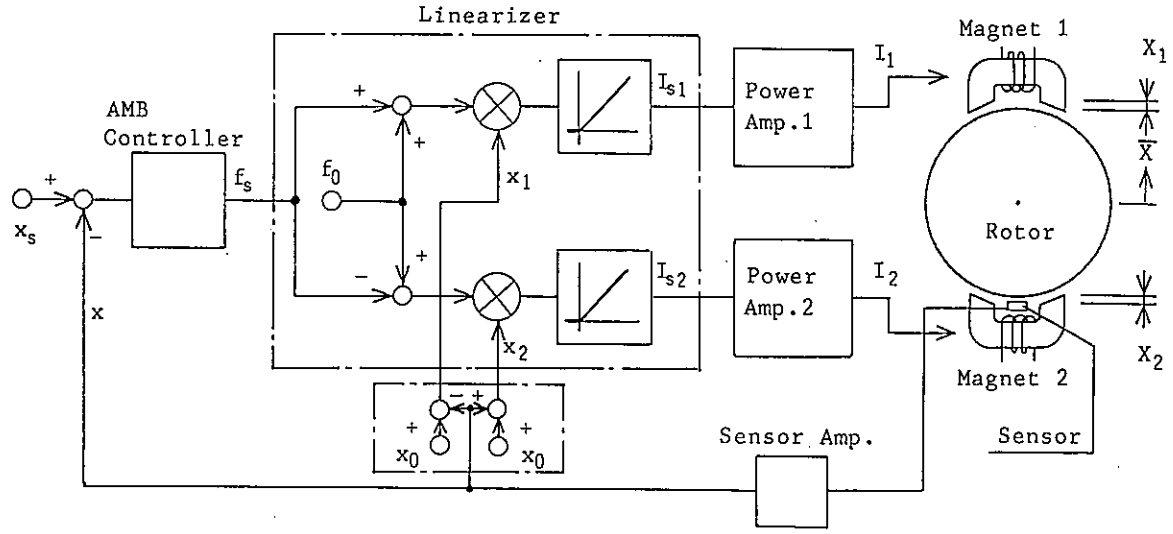

Fig. 4 AMB Block Diagram (B Method)

expressed : $\gamma_1=k_P X_1, \gamma_2=k_P X_2$
According to these relations, Equation (9) which shows the relation between controller command fs and force F is obtained, expressed as:

$$\begin{aligned} F&=F_1-F_2 \\ &=K[(\frac{K_i\gamma_1(f_o+f_s)}{X_1})^2-(\frac{K_i\gamma_2(f_o-f_s)}{X_2})^2] \\ &=4KK_i^2k_P^2\{(f_o+f_s)^2-(f_o-f_s)^2\} \\ &=kf_s \qquad (9) \\ &(k=4KK_i^2k_P^2f_o) \end{aligned}$$

This equation does not have a variable rotor deviation $\overline{X}$, that is to say, this equation is effective with or without considering a rotor levitating position. Thus, stable controlability is assured wherever a rotor is located only if the control system can be stabilized in the center position. This is because loop gain in the control system is not changed even if the rotor levitating position is changed.

As described above, in this method, by using two electromagnets which are applied with current, the attractive force difference can be in proportion to the controller command value. Controllr command fs becomes 0 when external force does not affect a rotor. However, current is always applied to two electromagnets since bias is added in the linearizer. Therefore, in addition to Joule heat generated in the electrmagnets' coils, heat loss is generated by eddy current in a rotor when the rotor rotates at high speed.

Since two electromagnets are required, this method is more applicable to rotating machine bearings than to magnetic levitation systems.

3.2 Square Root Method (R Method)

Fig.5 shows the second method proposed in this paper, a diagram of a linearizer. This method improves upon the OR method. A multiplier is provided in the output stage of the distributor shown in Fig.3. Then a command signal from the square root circuit is multiplied by a signal which corresponds to the air gap. The square root circuit just mentioned is provided in place of a bias addition circuit as in the B method. The two power amplifier commands are:

$$I_{s1}=\gamma_1\sqrt{f_s} \quad (0=<f_s)$$
$$I_{s2}=\gamma_2\sqrt{-f_s} \quad (f_s<0)$$

From these equations and displacement sensor's sensing factor k_P, Equation (10) which shows the relation between conroller command fs and force F, can be obtained as follows:

$$\begin{aligned} F&=K(\frac{K_i\gamma_1\sqrt{f_s}}{X_1})^2 \\ &\quad (0=<f_s \\ &\quad \text{only electromagnet 1 works.}) \\ &=K(\frac{K_i\gamma_2\sqrt{-f_s}}{X_2})^2 \\ &\quad (f_s<0 \\ &\quad \text{only electromagnet 2 works.}) \\ &=kf_s \qquad (10) \\ &(k=KK_i^2k_P^2) \end{aligned}$$

Since this equation does not have a variable rotor deviation $\overline{X}$, it can be established regardless of the rotor levitating position. Therefore, once an initial setting is stabilized, stable control status can be assured.

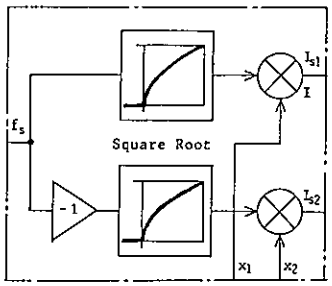

Fig.5 Linearizer in R Method

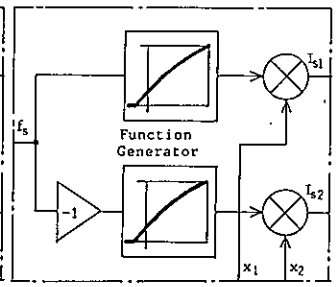

Fig.6 Linearizer in C Method

Because of the fact that two electromagnets are applied with current, B method cannot be employed for a bearing with only one electromagnet, while R method can be applied to bearings with either one or two electromagnets. When an external disturbance load is zero, the controller command and power amplifier command become zero and no current flows. Therefore, Joule heat becomes zero and heat loss will not be generated by eddy current in the rotor when the rotor rotates at high speed.

3.3 Combination Methd (C Method)

In B method, since current is always applied to two electromagnets, Joule heat cannot be avoided. Also heat loss is generated by eddy current in a rotor when the rotor rotates at high speed. In R method, due to a square root circuit, input-output ratio of the circuit becomes larger when the command is close to zero. A slight variation of the controller command value will change greatly the electromagnet coil's current. Thus, response of the force affecting a rotor becomes less when the controller command is

close to zero because of electric circuit and electromagnet inductance. In other words, one of the B method features is that there is no problem with reduced response. The combination method (C method), combining B and R methods and with intermediate features, is slightly more effective. Fig.6 shows a linearizer for this method.

In C method, two current commands I_{s1} and I_{s2} are in accordance with the following equations, corresponding to controller command f_s:

$$\begin{aligned}
&(1)\ -1=<f_s<-a: && I_{s1}=0,\quad I_{s2}=\gamma_2\sqrt{-f_s}\\
&(2)\ -a=<f_s<a: && I_{s1}=\frac{\gamma_1\sqrt{a}}{2}\left(1+\frac{f_s}{a}\right),\quad I_{s2}=\frac{\gamma_2\sqrt{a}}{2}\left(1-\frac{f_s}{a}\right)\\
&(3)\ a=<f_s=<1: && I_{s1}=\gamma_1\sqrt{f_s},\quad I_{s2}=0\\
&\quad (0<a<1) && \qquad (11)
\end{aligned}$$

Fig.7 shows the relation between controller command f_s, and signal f_{s1} or f_{s2} which has not yet been multiplied by air gap signal γ_1 or γ_2. In the above-mentioned three ranges, (1) and (3) are exactly the same as the range of R method. While (2) is the same as that of B method. However, inclination is changed according to the size of value a. From these equations and displacement sensor's sensing factor kp, Equation (12) showing the relation between controller command fs and force F can be obtained as follows:

$$F=F_1-F_2=kf_s \qquad (12)$$
$$(k=KK_i^2k_P^2)$$

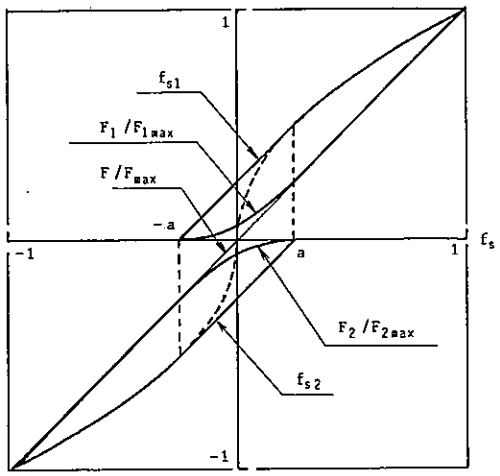

Fig.7 Signal in C Method

Since this equation does not have variable $\bar{X}$ as do the other two methods, it can be establised regardless of the rotor levitating position. Fig.7 also shows action forces F1, F2, and resultant force F.

In the above three methods (B, R, C methods), special sensors are not required. Apparently, by only employing displacement sensors used for magnetic bearings, we can, ipso facto, linearize magnet non-linearity. In any case, the most remarkable feature is that a multiplier is used to multiply command signal by each electromagnet's gap signal. However, to obtain a linearizer with higher accuracy, Equation (4) $X_{oo}=1\mu_o/2\mu$ must not be omitted. This equation can be established only by adding γ_{oo} to gap signal γ_1 or γ_2.

4 Experimental Results

An experiment to compare two of the proposed methods with the ordinary methods was performed. For this experiment, a magnetic bearing motor of 5-axis control type was used. Fig.8 shows a configuration of its radial bearing. A PID controller was used to control magnetic bearings. Each method mentioned above was applied to the same single axis. B method was applied to all the other 4 axes.

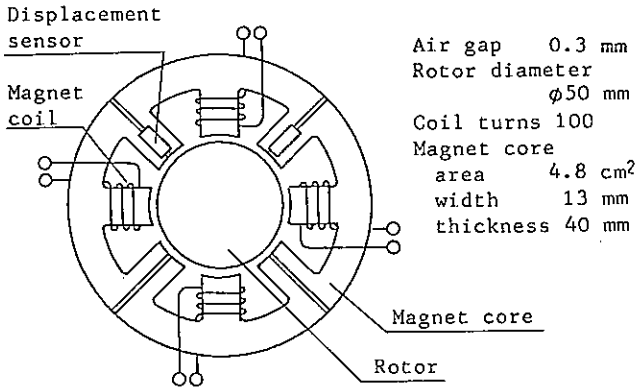

Fig.8 Radial Bearing Configuration

First, stationary characteristics were compared. Fig.9 shows a diagram where the relation between controller command fs and force F was measured using the ordinary methods.

In the OB method, when rotor deviation is zero ($\bar{X}=0$), action force F has a proportional relation with command fs. However, when the deviation is not 0, F does not pass the zero point and become non-linear. In the OR method, regardless of rotor deviation, F and fs have a proportional

relation. However, eccentricity changes the ratio. Fig.10 shows the experiment results of two proposed methods (B method, R method), in the measurable range. In both cases, the relation between command fs and action force F is proportional. According to these results, great effect could be obtained by improving the OB method. On the other hand, improvement could not be expected for the OR method. The gradient in the B method which was approx. 1.6 times larger than that in the R method is given by setting bias f_o to 0.4. By setting f_o to 0.25, all gains can coincide.

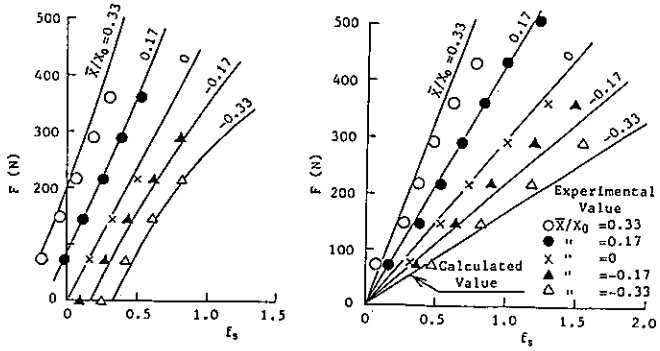

(a)OB Method (b)OR Method

Fig.9 fs-F Characteristics in Ordinary Method

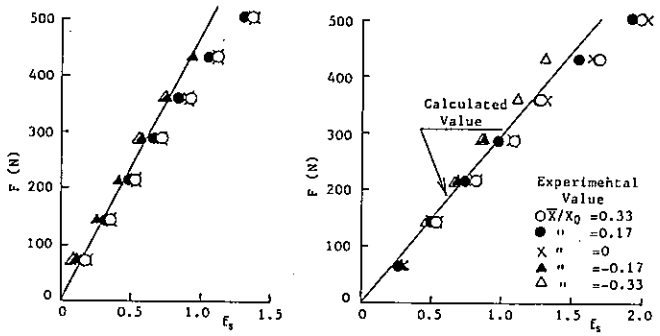

(a)B Method (b)R Method

Fig.10 fs-F Characteristics in New Method

Fig.11 shows the results of measured dynamic characteristics in new(B) and ordinary(OB) bias methods. Both new and ordinary square root methods have the same result as ①. In the OB method, gain becomes high at 40Hz and 1500Hz. The peak at 1500Hz is due to resonance with vibration peculiar to rotor bending. To lower this peak, loop gain is reduced to 80%. There is larger vibration around 35Hz as shown in ③, and stiffness is lowered.

In Fig.12, 10% recovery time after half the period is compared. In OR method, there is not a remarkable difference between when a large impulse is given and when the levitating position is eccentrized. Generally, difference by amplitude of impulse exciting force is small. However, the recovery time is shorter in the bias or square root methods proposed in this paper, which show us how well they are improved.

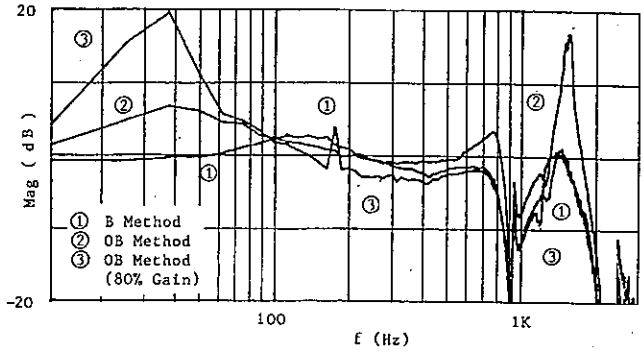

Fig.11 Bode Diagram of B and OB Method

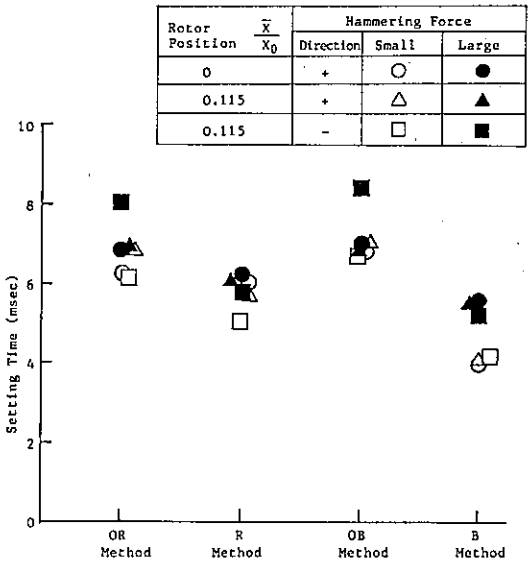

Fig.12 Setting time for each Methods (semi period 10%)

5. Applications

A few examples of actual applications of the proposed methods will be described. Fig.13 shows a magnetic levitation unit, developed by YASKAWA, to transport a semi-conducter wafer in a vacuum tank. To levitate a carrier, there are two ways:(1)only electromagnets for lifting are used or (2)electromagnets for lifting and small-size electromagnets for pulling down are used. 2nd way makes use of an over-

hang system. Both ways employ the R method. Before introduction of the R method, it had been impossible to levitate a carrier. By applying the R method, unstable control due to electromagnet non-linear characteristics could be solved and stable levitating became possible.

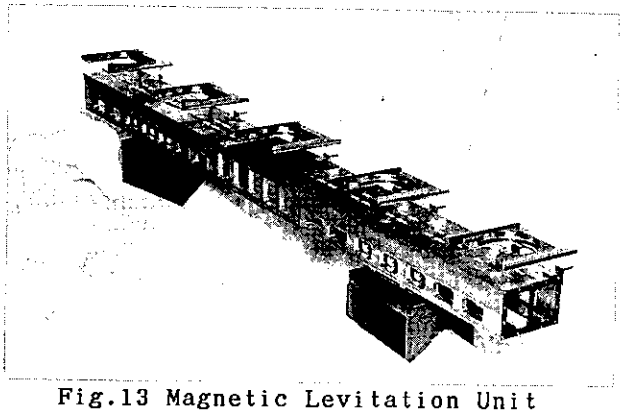

Fig.13 Magnetic Levitation Unit

A typical external force is applied when a bearing is activated. The following describes a state when a motor with 4- or 5-axis control magnetic bearings is started up. In the B or R method, stable levitating exists when a rotor is placed in the center position without any special circuits provided. Levitating without making any acoustic noise is possible especially in the R method. However, in the ordinary methods, any such levitating is very difficult to realize.

Another typical large external force is applied when a rotor rotates at high speed because of unbalance mass. This vibration is especially large as the rotor exceeds or passes through the critical speed of the rotor bending mode. In this case, special compensation circuits are required to function as dampers of the rotor bending mode. However, by using either the B or R method together with these special circuits, stability can be improved. When B method is used for an experiment where the critical speed of the rotor bending mode is approx. 90,000rpm (1,500Hz), the bearing section is sometimes skewed greatly (approx. 50μm) owing to unbalance mass. But bearing stability is always available[8]. However, in the OR methods, it is sometimes impossible to suspend the rotor when a rotor starts to make a large deviation.

6. Dynamic linear compensation

Stationary non-linear characteristics of an electromagnet could be compensated for by multiplying command signal by gap signals as mentioned above. It is also considered that electromagnet dynamic characteristics are compensated for since they are changed by the air gap and affected by control system conditions. Dynamic characteristics are changed since coil inductance varies according to the air gap. Therefore, by providing a compensation circuit to cancel such change, the characteristics can be compensated for.

In relation to electromagnets, the 2 following equations, in addition to Equations (1) through (3) are established[9].

$$E=L\frac{dI}{dt}+RI \qquad (13)$$

$$E=N\frac{d\Phi}{dt}+RI \qquad (14)$$

E:electromagnet coil terminal voltage
L:electromagnet coil inductance
R:electromagnet coil resistance

From the above equations and Equation (2), Equation (15) is obtained.

$$L=\frac{2K}{X+X_{oo}} \qquad (15)$$

For better current rise and for smaller loss, power MOS-FET is used as a power amplifier in the PWM method to perform current feedback control. When coil-applied voltage is increased, the second term in Equation (13) can be omitted and the current rising rate becomes: $dI/dt=E/L$.
Assuming that current is applied in sine wave $I=I_o\sin 2\pi ft$ and that maximum response frequency fmax is provided at a point where maximum rising rate $|dI/dt|=2\pi fI_o$ coincides with rising rate E/L, then the equation $fmax=E/2\pi I_oL$ is obtained. By using this equation, when current time constant T is defined as $T=1/2\pi fmax$ Equation (16) can be obtained:

$$T=\frac{2\pi I_oL}{E}=k_LL=\frac{k_X}{X+X_{oo}} \qquad (16)$$
$$(k_L=2\pi I_o/E,\ k_X=4\pi KI_o/E)$$

From the above equation, time constant T is varied by the air gap and is more or less in inverse proportion to the air gap.

Assume that X_{oo} is one tenth of central gap X_o, rotor deviation is one half of X_o and the cut-off frequency of the rotor levitating in its central position is $f_c=1/2\pi T(X_o)$. In this case, phase and gain are varied acco-

rding to rotor deviation in the range shown in Table 1. Phase and gain of magnetic attractive force will be larger since it is in proportion to the square of the current. Therefore, there is no problem when control system relative stability is large enough. Otherwise, instability may be created by gap variation.

f	$0.5f_o$	f_o	$1.5f_o$
Phase (deg)	-17~ -40	-32~ -59	-43~ -68
Mag/Mag(f=0)	0.95~0.77	0.85~0.51	0.73~0.37

Table.1

Fig.14 shows a block diagram of a compensator to compensate for variation of dynamic characteristics. In this circuit, the time constant of differentiator is changed according to air gap signal χ. The circuit is inserted in the stage before a power amplifier. One-side input of the differentiator is multiplied by coefficient k_3 to change the time constant variable. Coefficient k_3 is obtained by a function generator with an air gap signal as input signal and it(k_3) functions as in Equation (17):

$$k_3=\frac{k_1}{\chi+\chi_{oo}}-k_2 \qquad (17)$$

($k_1=k_X k_P/RC$, $k_2=r/R$)

r,R : resister resistance

C : capacitor capacity

The transfer function of configurated compensator is as follows:

$$\frac{I_{s1}^*}{I_{s1}}=\frac{1+(r+k_3R)CS}{1+rCS}=\frac{1+TS}{1+tS} \qquad (18)$$

($t=rC$, $T=(r+k_3R)C$)

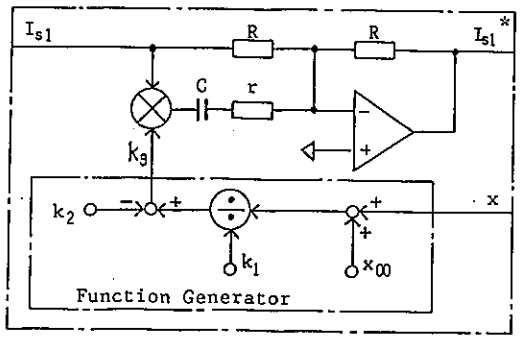

Fig.14 Dynamic Linearizer

By using displacement sensor's sensing factor k_P, we arrive at the equation $T=k_X/(X+X_{oo})$. Therefore, the transfer function between this compensator input signal I_{s1} and electromagnet current I_1 is as follows:

$$\frac{I_1}{I_{s1}}=\frac{K_1}{1+tS} \qquad (19)$$

As a result, time constant t does not depend on rotor deviation $\bar{X}$ in the above equation. That is, dynamic characteristics are held constant. Therefore, by using this method, change of dynamic characteristics and unstable control system can be avoided.

7. Conclusion

In this paper, three methods to compensate for stationary non-linear characteristics of electromagnets to be used for active magnetic bearings have been described and the effects of two have been compared. Results show the B method had better effects. However, in actual experiments, both the B and R methods were found to be effective. Concerning compensation for varying dynamic characteristics caused by an air gap, only the method in Fig.14 is proposed. The results of all of the above methods will be checked by performing other tests.

The author anticipates the methods proposed in this paper will be employed widely and will continue to be developed for more practical uses.

References

[1]Habermann,H.,and Liard,G.L., IEEE Spectrum,Sept.,1979,26.
[2]Matsumura,F.,et al., Trans.IEEJ,C-101-6,137(1981)
[3]Matsumura,F., Systems and Control,26-4,209(1982)
[4]Higuchi,T.,et al., Seisan-Kenkyu,34-6,101(1982)
[5]Mizuno,T.,et al., Trans.SICE,19-12,68(1983)
[6]Ohsima,S.,Nakazeki,T., Nikkei Mechanical,10.22.102(1984)
[7]Kanemitsu,Y.,et al., 1st Int.Symp.on M.B.,Zurich(1988)
[8]Ishida,S.,Preprint of 2nd Symp. Dynamics related with Magnetic Force June,1990
[9]Watanabe,T.,et al., Trans.JSME,36-284,578(1970)
[10]Jpn.Koukoku 61-37643(1986)
[11]Jpn.Koukoku 61-41001(1986)
[12]Ishida,S.,Preprint of JSME in Kurume 301,Jly,1987

2nd International Symposium on Magnetic Beaing
July 12-14, 1990, Tokyo, Japan

FLEXIBLE SHELL STRUCTURED ROTOR CONTROLLED BY DIGITAL MAGNETIC BEARINGS (TRANSPUTER CONTROL)

H. Zhang*, T. Nagata**, Y. Okada** and J. Tani*

* Tohoku University, 2-1-1 Katahira, Sendai, 980, JAPAN
** Ibaraki University, 4-12-1 Nakanarusawa, Hitachi, 316, JAPAN

Vibration control using magnetic bearings is applied to a shell structured rotor and a traveling steel sheet. It is intended that the rotor is to be light and to have a wide supporting region of magnetic flux, hence it is made of a flexible shell structure. These structures are apt to produce the shell vibrations, in addition to bending vibrations of the rotating shaft.

To improve the damping property of the structure, a new control scheme for a magnetic bearing is introduced. Each magnet is controlled individually, leading to favorable structural damping, which contrasts to the traditional controller where a pair of magnets are controlled in a push-pull operation.

An alternative similar application of this vibration control is a traveling steel sheet. The rolling process of a thin steel plate sometimes produces bending vibration, which affects adversely the surface finishing quality. Magnetic damper controlled by transputer is applied to reduce the vibration, and tested its capability.

INTRODUCTION

The use of electro-magnetic bearing systems has increased for clean or high speed rotors, mainly because of their noncontact supporting capability. The primary control for this is an analog controller [1,2].

A primary defect of magnetic bearings is poor supporting capability. Here it is intended that the rotor is to be light and to have a wide supporting region of magnetic flux. This paper introduces a flexible shell structured rotor controlled by a magnetic bearing. These structures are apt to result in the shell vibrations.

To improve the damping characteristics of the structure, a new control scheme for magnetic bearing is introduced: Four magnetic actuators are mounted on the shell structure. However, each magnetic actuator is controlled individually to achieve favorable structural damping, which is in contrast to the traditional controller where a pair of magnets are controlled in a push-pull operation.

An alternative application of this vibration control is a traveling steel sheet. The rolling process of a thin steel plate sometimes produces bending vibrations which affect adversely the surface finishing quality [3]. Magnetic damper controlled by transputer is applied to reduce the vibration, and to test its capability.

Digital control has the advantage of flexibility, including the use of higher level controls such as state feedback or adaptive control, and their use has been attempted for the control of magnetic bearings [4,5,6,7,8,9].

A theoretical treatment of digital control for radial bearings was given by Schweitzer and Ulbrich [4]. Bleuler and Schweitzer [5] analyzed the use of decentralized control for radial magnetic bearings which was prepared for the application of microprocessor-based digital control. Traxler, et al. [6] described a radial bearing using a microprocessor-based digital control. Larsonneur and Herzog [7] applied a digital output optimal control. Bleuler and Salm [8] controlled an elastic rotor with a signal processor.

One of the main purposes of this paper is to test the capability of parallel computing transputer control to the magnetic bearing. Analog control of local PD operation is also tested and compared. Then the digital PD control and the state feedback is tried. The results are compared and discussed.

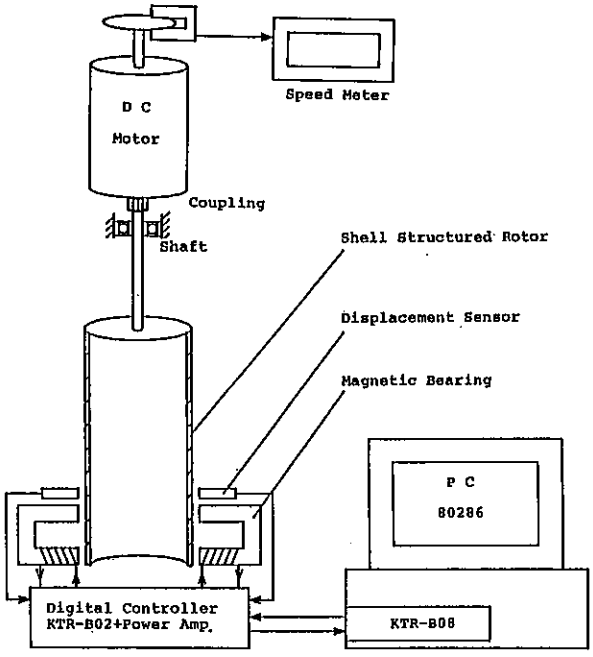

Fig. 1. The Experimental Rotor and Control System

MODELING OF THE PROPOSED ROTOR AND BEARING SYSTEM

The schematic diagram of experimental apparatus is shown in Fig. 1. The upper part of the rotor is a thin shaft supported by a ball bearing. The rotating torque is given by a DC motor through coupling. The shell structured rotor is the lower part which is controlled by a magnetic bearing.

This shell structured rotor has two types of motion: longitudinal bending motion and cylindrical bending vibration. If coupling between them is ignored, the two types of motion can be analyzed separately.

Longitudinal Bending Motion

The equation of motion of the longitudinal bending motion is given by

$$\begin{aligned} m\ddot{x} + kx &= f_x \\ m\ddot{y} + ky &= f_y \end{aligned} \tag{1}$$

where x and y are the deformations and f_x and f_y are the control forces, respectively. The m and k are the mass and stiffness matrices.

Cylindrical Bending Motion

If it is assumed that cylindrical bending vibration is not affected by the longitudinal bending motion, the equation of ring bending motion applies.

$$\begin{aligned} &\Lambda\left(\frac{\partial^6 w}{\partial\theta^6} + 2\frac{\partial^4 w}{\partial\theta^4} + \frac{\partial^2 w}{\partial\theta^2}\right) \\ &+\gamma\left(\frac{\partial^4 w}{\partial\theta^2\partial t^2} + 2\Omega\frac{\partial^4 w}{\partial\theta^3\partial t} + 2\Omega\frac{\partial^2 w}{\partial\theta\partial t}\right) \\ &= \frac{R^2}{D}\sum_{j=1}^{n} f_j \frac{\partial^2}{\partial\theta^2}\left\{\delta\left(\theta - \frac{2(j-1)\pi}{n}\right)\right\} \end{aligned} \tag{2}$$

Here w is the bending displacements corresponding to the coordinate system which are shown in Fig. 2. Ω is the rotating speed and, Λ and γ are the stiffness coefficients determined by the shell parameters, n is the number of actuators ($n = 4$ in this case).

The solutions w can be assumed as

$$w = \sum_{i=2}^{\infty}(w_{1i}\cos i\theta + w_{2i}\sin i\theta) \tag{3}$$

Substituting eq.(3) into eq.(2) and rearranging them by means of the generalized variable $q_i = \{w_{1i}, w_{2i}\}^T$, we obtain the following equation.

$$\begin{aligned} &M_i\ddot{q}_i + C_i\dot{q}_i + K_i q_i = Q_i \\ &M_i = \begin{bmatrix} \gamma(i^2+1) & 0 \\ 0 & \gamma(i^2+1) \end{bmatrix} \\ &C_i = \begin{bmatrix} 0 & 2\gamma\Omega i(i^2-1) \\ -2\gamma\Omega i(i^2-1) & 0 \end{bmatrix} \\ &K_i = \begin{bmatrix} \Lambda i^2(i^2-1)^2 & 0 \\ 0 & \Lambda i^2(i^2-1)^2 \end{bmatrix} \\ &Q_i = \frac{R^2 i^2}{D}\begin{bmatrix} \sum_{j=1}^{n} f_j \cos\frac{2i(j-1)\pi}{n} \\ \sum_{j=1}^{n} f_j \sin\frac{2i(j-1)\pi}{n} \end{bmatrix} \end{aligned} \tag{4}$$

M_i, C_i and K_i are the generalized mass, damping and stiffness matrices and Q_i is the i-th generalized control force.

CONTROL SYSTEM

Two types of control system is considered to apply to the shell structured rotor and magnetic bearings.

PD Control

Four magnetic actuators are mounted 90 deg apart on the cylindrical shell. They are controlled individually by the measured signal from four sensors. First, the analog PD controller of

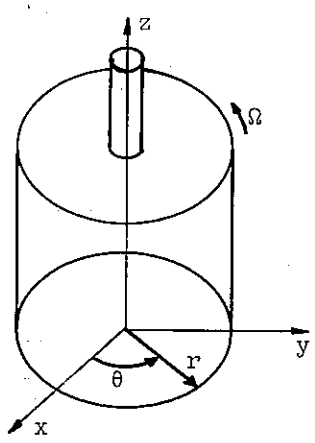

Fig. 2. The Coordinate System

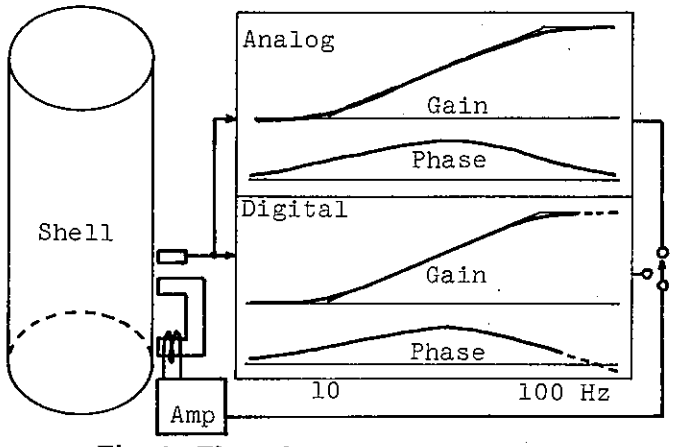

Fig. 3. The Scheme for Analog and Digital PD Controller

$$G(s) = K_P + \frac{K_D s}{T_D s + 1} \tag{5}$$

is installed in the individual actuator, with the sensor as shown in Fig. 3. The equivalent digital PD controller of

$$G(z) = K_P + \frac{K_D(z-1)}{T_D(z - \exp(-\tau/T_D))} \tag{6}$$

is realized by the transputer (KTR-B02, -B08). The frequency responses of the controller are also indicated in Fig. 3.

The State Feedback Controller

The structural vibration should be controlled softly and adding the damping, while the body motion of the rotor should be controlled rigidly. This control algorithm can be realized using state feedback. For the rotating speed of our system (up to 10,000 rpm), only the rigid motion of the longitudinal axis and the first bending ($i = 2$) vibration of the cylindrical axis should be controlled. Hence the state equation for the longitudinal bending motion

$$\begin{aligned} &x_b(k+1) = \Phi_b x_b(k) + \Gamma_b u_b(k) \\ &x_b = \{x, \dot{x}, y, \dot{y}\}^T, u_b = \{f_x, f_y\}^T \\ &\Phi_b = \exp(A_b\tau), \Gamma_b = \int_0^\tau \exp A_b(\tau - t) B_b dt \\ &A_b = \begin{bmatrix} 0 & I & 0 & 0 \\ -m^{-1}k & 0 & 0 & 0 \\ 0 & 0 & 0 & I \\ 0 & 0 & -m^{-1}k & 0 \end{bmatrix}, B_b = \begin{bmatrix} 0 & 0 \\ m^{-1} & 0 \\ 0 & 0 \\ 0 & m^{-1} \end{bmatrix} \end{aligned} \tag{7}$$

and the equation for the cylindrical bending motion

$$\begin{aligned} &x_s(k+1) = \Phi_s x_s(k) + \Gamma_s u_s(k) \\ &\Phi_s = \exp(A_s\tau), \Gamma_s = \int_0^\tau \exp A_s(\tau - t) B_s dt \\ &A_s = \begin{bmatrix} 0 & I \\ -M_s^{-1}K_s & -M_s^{-1}C_s \end{bmatrix}, B_s = \begin{bmatrix} 0 \\ M_s^{-1} \end{bmatrix} \end{aligned} \tag{8}$$

can be treated separately. The state feedback controller is simplified and shown in Fig. 4, where K_{Pb} and K_{Db} are the proportional and derivative gains for the longitudinal bending motion (rigid motion), and K_{Ps} and K_{Ds} are the gains for cylindrical bending vibration.

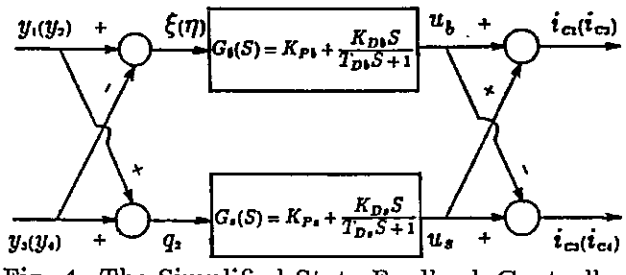

Fig. 4. The Simplified State Feedback Controller

EXPERIMENTAL RESULTS

The proposed rotor and magnetic bearing system are made as shown in Fig. 1. The cylindrical shell is made of 42 mm diameter and 0.5 mm thickness steel. The bearing actuator is diverted from a stator of a 4 phase stepping motor. The unbalance response obtained by an analog PD controller is indicated in Fig. 5. Four curves are obtained from four gap sensors. The fundamental peak near 5,000 *rpm* can be identified. However, the cylindrical bending vibration is far higher than the top speed of the system. Even without bending vibration control, it can run to the top speed. Similar results are obtained by the digital PD controller which are shown in Fig. 6. The control algorithm is realized by a parallel C program on two transputers (B02 and B08). The 4 channel PD control is realized with the sampling interval τ=0.13 ms. However the results are slightly worse than the analog ones. The state feedback has not been applied because of high bending resonant frequency. A large cylindrical shell is now being made to test the state feedback control.

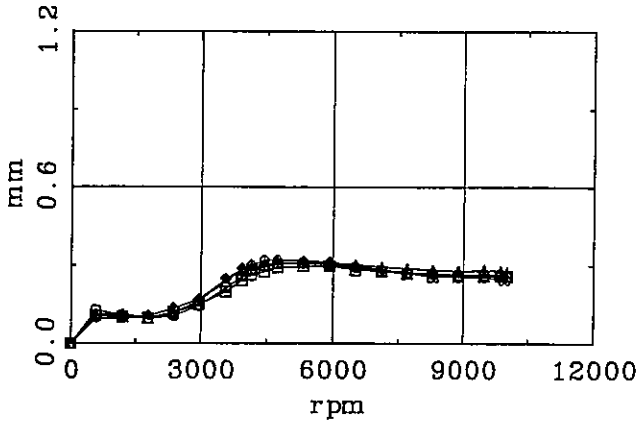

Fig. 5. The Unbalance Response Controlled by Analog PD Controller

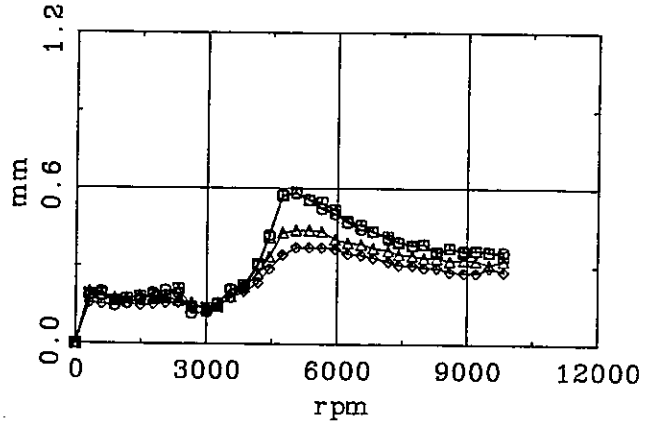

Fig. 6. The Unbalance Response Controlled by Digital PD Controller

APPLICATION TO VIBRATION CONTROL OF A TRAVELING SHEET

Similar control can be applicable to the rolling process of a thin steel sheet. Between the rollers, a sheet is apt to vibrate causing a bad surface finishing. Noncontact vibration control is highly desirable [3]. The schematic diagram is shown in Fig. 7. For experimental convenience, the plate is not moving, which is clamped in x-direction and free in y-direction. Two gap sensors are arranged on the upper side of the sheet, while two actuators are installed under the sheet.

The Vibrating Modes of the Sheet

The equation of plate motion is written by

$$\rho h\frac{\partial^2 w(x,y,t)}{\partial t^2} + D\nabla^4 w(x,y,t) - Th\frac{\partial^2 w(x,y,t)}{\partial x^2} = \sum_{n=1}^{2} f_n(t)\delta(x-x_n)\delta(y-y_n) \tag{9}$$

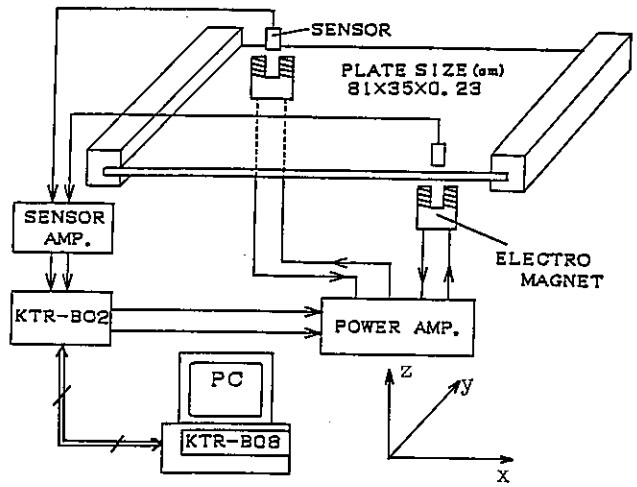

Fig. 7. The Scheme of the Vibration Control of Plate System

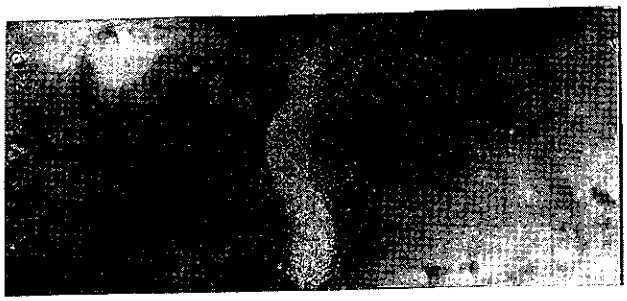

(a) 2nd (2,1) Mode, 30.5 Hz

(b) 3rd (1,2) Mode, 40 Hz

(c) 4th (2,2) Mode, 43.5 Hz

(d) 5th (3,1) Mode, 58 Hz

(e) 6th (3,2) Mode, 76.5 Hz

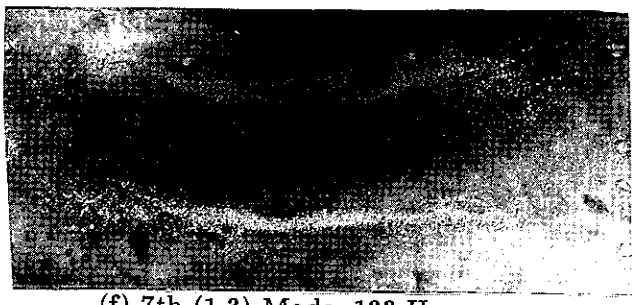

(f) 7th (1,3) Mode, 133 Hz

Fig. 8. The Experimental Modal Shapes of the Clamped-Free Plate

If the vibrating mode is approximated by a product of x and y directional beam modes, then

$$w(x,y,t) = \sum_{i=1}^{\infty} X_n(x) Y_m(y) w_i(t) \qquad (10)$$

can be used. Where $X_n(x)$ is the n-th mode of clamped beam and $Y_m(y)$ is the m-th mode of free beam.

The experimental vibrating modes are obtained by forcing the plate with a sinusoidal signal and taking the picture of the modal shape. The modes of $2.3 \times 810 \times 350mm$ plate are shown in Fig. 8. Unfortunately, the higher mode is not clear. Especially, the mode of thinner plate could not be measured. Hence the actuator location method which eliminate a specific resonances, i.e. pole/zero cancellation, can not be applicable. In this paper a local PD control is used to reduce the plate vibration.

Experimental Results

First, the impulse response test is conducted by forcing the plate with a dropping elastic ball and measuring the response. They are shown in Fig. 9. Where, (a) indicates the response without feedback, (b) is the response with analog PD control, while (c) is the response obtained with digital PD control. The frequency response test is also conducted and shown in Fig. 10. The peaks between 10 - 200 Hz are reduced significantly with the feedback. However, the peak near 500 Hz becomes unstable with a high feedback gain. The previously mentioned digital PD controller is also applied. The results are similar, but not as good as for the analog controller.

CONCLUSIONS

For the purpose of light weight and high load capability, a shell structured rotor is proposed. To reduce the structural vibration, four actuators are arranged and controlled individually from the measured shell displacements. Digital transputer control as well as an analog PD are applied to the magnetic bearing. The control algorithm is easily implemented by a parallel C program. However, the test shell rotor is so small that the resonant frequency of structural vibration is several times higher than the top speed of the system and could not be recognized.

Similar vibration control can be applied to the rolling process of the thin steel plate. Plate vibration occurs between the rollers. The resonances between 10 - 100 Hz are reduced significantly by the PD controller. However, the peak near 500 Hz becomes unstable with a high feedback gain. An improved control algorithm is needed for this system.

REFERENCES

1) Humphris, R. R., Kelm, R. D., Lewis, D. W. and Allaire, P. E., "Effect of Control Algorithms on Magnetic Journal Bearing Properties", J. of Eng. for Gas Turbines and Power, Trans. ASME, Vol.108, Oct. 1986, p.624-632

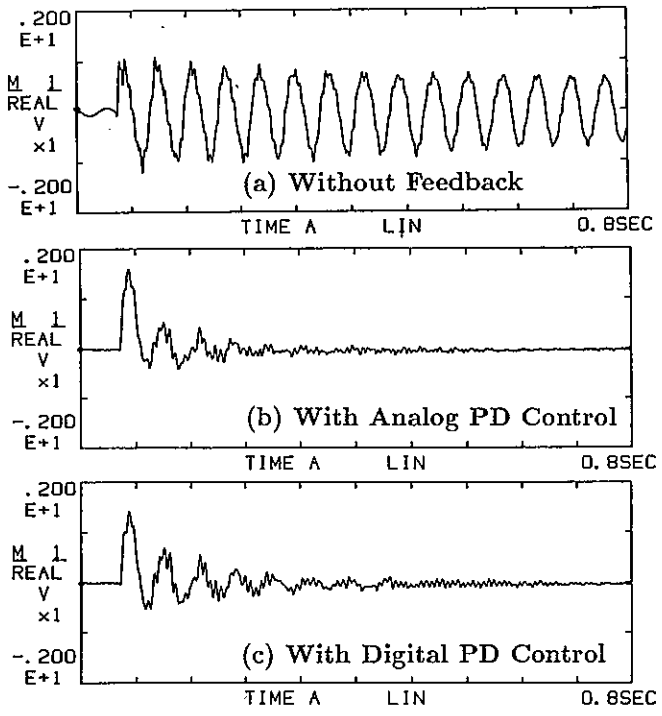

Fig. 9. The Comparison of Impulse Responses Without Feedback, With Analog PD and Digital PD Control

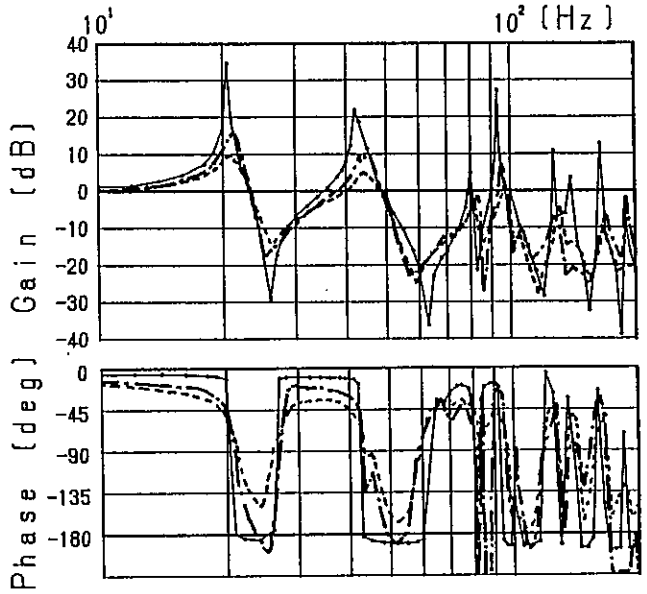

(a) Without Feedback
(b) With Analog PD Control
(c) With Digital PD Control

Fig. 10. The Comparison of Frequency Responses Without Feedback, With Analog PD and Digital PD Control

2) Matsushita, O., Takahagi, M., Tsumaki, N., Yoneyama, M., Sugaya, T., Bleuler, H., "Flexible Rotor Vibration Analysis Combined with Active Magnetic Bearing Control", Int. Conf. on Rotordynamics, IFToMM & JSME, Tokyo, Japan, Sept. 1986

3) Y. Oshima and T. Shimogo, "Electro-Magnetic Levitation Control of a Travelling Elastic Plate", Proc. of The Int. Conf. on Advanced Mechatronics, May 21-24, 1989, Tokyo, Japan.

4) Schweitzer, G. and Ulbrich, H., "Magnetic Bearings - A Novel Type of Suspension", Institution of Mechanical Engineers, Second Int. Conf. on Vibrations in Rotating Machinery, Cambridge, U. K., Sept. 1980, Paper C273/80

5) Bleuler, H., Schweitzer, G., "Dynamics of a Magnetically Suspended Rotor with Decentralized Control", First IASTED Int. Sym. on Applied Control and Identification, Copenhagen, Denmark, June 28-July 1, 1983, p.17-22

6) Traxler, A., Meyer, F. and Murbach, H. P., "Fast Digital Control of a Magnetic Bearing with a Microprocessor", Int. Kongress Mikroelektonik, Munich, Germany, Nov. 13-15, 1984

7) Larsonneur, R. and Herzog, R., "Optimal Design of Structure Predefined Discrete Control for Magnetic Bearings (SPOC-D)", Proc. of First Int. Sym. on Magnetic Bearings, June 6-8, 1988, Zurich, Switherland.

8) Bleuler, H. and Salm, J., "Active Electro-Magnetic Suspension and Vibration Control of an Elastic Rotor with a Signal Processor", 4th Int. Conf. on Vibrations in Rotating Machinery, Sep. 1988, Edinburgh, Scotland.

9) Okada, Y., Nagai, B. and Shimane, T., "Digital Control of Magnetic Bearing with Rotationally Synchronized Interruption", Proc. of First Int. Sym. on Magnetic Bearings, June 6-8, 1988, Zurich, Switzerland.

2nd International Symposium on Magnetic Beaing
July 12-14, 1990, Tokyo, Japan

STABILITY ANALYSIS FOR ROTORS SUPPORTED BY ACTIVE MAGNETIC BEARINGS

H. M. CHEN, D. WILSON, P. LEWIS, J. HURLEY
Mechanical Technology Incorporated
Latham, New York

Abstract

This paper presents an analytical method for tying active magnetic bearing (AMB) controller parameters to rotordynamic stability analysis. The controller, represented by its component transfer functions, is written into a subroutine appended to a finite-element rotordynamic program. The controller parameters can be modified until several lower system modes are stabilized. This method facilitates the controller design and shortens the tuning effort in installing rotor-AMB systems.

Introduction

Turbomachinery users and manufacturers are gradually accepting AMBs for the advantages they offer, i.e., elimination of the lubrication system and ability to control stiffness and damping. Stiffness and damping can be manipulated to desired values without any mechanical modifications by changing resistors and capacitors of an analog controller, or by changing equivalent parameters of a digital controller. However, the "desired values" are not yet well defined for these new rotor-AMB systems.

In conventional rotor systems with oil-film bearings, the stability of natural modes above operating speed is seldom a problem. However, it can be a controller design struggle to stabilize up to two or three of these modes in a rotor-AMB system. If the controllers are not properly tuned, it is not unusual for a rotor on AMBs to vibrate out of control during start-up. As reported in a recent conference*, a rotor was damaged during the installation and controller-tuning process. Tuning is a time-consuming process that involves adjusting and/or modifying the controller until the rotor-AMB system is stable and well damped at the lower modes.

Guiding the controller design with system stability analysis reduces the risk and effort of tuning. However, there is a lack of suitable computing tools for rotor-AMB systems. The stability programs developed during the last two or three decades for conventional bearings are awkward for use with rotor-AMB systems for the following reasons:

- AMB stiffness and damping are functions of rotor whirl frequency, not rotor speed.
- AMB reaction forces are proportional to displacements measured at rotor locations offset axially from the bearing. [1]**

To account for these unusual AMB features, Chen presented an extended state variable approach in which AMB dynamic behavior was represented by a set of first-order differential equations appended to the rotor equations of motion. [2] A different method is presented herein to facilitate the controller design.

Stability Analysis Formulation

Bearing force is defined as

$$F_b = -K_i\, G(S)\, Y_p + K_m\, Y_b \qquad (1)$$

where

F_b = AMB force exerted on rotor
K_i = Current stiffness
K_m = Magnetic stiffness
Y_b = AMB center displacement
Y_p = Displacement at AMB sensor
$G(S)$ = Controller transfer function
S = Laplace variable.

The stiffnesses K_i and K_m are functions of bias (steady state) currents in the magnetizing coils and are key parameters in the linearized control of AMBs.

The transfer function G(S) represents a series of component transfer functions that are typically multiplied together as shown in Equation 2.

$$G(S) = G_1(S)\, G_2(S)\, G_3(S)\, G_4(S) \qquad (2)$$

where G_1, G_2, G_3, and G_4 are, for example, the transfer functions of the sensor, PID controller, phase compensator, and power amplifier/coils, respectively.

Additional filtering schemes, such as band-pass or band-reject (notch) filters, can be added to Equation 2 as transfer function multipliers.

A radial AMB has two identically controlled axes, each represented by Equation 1. The two axes are perpendicular to each other and are usually located at 45° angles from vertical to share the rotor weight. Therefore, the dynamic properties of the axes, i.e., stiffness and damping, can be made identical. Since AMBs are generally an order of magnitude less stiff than the conventional bearings and their pedestals or casings, for most turbomachinery applications it is adequate to assume circular rotor whirl orbits in the stability analysis. The resulting equations of motion of a rotor can be represented by Equation 3.

$$[M]\,[\ddot{X}] + [C]\,[\dot{X}] + [K]\,[X] = \{F\} \qquad (3)$$

where

$[M]$ = Rotor mass matrix; an assembly of beam element 4 x 4 consistent mass matrices, and concentrated masses and transverse moments of inertia. [3]
$\{X\}'$ = $(Y_1, \theta_1, Y_2, \theta_2 \ldots\ldots)$; state vector
$[C]$ = diag. $(0, -jI_{P_1}\Omega, 0, -jI_{P_2}\Omega \ldots\ldots)$; diagonal matrix containing only gyroscopic terms
j = $\sqrt{-1}$

*REVOLVE '89 - A Symposium On Dry Seals and Magnetic Bearings, September 26, 1989. Calgary, Canada.

**Numbers in brackets indicate references cited herein.

Y_i = Linear displacement of i^{th} station

θ_i = Angular displacement of i^{th} station

I_{pi} = Polar moment of inertia of i^{th} station

Ω = Rotating speed (rad/sec)

[K] = Rotor stiffness matrix; an assembly of beam element 4 x 4 stiffness matrices, including the shear effect [3]

$\{F\}'$ = (---0---F_{b1}---0---F_{b2}---0---); forcing vector containing only bearing reactions for stability analysis

F_{bm} = Reaction of m^{th} AMB.

For a rotor model containing n stations, the above matrices and vectors would have an order of 2n.

Stability Analysis Method

Substituting the AMB forces of Equation 1 into the forcing vector {F} of Equation 3, and rearranging {F} to the left-hand side of Equation 3, a homogeneous system matrix equation is established for eigenvalue/eigenvector solution (damped system modes). Since each F_b term is a function of rotor whirl frequency, an iterative numerical scheme is required to obtain the solution. The steps in this scheme are:

1. Generate a conventional undamped natural frequency map at a fixed rotor speed. The AMBs are represented by incremental stiffnesses. At each stiffness, calculate the undamped natural frequencies. The natural frequencies for a given mode, calculated at different stiffnesses, are connected in a curve.
2. Superimpose the AMB stiffnesses as functions of whirl frequency on the map and locate the approximate system modal frequencies.
3. For each mode, begin by using these approximate frequencies as the rotor whirl frequency and calculate the corresponding stiffness and damping of the AMBs. Use these dynamic properties to calculate the damped system modes. If the assumed whirl frequency is equal to (or close to) the calculated damped frequency, a solution for one mode is obtained. If not, use the newly calculated frequency (or one close to it) as the new assumed whirl frequency and repeat this step.

In step 3, the AMB stiffness and damping coefficients at an assumed rotor whirl frequency are calculated through a program subroutine that implements a closed-form solution of Equation 2.

Numerical Example

Figure 1 shows a fan rotor supported by two radial AMBs and a thrust AMB. The rotor has a large fan wheel at one end. The radial AMBs, which are identical, each have 8 poles, 1-in. length, and a 2.5-in. journal outer diameter. Pertinent rotor and bearing data are listed on Figure 1. Dynamically, the AMBs are tuned to have approximately the stiffness and damping shown in Figure 2.

A stability analysis program was coded in Fortran with a static condensation option for saving computing time. [4] Twelve

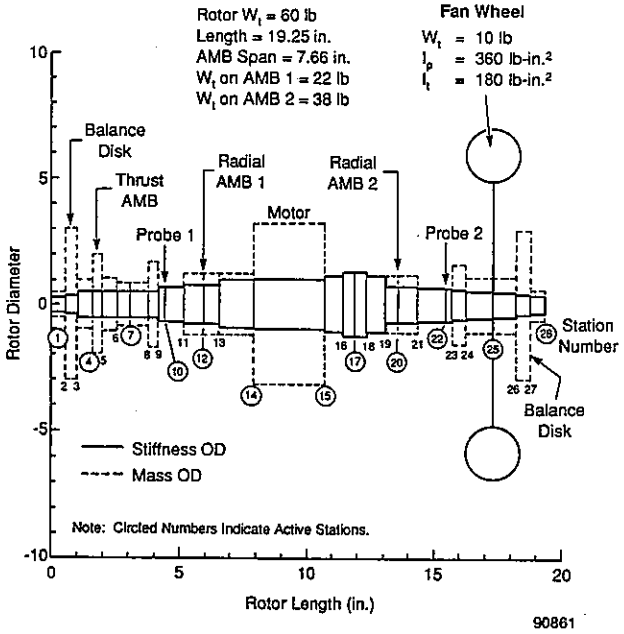

Fig. 1 Fan Rotor Model

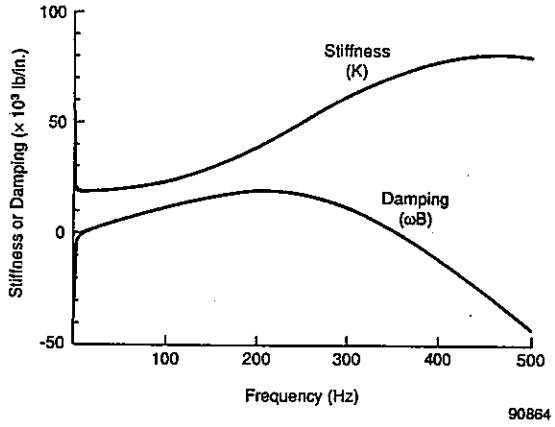

Fig. 2 AMB Stiffness and Damping

of the rotor model's 28 stations were taken as "active" stations, as indicated by the circled numbers in Figure 1.

The undamped natural frequencies at a rotating speed of 1800 rpm were calculated at bearing stiffnesses of 1×10^4, 4×10^4, and 1×10^5 lb/in. The natural frequency map for these calculations is presented in Figure 3. The superimposed AMB stiffness curve shows the first four forward modes as 55, 85, 250, and 480 Hz, respectively.

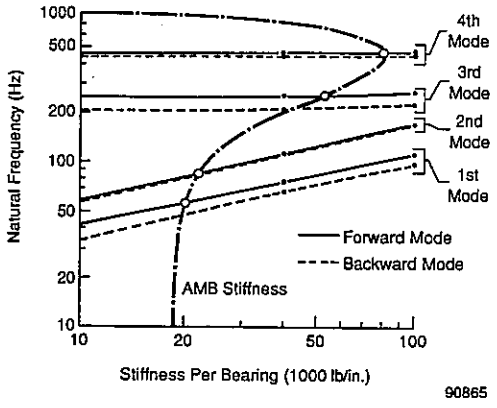

Fig. 3 Natural Frequency Map at 1800 rpm

The undamped mode shapes calculated at 4×10^4 lb/in./bearing are plotted in Figure 4. The mode shapes show that the displacements of an AMB and its associated probe have the same sign (i.e., positive value or negative value). Therefore, the probe locations are correct for the AMB control. The third mode has a node at one AMB, which could make controlling this mode difficult. These mode shapes provide a reference for evaluating the damped results.

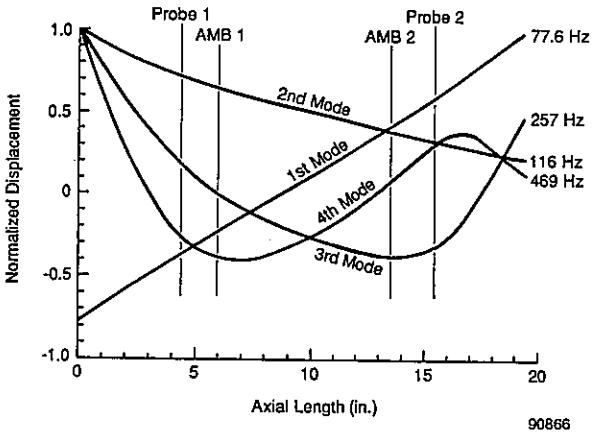

Fig. 4 Undamped Mode Shapes at 1800 rpm (4×10^4 lb/in./bearing)

To perform the damped analysis, a magnetic bearing subroutine that is applicable to both AMBs, MAGBRG, was written according to the control scheme in Figure 5. The subroutine's first two data statements contain all the essential control parameters and can be changed at the keyboard. The subroutine is compiled separately and is called by the main program. The subroutine Fortran statements are simple and straightforward.

Damped natural frequencies are plotted against assumed whirl frequencies with a 45° straight line superimposed. The log decrements of the calculated whirl modes are marked on the plot. Numerical iteration efforts to calculate the exact damped frequencies and the associated log decrements are not necessary as long as there are calculated points nearby. However, for cases of significant gyroscopic effect, this plot should be constructed twice — once at zero speed and once at full speed.

The results of searching the damped natural modes are presented in Figure 6. Only the forward modes are included as an example. The first two modes are well damped. This should be evident by examining their mode shapes in Figure 4 and the dynamic properties of Figure 2. The third mode (first bending) is very lightly damped because a node exists at one AMB. The fourth mode (second bending) is unstable. Although the rotating speed is low, the fourth mode is at a frequency of high stiffness and is likely to be excited.

To improve the damping of the two bending modes, a notch filter is placed to the left of each mode. As shown in Figure 7, these bending modes are riding on the right-hand slopes of the notches where large phase leads exist. Even with these large phase leads, the third mode log decrement is only slightly improved. The fourth mode, however, became stable.

Conclusions

Stability analysis is crucial to the design process for rotors supported by AMBs, since instability can be detrimental to these systems. Separating the dynamics of the AMB from the dynamics of the rotor during the analysis imposes uncertainty in the stability results and can lead to lengthy tuning time during system installation. This paper presents an analytical method for tying the AMB controller design directly to the rotor mechanical stability. The controller parameters can be readily modified until satisfactory log decrements are achieved for several lower modes. This method, when properly computerized, will take away the guesswork and in the future may make the installation tuning process unnecessary.

References

[1] KIRK, R. G., et al.: "Influence of Active Magnetic Bearing Sensor Location on the Calculated Critical Speeds of Turbomachinery," ASME, 12th Biennial Conference on Mechanical Vibration and Noise, Montreal, Canada, September 17-21, 1989.

[2] CHEN, H. M.: "Magnetic Bearing and Flexible Rotor Dynamics," STLE Annular Meeting at Cleveland, Ohio, May 9-12, 1988.

[3] ZORZI, E. S., and NELSON, H. D.: "Finite Element Simulation of Rotor-Bearing Systems with Internal Damping," ASME Paper No. 76-GT-89.

[4] COOK, R. D.: "Concepts and Applications of Finite Element Analysis," John Wiley and Sons, Inc., 1974, pp 242-48.

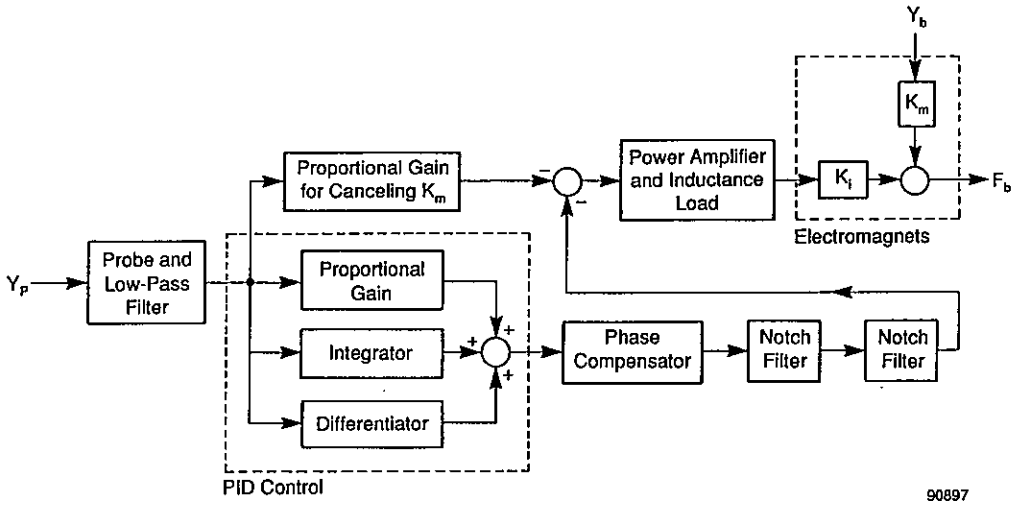

Fig. 5 Control Scheme Implemented in Subroutine MAGBRG

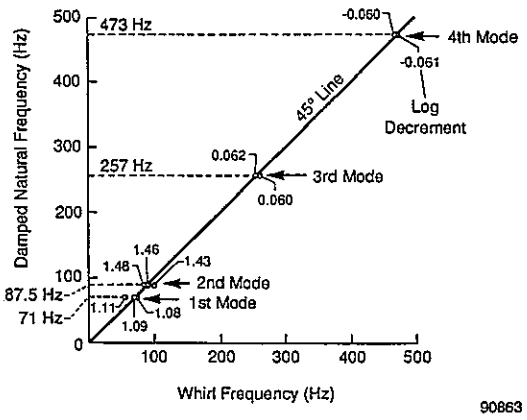

Fig. 6 Stability Analysis Results for Forward Modes at 1800 rpm

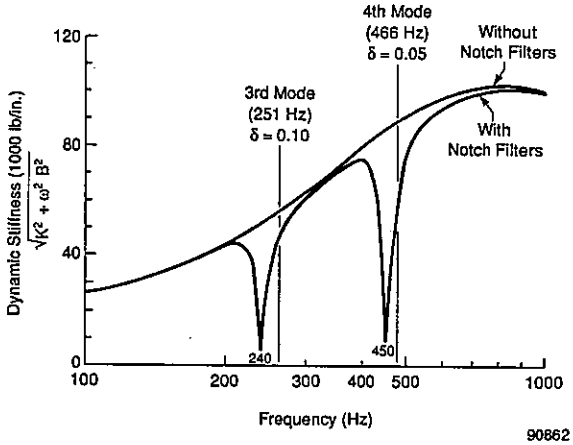

Fig. 7 Bending Mode Control Using Notch Filters

2nd International Symposium on Magnetic Beaing
July 12-14, 1990, Tokyo, Japan

A SELF-EXCITED VIBRATION OF MAGNETIC BEARING SYSTEM WITH FLEXIBLE STRUCTURE

I.SATOH*1, C.MURAKAMI*2, A.NAKAJIMA*3 and Y.KANEMITSU*1

*1 Ebara Research Co.Ltd,Honfujisawa, Fujisawa 251, Japan
*2 Tokyo Metropolitan Institute of Technology, Hino, Tokyo 191, Japan
*3 National Aerospace Laboratory, Chofu, Tokyo 182, Japan

Abstract

A self-excited vibration with two different frequencies was observed on our 4-axis-active type magnetic bearing system which has been developed for high speed rotating machinery. In this paper, we discuss the cause and mechanism of the self-excited vibration. Experiments indicated that the cause of the self-excited vibration is interaction between nonlinearity of the electromagnet system and flexibility of the structure. Clarification on the mechanism of this self-excited vibration was made through analysis with nonlinear model, applying a method wherein both the root-locus method and a describing function method were used.

1. Introduction

It is well known that self-excited vibration in passive axis of magnetic bearing may be caused by increasing of internal damping when the rotor is driven over critical speed. Shimizu[1] and Kawamoto[2] investigated the cause of the self-excited vibration, and they obtained the same results indicating that the self-excited vibration is caused by energy loss such as eddy current loss act as internal damping. On the other hand, another type self-excited vibration may occurs even in the active-axis of magnetic bearing, if the magnetic bearing system has flexible structures. Since cause of the self-excited vibration is not clarified, it is difficult to obtaining stable high speed rotation in magnetic bearing system with flexible structures. A self-excited vibration with two different frequencies was observed on our 4-axis-active type magnetic bearing system which has been developed for high speed rotating machinery.

In this paper, we discuss the cause and mechanism of the self-excited vibration. The experimental results and computer simulations proved that the self-excited vibration is caused by interaction between nonlinearity of electromagnet systems and structural flexibility. The self-excited vibration mechanism is clarified by applying the root-locus method and approximate dual-input describing function method.

2. Characteristics of the self-excited vibration

To summarize the main characteristics of the self-excited vibration obtained from experiments, we have following:

(1) The self-excited vibration is caused by relatively low-level disturbance, if loop gains are set at relatively high value.

(2) Even if the loop gains are set at relatively low-level, high-level disturbance such as hammering causes the self-excited vibration.

Figure 1 shows an example of the self-excited vibration observed in case of non-rotation. In this wave form, high frequency vibration may be first bending mode of the stator shaft, and low frequency vibration may be rigid mode of the rotor. Thus, the self-excited vibration is composed of two vibrations with different frequencies and become continuous vibration (limit cycle) in case of non-rotation state.

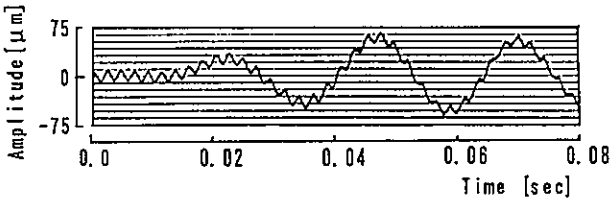

Fig.1 An example of the self-excited vibration

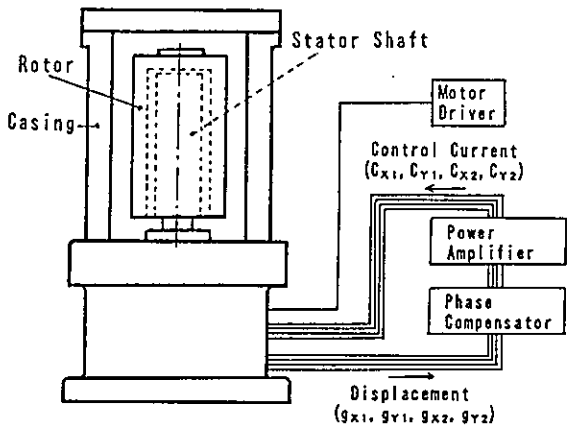

Fig.2 Four-axis-active type magnetic bearing system

3. Magnetic bearing system

A magnetic bearing system, shown in Fig.2, is consist of 4-axis-active type magnetic bearing which is located inside of a casing, its compensators and its power amplifiers which generate control currents. In the following, we give brief explanations and models of them for analysis.

3.1 Four-axis-active type magnetic bearing

3.1.1 Mechanical structure The mechanical structure of the 4-axis-active type magnetic bearing is shown in Fig.3, where the rotor has hanging bell shape and stator is a cantilever. The 4-axis-active type magnetic bearing is consist of two radially-active type magnetic bearings which are located on both side of the high speed motor. The radially-active type magnetic bearings contain permanent magnets and electromagnets. The rotor is passively stabilized in the axial direction by the restoring attractive force of the permanent magnets. However, the magnetic bearing even has imbalance stiffness, which is expressed as a negative spring constant, in the radial direction due to the attractive force of the permanent magnets. The electromagnets regulate radial clearance between rotor and stator and cancel the radial imbalance stiffness. Static characteristics for the rotor are shown in Table 1.

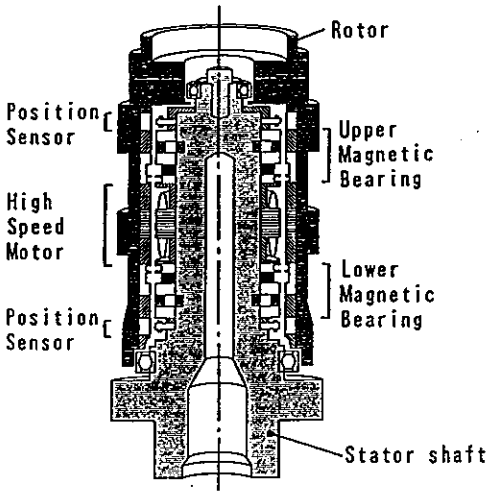

Fig.3 Mechanical structure of the 4-axis-active type magnetic bearing

3.1.2 Model of the dynamics Since the 4-axis-active type magnetic bearing is outer-rotor type, the first-bending-mode frequency of the rotor could be set at a rather high value, and only the rigid mode should be considered for the rotor. However, a first-bending-mode frequency of the stator shaft, which swings largely at the top part of the shaft but little at the bottom, is in the rotational region. Therefore, we adopt the simplified 2-DOF model shown in Fig.4, where only the radial motion of the upper side magnetic bearing is considered. Modal coefficients of the stator shaft are shown in Table 2.

Table 1 Static characteristics

Rotor Mass	$M = 5.7$	[kg]
Rotor Inertia		
Spin Axis	$I_p = 15.9\times10^{-3}$	[kg・m²]
Radial Axis	$I_d = 31.5\times10^{-3}$	[kg・m²]
Ratio	$\gamma = I_p/I_d = 0.504$	
Radial Unbalance Stiffness	$K_u = 12.7\times10^5$	[N/m]
Axial Stiffness	$K_z = 2.46\times10^5$	[N/m]

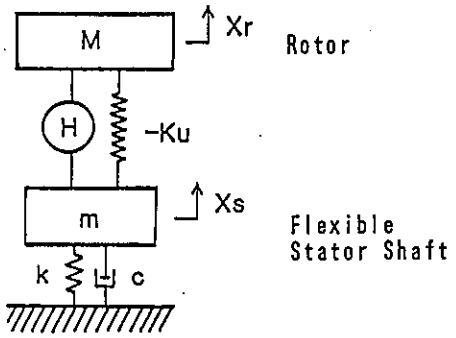

H : Controller

−Ku : Unbalance Stiffness

Fig.4 Dynamical model

Table 2 Modal coefficients of the stator shaft

Mass	$m = 2.2$	[kg]
Damping Coefficient	$c = 209$	[Ns/m]
Stiffness	$k = 2.21\times10^7$	[N/m]
Resonace Frequency	$\omega_n = 504$	[Hz]
Damping ratio	$\zeta = 0.015$	

3.2 Compensators

The independent control method for each axis, which does not separate the motion into translational and rotational modes, was adopted for simplicity of the control system. Every axis has a same phase compensator, whose transfer function is as follows.

$$H(s)=\frac{1+T_1 s}{1+T_2 s} \qquad (T_1>T_2)$$

3.3 Electromagnet system

An electromagnet system for the magnetic bearing, which is composed of a power amplifier

and electromagnetic coils, has a wide range bandwidth generally. Therefore, transfer functions for the electromagnet system have as far been expressed by constant element or first-order lag element at most. These models are valid when the low frequency vibration problems such as rigid mode are discussed. However, characteristics of the electromagnet system tend to become worse in high frequency region. Therefore, nonlinear model for electromagnet system should be adopted when the system includes flexible mode of which resonance frequency is several hundreds Hz.

3.3.1 Experimental results Figure 5 shows a circuit diagram of the power amplifier used in this system. The power amplifier is push-pull type and utilize 24 [V] power supply. Figure 6 shows frequency characteristic curves of the electromagnet system, when the input voltage was changed in three steps. It is obvious from this figure that the electromagnet system has nonlinearity in which phase characteristic becomes worse in the case where high-frequency, large amplitude signals are applied.

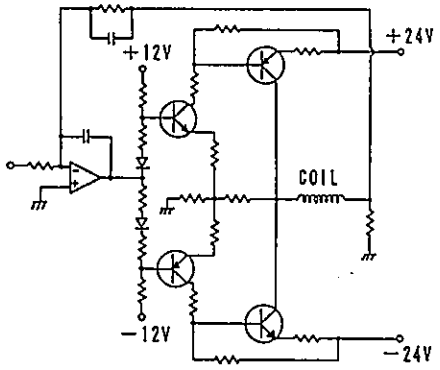

Fig.5 Circuit diagram of the power amplifier

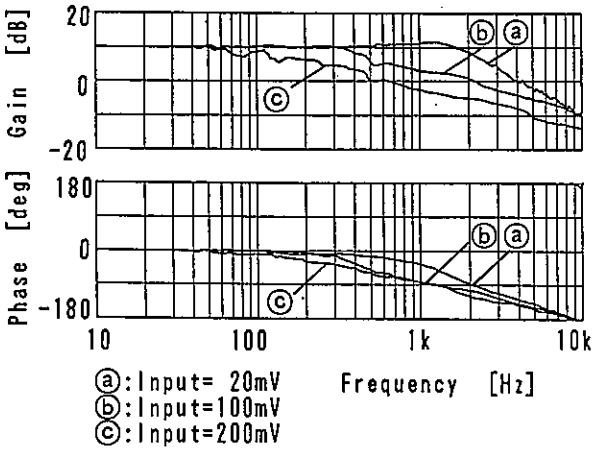

Fig.6 Frequency characteristic curves of the electromagnet system (Experiments)

3.3.2 Model for electromagnet system Considering the experimental results of electromagnet system, we adopted the model shown in Fig.7. The model consist of a saturation element and 2nd-order lag element, which are negatively fedback by constant gain element K_F.[3] Figure 8 shows frequency characteristic curves for the electromagnet system obtained form calculation by using the model. This figure proves validity of the model.

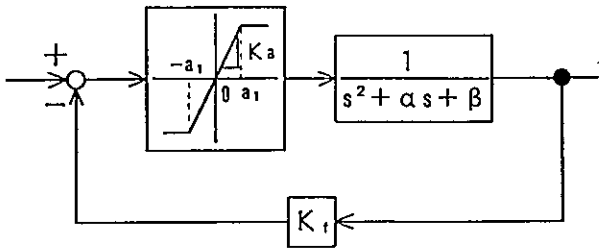

Fig.7 Nonlinear model of the electromagnet system

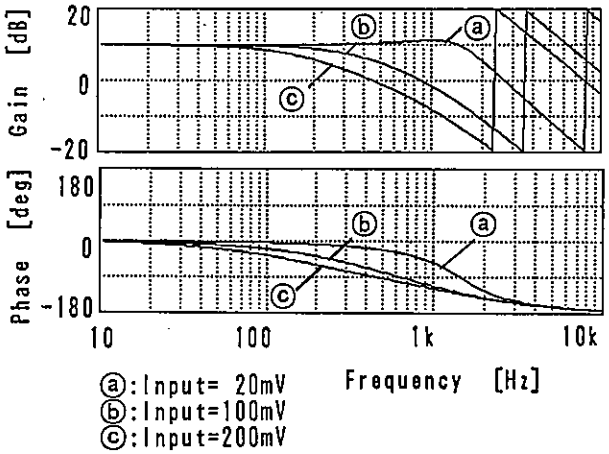

Fig.8 Frequency characteristic curves of the electromagnet system (Simulations)

4. Simulations

Figure 9 shows a block diagram of the whole system including nonlinear electromagnet system and a flexible structure. Figure 10(a) shows the wave forms of the self-excited vibration obtained from experiments. In this figure, upper side wave form represents relative displacement between rotor and stator shaft, and lower side wave form represents control current. As it is clear from this figure, both signals do continuous vibration which are composed of two different frequency vibrations. Figure 10(b) shows simulation results used the system shown in Fig.9. Similarly to the experimental results, both signals of the simulation show continuous vibration including two different frequency vibrations.

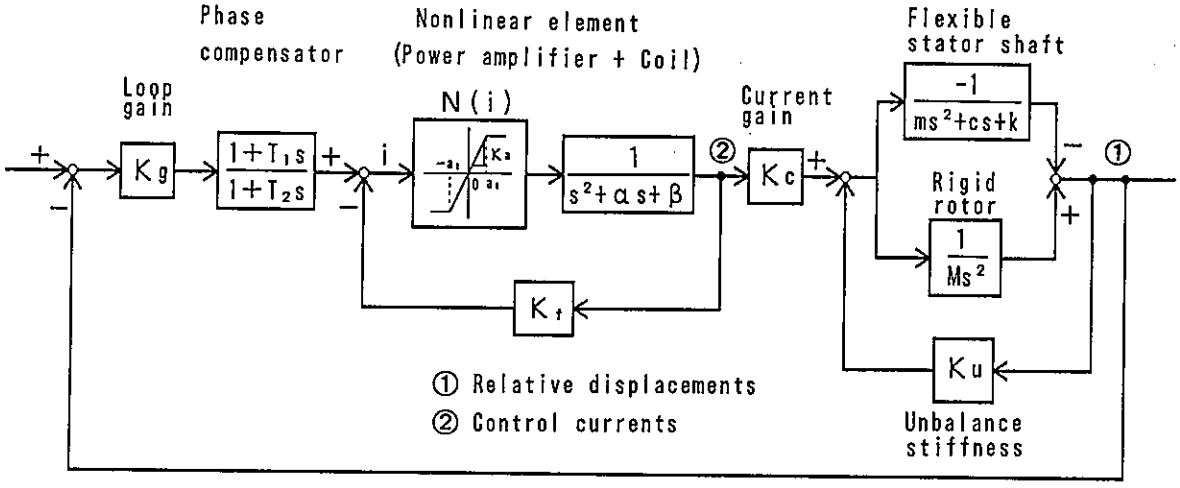

Fig.9 Block diagram of the system

Because of modeling approximation, the amplitude of the high frequency vibration in simulation is about one third times as small as the experimental results, though the amplitude of the low frequency vibration indicates good agreement between simulations and experiments.

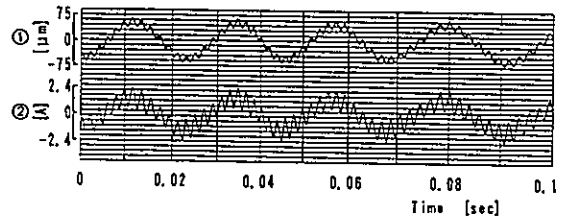

(a) Experimental results

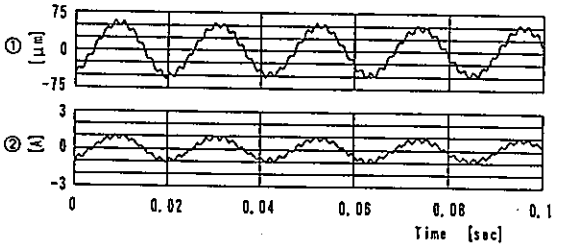

(b) Simulations

① Relative displacements
② Control currents

Fig.10 The self-excited vibration

5. Analysis for self-excited vibration

By using root-locus method and describing function(DF) method, occurrence mechanism of the self-excited vibration will be discussed.

5.1 Root-loci in nonlinear domain

The DF of the saturation element is represents only by change of gain, which depends on the amplitude of input signal. Therefore, root-loci of the system in nonlinear domain can be calculated by replacing the saturation element by linear gain element N. Figure 11 shows the root-loci of a rigid mode and flexible mode. In this figure, the root-loci by varying the loop gain Kg are shown by dotted lines and marks show the operating point in the linear domain. Solid lines show the change of characteristic roots by varying the ψ ($=N/K_a$) at the operating points. The relationship between ψ and the stability of the two modes are clarified from this figure as follows.

(1) Stable region of the rigid mode

$$0.066 < \psi < 1 \qquad (1)$$

(2) Stable region of the flexible mode

$$\psi < 0.092 \ , \ 0.224 < \psi < 1 \qquad (2).$$

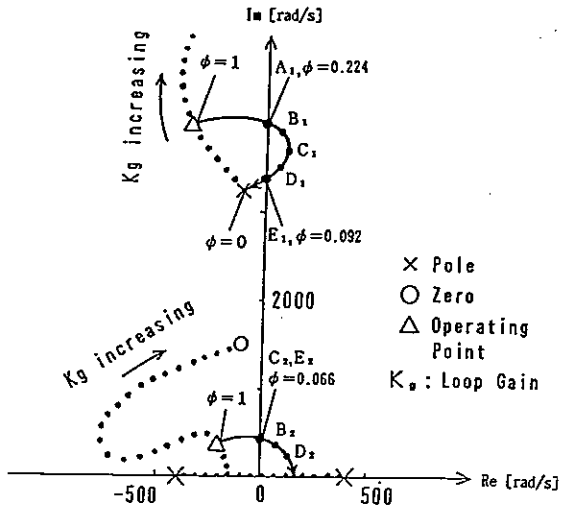

Fig.11 Root-loci of the system

5.2 Approximate dual-input describing function (ADIDF) method

In order to obtain the relationship between amplitude of the input signal and stability of the system, the value ψ of saturation element will be calculated by utilizing DF method. As is mentioned earlier, this self-excited vibration is composed of two different frequency oscillations so that dual-input describing function(DIDF), should be calculated. The DIDF method is based on consideration of two sinusoids as a input, shown in Eq.(3), being applied to the nonlinear element.

$$i = a_0\sin(\omega t) + b_0\sin(\beta t) \qquad (3)$$

Since the frequency of the two vibrations separate enough(ω =530Hz, β =40Hz), an ADIDF method could be utilized in this case. Assume that change of the low frequency component can be neglected while one any cycle of the high frequency component, the input signal is considered as shown in Eq.(4), which is composed of DC-bias and high-frequency oscillatory component.

$$i = a_0\sin(\omega t) + B_D \qquad (4)$$

Then, output signal from the nonlinear element can be approximated as

$$y = \frac{A_0}{2} + a_1\sin(\omega t) \qquad (5)$$

By adopting Fourier analysis to these equations, next two equivalent gains can be defined.

(1) Equivalent gain for DC component of the input signal (Equivalent DC gain)

$$K_{ed} = A_0/2B_D \qquad (6)$$

(2) Equivalent gain for sinusoidal component of the input signal

$$K_{ea} = a_1/a_0 \qquad (7)$$

These two equivalent gains are not independent each other but dependent on each amplitude of the high and low frequency component including of signal. These gains for saturation element are obtained as follows.

$$K_{ed} = \frac{K_a}{\pi}\left[\phi_1+\phi_2+\frac{a_0}{B_D}(\cos\phi_2-\cos\phi_1) + \frac{a_1}{B_D}(\phi_2-\phi_1)\right] \qquad (8)$$

$$K_{ea} = \frac{2K_a}{\pi}\left[\frac{a_1-B_D}{a_0}\cos\phi_1+\frac{a_1+B_D}{a_0}\cos\phi_2+ +\frac{1}{4}\{2(\phi_1+\phi_2)-(\sin2\phi_1+\sin2\phi_2)\}\right] \qquad (9)$$

where $\phi_1=\sin^{-1}\left(\frac{a_1-B_D}{a_0}\right)$, $\phi_2=\sin^{-1}\left(\frac{a_1+B_D}{a_0}\right)$

5.2.1 ADIDF for low frequency component Boyer [4] developed ADIDF for low frequency component of input signal by applying above-mentioned equivalent DC gain K_{ed}. Average value of output signal from nonlinear element can be calculated by product of B_D and K_{ed}. The "representative output wave" is determined to join the obtained value by smooth line as shown in Fig.12. By adopting the Fourier analysis to this wave form directory, the amplitude of fundamental wave(b_1) is obtained. Therefore, ADIDF for high frequency component is calculated by next equation.

$$N_r = b_1/b_0 \qquad (10)$$

Figure 13 shows the ADIDF for saturation element calculated by Boyer's method. If each amplitude ratio ε_r (= b_0/a_1), ε_r (= a_0/a_1) of low and high frequency component in input signal are known, ADIDF ratio of low frequency component ψ_r (=N_r/K_a) can be obtained from this figure. The shadowed portion in this figure is defined as a stable region of the low frequency component by Eq.(1) obtained form root-loci shown in Fig.11.

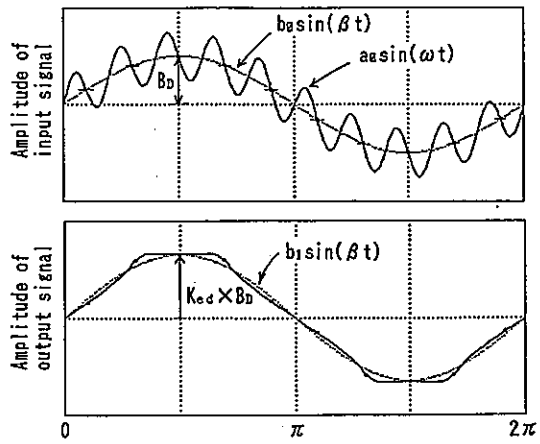

Fig.12 Representative output wave for low frequency component

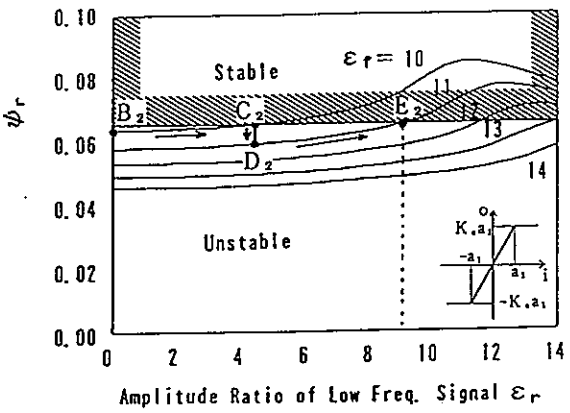

Fig.13 ADIDF of saturation element for low frequency component

5.2.2 ADIDF for high frequency component The equivalent gain for high frequency component K_{ea} can be calculated from Eq.(7), if the DC value B_D is fixed. Then, we regard the low frequency component as a DC-bias, because the change of low frequency component in a cycle of the high frequency component is so slow that we can neglect it. Since K_{ea} is changed with B_D, the change of K_{ea} in a cycle of low frequency is shown in Fig.14, where K_{ea} indicates maximum value when the amplitude of the low frequency component is zero and indicates minimum value when the amplitude of the low frequency component is maximum. In this analysis, we defined the average of K_{ea} as an ADIDF of the high frequency component. Figure 15 shows the ADIDF ration for high frequency component ψ_f ($=N_f/K_a$) obtained from above-mentioned method. The shadowed portion in this figure shows stable region of the ADIDF for high frequency component determined by Eq.(2).

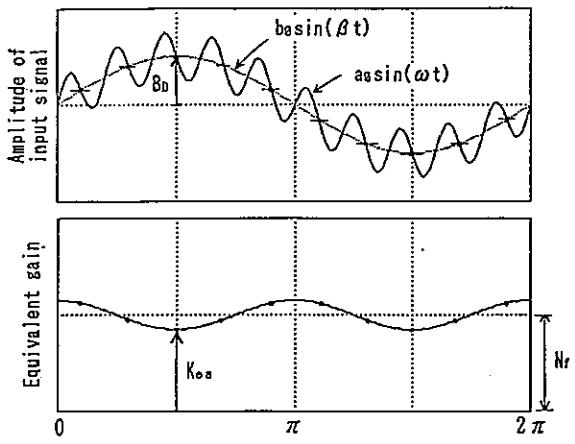

Fig.14 Equivalent gain for high frequency component

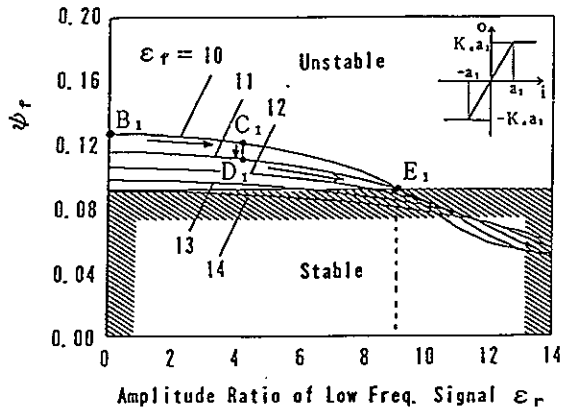

Fig.15 ADIDF of saturation element for high frequency component

5.3 Occurrence mechanism of the self-excited vibration

By using Figs.11,13 and 15, the process from resonance vibration of stator shaft to the self-excited vibration is explained as follows;

(1) If the stator shaft is excited by some disturbance as impulse force, the ADIDF for flexible mode (corresponding to the high frequency component) ψ_f is defined according to the amplitude of the vibration. As it is obvious from Fig.11, the characteristic roots of flexible mode exist in left-half plane within the range of $1> \psi_f >0.224$ so that the vibration is damped. However, if the amplitude of the vibration becomes larger, the ψ_f decrease under 0.224. Therefore, the characteristic roots of flexible mode moves into right-half plane and the vibration tends to diverge.

(2)Now we consider the condition that ε_f =10, ε_r = 0, then ψ_f and ψ_r are pointed by B_1,B_2 in Figs.12 and 14, respectively. As it is clear from these figures, both the flexible mode and the rigid mode(corresponding to the low frequency component) is unstable. Therefore, both vibrations tend to diverge.

(3)Firstly, we pay attention to the rigid mode. As it is clear from Fig.13, ψ_r increases with increment of ε_r in the region of $0< \varepsilon_r <10$ when ε_f is constant. In case of ε_f =10, ψ_r reaches the threshold between stable and unstable region when ε_r is about 4.5(point C_2). This point is a kind of equilibrium point, because if ε_r increases more than 4.5, the characteristic roots of rigid mode moves into stable region therefore the amplitude of the rigid mode tends to damp. On the other hand, if ε_r decrease less than 4.5 due to decrease of amplitude of the rigid mode, the characteristic roots of the rigid mode come back to the unstable region therefore the amplitude of the rigid mode tends to diverge. Consequently, the amplitude of the rigid mode keep balance in this point.

(4)Secondly, as it is clear from Fig.15, the flexible mode is still unstable in point C_1 (corresponding to the point C_2 in Fig.13) so that the amplitude of the flexible mode tends to increase. Now we assume that the amplitude of flexible mode increase up to ε_f =10(point D_1). As seen from Fig.13, the rigid mode becomes unstable again at point D_2(corresponding to the point D_1 in Fig.15), because ψ_r decreases with increment of ε_f when ε_r is constant.

(5)Thus, amplitude of the both rigid and flexible mode increase as they are influenced each other. Consequently, they balance at the boundary point (E_1,E_2) between stable and unstable region, when ψ_r =9 and ψ_f =11. As it is clear from Fig.11 that both E_1 and E_2 are located on the imaginary axis, continuous vibration including two frequency components occurs.

Considering the circumstances mentioned above, it is obvious that rigid mode is caused by flexible mode. And the flexible mode becomes stable limit cycle, when ψ_f decreases less than 0.224 due to the increasing of amplitude of the vibration, in case that the disturbance causing the vibration is not continuous, but impactive. Therefore, the self-excited vibration with two different frequency will be occurred. However, the rigid mode tends to toward unstable region when the amplitude of the flexible mode becomes large, though the flexible mode tends to toward stable region when the amplitude of the rigid mode becomes large. Therefore, if the amplitude of flexible mode becomes larger than ψ_f =0.092 due to forced disturbance such as unbalanced force, rigid mode becomes unstable.

6. Conclusions

In this paper, we discuss the cause and mechanism of the self-excited vibration occurs on our 4-axis-active type magnetic bearing which has been developed for high speed rotating machinery. The results of this research are summarized as follows.

(1)The self-excited vibration caused by interaction between flexibility of the stator shaft and nonlinearity of the electromagnet system in which phase characteristic becomes worse in the case where high-frequency, large-amplitude signals are applied.

(2)The self-excited vibration contain two different frequency vibrations, and the rigid mode(low frequency component) is caused by flexible mode (high frequency component).

(3)The rigid mode vibration has apprehension to become unstable in case that the flexible mode vibration become large, though the flexible mode surely becomes stable limit cycle regardless of the amplitude of rigid mode vibration.

7. Acknowledgment

The authors would like to express special thanks to Mr.Makoto IMAI, then a graduate student of Tokyo Denki University, for assistance in the simulations and experiments.

8. References

[1] H.Shimizu, H.Ozawa, O.Taniguchi, Trans. Jpn. Soc. Mech. Eng.,(in Japanese), Vol.36, No.290, 1(1970), p.1656.

[2] H.Kawamoto, K.Kikuchi, Trans. Jpn. Soc. Mech. Eng., (in Japanese), Vol.47, No.419, C(1981), p.849.

[3] A.Nakajima, M.Imai, I.Satoh, J.Nagahiro and C.Murakami, Proc. China-Japan Symp. on Mechatronics, (1988), p.63

[4] J.Gibson, "Nonlinear Automatic Control", McGraw-Hill Book Company, New York, 1963.

On the Static Stability Problem of Magnetic Levitation from Rigid Body to Flexible Plate

Shigeki Morii*, Noriyuki Kawada*, Keiichi Katayama*, and Yoshiro Takahashi*
* Hiroshima Research & Development Center, Mitsubishi Heavy Industries,LTD., Nishi-ku, Hiroshima 733 ,Japan

Abstract
It is an important item that how many magnets and control axis are necessary to be able to suspend the body by the magnetic force. The magnet has the attraction force originally,and the couple force i.e. the attraction moment in spite of it is controlled by the position feedback.
This paper presents the conditions of static stability which are necessary in order to determine the arrangements of magnetic bearings especially for flexible body.

1. Introduction

When the body is levitatied by magnetic force, the possibility of levitation is restricted by Earnshow's Theorem. Earnshow's Theorem shows that it is impossible for a position of stable equilibrium, and a current of the electromagnet has to be controlled by position feedback.

It is the important item that how many magnets and control axis are necessary to be able to suspend the body, especially the long body.
The magnet has the attraction force originally and the couple force i.e. attraction moment in spite of it is controlled by the position feedback. We have already presented that it was necessary to consider the couple force of every axis in order to discuss the stability of the full magnetic bearing type rotor(ref.[1]).

This paper presents the relations between the static stability conditions and the magnetic bearing arrangements under considering the above-mentioned original force of magnets theoreticaly.

Recently, many works have continued for applying the active magnetic bearings to the flexible body levitation (ref.[3], [4]). We are studying the magnetic levitation technologies of the thin steal plate in order to make good use of non-contact merit(ref.[2]).

At first,we make it be clear that is the static stability condition considering the magnetic couple force at the rigid body levitation. Secondly we discuss the static stability condition to determine the pitch of the bearings at the flexible beam levitation. And we investigate the instability problem caused by difference between the magnetic field and the position of feedback sensor.

2. Characteristics of Magnetic Bearing

In order to investigate the stability of magnetic levitation system, we have to make it clear that the static characteristic of the active magnetic bearing unit itseif first of all.

The bearing unit consists of twin electromagnets, their drive circuits, a position sensor, and a position feedback line as shown in Fig.1. As it's static characteristic, the transfer function from a displacement of the body to the electromagnetic forces has to be clear. There are two kind of electromagnetic forces for the displacement as follows.

(1)Passive Part:

$$F_P = K_M \cdot X_P \tag{1}$$

$$K_M = -4K(I_0^2 + I_C^2)/\delta_0^3$$

(2)Active Part:

$$F_A = K_F \cdot I_A \tag{2}$$

$$I_A = K_P \cdot X_A \tag{3}$$

$$K_F = 4K I_0/\delta_0^2$$

where F :electromagnetic force
X :displacement of the body
I_A:control current
K_P:proportional gain
K :electromagnetic constant
δ_O:aimed gap
I_O:bias current
I_C:load balance current
P :passive , A : active

These functions are led as the concentrated system. The displacement X_A used in the active part is measured by sensor, and then means that of one point

of the body. On the other hand, the displacement X_P used in the passive part means the distribution of the body, being concerned with the magnetic field. And both the passive part F_P and the active part F_A of the electromagnetic force act on the magnetic field as the distribution. Really, the displacement X_A which is the position feedback signal, only is as a cencentrated system, the others are as the distribution system. Then, the above-mentioned functions are realized, only when the body is rigid and displaces parallel to the electromagnet.

If the body rotates at the axis perpendicular to the displacement X_A, the position sensor can not measure the rotation movement, and the electromagnetic force F_A does not act to the body at all. But the electromagnetic force F_P acts to the body as the moment, as the displacement X_P is concerned with the rotation movement. Then, this phenomena is written as the following equations.

$$M_P = K_\theta \cdot \theta$$
$$K_\theta = \frac{1}{12} K_M \cdot \ell^2 \qquad (4)$$

where M_P :moment (coupled force)
θ :the rotation angle of the body
ℓ :The equivalent electromagneto width

The equation (4) is realized only when the body is rigid too. If the flexible body such as thin plate is levitated by such some magnetic bearing units, there are the following subjects.
(1) We wish that the distance between the magnetic bearing units is as much as possible.
(2) We wish that the width of the electromagnet is as mush as possible.
These subjects means that the number of the bearing units is reduced. The static stablity problem is studied from a viewpoint of each subject theoretically.

3. Stability Problem of Rigid Body

The static stability problem is studied for the rigid body of the system shown in Fig.2. In Fig.2, the body is suspent by 4 bearing units. Rotational stiffness of both rolling and yawing direction is ensured by each 2 bearing units. The distance of 2 bearing units is not much longer than the width of electromagnet. Then, the passive rotational stiffness K_θ is important to ensure the static stability. The static stability condition is as follows.

$$K_F \cdot K_P + K_M > 0 \qquad (5)$$

for each bearing unit

$$2 \cdot \frac{L^2}{4} (K_F \cdot K_P + K_M) + 2K_\theta > 0 \qquad (6)$$

for rolling and yawing direction where L:the distance of bearing units As K_θ is negative, it is sufficient to satisfy equation (6). Equation (6) becomes the following equation.

$$K_F \cdot K_P + \left(1 + \frac{\ell^2}{12L^2}\right) K_M > 0 \qquad (7)$$

And,it is a very important selection that the body is levitated by either attraction magnetic force or repulsion magnetic force. As using the attraction magnetic force, the stability check of pitching is necessary. And the couple force is added to the left hand of equation (6). Then, the feedback gain K_P increases at using the attraction force.

When the body is levitated by the electromagnet, the plate contacts with electromagnet. In order to clear the reason, the eigenvalue of the model shown in Fig.2 is analized by the program shown in ref.[6]. These results are shown in Fig.3. Fig.3 shows that the rigidity of plate is small to secure the static stability under keeping 4 bearing units. This problem is solved by analizing the precise model such as Fig.2.

4. Stability Problem of Steal Plate

When the thin and long steal plate is levitatied by the magnetic force, it is very important to determine the pitch of bearing units and the width of electromagnet. To be clear this subject, the static stability problem is studied. When this static stability problem is solved, the following items are assumed.
(1)The steal plate is analized as the beam model (ref.[5]).
(2)The steal plate is free in tension.
(3)The steal plate is not transfered.
And, the precise model is shown in Fig.4.

4.1 Pitch of Bearings and Stability

First of all, the ratio of steal strip area to electromagnet area is determined by the load capacity of bearing. Relations between the ratio of load capacity to strip weight and the thickness of strip is shown in Fig.5 (Ref[2]). The ratio of strip area to electromagnet area must be smaller than the value of the perpendicular axis in Fig.5.

Next the condition which determines the pitch of bearing units is introduced from the study of static stability. In Fig.4, the concentrated model mentioned in paragraph 2 is used as the

characteristics of bearing units. The eigenvalues are calculated as the values of rotational stiffness K_θ are parameter (ref.[5]). These results are shown in Fig.6. Fig.6 shows the following things.
(1)The 3rd eigenvalue is unstable at K_θ= -3.5 N·m/rad. And 2nd eigenvalue is unstable at K_θ =-5.9N·m/rad.
(2)When these eigenvalues become unstable, the mode of 3rd eigenvalue looks like that of 1st eigenvalue at pin support and that of 2nd eigenvalue looks like that of 2nd eigenvalue at pin support.

Then, the following stability criterion is gotten from the comparsion between the bendings stiffness of the above-mentioned mode and the rotational stiffness of bearing unit.

$$\frac{2EI}{L} + 2K_\theta > 0 \qquad (8)$$

for 3rd eigenvalue.

$$1 \Big/ \left(\frac{2}{\tilde{K} \cdot L^2} + \frac{L}{12EI} \right) + 2K_\theta > 0 \qquad (9)$$

for 2nd eigenvalue.

where, $\tilde{K}=K_F \cdot K_D + K_M$
EI:bending stiffness of beam
The results compared between the eigenvalue analysis and the criteria equation are shown in Fig.7. This simple criterion coincides with the results of the eigenvalue analysis. Usually, if equation (8) is satisfied, equation (9) is satisfied. Then, the pitch of bearing has to determined from the criterion of equation (8).

4.2 Width of Electromagnet and Stability

There is a question that how much area of electromagnet it is good for one feedback sensor. In order to confirm this question, the eigenvalues of the part of only a bearing unit shown in Fig.8. In Fig.8, both the passive stiffness K_M and the active magnetic force F_A act on the magnetic field which is different from the point of sensor. The root loci with the parameter of $\bar{K}=K_F \cdot K_A$ is shown in Fig.9. As the 2nd eigenvalue is unstable naturally and the 4th eigenvalue is stable, these are omitted. Only 1st and 3rd eigenvalues are plotted in Fig.9. Fig.9 shows the following results.
(1) As feedback $\bar{K}$ increases, 1st eigenfreguency increases and 3rd eigenfrequency decreases.
(2) At $\bar{K}$=4850N/m, 1st eigenfrequency coincides with 3rd eigenfrequency.
(3) When $\bar{K}$ is greater 4850N/m, 1st and 3rd eigenvalues are coupled, and both eigenvalues are dynamic unstable.
Fig.10 shows each mode of beam when 2 eigenvalues are both uncoupled and coupled. Such a feedback gain has the effect which is bending the beam.

Then, the following stable criterion is able to be made from the considence of both 1st and 3rd eigenfrequencies.

$$K_F \cdot K_P + K_H > \alpha \frac{48 \cdot EI}{\ell^3} \qquad (10)$$

where, 2·l:width of electromagnet
As the constant α is estimated from these results, α equals 0.15. The bearing unit is determined by the existance of K_F which is satisfied with both equation (8) and (10).

4.3 Results of Total System

To confirm the above-mentioned results, the eigenvalues of the precise model shown in Fig.4 is analized. Dimentions of strip and bearing are as t=0.3mm, L=570mm and l=70mm. The results of eigenvalue analysis are shown in Table 1. This system doesn't satisfy equation (8). Then, 1st eigenvalue is static unstable. And, as $K_F \cdot K_A$=5000N/m, this system doesn't satisfy equation (10). Then, Table 1. shows that 5th and 6th eigenvalues are dynamic unstable. Next, when the width of electromagnet is made smaller, the eigenvalues are shown in Table. 2. As $K_F \cdot K_D$=5000N/m, all of eigenvalues are stable. This system satisfies both equation (8) and (9).

5. Conclutions

According to the theoretical study above mentioned, satisfing the following conditions are necesary to determine the arrangement of magnetic bearing units.
(1) The ratio of strip weight to load capacity is determined.
(2) The pitch of bearing units satifies equation (8).
(3) And, the selected feedback gain satisfies equation (10).

From now on, we will develop these idea to the following status.
(1) From the beam model to the plate model.
(2) The strip is contrained by tention. We succeeded in the levitation of thin steal strip(2m×3m×0.6mm~6.0mm) shown in ref.[2]. The above-mentioned phenomena has to be confirmed by the test in the near future.

References.

[1] S.Morii, K.Katayama : On the Stability of Rotor with Active Magnetic Bearings. Symposium=Dynamics

concerning with Electro-Magnetic Force '89 (in Japanese)
[2] N.Kawada, S.Morii, K.Katayama, Y.Takahashi : On the Magnetic Levitation Characteristics of Thin Steal Strip. 2nd Symposium=Dynamics concerning with Electro-Magnetic Force '90(in Japanese)
[3] F.Matsumura, M.Fujita : Electro-Magnetic Levitation Control of an Elastic Plate. Maglev '89 p423
[4] T.Shimoga, Y.Oshinoya : Stabilization for Flexible Beam System Controlled by Magnetic Suspention. Maglev '89 p435
[5] M.Kawashima, S.Morii, et al : Vibration Analysis of Rotor-Bearing System by Finite Element Method. Mitsubishi Juko Giho Vol.20 No.4, 1983. p1(in Japanese)
[6] K.Katayama, S.Morii, M.Kawashima : Development of Rotor Dynamics Analysis System Considering Control System. Mitsubishi Juko Giho Vol.26 No.3, 1989, p253(in Japanese)

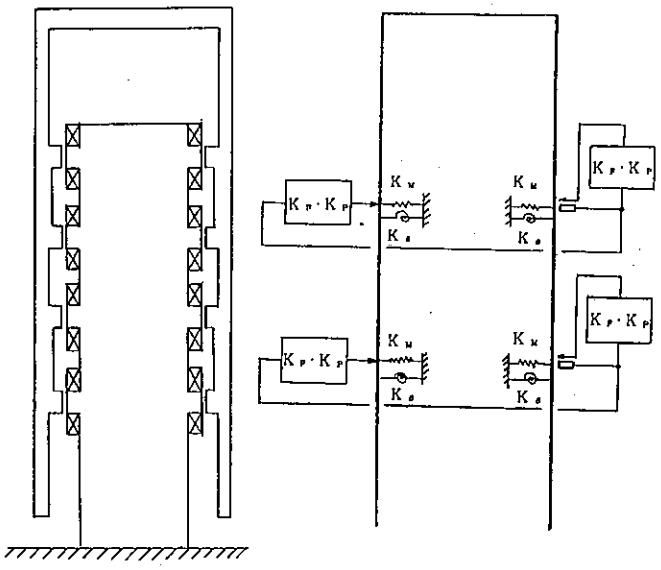

Fig.2 Model of Rigid Body Levitation

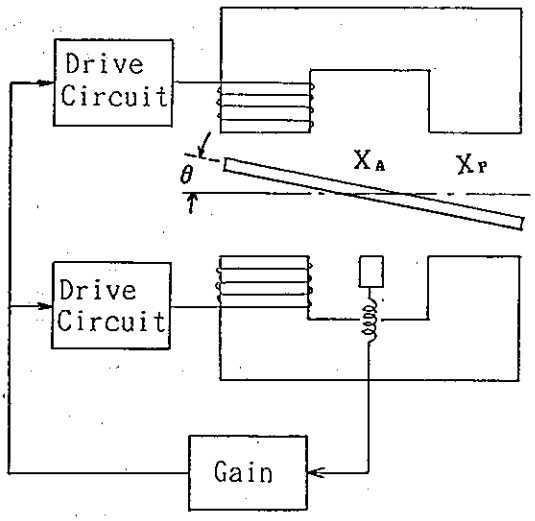

Fig.1 Magnetic Bearing Unit

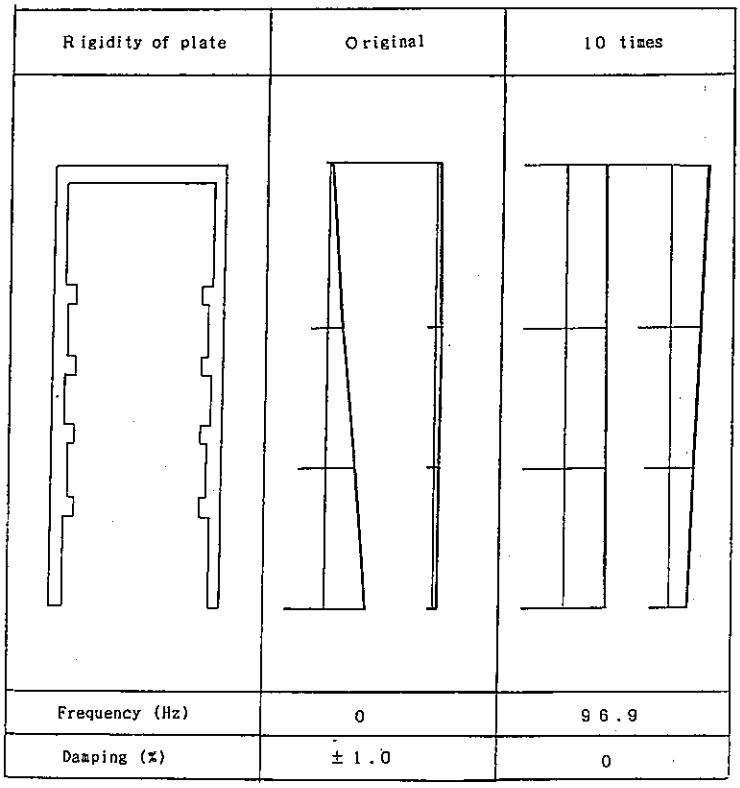

Fig.3 Static Stability Analysis Results

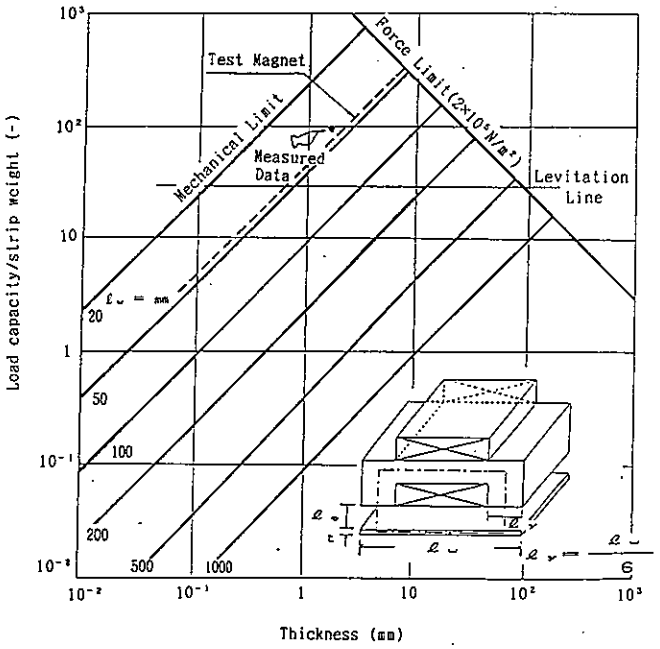

Fig.4 Load Capacity for Steal Plate

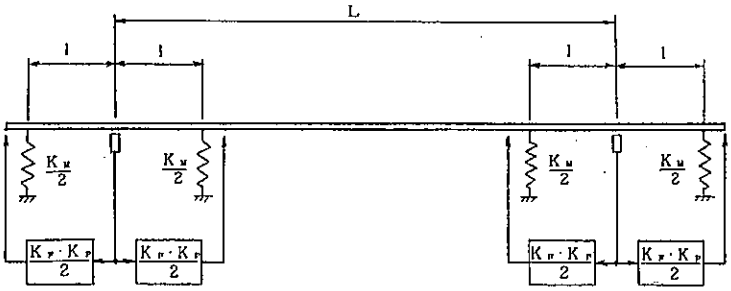

Fig.5 Beam Model of Plate Levitation

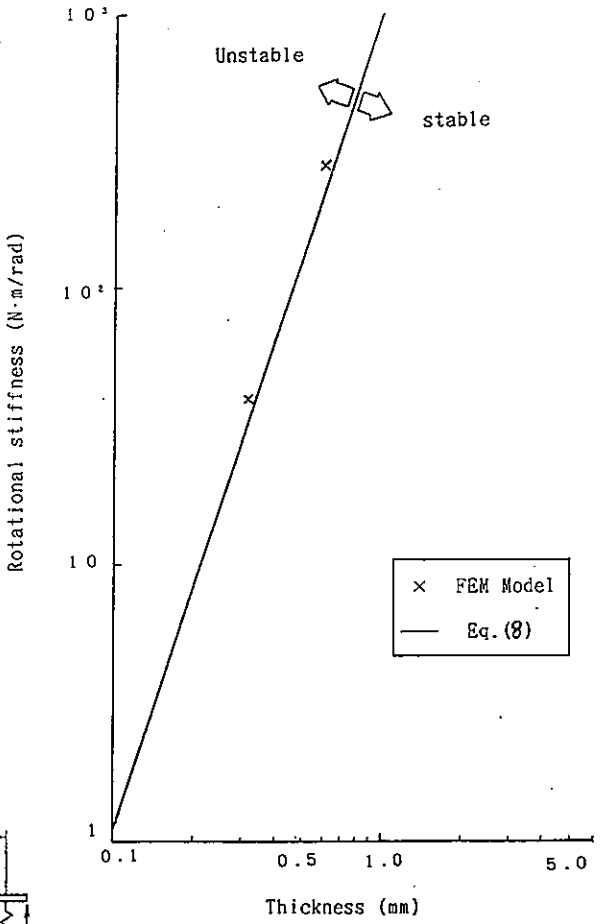

Fig.7 Stability Criterion concerning with Electromagnetic Width

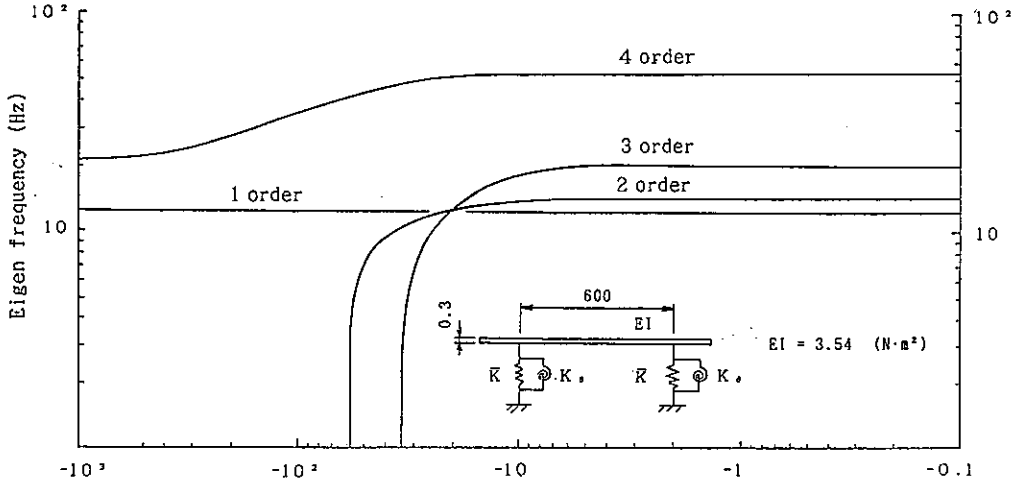

Fig.6 Eigenfrequency & Magneto Stiffness

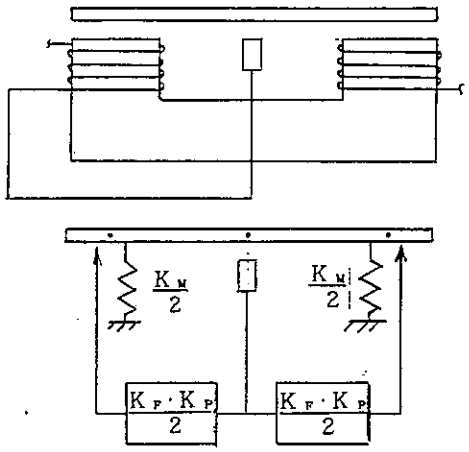

Fig.8 Model of Bearing Unit

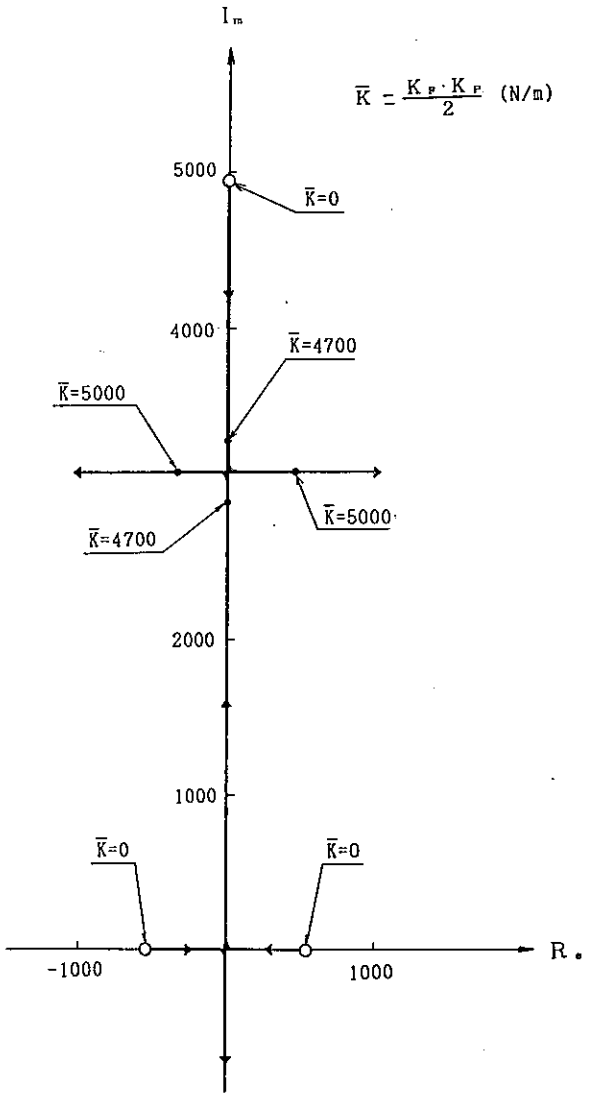

Fig.9 Root Loci

Proportional gain $\bar{K} = \frac{K_P \cdot K_P}{2}$ (N/m)	4700		5000	
	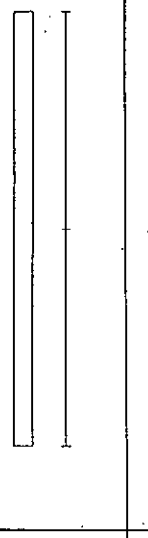	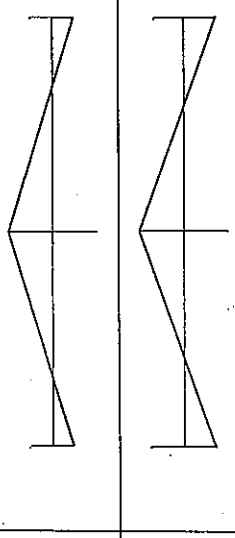	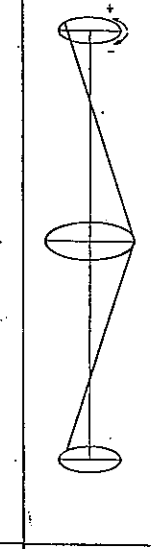	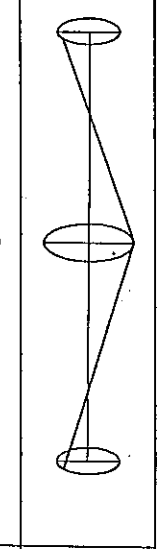
FREQUENCY (HZ)	456.5	519.2	489.7	489.7
DAMPING (%)	0	0	-0.145	0.145

Fig.10 Stability Analysis Results

Table 1. Stability Analysis Results (L=570,l=70)

	$K_P \cdot K_P$ = 1000 (N/m)		$K_P \cdot K_P$ = 5000 (N/m)	
	Frequency (Hz)	ζ (-)	Frequency (Hz)	ζ (-)
1-Order	0.	±1.0	0.	±1.0
2-Order	45.6	0.	46.3	0.
3-Order	103.2	0.	150.0	0.
4-Order	107.0	0.	302.6	0.15
5-Order	142.1	0.	302.6	-0.15
6-Order	263.9	0.	351.1	-0.21
7-Order	408.3	0.	351.1	0.21
8-Order	600.6	0.	519.1	0.

Table 2. Stability Analysis Resuits (L=330, l=70, $K_P \cdot K_P$ =5000N/m)

	Frequency (Hz)	ζ (-)
1-Order	76.7	0.
2-Order	315.2	0.32
3-Order	315.2	0.32
4-Order	315.2	-0.32
5-Order	315.2	-0.32
6-Order	619.8	0.
7-Order	1253.2	0.

2nd International Symposium on Magnetic Beaing
July 12-14, 1990, Tokyo, Japan

STIFF AMB CONTROL USING AN $\mathcal{H}^\infty$ APPROACH

R. HERZOG[1] AND DR. H. BLEULER[2]
Institute for Robotics, ETH Zurich, Switzerland

Abstract

An important requirement in most practical AMB (active magnetic bearing) applications is: "Stiffness of the controlled mechanical parts, subjected to *unknown dynamic* disturbance forces or loads, should not be below a given value *for all relevant frequencies.*" This requirement can be viewed as a *wide-band* disturbance attenuation problem in an $\mathcal{H}^\infty$ setting. This approach is particularly well-suited for applications where the *"worst case"* exciting frequency of disturbance forces must be considered.

The present contribution deals with trade-offs involved in the frequency domain. As in all control synthesis problems there are several *conflicting* requirements. A sample AMB problem is shown where the *achievable performance*, i.e. the worst-case compliance of the mechanical parts, is calculated numerically. Two basic ways of how *compromises* can be made and how several conflicting requirements can be incorporated in the $\mathcal{H}^\infty$ framework are considered.

1 Industrial Background

Electromagnetically supported milling spindles are examples for AMB application where stiff and precise suspension is indispensable [5][3]. The milling process induces wide-band cutting forces which may cause intolerable vibrations of the milling tool. The controller should provide a satisfactory "attenuation" of these vibrations.

2 A Sample AMB Problem

Consider the controlled mechanical system in figure 1 which stands for a simple electromagnetically supported *elastic* shaft. The system is assumed to be subjected to an *unknown* disturbance force $w(t)$ acting on the bottom mass m_1. Let $z(t)$ denote the displacement of m_1 caused by $w(t)$, and let $T_1(s)$ be the frequency-domain compliance of the bottom mass m_1: $z(s) = T_1(s)\, w(s)$.

For the time being, let the *objectives* of the controller C consist in *stabilizing* plant P and in maintaining dynamic *compliance* $T_1(s)$ *uniformly low*: $|T_1(i\omega)| \leq \alpha$, over all frequencies ω. The main goal

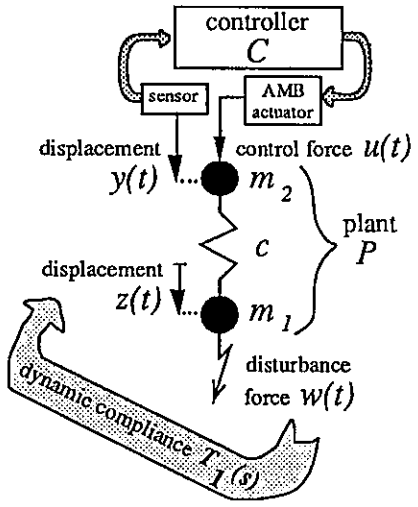

Figure 1: A sample AMB problem

of this paper is to seek such controllers and to gain an understanding of what happens if α is low.

The equations of motion are given by the following linear second order system:

$$\begin{cases} m_1 \ddot{y} &= c(z-y) + u \\ m_2 \ddot{z} &= c(y-z) + w \end{cases} \qquad (1)$$

Remark 2.1 For the sake of simplicity we do not consider the "negative stiffness" of the AMB, and we fix the parameter values to unity: $m_1 = m_2 = c = 1$.

[1] E-mail: raoul@sys.ife.ethz.chunet
[2] Fax: ++41-1-252 0276
[3] Session 7 of this conference is also concerned with machine tool spindles.

Figure 2 shows the interconnections between plant P and controller C.

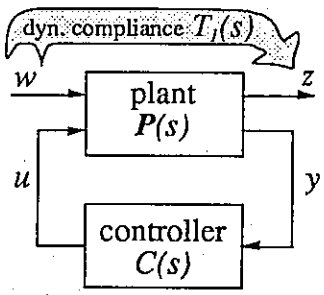

Figure 2: Interconnections

The corresponding algebraic equations in the Laplace–domain are:

$$\begin{bmatrix} z(s) \\ y(s) \end{bmatrix} = \begin{bmatrix} P_{11}(s) & P_{12}(s) \\ P_{21}(s) & P_{22}(s) \end{bmatrix} \begin{bmatrix} w(s) \\ u(s) \end{bmatrix} \quad (2)$$
$$u(s) = C(s)\, y(s)$$

The Laplace transformation of (1) gives:

$$P(s) = \begin{bmatrix} \frac{s^2+1}{s^2(s^2+2)} & \frac{1}{s^2(s^2+2)} \\ \frac{1}{s^2(s^2+2)} & \frac{s^2+1}{s^2(s^2+2)} \end{bmatrix} \quad (3)$$

It is a well–known fact that all closed–loop functions, of course including compliance T_1, can be expressed by *linear fractional maps* of controller C:

$$T_1(s) = P_{11} + P_{12}C(1 - P_{22}C)^{-1}P_{21}$$
$$\stackrel{\text{def}}{=:} \mathcal{F}_P(C(s)) \quad \text{(linear–fractional map)}$$
$$= \frac{C(s) - (s^2+1)}{(s^2+1)C(s) - s^2(s^2+2)} \quad (4)$$

Definition 2.2 Let $\| T \|_\infty$ denote the *"worst case"* compliance defined by its peak value in the frequency response:

$$\| T \|_\infty \stackrel{\text{def}}{:=} \sup_{0 \le \omega < \infty} |T(i\omega)|$$

Design engineers do appreciate $\| \cdot \|_\infty$–norms, because they are handy and easy to measure. Now let us formulate the central problem of this paper:

Problem 2.3 Find *stabilizing* controllers C, such that the worst case compliance of the bottom mass m_1 is *"better"* than α, i.e. $\| T_1 \|_\infty \le \alpha$, where $\alpha > 0$ is a given user–specific value. What happens if α is low? Does an "optimal" controller $\breve{C}$ exist?

The first step towards the solution of problem 2.3 is to get an understanding of what a stabilizing controller actually is. The next section will clarify this point.

3 Closed–Loop Stability implies Interpolation Conditions on T_1

Let us start with an introductory question. Is the following procedure a legitimate way to obtain stabilizing controllers: "Choose an *arbitrary stable* compliance $T_1(s)$ and compute $C(s)$ using equation (4)"? We shall see that the answer is *no!* This section will provide mandatory constraints[4] on T_1.

Recall the basic definition of internal closed–loop stability:

Definition 3.1 First let us introduce two additional inputs v_1, v_2 and outputs u, y according to figure 3. The closed–loop $[P, C]$ is termed *internally stable* [2] iff the augmented closed–loop transfer matrix $H(P, C)$ defined in equation (5) exists and belongs to $\mathcal{H}^\infty_{3\times 3}$; see next definition.

Definition 3.2 The *Hardy space* $\mathcal{H}^\infty$, or $\mathcal{H}^\infty_{m\times n}$ more precisely, consists of all complex functions of s (scalar–valued, vector–valued or matrix–valued according to m, n), which are *analytic* and *bounded* in $\{\Re\mathrm{e}(s) > 0\}$. For the subset of *rational* functions arising from lumped systems an equivalent definition is: every entry $H_{ij}(s)$ must be *proper* ($H_{ij}(\infty)$ is finite) and *stable* (no poles in $\{\Re\mathrm{e}(s) \ge 0\}$).

Definition 3.3 Let $\mathcal{S}(P)$ denote the *set* of all linear controllers $C(s)$ which *stabilize* P.

Here is the (3×3) transfer matrix $H(P, C)$:

$$\begin{bmatrix} z \\ u \\ y \end{bmatrix} = \begin{bmatrix} H_{11} & H_{12} & H_{13} \\ H_{21} & H_{22} & H_{23} \\ H_{31} & H_{32} & H_{33} \end{bmatrix} \begin{bmatrix} w \\ v_1 \\ v_2 \end{bmatrix} \quad (5)$$

Using the one–to–one correspondence between controller C and compliance T_1 in equation (4), we compute H as a function of T_1:

[4] An alternative approach [2] is coprime factorization of P_{22}.

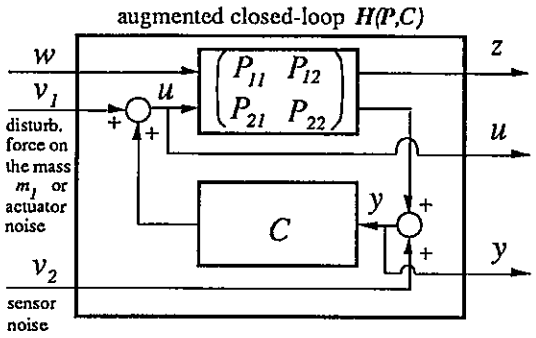

Figure 3: Diagram for stability definition

$$1.\ \text{col. of } \boldsymbol{H}: \begin{bmatrix} T_1 \\ s^2(s^2+2)T_1 - (s^2+1) \\ (s^2+1)T_1 - 1 \end{bmatrix}$$

$$2.\ \text{col. of } \boldsymbol{H}: \begin{bmatrix} (s^2+1)T_1 - 1 \\ s^2(s^2+2)\left((s^2+1)T_1 - 1\right) \\ (s^2+1)\left((s^2+1)T_1 - 1\right) \end{bmatrix}$$

$$3.\ \text{col. of } \boldsymbol{H}: \begin{bmatrix} s^2(s^2+2)T_1 - (s^2+1) \\ s^2(s^2+2)\left(s^2(s^2+2)T_1 - (s^2+1)\right) \\ s^2(s^2+2)\left((s^2+1)T_1 - 1\right) \end{bmatrix}$$

In fact, $\boldsymbol{H}$ is an *affine* function of T_1:

$$H_{ij}(s) = p_{ij}(s)\,T_1(s) + q_{ij}(s) \qquad (6)$$

where $p_{ij}(s)$ and $q_{ij}(s)$ are given *polynomials* in s. Therefore, $\boldsymbol{H}$ and T_1 share the same poles, except possibly for $s = \infty$. A *necessary* condition for internal stability is $T_1 \in \mathcal{H}^\infty$, but of course this is insufficient to meet the boundedness of $\boldsymbol{H}(\infty)$. Expand $T_1 \in \mathcal{H}^\infty$ as Laurent series around infinity:

$$T_1(s) = a_0 + \frac{a_{-1}}{s} + \frac{a_{-2}}{s^2} + \frac{a_{-3}}{s^3} + \ldots \qquad (7)$$

Insert (7) into (6) in order to get the asymptotic Laurent expansions of $\boldsymbol{H}_{ij}(s)$. Obviously, all positive powers in s have to vanish, which leads to the following conditions for the coefficients $a_0 \ldots a_{-7}$:

$$\begin{cases} a_0 = 0, & a_{-1} = 0 \\ a_{-2} = 1, & a_{-3} = 0 \\ a_{-4} = -1, & a_{-5} = 0 \\ a_{-6} = 2, & a_{-7} = 0 \end{cases} \qquad (8)$$

The coefficients $a_{-8}, a_{-9}, \ldots$ *freely* depend on the controller C.

Statement 3.4 *The closed loop $[P, C]$ is internally stable iff compliance $T_1(s)$ is stable and meets the interpolation conditions (8). We will call T_1 to be admissible iff these two conditions are met. Section 3 established the following equivalence relation: C stabilizing $\iff \boldsymbol{H}(P,C) \in \mathcal{H}^\infty_{3\times 3} \iff T_1$ admissible*

4 The "forbidden" controller C_0

Set $T_1(s) \equiv 0$ which *violates* the interpolation conditions (8)! Equation (4) gives:

$$C_0(s) = s^2 + 1 \notin \mathcal{S}(P)$$

Figure 4 helps to clarify the behaviour of C_0. Of

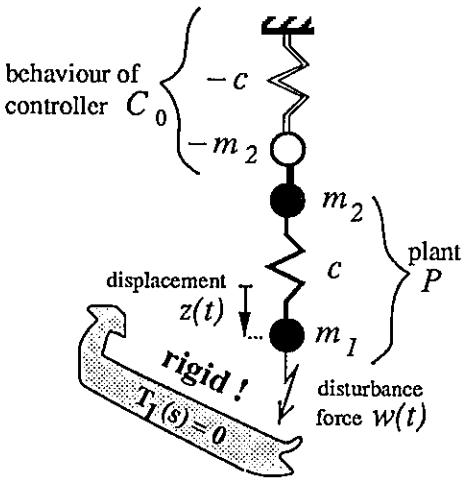

Figure 4: Behaviour of controller C_0

course, C_0 is neither stabilizing nor is it implementable (differentiators do not exist physically). Let us take a look at the corresponding closed-loop matrix $\boldsymbol{H}_0 := \boldsymbol{H}(P, C_0)$:

$$\boldsymbol{H}_0(s) = \begin{bmatrix} 0 & -1 & -s^2-1 \\ -s^2-1 & -s^4-2s^2 & -s^2(s^2+1)(s^2+2) \\ -1 & -s^2-1 & -s^4-2s^2 \end{bmatrix} \notin \mathcal{H}^\infty_{3\times 3}$$

Most of the $[\boldsymbol{H}_0]_{ij}$ are unbounded for $s \to \infty$: *high frequency* sensor (actuator) noise causes actuator (sensor) *saturation*. So, most of the functions H_{ij}

conflict with a low compliance $\| T_1 \|_\infty$. Note the practical meaning of each of the H_{ij}: we already introduced $H_{11} = T_1$ which is the local compliance of the *bottom* mass m_1. $T_2 := H_{32}$ denotes the local compliance of the *top* mass m_2.

The following statement 4.1 will fully make sense to the reader at the latest when he has finished reading this paper!

Statement **4.1**

- *There are stabilizing controllers C_j which permit an arbitrary low worst case compliance $\| T_1 \|_\infty$ of the bottom mass m_1.*
- *There are also stabilizing controllers $\widetilde{C}_j$ which permit an arbitrary low worst case compliance $\| T_2 \|_\infty$ of the top mass m_2.*
- *However, controllers which permit both at the same time do not exist.*

In fact, the optimization problem "min $\| T \|_\infty$" turned out to be a degenerate *boundary interpolation* problem at $s = \infty$ (see [1], [4]), because it lacks any *controller bandwidth limitation*. In order to take this essential aspect into consideration we now present two approaches.

5 First approach

The first approach is somehow indirect: we must prevent the closed–loop poles from "migrating too far to the left". This can be achieved by reducing the allowed pole region to a disk by means of a bilinear map, see figure 5. Parameter β governs the size of this disk. As β approaches 1, the disk grows to cover the whole left half plane $\{\Re\mathrm{e}(s) < 0\}$. So, the modified version of problem 2.3 is:

Problem 5.1 Define the disk $\mathcal{D}_\beta := \{|s + (1-\beta)^{-1}| < (1-\beta)^{-1}\}$. A compliance function $T_1(s)$ will be called *β-admissible*, if *all* of its poles are located in $\mathcal{D}_\beta$ *and* if it meets the interpolation conditions (8). Now, find a compliance function $\breve{T}_\beta$ which solves the following Min–Max problem:

$$\inf_{T_1 \ \beta\text{–admissible}} \left\{ \sup_{s \in \partial\mathcal{D}_\beta} |T_1(s)| \right\}$$

The optimal value[5] is denoted by $\breve{\alpha}(\beta)$.

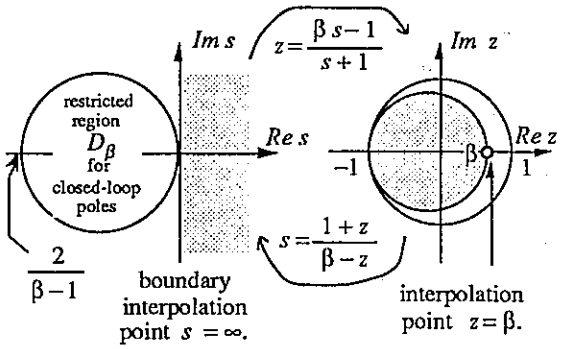

Figure 5: Bilinear map

Here is a brief outline of the standard "machinery" [2][6] we used to compute the solution of problem 5.1:

- Transform the interpolation conditions (8) in the z–plane. The new interpolation point is $z_* = \beta$. The function values up to the seventh derivative are prescribed at z_*.
- Set up the "model matching" problem $\inf \| T_a - QT_b \|_\infty$. The Blaschke product $(z-\beta)^8/(1-z\beta)^8$ is a good choice for T_b.
- Set up the "Nehari" problem $\inf \| R - X \|_\infty$.
- Solve the Nehari problem (by solving Lyapunov equations and eigenvalue problems).
- Backsubstitute and use the reverse bilinear map. Finally use (4) to obtain the corresponding controller $\breve{C}_\beta$.

Example 5.2 Choose $\beta = 0.6$. Thus the closed–loop pole locations are restricted to the disk $\{|s + 2.5| < 2.5\}$. For this value of β we obtained the following numerical solution:

$$\| \breve{T}_{\beta=0.6}(s) \|_\infty = \breve{\alpha}(0.6) \approx 1.727$$

The resulting controller $\breve{C}_{\beta=0.6}$ is:

$$\approx \frac{-2.55798s^3 + 0.7724s^2 - 4.68039s - 2.14526}{0.001s^3 + 0.01979s^2 - 2.38978s + 1.55966}$$

Note that compliance $|\breve{T}_{\beta=0.6}(s)|$ is *constant* on the circle $\{|s + 2.5| = 2.5\}$.

[5] Note that by the maximum modulus theorem $\| \breve{T} \|_\infty \leq \breve{\alpha}$. In fact, the right hand side equals the left due to the "all pass" property of solution $\breve{T}_\beta$.

[6] Recently, a new state space approach appeared in literature, see [Doyle, Glover, Khargonekar, Francis, IEEE 8, 1989]. This new method avoids the cumbersome backsubstitution.

Remark 5.3 Note that the order of $\check{C}$ is $n-1=3$. This is a well-known result in $\mathcal{H}^\infty$ control theory.

Figure 6 shows the set of solutions as β varies. We see that the optimum value of the worst-case compliance decreases to zero as $\beta \to 1$; at the same time the gain of the corresponding controllers $\check{C}_\beta$ keeps increasing.

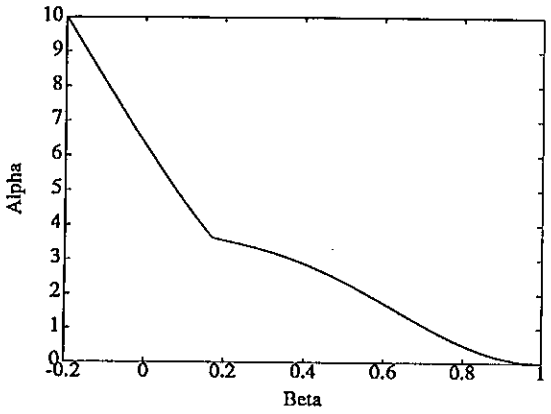

Figure 6: Numerical evaluation of $\check{\alpha}(\beta)$

6 Second approach

One disadvantage of the first approach is: parameter β of the bilinear map offers only insufficient control of the "size" of the functions $H_{ij}(s)$ conflicting with a low compliance $\| T_1 \|_\infty$. An interesting step towards a remedy would be a *quantitative* version of statement 4.1, namely: we already know that *no* controller C exists which permits *arbitrary low* values of *both* $\| T_1 \|_\infty$ *and* $\| T_2 \|_\infty$. But what about minimizing one of those while keeping the other one under a given tolerable bound ϱ? For the sake of simplicity we now don't care about sensor noise and actuator saturation.

Problem 6.1 Find a *stabilizing* controller C_ϱ which minimizes $\| T_1 \|_\infty$ under the *constraint* $\| T_2 \|_\infty \leq \varrho$, where $\varrho > 0$ is given.

Unfortunately, problem 6.1 is a very intricate one, and it cannot be solved in this setting. We now give a solvable problem slightly related to 6.1:

Problem 6.2 Define the dynamic "cross"-compliances $T_{12} := H_{12}$ and $T_{21} := H_{31}$. Note that $T_{12} = T_{21}$ because of the *reciprocity* of non-gyroscopic mechanical systems. Define a diagonally ϱ-weighted compliance matrix $W_\varrho(s)$ according to figure 7. Our optimization problem is[7]:

$$\inf_{T_1 \text{ admissible}} \Big\| \underbrace{\begin{bmatrix} \varrho^2 T_1 & T_{12} \\ T_{12} & \varrho^{-2} T_2 \end{bmatrix}}_{=: W_\varrho(s)} \Big\|_\infty$$

Recall that the $\| \cdot \|_\infty$-norm for matrix-valued transfer functions is defined by its maximum singular value over the $i\omega$ frequency axis.

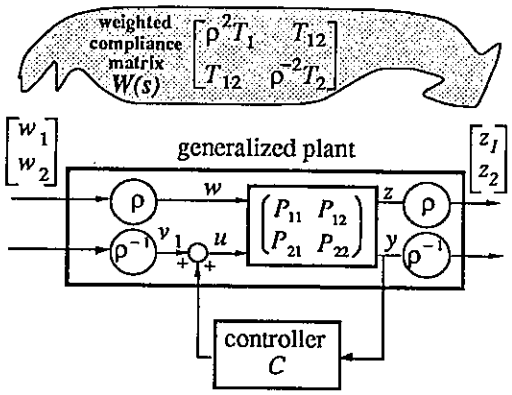

Figure 7: Seeking compromises by weighting

A careful analysis [3] of problem 6.2 shows that the infimum over all *admissible* T_1's is not achieved[8] but it is approached by a sequence of admissible T_1's. In order to compute the limit $\check{T}_1$ of this sequence which is not admissible in the sense of statement 3.4 we will temporarily relax the interpolation conditions. For the moment let us only insist on the first four conditions on $a_0 \ldots a_{-3}$. Then the corresponding "model matching" problem is easily shown [3] to be:

$$\check{\alpha}(\varrho) := \inf_{Q \in \mathcal{H}^\infty_{1\times 1}} \Big\| \underbrace{T_a - T_b Q T_c}_{= W_\varrho(s)} \Big\|_\infty$$

$T_a \in \mathcal{H}^\infty_{2\times 2}$, $T_b \in \mathcal{H}^\infty_{2\times 1}$ and $T_c \in \mathcal{H}^\infty_{1\times 2}$ are as follows:

$$T_a(s) := \begin{bmatrix} \dfrac{\varrho^2 (s^2+2s+2)}{(s^2+s+1)^2} & \dfrac{1}{(s^2+s+1)^2} \\ \dfrac{1}{(s^2+s+1)^2} & \dfrac{\varrho^{-2}(s^2+1)}{(s^2+s+1)^2} \end{bmatrix}$$

[7] Recall that T_1 uniquely determines T_2 and T_{12}.

[8] The reason for this is that we did not incorporate H_{23} in the optimization problem. Note that the order of the polynomial $p_{23}(s)$ in equation (6) is the highest and comes to 8.

$$T_c(s) := T_b^T(s) := \begin{bmatrix} \frac{\varrho}{(s+1)^2} & \frac{\varrho^{-1}(s^2+1)}{(s+1)^2} \end{bmatrix}$$

We solved this model matching problem by using the standard technique [2] (reduce it to the "4-block" problem which can be iteratively solved).

Example 6.3 Choose $\varrho = 0.95$. We obtained the following numerical solution:

$$\| \check{W}_{\varrho=0.95}(s) \|_\infty = \check{\alpha}(0.95) \approx 1.7028$$

$$\| \check{T}_1 \|_\infty \approx 1.562, \quad \| \check{T}_2 \|_\infty \approx 1.537$$

The corresponding controller $\check{C}_{\varrho=0.95}$ is:

$$\approx \frac{-1.5368s^3 + 0.6490s^2 - 2.5368s - 1.1543}{-1.5368s + 0.6490}$$

Of course, $\check{C}$ has to be "replaced" by a *proper* stabilizing controller. This can be done either prior to this stage (e.g. by the method of section 5) or afterwards (e.g. by "cutting off" Q, see [3]). The limitation of the controller bandwidth further reduces the achievable performance, see section 5.

Figure 8 shows the set of trade-off solutions as the weighting parameter ϱ varies. Choosing ϱ large implies a low worst-case compliance of mass m_1 at the expense of a large worst-case compliance of mass m_2. Choosing ϱ small reverses the situation. Statement 4.1 is thus fully confirmed.

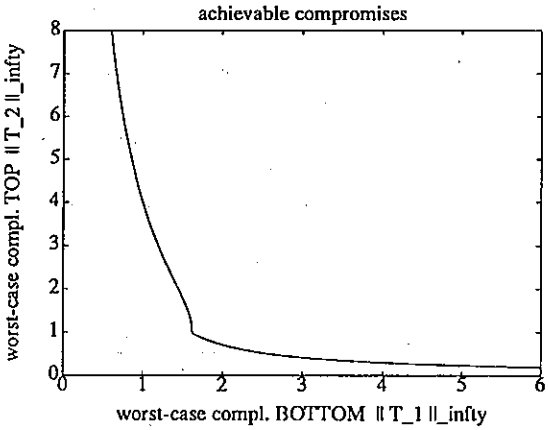

Figure 8: $\varrho \mapsto (\| \check{T}_1 \|_\infty, \| \check{T}_2 \|_\infty)$: Parametric plot for ϱ sweeping from $0.35 \ldots 2$.

7 Conclusions and Outlook

This paper gives some insight into how modern $\mathcal{H}^\infty$ control theory can be used to treat *wide-band stiffness requirements* in AMB applications.

We are convinced that $\mathcal{H}^\infty$ approaches are a *powerful* and *extremely versatile* tool to determine the achievable performance in AMB feedback systems, and to design the corresponding controllers. Of course, one has to learn how to use this new tool and how to choose *"appropriate"* $\mathcal{H}^\infty$ design criteria. The meaning of "appropriate" inherently depends on the practical application.

Some future problems we want to tackle are robustness aspects in AMB control and design of positive real controllers using $\mathcal{H}^\infty$ optimality criteria. It should be intuitively clear that "highly stiff" AMB controllers have only poor "robustness properties". Recall that we identified the "stiffest" controller C_0 with a *negative* mass and a *negative* spring. Positive real controllers are exactly the opposite: they behave as an interconnection of *positive* dampers, masses and springs. We expect this conservatism to improve the "robustness properties" at the expense of "lower performance".

References

[1] J. A. Ball, J. W. Helton, *"Interpolation problems of Pick-Nevanlinna and Loewner types for meromorphic matrix functions: Parametrization of the set of all solutions"*, Integral Equations and Operator Theory 1986, Vol. 9, p. 155–203.

[2] B. A. Francis, *"A Course in $\mathcal{H}^\infty$ Control Theory"*, Lecture Notes in Control and Information Sciences, Springer 1987.

[3] R. Herzog, *"Ein Beitrag zur Regelung elastischer Strukturen mittels positiv reeller Funktionen und $\mathcal{H}^\infty$-Optimierung"*, thesis ETH Zurich, to appear in 1990.

[4] S. D. O'Young, I. Postlethwaite, D. W. Gu, *"A Treatment of $j\omega$- Axis Model-Matching Transformation Zeros in the Optimal $\mathcal{H}^2$ and $\mathcal{H}^\infty$ Control Designs"*, IEEE Trans. Contr., May 1989, vol. 34, no. 5., p. 551.

[5] R. Siegwart, *"Aktive magnetische Lagerung einer Hochleistungs-Fräs(„spindel mit digitaler Regelung"*, thesis ETH Zurich, 1989, No. 8962.

2nd International Symposium on Magnetic Bearing
July 12-14, 1990, Tokyo, Japan

H^∞ Robust Control Design for a Magnetic Suspension System

Masayuki Fujita, Fumio Matsumura, and Masanao Shimizu

Department of Electrical and Computer Engineering, Kanazawa University,
Kodatsuno 2-40-20, Kanazawa 920, Japan

Abstract: This paper presents an H^∞ robust control design for a magnetic suspension system with a flexible beam. The experimental apparatus utilized in this study is a simplified model of a magnetic bearing with a flexible rotor. Firstly, we describe the apparatus and formulate the mathematical model. Secondly, we set up an H^∞ control problem as the mixed sensitivity problem where the augmented plant is constructed with frequency weighting functions. The iterative computing environment MATLAB is then employed to calculate the controller. Thirdly, the controller is implemented using a digital signal processor NEC μPD77230 with 12-bit A/D and D/A converters. Finally, some experiments are carried out in order to evaluate the robustness of the H^∞ design. These experimental results show that the magnetic suspension system is robustly stable against various parameter changes and uncertainties.

1. Introduction

Magnetic bearings are bearings where the suspension forces are generated magnetically without any contact [1]. The structure of a magnetic bearing is shown schematically in Fig. 1. Several pairs of electromagnets are arranged radially around a rotor. By utilizing the magnetical forces of the electromagnets, we can support the rotor without any contact. It should be noted that these forces have to be controlled according to the motion of the rotor, since it is unstable in nature. Modeling and control of a magnetic bearing with its rigid body motion have been reported elsewhere (see, e.g., [2] - [8]). In case of high speed rotation, however, the rotor should be treated as a flexible one due to the effect of the deflection of the shaft. Now the control of magnetic bearings with a flexible rotor becomes more and more an important issue. In this paper, as a simplified model of an elastic rotor in a magnetic bearing, a magnetic suspension system with a flexible beam is fully utilized [9]. Further, in order to achieve robust stabilization, we try to apply the H^∞ control theory.

Recently the state-space formulae for the H^∞ control has been found (see [10],[11], and the references therein). The formulae involve the stabilizing solutions to two indefinite algebraic Riccati equations, which have the same form as those arising in the linear quadratic differential games [11],[12]. A direct consequence of the above results is that the associated complexity of computation is fairly reduced. Further, there has been a substantial development in the computer aided control systems design packages, such as Robust-Control Toolbox with MATLAB [13]. Accordingly, we could readily practice this powerful control methodology. Note that, despite voluminous publications on its theory, there have been few experimental evaluations for the performance of the H^∞ controller. Hence an application oriented study of the H^∞ control is also an challenging issue.

This paper presents an H^∞ robust control design for a magnetic suspension system with a flexible beam. In Section 2, we describe the experimental apparatus and formulate the mathematical model. In the apparatus, we intend to emphasize the first vibrational mode of the flexible beam. Section 3 is devoted to the control problem setup and the design of a controller. We set up an H^∞ control problem as the mixed sensitivity problem where the augmented plant is constructed with frequency weighting functions. The iterative computing environment MATLAB is then employed to calculate the controller. In Section 4, the controller is implemented using a digital signal processor NEC μPD77230 with 12-bit A/D and D/A converters. Several experiments are carried out in order to evaluate the robustness of the H^∞ design. These experimental results show that the magnetic suspension system is robustly stable against various parameter changes and uncertainties.

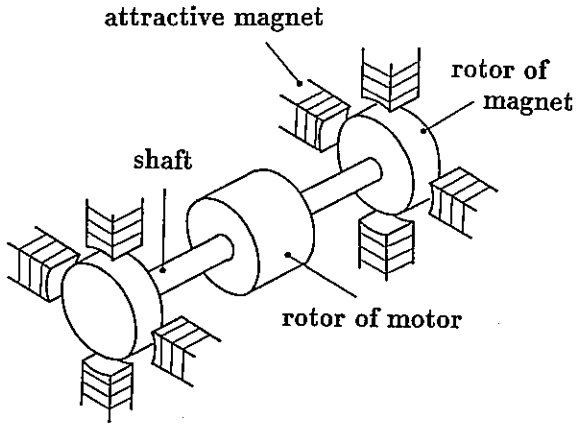

Fig. 1. Schematic diagram of magnetic bearing.

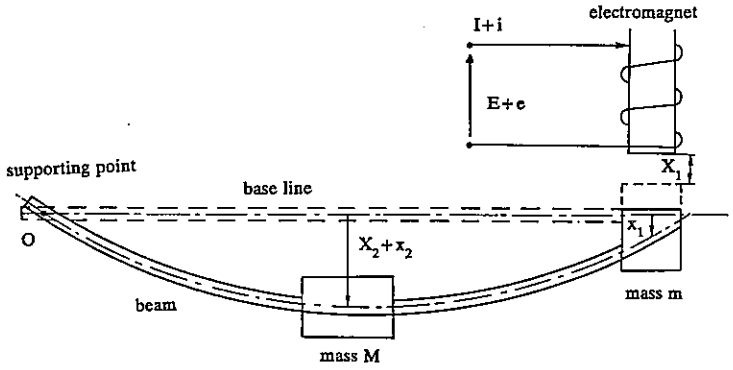

Fig. 2. Magnetic suspension system.

Table 1. Parameters.

parameter	symbols	values	units
beam length	2l	3.8	m
first order resonance frequency	f_n	4.5	Hz
deflection of the beam	X_2	12.3×10^{-3}	m
mass m	m	5.8	kg
mass M	M	10.36	kg
stationary gap of the electromagnet	X_1	5.0×10^{-3}	m
steady state current of the electromagnet	I	0.885	A
resistance of the electromagnet	R	57	Ω
inductance of the electromagnet	L	3.16	H

2. System Description and Modeling

2.1. Description of Apparatus

As a simplified model of a magnetic bearing for a flexible rotor, we consider a magnetic suspension system with a flexible beam shown in Fig. 2 [9]. The experimental configuration which is fully utilized throughout the paper, consists of a flexible aluminum beam with a electromagnet and a gap sensor. The beam is supported by a hinge at the left side and it will be suspended stably by the force of the electromagnet at the right side. The beam is reasonably stiff in torsion bending and is free to rotate at the supporting point O. Thus it can be assumed that the motion of the beam is confined to the vertical plane. As in Fig. 2, a mass m is attached at the right side of the beam and a mass M is attached at the center. It is noted that m is corresponding to the rotor of the electromagnet, M is corresponding to the rotor of the motor, and the beam is corresponding to the shaft (see Fig. 1). In this configuration, we intend to emphasize the first vibrational mode of the flexible beam. An U-shaped electromagnet is located as an actuator at the right side. As a gap sensor, a standard induction probe of eddy-current type is placed at the same position in the right side of the beam. Parameters of this experimental apparatus are given in Table 1. The beam weight, including m and M, is supported by having a steady-state current I (or, a steady-state voltage E). Stabilization of the system can be accomplished by controlling the corresponding voltage perturbation e.

2.2. Model Formulation

Several approaches can be considered to obtain its mathematical model; e.g., a purely analytic approach which results in complex distributed-parameter systems represented by partial differential equations, or a finite-element approach with the assistance of computer programs which usually generates high-order finite-dimensional systems represented by ordinally differential equations. Among them, the approach taken here may be the simplest one. In the following, the beam is described by a simple multi-mass linear system. Due to the structure of the apparatus, we will include up to the first vibrational mode of the beam, as well as the rigid body motion, in the model. There is no need to say that, if necessary, we can build a more precise mathematical model using the approach mentioned above.

We assume that a half of the mass of the beam can be included into M, and a quarter of it can be included into m. Under these assumptions, we will consider the dynamical equations for m and M, respectively. This naturally leads to a simple lumped-parameter model of the beam, in which the effect of the first vibrational mode is taken into account. Let X_1 be the steady-state gap between the electromagnet and the beam at the position of m, X_2 be the steady-state deflection of the beam from the base line at the position of M, I be the coil current in the steady-state, and E be the corresponding voltage. Further, let the small perturbations of the above quantities be x_1, x_2, i, and e, respectively (see Fig. 2). Then the following equations of motions can be obtained.

$$m\frac{d^2x_1}{dt^2} = mg-k\left(\frac{I+i}{X_1+x_1}\right)^2+\alpha[2(X_2+x_2)-x_1] +\beta\frac{d}{dt}[2(X_2+x_2)-x_1] \quad (1)$$

$$M\frac{d^2x_2}{dt^2} = Mg-2\alpha[2(X_2+x_2)-x_1] -2\beta\frac{d}{dt}[2(X_2+x_2)-x_1]. \quad (2)$$

The second term in the right-hand side of (1) represents the attractive force of the electromagnet and k, which will be determined by experimental data, denotes the corresponding coefficient. Both the third and the fourth terms in the right-hand side of (1) represent the restoring force generated by the deflection of the beam. The coefficients α and β will be also determined by experimentally obtained data. While, both the second and the third terms in the right-hand side of (2) represent the reaction of the above stated force.

Although these equations are nonliner, as is well known, we can easily obtain the linearized equations for the small perturbations around the steady-state points. In the steady-state, we have

$$0 = mg-k\left(\frac{I}{X_1}\right)^2+2\alpha X_2, \quad 0 = Mg-4\alpha X_2. \quad (3)$$

From this, the linearized equations are

$$m\frac{d^2x_1}{dt^2} = \left(\frac{M+2m}{X_1}g-\alpha\right)x_1+2\alpha x_2 -\frac{(M+2m)g}{I}i-\beta\frac{dx_1}{dt}+2\beta\frac{dx_2}{dt} \quad (4)$$

$$M\frac{d^2x_2}{dt^2} = 2\alpha x_1-4\alpha x_2+2\beta\frac{dx_1}{dt}-4\beta\frac{dx_2}{dt}. \quad (5)$$

For the relationship between the applied voltage e and the coil current i, the equation can be

$$Ri+L\frac{di}{dt} = e \quad (6)$$

where R and L denote the resistance and the inductance of the electromagnet, respectively. The values of R and L have been determined by experiments.

The sensor provides us with the information for the gap x_1. Hence the measurement equation is

$$y_g = x_1. \quad (7)$$

Now, from experimentally obtained data, we can determine the following values; k = 0.0034 $\mathrm{Nm^2/A^2}$, α = 2064 N/m, and β = 0.327 Ns/m. Thus, summing up the results, the state equations for the magnetic suspension system are

$$\dot{x}_g = A_gx_g+B_gu_g, \quad y_g = C_gx_g \quad (8)$$

where $x_g := [x_1\ x_2\ \dot{x}_1\ \dot{x}_2\ i]^T$, $u_g := e$ and

$$A_g=\begin{bmatrix} 0.0 & 0.0 & 1.0 & 0.0 & 0.0 \\ 0.0 & 0.0 & 0.0 & 1.0 & 0.0 \\ 7070 & 712 & -0.327 & 0.654 & -41.9 \\ 399 & -797 & 0.654 & -1.31 & 0.0 \\ 0.0 & 0.0 & 0.0 & 0.0 & -18.0 \end{bmatrix} \quad (9a)$$

$$B_g=\begin{bmatrix} 0.0 \\ 0.0 \\ 0.0 \\ 0.0 \\ 0.317 \end{bmatrix} \quad C_g=\begin{bmatrix} 1 & 0 & 0 & 0 & 0 \end{bmatrix} \quad (9b)$$

with (A_g, B_g) controllable, and (A_g, C_g) observable. The transfer function of this system is

$$G(s) = \frac{-13.3}{(s+18.0)(s+84.4)(s-84.1)} \times\frac{(s+0.654-j28.2)(s+0.654+j28.2)}{(s+0.697-j28.8)(s+0.697+j28.8)}. \quad (10)$$

For the magnetic suspension system described above, our principal objective is stabilization. Further, the system should be stabilized robustly against the followings; i.e., the unmodeled higher order vibrational dynamics of the beam, the neglected higher order terms in the Taylor series expansions in the linearization procedure, the parameter errors in the beam and in the electromagnet such as k, α, β, m, M, R and L, the effect of the eddy-current in the electromagnet, and so on. To this end, we will use the H^∞ control theory in the next section.

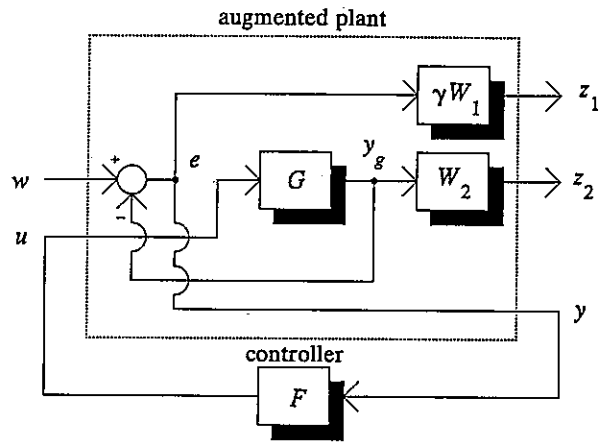

Fig. 3. Plant augmentation.

3. Controller Design

3.1. Mixed Sensitivity Problem

Consider the system shown in Fig. 3. Let us focus our attention on the transfer function from w to e, called the sensitivity function $S(s)$, and the transfer function from w to y_g, called the complementary sensitivity function $T(s)$. The sensitivity function $S(s)$ and the complementary sensitivity function $T(s)$ are defined as

$$S(s) := (I+L(s))^{-1} \tag{11}$$

$$T(s) := L(s)(I+L(s))^{-1} = I-S(s) \tag{12}$$

where $L(s) := G(s)F(s)$ denotes the loop transfer function. It is well known that these functions play an important role in robust feedback control system design. In the following, $\overline{\sigma}(\cdot)$ denotes the greatest singular value of a matrix, and the H^∞-norm is defined as

$$\| \Phi(s) \|_\infty := \sup_\omega \overline{\sigma}(\Phi(j\omega)) \tag{13}$$

for a proper stable transfer function $\Phi(s)$.

Firstly, it is known that the requirement for disturbance attenuation in the feedback system can be specified with the sensitivity function $S(s)$ as

$$\overline{\sigma}(S(j\omega)) < | \gamma^{-1} W_1^{-1}(j\omega) | \quad \text{for all } \omega. \tag{14}$$

In (14), $W_1(s)$ is a desired frequency weighting factor whose gain is relatively large in a low frequency range and $\gamma > 0$ is an adjusting scalar parameter. It is easy to see that the disturbance attenuation requirement (14) can be rewritten as

$$\| \gamma W_1(s) S(s) \|_\infty < 1. \tag{15}$$

Secondly, let us consider robust stability of the feedback system in terms of the complementary sensitivity function $T(s)$. Suppose that the plant $G(s)$ is perturbed as

$$G'(s) = (I+\Delta(s))G(s) \tag{16}$$

where $\Delta(s)$ denotes multiplicative plant perturbations. We will assume that $G'(s)$ has the same number of unstable modes as $G(s)$, and that the nominal feedback system is stable. Then, if

$$\overline{\sigma}(T(j\omega)) < | W_2^{-1}(j\omega) | \quad \text{for all } \omega \tag{17}$$

the system remains stable for all $\Delta(s)$ satisfying

$$\overline{\sigma}(\Delta(j\omega)) \le | W_2(j\omega) | \quad \text{for all } \omega. \tag{18}$$

Hence, as the robust stability condition, we have

$$\| W_2(s) T(s) \|_\infty < 1. \tag{19}$$

The frequency weighting factor $W_2(s)$ is usually small at low frequencies and increases its magnitude at higher frequencies.

The design specifications as in (15) and (19) can be combined into a single H^∞-norm specification

$$\left\| \begin{matrix} \gamma W_1(s) S(s) \\ W_2(s) T(s) \end{matrix} \right\|_\infty < 1 \tag{20}$$

where we have used the following matrix inequality

$$\frac{1}{\sqrt{2}} \overline{\sigma}\left(\begin{bmatrix} A \\ B \end{bmatrix} \right) \le \max \{ \overline{\sigma}(A), \overline{\sigma}(B) \} \le \overline{\sigma}\left(\begin{bmatrix} A \\ B \end{bmatrix} \right). \tag{21}$$

This ensures that the requirements (15) and (19) are reasonably approximated (within 3 dB). Now the mixed sensitivity problem is to find a controller $F(s)$ such that the system is internally stable and the specification (20) is satisfied.

3.2. H^∞ Design

In this study, the weighting functions $W_1(s)$ and $W_2(s)$ are chosen as

$$W_1(s) = \frac{1.3298}{1+s/(2\pi \cdot 0.016)} \tag{22}$$

$$W_2(s) = 10^{-4} \left(1+\frac{s}{2\pi \cdot 0.002} \right) \times \left(1+\frac{s}{2\pi \cdot 160} \right) \left(1+\frac{s}{2\pi \cdot 200} \right). \tag{23}$$

While the value of γ will be increased according to the design iterations until the specification (20) can be no longer satisfied (γ-iteration).

Table 2. State-space realization of augmented plant.

$$A=\begin{bmatrix} 0.00 & 0.00 & 1.00 & 0.00 & 0.00 & 0.00 \\ 0.00 & 0.00 & 0.00 & 1.00 & 0.00 & 0.00 \\ 7.07\times10^{3} & 7.12\times10^{2} & -3.27\times10^{-1} & 6.54\times10^{-1} & -4.19\times10 & 0.00 \\ 3.99\times10^{2} & -7.97\times10^{2} & 6.54\times10^{-1} & -1.31 & 0.00 & 0.00 \\ 0.00 & 0.00 & 0.00 & 0.00 & -1.80\times10 & 0.00 \\ -1.00 & 0.00 & 0.00 & 0.00 & 0.00 & -1.01\times10^{-1} \end{bmatrix}, \quad [B_1 \;\; B_2]=\begin{bmatrix} 0.00 & 0.00 \\ 0.00 & 0.00 \\ 0.00 & 0.00 \\ 0.00 & 0.00 \\ 0.00 & 3.17\times10^{-1} \\ 1.00 & 0.00 \end{bmatrix}$$

$$\begin{bmatrix} C_1 \\ C_2 \end{bmatrix}=\begin{bmatrix} 0.00 & 0.00 & 0.00 & 0.00 & 0.00 & 2.30 \\ 1.01\times10^{-1} & 1.01\times10^{-2} & 7.99\times10^{-3} & 1.38\times10^{-5} & -5.92\times10^{-4} & 0.00 \\ -1.00 & 0.00 & 0.00 & 0.00 & 0.00 & 0.00 \end{bmatrix}, \quad \begin{bmatrix} D_{11} & D_{12} \\ D_{21} & D_{21} \end{bmatrix}=\begin{bmatrix} 0.00 & 0.00 \\ 0.00 & -8.35\times10^{-8} \\ 1.00 & 0.00 \end{bmatrix}$$

Table 3. State-space realization of controller.

$$A_f=\begin{bmatrix} -2.98\times10^{3} & -1.40 & -3.49 & -1.29\times10^{-3} & 8.27\times10^{-2} & 3.06\times10^{4} \\ -1.69\times10^{2} & -7.97\times10^{-2} & -2.55\times10^{-1} & 1.00 & 4.69\times10^{-3} & 1.73\times10^{3} \\ -2.44\times10^{5} & 5.94\times10^{2} & -3.78\times10^{2} & 5.45\times10^{-1} & -3.49\times10 & 2.57\times10^{6} \\ -1.38\times10^{4} & -8.04\times10^{2} & -2.08\times10 & -1.31 & 3.95\times10^{-1} & 1.46\times10^{5} \\ 3.02\times10^{7} & 5.47\times10^{4} & 8.25\times10^{4} & 6.73\times10 & -3.22\times10^{3} & -3.56\times10^{8} \\ 0.00 & 0.00 & 0.00 & 0.00 & 0.00 & -1.01\times10^{-1} \end{bmatrix}$$

$$B_f=\begin{bmatrix} -4.20\times10^{2} & -2.39\times10 & -3.54\times10^{4} & -2.01\times10^{3} & 0.00 & 1.00 \end{bmatrix}^T$$

$$C_f=\begin{bmatrix} 9.54\times10^{7} & 1.73\times10^{5} & 2.61\times10^{5} & 2.12\times10^{2} & -1.01\times10^{4} & -1.12\times10^{9} \end{bmatrix}$$

Recall that the open-loop plant $G(s)$ has three more poles than zeros. Hence we need at least -60 dB/decade roll-off for the complementary sensitivity, which is the same as the open-loop plant. As a result, $W_2(s)$ becomes an improper function as in (23). But this ensures that the direct feedthrough matrix D_{12} in (24) has full rank (see Table 2) and the resulting controller is proper. The frequency weighting $W_2(s)$ has been determined so that the closed-loop system possesses sufficient robust stability against uncertainties such as the unmodeled higher order vibrational dynamics. Subject to these constraints, we try to minimize the weighted sensitivity $W_1(s)S(s)$ as much as possible using γ-iteration.

With the weighting functions $\gamma W_1(s)$ and $W_2(s)$, let us form an augmented plant as shown in Fig. 3. A few hand calculations enable us to obtain the state-space realization of the augmented plant as follows (see Table 2)

$$\dot{x} = Ax+B_1w+B_2u \tag{24a}$$

$$z = C_1x+D_{11}w+D_{12}u \tag{24b}$$

$$y = C_2x+D_{21}w+D_{22}u \tag{24c}$$

where we have chosen $\gamma = 17.2$. It is noted that the maximal value of γ for which (20) holds, is 21.0. These H^∞ designs have been carried out using the iterative computing environment MATLAB [13].

The obtained H^∞ "central" controller [10],[11] is

$$F(s) = C_f(sI-A_f)^{-1}B_f$$

$$= \frac{-5.05\times10^{10}(s+1.972)(s+18.0)(s+84.4)}{(s+0.101)(s+1176-j401)(s+1176+j401)(s+4232)} \times\frac{(s+0.697-j28.8)(s+0.697+j28.8)}{(s+0.654-j28.2)(s+0.654+j28.2)} \tag{25}$$

(see Table 3). This controller has six state variables, which is the same as the augmented plant, is stable and is strictly proper.

The Bode plots of the sensitivity S with $\gamma^{-1}W_1^{-1}$, and the complementary sensitivity T with W_2^{-1} are shown in Fig. 4 and Fig. 5, respectively. As in Fig. 4 and 5, the sensitivity S approaches to $\gamma^{-1}W_1^{-1}$ at low frequencies, and the complementary sensitivity T approaches to W_2^{-1} at high frequencies. These are essentially based on the remarkable all-pass property in the H^∞ theory. Thus the H^∞ theory provides a direct method for achieving a loop-shaping in the frequency domain. In Fig. 6, the Bode plots of the loop transfer function are shown. At low frequencies, the loop transfer function has a large gain. An increasing phase-lead can be seen in the middle frequency range, which shows the gain margin of 22.5 dB and the phase margin of 26 degrees. The crossover frequency is about 9 Hz and the desirable roll-off property can be seen at high frequencies.

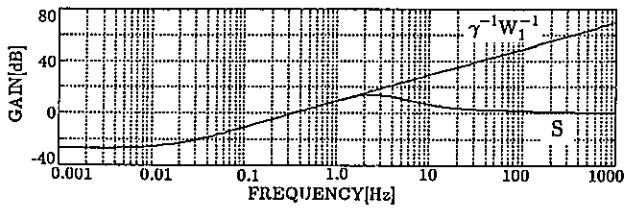

Fig. 4. Sensitivity function.

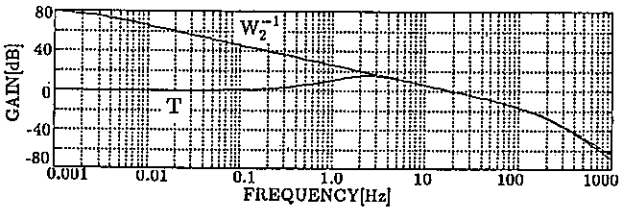

Fig. 5. Complementary sensitivity function.

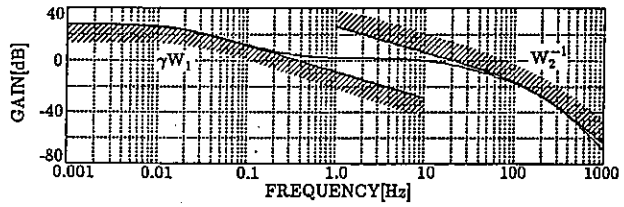

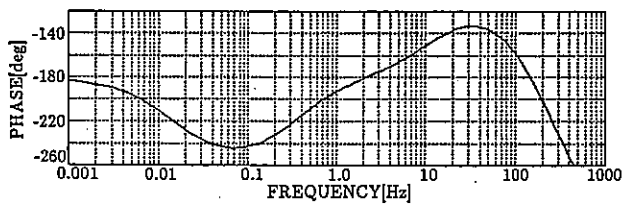

Fig. 6. Loop transfer function.

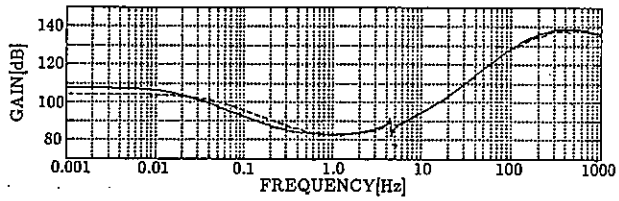

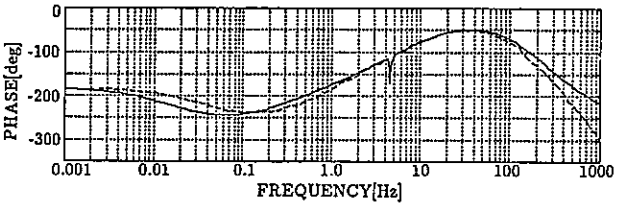

Fig. 7. Controller.

4. Implementation and Experimental Results

4.1. Implementation of Digital Controller

The obtained continuous-time controller (25) is discretized via the popular Tustin transform

$$s = \frac{2}{T}\frac{z-1}{z+1} \tag{26}$$

at the sampling rate of 40 μs. The Bode plots of the controller are given in Fig. 7. The solid line in the figure shows the ideal continuous-time controller and the broken line shows the discretized controller with the transformation (26).

The structure of the digital signal processor (DSP)-based controller is shown in Fig. 8. Real-time control is accomplished via the processor NEC μPD77230 on a special board, which can execute one instruction in 150 ns with 32-bit floating point arithmetic. The control algorithm is written in the assembly language for the DSP and the software development is assisted by the host personal computer NEC PC9801. The data acquisition boards consist of a 12-bit A/D converter module DATEL ADC-B500 with the maximum conversion speed of 0.8 μs and a 12-bit D/A converter DATEL DAC-HK12 with the maximum conversion speed of 3 μs.

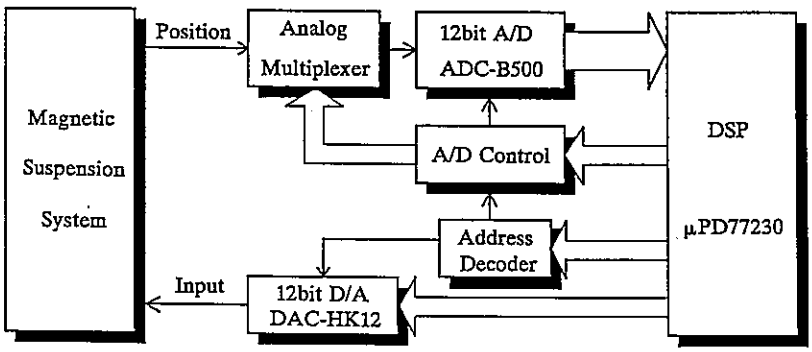

Fig. 8. DSP-based controller.

4.2. Experimental Results

We first evaluate the nominal stability of the designed control system with time-responses for a step-type disturbance. The disturbance is added as an applied voltage in the electromagnet, which in fact amounts to about 20 % of the steady-state force. Fig. 9 shows the displacements of x_1 and x_2. From this result, we can see that the nominal stabilization of the system is achieved. In Fig. 10, the stiffness at the position of the electromagnet is also shown. From these data, we can see that high stiffness has been achieved at low frequencies. Further, it should be noted that the stiffness is not necessarily deteriorated near the resonance frequencies. This implies that the system is well stabilized.

Since our concerns are also in robust stability against various model uncertainties, we further continue the same experiments with the plant parameters changed. The parameters have changed in the following ways;

(i) m = 6.95 kg, which amounts to a 20 % increase for the nominal value of 5.8 kg,

(ii) M = 12.31 kg, which amounts to a 20 % increase for the nominal value of 10.36 kg,

(iii) R = 61.7 Ω, which amounts to a 10 % increase for the nominal value of 57.0 Ω.

The results are shown in Fig. 11 - 13. In any case it can be seen that the beam is still suspended stably by the controlled magnetical forces. Therefore, these experimental results confirm us that the designed magnetic suspension system is robustly stable against various parameter changes.

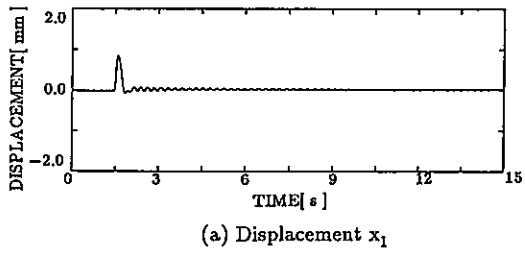

(a) Displacement x_1

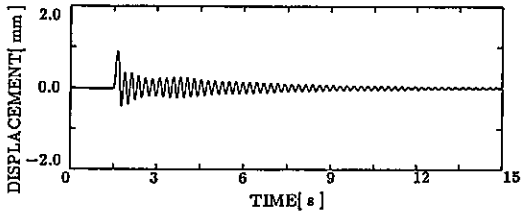

(b) Displacement x_2

Fig. 9. Responses for step-type disturbance (nominal).

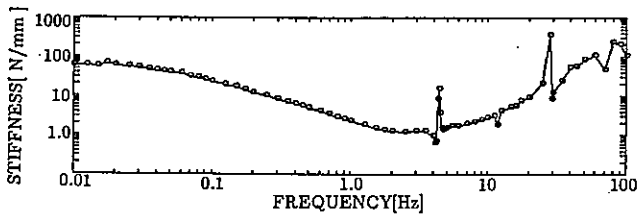

Fig. 10. Stiffness.

5. Conclusions

In this paper, an H^∞ robust control design for a magnetic suspension system with a flexible beam has been presented. Several experimental results showed that the designed magnetic suspension system is robustly stable against various plant perturbations. For the related experimental studies of the H^∞ control, see [14],[15].

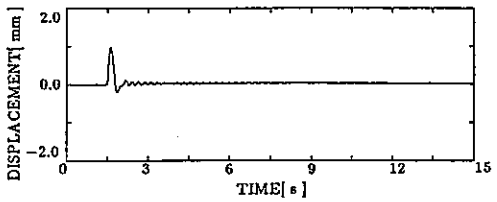

(a) Displacement x_1

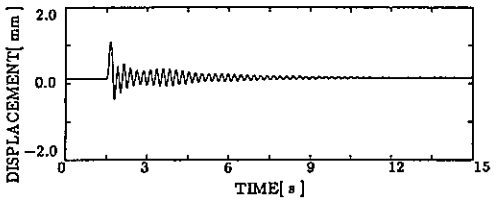

(b) Displacement x_2

Fig. 11. Responses for step-type disturbance (m = 6.95 kg).

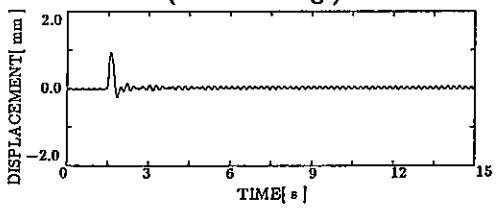

(a) Displacement x_1

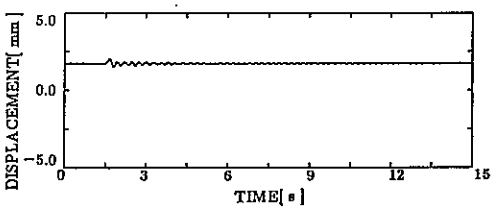

(b) Displacement x_2

Fig. 12. Responses for step-type disturbance (M = 12.31 kg).

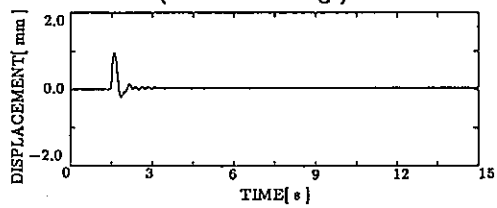

(a) Displacement x_1

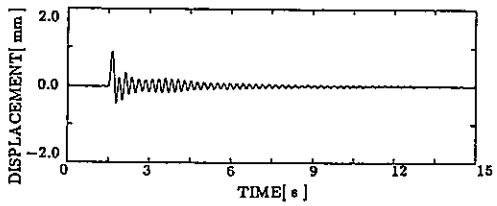

(b) Displacement x_2

Fig. 13. Responses for step-type disturbance (R = 61.7 Ω).

References

[1] G. Schweitzer, Ed., *Magnetic Bearings: Proc. First Int. Symp. Magnetic Bearings.* Berlin: Springer-Verlag, 1989.

[2] F. Matsumura, H. Kobayashi, and Y. Akiyama, "Fundamental equation of horizontal shaft magnetic bearing and its control system design (in Japanese)," *Trans. IEE of Japan*, vol. **101-C**, pp. 137-144, 1981.

[3] F. Matsumura and T. Yoshimoto, "System modeling and control design of a horizontal-shaft magnetic-bearing system," *IEEE Trans. Magnetics*, vol. **MAG-22**, pp. 196-203, 1986.

[4] F. Matsumura, M. Fujita, A. Higashide, and C. Oida, "Stabilizing control of magnetic bearing combining radial control and thrust control using the In-the-Region pole allocation method (in Japanese)," *Trans. IEE of Japan*, vol. **107-D**, pp. 35-41, 1987.

[5] F. Matsumura, M. Fujita, and C. Oida, "Theory and experiment of magnetic bearing combining radial control and thrust control," *IEEE Trans. Magnetics*, vol. **MAG-23**, pp. 2581-2583, 1987.

[6] F. Matsumura, M. Fujita, C. Oida, and A. Higashide, "A damping control for the vibration in a magnetic bearing using the selective turn-over method (in Japanese)," *Trans. IEE of Japan*, vol. **108-C**, pp. 47-54, 1988.

[7] F. Matsumura, M. Fujita, and K. Okawa, "Modeling and control of magnetic bearing systems achieving a rotation around the axis of inertia," to be presented at the *2nd Int. Symp. Magnetic Bearings*, Tokyo, Japan, July 12-14, 1990.

[8] F. Matsumura, M. Fujita, and H. Takahashi, "An observer-based robust stabilization of 3-axes controlled type magnetic bearings using a digital signal processor," to be presented at the *11th IFAC World Congress*, Tallinn, USSR, Aug. 13-17, 1990.

[9] F. Matsumura, M. Fujita, Y. Ozaki, and M. Shimizu, "Stabilization for flexible beam system controlled by magnetic suspension," in *Proc. 11th Int. Conf. Magnetically Levitated Systems and Linear Drives*, Yokohama, Japan, July 7-11, 1989.

[10] K. Glover and J.C. Doyle, "State-space formulae for all stabilizing controllers that satisfy an H_∞-norm bound and relations to risk sensitivity", *Syst. Contr. Lett.*, vol. **11**, pp. 167-172, 1988.

[11] J.C. Doyle, K. Glover, P.P. Khargonekar, and B.A. Francis, "State-space solutions to standard H_2 and H_∞ control problems," *IEEE Trans. Automat. Contr.*, vol. **AC-34**, pp. 831-847, 1989.

[12] K. Uchida and M. Fujita, H^∞ control theory and game theory (in Japanese)," *J. SICE*, vol. **29**, pp. 136-141, 1990.

[13] R.Y. Chiang and M.G. Safonov, *Robust-Control Toolbox User's Guide.* The Math Works, Inc., 1988.

[14] F. Matsumura, M. Fujita, and M. Shimizu, "Robust stabilization of a magnetic suspension system using H^∞ control theory (in Japanese)," *Trans. IEE of Japan*, 1990, submitted for publication.

[15] M. Fujita and F. Matsumura, "H^∞ control of a magnetic suspension system (in Japanese)," *J. IEE of Japan*, 1990, to be published.

2nd International Symposium on Magnetic Beaing
July 12-14, 1990, Tokyo, Japan

APPLICATION AND TESTING OF MAGNETIC BEARINGS AND DRY GAS SEALING IN AXIAL INLET PROCESS COMPRESSORS

C.W. PEARSON - DELAVAL-STORK, HENGELO, THE NETHERLANDS
H.J. AARNINK - DELAVAL-STORK, HENGELO , THE NETHERLANDS
J. MAGEE - DELAVAL-STORK, HENGELO, THE NETHERLANDS
J.G.H. DERKINK - DELAVAL-STORK, HENGELO, THE NETHERLANDS

ABSTRACT

Modern day large scale gas phase synthesis processes require a centrifugal compressor for recycling process gas around the synthesis loop, which is a very severe duty.

In order to provide for safe, reliable and efficient plant operation, the recycle compressor must be carefully designed and manufactured to provide optimum operation efficiency and minimum maintenance downtime.

Environment, noise and safety of operation are major areas of attention. The development from WET-WET to DRY-DRY technology is seen as a distinct opportunity to develop and improve machinery in these areas.

ROTOR CARTRIDGE DESIGN

The severe application for this specific compressor is the main reason for utilizing magnetic bearings outside of the process gas environment, see figures 1 and 2.

During the design phase, it was decided to carry out a number of critical engineering analyses.

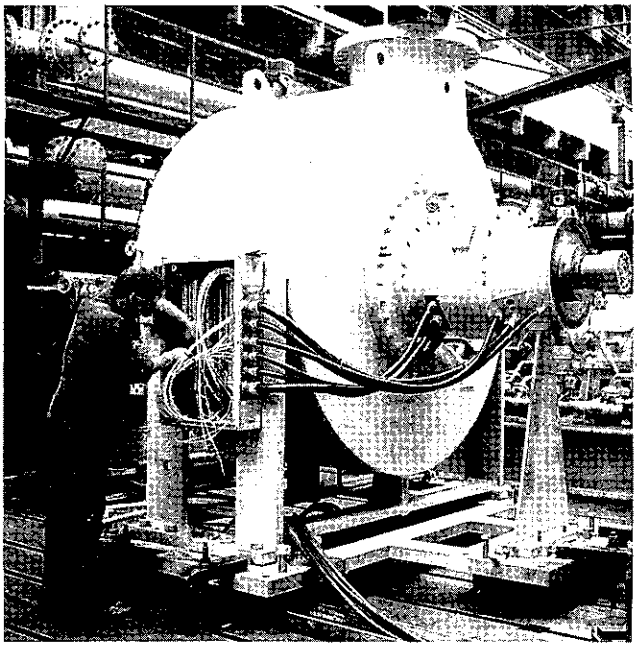

Figure 1 - DRY-DRY PV Compressor

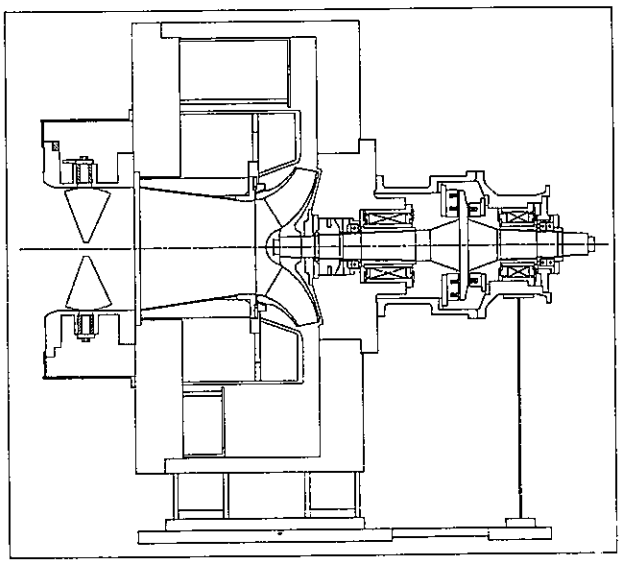

Figure 2 - Compressor Assembly

1 Dynamic Analysis

1a Undamped Critical Speed Map

Figure 3 shows the actual undamped critical speed map. This map is based on identical transfer function for both radial bearings and results in simple hardware and control circuitry.

1b Damped Response Analysis

The response analysis indicates that both the first two response modes are well damped, which is typical for overhung machines of this type with the first mode being a conical one and the second being a bouncing

mode. The results show that integration of sensors of both sides of the journal bearing will make the control less noisy, particularly on the impeller side.

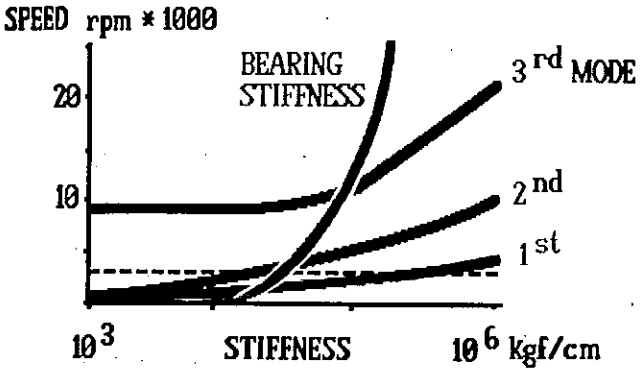

Figure 3 - Undamped Critical Speed Map

1c Stability Analysis

The stability analysis (figure 4) indicates a generous stability margin at the expected aerodynamic excitation, as would be expected of a rigid rotor configuration, even if the actual damping is only 50% of the expected damping value.

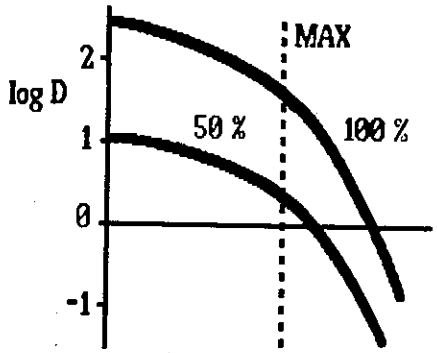

Figure 4 - Stability Analysis

2 Performance Analysis

The characteristic of the impeller for this application is its high specific speed due to high flow and low head requirements. Delaval has a vast experience in designing the mixed flow impellers for this and other applications.

3 Stress Analysis

Specific areas of design require stress analysis. As a result of these analyses, additional features are integrated in the design, see figure 5.

- Shrunk on sleeves, using hydraulic-fit on conical taper, modified to suit this specific application. These allow for operational speeds up to 7000 RPM.
- Integral thrust collar on the shaft.
- The bearing bracket for this DRY-DRY PV compressor is a barrel design.

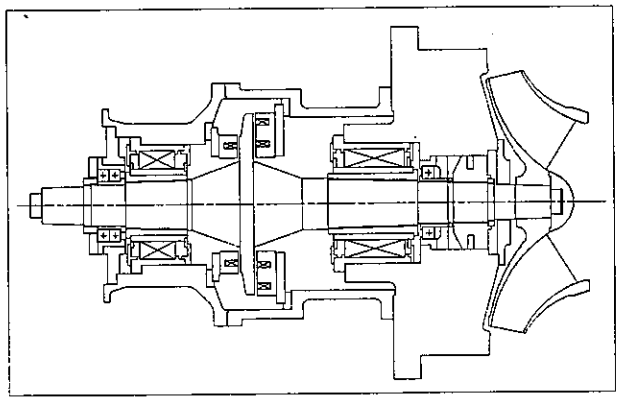

Figure 5 - Rotor Cartridge Assembly

4 Electrical Analysis

Features included in the design are:

- The speed sensor, which is modified from a magnetic type into a conventional proximity type.
- This is the first commercially installed air cooled control cabinet. Its reliability has been enhanced by utilizing fan redundancy, automatic battery check, electrical counter for full speed landings and double power supply units.

5 Auxiliary Bearing Analysis

An extensive analysis of the auxiliary bearings has been undertaken. Specific items of interest covered the potential wind-milling of these bearings, its landing capacity under full load, detection methods and registration methods.

6 Thrust Analysis

Inherent in the overhung design compressor is the high thrust load at standstill as shown in figure 6. This has been overcome by the asymmetrical magnetic thrust bearing design.

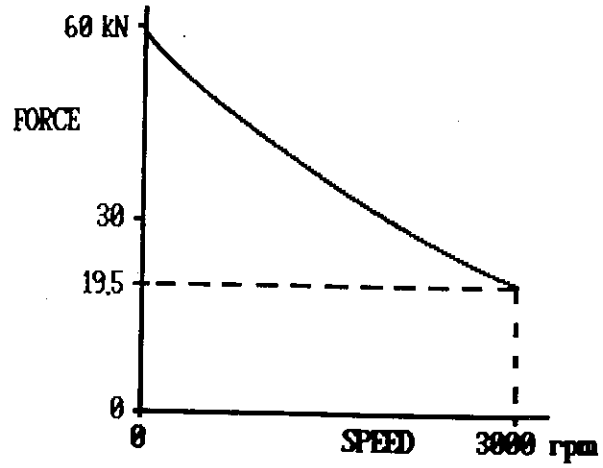

Figure 6 - Actual Force during Start-Up

7 Maintenance Analysis

Maintainability of the machine is also a major area of interest. During the design phase this has led to several improvements in the design, resulting in a backward pull-out rotor cartridge design with a barrel type bearing bracket. This cartridge incorporates all major compressor components, including: impeller, bearings and seals, resulting in a compressor which is easy to maintain, see figure 5.

TEST PROGRAM

A new concept requires exhaustive testing in order to prove that design parameters have been met. This involves more detailed testing of components and of the complete machine than are normally involved in the provision of a conventional design. Some of these tests are quite unique.

1 Dry Gas Seal Testing

Delaval has its own extensive test procedure for dry gas seals.

Each seal is full-load shop-tested by the subvendor. This seal was full-load tested at 3300 rpm, 28 barg and 160 °C. The guaranteed leakage rates are 14 l/min. in the primary seal and less than 2.5 l/min. in the secondary seal. The test values are 8.6 l/min. and less than 2.5 l/min. respectively.

2 Magnetic Bearing Testing

The manufacturer of the magnetic bearings executes specific tests during the manufacturing phase. For this compressor it was decided to carry out additional exhaustive testing in the actual compressor.

3 Rotor Excitation Free-Free Modes

Natural frequencies are calculated at 107, 220, 443 and 813 Hz. The free-free modes of the compressor rotor have been checked by exciting the rotor suspended in slings. This has been done firstly to check the engineering lateral analysis and secondly to have a starting point for the tuning of the bearing system. The measured free-free modes are in good correlation with the results of the engineering analysis.

	TEST (Hz)	CALC. (Hz)
1st mode	106.7	107.1
2nd mode	221.7	219.9
3rd mode (see fig. 7)	426.7	443.2
4th mode	805.0	812.9

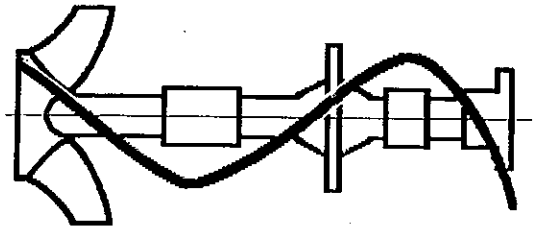

Figure 7 - Third Mode Response

4 Magnetic Bearing Tuning

The concept of the rotor layout, the sizing of the bearing and the selection of the controls has been done in the design phase. After assembly of the compressor, these three elements have to be tuned to each other in order to build a stable control loop, which will perform the normal and transient duties.

First the rotor is balanced at low speed and then the tuning starts with the information from the free-free mode excitation. Each bearing has a displacement sensor on each side. The final tuning includes both sensors on the inboard bearing and one sensor on the outboard bearing. The total tuning was finished within two weeks.

5 Static Load Testing Radial Bearing

Each radial bearing capability has been checked against measured bearing reaction force, see figure 8. The curve shows the S-shape curve for flux and force as a function of current to the bearing. The current is limited to avoid saturation of the magnets. This limit is indicated. The measured current at the reference point is in close agreement with the design value. The difference in current, as shown, is available to counterbalance the dynamic forces when the compressor is in operation.

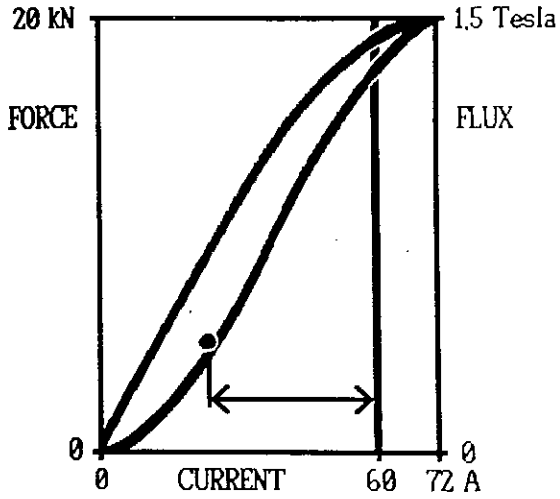

Figure 8 - Static Load Test Radial Bearing

6 Static Load Testing Axial Bearing

The axial bearing consists of three coils, which develop identical force. Two coils: Z1A & Z1B are located at NDE side and one coil: Z2 is located at DE side. The basic curve of each coil is very similar to that of the radial bearing. However, it should be pointed out that both sides of the axial bearing are pulling. An axial load on the rotor will cause a change in the current on both sides of the axial bearing such that the difference in the pulling forces of the magnets will counterbalance the axial load of the rotor, see figure 9. The axial bearing is designed for 80 kN. The difference in current between normal duty and the design point is available for dynamic forces which can occur at surge and other transient operating conditions.

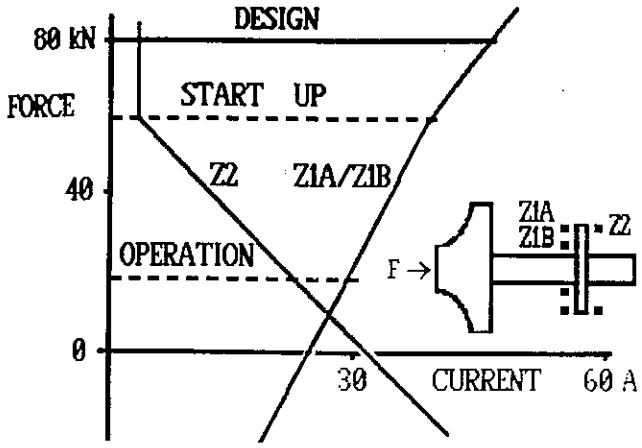

Figure 9 - Static Load Test Actual Bearing

7 Dynamic Testing Axial Bearing Capability

All pressurized overhung compressors have a high axial force at standstill. The static force at standstill for this compressor is 60 kN, which reduces to 19.5 kN at full speed, see figure 6. The bearing can handle this rapid change in force without any overshoot in the control system.

8 Simulation of Surge Condition

Surge in a centrifugal compressor creates a major upset in the axial loading of the rotor. To simulate the surge condition the compressor has been rebuilt. The impeller was replaced by a dummy with identical rotor dynamic characteristics as the original impeller. In front of the impeller a chamber has been created, which can be loaded by external pressure. By fluctuating this external pressure a dynamic load on the rotor is created, which has the same magnitude as the static load.

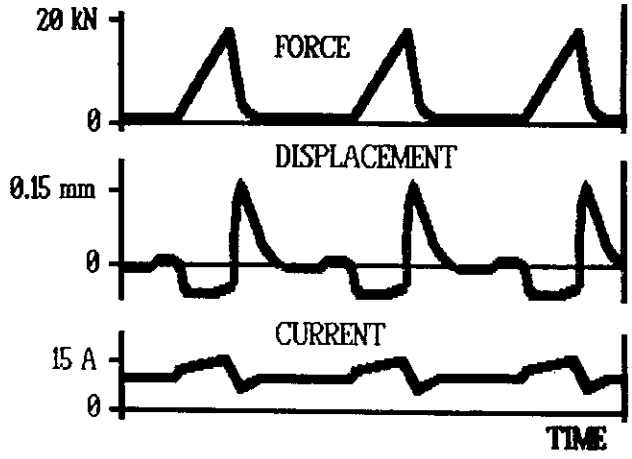

Figure 10 - Surge Simulation Test

Figure 10 shows force, displacement and current as a function of time. This unique test proves that the bearing system can handle these fluctuating loads without overshoot and well within the capability of the bearing.

9 Unbalance Response Testing

An unbalance weight corresponding to five times the API 617 value was added to the impeller. The frequency scan recorded at full running speed, shows neither subsynchronous vibrations, nor harmonics. The system has good control over the unbalanced rotor, however, the displacements are larger than calculated, indicating that stiffness of the bearing system is lower than expected.

10 Sudden Unbalance Response Testing

An important check is how the bearing system reacts in case a sudden unbalance occurs when the compressor is rotating at full speed. For this test the dummy impeller is used again with two unbalance weights, such that the rotor as a whole is perfectly balanced. Then at full speed the unbalance weight is removed.

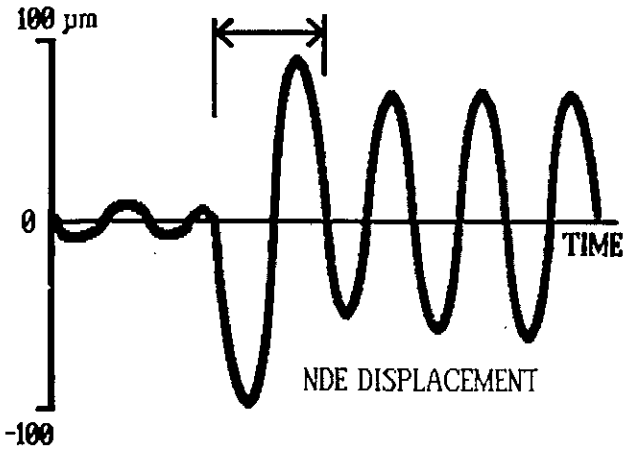

Figure 11 - Sudden Unbalance Response Test

Figure 11 shows that there is an instantaneous reaction of the bearing system on the sudden change in unbalance and it is practically demonstrated that the system can handle this situation with just a small overshoot and then come to the stable condition, within one revolution (1/50th of a second).

11 Auxiliary Bearings Non-Rotating Testing

The auxiliary bearings should not rotate when the compressor is in normal operation. To check this the end cap of the bearing bracket at the drive end side was removed. The video pictures taken, prove that the auxiliary bearing is not windmilling.

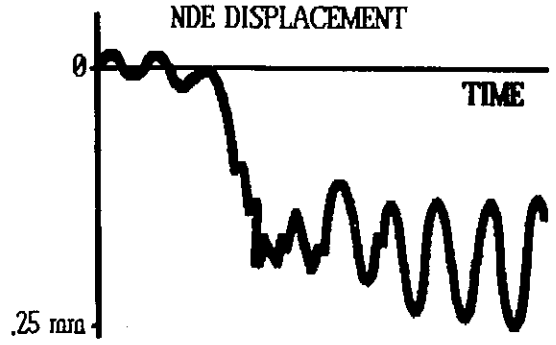

Figure 12 - Rotor Landing under Actual Load

12 Rotor Landing Under Axial Load

In general auxiliary bearings should never operate. The first line of protection is the battery back-up which allows five minutes of continuous operation without electrical power supply to the cabinet. Only if the cable between cabinet and compressor should fail, then the auxiliary bearings will safely bring the rotor to standstill. Further it is of interest to check if the auxiliary bearings can withstand one or more landings. Figure 12 shows the NDE bearing with the auxiliary bearing engaged. Due to the overhung rotor, the radial load on the DE bearing is very low. The reading of the DE bearing, figure 13, shows therefore a different behavior, which means that the rotor does not drop to its lowest position, but circulates in the full space available within the auxiliary bearing. After the landings, the bearings have been removed and extensively examined and show no signs of wear, deformation or cracks.

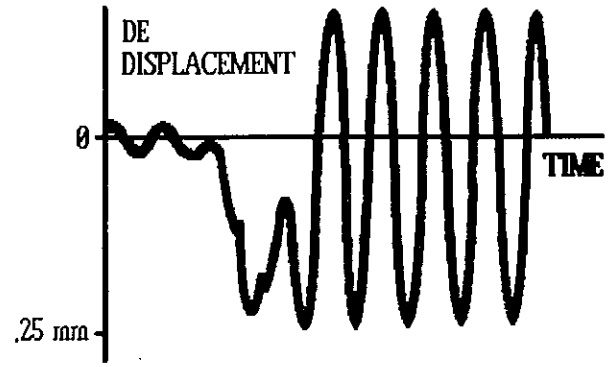

Figure 13 - Rotor Landing under Actual Load

13 System Temperature Sensitivity Testing

The heat developed by the magnets in the bearing cartridge is so low that the winding temperature without additional cooling does not exceed 60 degrees Celsius.

14 Faulty Magnet Tests

During one of the landing tests a landing has been initiated by simulating a faulty magnet. The result of this test is identical to the other landing tests.

15 Battery Capacity Test

To check the battery, the electrical supply from the control cabinet has been disconnected, whilst the compressor is in operation. The battery took over the

duty without any negative effect and continued to operate for seven minutes whilst the supply voltage from the battery dropped from 110 to 106 V, thus exceeding the specified capacity by two minutes.

CONCLUSION

The results of the extensive test program on this DRY-DRY PV, as shown above, prove that active magnetic bearings combined with dry gas seals are eminently suitable for arduous continuous process duties.

We foresee that dry seal and dry bearing technology will become accepted in general practice in the near future. It will enable the centrifugal compressor designer to simplify construction, improve reliability, safety and maintainability, reduce weight and space for both onshore and offshore applications and provide an environmentally friendly concept.